

REVISTA **Processos
Químicos**

Revista Científica da Faculdade de
Tecnologia SENAI Roberto Mange

Ano 9
n° 18
Jul/Dez
2015

www.rpqsenai.org.br

Simpósio Brasileiro de Química Teórica

SBQT

2 0 1 5

ISSN 1981-8521

REVISTA **Processos Químicos**

Revista Científica da Faculdade de
Tecnologia SENAI Roberto Mange



Goiânia, v.9, n.18, ano 9, jul/dez 2015.

Edição Especial XVIII SBQT

Pedro Alves de Oliveira

Presidente do Conselho Regional do SENAI

Paulo Vargas

Diretor Regional do SENAI

Ivone Maria Elias Moreyra

Diretora de Educação e Tecnologia

Jorge Quirino Pereira Sobrinho

Gerente de Educação Profissional

Aroldo dos Reis Nogueira

Diretor da Faculdade de Tecnologia SENAI Roberto Mange

Wilson de Paula e Silva

Gerente de Educação e Tecnologia

Joana Darc Silva Borges

Coordenadora da Área de Química

Corpo Editorial

Ademir João Camargo

Anselmo Eucana de Oliveira

Carlito Lariucci

Eurípedes de Almeida Ribeiro Júnior

Gilberto Lúcio Benedito Aquino

Guilherme Roberto de Oliveira

Hamilton Barbosa Napolitano

Kleber Carlos Mundim

Maria Assima Bittar Gonçalves

Roberta Signini

Solemar Silva Oliveira

Valter Henrique Carvalho Silva

Revista Processos Químicos / SENAI.

Departamento Regional de Goiás - v.9,
n.18 (jul/dez 2015). Goiânia: SENAI/
DR. Gerência de Educação Profissional /
Faculdade de Tecnologia SENAI Roberto
Mange, 2015.
v.: il.

Semestral

Núcleo de Material Didático da Gerência
de Educação Profissional do SENAI/DR/GO
Capa e Diagramação: Juliano Rodrigues
Revisão Linguística: Fernanda Marques

ISSN 1981-8521

1. Educação Profissional - Periódicos. 2.
Processos Químicos.

I. SENAI. Departamento Regional de
Goiás

CDD - 540

Tiragem: 1.500 exemplares

Faculdade de Tecnologia SENAI Roberto Mange
Av. Engenheiro Roberto Mange, nº 239
Bairro Jundiá - CEP 75113-630 - Anápolis-GO
Fone: (62) 3902-6200 - Fax: (62) 3902-6226
e-mail: revistapq.senai@sistemapq.org.br

ARTIGOS GERAIS

- 13 **Classic Study on the Growth of Metal Clusters Al_xNaN-x ($3 \leq N \leq 55$) Using Genetic Algorithms Modeled by the Gupta Potential**
Acassio R. Santos, Breno R. L. Galvão, Caio L. Firmea, Fabrício de L. Fariasa & Jadson C. Belchior
- 23 **PEDOT Chain Length and Excitation Energy Dependence From Time-Dependent Density Functional Theory**
Ageo M. de Andrade, Luis H. Lacerda, Renan A. P. Ribeiro, Sergio R. de Lazaro & Alexandre C. Junior
- 29 **Zn-doped BaTiO₃ Materials: A DFT Investigation for Optoelectronic and Ferroelectric Properties Improvement**
Luis H. S. Lacerda, Renan A. P. Ribeiro, Ageo M. Andrade, Alexandre C. Jr. & Sérgio R. Lazaro
- 36 **Structural Determination of Complex Natural Products by Quantum Mechanical Calculations of ¹³C NMR Chemical Shifts: Development of a Parameterized Protocol for Terpenes**
Ana Carolina F. Albuquerque, Daniel J. Ribeiro & Mauro B. Amorim
- 40 **Virtual HTS and Free Energy Calculation of Brazilian Natural Compounds Using OOMT as Pharmacological Targets Database**
Ana Paula Carregal, Flávia V. Maciel, Juliano B. Carregal & Alex G. Taranto
- 45 **Dispersion-Corrected Density Functional for the Correct Description on Regioselectivity Trends in Heck-Mizoroki Reaction Catalyzed by Anionic (N-Heterocycle Carbene)-Palladium Complexes**
Vitor H. M. Silva, Oscar Navarro & Ataulpa A. C. Braga
- 50 **Experimental and Theoretical Infrared Study of Homogalacturonans in the Psidium Myrtoides – *Nothotrioza Myrtoidis* System**
Renê G. S. Carneiro, Rosy M. S. Isaias, Bárbara D. L. Ferreira, Breno R. L. Galvão, Cláudio L. Donnici & Rita C. O. Sebastião
- 53 **Estudo Eletrônico dos Processos de Redução de Complexos de Pt(IV) à Pt(II).**
Bruna L. Silva & Juliana F. Lopes
- 57 **Structural Dependence of Photochromism in MEH-PPV Solutions**
C.E. Magalhães, R. M. L. Savedra, K. S. Dias, R. Ramos & M.F. Siqueira
- 60 **Accurate Multireference Electronic Structure Calculations on the Si₃ Molecule**
C. E. M. Gonçalves, B. R. L. Galvão & J. P. Braga
- 63 **Estudo das Interações dos Modelos da Proteína ATP7A no Mecanismo de Resistência à Cisplatina**
Christina T. Borges, Guilherme F. Lima & Juliana F. Lopes
- 66 **Investigation of the Pseudopotential Stuttgart/Dresden in the G3(MP2,CSSD,rel) Theory for Compounds Containing Transition Elements**
Cleuton S. Silva & Rogério Custodio
- 68 **QM/MM (ONIOM) Calculation on FAK/Dasatinib Docking**
Daniel Augusto Barra de Oliveira & João Batista Lopes Martins

- 73** **Evaluation of the Photophysics of Four Ru(II) Phthalocyanine/TiO₂ (Anatase) Complexes Using DFT Methods**
D. M. S. Araújo, L. T. Ueno, A. O. T. Patrocinio & A. E. H. Machado
- 78** **Estudo Teórico de Propriedades Geométricas e Eletrônicas da Nimesulida no Vácuo Utilizando Dinâmica Molecular de Car-Parrinello**
Eduardo C. Vaz, Ademir J. Camargo & Solemar S. Oliveira
- 81** **Planejamento Fatorial para a Investigação das Propriedades Espectroscópicas, Efeitos Relativísticos e de Solvatação de Derivados Halogenados da 2-Amino-1,4-Naftoquinona**
Eduardo P. Rocha, Livia C. T. Lacerda, Mateus A. Gonçalves, Máira S. Pires, Telles C. Silva, Henrique A. Rodrigues & Teodorico C. Ramalho
- 88** **Investigação Teórica de Adições Aldólicas de Monocarbonilas e β -Dicarbonilas Catalisadas**
Ellen V. D'Alessandro & Josefredo R. Pliego Jr.
- 91** **An improved Method of ¹³C NMR Chemical Shift by GIAO-DFT Calculations in the Study of a Synthetic Prenylated Chalcone**
Fabio L. P. Costa & Gunar V. S. Mota
- 94** **Modeling Polymer/Fullerene Heterojunctions: a Case Study for the Interfaces PTPD3T/PCBM and PBTI3T/PCBM**
Rodrigo M. D. Ledo, Luciano A. Leal, Luiz A. R. Juniora & Antônio L. A. Fonseca
- 97** **Impact of Coulomb Interactions on The Exciton Dissociation in Polymer Heterojunctions**
Gesiel G. Silva, Luiz A. R. Junior & Antonio L. A. Fonseca
- 101** **An Experimental Spectroscopic and Theoretic Study of Acetylberginin**
Gisele F. de Castro, Diego dos S. Freitas, Alberto S Marques & YujiTakahata.
- 106** **Theoretical Evidence to Cis Folding in PhoR Histidine Kinase of Corynebacterium Pseudotuberculosis**
Gleiciane L. Moraes, Guelber Cardoso, Cláudio N. Alves & Jerônimo Lameira
- 111** **Fully Anharmonic Resonance Raman Spectrum of Diatomic Molecules Through Numerical Solution of the Vibrational Schrodinger Equation**
Gustavo J. Costa, Rogério Custodio, Pedro A. M. Vazquez & Luciano N. Vidal
- 114** **Analysis of Titanium Dioxide Nanotubes, Rutile (110) and Anatase (101)**
G.O. Silva, J.D. Santos, J.B.L. Martins, C.A.Taft & E. Longo
- 118** **Proposal of Calculation Protocols for Implicit Solvation Methods in Conformational Analysis Involving the Gauche Effect**
Filipe B. de Lima, Carlos R. M. Cavalcante, Keyla M. N. de Souza, Juliana A. B. da Silva & Hélcio J. Batista
- 122** **A Theoretical Kinetic and Thermodynamics Study about the Effect of Substituents in the Synthesis of Chalcones**
H. G. Machado, H. C. B. Oliveira, G. R. Oliveira, W. A. Silva & V. H. Carvalho
- 125** **Electronic Spectra of Nitrosyl Chloride: A Reinvestigation Using Coupled Cluster and DFT Calculations**
Iran da Luz Sousa, Pedro A. M. Vazquez & Nelson H. Morgon

128 Construction of Brn2 Protein in Complex with MORE DNA Through In Silico Methods

Ivan E. V. Coelho, Denise C. A. & Alex G. Taranto

133 Estudo QTAIM/NBO das Interações Estabilizante do Empacotamento do (E)-1,1,1-Tricloro-5, 5-Difenil-4-Metoxipent-3-en-2-ona (CL3ONA)

José A. S. de Freitas, Mariano A. Pereira, Alex F. C. Flores, Davi A. C. Ferreira & Tatiane L. Balliano

136 Adsorption of Atoms on Cubic -MoC (001) Surface

José R. S. Politi & Alanna P. C. Dantas

139 Synthetic Routes of the Fundamental Building Blocks of Life: Computational Study of The Reaction Free Energy

Kelson M. T. Oliveira & Elaine Harada

144 Conformational Analysis, MC Simulation, Experimental and GIAO-DFT ¹³C NMR Calculation on 2'-Hydroxy-3,4,5-Trimethoxy-Chalcone

Leandro O. Duarte, Paulo G. Freitas, Andressa K. Silva, Luciano M. Lião & Fabio L. P. Costa

147 Proposta para o Cálculo do Coeficiente de Partição Gás/Aerossol de Compostos Orgânicos Voláteis Utilizando Métodos DFT Associados ao Modelo IEFPCM

Leonardo Baptista & Lillian L. Castilho

150 Análise termodinâmica e cinética de reações de mecanismo de ação para Compostos de Platina (II) Análogos a cisplatina com ligantes derivados de terpenos.

Lucas C. Santana & Juliana F. Lopes

154 Multiple Hartree-Fock Solutions of Systems Constituted with First Line Atoms: BH and FH molecules using the Double Zeta Base.

L. A. C. Malbouisson, A. M. de C. Sobrinho & M. D. de Andrade

157 The Confined Helium Atom in Hyperspherical Coordinates

M. N. Guimarães & F. V. Prudente

160 Quasiperiodic CH₂/SiH₂ Molecular Nanowires

David L. Azevedo, M.S. Vasconcelos, Marco A. de Andrade, Kleber A. T. da Silva, Fábio F. Monteiro & Antonio L. A. Fonseca

163 A Theoretical Study of CCD4a Dioxygenase of Citrus, a Cleavage Enzyme of Carotenoids in Plants.

Mauricio Vega-Tejido, Margot P. Zunini, Carolina López & Maria J. Rodrigo

166 Solving the Schrödinger equation using anharmonic potentials and a variational quantum Monte Carlo method

Maurício G. Rodrigues, Régis C. Leal & Rogério Custodio

170 Estudo de Acoplamento Molecular e NBO das interações entre a molécula 5-FU e o alvo biológico HER-2

Michell O. Almeida, Daiane A. S. Barros, Sheila C. Araújo, Sergio H. D. M. Faria & Kathia Maria Honório

173 Effect of the Methyl Group on the Stability and Twisting of Flavonoids

Milene A. R. de Oliveira, Keylla U. Bicalho & João B. Fernandes

177 Aspectos Moleculares da Solvatação do Íon Fluoreto em Água e DMSO

Natália M. Silva & Josefredo R. Pliego Jr.

- 180** **Glucose-6-Phosphate Dehydrogenase as Potential and Selective Target Against Malaria**
Nelson A. N. de Alencara, Jordi Jimenez Juarez, Jeronimo Lameira Silva & Javier Luque Garriga.
- 183** **Modelagem do Equilíbrio de Fases do Pentano e da Mistura de Pentano e CO₂**
Patrícia B. Gusmão, Leonardo Baptista & Márcio Paredes
- 186** **Cooperativity Effects on the Hydrogen Bonds Within HCN and HNC Complexes**
Paulo M. C. de Oliveira, Juliana A. B. Silva & Ricardo L. Longo
- 190** **Application of the G3(MP2)-CEP Theory in Understanding Diels-Alder Mechanism**
Régis C. Leal, Douglas H. Pereira & Rogério Custodio
- 195** **Interplay Between Interatomic Distance and Orbital Overlap at Control of Magnetism in FeBO₃ (B = Ti, Ge, Zr, Sn) ilmenites**
Renan A. P. Ribeiro, Ageo M. de Andrade, Luis H. S. Lacerda, Alexandre C. Jr. & Sergio R. de Lázaro
- 202** **Success Case of the Application of Virtual High Throughput Screening Against Molecular Antimalarial Targets**
Renata R. Nunes, Rafael C. R. Chagas, Fernando P. Varotti & Alex G. Taranto
- 207** **Theoretical Quantum Study of the Molecular System XLi₂, with X=D,T, and Mu**
Ricardo Gargano, Thiago F. da Cunha, Henrique V. R. Vila, Wiliam F. da Cunha, Luciano A. Leal & Geraldo M. e Silva
- 209** **Angular Momentum Coupling and Discrete Quantum Mechanics: the 10-Spin Network, the Pentagonal Relationship, an Eigenvalue Equation and Semiclassical Limits**
Robenilson F. dos Santos, Mirco Ragni, Ana Carla P. Bitencourt, Frederico V. Prudente & Vincenzo Aquilanti
- 213** **Cálculo da Segunda Hiperpolarizabilidade da L-arginina Fosfatada Monohidratada Considerando o Efeito do Ambiente Cristalino**
Rosemberg Fortes Nunes Rodrigues, Clodoaldo Valverde, Basílio Baseia & Heibbe C. B. de Oliveira
- 216** **The Charge Carrier Density Influence and Thermal Effects on Charge transport in Organic Semiconductors.**
Sara Santiago de Brito, Wiliam Ferreira da Cunha, Demétrio Antônio da Silva Filho & Pedro Henrique de Oliveira Neto.
- 219** **Estudo Termodinâmico e Cinético da Formação de Modelos Químicos derivados de Adamantano para a Interação com Ciclodextrinas**
Selma F. Bazan, Clara H. S. Braga, Frederico B. de Sousa & Juliana F. Lopes
- 223** **N-Deethylation Process of Rhodamine B in Aluminum Polyphosphate Gel: Theoretical and Experimental Study.**
Sheila C.S. Costa, Paula A. Jaramillo, Rodrigo J. Oliveira & Marcos S. Amaral.
- 226** **Deformed Transition State Theory: Inclusion of the Tunneling Effect by Euler Exponential, Limit of Validity and Description of Bimolecular Reactions**
V. H. Carvalho, V. Aquilanti, H. C. B. Oliveira & K.C. Mundim
- 229** **Inverse Virtual Screening of Bradyoxetin and a Synthetic Intermediate using OOMD as a Source Database**
Vanildo M. L. Braga & Alex Taranto

- 234** **Conjugation and Hyperconjugation Effects: Comparative Studies Through Localized Molecular Orbitals Energy Decomposition Analysis (LMO-EDA) and Natural Bond Orbitals (NBO)**
V. A. V. Ferreira, V. G. do Nascimento & M. B. de Amorim
- 240** **Unconventional Channel of Atmospheric Reaction $\text{NO} + \text{O}_3 \rightarrow \text{NO}_2 + \text{O}_2$: A Mechanistic Study Using Born-Oppenheimer Molecular Dynamics**
Yago S. de Sousa; Ademir J. Camargo; Heibbe C. Oliveira & Valter H. Carvalho
- 243** **Theoretical Study of the Mechanism and Rate Constant Calculations of the Reaction of Carbon Monoxide with Ethylene.**
Washington B. Silva & Alessandra F. Albernaz
- 247** **Anacardic Acid Derivatives as Potential Acetylcholinesterase Inhibitors**
A. S. Kiametis, M. Abreu, R. Gargano & L. A. S. Romeiro
- 250** **The NH_2^+ and Be^{2+} Vibrational Spectroscopic Constants From use of the New Analytical Potential Energy Function**
Ana Paula de Oliveira, Valter Henrique Carvalho Silva, Kleber C. Mundim, Ricardo Gargano, Heibbe Cristhian B. de Oliveira & Luciano Ribeiro
- 254** **Width Influence on the Polaron Dynamics in Graphene Nanoribbons**
Ana V. P. Abreu, Luiz A. R. Junior, Antonio L. A. Fonseca
- 258** **Parameterization Study of LRC Functional Applied to Optical Properties of Carotenoids**
Andriele S. Prado, Luiz A. R. Júnior & Wiliam F. da Cunha
- 263** **Theoretical Characterization of the Resonance-Energy Transfer Between Organic Molecules**
Demétrio A. S. Filho
- 265** **Evaluation of the Best Theoretic Approach DFT Based for Indirect Spin-Spin Coupling Constants of 3-Ishwarone**
Eduardo da Conceição & Mauro B. de Amorim
- 267** **$\text{H}_2\text{O}_2 + \text{Ng}$ Excited Electronic State Description**
Luciano Almeida Leal, Jonathan Teixeira, Luiz Fernando Roncaratti, Geraldo Magela e Silva & Ricardo Gargano
- 269** **Cálculo do fator de Debye-Waller na Níquel-Fluorohectorita por EXAFS**
Matheus N. Jácome & Luciano Ribeiro
- 271** **Theoretical Study of Thermodynamic Properties of Liquid Methyl Tert-Butyl Ether (MTBE) Using Ab Initio Calculations and Monte Carlo Simulation**
Luciene B. Silva & Luiz C. G. Freitas
- 274** **Zn-doped BaTiO_3 Materials: A DFT Investigation for Optoelectronic and Ferroelectric Properties Improvement**
Luis H. S. Lacerda, Renan A. P. Ribeiro, Ageo M. de Andrade & Sérgio R. de Lazaro
- 281** **Polaron Dynamics in Organic Molecular Stacks**
Luiz A. R. Júnior
- 285** **Desenvolvimento de Ferramenta para a Inserção com Baixa Perturbação de Proteínas de Membrana em Bicamadas Lipídicas para Simulações de Dinâmica Molecular**
Luiz F. C. Zonetti & Alexandre S. Araújo

- 291 **Analysis of Aluminium-Magnesium Alloy Clusters Through Genetic Algorithm**
Mateus A. M. Paiva & Breno R. L. Galvão
- 295 **Parametrização de Campo de Força e Estudo Teórico do Comportamento Estrutural e Eletrônico de FAD e TPP – cofatores da enzima AHAS.**
Renan F. Guerra & Eduardo F. Franca
- 298 **Stretching-Dependent Thermoelectric Properties of a BDT Single-Molecule Junction**
Renato B. Pontes, Alberto Torres, Antônio J. R. da Silva & Adalberto Fazio
- 301 **Molecular Modeling and Computer Simulation involving the Encapsulation of β -carotene in Boron Nitride Nanotubes**
Charles de A. O. Rocha, David L. Azevedo, Fábio F. Monteiro & Antonio L. de A. Fonseca

OPINIÃO

- 304 **Development of a Transition State Database from Chemical Reactions**
F. O. S. Neto & V. H. Carvalho

Apresentação

O Simpósio Brasileiro de Química Teórica (SBQT), na sua XVIII edição em 2015, completa 34 anos. O sucesso verificado nos encontros anteriores avaliza o fato de que esse evento se torna progressivamente a maior instância, nacional e latino americana, de expressão da comunidade de Química Teórica. Este sucesso alcançado pelo SBQT reside no fato dele permitir a articulação dos grupos de pesquisa em Física, Química e áreas Biológicas direcionando e otimizando os esforços para o desenvolvimento de métodos teóricos e computacionais de interesse comum e para a utilização e aprimoramento de técnicas experimentais existentes no país. Atualmente, a Química Teórica no Brasil engloba contribuições de diversas áreas específicas tais como Química Quântica, Dinâmica Atômica e Molecular, Simulação Computacional de Sistemas Líquidos e Sólidos, Modelagem Molecular de Sistemas de Interesse Biológico e Tecnológico, Catálise Química, Físico-Química Orgânica, entre outras. Nesse contexto, são inegáveis as contribuições do SBQT para o desenvolvimento da área no país.

A tecnologia e a inovação tecnológica exercem um papel importante e fundamental na vida das pessoas e na economia dos países. Seria inconcebível pensarmos o desenvolvimento do mundo contemporâneo sem a presença da tecnologia e dos seus impactos. Importantes instituições, como o Conselho Econômico e Social das Nações Unidas, têm discutido Ciência, Tecnologia e Inovação e seus impactos na economia do século 21. No Brasil, várias ações, envolvendo diversas instituições, têm sido realizadas nesta direção. Dentre elas, destacam-se o Plano Brasil Maior do Ministério do Desenvolvimento, Indústria e Comércio Exterior e a criação da Empresa Brasileira de Pesquisa e Inovação Industrial (Embrapii). A Revista Processos Químicos do Serviço Nacional de Aprendizagem Industrial (SENAI), comprometida com a inovação e a transferência de tecnologias industriais, edita esse volume especial dedicado ao SBQT, considerando a ampla contribuição que a Química Teórica tem dado à tecnologia e à inovação tecnológica, e portanto ao fortalecimento da competitividade da indústria brasileira.

Kleber C. Mundim
Hamilton B. Napolitano

Editores da Revista Processos Químicos

Classic Study on the Growth of Metal Clusters $\text{Al}_x\text{Na}_{N-x}$ ($3 \leq N \leq 55$) Using Genetic Algorithms Modeled by the Gupta Potential

Acassio R. Santos, Breno R. L. Galvão, Caio L. Firmea, Fabrício de L. Fariasa & Jadson C. Belchiorb

Introduction

As a new area of research, nanoscience has been in development since the 1980s. Its main scope is the study of nanoscopic phenomena ($1\text{nm} = 10^{-9}\text{m}$), where clusters refer to a new type of materials (nanoparticles), in the order of 2 to $10n$ ($n = 6$ or 7) atoms or molecules. These particles may be identical or related to two or more distinct species: monoatomic and monomolecular clusters, polyatomic and/or polymolecular clusters, or molecular clusters. Clusters consisting of a small amount of atoms (2 - 1000 atoms) are denominated nanoclusters. Such systems are adequate models of researching by the means of theoretical methodologies, as they have a smaller number of particles. On the other hand, they may present difficulties regarding experimental studies, such as structural determination.¹

Theoretical studies concerning clusters are relevant and contribute to the interpretation of experimental measures. Among these studies, we may find those that determine the structures of atomic and/or molecular clusters, possibly using mathematical tools related to spatial geometry applied according to theoretical models. Besides, the quantitative study of potential energy provides us with the basis for the understanding of chemical and physical phenomena of atomic and molecular clusters.²

Particularly, the determination of isomers of greater cluster stability has ample relevance to the development of new materials, where the more stable structure of cluster corresponds to that of lower energy. In order to

determine the cluster structure and energies, one should calculate the conformation of lower energy on the potential energy surface (PES), i. e. the global minimum (GM). Generally, the determination of a minimum is considered an optimization problem. The sheer number of isomers with diverse structures constitute one of the chief difficulties in the determination of the GM in PESs, where it may be verified that there is an almost exponential growth in the number of minimum structures related to the number of particles, i. e., the system size^{3,4}. Therefore, optimization methods have been developed in order to contribute to the above-mentioned difficulties, whether they are biased or non-biased. The former utilize chemical or physical information regarding the material and initial conditions such as starting geometry, whilst the latter, in contrast, does not use previous information, and the initial geometry is instead defined at random and thus optimized until a minimum of lower energy is found.

This current study proposes the application of non-biased methods, since they may reduce the occurrence of problems such as the determination of local minima, which are recurring in other methods due to the imposition of certain types of geometries or of a PES region. The non-biased methods of optimization have two instruments that may be considered the most effective overall: 1) the exhaustive utilization of local minimization, and 2) the discovered structures of local minima, used as initial conditions to the comparison and selection of new structures to be minimized. Among

these methods, the Basin-Hopping^{5,6} and the Genetic Algorithm (GA)⁷ have been the most promising^{5, 6, 8, 9}, incorporating the two above-mentioned instruments. Within this work, we will focus on the applications of GA in the research of nanoalloys of Al and Na. In traditional non-biased methods, such as the Monte Carlo and the Molecular Dynamics Simulated Annealing approaches, the difficulties on finding the global minima (GMs) remain^{10, 11}.

The interest in the research of metal clusters arises mostly from the possibility of creating new alloys from materials in nanoscale, the so-called “nanoalloys”. The theoretical research of nanoalloys has an important role in materials science, and some of its most relevant objectives are: the prediction of stability in structures, their growth, and assistance in the interpretation of spectroscopic and other experimental measures. In this context, it should be highlighted that a great number of methods were reported in the last few years regarding the effective global optimization of atomic and molecular systems.

Methodology

Inspired by Darwin's theory of evolution by natural selection, the genetic algorithms (GA) concern the field of artificial intelligence, and, more specifically, evolutionary computation. It consists in a technique that solves a problem by using an evolutionary process where the surviving solution is, consequently, the best adapted, i. e., developed.

We may compare the GA method with the cells of a living organism – DNA blocks – located in specific positions and components of the same group of chromosomes. These blocks codify certain proteins as well as a given feature of the organism, such as skin color. The parental gene pool crossover is to combine during the reproductive process, resulting in a new chromosome that may mutate due to alterations in the DNA, which are usually caused by some factors such as failure in the copies from the parental gene pool. Biologically formed, the offspring adapts or not to its environment, where survival is a measure to its adaptation¹². The mathematical modeling of this analogy consists in the application of the GA technique to the resolution of a problem by searching

a solution that may come up among a variety of other possible solutions and be considered the best option, according to the marking of possible solutions in conformity with its adequacy to the intended answer. In this context, the GA have often been employed in the determination of maxima to the adequacy values regarding the potential energy surfaces associated to the cluster structure^{13,14}. Once the GA standard method is applied, the use of evolutionary genetic operators (OP) becomes quite common, bearing resemblance to the crossover operators among individuals (also known as the mating operator), as well as to the Mutation and Natural Selection operators, used towards a test population with the purpose of optimizing, for instance, the cluster structure. The determination of the best-adapted individuals depends on the “quality” assessment, i. e., on the adequacy of each individual that contributes to the system. In the GA model, such assessment is obtained according to the Fitness Function (FF)¹⁵ that, in the context of the clusters, is used to assess the respective energies.

The solutions found in the use of the observed technique (GA) are usually considered adequate, since it is not always possible to find or prove which solution is optimal. The GA used in this research has two other evolutionary operators that distinguish them from the standard GA: the Annihilator (AN) and the History (H)^{16,17}.

Considering the composition and size of the cluster (total amount of atoms), its population is generated at random, given that the spatial coordinates from each atom in each cluster are generated at random inside a search space previously defined. After this stage, the GA method uses a list of atomic Cartesian coordinates from each cluster, with the purpose of generating their respective genes, which evolve to the next generation by the application of genetic evolutionary operators from the standard method of Crossover, Mutation and Natural Selection. In this context, the genetic operators are applied to the current population, immediately after each individual of this population is relocated to its nearest local minimum according to the quasi-Newtonian standard method (BFGS)¹⁸.

In the current research, the parental individuals are chosen to the application of the Crossover OP through

the roulette-wheel selection method. Therefore, the probability of a choice depends on the adequacy of the individual. Once this process occurs, the use of the Mutation OP may or may not be put into effect, considering that this operator is slow and less frequent, so that its application may occur strictly to a fraction of a population from each generation. This does in no way differ from the GA standard method, and yet, in the Mutation OP, the AN removes both offspring individuals and mutants yielding the same energy when compared to already existent individuals from the same generation, while H “memorizes” information concerning the population of that generation for a next use. Hence, the remaining individuals are classified in a list and arranged according to their FF values, where the last-placed in the list are discarded, so it may persist with a constant number of clusters within the population (Natural Selection)¹⁹.

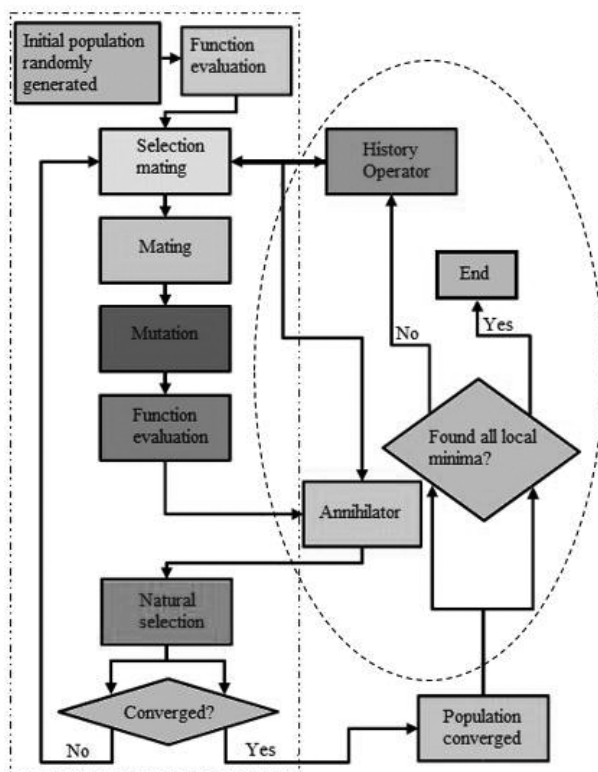


Figure 1: Flow chart indicating the operation of the GA used in this research. The traced box on the left corresponds to the operators of the standard method, while the traced ellipsis to the right indicates the new operators.

The described procedure is a loop from the standard GA (except for a minor interference of AN and H) and is repeated in a determined number of times until convergence, in which it is not possible to produce any more energy. To the GA, henceforth, the global minimum has been found. However, since it is a stochastic process, it is possible that the true global minimum may not be found. For this reason, the better improvement of the modified GA in this research lies in the realization of new cycles, starting from the point where the AN promotes a mass extinction of the system optimized by the standard method. In this case, the procedure reboots and the initial population is no longer generated at random, but provided by H. This new complete loop may now be repeated until, after a determined number of times, no isomer with energy lower than the last more stable obtained is found¹⁷.

Thus, considering the basic functioning of the GA, it is pointless to target a problem regarding clusters with overly strict ab initio treatments, such as the DFT method (Density Functional Theory), due to the great quantity of local minimizations that the optimization algorithm is supposed to perform. For this reason, an analytical description, experimentally parameterized to the potential energy among the atoms of the system (demanding much simpler computational requirements), is the most reasonable option. Expressions used in potential energy associated to a many-body system are denominated “empirical many-body potentials”, widely recognized for being capable of modeling in close approximation the bonds between metal atoms, as well as of reproducing accurately the thermodynamic and structural properties, mainly from most of the transition metals^{17,20}.

Currently, it is recognized that the empirical many-body potential energy expressions are capable of reproducing thermodynamic and structural properties of many transition metals with good accuracy, such as the energy of sublimation, the constant of network, elastic constants and vacancy formation energy^{21,22}. This is, to the date, one of the most practical manners of addressing simulations of punctual or extended defects, as much as interface or surface properties in metal alloys¹⁶. Thus, in the last few years, there has been frequent use

of empirical potentials towards the analysis of several problems, in the example of the materials science.

The empirical many-body potential energy expressions present a superior efficiency when compared to simpler potential expressions that only add contributions due to pair interaction, from which the latter is usually the most adequate in the reproduction of basic features of metal systems. This occurs because in the former it is included the essential feature of band regarding metal alloys²⁰. Such expressions concern the effect of each individual (j) from the system in reference to one of the components (i) of the same system, not inasmuch as it depends solely on the interaction of each pair (ij), but considering also the influence in which the neighbors, so far as to a certain distance from each individual in question (j), exert on the caused effect in the assessed component (i). We must highlight that all these contributions are added to all existent i and j in the system.

We have it that the Gupta potential belongs to a class of pair-functional potentials based on the Tight-Binding Second-Moment Model. The Gupta potential may be written in the manner of repulsive pairs V_r and term of many-body coupling V_m . The energy of a given atom i constituted by the interaction with all the neighboring atoms j is, accordingly:

$$V_{clus} = \sum_i^n (V_r(n) - V_m(n)) \quad 01$$

where V_r represents pair repulsion among metal ions, and is given by:

$$V_r(n) = \sum_i^n A \exp \left(-p \left(\frac{r_{ij}}{r_0} - 1 \right) \right) \quad 02$$

Subsequently, the many-body term, V_m , represents the cohesion of many bodies given by the valence band, i. e.,

$$V_m(n) = \left[\sum_i^n \zeta \exp \left(-2q \left(\frac{r_{ij}}{r_0} - 1 \right) \right) \right]^{\frac{1}{2}} \quad 03$$

The parameters A , p , r_0 , ζ e q are values obtained from adjustments in experimental data of the cohesion energy, parameters of network and elastic constants, independent of the crystalline structure at 0 K, not only to pure metals but also to alloys. The term r_{ij} is the distance between atoms i and j; the parameters q and p are dimensionless and determine the extent of the terms of band and repulsion, respectively; whereas A and ζ have energy units and establish the force of these terms. The term r_0 is the average distance to the atom's nearest neighbors in the bulk of the metal²³.

The parameters to homodiatomic interactions (Al-Al, Na-Na) within this research were obtained from the literature^{24,25}. Simple arithmetic means were used in order to address the heterodiatomic interactions (Al-Na)²³. In this context, the Gupta potential may be used to model an extensive diversity of solids and clusters, as well as of some alloys.

At Table 1 we present the values of the parameters used in this research.

Table 1: Empirical parameters of the Gupta potential to the system Al-Na

	r_0 (Å)	ζ (eV)	p	q	A (eV)
Al-Al	2,8637	1,316	8,612	2,516	0,1221
Na- Na	3,6989	0,2911	10,13	1,30	0,01596
Al-Na	3,2818	0,8035	9,371	1,90	0,06903

The average bond energy is an important quantity that may be associated to the clusters and defined as¹⁶:

$$E_b = \frac{-V_{clus}(N)}{N} \quad 04$$

The value of E_b must be asymptotically close to the value of the cohesion energy of the bulk related to the atoms that compose the cluster, in the case the clusters are relatively sizable¹⁶.

The second difference of average bond energy among clusters is also a useful quantity to the analyzed structures^{26,27}. Its calculation may be performed by the following equation:

$$\Delta_2 E_b(N) = 2E_b(N) - E_b(N-1) - E_b(N+1) \quad 05$$

Through this expression, it becomes possible to assess the energetic behavior of a cluster of N atoms in reference to its “neighbors”, i. e., a cluster of $N + 1$ and another of $N - 1$. Hence, we may observe stability peaks when $\Delta_2 E_b(N) > 0$ or instability when $\Delta_2 E_b(N) < 0$.¹⁶

In spite of being a useful quantity, the efficiency of the second energy difference may be, in some fashion, unreliable, since the stability comparison occurs only to the neighboring clusters. For instance: there might be cases where neighboring clusters may present a very high energetic instability, leading to the demonstration of a stability peak by the cluster of N atoms, not because the structure is stable, but otherwise, because the neighboring clusters were too unstable.

In order to analyze the alloy clusters, the excessive energy provides another useful quantity, which may give information regarding the likelihood of the alloy formation in relation to the formation of the corresponding pure cluster^{28,29}. In our approach, the excessive energy of an agglomeration of N atoms in a $\text{Al}_x\text{Na}_{N-x}$ alloy is given by:

$$E_{\text{exc}}(\text{Al}_x\text{BN}_{N-x}) = V_{\text{clus}}(\text{Al}_x\text{BN}_{N-x}) - x \frac{V_{\text{clus}}(\text{Al}_N)}{N} - (N-x) \frac{V_{\text{clus}}(\text{B}_N)}{N} \quad 06$$

Negative values to $E_{\text{exc}}(\text{Al}_x\text{BN}_{N-x})$ favor the formation of the corresponding nanoalloy. In this research, we performed the calculation of the excessive energy to all combinations of $\text{Al}_x\text{Na}_{N-x}$ where $3 \leq N \leq 55$.

Results and Discussions

The results obtained regarding the geometries of pure aluminum (Figure 2) and pure sodium (Figure 3) clusters were analogue, and agree with the literature^{25,30} concerning systems of this type, where, however, other methods were utilized to deal with the issue.

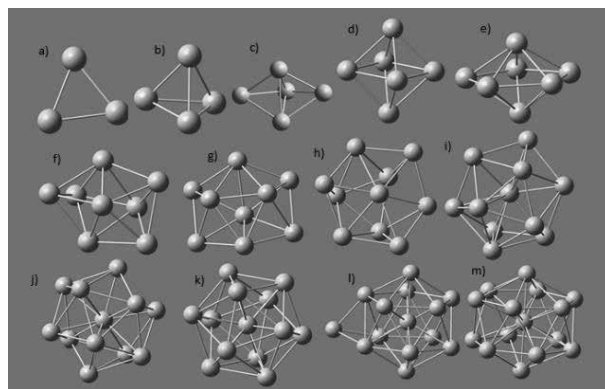


Figure 2: Structures obtained as global minima using the GA regarding pure Aluminum clusters from: a) Al_3 to m) Al_{15} .

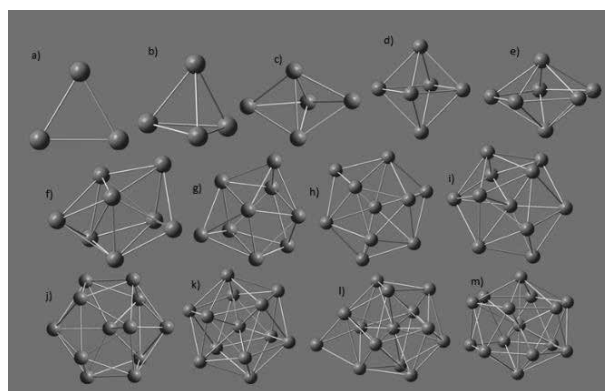


Figure 3: Structures obtained as global minima using the GA regarding pure Sodium clusters from: a) Na_3 to m) Na_{15} .

The pure aluminum structures present sturdier atom compaction if compared to those of sodium. This may be explained by the differences in the atomic radius between those two elements, which are reflected in the equilibrium of interatomic distances provided by the Gupta potential to distinguished atoms. We have verified that the structures of the pure Al clusters are quite similar to those of pure Na, whereas the most important difference occurs in the clusters of 9 and 11 atoms. We noticed that the dihedral angle in the sodium clusters is sharper when compared to the aluminum clusters. Once we compared the structures obtained by the GA using the many-body Gupta potential to the pure aluminum with recent results from the literature, such as those from

Kiohara et al. (2013)³¹, we verified that the Gupta potential, despite being a classic method, presented the cluster structure to the systems Al_2 , Al_3 , Al_6 , Al_8 and Al_9 with striking resemblance to those obtained via ab initio calculations, such as DFT and CCSD(T). Since we did not find aluminum doped with sodium clusters in the literature, we managed to provide a few assumptions and observations concerning the behavior of their structures from the analysis of pure sodium and pure aluminum clusters. The following figures present some results to the second energy difference of the clusters Al_xNa_y regarding different nuclearities.

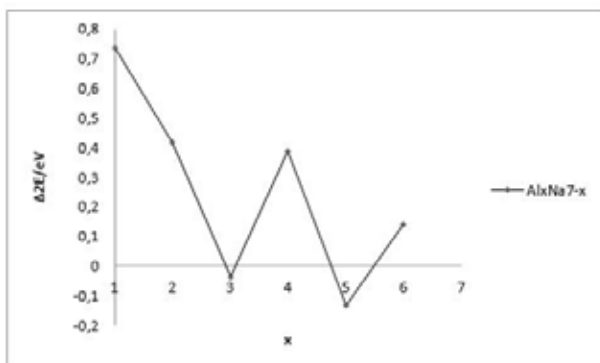


Figure 4: Second energy difference of the clusters aluminum-sodium of 7 atoms.

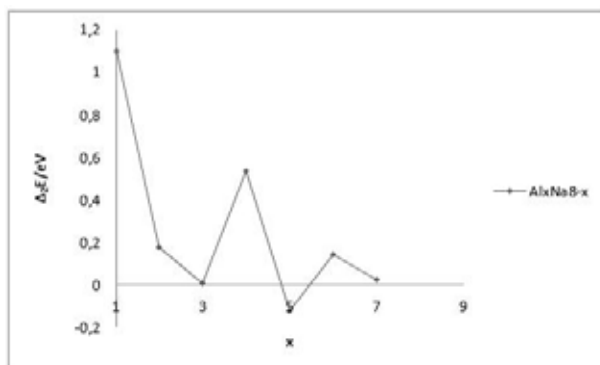


Figure 5: Second energy difference of the clusters aluminum-sodium of 8 atoms.

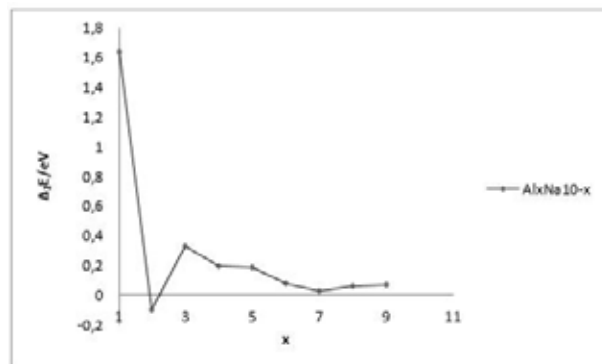


Figure 6: Second energy difference of the clusters aluminum-sodium of 10 atoms.

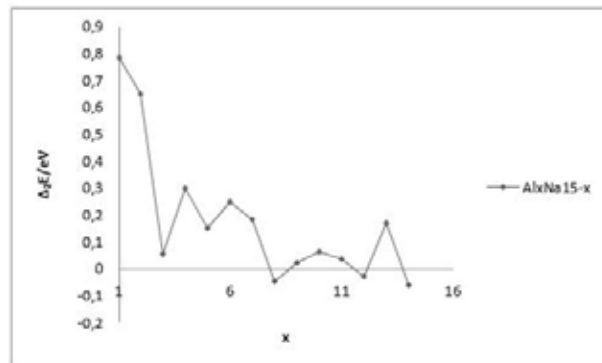


Figure 7: Second energy difference of the clusters aluminum-sodium of 15 atoms.

By performing an analysis of the second energy difference to the aluminum-sodium mixtures, we verified that higher stability peaks occurred with a value of $x=1$, i. e., when we had but a single atom of aluminum in the cluster structure. However, considering a more detailed analysis of the clusters in an alloy, the excessive energy may become a useful quantity, because it provides the likelihood of the bimetallic alloy formation, when compared to the pure corresponding cluster^{28,29}. Next, we present the results from the excessive energies (E_{exc}) concerning varying compositions of clusters of Al_xNa_{N-x} ($3 \leq N \leq 55$).

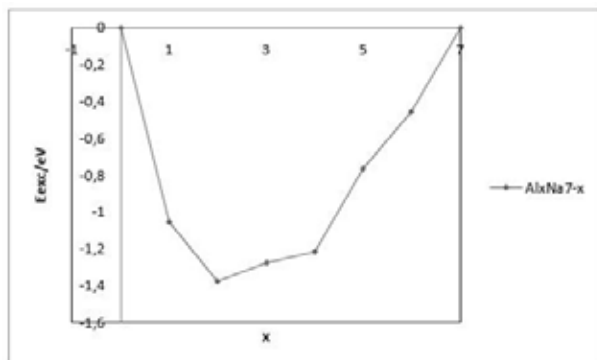


Figure 8: Excessive energy to aluminum-sodium clusters of 7 atoms.

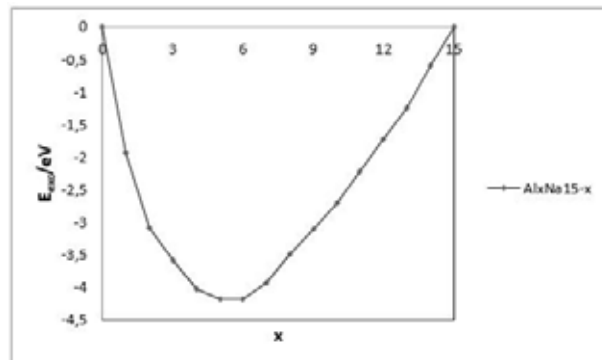


Figure 11: Excessive energy to aluminum-sodium clusters of 15 atoms.

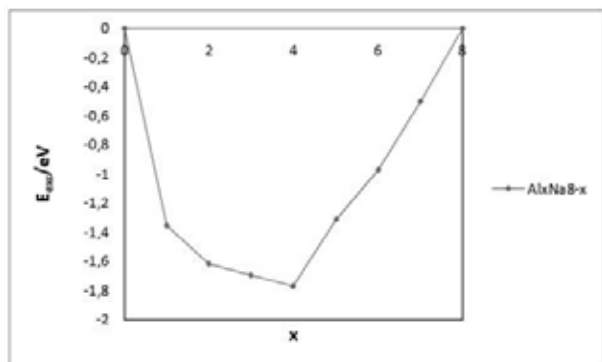


Figure 9: Excessive energy to aluminum-sodium clusters of 8 atoms.

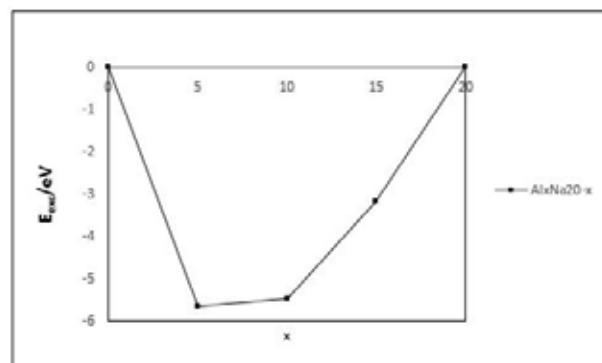


Figure 12: Excessive energy to aluminum-sodium clusters of 20 atoms.

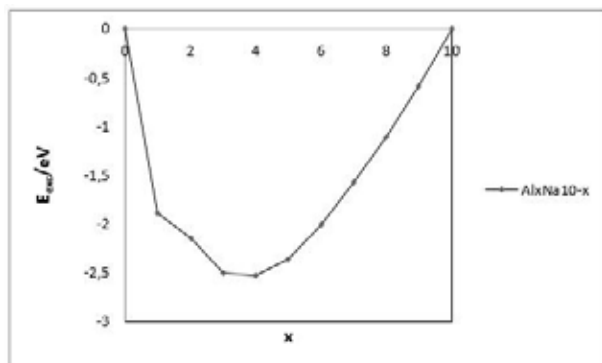


Figure 10: Excessive energy to aluminum-sodium clusters of 10 atoms.

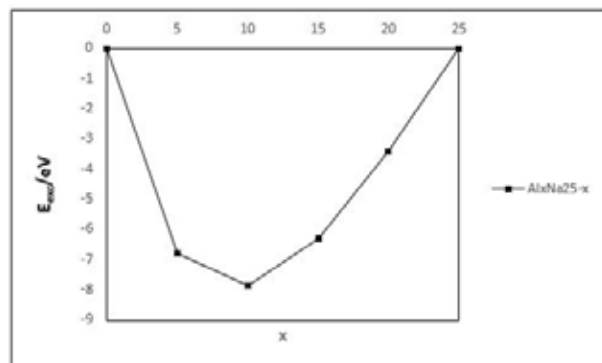


Figure 13: Excessive energy to aluminum-sodium clusters of 25 atoms.

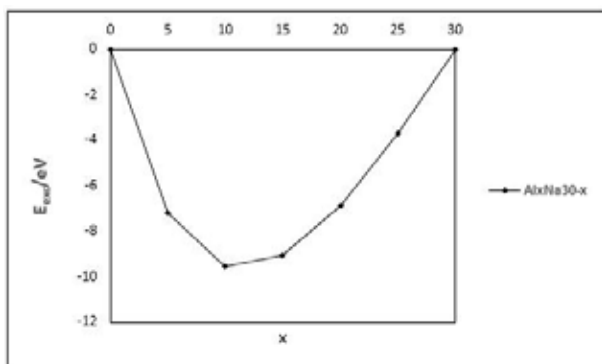


Figure 14: Excessive energy to aluminum-sodium clusters of 30 atoms.

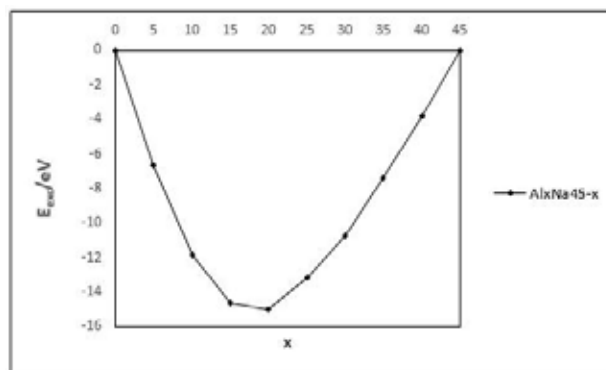


Figure 17: Excessive energy to aluminum-sodium clusters of 45 atoms.

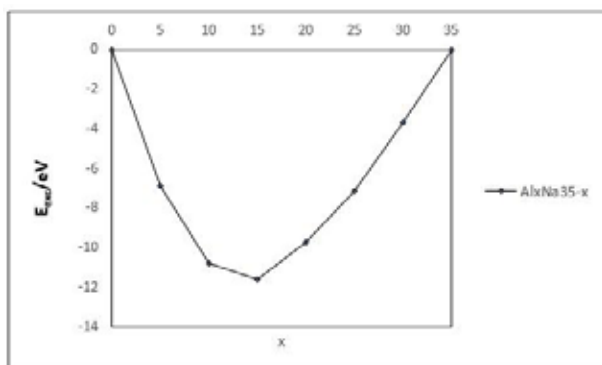


Figure 15: Excessive energy to aluminum-sodium clusters of 35 atoms.

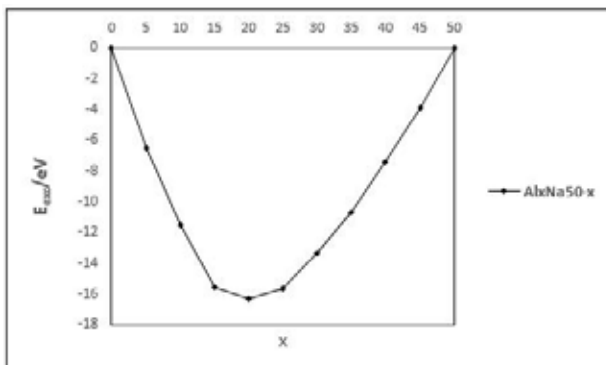


Figure 18: Excessive energy to aluminum-sodium clusters of 50 atoms.

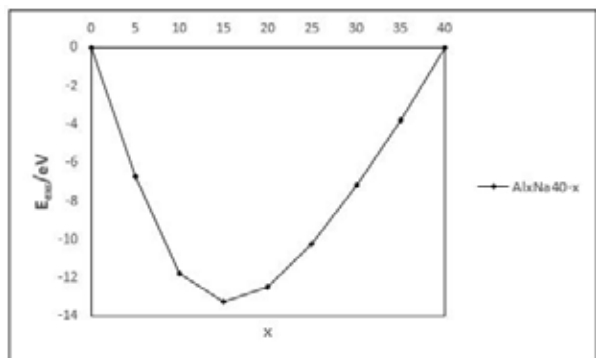


Figure 16: Excessive energy to aluminum-sodium clusters of 40 atoms.

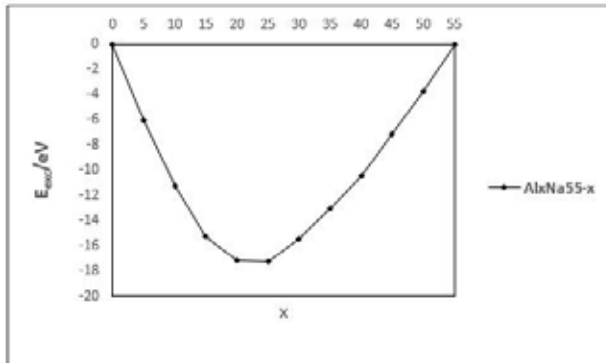


Figure 19: Excessive energy to aluminum-sodium clusters of 55 atoms.

By analyzing the excessive energy graphics, we observe that clusters with 3, 4, 5, 6 and 7 atoms have better stability when the agglomerations are composed of 2 aluminum atoms; in other words, the structures Al_2Na_1 , Al_2Na_2 , Al_2Na_3 , Al_2Na_4 , Al_2Na_5 are the ones most prone to be formed. When, considering the structures of nuclearities 8, 9, 10, 11, 12 and 13, the composition is altered and then presents stronger trend to form clusters with the composition of 4 aluminum atoms - Al_4Na_4 , Al_4Na_5 , Al_4Na_6 , Al_4Na_7 , Al_4Na_8 and Al_4Na_9 . Regarding agglomerations of 14 atoms, the most stable structure was Al_6Na_8 , and, to those of 15 atoms, the most stable composition was $\text{Al}_5\text{Na}_{10}$. To clusters of 20 atoms, the most stable structure presented 1 aluminum atom. Clusters with nuclearity of 25 and 30 presented better stability with 2 atoms of aluminum in the structure. Agglomerations of 35 and 40 atoms presented better stability with 3 aluminum atoms. Finally, structures of 45, 50 and 55 atoms presented themselves more stable with 4 aluminum atoms in the structure of the nanoalloy. In Figure 20 we present alloy structures with nuclearity up to 15 atoms.

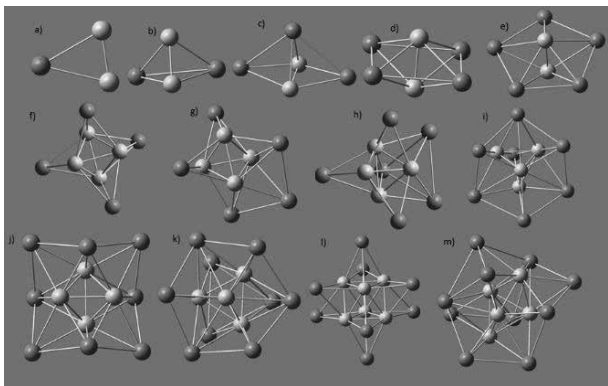


Figure 20: Structure of the compositions Al_2Na_1 , Al_2Na_2 , Al_2Na_3 , Al_2Na_4 , Al_2Na_5 , Al_4Na_4 , Al_4Na_5 , Al_4Na_6 , Al_4Na_7 , Al_4Na_8 , Al_4Na_9 , Al_6Na_8 and $\text{Al}_5\text{Na}_{10}$.

We have observed that, regarding sodium structures doped with a single atom of aluminum, the aluminum atoms tend to occupy central positions, whilst sodium atoms tend to occupy peripheral areas within the structure. It is compelling to notice that there is an ordered growth in the structure to the compositions of

4 aluminum atoms (20-f, 20-g, 20-h, 20-i, 20-j and 20-k), in which these atoms form a regular tetrahedron in the center and the sodium atoms agglomerate around those of aluminum, in a very similar fashion to a micelle. We have also verified that the 20-a, 20-b, 20-c, 20-d and 20-e structures presented great similarity to those of pure aluminum and pure sodium with the same nuclearity. With $N=8$, the structures then started presenting configurations much different from those obtained from pure clusters.

Conclusions

In the current research, all clusters to the system $\text{Al}_x\text{Na}_{N-x}$ ($3 \leq N \leq 55$) presented structures that may be considered of lesser energy according to the modified genetic algorithm method, along with the many-body Gupta potential^{16,17}. We realized that the pure aluminum structures present sturdier atom compaction when compared to those of sodium, which may be explained by the differences in the atomic radius between sodium and aluminum.

Such differences are observed in the equilibrium of interatomic distances provided by the Gupta potential to distinct atoms. Since there is no further research in the literature regarding aluminum-sodium clusters, we started from the obtained structures of pure aluminum and pure sodium in order to predict information regarding to corresponding nanoalloys. Once we considered that the aluminum clusters presented more stability than those of sodium, we focused in the use of pure aluminum structures to serve as a comparative basis for the GA method with the Gupta potential. By confronting the obtained structures using the GA with the many-body Gupta potential to pure aluminum, consonant with recent studies in the literature such as those of Kiohara et al. (2013)³¹, we have verified that, despite being a classic method, the Gupta potential presented cluster structures to systems Al_2 , Al_3 , Al_6 , Al_8 and Al_9 in a very similar manner to those obtained from ab initio calculations, such as the DFT and the CCSD(T).

In conformity with what has been explained, it became possible to demonstrate that the genetic algorithms applied to the Gupta potential may be an effective tool in the search for global minima structures.

Acknowledgments

Work supported by CNPq, FAPEMIG, FAPERN.

References

- Schmid G. Metal Clusters in Chemistry I. Wiley-VCH, Weinheim, **1999**.
- Available at: <http://www.tc.bham.ac.uk/~roy/Research/clusters.html>. Accessed on July 10, **2015**.
- Berry R. S., Braier P., Hinde R. J. Tumer, G.W.; Johnston, R. L.; WILSON, N. T, J. Chem. Phys. 112, 4773 (2000) P., Israel J. Chem., 30 39, **1990**.
- Hartke B., Chem. Phys. Lett., 258 144, **1996**.
- Wales D. J. e Scheraga H. A., Science, 285 1368, **1999**.
- White R. P. e Mayne H. R., Chem. Phys. Lett., 289 463, **1998**.
- Holland J. H., Sci. Am., 267 66, **1992**.
- Hartke B., Phys. Chem, 214 1251, **2000**.
- White R. P., Niesse J. A. E H. R. Mayne., J. Chem. Phy., 108 2208, **1998**.
- Doye J. P. K., Wales D. J. E Berry R. S., J. Chem. Phys., 103 4234, **1995**.
- Doyce J. P. K. e Wales D. J., J. Chem. Soc. Faraday, Trans., 93 4233, **1997**.
- Disponível em: <http://professor.webizu.org/ga/>, accessed in May 10, **2014**.
- Hartke, B., Z. Phys. Chem. 214 (**2000**) 1251.
- Johnston, R. L.; Roberts, Soft Computing Approaches in Chemistry, edited by H. Cartwright, L. Sztandera (Physica-Verlag, Heidelberg, **2001**).
- Silva, E. S. A.; Duarte, H. A.; Belchior, J. C., Chemical Physics 323 (**2006**) 553–562.
- Lordeiro, R. A.; Guimarães, F. F.; Belchior, J. C.; Johnston, R. L., International Journal of Quantum Chemistry 95 (**2003**) 112.
- Guimarães, F. F.; Belchior, J. C.; Johnston, R. L.; Roberts, C., Journal of Chemical Physics, 116 n°19 (**2002**) 8327.
- Schlegel, H.B., Adv. Chem. Phys. 67 (**1987**) 249.
- Rodrigues, D.D.C.; Nascimento, A.M.; Duarte, H.A.; Belchior, J.C., Chemical Physics 349 (**2008**) 91.
- Cleri, F.; Rosato, V., Physical Review B, 48 n°1 (**1993**) 22.
- Daw, M. S.; Baskes, M. I., Phys. Rev. Lett. 50, 1285 (**1983**); Phys. Rev. B29, 6443 (1984).
- Rosato, V.; Guillope, M.; Legrand, B., Philos. Mag. A 59, 321 (**1989**).
- Aguado, A.; López, J. M., The Journal of Chemical Physics 133 (**2010**) 094302-1.
- Li, Y.; Blaisten-Barojas, E., Physical Review B 57 n°24 (**1998**) 15 519.
- Tumer, G.W.; Johnston, R. L.; WILSON, N. T, J. Chem. Phys. 112, 4773 (**2000**)
- Wilson, N. T.; Johnston, R. L., Eur. Phys. J D (**2000**), 12, 161.
- Rao, B. K.; Jena, P., J. Chem. Phys. (**1999**) 111 1890.
- A. Aguado and J. M. L'opez, J. Chem. Phys. 133 (**2010**) 094302
- R. Ferrando, J. Jellinek and R. L. Johnston, Chem. Rev. (Washington, D.C.) 108 (**2008**) 845.
- Lai, S. K.; Hsu, P. J.; Wu, K. L.; Liu, W. K.; Iwamatsu, M., Journal of Chemical Physics 117 n°23 (**2002**) 10715.
- Valéria O. Kiohara; Edson F.V. Carvalho; Carlos W.A. Paschoal; Francisco B. C. Machado; Orlando Roberto-Neto. Chem. Physics Letters 568–569 (**2013**) 42–48.

Acassio R. Santos^{a*}, Breno R. L. Galvão^c,
Caio L. Firme^a, Fabrício de L. Farias^a and
Jadson C. Belchior^b

^a Chemistry Institute, Universidade Federal do Rio Grande do Norte, Av. Senador Salgado Filho, 3000, Lagoa Nova, (59.072-970), Natal, Rio Grande do Norte, Brazil.

^b Chemistry Department, Universidade Federal de Minas Gerais, Av. Antonio Carlos 6627, Pampulha, (31.270-901), Belo Horizonte, Minas Gerais, Brazil

^c Chemistry Department, Centro Federal de Educação Tecnológica de Minas Gerais, CEFET-MG, Av. Amazonas, 5253 (30.421-169), Belo Horizonte, Minas Gerais, Brazil

*E-mail: acassioroch@hotmail.com

PEDOT Chain Length and Excitation Energy Dependence from Time-Dependent Density Functional Theory

Ageo M. de Andrade, Luis H. Lacerda, Renan A. P. Ribeiro, Sergio R. de Lazaro & Alexandre C. Junior

Introduction

Nowadays, the need to produce alternative energy sources which can substitute fossil fuels is a worldwide challenge. Furthermore, policy efforts must be made to become the clean energy technologies competitive to cheaper energy sources, and its application in the society, especially for reducing global warming¹. Since 1970, solar photovoltaic devices has been developed with objective to reach new low energy cost devices, but its application was limited by low energy conversion efficiency. During last decades, solar energy conversion up to 30% was achieved in inorganic devices based on crystalline silicon devices; however, they are limited by high cost and short durability².

One way to avoid the high effective cost of solar cell devices is to replace silicon by organic semiconductors (OS) because its potential for easy roll-to-roll fabrication has more processable advantages mainly, high flexibility, easy to synthesize and endless possibilities on discovering new materials by organic modification, and capacity to use in flexible substrates³. However, such OS also have the problem of the low efficiency at energy conversion⁴. Recently, studies with multiple organic solar cells called “sandwich” solar cells have shown good candidates to avoid the limited absorption range^{5,6}. Furthermore, OS can be associated with inorganic semiconductors to produce flexible thin film devices with good charge transport properties⁷. The role of organic materials that can be used for application in solar cell devices is widespread in different organic classes, but the main characteristic found in all compounds is π conjugation length allowing a high charge mobility between HOMO and

LUMO orbitals^{8,9}.

Organic polymeric materials used in solar cell devices must show high structure ordering of polymer bulk, once this molecular property contribute significantly for charge transport between HOMO-LUMO orbitals spread in polymeric chain^{8,10,11}. For better bulk formation efficiency, polymeric materials must show planar chain among monomers to produce charge carriers on polymeric chain¹². Considering such property, the class of polythiophenes (PT) have attached attention, especially by experimental results in different synthesis routes^{13,14}. From many PT derivatives, Poly(3,4-ethylenedioxythiophene) (PEDOT – Chart 1) has been investigated since 1970, initially on BAYER laboratories, become it an interesting candidate for application as OS, once PEDOT is easy to process in non-aqueous solvents, and it has excellent hole transport properties, allowing the application on different electronic devices, such as antistatic coatings, cathodes in capacitors, organic light emitting diodes (OLEDs), photovoltaic, and electrochromic films^{15,16}.

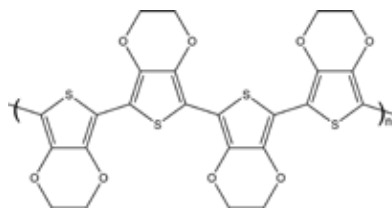


Chart 1. Chemical structure of Poly(3,4-ethylenedioxythiophene) (PEDOT)

PEDOT has been investigated to understand the contribution of p conjugations on optical properties. Apperloo and co-workers¹⁷ investigated the relation between monomeric units and ultraviolet absorption through experimental and semi-empirical results, but from this contribution there is no significant theoretical contributions for a better understanding of the relation between molecular geometry, electronic structure and absorption spectra.

In this work we present a Time-Dependent Density Functional Theory (TD-DFT) investigation from monomer to sixamer PEDOT to deep on optical property, molecular geometry, π conjugation length, electronic properties (HOMO and LUMO) and excitation profiles. The discussion is based on theoretical results of excitation levels on each oligomeric size comparing the differences between each geometry from molecular orbital and electronic property.

Computacional Procedure

3,4-ethylenedioxythiophene (EDOT) structures from monomer to decamer (1-EDOT to 10-EDOT) were optimized using PM618 semi-empirical methodology available in Molecular Package 2012 (MOPAC2012) Program¹⁹, where the gradient minimization was specified as 0.01 kcal.mol⁻¹ applying Pulay and Camp²⁰ routines for SCF calculation. From optimized geometries, single-point calculation using GAMESS²¹⁻²³ was applied using B3LYP/6-31+G(d,p) level of theory, with geometry gradient convergence tolerance of 1x10⁻⁶ Hartree, and SCF density convergence criteria set as 1x10⁻⁶ applying Pulay's²⁴ routine on SCF cycles. From single point calculations, orbital and gap energies and orbital densities were obtained. Time-Dependent Density Functional Theory (TD-DFT)²⁵ was applied up to 6-EDOT to investigate excitations in gas phase with B3LYP/6-31+G level of theory for first 30 excited states for each EDOT geometry producing ultraviolet-visible (UV-Vis) spectra for all geometries of interest (Chart 1). The discussions are centered on comparison between theoretical and experimental UV-Vis spectra results, the contribution of an orbital in particular for the excited state and how the oligomer size affect the UV-Vis spectra.

Results and Discussion

Optimized molecular geometries from 1-EDOT to 10-EDOT are shown in Figure 2, they present good agreement for a polymeric planar chain. Other theoretical works showed similar results, where were calculated a dihedral angle between monomers close to 180 degrees^{26,27}. From PM6 semi-empirical methodology, the mean dihedral angle calculated for each oligomer is shown in Table 1. Such result shows that is possible to produce good results for conductive polymers applying semi-empirical methodology with much less computational cost comparing to Hartree-Fock (HF) or DFT theory levels, once the main objective of the semi-empirical calculations is produce a start molecular geometries to investigate electronic property.

Table 1. Mean Dihedral Angle (in degrees) between monomers from 1-EDOT to 10-EDOT from PM6 semi-empirical methodology.

Geometry	Mean Dihedral Angle
1-EDOT	--
2-EDOT	179.89
3-EDOT	179.61
4-EDOT	179.35
5-EDOT	179.19
6-EDOT	179.98
7-EDOT	179.06
8-EDOT	178.98
9-EDOT	179.07
10-EDOT	179.13

Considering the good agreement produced by PM6 methodology for PEDOT oligomers geometry, a new electronic structure calculation was performed through DFT theory. The choice to produce molecular geometries by semi-empirical calculations, analyzing electronic structure through DFT theory was made considering low computational cost to produce optimized geometries, and better electronic description, respectively^{8,25}. From 1-EDOT to 10-EDOT molecular structures (Figure 1) were calculated HOMO and LUMO orbitals, which are located over all oligomeric chain. It is possible to purpose that charge transport occur between sulfur atoms and π -type conjugated bonds over the neighbor monomers. The more acceptable electronic mechanism in solid state theory is based on excitation of the electrons from HOMO orbital to LUMO orbital. These electrons in LUMO orbital

are available to perform the charge transfer or electronic conduction through oligomeric chain^{8,28}. Such charge transport is often called charge way because the charge

distribution is continuous in all molecular structure⁸. In fact, good results for PEDOT conductivity²⁹ are explained by π conjugation length as shown in Figure 1.

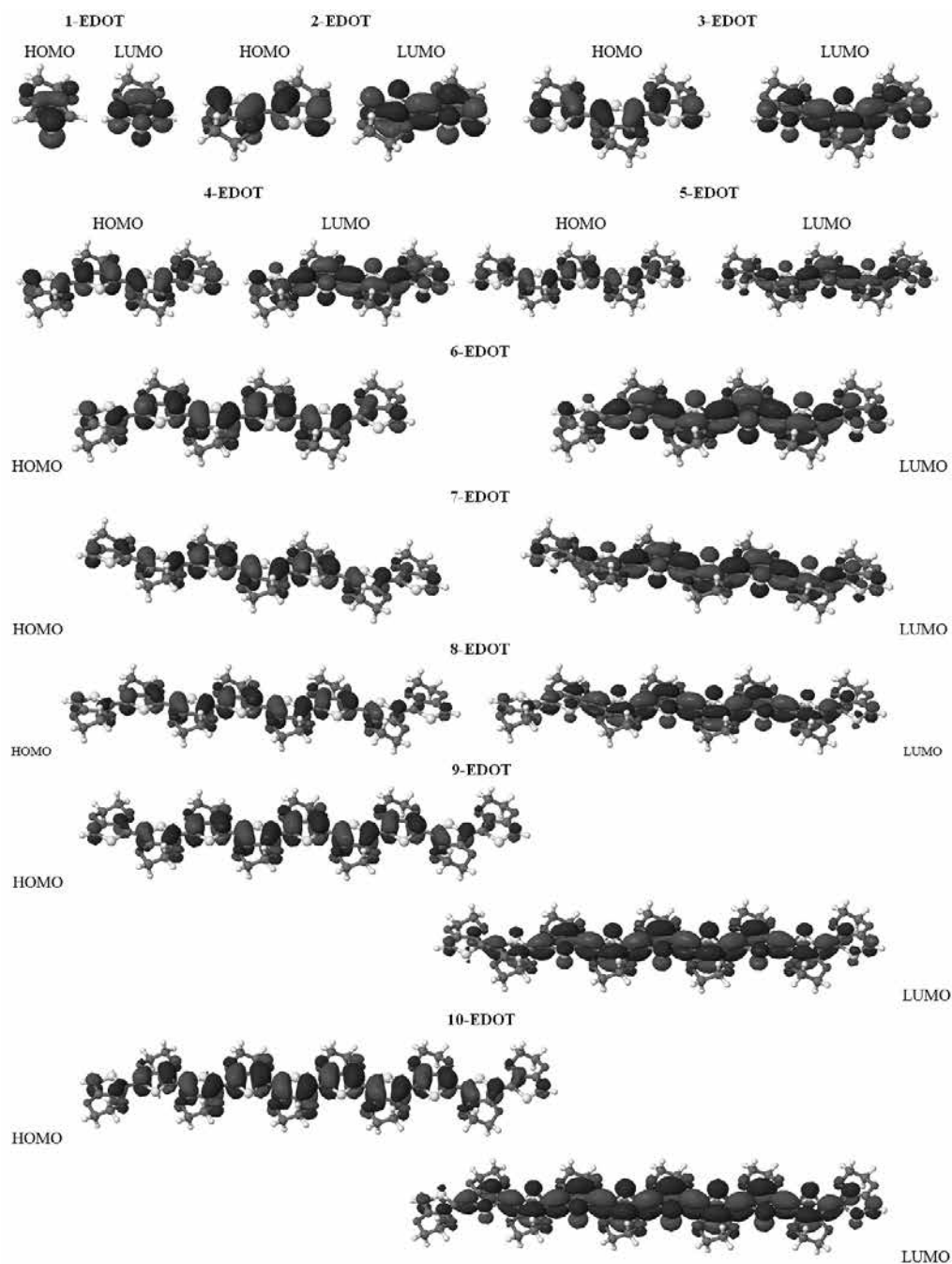


Figure 1. Electronic densities for π conjugated length located as HOMO and LUMO orbitals from 1-EDOT

Potential Energy Surface (PES - Figure 2) results from 1-EDOT to 10-EDOT show that growth oligomeric chain cause bulk formation inside chain producing a charge way in center of the oligomer. This effect is only visualized from six monomeric units or 6-EDOT model. In the same context, these PES results provided information about why

PEDOT produces better results for electronic conduction in large oligomeric size than a few monomeric units, such as, 1-EDOT to 5-EDOT. Another point, for PEDOT macrostructure there is no intramolecular interaction becoming hard to perform charge transfer through π - π stacking interaction among neighbor oligomeric chains.

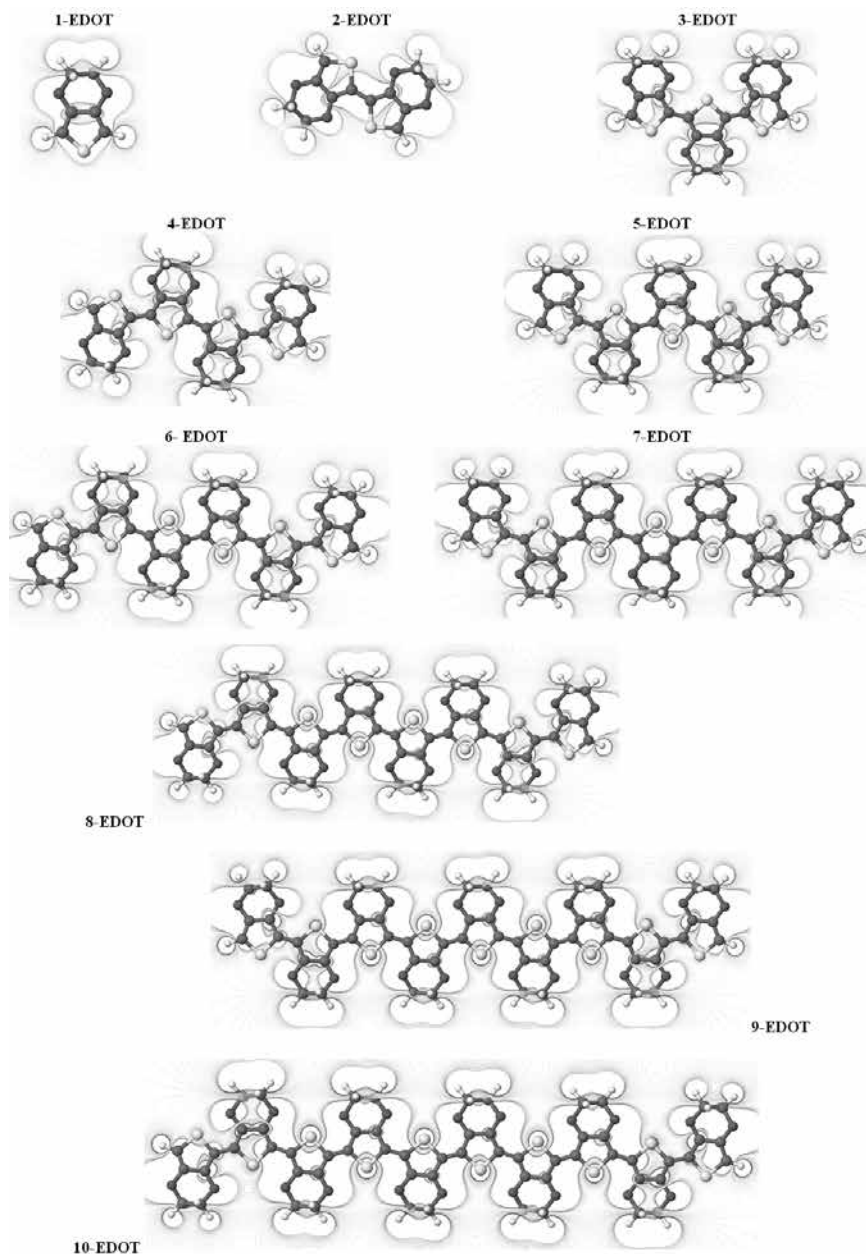


Figure 2. Potential energy surface (PES) calculated from 1-EDOT to 10-EDOT models using DFT/B3LYP

Recently, TD-DFT have gained attention of computational chemists to provide information about specific excitation of frontier orbitals. This approach has produced better understanding of electron-hole transfers from simulations based on Theory Orbital Molecular (TOM). Specially for organic semiconductors is possible to visualize where charge transport phenomenon is localized on molecular structure. Thus, TD-DFT simulations have represented better band-gap energy (E_g), PES and Density of States (DOS) results, mainly from calculations based on singlet excitation of the molecule. In our investigation, TD-DFT calculations from 1-EDOT to 6-EDOT electronic excitation have the dependence from oligomer size as shown in Figure 5. A red shift is observable as oligomeric size increases; however, from 7 monomeric units, TD-DFT calculations showed a high computationally cost and it was not possible to perform such calculations.

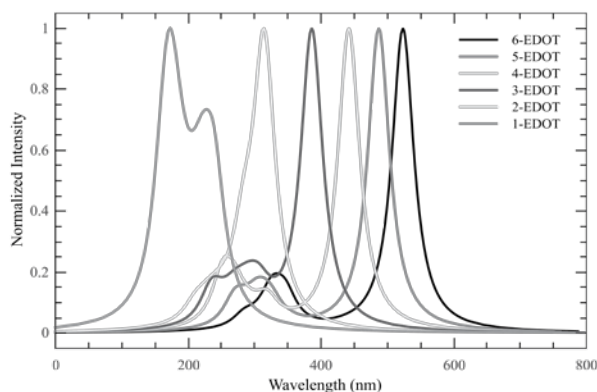


Figure 5. TD-DFT results for electronic excitation spectra from 1-EDOT to 6-EDOT molecules. Red shift is function of oligomer size.

Results for contribution of orbital excitation are shown in Table 2. Lower excitation energies are always associated to HOMO-LUMO excitation state for all simulated molecular structures. Furthermore, the HOMO-LUMO excitation energy or E_g is reduced from 5.18 eV (1-EDOT) to 2.37 eV (6-EDOT), showing a dependence of the E_g in relation to π conjugation length. Other possible excitation states from HOMO -2, HOMO -1 and LUMO +1 orbitals have also important contributions for excitation energy. For 1-EDOT molecule, the electronic excitation between HOMO -1 to LUMO orbitals represents 93% of the total contribution for excitation in 5.57 eV; whereas, for 2-EDOT molecule, the same electronic excitation has 4.37 eV. However, two oscillator strength were produced with different contributions of 51% and 43% from HOMO -2 and HOMO

-1 orbitals to LUMO orbital, respectively. Oscillator strengths associated to such electronic transitions are equals to 0.05 a. u. and 0.07 a. u.; nevertheless, these oscillator strengths have opposite signals for contributions, suggesting that electronic excitation from both orbitals is possible. In the 4-EDOT oligomer, the excitation in 3.85 eV is connected to HOMO -2 to LUMO electronic transition representing 44% of the total contribution of the excitation; whereas, in 4.61 eV the total contribution is 40% of the excitation energy corresponding to HOMO -1 to LUMO +1 excitation. For 5-EDOT molecule there is a HOMO -3 to LUMO excitation in 3.78 eV, correspondent to 55% of excitation energy and a HOMO -1 to LUMO +1 contribution is associated to two important excitation energies, in 3.98 eV and 4.11 eV. At last, 6-EDOT molecule shows an electronic transition between HOMO -1 and LUMO +1 orbitals with 34% of contribution for excitation energy in 3.58 eV. All these results suggest that HOMO and LUMO orbitals are the most important frontier orbitals because show the lowest energy excitation; however, HOMO -3, HOMO -2, HOMO -1 and LUMO +1 are also important for charge transport.

Table 2. Excitation Energy (E), Oscillator Strength (fosc), Contribution of the Main Configuration Orbital (H = HOMO and L = LUMO) and States related to singlet excitation on different EDOT oligomers from TD-DFT.

Geometry	E (eV)	Fosc (a. u.)	Main conf.	Contrib.
1-EDOT	5.18	0.15	H \rightarrow L	92%
	5.57	0.09	H -1 \rightarrow L	93%
2-EDOT	3.94	0.52	H \rightarrow L	98%
	4.37	0.05	H -2 \rightarrow L	51%
			H -1 \rightarrow L	43%
	4.37	0.07	H -1 \rightarrow L	51%
			H -2 \rightarrow L	43%
3-EDOT	3.21	0.88	H \rightarrow L	99%
	4.06	0.07	H -3 \rightarrow L	80%
	5.26	0.05	H -3 \rightarrow L +1	63%
4-EDOT	2.80	1.30	H \rightarrow L	99%
	3.85	0.05	H -2 \rightarrow L	44%
	4.61	0.06	H -1 \rightarrow L +1	40%
5-EDOT	2.55	1.70	H \rightarrow L	99%
	3.78	0.07	H -3 \rightarrow L	55%
	3.98	0.08	H -1 \rightarrow L +1	50%
	4.11	0.08	H -1 \rightarrow L +1	30%
6-EDOT	2.37	2.08	H \rightarrow L	99%
	3.58	0.19	H -1 \rightarrow L +1	34%

In fact, experimental results³⁰ show a second electronic excitation state more energetic than HOMO-LUMO excitation; however, the researchers do not confirm which molecular excitation produced such electronic absorption. Our TD-DFT single excitation calculations identify this electronic excitation as different transitions among HOMO -3, HOMO -2, HOMO -1 and LUMO +1 orbitals; however, such electronic transitions confirmed are dependents from oligomer size simulated. Therefore, the amount of energy levels are fundamentals to rise this electronic transition of high energy. This result is consequence of the introduction of energy levels inside band-gap in according to Theory of Bands for solid state²⁸.

Conclusion

The results showed in this work provided better understanding of charge transport properties in EDOT oligomers and PEDOT. From optimized geometries with low computational cost, electronic structure was determined from DFT calculations, showing bulk formation from 6 monomeric units extending for longer polymeric chains. The same calculations provided information about frontier orbital location, showing polymeric central region the most important for charge transport properties. DOS explains how band-gap energy was reduced from increase of monomeric units, showing π conjugation dependence between electronic and geometric structures. The same relation was observed on singlet excitation theory applying TD-DFT calculations. These results are in good agreement with experimental data for excitation energy, becoming possible to understand the main excitation bands in UV-Vis spectra for EDOT oligomers and PEDOT and its relation with frontier orbitals.

References

- IEA and OECD, (2011).
- J.-P. Kleider, J. Alvarez, A. Br  zard-Oudot, M.-E. Gueunier-Farret and O. Maslova, *Sol. Energy Mater. Sol. Cells*, 135, 8, (2015).
- S. Hedstr  m and P. Persson, *J. Phys. Chem. C*, 116, 26700, (2012).
- I. Constantinou, T.-H. Lai, D. Zhao, E. D. Klump, J. J. Deininger, C. K. Lo, J. R. Reynolds and F. So, *ACS Appl. Mater. Interfaces*, 7, 4826, (2015).
- M. Lanzi, E. Salattelli, T. Benelli, D. Caretti, L. Giorgini and F. P. Di-Nicola, *J. Appl. Polym. Sci.*, 132, n/a, (2015).
- F. Hermerschmidt, A. S. Kalogirou, J. Min, G. A. Zissimou, S. M. Tuladhar, T. Ameri, H. Faber, G. Itskos, S. A. Choulis, T. D. Anthopoulos, D. D. C. Bradley, J. Nelson, C. J. Brabec and P. A. Koutentis, *J. Mater. Chem. C*, 3, 2358, (2015).
- M. Ra  ssi, L. Vignau, E. Cloutet and B. Ratier, *Org. Electron.*, 21, 86, (2015).
- V. Coropceanu, J. Cornil, D. A. da Silva Filho, Y. Olivier, R. Silbey and J.-L. Bredas, *Chem. Rev.*, 107, 926, (2007).
- A. Facchetti, *Chem. Mater.*, 23, 733, (2011).
- G. Tu, A. Bilge, S. Adamczyk, M. Forster, R. Heiderhoff, L. J. Balk, D. M  hlbacher, M. Morana, M. Koppe, M. C. Scharber, S. A. Choulis, C. J. Brabec and U. Scherf, *Macromol. Rapid Commun.*, 28, 1781, (2007).
- M. T. Dang, L. Hirsch, G. Wantz and J. D. Wuest, *Chem. Rev.*, 113, 3734, (2013).
- H. Nikoofard and M. Gholami, *Comptes Rendus Chim.*, 17, 1034, (2014).
- L. Wen, D.-C. Jeong, A. Javid, S. Kim, J.-D. Nam, C. Song and J. G. Han, *Thin Solid Films*, 587, 66, (2015).
- S. Das, D. P. Chatterjee, R. Ghosh and A. K. Nandi, *RSC Adv.*, 5, 20160, (2015).
- J. Liu, S. Pathak, T. Stergiopoulos, T. Leijtens, K. Wojciechowski, S. Schumann, N. Kausch-Busies and H. J. Snaith, *J. Phys. Chem. Lett.*, 6, 1666, (2015).
- B. Park, M. Pazoki, K. Aitola, S. Jeong, E. M. J. Johansson, A. Hagfeldt and G. Boschloo, *ACS Appl. Mater. Interfaces*, 6, 2074, (2014).
- J. J. Apperloo, L. 'Bert' Groenendaal, H. Verheyen, M. Jayakannan, R. A. J. Janssen, A. Dkhissi, D. Beljonne, R. Lazzaroni and J.-L. Br  das, *Chem. – Eur. J.*, 8, 2384, (2002).
- J. J. P. Stewart, *J. Mol. Model.*, 13, 1173, (2007).
- J. Stewart, ([HTTP://OpenMOPAC.net](http://OpenMOPAC.net)).
- R. N. Camp and H. F. King, *J. Chem. Phys.*, 75, 268, (1981).
- M. S. Gordon and M. W. Schmidt, pp. 75–83.
- M. S. Gordon and M. W. Schmidt, (2005), pp. 1167–1189.
- M. W. Schmidt, K. K. Baldridge, J. A. Boatz, S. T. Elbert, M. S. Gordon, J. H. Jensen, S. Koseki, N. Matsunaga, K. A. Nguyen, S. Su, T. L. Windus, M. Dupuis and J. A. Montgomery, *J. Comput. Chem.*, 14, 1347, (1993).
- P. Pulay, *J. Comput. Chem.*, 3, 556, (1982).
- P. Elliott, F. Furche and K. Burke, (2008), pp. 91–165.
- J. A. Dur  es, D. A. da S. Filho, A. M. Ceschin, M. J. A. Sales and J. B. L. Martins, *J. Mol. Model.*, 20, 1, (2014).
- T. P. Kaloni, G. Schreckenbach and M. S. Freund, *J. Phys. Chem. C*, 119, 3979, (2015).
- W. A. Harrison, (2005).
- L. Groenendaal, F. Jonas, D. Freitag, H. Pielartzik and J. R. Reynolds, *Adv. Mater.*, 12, 481, (2000).
- D. Wasserberg, S. C. J. Meskers, R. A. J. Janssen, E. Mena-Osteritz and P. B  uerle, *J. Am. Chem. Soc.*, 128, 17007, (2006).

Ageo M. de Andrade^{*a}, Luis H. Lacerda^a,
Renan A. P. Ribeiro^a, Sergio R. de Lazaro,
Alexandre C. Junior^b

^a Department of Chemistry, State University of Ponta Grossa, Av. General Carlos Cavalcanti, 4748, 84030-900, Ponta Grossa, PR, Brazil

^b Department of Physics, State University of Ponta Grossa, Av. General Carlos Cavalcanti, 4748, 84030-900, Ponta Grossa, PR, Brazil

*E-mail: aageo25@gmail.com

Zn-doped BaTiO_3 Materials: A DFT Investigation for Optoelectronic and Ferroelectric Properties Improvement

Luis H. S. Lacerda, Renan A. P. Ribeiro, Ageo M. Andrade, Alexandre C. Jr. & Sérgio R. Lazaro

Introduction

Theoretical methods based on quantum mechanical simulations are an important tool to study material properties. Such methodologies are used for analyzing the electronic, optical, structural, pyro-, piezo- and ferroelectric properties of any materials. In case of crystalline semiconductors materials, these properties are highly dependent on chemical composition due to chemical bond character. Among the crystalline materials, the semiconductors materials stand out once are largely employed to develop electronic, optical devices, piezoelectric and memory devices because of its spontaneous polarization¹⁻¹². Then, the perovskite materials are an important group of materials since are the most abundant minerals in Earth.¹³ This material has ABX_3 stoichiometry since A is a mono or bivalent cation; B is tetra or pentavalent cation and X is a non-metallic element, in most cases oxygen. As well as the other semiconductor materials, the properties of perovskite materials are dependent of chemical bonds and symmetry of crystalline structure.

Among the perovskite materials, a most important is BaTiO_3 material (BTO). This material is a solid that can be found in five crystalline structures which differ according to central atom (Ti) in unit cell. The stability of each crystalline structure of BTO is dependent of temperature variation as showed in Figure 1. At room

temperature (298 K), the BTO has tetragonal structure. Such structure is characterized by Ti position out of symmetric center of unit cell resulting in properties, such as: optical, electronic, pyro-, piezo- and ferroelectric properties.¹⁴⁻¹⁶

In this work, the tetragonal phase was investigated. This material has a band gap of 3.30 eV and is employed to development of integrated circuits, energy storage device, temperature coefficient resistance thermistor, piezoelectric sensors, sensing and monitoring devices, thin films, optoelectronic devices, actuators and others.¹⁶⁻²¹

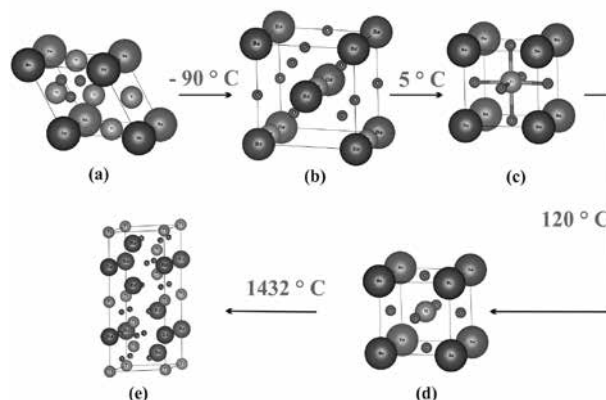


Figure 1. Crystalline Structures of barium titanate. a) Rhombohedral, b) Orthorhombic, c) Tetragonal, d) Cubic and e) Hexagonal.

Although BTO is a not a recent discovery, such material still is largely studied in order to improve innumerable devices, once its properties can be improved through of doping process. This process consists in adding a controlled amount of impurities in semiconductor structure that changes drastically the properties of a semiconductor material without changing its crystalline structure and controlling their properties.^{22, 23} In case of BTO, the doping process is possible by substitution of Ba, Ti or O atoms.²⁴⁻²⁸ Among these substitutions, the replacement of Ba atoms for Zn atoms (BZTO) was not largely analyzed due to few works focused in this system. Such manuscripts evaluated only the structural, optical, electronic properties, the grain growth and photocatalysis application of Zn-doped BTO.^{24-26, 29, 30} Therefore, we propose a BZTO theoretical investigation based on DFT/B3LYP to evaluate the effects of Zn-doping in different amounts on BTO structural, electronic, optical and ferroelectric properties.

Methods

BTO material simulation was performed based on a tetragonal structure. This structure is composed by one Ba atom, one Ti atom and two O atoms arranged on P4mm (99) space group with lattice parameters $a = b = 3.98601 \text{ \AA}$, $c = 4.0259 \text{ \AA}$ and angles $\alpha = \beta = \gamma = 90^\circ$.¹⁶ The BZTO models was developed from unit cell expansion in the direction of axes a and b resulting at 25-100% doping (Table 1). For all models, the TZVP³¹ basis set was employed to describe the Ti, O and Zn atoms; whereas, the Ba atoms were described by Zagorac³² basis set employing the HAYWSC³³ pseudopotential.

Table 1. Description of the unit cells used for simulating the Zn-doping on BaTiO₃ material.

Doped amount (%)	Unit cell expansion	Ba atoms replaced
0	2x2x1	0
25	2x2x1	1
50	2x2x1	2
75	2x2x1	3
100	2x2x1	4

The calculation level applied was based on the Density Functional Theory (DFT) at set B3LYP hybrid functional^{34, 35}; SCF convergence was truncated in 10^{-8} Hartree and Mohnkhost-Pach36 method defined as 8x8x8 using CRYSTAL09^{37, 38} software. Vibrational calculations were also performed using optimized results for all models to evaluation of thermodynamic stability at room temperature (298.5 K) and 1 atm. The theoretical results discussed in this manuscript are Density of States (DOS) Projections and Band Structure analysis. XCrysden^{39, 40} Software was used for structural analysis. Personal computer using Ubuntu Linux operational system made up by quad-core AMD processor with 32 GB of RAM and data storage capability of 3.5 TB was used in all simulations.

Results and Discussion

STRUCTURAL PROPERTIES

The evaluation of Zn influence on structural properties of BTO material (Table 2) was performed through lattice parameters, unit cell angles, tetragonality factor (c/a) and μ structural coefficient (Equation 1). Such results indicate that unit cell symmetry was not affected by Zn-doping. While Zn-doping amount increases, a , b and c lattice parameters decrease linearly (Figures 2). The linear variation of lattice parameters was evaluated based on Vegard's Law^{41, 42} that provides a linear relationship between lattice parameters and impurity amount. According to this empirical rule the linear variation of lattice parameters with dopant amount variation indicates an ideal behavior for solid solution. Then, the Zn insertion in the BTO structure is characterized by an ideal behaviour indicating the possible formation of solid solution. The stability of BZTO materials are better discussed in Thermodynamic Stability Evaluation Section. For 50 % model, the lattice parameter c are bigger than for BTO model due to the equal amount of Ba and Zn in crystalline structure which causes the perturbation through of replaced atoms distribution. However, the tetragonality index and μ values indicate that the tetragonal symmetry of unit cell is kept.

The lattice parameters are changed due to bond length decrease in crystalline structure, once for BTO model the average bond length for Ba – O and Ti – O are 2.865 \AA

and 2.033 Å, respectively. As the Zn quantity increases, these values are reduced. Thus, for Zn-doped BTO at 100 % such bonds have average bond length of 2.685 Å and 1.928 Å, respectively. Although Ti – O bonds were changed, the μ coefficient structural evaluation indicates that the Ti position is slightly modified; therefore, it is expected the arising of ferroelectric and piezoelectric properties for BZTO materials are not smaller regarding to BTO.

$$\mu = d_{\text{(Ti-O axial)}}/c$$

Equation 1

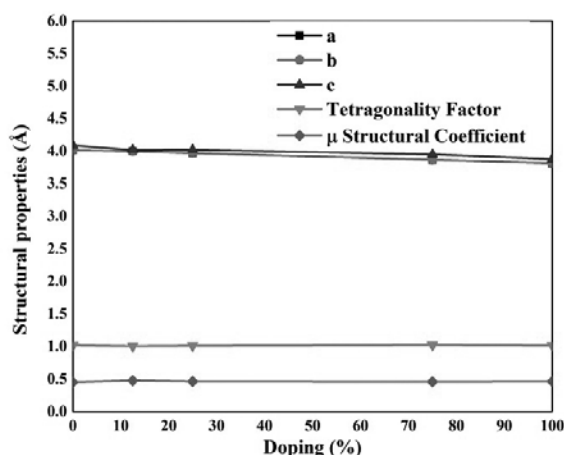


Figure 2. Variation of Lattice parameters (in Å), unit cell angles (in degrees), Tetragonal factor (a/c) and structural coefficient μ for BTO and BZTO models according to dopant amount.

ELECTRONIC PROPERTIES

The electronic properties of BTO and BZTO materials were evaluated through the projected Density of States (DOS) for analysing models, evaluated from last five energy bands of the Valence Band (VB) and the first five energy bands of the Conduction Band (CB) featuring the band gap region (E_g). For BTO model, the O atoms largely contribute to the composition on all VB and for lower energy levels of CB through 2s and 2p orbitals; whereas, Ti atoms have low contribution for VB through

of 3d and 3p orbitals and compose majority in CB through 3d orbitals. In turn, Ba atoms lightly contribute for VB through 5sp and 6sp orbitals; while, its 3d orbitals contributed for CB. The doping process has showed low influence on O and Ba contributions in VB and CB. Nevertheless, the Ti contribution in CB was observed in a higher energy level than in BTO model. Zn contribution was made by 4s orbitals that has low contribution in VB and average contribution in CB. This insertion of Zn atoms shows a strong effect on the energy at the top of the VB in relation to the BTO material, causing degeneration of such energy levels, as well as reducing the contribution of the Ti atoms in CB.

OPTICAL PROPERTIES

The optical property of a solid is defined as the interaction between a solid and electromagnetic radiation. In case of semiconductor materials, the interaction only occurs with electromagnetic energy equal to or higher than $E_g^{22, 43}$. The optical property of BTO and BZTO material were evaluated through of E_g values (Table 3) showing that a decrease linearly with the Zn doping. Therefore, the presence of Zn atoms in the crystalline structure cause changes in the electronic structure from Zn orbitals insertion energy lower than Ti orbitals in the CB. The band gap change after doping process is large, once for BTO the characteristic wavelength is located on Ultraviolet-Visible (UV-Vis); whereas, for BZTO at 100 % the radiation characteristic is observed on Infrared region. As shown on Table 3, all the E_g are referred to an indirect excitation, except for 75 % model that present a direct excitation along the G symmetry points.

Table 3. Theoretical results calculated for indirect and direct band gaps (E_g in eV), wavelength (in nm), electromagnetic radiation range in relation to doping amount (in %).

Doping %	E_g (eV)	λ (nm)	Radiation
0	3.28 (M – G)	377.91	UV-Visible
25	2.89 (R – M)	429.33	Visible
50	2.2 (Λ – G)	561.40	Visible
75	1.62 (G – G)	764.53	Infrared
100	0.75 (A – G)	1656.50	Infrared

The Figure 3 shows the band-gap variation (ΔE_g) for BZTO models in relation to BTO indicating a linear decrease. Then, all BZTO models have band-gap below to of BTO material. Such variation is caused by displacement of bottom of CB to a lower energy level than in BTO material due to Zn orbitals contribution. Figure 4 shows the results for top of VB and bottom of CB energy levels for all models investigated. These results indicate that the VB level for Zn-doped models is slightly different of the energy level observed in BTO material. In order hand, the influence of Zn-doping process on CB energy level is strong, since the energy level is reduced largely.

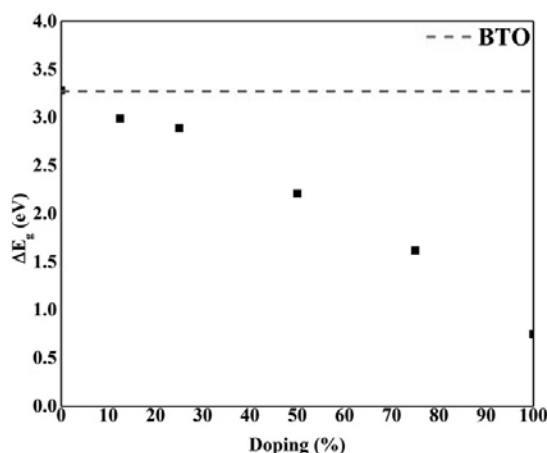


Figure 3. Theoretical results for BTO band gap according to Zn-dopant amount.

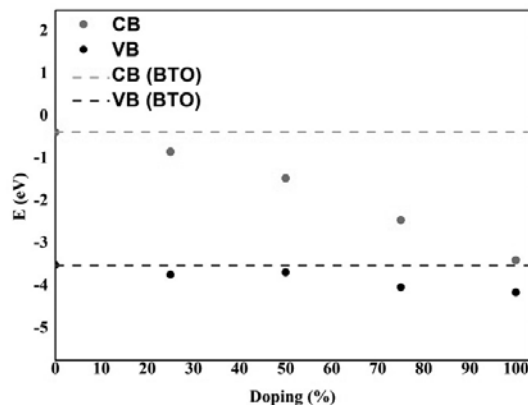


Figure 4. Energy levels calculated from DFT/B3LYP at the top of Valence Band (VB) and the bottom of Conduction Band (CB) according to Zn-doping amount.

FERROELECTRIC PROPERTIES

Nowadays, the perovskite-type materials have been largely applied in the development of ferroelectric memories and charge storage devices because of high values for polarizability and dielectric constants presented by these materials.⁴⁴⁻⁴⁹ In a ferroelectric material the direction of charge polarization can be reverted applying an external electrical field, which is very important to the charge storage property.

In general, the dielectric constant (ϵ) determines the charge storage capacity; whereas, the polarizability (α) describes how much a material is polarizable under an electrical field.⁴³ These measures were developed by solid state theory, in order to better understand the ferroelectric property of the materials and they are dependent on the tensor matrix; which is directed similarly to the Cartesian coordinates system. For BTO and BZTO materials, the ϵ and α amount were investigated based on components presented in Figure 5.

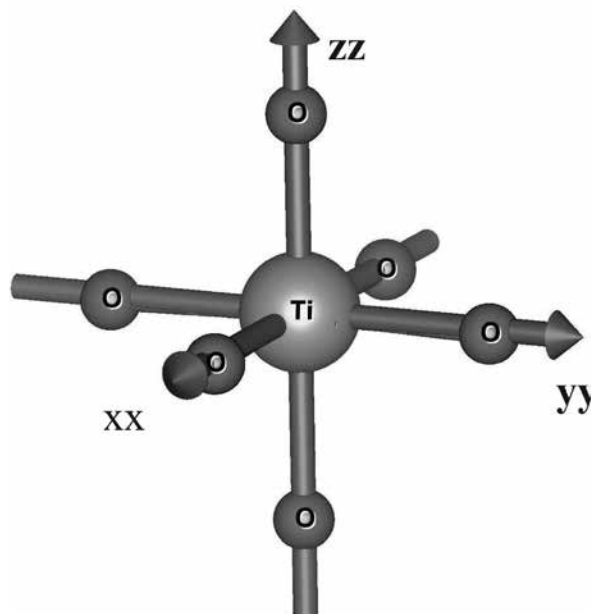


Figure 5. Octahedral sites for tetragonal-BTO and xx, yy and zz components used for calculating dielectric constants and polarizability.

Table 4. Polarizability (α) and dielectric constants (ϵ) for BTO and BZTO models.

Dopagem (%)	α			ϵ		
	Componente			Componente		
	xx	yy	zz	xx	yy	zz
0	154,1379	-	6216,2654	5,3564	-	176,6886
25	320,0193	-	8975,2729	5,7011	-	66,9239
50	295,1744	298,6174	301,6386 . 105	5,3724	5,4234	223,41 . 103
75	333,3171	331,4823	474,9845 . 107	6,2531	6,2241	374,29 . 105
100	162,264	-	150,181	6,359	-	5,960

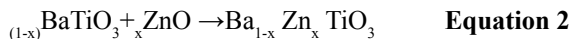
The ϵ and α results for BTO and BZTO models are shown in the Table 4 and indicate that doping process improves largely the ferroelectric property because theoretically there is an increase in all tensor matrix components in relation to BTO; except for BZTO at 100 % model, which shows a decrease for both ϵ and α regarding to pure material. Thus, the higher values for ϵ and α were observed to BZTO at 75 % doping. The increase observed in relation to Zn-doping, can be understood because the octahedron distortion in the crystalline structure that are responsible for the increase of the dielectric constants and polarizability. Another point is associated to the atoms random distribution in crystalline structure causing a lower symmetry in relation to BTO; consequently, the electronic density is randomly distributed providing ferroelectric and dielectric properties higher than those in the BTO.

Table 5. Theoretical values for mixing Gibbs Free Energy variation (ΔG_{mix}) and Gibbs Free Energy variation in relation to pure BTO ($\Delta \Delta G$) for BZTO material

Modelo (%)	ΔG (kJ.mol ⁻¹)	$\Delta \Delta G$ (kJ.mol ⁻¹)
0	0	0
25	-68.8969	-51.4552
50	-41.6027	-24.1609
100	0	-45.7471

THERMODYNAMIC STABILITY EVALUATION

According to Vegard's law, the structural results for BZTO models indicate that this solid solution shows an ideal character; then, it is expected that these materials can be obtained by experimental techniques, once the crystalline structure is linearly changed from dopant amount. In literature, BZTO materials were synthesized from 0 to 10 %. In manuscript of Caballero and coauthors³⁰ is not founded information of Zn solubility limit on BTO crystalline structure. Assuming that the Vegard's law prevision is not enough to determine the stability of BZTO materials, vibrational calculations were performed. Such vibrational calculations were based on DFT/B3LYP and we calculate the mixing Gibbs Free Energy (ΔG_{mix} – Equation 2) and Gibbs Free Energy in relation to BTO material ($\Delta \Delta G$ – Equation 3).



$$\Delta \Delta G = \Delta G_{\text{mix}} - \Delta G_{\text{BTO}} \quad \text{Equation 3}$$

The positive value for $\Delta \Delta G$ indicates that these models are not favorable thermodynamically to be obtained the crystalline structure; while, the negative values suggest a thermodynamically factor favorable obtained the crystalline structure. The thermodynamically stability results for BTO and BZTO are present on Table 5. For

all BZTO models, the DDGmix results are negatives in relation to BTO suggesting that such models are stable at room conditions. Then, these results corroborate with structural results provided by Vegard's law discussed before and they strongly suggest that BZTO materials a viable alternative to development of electronic, optical and ferroelectric devices and they are expected to show excellent fluorescence properties.⁵⁰⁻⁵²

Conclusions

We used DFT with periodic model to evaluate the structure, electronic, optical and ferroelectric properties for Zn-doping in barium titanate. Electronic and optical properties showed that Zn-doping are potential alternatives to be employed in electronic and optical devices, once the band-gap decrease changes the profile wavelength to the visible and infrared range of electromagnetic spectrum. The band-gap variation is caused by Zn atoms influencing as Valence Band as Conduction Band of BaTiO₃ material. The ferroelectric property was evaluated for all models and presented that Zn atoms insertion is a good alternative to improve the ferroelectric properties of BaTiO₃ materials. The vibrational frequencies and structure results for BZTO materials indicates that all models investigated are stable at room condition.

Then, it is concluded that the Zn-doping on BaTiO₃ crystalline structure improve electronic, optical and ferroelectric properties and it is a potential alternatives to application in ferroelectric devices employed in several electronic and optical devices, solar cells, and photocatalysis processes.

Acknowledgments

The authors acknowledge support from CNPq, CAPES and Fundação Araucária.

References

1. Z. J. Chew and L. Li, Materials Letters, 91, (2013).
2. C. Xun, L. Xiaomin, G. Xiangdong, L. Xinjun, Y. Chang, Y. Rui and J. Ping, Journal of Physics D: Applied Physics, 44, (2011).
3. M. K. Gupta, N. Sinha and B. Kumar, Journal of Applied Physics, 112, (2012).
4. F. Zhang, X. Li, X. Gao, L. Wu, F. Zhuge, Q. Wang, X. Liu, R. Yang and Y. He, Solid State Communications, 152, (2012).
5. S. Nedic, Y. Tea Chun, W.-K. Hong, D. Chu and M. Welland, Applied Physics Letters, 104, (2014).
6. M. K. Gupta and B. Kumar, Journal of Materials Chemistry, 21, (2011).
7. T. Qiuhong, W. Jinbin, Z. Xiangli, Z. Yichun, W. Qianjin, Z. Yi, X. Zhang and S. Huang, Electron Devices, IEEE Transactions on, 58, (2011).
8. J. I. Sohn, S. S. Choi, S. M. Morris, J. S. Bendall, H. J. Coles, W.-K. Hong, G. Jo, T. Lee and M. E. Welland, Nano Letters, 10, (2010).
9. S. Lee, H. Kim, D.-J. Yun, S.-W. Rhee and K. Yong, Applied Physics Letters, 95, (2009).
10. D. U. Lee, E. K. Kim, W.-J. Cho, Y.-H. Kim and H. Im, Thin Solid Films, 521, (2012).
11. J.-W. Zhao, F.-J. Liu, H.-Q. Huang, Z.-F. Hu and X.-Q. Zhang, Chinese Physics B, 21, (2012).
12. Y. H. Kang, J.-H. Choi, T. I. Lee, W. Lee and J.-M. Myoung, Solid State Communications, 151, (2011).
13. M. W. Davidson and G. E. Lofgren, Journal of Geological Education, 39, (1991).
14. P. Erhart and K. Albe, Journal of Applied Physics, 102, (2007).
15. M. Yashima, T. Hoshina, D. Ishimura, S. Kobayashi, W. Nakamura, T. Tsurumi and S. Wada, Journal of Applied Physics, 98, (2005).
16. R. A. Evarestov and A. V. Bandura, Journal of Computational Chemistry, 33, (2012).
17. P. Kumar, S. Singh, M. Spah, J. K. Juneja, C. Prakash and K. K. Raina, Journal of Alloys and Compounds, 489, (2010).
18. S.-H. Yao, J.-K. Yuan, P. Gonon, J. Bai, S. Pairis and A. Sylvestre, Journal of Applied Physics, 111, (2012).
19. Z.-X. Chen, Y. Chen and Y.-S. Jiang, The Journal of Physical Chemistry B, 105, (2001).
20. B. Wodecka-Dus and D. Czekaj, Archives of Metallurgy and Materials, 54, (2009).
21. J. A. Dawson, J. H. Harding, H. Chen and D. C. Sinclair, Journal of Applied Physics, 111, (2012).
22. H. L. Kwok, Electronic Materials (PWS Publishing Company, Boston, 1997).
23. A. R. West, Basic solid state chemistry (John Wiley & Sons, Chichester, 2006), 2 ed. edn.
24. A. Y. Fasasi, M. Maaza, E. G. Rohwer, D. Knoessen, C. Theron, A. Leitch and U. Buttner, Thin Solid Films, 516, (2008).
25. A. Y. Fasasi, M. Maaza, C. Theron, P. Neethling, U. Buttner, A. Leitch and A. K. Chaudhary, Thin Solid Films, 516, (2008).
26. J.-P. Zou, L.-Z. Zhang, S.-L. Luo, L.-H. Leng, X.-B. Luo, M.-J.

- Zhang, Y. Luo and G.-C. Guo, *International Journal of Hydrogen Energy*, 37, (2012).
27. H.-S. Kwon, H.-I. Yoo, C.-H. Kim and K.-H. Hur, *Journal of Applied Physics*, 107, (2010).
 28. C. Tian, Z. Yue, Y. Zhou and L. Li, *Journal of Solid State Chemistry*, 197, (2013).
 29. A. C. Caballero, J. F. Fernández, C. Moure and P. Durán, *Journal of the European Ceramic Society*, 17, (1997).
 30. A. C. Caballero, J. F. Fernández, C. Moure, P. Durán and Y.-M. Chiang, *Journal of the American Ceramic Society*, 81, (1998).
 31. M. F. Peintinger, D. V. Oliveira and T. Bredow, *J. Comput. Chem.*, 34, (2013).
 32. D. Zagorac, K. Doll, J. C. Schön and M. Jansen, *Chemistry - A European Journal*, 18, (2012).
 33. P. J. Hay and W. R. Wadt, *J. Chem. Phys.*, 82, (1985).
 34. A. D. Becke, *J. Chem. Phys.*, 98, (1993).
 35. A. D. Becke, *Phys. Rev. A*, 38, (1988).
 36. C. Pisani, R. Dovesi and C. Roetti, *Hartree-Fock ab initio Treatment of Crystalline Systems*. (Springer Berlin Heidelberg, 1988), *Lecture Notes in Chemistry*, 48.
 37. R. Dovesi, R. Orlando, B. Civalleri, C. Roetti, V. R. Saunders and C.-M. Zicovich-Wilson, *Zeitschrift für Kristallographie*, 220, (2005).
 38. R. Dovesi, V. R. Saunders, C. Roetti, R. Orlando, C. M. Zicovich-Wilson, F. Pascale, B. Civalleri, K. Doll, N. M. Harrison, I. J. Bush, P. D'Arco and M. Llunell, *CRYSTAL09 User's Manual* (University of Torino, Torino, 2009).
 39. A. Kokalj, *J. Mol. Graphics Modell.*, 17, (1999).
 40. A. Kokalj, *Comput. Mater. Sci.*, 28, (2003).
 41. A. R. Denton and N. W. Ashcroft, *Phys. Rev. A*, 43, (1991).
 42. L. Vegard, *Zeitschrift für Physik*, 5, (1921).
 43. L. E. Smart, *Solid state chemistry: an introduction*. (Taylor & Francis, Boca Raton, 2005), 3 ed. edn.
 44. W. Wang, Q. Zhao, J. Xu and D. Yu, *CrystEngComm*, 14, (2012).
 45. S. Cho, S. Kim, E. Oh, S.-H. Jung and K.-H. Lee, *CrystEngComm*, 11, (2009).
 46. P. Chen, L. Gu and X. Cao, *CrystEngComm*, 12, (2010).
 47. Y. Yang, J. Qi, W. Guo, Q. Liao and Y. Zhang, *CrystEngComm*, 12, (2010).
 48. L. J. Brillson and Y. Lu, *Journal of Applied Physics*, 109, (2011).
 49. Y. Lee, S. Lee, H. T. Ryu and D. Y. Kim, *AIP Conference Proceedings*, 1399, (2011).
 50. J.-Z. Kong, A.-D. Li, H.-F. Zhai, H. Li, Q.-Y. Yan, J. Ma and D. Wu, *Journal of Hazardous Materials*, 171, (2009).
 51. Z. Ali, S. Ali, I. Ahmad, I. Khan and H. A. Rahnamaye Aliabad, *Physica B: Condensed Matter*, 420, (2013).
 52. Q.-J. Liu, N.-C. Zhang, F.-S. Liu, H.-Y. Wang and Z.-T. Liu, *physica status solidi (b)*, 250, (2013).

Luis Henrique da Silveira Lacerda^{1*}, Renan Augusto Pontes Ribeiro¹, Ageo Meier de Andrade¹, Alexandre Camilo Jr.², Sérgio Ricardo de Lazaro¹

¹ Ponta Grossa State University, Department of Chemistry, PR

² Ponta Grossa State University, Department of Physics, PR

*E-mail: lhslacerda1@gmail.com

Structural Determination of Complex Natural Products by Quantum Mechanical Calculations of ^{13}C NMR Chemical Shifts: Development of a Parameterized Protocol for Terpenes

Ana Carolina F. Albuquerque, Daniel J. Ribeiro & Mauro B. Amorim

Introduction

In the last decades, Nuclear Magnetic Resonance (NMR) spectroscopy has established itself as one of the most important techniques for structural determination of natural products.¹ Despite the current advances in multidimensional techniques and in probe technology,^{1,2} instances of revision of structures erroneously established for natural products are still common in the literature.³ With the recent development of quantum mechanical methods and the availability of modern computers, the prediction of chemical shifts through *ab initio* and Density Functional Theory (DFT) calculations has become a very powerful tool for assistance in the assignment of chemical shifts and in the structural determination of complex organic molecules, such as natural products.⁴⁻⁶

With the aim to achieve a good ratio between accuracy and computational cost, calculated chemical shifts can be corrected through the use of scaling factor procedures. It has been established in the literature that the application of this approach can reduce systematic errors inherent in theoretical calculations.⁶ Even though in recent years there has been the development of several scaling factors,⁷⁻¹¹ there are no studies in the literature reporting the use of scaling factors parameterized for a specific class of natural products.

In this work, we present the development of a calculation protocol for terpenes, a class of natural products with a board distribution among plant species and with great importance due to its biological and pharmacological activities.¹² This protocol consists of GIAO-DFT calculations of chemical shifts and application of a scaling factor parameterized with

terpenes, in order to ensure accurate structural determination of this class of natural products.

Methods

In order to reduce the computational costs in our calculations, we parameterized the scaling factor using sesquiterpene molecules, a sub-class of terpenes with structural frameworks containing only 15 carbon atoms.¹³

A set of 10 sesquiterpene molecules (figure 1), whose structures have been reliably elucidated in literature,¹⁴⁻²³ were selected and submitted to randomized conformational searches using Monte Carlo method and MMFF force field. The most significant conformations of each compound, considering an initial energy cutoff of 10 kcal.mol⁻¹, were selected to single-point energy calculations at the B3LYP/6-31G(d) level of theory. All conformations within 5 kcal.mol⁻¹ of energy were selected to geometry optimization calculations carried out at the mPW1PW91/6-31G(d) level of theory. Population-averaged ^{13}C nuclear magnetic shielding constants (δ) were calculated using GIAO method at the same level of theory and assuming Boltzmann statistics. Chemical shifts (δ) were obtained as $\delta_{\text{calc}} = \delta_{\text{TMS}} - \delta$, where δ_{TMS} is the shielding constant of the reference compound, tetramethylsilane (TMS), calculated at the same level of theory. All quantum mechanical calculations were performed in gas phase, using Gaussian 09 software package.²⁴

The scaling factor was generated by plotting calculated (δ_{calc}) against experimental chemical shifts of the set of sesquiterpenes. Thus, slope (a) and intercept (b) values

obtained from this linear regression can be used to generate scaled chemical shifts (δ_{scal}) from as δ_{calc} , using the expression $\delta_{\text{scal}} = a \cdot \delta_{\text{calc}} + b$.

In order to validate the protocol, the scaling factor was used to obtain δ_{scal} for (4S)-3-ishwarone (11), with a rare ishwarane skeleton,²⁵ and 9-*epi*-presilphiperfolan-1-ol (13), a triquinane sesquiterpene.²⁶ Additionally, aiming to evaluate the ability of the method to distinguish possible isomers of the terpenes, we also computed chemical shifts for the (4R)-diastereomer of 3-ishwarone (12),²⁷ and for the known regioisomer of 9-*epi*-presilphiperfolan-1-ol, presilphiperfolan-9-ol (14)²⁸ (figure 2).

Finally, with the purpose of demonstrating that this calculation protocol can be applied for the prediction of chemical shifts of larger terpenes, we computed chemical shifts for the triterpene oleana-12(13),15(16)-dienoic acid (15)²⁹ (figure 2).

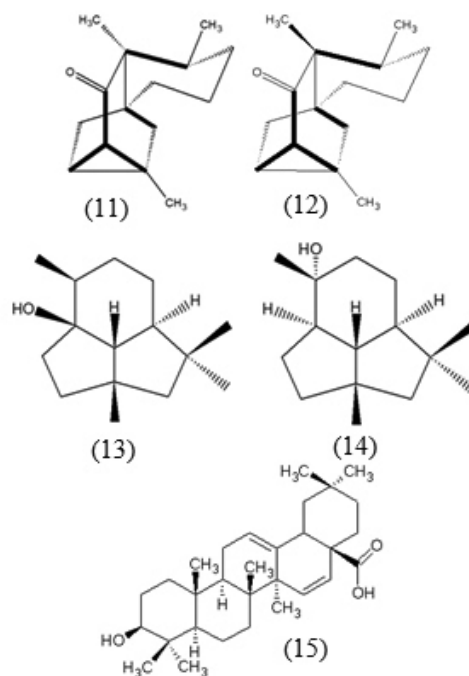


Figure 2. Structures of (4S)-3-ishwarone (11), (4R)-3-ishwarone (12), 9-*epi*-presilphiperfolan-1-ol (13), presilphiperfolan-9-ol (14) and oleana-12(13), 15(16)-dienoic acid (15).

Results and Discussion

With the purpose to ensure that the calculation protocol could be applied to any terpene, it was selected a series of sesquiterpenes with varied and complex structural frameworks (figure 1). Its ^{13}C chemical shifts were calculated according to procedures described in previous section. Statistical parameters, obtained from calculated and experimental chemical shifts of molecules 1-10, are shown in table 1.

Table 1. Statistical parameters obtained from δ_{calc} and δ_{exp} ^{13}C chemical shifts of molecules 1-10.

Statistical parameters	Values
Mean Absolute Deviation (MAD)	2.91 ppm
Root Mean Square Deviation (RMSD)	4.08 ppm
Correlation coefficient (r^2)	0.9987
Slope (a)	1.0564
Intercept (b)	-2.1945

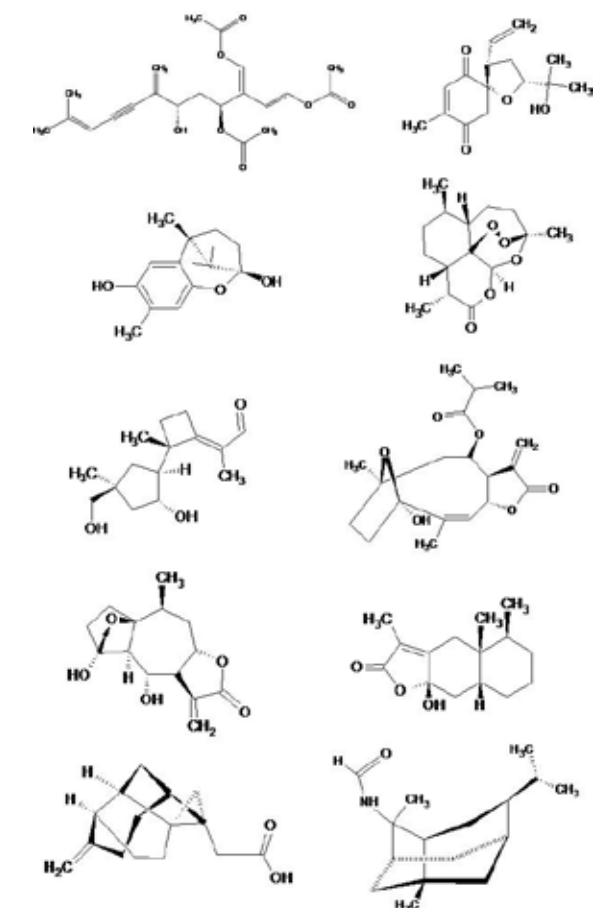


Figure 1. Structures of sesquiterpenes 1-10, used for parameterization.

Both MAD and RMSD parameters indicate errors between theoretical and experimental data within the range of expected deviations for ^{13}C nuclei calculated with DFT.6 Furthermore, r^2 value also indicates an excellent correlation between calculated and experimental chemical shifts.

Thereby, results in table 1 show that the calculation protocol employed in this work, even without the application of a scaling factor, can reproduce experimental ^{13}C chemical shifts with satisfactory accuracy.

Slope (a) and intercept (b) values in table 1 were used to obtain scaled chemical shifts for terpenes 11-15. Table 2 shows MAD, RMSD, maximum error (E_{\max}) and r^2 values, obtained from theoretical and experimental data, before and after application of the scaling factor, for molecules 11, 13 and 15.

Table 2. MAD, RMSD, E_{\max} and r^2 values obtained from theoretical and experimental ^{13}C chemical shifts for molecules 11, 13 and 15.

Statistical parameters	(4S)-3-ishwarone (11)	
	Before linear scaling	After linear scaling
MAD	1.33	0.46
RMSD	2.56	0.60
E_{\max}	9.30	1.20
r^2	0.9999	0.9999
9- <i>epi</i> -presilphiperfolan-1-ol (13)		
	Before linear scaling	After linear scaling
MAD	1.11	0.54
RMSD	1.49	0.75
E_{\max}	2.90	1.85
r^2	0.9988	0.9988
Oleana-12(13),15(16)-dienoic acid (15)		
	Before linear scaling	After linear scaling
MAD	1.71	1.35
RMSD	2.84	1.89
E_{\max}	10.96	5.96
r^2	0.9982	0.9982

The values of the statistical parameters, shown in table 2, indicate once again that the calculation protocol employed to the three validation molecules (11, 13 and 15) can generate theoretical chemical shifts well converged towards experimental values.

Particularly, the significant reduction in MAD, RMSD and E_{\max} values after application of a linear scaling procedure shows that this is a powerful tool to reduce errors from calculated chemical shifts.

Furthermore, the results obtained for triterpene 15 show that the calculation protocol developed in this work can be applied for the prediction of ^{13}C chemical shifts of higher classes of terpenes with reasonable accuracy.

In order to demonstrate that the theoretical method employed in this work is able to accurately distinguish (4S)-3-ishwarone (11) from its diastereomers, we made a comparison of the experimental data obtained for 11 with the theoretical data for its (4R)-diastereomer, 12. Statistical values obtained from this comparison are presented in table 3.

Table 3. MAD, RMSD, E_{\max} and r^2 values obtained from theoretical ^{13}C chemical shifts of molecule 12 and experimental data of molecule 11.

Statistical parameters	Before linear scaling	After linear scaling
MAD	3.23	2.47
RMSD	4.66	3.68
E_{\max}	11.64	10.78
r^2	0.9939	0.9939

The comparison between experimental chemical shifts from the (4S)-diastereomer of 3-ishwarone (11) with theoretical chemical shifts from the (4R)-diastereomer (12) yield significantly larger deviations than those shown in table 2. Therefore, these data indicate that the calculation protocol is able to successfully distinguish between diastereomers.

In a similar manner, with the purpose to evaluate the ability of the method to distinguish regioisomers, we also made a comparison between the experimental data from 9-*epi*-presilphiperfolan-1-ol (13) with the theoretical data obtained for one of its regioisomers, presilphiperfolan-9-ol (14). Statistical values obtained from this comparison are presented in table 4.

Table 4. MAD, RMSD, E_{\max} and r^2 values obtained from theoretical ^{13}C chemical shifts of molecule 14 and experimental data of molecule 13.

Statistical parameters	Before linear scaling	After linear scaling
MAD	8.45	8.35
RMSD	12.64	12.88
E _{max}	35.57	37.45
r^2	0.5301	0.5301

Statistical values shown in table 4 indicate a worst correlation and larger deviations between the two data sets than those in table 2. Thereby, we can safely assume that the calculation protocol employed in this work is able to accurately distinguish between two regioisomers.

Conclusions

Considering a set of 10 sesquiterpenes, we developed a parameterized protocol for the calculation of ^{13}C NMR chemical shifts of terpenes. This protocol, consisted of GIAO-DFT calculations and a linear scaling factor, was able to yield calculated chemical shifts with satisfactory accuracy.

Therefore, the calculation protocol developed in this work is a very attractive tool as an alternative to more computationally demanding approaches for the calculation of complex organic structures, such as terpenes.

Acknowledgments

The authors are grateful for the support given from FAPERJ, CAPES and CNPq.

References

1. A. G. Petrovic, A. Navarro-Vázquez, J. L. Alonso-Gómez, *Curr. Org. Chem.*, **14**, 1612, **2010**
2. F. E. Koehn and G. T. Carter, *Nat. Rev.*, **4**, 206, **2005**
3. K. C. Nicolaou and S. A. Snyder, *Ang. Chem. Int. Ed.*, **44**, 1012, **2005**
4. T. Helgaker, M. Jaszunski, K. Ruud, *Chem. Rev.*, **99**, 293, **1999**
5. G. Bifulco, P. Dambruoso, L. Gomez-Paloma, R. Riccio, *Chem. Rev.*, **107**, 3744, **2007**
6. M. W. Lodewyk, M. R. Siebert, D. J. Tantillo, *Chem. Rev.*, **112**, 1839, **2012**
7. N. J. R. van E. Hommes and T. Clark, *J. Mol. Model.*, **11**, 175, **2005**
8. G. K. Pierens, *J. Comput. Chem.*, **35**, 1388, **2014**
9. A. E. Aliev, D. Courtier-Murias, S. Zhou, *J. Mol. Struct. (THEOCHEM)*, **893**, 1, **2009**
10. F. L. P. Costa, A. C. F. de Albuquerque, R. M. Borges, F. M. dos S. Junior, M. B. de Amorim, *J. Comput. Theor. Nanosci.*, **11**, 1, **2014**
11. F. L. P. Costa, A. C. F. de Albuquerque, F. M. dos S. Junior, M. B. de Amorim, *J. Phys. Org. Chem.*, **23**, 972, **2010**
12. P. M. Dewick, *Medicinal Natural Products: A Biosynthetic Approach*, 3 ed., Wiley, **2007**
13. B. M. Fraga, *Nat. Prod. Rep.*, **30**, 1226, **2013**
14. L. Commeiras, J. Thibonnet, J. L. Parrain, *Org. Biomol. Chem.*, **7**, 425, **2009**
15. C. Huang and B. Liu, *Chem. Commun.*, **46**, 5280, **2010**
16. M. Yoshida, Y. Shoji, K. Shishido, *Org. Lett.*, **11**, 1441, **2009**
17. J. S. Yadav, B. Thirupathaiah, P. Srihari, *Tetrahedron*, **66**, 2005, **2010**
18. G. R. Pettit, Y. Meng, R. K. Pettit, D. L. Herald, F. Hogan, Z. A. Cichacz, *Bioorg. Med. Chem.*, **18**, 4879, **2010**
19. T. Nakamura, K. Tsuboi, M. Oshida, T. Nomura, A. Nakazaki, S. Kobayashi, *Tetrah. Lett.*, **50**, 2835, **2009**
20. S. Rosselli, A. Maggio, R. A. Raccuglia, M. Bruno, *Eur. J. Org. Chem.*, **2010**, 3093, **2010**
21. A. Bodensieck, W. M. F. Fabian, O. Kunert, F. Belaj, S. Jahangir, W. S. Hly, R. Bauer, *Chirality*, **22**, 308, **2010**
22. T. Magauer, J. Mulzer, K. Tiefenbacher, *Org. Lett.*, **11**, 5306, **2009**
23. A. Srikrishna, G. Ravi, D. R. C. V. Subbaiah, *Synlett*, **1**, 32, **2009**
24. Gaussian 09, Revision D.01, Gaussian, Inc., Wallingford CT, **2009**
25. J. H. G. Lago, A. Oliveira, E. F. Guimarães, M. J. Kato, *J. Braz. Chem. Soc.*, **18**, 638, **2007**
26. P. Joseph-Nathan, S. G. Leitão, S. C. Pinto, G. G. Leitão, H. R. Bizzo, F. L. P. Costa, M. B. de Amorim, N. Martínez, E. Dellacassa, A. Hernández-Barragán, N. Pérez-Hernández, *Tetrah. Lett.*, **51**, 1963, **2010**
27. F. M. dos Santos Jr., L. S. M. Velozo, E. M. de Carvalho, A. M. Marques, R. M. Borges, A. P. F. Trindade, M. I. S. dos Santos, A. C. F. de Albuquerque, F. L. P. Costa, M. A. C. Kaplan, M. B. de Amorim, *Molecules*, **18**, 13520, **2013**
28. J. A. Marco, J. F. Sanz-Cervera, M. D. Morante, V. García-Lliso, J. Vallés-Xirau, J. Jakupovic, *Phytochem.*, **41**, 837, **1996**
29. J. Bhattacharyya and E. V. L. Cunha, *Phytochem.*, **31**, 2546, **1992**

Ana Carolina Ferreira de Albuquerque^{a*},
Daniel Joras Ribeiro^a & Mauro Barbosa de Amorim^a

^aInstituto de Pesquisas de Produtos Naturais – Universidade Federal do Rio de Janeiro

*E-mail: maurobdeamorim@gmail.com

Virtual HTS and Free Energy Calculation of Brazilian Natural Compounds Using OOMT as Pharmacological Targets Database

Ana Paula Carregal, Flávia V. Maciel, Juliano B. Carregal & Alex G. Taranto

Introduction

The Virtual Screening (VS) methods are useful to perform in silico search of lead compounds in large data base. This methodology selects the compounds with the best interaction energies for performing biological assays. Considering the natural products are a major source of lead compounds, VS applied to them have great possibilities for the development of a new drugs^{1,2}. In general, the first step in the development of a new drug is understanding of the molecular target of interest. The Our Own Molecular Targets (OOMT) is a bank of proteins containing selected molecular targets for cancer, malaria and dengue³. In this context, VS was carried out on natural compounds against molecular targets on OOMT for the identification of hits for diseases that require new therapeutic alternatives.

Methods

The Brazilian natural compounds database was obtained from ZINC platform⁴, which consist of 473 compounds deposited by State University of Feira de Santana. These compounds were selected for VS methodology applied on OOMT. The geometry of the compounds were optimized through the universal force field⁵ (UFF) implemented in the Gaussian 09W⁶ software.

Next, docking calculation was performed against 36 receptors deposited on OOMT. The AutoDock Vina⁷ software was used for docking simulation. The effectiveness of AutoDock Vina program and the affinity

of the compounds were evaluated using the redocking methodology⁸. The intermolecular interactions were described by Discovery Studio⁹ software. The resultant binding energy of each natural compounds obtained from docking step was divided by the crystallographic binding energy generating δ values (Equation 1). Natural compounds with δ value equal or bigger than one will be sent for further biological assay¹⁰.

$$\delta = \frac{\text{Natural compounds binding energy}}{\text{Crystallographic ligand binding energy}}$$

Equation 1. Determination of δ values.

Then, drug-likeness property was calculated in DataWarrior¹¹ program to select compounds with better pharmacokinetic properties¹². Following, the previous Autodock Vina results were refinement by free energy calculations using Dock6 software. Hence, the natural compounds selected by the delta value and by the drug-likeness were submitted to the calculation of molecular docking, energy minimization and molecular dynamics (MD) using Dock6¹³ program. The system was minimized at 5000 cycles, and then 30000 MD steps were run at 310 K, followed by a further 5000 cycles of minimization. These calculations were run for protein, the ligand and for the complex respectively. In this study were selected the three most promising ligands to describe the binding energy and intermolecular interactions.

Results and Discussion

As a result of docking simulation among 473 ligands against 36 molecular targets generated 17028 complex ligand-receptor. The delta values showed the most of the natural compounds had a better binding energy than crystallographic ligand for various OOMT proteins. This allowed to identify the best molecular targets for this study. The highest δ values obtained were the molecular targets with PDB code: 1W6M, 2QHN and 3JYA. The 1W6M, 2QHN and 3JYA receptors are involved in cancer process. Figure 1 shows the tertiary structure of molecular targets complexed with docked ligands. As can be seen, the ligands ZINC69482333, ZINC01721695 and ZINC01557254 were able to binding to 1W6M, 2QHN and 3JYA, respectively.

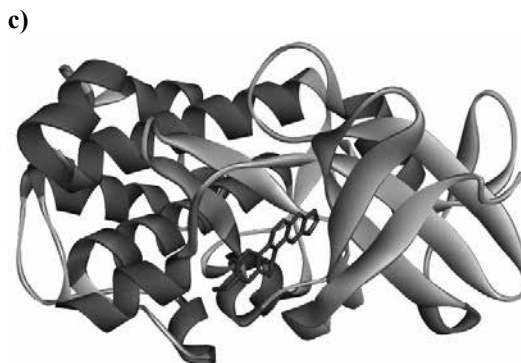
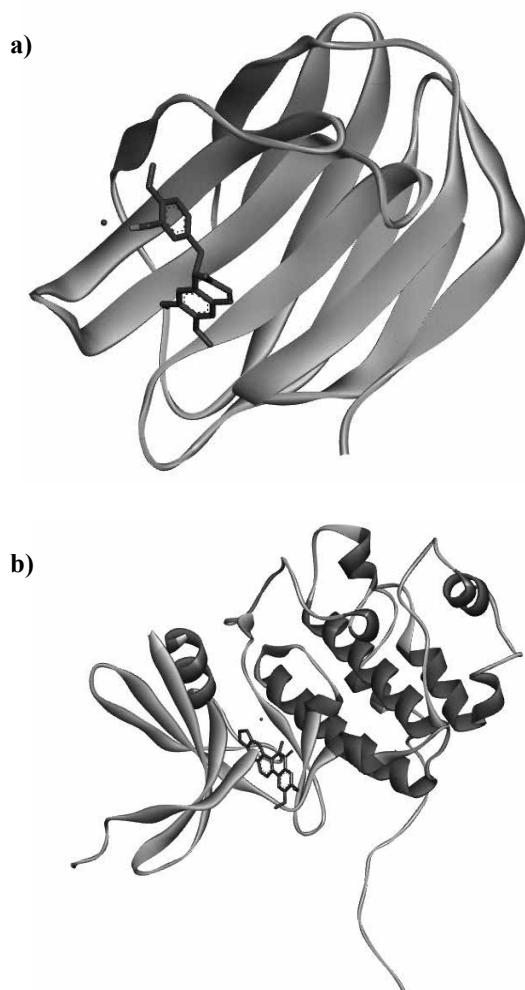


Figure 1. VS results of natural compounds on OOMT. a) Ligand ZINC69482333 complexed with 1W6M; b) Ligand ZINC01721695 complexed to the receptor 2QHN; c) Ligand ZINC01557254 complexed to 3JYA.

In this study all molecular targets selected have involved in the cancer process. The 1W6M protein is involved in the regulation of cell migration. It has been associated with tumor malignancy. The possibility of the development of an inhibitor for this molecular target would result in inhibition of tumor migration¹⁴.

The 2QHN receptor, known as checkpoint kinase Chk1, performs the verification of the DNA and cell cycle delay for the cell to repair DNA. This function is carried out in conjunction with other proteins that in most cancers are inhibited. The Chk1 alone can not accomplish this DNA check function and cell death of cells with damaged DNA would be the best option to stop tumor growth. Inhibition of Chk1 stops the cell cycle leading it to death¹⁵.

The 3JYA protein is a cytoplasmic Pim kinase that controls programmed cell death by phosphorylation of substrates that regulate apoptosis and the cell metabolism. The pharmacological manipulation of these kinases may be useful for the treatment of various diseases such as cancer, inflammatory diseases and ischemic disorders¹⁶.

In addition to the δ values, druglikeness was used to select the best compounds. A positive value of druglikeness indicates that the molecule contains predominantly fragments which are frequently present in commercial drugs. Figure 2 shows the three ligands selected by the VS methodology and druglikeness. The ligands ZINC69482333, ZINC01721695 and ZINC01557254 showed druglikeness values of 2,14; 2,22 and 2,42 respectively.

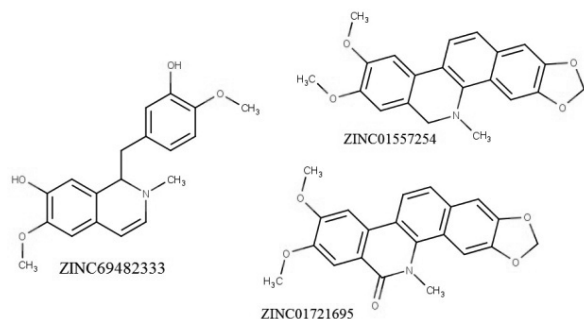


Figure 2. VS results of natural compounds on OOMT.

Summarising the VS results, table 1 shows the binding energy and delta values for ZINC69482333, ZINC01721695 and ZINC01557254 ligands against 1W6M, 2QHN and 3JYA molecular targets.

The binding energy of the complex was determined by three methods, the first one using the AutoDock Vina and the others through Dock6 (Grid and Amber Score Score). This protocol was applied to decrease false positive results. The first filter for elimination of false positive results (δ value) was applied to the results provided by AutoDock Vina program. The Complex 1W6M-ZINC69482333, 2QHN-ZINC01721695, and 3JYA-ZINC01557254 were those with the largest delta values, and therefore were subjected to energy minimization and molecular dynamics calculations. The Table 1 shows that natural compounds can complex with the targets in all methods studied. In order to improve the docking results the free energy of the complex were carried out using AMBER Score implanted in the Dock6 program. The AMBER score implements molecular mechanics simulations with implicit solvent

(Generalized Born solvation model17) applying the all-atom force field AMBER traditional for all protein atoms and the general AMBER force field (GAFF18) for the ligand atoms. After these calculations it was observed that natural compounds showed a better energy value than those displayed by crystallographic ligands. These results showed that the compounds ZINC69482333, and ZINC01721695 ZINC01557254 can bind the molecular targets 1W6M, 2QHN and 3JYA, respectively.

The intermolecular interactions between ligands and receptors are shown in the figure 3. In the 3D representation the green and pink colour represent hydrogen bond acceptor and donor regions in the binding site, respectively; the green dash lines show hydrogen bonds and hydrophobic interactions. In addition, 2D pharmacophoric map shows van der Waals and electrostatics interactions by green and pink colours, respectively. In this context, the figures 3a, 3c and 3e depict the 3D intermolecular interactions; whereas the figures 3b, 3d and 3f summarize the 2D pharmacophoric map formed by ligands ZINC69482333, ZINC01721695 and ZINC01557254 with the proteins 1W6M, 2QHN and 3JYA, respectively.

In general, in complex 1W6M - ZINC69482333, the electrostatic interaction occurred with Ser1029, Asn1046, Arg1048, His1052 and Glu1071. In addition, van der Waals interactions were carried out with Val1031, His1044, Asn1061, Trp1068 and Gly1069. Furthermore, a pi-stack interaction was formed between amino acid Trp1068 and aromatic moiety of ligand ZINC69482333 in the protein 1W6M protein.

Similar, the intermolecular interaction standard was observed for the interaction between ZINC01721695 and 2QHN. The electrostatic interactions can be observed

Table 1. Binding energy and δ value of the selected compounds.

Molecular Target	Ligand	δ Value	Energy (kcal/mol)		
			Autodock Vina	Dock (standard)	Dock (AMBER)
1W6M	Crystallographic	1.44	-4.3	-26.74	-18.93
	ZINC69482333		-6.2	-33.54	-26.55
2QHN	Crystallographic	1.19	-7.4	-37.56	-46.08
	ZINC01721695		-8.8	-41.43	-47.41
3JYA	Crystallographic	1.11	-8.4	-33.59	-64.00
	ZINC01557254		-9.3	-35.92	-77.94

with Leu15, Glu91. On the other hand, van der Waals interactions were carried out with Gln13, Val23, Ala36, Leu137, Leu84, Glu85, Tyr86, Cys87 (Figure 3c and 3d). Additionally, Figure 2d highlights a hydrogen bond between a water molecule and the ligand.

Finally, figure 3e and 3f shows the interactions of ZINC01557254 with the 3JYA molecular target. The

electrostatic interaction occurred with Lys76, Val126 and Asp186. Besides, van der Waals interactions were carried out with Leu44, Gly45, Ala65, Ile104, Leu120, Glu124, Asp131, Leu174 and Ile185. Additionally, in Figure 2f possible to visualize the formation of Pi interactions between two amino acids (Leu 44 and Ile185) and 3JYA binding site of the protein).

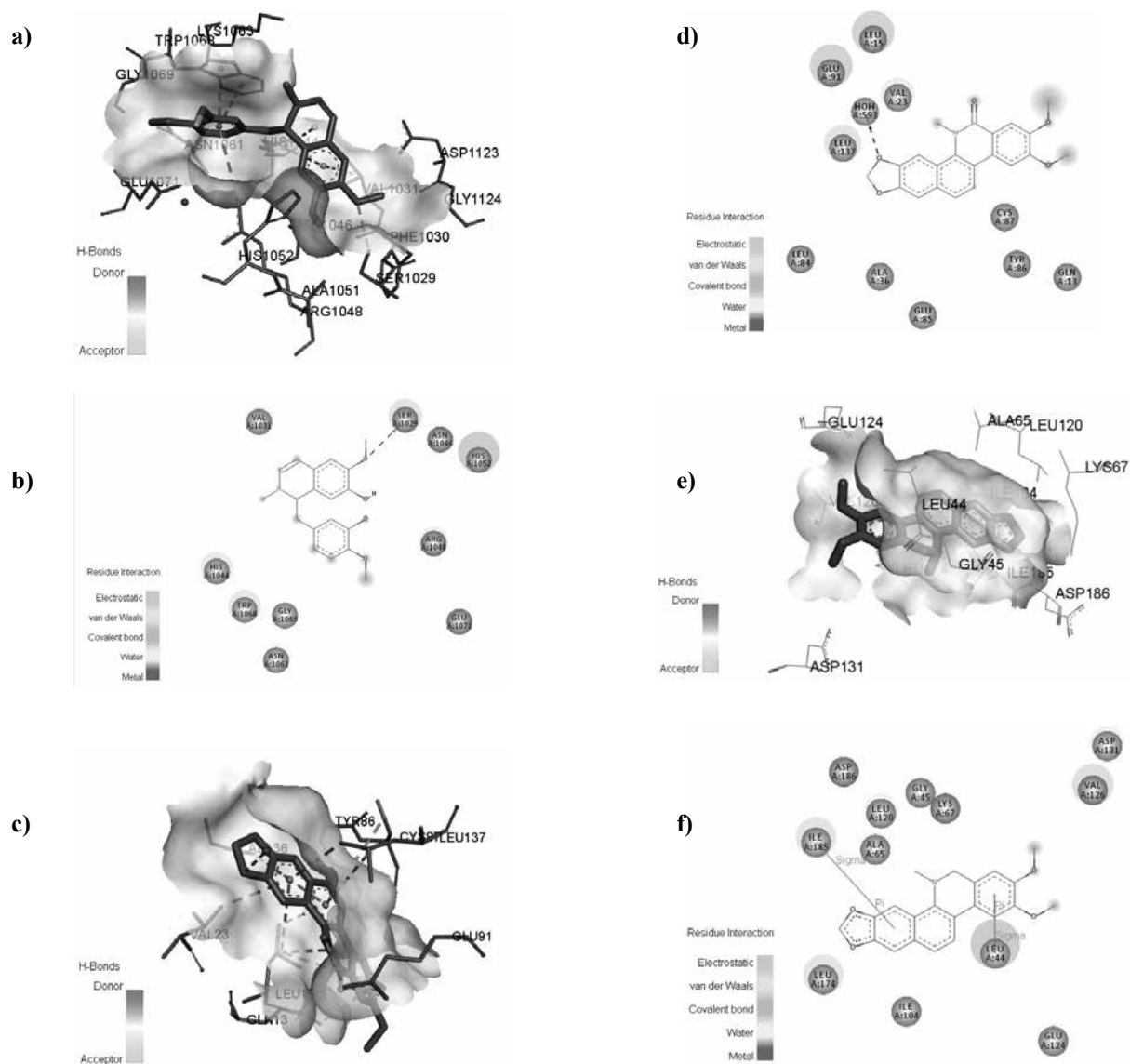


Figure 3. a) ligand ZINC69482333 - 1W6M in 3D; b) ligand ZINC69482333 - 1W6M in 2D; c) ligand ZINC01721695 - 2QHN in 3D d) ligand ZINC01721695 - 2QHN in 2D; e) ZINC01557254 - 3JYA in 3D; f) ZINC01557254 - 3JYA in 2D.

Conclusions

Among 473 natural compounds studied using OOMT data base, three of them showed a binding energy profile better than the crystallographic ligands. The calculation of free energy has shown that natural compounds can complex with molecular targets 1W6M, 2QHN and 3JYA. Consequently, new hits were formed in drug discovery context. These findings suggested the respective molecular target for these natural compounds. Further, a ligand optimization process can be initiated as a cycle between semi-synthesis and biological assay improving the anticancer property.

Acknowledgments

The authors are grateful for the support given from the FAPEMIG (APQ-00557-14), CAPES, CNPq (UNIVERSAL 449984/2014-1) and PPGCF/UFSJ .

References

1. R. S. Ferreira and B. Oliva, *Quim. Nova*, 34, 1770, (2011).
2. M. S. Butler, *J. Nat. Prod.*, 67, 2141, (2004).
3. A. P. Carregal, M. Comar Jr, A. G. Taranto, *Biochem. Biotechnol. Reports*, 2, 14, (2013).
4. J. J. Irwin, T. Sterling, M. M. Mysinger, E. S. Bolstad, R. G. Coleman, *J. Chem. Inf. Model*, 52, 1757, (2012).
5. A. K. Rappe, C. J. Casewit, K. S. Colwell, W. Goddard, W. M. Skiff, *J. Am. Chem. Soc.*, 114, 10024, (1992).
6. M. J. Frisch, G. W. Trucks, H. B. Schlegel, G. E. Scuseria, M. A. Robb, J. R. Cheeseman, G. Scalmani, V. Barone, B. Mennucci, G. A. Petersson, H. Nakatsuji, M. Caricato, X. Li, H. P. Hratchian, A. F. Izmaylov, J. Bloino, G. Zheng, J. L. Sonnenberg, M. Hada, M. Ehara, K. Toyota, R. Fukuda, J. Hasegawa, M. Ishida, T. Nakajima, Y. Honda, O. Kitao, H. Nakai, T. Vreven, J. A. Montgomery, Jr., J. E. Peralta, F. Ogliaro, M. Bearpark, J. J. Heyd, E. Brothers, K. N. Kudin, V. N. Staroverov, R. Kobayashi, J. Normand, K. Raghavachari, A. Rendell, J. C. Burant, S. S. Iyengar, J. Tomasi, M. Cossi, N. Rega, J. M. Millam, M. Klene, J. E. Knox, J. B. Cross, V. Bakken, C. Adamo, J. Jaramillo, R. Gomperts, R. E. Stratmann, O. Yazyev, A. J. Austin, R. Cammi, C. Pomelli, J. W. Ochterski, R. L. Martin, K. Morokuma, V. G. Zakrzewski, G. A. Voth, P. Salvador, J. J. Dannenberg, S. Dapprich, A. D. Daniels, Ö. Farkas, J. B. Foresman, J. V. Ortiz, J. Cioslowski, and D. J. Fox, Gaussian, Inc., Wallingford CT, 2009.
7. O. Trott and A. J. Olson, *J. Comput. Chem.*, 31, 455, (2010).
8. B. D. Bursulaya, M. Totrov, R. Abagyan, C. L. Brooks, J. *Comput. Aided. Mol. Des.*, 17, 755, (2004).
9. Accelrys Software Inc., Discovery Studio Modeling Environment, Release 3.1, San Diego: Accelrys Software Inc., 2009.
10. G. Lauro, A. Romano, R. Riccio, G. Bifulco, *J. Nat. Prod.*, 74, 1401, (2011).
11. Inc.. All Rights Reserved. Copyright © 2008 Scientific Data Systems Inc.. All Rights Reserved. (2008).
12. W. P. Walters, M. Murcko, *Adv. Drug Deliv. Rev.*, 54, 255, (2002).
13. P. T. Lang, S. R. Brozell, S. Mukherjee, E. F. Pettersen, E. C. Meng, V. Thomas, R. C. Rizzo, D. Case, T. L. James, I. D. Kuntz, *RNA*, 15, 1219, (2009).
14. M. F. López-Lucendo, D. Sólis, S. A. J. Hirabayashi, K. Kasai, H. Kaltner, H. Gabius, A. Romero, *J. Mol. Biol.*, 343, 957, (2004).
15. E. J. Brnardic, R. M. Garbaccio, M. E. Fraley, E. S. Tasber, J. T. Steen, K. L. Arrington, V. Y. Dudkin, G. D. Hartman, S. M. Stirdivant, B. Drakas, K. Rickert, E. S. Walsh, K. Hamilton, C. Buser, J. Hardwick, W. Tao, S. C. Back, X. Mao, R. B. Lobell, L. Sepp-Lorenzino, Y. Yan, M. Ikuta, S. K. Munshi, L. C. Kuo, C. Kreatsoulas, *Bioorganic Med. Chem. Lett.*, 17, 5989, (2007).
16. R. Amaravadi and C. B. Thompson, *J. Clin. Invest.*, 115, 2618, (2005).
17. A. Onufriev, D. Bashford, D. Case, *Proteins Struct. Funct. Genet.*, 55, 383, (2004).
18. J. Wang, R. M. Wolf, J. W. Caldwell, P. A Kollman, D. A. Case, *J. Comput. Chem.*, 25, 1157, (2004).

Ana Paula Carregal*, Flávia V. Maciel,
Juliano B. Carregal & Alex G. Taranto

Universidade Federal de São João del Rei – campus Centro-Oeste
35501-296, Divinópolis-MG, Brazil.

*E-mail: anapaulacarregal@gmail.com

Dispersion-Corrected Density Functional for the Correct Description on Regioselectivity Trends in Heck-Mizoroki Reaction Catalyzed by Anionic (N-Heterocycle Carbene)-Palladium Complexes

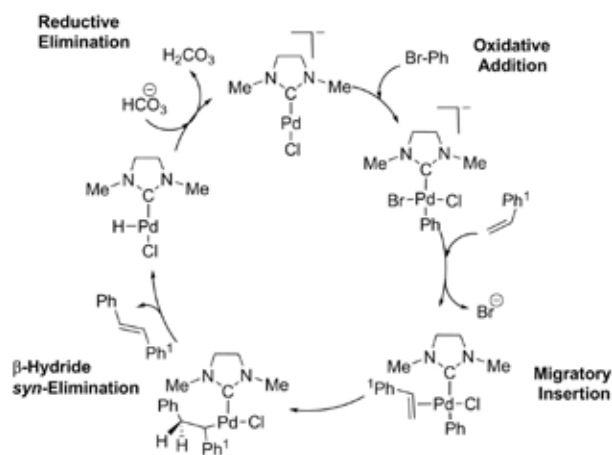
Vitor H. M. Silva, Oscar Navarro & Ataulpa A. C. Braga

Introduction

Palladium-catalyzed cross-coupling reactions are an important field in organic synthesis and organometallic chemistry. Its importance was recognized in 2010 by awarding Richard Heck, Ei-ichi Negishi and Arika Suzuki the Nobel Prize of Chemistry, for the prominent contribution to this field.¹ The Heck-Mizoroki (HM) reaction is an excellent tool for C-C sp^2 bond construction.² Historically, phosphines have been used as main ligands for palladium complexes furthering high catalytic activity in HM process, in particular cases, with excellent regio- and stereoselectivity control.³ In past decade, the N-heterocyclic carbenes (NHCs) emerged as new class of ligands in a number of cross-coupling reactions.⁴

The NHCs are strong σ -donors ligands, thus they are capable to provide better stability to transition metal complexes with highest oxidation state. Furthermore, NHCs are usually more sterically demanding than phosphines. The N-substituted pendants groups from central imidazole ring can play an important role in the reactivity and selectivity of catalyzed systems. Recently, density functional calculations were used to rationalize the role of the ionic (NHC)PdCl complex as pre-catalyst in a HM coupling reaction involving PhBr and styrene in the presence of HCO_3^- as base (Scheme 1).⁵ In this case, computational studies were applied to a

model system, in which the two SIPr groups (SIPr = 2,6-diisopropylphenyl) were replaced by Me groups (Me = methyl). Although this model system was able to provide new insights from the electronic influence of the NHC ligand in the reactivity and selectivity in HM coupling, the influence of the steric bulk from the real system over the selectivity of the catalyzed system still remains unclear.



Scheme 1. Plausible HM catalytic cycle for the (NHC)PdCl. The model system was constructed using Me groups as N-substituted in NHC ligand.

Computational studies have indicated that a correct description of dispersion interactions is crucial for modeling hindered phosphine (PPh_3) ligands in Pd-catalyzed cross-coupling reactions.⁶ Recently, Schoenebeck and collaborators showed that dispersion forces are key controlling factor to the correct description of the oxidative addition pathways involving crowded trialkyl substituent in palladium complexes.⁷ Norrby and Sigman performed theoretical calculations for the enantioselective Heck-Matsuda reaction using a *N,N*-PyOx ligand with *tert*-butyl substituent. Only dispersion-corrected density functionals were able to provide the correct stereochemistry of the product.⁸

Herein, we performed a computational study based on the density functional theory (DFT) to investigate how the real (NHC)PdCl- pre-catalyst influences the HM mechanism reaction. The main goal of this work is to analyze the regioselectivity trends by different exchange-correlation density functionals.

Methods

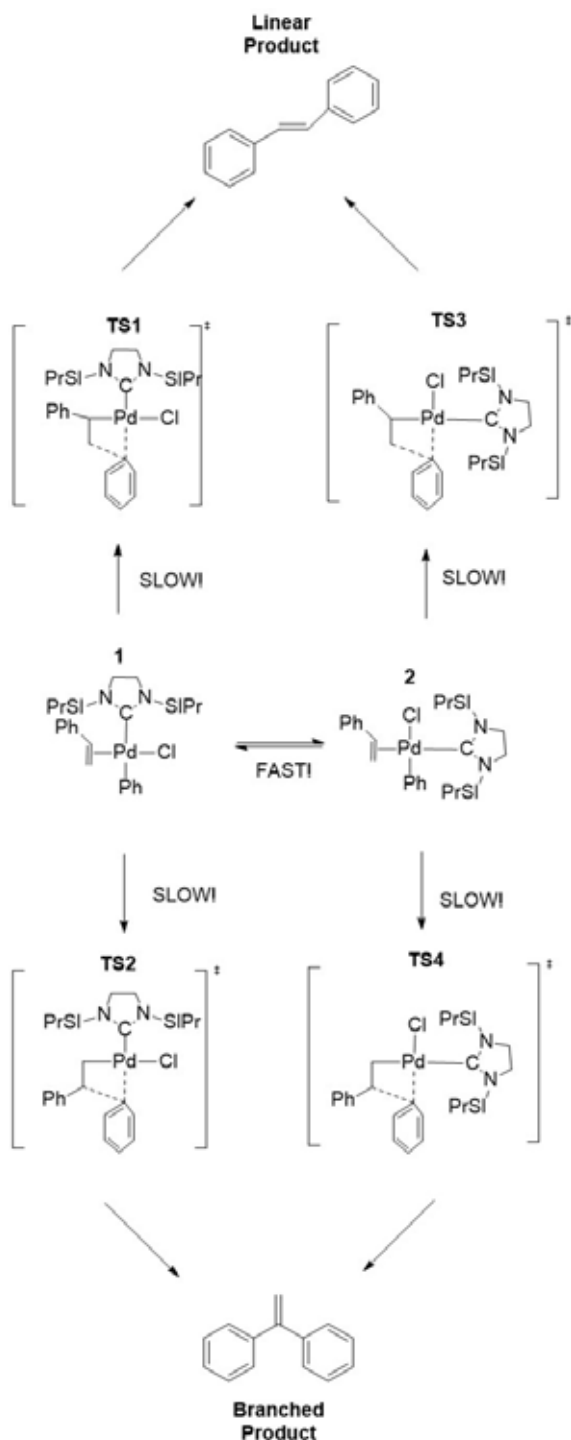
All electronic structure calculations were carried out within the DFT formalism using Gaussian09 suite of quantum chemical programs.⁹⁻¹⁰ Geometries optimizations, without any symmetry restriction were carried out in gas-phase using the GGA hybrid functionals PBE0¹¹ and B3LYP¹². The dispersion-corrected local and hybrid functional meta-GGA M06L¹³ and M06¹⁴ also were used in the current study, because these approaches have been proved to be reliable methods for transition metal kinetics-thermochemistry. The long-range-corrected hybrid GGA functional ω B97XD¹⁵ with the Grimme's empirical damped pair-wise dispersion terms (DFT-D2) was also explored.¹⁶ The SDD basis set was adopted to Pd¹⁷ and the 6-31G(d) basis set for the remaining atoms. This basis set approach is denoted as BS1 (6-31G(d), SDD (Pd)). Frequency calculations were performed in order to verify the nature of all stationary points on the potential energy surface (PES). The vibrational analysis was performed within the harmonic approximation with thermochemical data calculated at 298 K and 1 atm. Intrinsic reaction coordinate (IRC)¹⁸ calculations were used to connect reactants to products. Solvents effects were taken into account with the continuum solvation model SMD¹⁹ with DMF as the solvent. The

SMD calculations were performed as single-point energies calculations (SMD) on the optimized gas-phase geometries. In specific cases, single-point energies have been calculated using the SMD-6-311+G(d), SDD(Pd) level of theory. This basis set approaches denoted as BS2 (6-311+G(d), SDD (Pd)). All energies are presented in kcal/mol with respect to the lowest energy structure, unless otherwise specified.

Results and Discussion

The regioselective proposal for the catalyzed HM arylation is depicted in Scheme 2. The real (NHC)PdCl-complex is the catalyst. The starting aryl-palladium (II) complexes has two possible configurations, 1 and 2, with the Ph group (Ph=aryl) *trans* or *cis* to the NHC ligand, respectively. The stereoisomer 1 was found to be 10 kcal/mol higher than 2 at free energy surface, at SMD-PBE0/BS1 level of theory. It is noted the strongest NHC *trans* influence over the aryl group, increasing the energy of the intermediate 1. Besides the thermodynamic driving force in the isomerization of 1 towards to 2, we were unable to find the transition state for the isomerization via an associative or a dissociative process. A Berry pseudorotation mechanism was discarded, once a hindered steric bulk of the SIPr groups in imidazole ring is present.

In addition, it is well-known that a *cis-trans* isomerization is accelerated,^{1, 6b,8,21} when chlorine and basic ligands are present in HM catalyzed systems. Therefore, it is expected that the isomerization process would be faster than the migratory insertion of olefin into the starting intermediates 1 and 2. Consequently, the selectivity-determining step is the migratory insertion under Curtin-Hammett condition, in which the regioselectivity is determined solely by the relative energies of the competing insertion migratory transition states.²⁰ The transition states TS1 and TS3 are associated to the linear product, while the TS2 and TS4 yield the branched product. It is worthy to mention that only the linear product is detected by the experimental work, see the catalytic cycle in Scheme 1. The search for linear and branched transition states, having the full ligand SIPr, was made using DFT calculations. The dispersion-free density functional, PBE0 and B3LYP, and density functionals that take into account the dispersion forces (M06L, M06 and ω B97XD) were used.



Scheme 2. β - and γ - insertion migratory pathways starting through an isomerization between aryl-palladium (II) alkenes intermediates

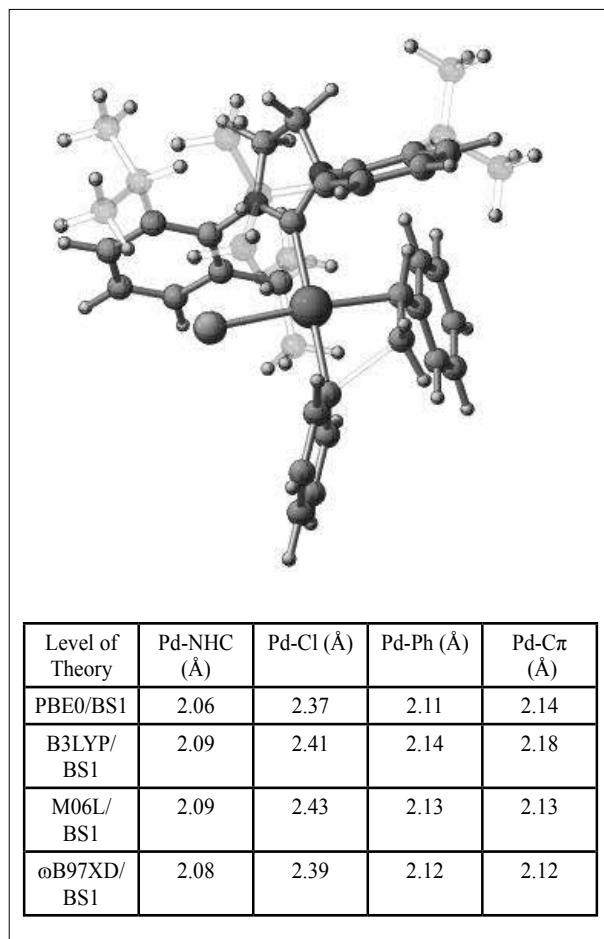


Figure 1. Crucial optimized features of TS1.

The optimized TS1 associated to linear products is illustrated in Figure 1. Its molecular structure clearly shows the C-C bond formation *via* four-membered arrangement. The dispersion has no significant impact on TS arrangement with respect to the calculations obtained using the model system. The Pd-NHC and Pd-C π bonds in NHC model (R = Me) were found to be 2.04 and 2.10 Å, respectively, at M06L/6-31+G(d), SDD (Pd) level of theory. For the real system, this bond distance is about 2.09 and 2.10 Å, respectively, at M06L/BS1. The geometries obtained using M06L and wB97XD dispersion-corrected functionals are quite close; except in the case of Pd-Cl distance where the difference was 0.4 Å shorter using wB97XD functional. Calculations

based on PBE0 and B3LYP showed larger differences compared to the dispersion-corrected methods.

The electronic influence of NHC on the reaction regioselectivity was explored with Me groups in the NHC ligand.⁵ In the model system, the β -carbon addition was preferential, and the final product was in agreement with the experimental reports. The regioselectivity trends can be understood in terms of how metal-ligand bond changes during the course of the C-C bond formation.²⁰ As the new bond is forming, relative to the β -carbon ($C\pi$), a negative charge is generated in the neighbor carbon, which results in a stronger interaction with the palladium center. In the linear transition states, this carbanion is stabilized by conjugation with the styrene, decreasing its *trans* influence. On the other hand, in the branched transition state structures, the negative charge on alkyl group is free causing strongest *trans* influence over the ligands. The NHC ligand, a stronger σ -donor ligand and π -acceptor, once the *trans* to the localized carbanion, it is expect a destabilization more pronounced in the transition states structures than to exerted by chlorine moiety, ligand with weak *trans* influence. Therefore, it is expected that TS3 and TS4 have higher energy than the TS1 and TS2. In addition, the charge separation stabilized by conjugation into TS1 and TS3 transition states structures explains the electronic influence on regioselectivity trends to the linear product. However, into the real NHC catalyst, the dispersion forces are correlated with the electronic influence of ligand, thus both chemical properties

contributed to regioselectivity of the reaction.

The computed enthalpies and Gibbs free energies in DFM solution related to the insertion transition states are shown in Table 1. The PBE0 and B3LYP density functional favor the branched product via the transition state TS2, in total disagreement with the regioselectivity reported in the experimental work.⁵ The M06L method improves the energies, decreasing in 3 and 5 kcal/mol, the stability of TS2 as predicted by the PBE0 and the B3LYP functionals, however, the free energies barriers stills report the branched configuration as preferential product. Only the long-range-corrected ω B97XD method favors the linear transition state TS1, in agreement with the experimental data. M06 single-points calculations at the B3LYP optimized geometries are a common tool in computational studies involving metal transition catalyzed systems.¹⁴ In the preset study, the B3LYP/BS1/M06/BS2 approach failed in predicting the right regioselectivity. In contrast, the ω B97XD/BS1/M06/BS2 approach was able to properly describe the experimental regioselectivity. These results show the importance of using computational approaches that account for dispersion effects. Such approaches should be use in geometry optimizations, mainly for crowded organometallics catalysts. Importantly, no matter whether dispersion is included or not, the highest energies are obtained for TS3 and TS4 transition sates, showing that the strong electronic influence of NHC ligand can overcome the attractive intramolecular dispersion forces

Table 1. Relative enthalpies and free energies in DFM solution. The energies are computed with respect to the lowest energy transition state structure.

Level of Theory	ΔH_{DMF} (kcal/mol)				ΔG_{DMF} (kcal/mol)			
	TS1	TS2	TS3	TS4	TS1	TS2	TS3	TS4
PBE0/BS1	3.0	0.0	7.8	10.2	4.1	0.0	8.7	10.9
B3LYP/BS1	4.2	0.0	8.6	10.9	6.0	0.0	10.2	12.0
M06L/BS1	0.0	0.4	4.4	7.8	1.1	0.0	6.5	10.9
ω B97XD/BS1	0.0	0.6	5.5	6.7	0.0	0.8	7.2	7.7
ω B97XD/BS1// ω B97XD/BS2	0.0	0.8	5.8	7.6	0.0	1.0	7.5	8.5
B3LYP/BS1// M06/BS2	0.7	0.0	3.6	6.5	2.5	0.0	5.2	7.6
ω B97XD/BS1// M06/BS2	0.0	0.2	3.9	6.7	0.0	0.5	5.7	7.6

of real ligands. Furthermore, our results suggest that the regioselectivity in the present system follows a typical Harper mechanism²¹, wherein the major product, in this case the linear configuration, arises from a preceding minor intermediate, the alkene-palladium (II) complex 1.

Conclusions

In conclusion, density functionals that account for dispersion correction are fundamental to predict the correct regioselectivity in insertion migratory step of the NHC-catalyzed Heck-Mizoroki reaction discussed. Herein, we explored the influence of real NHC ligand bulk, an extension of computational studies on model NHC ligand with methyl ligands reported in the literature. The use of B3LYP and PBE0 functionals result in a strikingly different regioselectivity compared to the experimental prediction. Only hybrid dispersion-corrected ω B97XD and *meta*-GGA M06 functionals were capable to describe the influence of real ligand to the reaction regioselectivity. We expected with complete elucidation on the selectivity-controlling this catalyzed system, to start investigations based on theoretical design of new NHC ligands.

Acknowledgments

The V.H.M.S. is thankful for scholarship grant #2013/04813-6, São Paulo Research Foundation, and appreciates the generous help for Ana P. de Lima Batista with manuscript editing and helpful suggestions. The authors are grateful for the financial support given from the grant #2015/01491-3, São Paulo Research Foundation.

References

1. C. C. C. Johansson Sechurn, M. O. Kitching, T. J. Colacot, V. Snieckus, *Angew.Chem. Int. Ed.*, 51, 5062 (2012).
2. F. R. Heck, J. P. Nolley, *J. Org. Chem.* 37, 2320 (1972) b) T. Mizoroki, K. Mori, A. Ozaki, *Bull. Chem. Soc. Jpn.*, 44, 581 (1971).
3. M. Garcia-Melchor, A. A. C. Braga, Llédos A., G. Ujaque, *Acc. Chem. Res.*, 46, 2626 (2013).
4. G. C. Fortman, S. P. Nolan, *Chem. Soc. Rev.*, 40, 5151 (2010).
5. D. Guest, V. H. Menezes da Silva, A. P. De Lima Batista, M. Roe, A. A. C. Braga, O. Navarro, *Organometallics*, 34, 2463 (2015).
6. a) S. Grimme, P. R. Schreiner, *Angew.Chem. Int. Ed.*, 50, 11794 (2011). b) M. S. G. Ahlquist, P. -O., Norrby, *Angew.Chem. Int. Ed.*, 50, 12639 (2011).
7. E. Lyngvi, I. A. Sanhueza, F. Schoenebeck, *Organometallics*, 34, 805 (2015).
8. L. Xu, M. J. Hilton, X. Zhang, P. -O. Norrby, Y. -D. Wu, M. S. Sigman, O. Wiest, *J. Am. Chem. Soc.*, 136, 1960 (2013).
9. a) P. Hohenberg, W. Kohn *Phys. Rev.* 136, B864, (1964). b) W. Kohn, L. Sham *Phys. Rev.* 140, A1113, (1965).
10. M. J. Frisch et al. Gaussian09, Revision D.01, Gaussian Inc., Wallingford, CT (2009).
11. J. P. Perdew, K. Burke, M. Ernzerhof, *Phys. Rev. Lett.*, 77, 3865 (1996).
12. A. D. Becke, *J. Chem. Phys.* 98, 5648 (1993). b) W. Kohn, A. D. Becke, R. G. Park, *J. Phys. Chem.* 100, 12974, (1996). c) C. Lee, W. Yang, R. G. Parr, *Phys. Rev. B*, 37, 785, (1988).
13. Y. Zhao, D. G. Truhlar, *J. Chem. Phys.*, 125, 194101 (2006).
14. Y. Zhao, D. G. Truhlar, *Theor. Chem. Acc.* 120, 215 (2008) b) Y. Zhao, D. G. Truhlar, *Acc. Chem. Res.*, 41, 157 (2008).
15. J. -D. Chai, M. Head-Gordon, *Phys. Chem. Chem. Phys.* 10, 6615 (2008).
16. Grimme, *J. Comp. Chem.* 27, 1787 (2006).
17. D. Andrae, U. Huermann, M. Dolg, H. Stoll, H. Preu, *Theor. Chim. Acta*, 77, 123, 1991.
18. H. P. Hratchian, H. B. Schlegel, *J. Chem. Theory Comput.*, 1, 61 (2005).
19. A. V. Marenich, C. J. Cramer, D. G. Truhlar, *J. Phys. Chem. B*, 113, 6378 (2009).
20. C. Bäcktorp, P. -O. Norrby, *J. Mol. Catal. A: Chem.*, 328, 108 (2010).
21. S. T. Henriksen, P. -O. Norrby, P. Kaukoranta, P. G. Andersson *J. Am. Chem. Soc.*, 130, 10414 (2008).

Vitor H. Menezes da Silva^{a*}, Oscar Navarro^b
& Ataulpa A. C. Braga^a

^aInstituto de Química, Departamento de Química Fundamental, Universidade de São Paulo, SP, Brasil.

^bDepartment of Chemistry, University of Sussex, Brighton, BN1 9QJ, United Kingdom

*E-mail: vhugomenezes@iq.usp.br

Experimental and Theoretical Infrared Study of Homogalacturonans in the *Psidium Myrtoides* – *Nothotrioza Myrtoidis* System

Renê G. S. Carneiro, Rosy M. S. Isaias, Bárbara D. L. Ferreira, Breno R. L. Galvão, Cláudio L. Donnici & Rita C. O. Sebastião

Introduction

Structural and functional properties of plant cells rely on the composition of cell walls, which may be altered by the influence of galling herbivores^{1,2}. The alteration of chemical compounds in plant cell walls may be detected by different techniques as the absorption of infrared light and nuclear magnetic resonance (NMR)^{3,4}. The use of infrared absorption spectra allows the identification of molecular structures by the fingerprint of chemical bonds and functional groups, and by chemometric methods analyzing the region of 1000-500 cm^{-1} ^{5,6}. The fingerprints of chemical compounds may be successfully assessed in complex mixtures, which is the case of plant cell walls⁷.

Plant epidermis mediates the interactions between plant organs and the surrounding environment by lining on both leaf surfaces, and on the inner and outer surface of galls⁸. In the *Psidium myrtoides* (Myrtaceae) – *Nothotrioza myrtoidis* (Psylloidea) system, the leaf epidermis undergoes distinct degrees of alterations during gall formation, as evidenced by anatomical, cytological and immunocytochemical analyses^{9,10}. The set of structural alterations in the galls of *N. myrtoidis* indicate that the inner epidermis is functionally altered¹¹. Even though the inner and outer gall surfaces have the same ontogenetic origin^{11,12}, their structure is distinct and so is the molecular composition of their cell walls. Based on this premise, current study proposes the investigation of the surfaces of non-galled leaves of *P. myrtoides* and leaf galls of *N. myrtoidis* using IR-ATR spectroscopy. Furthermore, we analyze the optimized structure of homogalacturonans (HGAs), which are the main pectins in the cell walls¹¹⁻¹³,

with different degrees of methylation/acetylation. The main objective is to check if gall establishment distinctly affects the molecular structure of the epidermal cell walls on both gall surfaces. We expect distinct fingerprint patterns for the gall and leaf epidermises related to the alterations in the structure of HGAs, with greater cell alterations occurring in the inner epidermis when compared to the outer epidermis of the galls. In addition, we evaluate the efficiency of experimental and theoretical chemical analyses in assessing the structure of HGAs, which should allow new insights on the biology of plant cell walls.

Methods

We have experimentally analyzed fresh non-galled leaves and galls using a zinc-selenium crystal ATR apparatus (Smart orbit ATR, Thermo Fisher Scientific Inc., Madison, USA), coupled with the spectrophotometer FTIR Nicolet 380 (Thermo Fisher Scientific Inc., Madison, USA), and submitted the samples to infrared radiation between 4000 - 525 cm^{-1} . Series of 32 scanings with the resolution of 2cm were performed. Additionally, we theoretically simulated the infrared spectrum of HGAs of several degrees of methylation, with and without acetyl groups. Given the large number of atoms involved, we have started the analysis at the Hartree-Fock level. However, we currently worked on higher level calculations, the DFT level, using the B3LYP functional, and including Grimme's empirical dispersion correction in order to improve the description of intra-molecular interactions^{13,14}. Geometry

optimizations are followed by calculations of the Hessian matrix, in order to extract the vibrational frequencies. All electronic structure calculations were performed using the GAMESS package¹⁶.

Results and Discussion

The experimental ATR-IR spectra of the adaxial epidermis of non-galled leaves and the inner epidermis of galls are remarkably different, especially at the 3500-3000 cm⁻¹ and 1750-1600 cm⁻¹ regions. In the spectra of non-galled leaves, three intense bands were found at 3360, 1727 and 1642 cm⁻¹, being the second band more intense (~ 87%, 75%, and 84% transmittance = T). In the spectra of galls, the band at 3360 cm⁻¹ is more intense than the corresponding band in the non-galled leaves (~ 57% T). The band at 1727 cm⁻¹ is less intense in galls (~ 89% T), and the band at 1642 cm⁻¹ is more intense in galls (~ 68% T) when compared to the bands of non-galled leaves. Immunocytochemical investigations using specific antibodies for homogalacturonans (HGAs) with different levels of methylation revealed that the adaxial epidermis of non-galled leaves have low methylated HGAs, and the inner epidermis of galls have high methylated HGAs in their cell walls¹. The strong intensity of OH bands in the spectra of galls could be attributed to intermolecular Hydrogen bonds (H bonds) occurring mainly in the low methylated HGAs. Nevertheless, this hypothesis needs to be proven, and led to the theoretical study.

For the theoretical study, ten molecular structures of HGAs were simulated. Each structure is composed by six monomers of galacturonic acid linked by glucoside bonds. Figure 1 represents the structure of the monomer, with H as R and R1 groups.

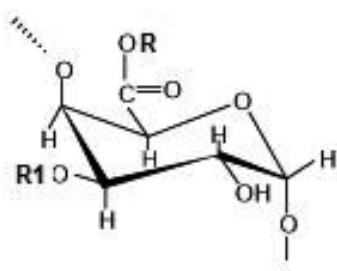


Figure 1. Galacturonic acid monomer.

The structures were divided into two sets: (a) with acetyl group in the R1 position of the fourth and sixth monomers and, (b) without acetyl groups. In both sets, the structures were methyl-esterified in the R position of the monomers: (i) 1,6; (ii) 1,2,6; (iii) 2,3,4,5; (iv) 3,4,5 and (v) 1,3,5.

The OH band analysis of simulated infrared spectra is presented in Table 1. The OH bands in acetylated structures always present stronger intensity than in the corresponding non-acetylated. The experimental infrared spectra of galls present similar behavior, i.e. show stronger intensity for OH band in galls when compared to non-galled leaves. This theoretical result suggests that the structure of HGAs in galls may be composed by acetylated monomers with high degree of methylation. This result adds new information to the experimental detections of high and low methylated HGAs in the plant cell walls using the monoclonal antibodies JIM5 and JIM7, which cannot assess the degree of acetylation of HGAs. Together, the theoretical and experimental studies show that the formation of galls affects both the methylation and acetylation of HGAs, with implications for the functional aspects of plant cell walls.

Table 1. Simulated infrared OH band with H bond analysis after geometry optimization.

Monomers methylation and/or acetylation	OH band		Intra Molecular H bond
	cm ⁻¹	Intensity	
1,6 methylated	4263.45	53.68417	HO---OH CO---OH
1,6 methylated and 4,6 acetylated	4238.58	66.93222	HO---OH CO---OH
1,2,6 methylated	4266.84	53.63021	HO---OH CO---OH
1,2,6 methylated and 4,6 acetylated	4243.64	65.38409	HO---OH CO---OH
1,3,5 methylated	4342.67	16.59795	HO---OH CO---OH
1,3,5 methylated and 4,6 acetylated	4306.84	28.14144	HO---OH CO---OH
2,3,4,5 methylated	4252.92	14.62813	HO---OH
2,3,4,5 methylated and 4,6 acetylated	4247.83	15.86863	HO---OH
3,4,5 methylated	4251.10	13.90583	HO---OH
3,4,5 methylated and 4,6 acetylated	4256.87	15.78891	HO---OH

Given that this study was performed on the isolated molecule (gas phase), the role of intermolecular H bond is not taken into account. Nevertheless, intramolecular H bond is an important factor that seems to be crucial on elucidating the experimental results. It should also be emphasized that the wave numbers presented in Table 1 are at the Hartree-Fock level, and thus cannot quantitatively describe the system. Our analysis are of qualitative nature, aiming to rationalize the experimental findings. In the structures with higher degree of methylation and/or acetylation, the CO-OH interaction between the monomers does not occur. The spatial aspect of the highly methylated and acetylated structure is linear and does not present helical configuration. Figure 2 shows the optimized structure for the (a) 1,6 methylated and (b) 3,4,5 methylated HGAs.

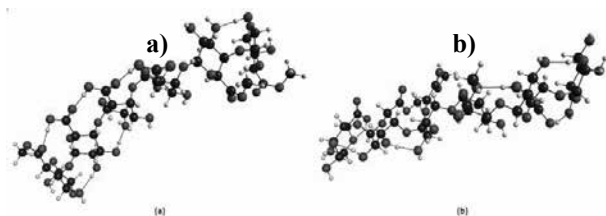


Figure 2. HGAs (a) 1,6 methylated and (b) 3,4,5 methylated.

The analyses of the CO band in the theoretical IR spectra show a general behavior for the structures (a), in which the acetylation determines a reduction in the calculated wavenumber, thus corroborating the experimental results.

Conclusions

Experimental and theoretical studies on the structure of HGAs represent new frontiers to help understanding the biology of plant cell walls, as far as the intramolecular and intermolecular forces of polymers are concerned. The simulated infrared absorption of HGAs showed that acetylation affects intramolecular bonds the most, thus being complementary to the immunocytochemical analyses for the degree of HGAs methylation. Further analyses considering the complexity of the cell wall matrix should help elucidating the role of fine structural details of polymers on the functional aspects of the cell walls.

Acknowledgments

The authors thank FAPEMIG and CNPQ for the financial support.

References

1. P. Albersheim, A. Darvill, K. Roberts, R. Sederoff, A. Staehelin, *Plant cell walls: from chemistry to biology*, Garland Science, New York, (2011).
2. D. Burckhardt, *Biology, ecology and evolution of gall-inducing psyllids (Hemiptera: Psylloidea)*. In: A. Raman, C. W. Schaefer, T. M. Withers, *Biology, ecology, and evolution of gall-inducing arthropods*, Science Publishers, Plymouth, (2005).
3. R. C. O. Sebastião, J. P. Braga, J. Magn. Reson., 177, 146, (2005).
4. R. C. O. Sebastião, C. N. Pacheco, J. P. Braga, D. Piló-Veloso, J. Magn. Reson., 182, 22, (2006).
5. R. G. S. Carneiro, R. M. S. Isaias, *Protoplasma*, 252, 637, (2014).
6. R. G. S. Carneiro, D. C. Oliveira, R. M. S. Isaias, *Pl. Cell. Rep.*, 33, 2093, (2014).
7. R. G. S. Carneiro, P. Pacheco, R. M. S. Isaias, *Plos One*, 10, e0129331, (2015).
8. A. A. Christy, S. Kasemsumran, Y. Du, Y. Ozaki, *Analytical Sci* 20, 935, (2004).
9. R. F. Evert *Esau's Plant Anatomy: Meristems, cells, and tissues of the plant body: their structure, function and development*, John Wiley & Sons, Inc., Hoboken, (2006).
10. A. Fahn, *Plant anatomy*. Pergamon Press, Oxford, (1990).
11. A. T. Formiga, D. C. Oliveira, B. G. Ferreira, T. A. Magalhães, A. C. Castro, G. W. Fernandes, R. M. S. Isaias, *Protoplasma*, 250, 899, (2013).
12. D. C. Oliveira, T. A. Magalhães, B. G. Ferreira, C. T. Teixeira, A. T. Formiga, G. W. Fernandes, R. M. S. Isaias, *Plos One*, 9, e94588, (2014a).
13. C. Pasquini, *J. Braz. Chem. Soc.*, 14, 198, (2003).
14. P. J. Stephens, F. J. Devlin, C. F. Chabalowski, M. J. Frisch, *J. Phys. Chem.*, 98, 11623, (1994).
15. S. Grimme, J. Antony, S. Ehrlich, H. Krieg, *J. Chem. Phys.*, 132, 154104, (2010).
16. M. W. Schmidt, K. K. Baldridge, J. A. Boatz, S. T. Elbert, M. S. Gordon, J. H. Jensen, S. Koseki, N. Matsunaga, K. A. Nguyen, S. Su, T. L. Windus, M. Dupuis, J. A. Montgomery, *J. Comput. Chem.*, 14, 1347, (1993).

Renê G. S. Carneiro^a, Rosy M. S. Isaias^a,
Bárbara D. L. Ferreira^b, Breno R. L. Galvão^c,
Cláudio L. Donnici^b, Rita C. O. Sebastião^{b*}

^aDepartamento de Botânica, Instituto de Ciências Biológicas, Universidade Federal de Minas Gerais-UFMG. Av. Antônio Carlos, 6627, Belo Horizonte – MG, Brazil

^bDepartamento de Química, Instituto de Ciências Exatas, Universidade Federal de Minas Gerais-UFMG. Av. Antônio Carlos, 6627, Belo Horizonte – MG, Brazil

^cCentro Federal de Educação Tecnológica de Minas Gerais- CEFET-MG. Av. Amazonas ,5253, Belo Horizonte – MG, Brazil

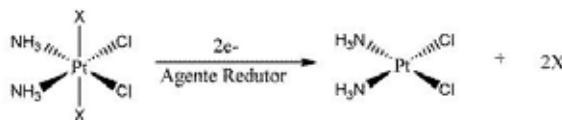
*E-mail: ritacos@ufmg.br

Estudo Eletrônico dos Processos de Redução de Complexos de Pt(IV) à Pt(II)

Bruna L. Silva & Juliana F. Lopes

Introduction

Atualmente, existe um grande interesse no desenvolvimento de uma nova geração de drogas anticâncer à base de platina incluindo complexos de Pt(IV), a fim de superar ou minimizar os efeitos tóxicos da cisplatina e carboplatina e/ou expandir o espectro terapêutico de câncer.¹ Apesar do mecanismo de ação desses compostos não ser totalmente conhecido, acredita-se que a redução destas espécies de Pt(IV) à complexos de Pt(II) seja uma etapa que determina a atividade anticâncer.² Em geral, variam-se os ligantes axiais e equatoriais, para alterar a lipofilicidade, carga, seletividade, segmentação e absorção celular dos complexos.³ O mecanismo padrão de redução para complexos de Pt(IV) octaédricos estabelece a saída dos ligantes axiais, o que seria explicado pela simetria dz^2 dos orbitais LUMO de complexos do tipo d^6 . Com a redução, este orbital seria populado com elétrons, desestabilizando as ligações na direção axial e liberando os ligantes axiais. Estudos recentes sobre redução de complexos de Pt(IV) evidenciam, entretanto, ser possível a saída dos ligantes equatoriais.^{4,5} Por envolverem a saída de ligantes, estes complexos apresentam comportamento de redução irreversível, e desta forma os potenciais padrão de redução são difíceis de serem determinados experimentalmente. Nesse sentido, metodologias de química teórica auxiliam na compreensão dos resultados experimentais obtidos, podendo, inclusive indicar o mecanismo provável de redução. Na reação do esquema 1, a redução está associada à saída de ligantes da esfera de coordenação e portanto, acontece um rearranjo estrutural.



Esquema 1. Conversão dos complexos de Pt+4 em Pt+2 por redução.

A redução da platina (IV) para platina (II) envolve a mudança de um arranjo octaédrico – hexacoordenado, para uma espécie quadrático-plana, envolvendo de acordo com o mecanismo clássico da química inorgânica a saída dos ligantes axiais. O objetivo deste trabalho é compreender eletronicamente os processos de redução envolvidos por meio de complexos modelo de Pt(IV), indicando possíveis mecanismos para a redução.

Métodos

Os cálculos foram feitos com o programa Gaussian 09 utilizando as metodologias DFT (funcional M06-2x) e MP2. O conjunto de funções de base 6-31g(d,p) foi aplicado para os átomos leves e o pseudopotencial LANL2DZ para o átomo de platina. Foram realizados cálculos de otimização de geometria, análise vibracional e eletrônica por meio do cálculo

de população para os complexos octaédricos *cis* e *trans*-Pt(NH₃)₂Cl₄, [Pt(NH₃)₃Cl₃]⁺¹, [Pt(NH₃)₄Cl₂]⁺², [Pt(NH₃)₅Cl]⁺³, [Pt(NH₃)Cl₅]⁻¹ e [Pt(NH₃)₆]⁺⁴ seguindo a análise NBO.

Resultados e Discussão

Todos os complexos tiveram suas geometrias otimizadas e foram caracterizados como mínimos locais em ambos os níveis de teoria utilizados. Todos se mantêm na geometria octaédrica, com as ligações no eixo axial mais alongadas do que as similares no plano equatorial. Utilizando cálculos NBO, verificou-se a energia dos orbitais moleculares ocupados (HOMO) e desocupados (LUMO). Nos processos de redução, os elétrons são adicionados no orbital LUMO, portanto a simetria e a energia destes orbitais se associam com o mecanismo da reação.

De forma geral, as energias dos orbitais LUMO e LUMO+1, determinados no MP2, são mais altas do que às calculadas no DFT. Em contrapartida, os orbitais HOMO são mais estáveis no MP2 do que os obtidos pelo funcional M06-2X. Este fato faz com que o *gap* HOMO-LUMO seja sempre maior quando determinado pelo método MP2.

As superfícies que indicam as simetrias dos LUMO para os complexos *cis* e *trans* Pt(NH₃)₂Cl₄ estão representados na Figura 1.

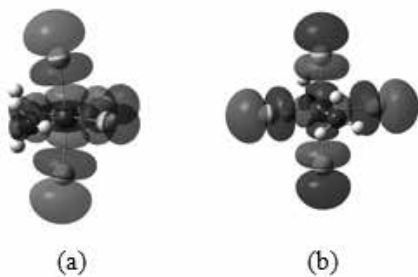


Figura 1. Orbitais moleculares LUMO dos complexos *cis* e *trans* Pt(NH₃)₂Cl₄. MP2/6-31g(d,p), isovalor=0,02.

As simetrias são confirmadas pela análise das regiões definidas e também pela composição destes orbitais descritas na análise NBO. Para o complexo *cis*-Pt(NH₃)₂Cl₄ tanto no nível M06-2X quanto para o

MP2 o orbital mais energético desocupado – LUMO, a simetria descrita por esse é do tipo dz², o que indica que aconteceria a saída dos ligantes do plano axial. O orbital LUMO +1 de simetria dx²-y², tem energia superior ao LUMO em mais de 0,02 u.a. (M06-2x) o que garante este mecanismo. Já para o complexo *trans*-Pt(NH₃)₂Cl₄ tanto para o nível M06-2x quanto para o MP2, o orbital LUMO apresenta simetria dx²-y², e contribuição dos orbitais atômicos p dos ligantes cloro, indicando um mecanismo de redução alternativo aos mecanismos clássicos de redução para compostos d⁶ com geometria octaédrica. Desta forma, é possível que os ligantes do plano equatorial saiam. Para o nível LUMO +1 a simetria do tipo d_z², entretanto esta energia é superior em 0,03 u.a. (M06-2x) e 0,05 u.a. (MP2) como descrito na tabela 1. Na Tabela 1 Δ_(L+1,L) indica a diferença energética entre os orbitais LUMO+1 e LUMO e o Δ_{L,H} indica a diferença energética entre os orbitais LUMO e HOMO.

Tabela 1. Diferença energética em u.a. (Hartree) entre orbitais para os complexos *cis* e *trans* Pt(NH₃)₂Cl₄

	cis-Pt(NH ₃) ₂ Cl ₄		trans-Pt(NH ₃) ₂ Cl ₄	
	M06-2X	MP2	M06-2X	MP2
ΔL+1,L	0,02	0,03	0,03	0,05
ΔL,H	0,23	0,38	0,23	0,38

Para o complexo triaminotricloroplatina (IV) em ambos níveis de cálculo a simetria que descreve o orbital LUMO é dz², indicando a possível saída dos ligantes axiais. Também para o complexo tetraminodichloroplatina (IV) o orbital LUMO de simetria dz² em ambos níveis de cálculo indica a saída dos ligantes do eixo axial.

Tabela 2. Diferença energética em u.a. (Hartree) entre orbitais para os complexos [Pt(NH₃)₃Cl₃]⁺¹ e [Pt(NH₃)₄Cl₂]⁺²

	[Pt(NH ₃) ₃ Cl ₃] ⁺¹		[Pt(NH ₃) ₄ Cl ₂] ⁺²	
	M06-2X	MP2	M06-2X	MP2
ΔL+1,L	0,02	0,04	0,02	0,05
ΔL,H	0,24	0,38	0,24	0,40

O orbital LUMO +1 tem energia superior ao LUMO em 0,02 u.a. (M06-2x) e 0,04 u.a. (MP2) para o complexo $[\text{Pt}(\text{NH}_3)_3\text{Cl}_3]^+1$ e 0,02 u.a. (M06-2x) e 0,05 u.a. (MP2) para o complexo $[\text{Pt}(\text{NH}_3)_4\text{Cl}_2]^+2$, como descrito na Tabela 2. Por a diferença energética entre o LUMO e o LUMO+1 é relativamente alta, 12,55 kcal mol⁻¹ (M06-2x) pode-se dizer que a reação de redução em ambos complexos aconteceria ocupando o LUMO, indicando a saída dos ligantes axiais, como prevê o mecanismo convencional.

Na Figura 3, são apresentados os níveis de energia para os íons complexos $[\text{Pt}(\text{NH}_3)_5\text{Cl}]^{+3}$ e $[\text{Pt}(\text{NH}_3)_6\text{Cl}_5]^{-1}$. Para o complexo pentaminocloroplatina(IV) tanto no nível M06-2X quanto para o MP2 o orbital mais energético desocupado – LUMO, a simetria descrita por esse é do tipo dz², o que indica que aconteceria a saída dos ligantes do eixo axial. Para o complexo aminopentacloroplatina (IV) o orbital LUMO é descrito pela simetria dx²-y², mais uma vez indicando que um mecanismo alternativo ao clássico pode acontecer.

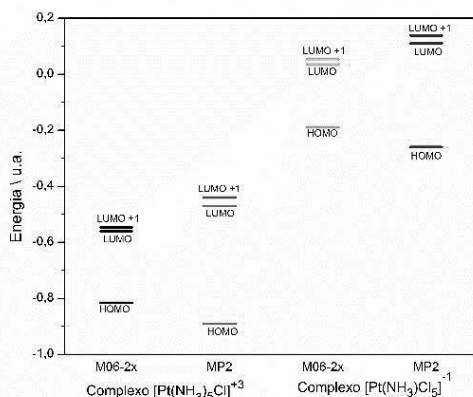


Figura 3. Diagrama de energia dos complexos $[\text{Pt}(\text{NH}_3)_5\text{Cl}]^{+3}$ e $[\text{Pt}(\text{NH}_3)_6\text{Cl}_5]^{-1}$

O orbital LUMO +1 tem energia superior ao LUMO em 0,01 u.a. (M06-2x) e 0,03 u.a. (MP2) para o complexo $[\text{Pt}(\text{NH}_3)_5\text{Cl}_3]^+3$, novamente, analisando a diferença de energia entre os orbitais LUMO e LUMO+1, pode-se dizer que a reação de redução aconteceria com a entrada dos dois elétrons ocupando apenas o LUMO, de menor

energia. No complexo $[\text{Pt}(\text{NH}_3)_5\text{Cl}_5]^-$ o orbital LUMO+1 tem energia superior ao LUMO em 0,02 u.a. (M06-2x) e 0,03 u.a. (MP2), neste caso a reação aconteceria preferencialmente com a saída dos ligantes equatoriais, de acordo com a simetria dx²-y² deste orbital.

Completando a série destes complexos “modelo”, realizamos também a análise para o complexo hexaminoplatina (IV). tanto no nível M06-2X quanto para o MP2 o orbital mais energético desocupado – LUMO, a simetria descrita por esse é do tipo dz², entretanto a simetria do LUMO+1 é dx²-y².

Tabela 4. Diferença energética entre orbitais para o complexo $[\text{Pt}(\text{NH}_3)_6]^{+4}$

$[\text{Pt}(\text{NH}_3)_6]^{+4}$		
	M06-2X	MP2
$\Delta_{L+1,L}$	0,00	0,00
$\Delta_{L,H}$	0,36	0,53

Os orbitais LUMO e LUMO +1 apresentam energias praticamente degeneradas (como mostrado na tabela 4), e desta forma conclui-se que ambos os mecanismos poderão ocorrer, com a saída dos ligantes equatoriais e/ ou axiais.

Como perspectivas futuras, há pretensão de se incluir o efeito do solvente (água e plasma), para se entender os processos de redução em solução. A perspectiva é que a simetria dos orbitais não se altere, mas que a energia seja modulada pelos efeitos do solvente. Outro aspecto a ser estudado, é a alteração de outros ligantes que podem ser doadores ou receptores de elétrons, para prever como estes mudam as propriedades eletrônicas e estruturais. Estes cálculos já estão sendo conduzidos e espera-se obter os resultados para apresentação no evento.

Conclusão

O entendimento dos processos de redução é extremamente importante para elucidar o mecanismos de ação destas moléculas modelo. Portanto, estudar as propriedades de simetria e energia envolvem os orbitais de fronteira, sabendo-se que a energia do LUMO pode

ser relacionada com o potencial de redução, e que sua simetria está relacionada com o complexo de Pt(II) a ser gerado, novas relações poderão ser obtidas para estabelecer estrutura na síntese de novos compostos poderá ser feita. Além disso, o mecanismo de ação deverá ser explorado, no sentido de incluir o mecanismo não tradicional que envolve a saída dos ligantes equatoriais.

Agradecimentos

Os autores agradecem à CAPES, FAPEMIG, CNPq, RQ-MG e ao PPGMQ-MG pelo apoio.

Referências

1. Ren, Y; et al. Transition Met Chem, v.40: p.347–353, **2015**.
2. Silva, G.B.; Vargas, M.D. Revista Virtual Química, v.4: p.102-117, **2012**
3. Wexselblatt, E., E. Yavin, and D. Gibson. Angewandte Chemie International Edition. v.52: p. 6059-6062, **2013**.
4. Nemirovski, A., Gibson, D. et.al; Chem. Commun., v.46:p.1842–1844, **2010**.
5. Lippard. S.J, Graf, N., Advanced Drug Delivery. Review., p.993-1004, **2012**.

Bruna L. Silva* & Juliana F. Lopes

LaQC- Laboratório de Química Computacional, Universidade Federal de Itajubá, Av. BPS nº1303, Bairro: Pinheirinho, 37500-903, Itajubá, MG, Brasil;

*E-mail: brunalemessilva@gmail.com

Structural Dependence of Photochromism in MEH-PPV Solutions

C. E. Magalhães, R. M. L. Savedra, K. S. Dias, R. Ramos & M.F. Siqueira

Introduction

Photochromism is a photoinduced reversible transformation of a molecular system, which undergoes to an appropriate molecular design. This phenomenon triggers changes in the optoelectronic properties of these compounds by electromagnetic radiation exposure.^{1,2} Therefore, these kind of compound can act as electro-optical switches at molecular scale, and there is an increasing interest for applications as optoelectronic devices.^{3,4} Previous literatures have reported the chromism effect on poly(p-phenylene vinylene) based polymers and its relationship to the structural arrangements.^{5,6} Accordingly, these reversible molecular events can allow the development of smart materials.

The semiconducting poly[2-methoxy-5-(2-ethylhexyloxy)-p-phenylene vinylene] (MEH-PPV), Figure 1, has been widely studied due to its electronic and mechanic properties due to its potential for applications in the field of organic electronics.⁷ MEH-PPV can be found as red phase and blue phase, which are morphologically distinct.^{6,8}

In this work, we have studied the structural

arrangements of MEH-PPV in tetrahydrofuran (THF) as solvent to evaluate the photochromism behavior. To this aim, we carried out simulations using Molecular Dynamic (MD) and Quantum Mechanics (QM) approaches.

Methods

A MEH-PPV oligomer with nine units (nonamers) was fully optimized in vacuum using the PM6-DH+ semi-empirical calculations,⁹ implemented in the MOPAC package.¹⁰ This molecular model was used as an initial guess for modeling of the polymer solution using Molecular Dynamic simulations.

Molecular dynamic simulations were performed using the GROMACS 5.0.1 package.¹¹ The MEH-PPV and THF were modeled using the GROMOS 53a6 force field parameters.¹² The initial topology was built adding 20 MEH-PPV nonamers in a cubic box of 25.0 nm edge and filled with THF solvent. The PME method with 1.0 nm cutoff was used for treatment of long-range electrostatic interaction. All bonds lengths were constrained to their equilibrium values by using the LINCS algorithm. The neighbor list for the calculation of nonbonded interaction was updated every 10 time step with a cutoff of 1.0 nm, the same cutoff for Lennard-Jones potential. The PME method with 1.0 nm cutoff was used for treatment of long-range electrostatic interaction. All bonds lengths were constrained to their equilibrium values by using the LINCS algorithm. The neighbor list for the calculation

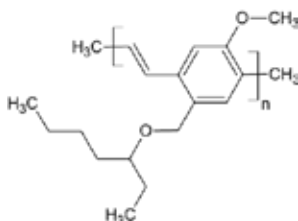


Figure 1. Chemical structure of MEH-PPV.

of nonbonded interaction was updated every 10 time step with a cutoff of 1.0 nm.

The system was submitted to steepest descent energy minimization methodology until the maximum force attained a tolerance of $10 \text{ kJ mol}^{-1}\text{nm}^{-1}$. Afterwards, from this minimized system we carried out 1.0 ns of simulation in the canonical (NVT) ensemble in order to allow the relaxing of the molecular bonds and then we carried out 1.0 ns of simulation in the isobaric-isothermal (NPT) ensemble at 300K and a small external pressure of 1 bar for 10 ns of simulation with a step size of 1 fs, using V-rescale thermostat and berendsen barostat with coupling time of $\tau_t = 0.1 \text{ ps}$ and $\tau_p = 2.0 \text{ ps}$. The MD protocols used herein are widely employed in the literature.

The UV-VIS spectra for all final oligomer structures obtained from last frame of Molecular Dynamics were calculated by ZINDO-S/CIS method,^{13,14} including 30 occupied to 30 unoccupied states for the single excitations. These calculations were performed with the Orca computational program, version 2.7.¹⁵

Results and Discussion

Figure 2(a) shows the initial topology of MEH-PPV:THF solution before molecular dynamic procedure. Afterward 5.0 ns of simulation we observed the clustering formation of MEH-PPV and solvent molecules, Figure 2(b). The aggregation occurs driven by the non-bonded interaction between molecules, besides temperature and solvent effects played a role into the final morphology.

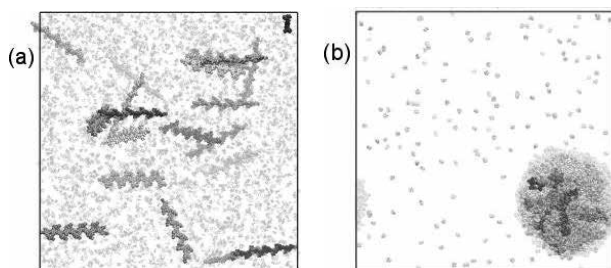


Figure 2. (a) Initial molecular system before the MD procedure. Box dimension with 25nm3 with 20 nonamers of MEH-PPV in THF as solvent. (a) Clustering formation of MEH-PPV molecules after 5.0 ns of MD simulation.

From the simulation we took two main structural arrangements found for the MEH-PPV oligomers in the solution: planar and twisted conformations. We selected two of these structures, as shown in the Figure 3(a) and 3(b). The difference between each other is the number of internal torsions which can lead to differences in the conjugation length (CL) of electronic states, being the larger CL found to the planar structure. For selected oligomers we calculate the UV-Vis spectra, presented in Figure 3(c).

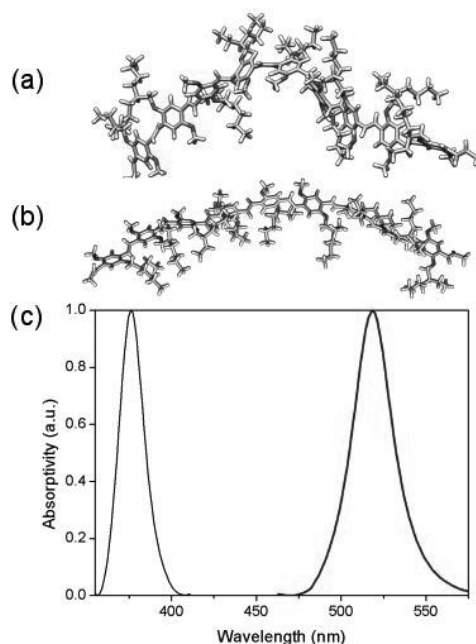


Figure 3. Conformational arrangements of two selected structures (a) twisted and (b) planar, from the sample after 5 ns of MD simulations. (c) Normalized first transition (HOMO-LUMO) from UV-Vis spectra calculated for these structures: in black color (for the twisted), and in blue color (for the planar); lorentzian broadening and a 11.28 half-width were added.

As it can be seen, the main electronic excitation of the twisted structure is found in the blue region. This can be directly attributed to the shorter conjugation lengths of the frontier orbitals. In the same sense, we found the main absorption transitions of the planar structure lying in the red region, which can be attributed to the larger conjugation length for these more ordered oligomers.

Therefore, the modeling support that the difference between red and blue phases found in MEH-PPV can be attributed to intrachain electronic effects resulting from differences on the conjugation length determined by the differences in the molecular morphology.

Conclusions

Our results support the proposal that even it would be possible to access many transient conformational arrangements under temperature effects, they will be finally converted in two main configuration: twisted and planar. Accordingly, these structural arrangements are then related to the chromism reported for these materials, the red phase is attributed to less disordered oligomers with higher electronic conjugation lengths and the blue phase is related to the shorter conjugation lengths imposed by twisted molecular morphology.

Acknowledgments

The authors thank the Brazilian funding agencies CNPq, FAPEMIG and CAPES, as well as the National Institute of Science and Technology on Organic Electronics (INEO/INCT) for financial support and fellowships.

References

1. M. Irie, Y. Yokoyama, and T. Seki, *New Frontiers in Photochromism* (Springer Science & Business Media, **2013**).
2. H. Dürr and H. Bouas-Laurent, *Photochromism: Molecules and Systems: Molecules and Systems* (Gulf Professional Publishing, **2003**).
3. S. Masi, S. Colella, A. Listorti, V. Roiati, A. Liscio, V. Palermo, A. Rizzo, and G. Gigli, *Sci. Rep.* **5**, (2015).
4. J.C. Yu, J.I. Jang, B.R. Lee, G.-W. Lee, J.T. Han, and M.H. Song, *ACS Appl. Mater. Interfaces*, **6**, 2067 (2014).
5. E.N. Hooley, A.J. Tilley, J.M. White, K.P. Ghiggino, and T.D.M. Bell, *Phys. Chem. Chem. Phys.*, **16**, 7108 (2014).
6. A. Köhler, S.T. Hoffmann, and H. Bässler, *J. Am. Chem. Soc.*, **134**, 11594 (2012).
7. E.S. Bronze-Uhle, J.F. Borin, A. Batagin-Neto, M.C.O. Alves, and C.F.O. Graeff, *Mater. Chem. Phys.*, **132**, 846 (2012).
8. F.A. Feist, M.F. Zickler, and T. Basché, *Chemphyschem Eur. J. Chem. Phys. Phys. Chem.*, **12**, 1499 (2011).
9. J. Řezáč, J. Fanfrlík, D. Salahub, and P. Hobza, *J. Chem. Theory Comput.*, **5**, 1749 (2009).
10. James P. Stewart, *MOPAC* (Stewart Computational Chemistry, **2008**).
11. J. Van der Spoel, E. Lindahl, B. Hess, G. Groenhof, A.E. Mark, and H.J.C. Berendsen, *J. Comput. Chem.*, **26**, 1701 (2005).
12. C. Oostenbrink, A. Villa, A.E. Mark, and W.F. Van Gunsteren, *J. Comput. Chem.*, **25**, 1656 (2004).
13. M.C. Zerner, in *Rev. Comput. Chem.*, edited by K.B. Lipkowitz and D.B. Boyd (John Wiley & Sons, Inc., **1991**), pp. 313–365.
14. J. Ridley and M. Zerner, *Theor. Chim. Acta*, **32**, 111 (1973).
15. F. Neese, *Wiley Interdiscip. Rev. Comput. Mol. Sci.*, **2**, 73 (2012).

C.E. Magalhães¹, R. M. L. Savedra², K. S. Dias¹, R. Ramos³ & M.F. Siqueira^{1*}

¹ Laboratory of Polymers and Electronic Properties of Materials, Department of Physics - Federal University of Ouro Preto, 35400-000, Ouro Preto – MG, Brazil

² Department of Chemistry, Federal University of Lavras, 37200-000, Lavras-MG, Brazil

³ Institute of Physics, Department of Material Physics and Mechanics, University of São Paulo, 05508-090, São Paulo - SP, Brazil

*E-mail: melissa@iceb.ufop.br

Accurate Multireference Electronic Structure Calculations on the Si₃ Molecule

C. E. M. Gonçalves, B. R. L. Galvão & J. P. Braga

Introduction

The properties of small silicon clusters have been discussed since the last century. The interest started from astrophysics research concerning the spectra of carbon-rich stars¹ and chemical vapor decomposition processes^{2,3}. Nowadays they are important for semiconductor devices and optoelectronic nanomaterials⁴⁻⁶.

The Si₃ system, in particular, has shown quite a challenge since even its ground state is difficult to determine, and the literature is not yet in consent⁷⁻¹³. Although many theoretical works agree with experimental results, the symmetry of the ground state is still in discussion, balancing between the singlet C_{2v} group and the triplet D_{3h} one. Oyedepo et al.¹³ recently performed multireference correlation consistent composite approach (MR-ccCA) calculations of Si₃, predicting geometries, total atomization energy (TAE) and the singlet-triplet gap (S-T Gap). They showed that this system have a strong multireference (MR) character.

Even the Si₂ potential energy surface (PES) has many low lying electronic states, with several crossings between them. Therefore, molecular dynamics simulations of the Si(³P)+Si₂ collision will have a myriad of states interfering in the reaction process. The electronic profile of Si₃, including its excited states and geometries, using high accurate MR methods is the main subject of this work.

Methods

All calculations were carried out with the MOLPRO 2012 package¹⁴, using the Multireference Configuration Interaction, MRCI(Q), with the Davidson correction^{15,16}. We use the correlation-consistent basis, aug-cc-pVQZ^{17,18}. All geometry optimization were carried out under the complete active space self-consistent field (CASSCF) with the same basis, using the quadratic steepest descent method.

The frequencies were obtained using CASSCF level of theory, with the aug-cc-pVQZ basis due to the high computational cost.

Results and Discussion

To test the accuracy of our calculations, we compare our results with the most recent theoretical results of the literature, using single or multireference methods, and the available experimental data. Table 1 shows the comparison of the geometries and frequencies, total atomization energy (TAE) and the S-T Gap.

Oyedepo *et al.*¹³ exposed that both singlet and triplet forms have a strong multireference (MR) character. A system with strong MR effects shows a C₀² (the magnitude of the SCF configurations to the CASSCF wave functions) value less than 0.90 while the T₁ and D1

Table 1. Comparison of the present methodology with experimental results and most recent theoretical values for the Si3 two lowest states. Energies are given in kJ/mol, frequencies (ω) in cm^{-1} , bond lengths in Å, and bond angles (θ) in degrees.

	Ref. 12	Ref. 13	Experimental Ref. 7,10,19	This work
TAE	719	710	705±16	700.863
S-T gap	0.8	0.8	4.19?	3.675
Singlet	RS _i -S _i	2.21	2.177	2.207
	θ	79.7	78.10	79.71
	ω_{sy}	549	550.6	528.9
	ω_{as}	524	525.1	518.4
	ω_{b}	180	*	175.8
Triplet	RS _i -S _i	2.31		2.322
	θ	60.0		60.00
	ω_{sy}	502	501±10	482.6
	ω_{def}	324	337±10	302.4
	ω_{def}	325	337±10	302.4

Only the most accurate coupled cluster result from Tam et al.12 is given. * Ref. 19 gives two possible values, 146.2 and 153.2 cm^{-1} .

diagnostics20-22 are larger than the generally accepted cutoff of 0.02 and 0.05. The Si₃ singlet state parameters are $C_0=0.822$, $T1 = 0.032$ and $D1 = 0.082$, therefore not properly described by a single-reference method by any of those criterion. The triplet state with $C_0=0.843$, $T1 = 0.031$ and $D1 = 0.082$ also fails the tests.

Tam *et al.*12 most accurate calculations used single reference coupled cluster with the large aug-cc-pVXZ basis expanded with tight d-functions, extrapolated to the complete basis set limit (CBS), including scalar relativistic, core-valence and spin-orbit corrections. Their best result for TAE (719 kJ/mol) deviates from the experimental value more than Oyedepo et al.13 (710 kJ/mol), probably because of the strong MR character of this molecule.

We made, instead of MR composite approach of Oyedepo *et al.*13, full MRCI(Q) calculations, with the large aug-cc-pVQZ basis. Our result, 700.863 kJ/mol, considering the zero point energy (ZPE), is closer to the experiment than Oyedepo's. All our geometries are in excellent agreement

with experiments, but our frequencies were systematically below experimental values, probably due to the lower level of theory in the calculations.

If the interest is to study the collisions that lead to Si₃, there will be a myriad of electronic states involved. The Si₂ molecule has two nearly degenerate states, ³Π_u and ³Σ_g⁻, and they alternate for the ground state with the distance. Figure 1 shows the PES of the Si₂ molecule, including some low-lying excited states that may not be accessible under normal circumstances, but are still below the dissociation limit.

Exploring a “T shaped” profile of the system, in which a silicon atom approaches the Si₂ molecule perpendicular to the bond axis and in its center-of-mass, one can have a preliminary insight of the collision reaction. Figure 2 shows the PES for singlet and triplet two-state calculations in C_{2v} symmetry for each wave function A₁, B₁, B₂ and A₂. The Si₂ bond distance is fixed at its equilibrium value of 2.17 Å. It can be seen several attractive states that will lead to a barrierless collision, and all of them are important to the cross sections and rate constants of reactive events23-25. In the dissociation limit the surfaces merge to two separated energies, and this separation gap, 4.5 kJ/mol, is very close to the one observed between the two lowest states of Si₂ molecule, 4.9 kJ/mol.

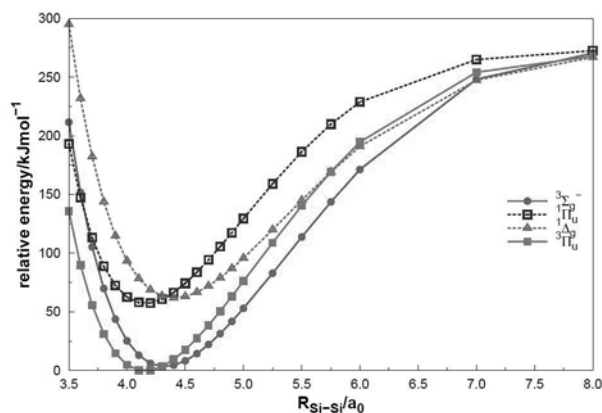


Figure 1. T-shaped atom-diatom interaction profile. Dashed lines represent the respective excited states; The Si2 separation is fixed at 2.17 Å.

Conclusions

We report new values for geometry, TAE, frequencies and S-T Gap for the singlet and triplet states of Si3

molecule, using a high accuracy MRCI(Q) with a large basis, since it is known that this system has a strong MR character. The first 16 lowest PES are also calculated showing several attractive states that lead to a barrierless collision, which means that they all contribute to cross sections and rate constants of reactive events. If one is aiming to study the dynamics of Si_3 molecule, all these non-barrier channels should be considered.

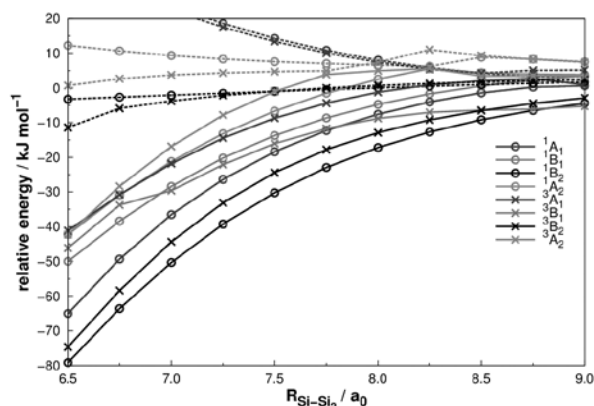


Figure 2. T-shaped atom-diatom interaction profile. Dashed lines represent the respective excited states; The Si_2 separation is fixed at 2.17 Å.

Acknowledgments

The authors are grateful for the support given from the FAPEMIG, CAPES and CNPQ.

References

1. P. W. Merrill, Publ. Astron. Soc. Pac., **1926**, 38, 175.
2. R. F. Sanford, Astrophys. J., **1950**, 111, 262.
3. P. Ho and W. G. Breiland, Appl. Phys. Lett., **1984**, 44, 51.
4. E. C. Honea, Nature (London) **1993**, 366, 42.
5. K. M. Ho, Nature (London) **1998**, 392, 582.
6. V. T. Ngan, P. Claes, P. Gréune, E. Janssens, G. Meijer, A. Fielicke, M. T. Nguyen, P. J. Lievens, Am. Chem. Soc. **2010**, 132, 15589.
7. R. W. Schmude, Q. Ran, K. A. Gingerich, and J. E. Kingcade, J. Chem. Phys., **1995**, 102(6), 2574–2579.
8. C. C. Arnold and D. M. Neumark, J. Chem. Phys., **1994**, 100(3), 1797–1804.
9. M. C. McCarthy and P. Thaddeus, Phys. Rev. Lett., **2003**, 90(21).
10. N. J. Reilly, D. L. Kokkin, X. Zhuang, V. Gupta, R. Nagarajan, R. C. Fortenberry, J. P. Maier, T. C. Steimle, J. F. Stanton, and M. C. McCarthy, J. Chem. Phys., **2012**, 136, 194307.
11. N. M. Tam, M. T. Nguyen, Chem. Phys. Lett., **2013**, 584, 147–154.
12. N. M. Tam, T. D. Hang, H. T. Pham, H. T. Nguyen, M. P. Pham-Ho, P. A. Denis, and M. T. Nguyen, J. Comput. Chem., **2015**, 36(11), 805–815.
13. G. A. Oyedepo, C. Peterson, and A. K. Wilson, J. Chem. Phys., **2011**, 135(9).
14. H.-J. Werner, P. J. Knowles, G. Knizia, F. R. Manby, M. Schütz, P. Celani, T. Korona, R. Lindh, A. Mitrushenkov, G. Rauhut, K. R. Shamasundar, T. B. Adler, R. D. Amos, A. Bernhardsson, A. Berning, D. L. Cooper, M. J. O. Deegan, A. J. Dobbyn, F. Eckert, E. Goll, C. Hampel, A. Hesselmann, G. Hetzer, T. Hrenar, G. Jansen, C. Köppl, Y. Liu, A. W. Lloyd, R. A. Mata, A. J. May, S. J. McNicholas, W. Meyer, M. E. Mura, A. Nicklass, D. P. O'Neill, P. Palmieri, D. Peng, K. Pflüger, R. Pitzer, M. Reiher, T. Shiozaki, H. Stoll, A. J. Stone, R. Tarroni, T. Thorsteinsson, and M. Wang, Molpro, version 2012.1, a package of ab initio programs, **2012**.
15. H. J. Werner and P. J. Knowles, J. Chem. Phys., **1988**, 89(9), 5803–5814.
16. P. J. Knowles and H. J. Werner, Chem. Phys. Lett., **1988**, 145(6), 514–522.
17. T. H. Dunning, J. Chem. Phys., **1989**, 90(2), 1007–1023.
18. R. A. Kendall, T. H. Dunning, and R. J. Harrison, J. Chem. Phys., **1992**, 96(9), 6796–6806.
19. S. Li, R. J. Vanze, W. Weltner, and K. Raghavachari, Chem. Phys. Lett., **1995**, 243(3-4), 275–280.
20. T. J. Lee and P. R. Taylor, Int. J. Quant. Chem. Symp., **1989**, 23, 199–207.
21. M. L. Leininger, I. M. B. Nielsen, T. D. Crawford, and C. L. Janssen, Chem. Phys., **2000**, 328, 431–436.
22. T. J. Lee, Chem. Phys. Lett., **2003**, 372, 362–367.
23. B. R. L. Galvão, J. P. Braga, J. C. Belchior, and A. J. C. Varandas, J. Chem. Theo. Comp., **2014**, 10(5), 1872–1877.
24. B. R. L. Galvão, A. J. C. Varandas, J. P. Braga, and J. C. Belchior, J. Phys. Chem. Lett., **2013**, 4(14), 2292–2297.
25. M. Boyukata, E. Borges, J. P. Braga, J. C. Belchior, J. Alloys Compd., **2005**, 403, 349–356.

C. E. M. Gonçalves^{1*}, B. R. L. Galvão² & J. P. Braga¹

¹Chemistry Department, Universidade Federal de Minas Gerais, Brazil.

²Chemistry Department, Centro Federal de Educação Tecnológica de Minas Gerais, Brazil.

*E-mail: cayoquimica@gmail.com

Estudo das Interações dos Modelos da Proteína ATP7A no Mecanismo de Resistência à Cisplatina

Christina T. Borges, Guilherme F. Lima & Juliana F. Lopes

Introdução

Um quimioterápico muito utilizado no tratamento de diversos tipos de câncer é o cis- diaminodicloroplatina (II), conhecido por cisplatina, que é um composto inorgânico neutro e possui geometria quadrático plana(figura 1).

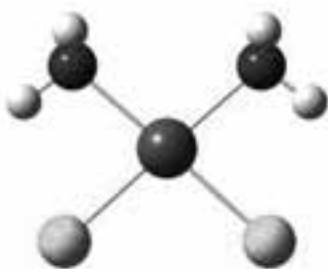


Figura 1: Estrutura da cisplatina

A resistência à cisplatina limita drasticamente seu uso e está associada, entre outros fatores, à redução da acumulação intracelular da droga o que pode estar relacionada à interações com várias biomoléculas tioladas, como por exemplo a proteína ATP7A (Figura 2), que é o foco desse estudo. A proteína ATP7A tem 40280 átomos e alguns domínios de ligação à metais, sendo responsável pelo controle de íons metálicos no organismo, principalmente íons de cobre e magnésio.



Figura 2: Proteína ATP7A¹ (1Y3J)

Métodos

Cálculos computacionais utilizando o programa Gaussian 09 e a metodologia híbrida QM/MM com o método ONIOM², foram feitos para a reação entre o sítio ativo do quinto domínio de ligação à metais da proteína ATP7A e a cisplatina. A opção pela metodologia ONIOM se fez necessária uma vez que a estrutura química/ eletrônica é grande, e ao mesmo tempo que é necessário contemplar o ambiente da proteína, precisamos avaliar a termodinâmica e cinética da formação de novas ligações químicas, o que é competência da química quântica. A escolha do quinto domínio de ligação à metais se deve à presença de dois aminoácidos do tipo cisteína, identificados na estrutura depositada no pdb por cys¹⁴ e cys¹⁷, que apresentam uma conformação passível de ser realizar uma coordenação de forma bidentada com o metal (Cu²⁺ ou Pt²⁺) e caracterizando assim uma estrutura termodinamicamente mais estável. O quinto domínio

possui 1194 átomos e foi dividido em duas camadas de nível de cálculo, tratadas com métodos computacionais diferentes. A camada alta, é evidenciada na Figura 3, com modelo “pau-bola” foi tratada com química quântica, por meio do nível de cálculo DFT (funcional pbe1pbe) e funções de base 6-31g(d,p), exceto para a platina, que foi definida com o pseudopotencial LanL2DZ. A camada baixa foi tratada com mecânica molecular, com uso do campo de força UFF e é apresentada com modelo de “varetas”.

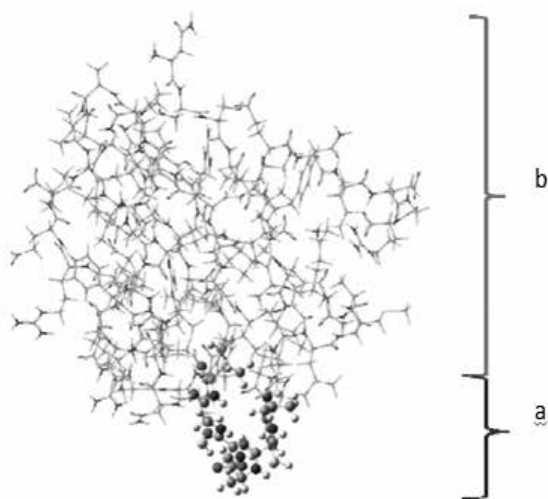
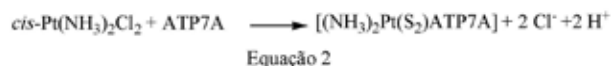
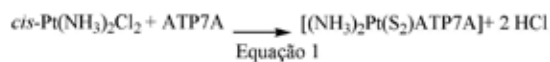
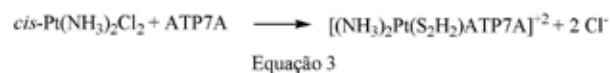


Figura 3: Divisão da estrutura do quinto domínio da ATP7A através da metodologia híbrida QM/MM: camada alta(a) e camada baixa(b).



Em meio biológico, é de se esperar que as espécies estejam dissociadas, entretanto a presença de íons na equação química, e tratados na aproximação da fase gasosa trará resultados superestimados para as energias dos produtos em relação às do reagente. Se não houver a desprotonação, haverá apenas a formação de dois íons cloreto, como mostrado na equação 3. A desprotonação ou não dos grupos tiol dependerá do pH do meio onde ocorre a reação.³



As estruturas otimizadas do quinto domínio da proteína ATP7A e desse domínio coordenado à cisplatina (representando os produto final da substituição) estão representados na Figura 4:

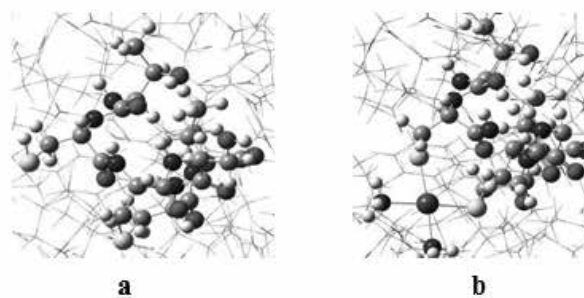


Figura 4: Estruturas otimizadas: a) do quinto domínio da proteína ATP7A b) do quinto domínio da proteína ATP7A coordenada à cisplatina

Resultados e Discussões

Inicialmente foram feitos cálculos de otimização de geometria e análise vibracional para as estruturas envolvidas na possível reação entre a cisplatina e o quinto domínio de ligação à metais da proteína ATP7A. Partindo das contribuições energéticas de cada reagente e cada produto, foram calculados os parâmetros termodinâmicos das reações globais, considerando a desprotonação ou não do grupo tiol das cisteínas. No caso da desprotonação, há possibilidade de duas reações diferentes, produzindo HCl ou H⁺ e Cl⁻, e essas reações estão representadas pela equações 1 e 2 :

A estrutura da proteína é simplificada na Figura 4, para verificar com mais facilidade a estrutura da camada alta, onde ocorre a reação. O produto, mantém a coordenação quadrático-plana ao redor da Platina e a coordenação não provoca grandes distorções na proteína.

Os dados termodinâmicos obtidos para cada reação estão mostrados abaixo, na tabela 1:

Tabela 1. Dados termodinâmicos para as equações químicas 1, 2, e 3.

Equação	$\Delta H(\text{kcal/mol})$	$\Delta G(\text{kcal/mol})$
1	+34,92	+30,35
2	+714,60	+339,30
3	+307,89	+306,90

De acordo com estes resultados, as reações são não espontâneas, indicando de forma incipiente que as reações não ocorreriam nas condições simuladas. Como se pode observar pela tabela 1, a equação 1 apresenta valores bem inferiores aos encontrados para as equações 2 e 3. Isso pode ser explicado pela ausência de espécies iônicas nessa equação, ao contrário das equações 2 e 3. Como os cálculos foram realizados em fase gás, a presença de espécies iônicas faz com que os valores encontrados fiquem superestimados. Quanto maior o número de espécies iônicas, maiores são os resultados obtidos. Os mesmos cálculos anteriores foram feitos com o Cu(II) isolado, no lugar da cisplatina uma vez que esta é a função biológica reconhecida da proteína. Novamente os dados termodinâmicos apontaram reações endotérmicas e não espontâneas, sendo que para a reação onde os grupos tiol estão protonados os valores obtidos foram $\Delta H = 6493,5$ kcal/mol e $\Delta G = 5798,5$ kcal/mol e para a reação onde os grupos desprotonados os valores foram $\Delta H = 6886,9$ kcal/mol e $\Delta G = 6196,3$ kcal/mol. Desta forma, o modelo computacional ainda precisa ser otimizado para definição mais adequada se as reações com a cisplatina e ATP7A ocorrerão em meio biológico colaborando então para a resistência deste fármaco.

Novas estratégias computacionais estão sendo estudadas para contornar esse problema da superestimação dos valores e vão ser colocadas em prática. Esses resultados indicam uma reação endotérmica, onde foi necessário um fornecimento de

energia às moléculas reagentes para haver quebra de ligações e formações de novas, o que é explicado pela maior presença de ligações intramoleculares nas moléculas reagentes em relação às moléculas dos produtos nas três reações. Os parâmetros cinéticos da reação dependem da estrutura de estado de transição caracterizada, o que ainda está sendo um desafio. Várias tentativas de se encontrar os estados de transição estão sendo realizados, além de novos cálculos incluindo outros procedimentos como: (i) diminuição do tamanho da camada alta; (ii) inclusão do solvente e (iii) estudos de outros sítios ativos da proteína ATP7A, para que se tenha uma visão geral do possível envolvimento ou não da proteína no mecanismo de resistência ao fármaco cisplatina.

Conclusões

A espontaneidade de uma reação química depende de diversos parâmetros e a combinação entre eles. A reação entre a proteína ATP7A e a cisplatina é uma reação que ocorre em meio biológico, com a presença de diversos solventes, que interagem com as moléculas participantes da reação. A inserção do solvente nos cálculos computacionais é de grande valia e já está sendo realizada, para que se possa obter uma conclusão mais precisa sobre a ocorrência ou não dessa reação.

Agradecimentos

Os autores agradecem o apoio recebido pela FAPEMIG, CAPES, CNPq, PPGMQ-MG, RQ- MG

Referências

1. www.pdb.org
2. S. Dapprich, I. Komaromi, K.S. Byun, K. Morokuma, and M.J. Frisch (1999). Journal of Molecular Structure, 461-462: 1
3. Rohr, A. K., M. Hammerstad, et al. Tuning of
4. Thioredoxin Redox Properties by Intramolecular
5. Hydrogen Bonds. Plos One, v.8, n.7, Jul, p.12.

Christina T. Borges*, Guilherme F. Lima, Juliana F. Lopes

Universidade Federal de Itajubá, LaQC- Laboratório de Química Computacional, Av. BPS nº1303, Bairro: Pinheirinho, 37500-903, Itajubá, MG, Brasil;

*E-mail: ctellesq@gmail.com

Investigation of the Pseudopotential Stuttgart/Dresden in the G3(MP2,CCSD,rel) Theory for Compounds Containing Transition Elements

Cleuton S. Silva & Rogério Custodio

Introduction

The Gaussian Theory^{1,2} has been developed over the last decades with the goal of approaching exact molecular energies using a set of calculations based primarily on ab initio molecular orbital theory with different levels of accuracy and basis set.

DeYonker et al.³ test set comprising 17 enthalpies of formation for transition metal compounds for testing their method referred to as the correlation consistent composite approach (ccCA). On this test set of 17 enthalpies, their ccCA method has a mean absolute deviation (MAD) of 5.6 kcal/mol, which is just under twice the average experimental uncertainty of 3.1 for this set of molecules.

Mayhall et al.⁴ Collected a test set comprising 20 enthalpies of formation for transition metal compounds for testing their method referred to as the G3(MP2,CCSD,rel). On this test set of 20 enthalpies, their G3(MP2,CCSD,rel) method has a mean absolute deviation (MAD) of 4.58 kcal/mol, which is just under twice the average experimental uncertainty of 1.5 Kcal/Mol.

Recently, the use of the CEP pseudopotential (Compact Effective Potential) along with the G3 theory⁵ proved to be possible preserving a high level of accuracy and providing a considerable gain in the CPU time. The objective of this work is to adapt the stuttgart/dresden pseudopotential in the G3(MP2,CCSD,rel).

Methods

The G3(MP2,CCSD,rel). composite model combines high-level correlation/moderate basis set calculations with lower level correlation/larger basis set calculations to approximate the results of a more expensive calculation. The composite energy is obtained from results using CCSD(T), MP2, and DKH calculations with progressively larger basis sets, and including first-order spin-orbit corrections for atoms and molecules (SO), zero-point energy corrections (ZPE), and an empirical higher level correction (HLC) that depends on the number of paired and unpaired electrons.

All steps of the original G3(MP2,CCSD,rel) theories were used and adapted to include the stuttgart/dresden pseudopotential G3(MP2,CCSD,rel,SDD) The scalar relativistic corrections to the energies are obtained from DKH-CCSD(T)/6-31G(d) single-point energy calculations using a second-order Douglas-Kroll-Hess (DKH) scalar relativistic Hamiltonian:

$$Eo[G3(MP2, CCSD, rel)] = CCSD(T)/6-31G(d) + \Delta E(MP2) + \Delta E(rel) + \Delta E(SO) + E(HLC) + E(ZPE) \quad (1)$$

And

$$\Delta E(MP2) = E[MP2/G3MP2LargeXP] - E[MP2/6-31G(d)] \quad (2)$$

$$\Delta E(rel) = E[DKH-CCSD(T)/6-31G(d)] - E[CCSD(T)/6-31G(d)] \quad (3)$$

Results and Discussion

Table 1 contains the total energies of the atoms Sc-Zn from the G3(MP2,CCSD,rel) and G3(MP2,CCSD,rel,SDD) methods. The deviations for all 20 molecules are given in this table with the mean absolute deviation at the bottom of the table. All of the deviations are in kilocalories per mole and calculated as experiment minus theory.

The MAD of 4.58 kcal/mol for G3(MP2,CCSD,rel) with a maximum deviation of 9.37 kcal/mol. The MAD of 4.39 kcal/mol for G3(MP2,CCSD,rel,SDD) with a maximum deviation of -16.07 kcal/mol. Most notable is the result for VO, where G3(MP2,CCSD,rel,SDD) differs by -16.07 kcal/mol from experiment while G3(MP2,CCSD,rel) differs by only -1.97 kcal/mol. If VO is excluded, the G3(MP2,CCSD,rel,SDD) mean absolute deviation is about the same as for G3(MP2,CCSD,rel).

Table 1: Comparison of G3(MP2,CCSD,rel) and 3(MP2,CCSD,rel,SDD) Methods for Calculation of ΔH_f (298 K) for a Test Set of 20 Molecules

Molecule	Experiment	G3(MP2, CCSD, rel)	G3(MP2, CCSD, rel, SDD)
ScO	-13.0±2.2	-2.4	-6.02
ScCl3	-160.5±2.1	5.97	0.37
TiO	-13.7±2.2	0.68	-4.89
TiF4	-370.8±1	5.48	0.24
VO	-31.8±2	-1.97	-16.07
CrCl	-31.0±0.6	1.13	1.87
CrO3	-77.3±1	9.12	2.67
MnCl	15.8±1.6	9.37	9.21
MnS	63.31±2	1.5	-3.10
FeCl	49.5±1.6	8.95	0.46
FeCl2	-32.8±1	7.71	-1.66
FeCl3	-60.5±1.2	9.43	5.45
CoCl2	-22.6±1	5.56	-0.63
CoCl3	-39.1±2.5	2.94	-5.29
NiCl2	-17.4±1	5.35	-0.17
NiF2	-77.8±1.1	8.9	7.73
CuH	65.9±2	-0.53	-10.32
CuCl	19.3±2	0.83	11.50
ZnH	62.9±0.5	0.31	0.14
Zn(CH3)2	12.86±2	3.52	0.04
MAD		4.58	4.39

The average uncertainty for the 20 molecule transition metal set is 1.5 kcal/mol, so the MAD is less than twice the

experimental uncertainty. In addition, some experimental atomic enthalpies of formation, such as for Ti, V, and Ni, have uncertainties of 2-4 kcal/mol. These are used in the calculation of the molecular enthalpies and may introduce uncertainties in the theoretical values. In a paper, Mayhall et al. G4(rel) the MAD of 4.07 kcal/mol with a maximum deviation of 21,31 kcal/mol. The MAD of 4.39 kcal/mol for G3(MP2,CCSD,rel,SDD) with a maximum deviation of -16.07 kcal/mol.

Conclusions

The G3(MP2,CCSD,rel,SDD) method, which includes scalar relativistic effects, has a mean absolute deviation of 4,39 kcal/mol and a maximum deviation of -16.07 kcal/mol for the test set of 20 enthalpies. Since the 20 enthalpies have an average experimental uncertainty of 1.5 kcal/mol, these results indicate that the G4(MP2,rel) method performs well for transition metals. The G3(MP2,CCSD,rel,SDD) failure stuttgart/dresden pseudopotential, which is particularly large for one molecule, VO.

Acknowledgments

The authors are grateful for the support given from the FAPEAM, CAPES, CNPQ and FAPESP e FAIPEX(UNICAMP).

References

1. L. Curtiss, R. Raghavachari, P. Radfern, V. Rassolov. J. Chem. Phys.,109 , 7764, (1998).
2. L. Curtiss, R. Raghavachari, P. Radfern, J. Chem. Phys.,126 , 084108, (2007).
3. J. DeYonker, K. Peterson, G. Steyl, A. Wilson, T. Cundari, J. Phys. Chem. A, 111 , 11269, (2009).
4. N. Mayhall, R. Raghavachari, P. Radfern, L. Curtiss. J. Phys. Chem. A, 113 , 5170, (2009).
5. D. Pereira, A. Ramos, N. Morgon, R. Custodio J. Chem. Phys. 135, 034106,(2011).

Cleuton S. Silva ^{a,b,*} & Rogério Custodio^b

^a Institute of Sciences Exact and technology, Federal University Of Amazonas, Cep: 69077-000, Itacoatiara-AM;

^b Department Of Physical Chemistry, Institute of Chemistry, State University of Campinas, Cep: 13083-872, Campinas-SP;

*E-mail: cleutonsouza@yahoo.com.br;

QM/MM (ONIOM) Calculation on FAK/Dasatinib Docking

Daniel A. B. de Oliveira & João B. L. Martins

Introduction

The cells perform several activities at every level through biochemical signaling. In general, every signal pathway is mediated by a receptor protein^{1,2}. The specific function of this class of enzyme is controlled by their molecular geometric covalent modification. These geometric molecular modifications are associated with the process know how phosphorylation. In this process phosphate groups originated from an ATP molecule react with the tyrosine amino-acids of the receptor tyrosine kinases modifying the original structure of the enzyme. This process is correlated with the normal division of the cell as well the control of cell proliferation through apoptosis. Cancer is a disease where an uncontrolled division of cells are observed. In this way, new cancer drugs are been developed from the knowledge of signal transduction^{3,4,5,6,7,8,9}. Focal adhesion kinase (FAK) is a non specific receptor tyrosine kinase, localized inside cytoplasm, that is implicated in regulation of a number of cell signaling pathways, including spreading, motility and apoptosis^{10,11,12,13,14,15,16}. The increase of phosphorylation in this kind of enzyme has been correlated with the interaction of integrins with fibronectins, which are adhesive proteins that help the cells adhere with cellular matrix.

Over expression of FAK has been correlated with several kinds of tumors^{17,18,19,20,21}. Experimentally, it has been showed that the uncontrolled division of cell is verified by a phosphorylation of aminoacid tyrosine 397 in FAK^{22,23,24,25,26,27}. The FAK phosphorylation is due of interaction between chemical signals and integrins with a non receptor tyrosine kinase. In the drug

design context, molecular modeling has contributed to understand the interaction between FAK and pyrrolopyrimidine inhibitors, helping in the discovery, development and optimization of new drugs^{28,29,30,31}.

Dasatinib is a known drug used in different cancers treatments and it is correlated with FAK inhibition³⁵. However the molecular interaction between FAK and the dasatinib is unknown. In this work it has been performed molecular docking between FAK and the drug dasatinib. In order to understand the chemical interaction between dasatinib and the catalytic site of FAK, it was employed QM/MM calculation using PM6, HF, AM1, RMNDO approach for the higher layer and molecular mechanic for lower layer. UFF force field was employed to describe low layer in QM/MM calculations. Molecular dynamics was performed to determine the behavior of dasatinib inside the catalytic site. The amino acids of catalytic site were selected based in recent publications that show the interaction between FAK and the respective inhibitors. ONIOM approach based in RMNDO/UFF and HF/UFF are the more adequate quantum mechanic methods to explain the interaction between FAK and dasatinib without internal error coordinate during the optimization. The calculation results show that dasatinib interact via hydrogen bond with the aminoacid ARG426 (Arginine 426), that is the hydrogen bond found in others FAK inhibitors.

Methods

Based in recent studies³⁰, it was performed molecular docking using AutoDockVina following

the next scripts. The docking was performed keeping the protein FAK frozen. For the ligand the dihedral angles were retained free. It was used a grid with follow dimensions: $x=-18$, $y=22$ and $z=16$ angstroms. Center grid was centered in catalytic site of protein FAK. The size box used on the grid had the follow orientation: $x=-0.444$, $y=10.627$ and $z=6.613$ angstroms. The time employed to proceed the exhaustiveness search of ligand conformations in catalytic site was 500 seconds. In order to understand the interaction between the molecule dasatinib and FAK it was employed QM/MM calculations based in ONIOM approach present in Gaussian program. It was chosen the aminoacids CYS 502, LYS 454, MET 499, ARG 426, ALA 452, GLU 471, GLU 506, ARG 508, ARG 550, ASP 564 in order to compose the higher layer in according of current literature³⁰. Quantum mechanics calculation based in PM6, B3LYP/6-31g, HF/6-31g, RMNDO were employed in higher layer that was optimized using the keyword quadmac, which does a quadratic step in the coordinates of all the atoms. 5000 SCF cycles were used in high layer optimization. UFF (Universal Force Field) was used in order to describe the Van-der Walls and electrostatic potential for the atoms in lower layer, that was maintained frozen during the optimization.

A short molecular dynamics with the classic force field CHARM and the program Hyperchem was employed in order to verify the dihedral angles displacements not observed during the optimization. For this purpose was used force field CHARM with one nanoseconds of simulation, a temperature of 300K and a dielectric constant equal 80 to simulate implicit solvent.

Results and Discussion

EQUILIBRIUM GEOMETRY AND MOLECULAR INTERACTIONS

Only the quantum mechanics calculation based in HF and MNDO approximation provided complete optimization of the system FAK-Dasatinib. The Table 1 show the energy associated with the interaction between FAK and the drug Dasatinib.

Table 1. Interaction obtained using HF/UFF and MNDO/UFF calculation.

METHOD	INTERACTION ENERGY IN kcal
HF	-108
MNDO	-176

The optimized QM/MM calculation, based in MNDO/UFF and HF/UFF, show that the drug Dasatinib interact with the aminoacid GLU471 via hydrogen bonding, as can be seen in the Figure 1.

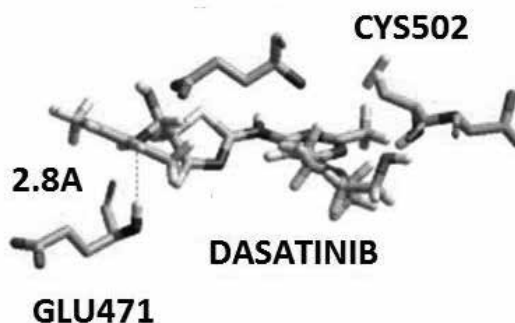


Figure 1. Interaction between Dasatinib and the aminoacid GLU471.

However when the molecular dynamics is performed, other hydrogen bonds into the catalytic site are found as shown in Figure 3. In these selected groups is observed dihedral angle rotations in dasatinib molecule during molecular dynamics as observed in Figure 2.

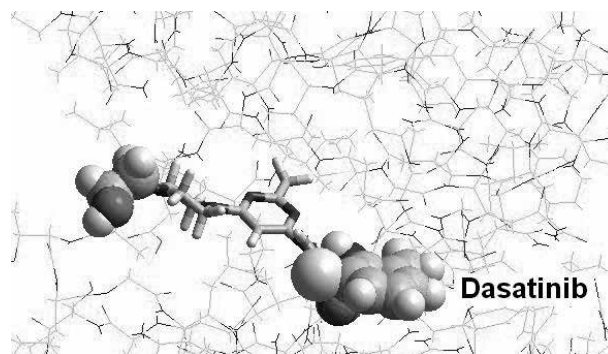


Figure 2. Chemical groups that showed dihedral rotation during the molecular dynamics.

The movement associated with the hydroxyl group allow the dasatinib perform hydrogen bond with the aminoacid ARG 426, as described in the Figure 3.

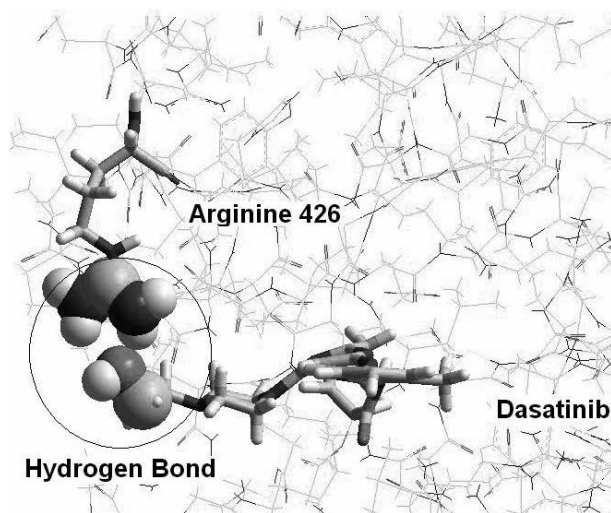


Figure 3: Hydrogen bond associated with the rotation of dihedral angle of group hydroxyl in the molecule of dasatinib.

This hydrogen bond is observed in others FAK inhibitors as noted in the literature³⁰.

THE PROBLEM ASSOCIATED WITH OPTIMIZATION

AM1, PM6 and B3LYP/3-21g were not useful to performed a complete optimization. These approximations revealed several errors in internal coordinates. In other hand HF/LANL2DZ and RMNDO performed a complete optimization of the complex FAK/dasatinib. In order to understand the optimization problem it was compared the molecular volume of Dasatinib with different FAK inhibitors. The molecule dasatinib occupy a large parcel of volume of the catalytic site. This fact may be corroborated when the volume of molecule dasatinib is compared with the volume of two know inhibitors. These results are showed below in the Table 2.

Table 2. Molecular Volume occupied by different FAK inhibitors.

Inibidor	Volume Molecular A3
Pirrolo -pirimidina	1510.93
ATP	1044.64
Dasatinibe	2303.61

It is known that the semi-empirical method MNDO do not describe very well noncovalent interactions. The FAK/dasatinib bonding is essentially hydrogen bond and noncovalent interaction. In other hand the quantum-semi-empirical PM6 replace MNDO core-core approximation by Voityuk diatomic expression resulting in a corresponding increased hydrogen bond interaction energy³³. There is also a problem associated with the HF method. The HF theory cannot describe the hydrogen bonding in some molecules³⁴. Although DFT does not predict true dispersion interactions in the weak interaction region of zero overlap, it can still be useful for predicting correlation energy and even dispersion-like interactions in the region of overlap near the equilibrium geometry of even noncovalent complexes if one has an accurate enough functional³⁴. Given these considerations we believe that during the energy optimization calculation via QM / MM, the inhibitor suffer deformation in their angles and dihedral, which cause errors in internal coordinates. These deformation are more pronounced for the functional B3LYP density and the quantum - semi-empirical PM6 method, that are more accurately methods to describe the interactions associated with dasatinib/FAK docking.

Conclusions

Dasatinib establish hydrogen bonds with the aminoacid GLU471 in according with ONIOM optimization. In other hand, molecular dynamics reveals the possibility of the hydrogen bond with the aminoacid ARG426. The problematic associated with the convergence errors in some methods of simulation such as AM1, PM6 and B3LYP, are associated with the size of molecular dasatinib into the catalytic site and the quality of methods used. Methods with high quality in

the description of interactions and bonds provide more angles displacements in dasatinib into the catalytic site.

Acknowledgments

The authors are grateful for the support given from the FAPEG, CAPES, CNPQ and FINATEC.

References

1. S. W. Benson and O. Dobis, *J. Phys. Chem. A*, **102**, 5175, (1998).
2. J. Liu, Z. Li, C. Sun, *J. Phys. Chem. A*, **105**, 7707, (2001). 3Tsai, P.-Y.; Che, D.-C.;
3. Nakamura, K. C. Lin, T. Kasai, *Phys. Chem. Chem. Phys.*, **12**, 2532, (2010).
4. Mukherjee, A.; Tang, M.; Pannu, H. S.; Chan-Hui, P.; Singh, S.; Mukherjee, A.; Pidaparthy, S.; Shi, Y.; Dua, R. Profiling one or more components of a signaling pathway by determining the status of receptor tyrosine kinase (RTK) signal transduction pathway activation, useful for measuring ErbB receptors and receptor complexes in cancer disorders. WO2005037071-A2; US2005131006-A1; EP1681983-A2; US7402399-B2; US7402398-B2; US2009011440-A1; WO2005037071-A3; US2009155818-A1; US8247180-B2.
5. Albagli, O.; Laget, M. P.; Chanut, F., Photoreceptor differentiation in *Drosophila*: Transduction and interpretation of the RTK signaling pathway. *M S-Medecine Sciences* **1997**, **13** (2), 184-191.
6. McCubrey, J. A.; Abrams, S. L.; Stadelman, K.; Chappell, W. H.; LaHair, M.; Ferland, R. A.; Steelman, L. S., Targeting signal transduction pathways to eliminate chemotherapeutic drug resistance and cancer stem cells. In *Advances in Enzyme Regulation*, Vol 50, Weber, G.; Weber, C. E. F.; Cocco, L., Eds. **2010**; Vol. 50, pp 285-307.
7. Collins, I.; Workman, P., Design and development of signal transduction inhibitors for cancer treatment: Experience and challenges with kinase targets. *Current Signal Transduction Therapy* **2006**, **1** (1), 13-23.
8. Fulda, S.; Debatin, K.-M., Signal transduction therapy targeting apoptosis pathways in cancers. *Current Signal Transduction Therapy* **2006**, **1** (2), 179-190.
9. Klein, S.; Levitzki, A., Signal transduction therapy for cancer - Whither now? *Current Signal Transduction Therapy* **2006**, **1** (1), 1-12.
10. Christoffersen, T.; Guren, T. K.; Spindler, K.-L. G.; Dahl, O.; Lonning, P. E.; Gjertsen, B. T., Cancer therapy targeted at cellular signal transduction mechanisms: Strategies, clinical results, and unresolved issues. *European Journal of Pharmacology* **2009**, **625** (1-3), 6-22.
11. Bidwell, G. L., III; Raucher, D., Therapeutic peptides for cancer therapy. Part I - peptide inhibitors of signal transduction cascades. *Expert Opinion on Drug Delivery* **2009**, **6** (10), 1033-1047.
12. Levitzki, A.; Klein, S., Signal transduction therapy of cancer. *Molecular Aspects of Medicine* **2010**, **31** (4), 287-329.
13. Huang, S.-M.; Hsu, P.-C.; Chen, M.-Y.; Li, W.-S.; More, S. V.; Lu, K.-T.; Wang, Y.-C., The novel indole compound SK228 induces apoptosis and FAK/Paxillin disruption in tumor cell lines and inhibits growth of tumor graft in the nude mouse. *International Journal of Cancer* **2012**, **131** (3), 722-732.
14. Chang, S. K.; Hindes, A.; Cornelius, L. A.; Efimova, T., Proline-rich tyrosine kinase 2 (Pyk2), a focal adhesion kinase (FAK) homologue, induces apoptosis in human malignant metastatic melanoma. *Journal of Investigative Dermatology* **2012**, **132**, S130-S130.
15. Kwak, S. W.; Park, E. S.; Lee, C. S., Parthenolide induces apoptosis by activating the mitochondrial and death receptor pathways and inhibits FAK-mediated cell invasion. *Molecular and Cellular Biochemistry* **2014**, **385** (1-2), 133-144.
16. Shieh, J.-M.; Wei, T.-T.; Tang, Y.-A.; Huang, S.-M.; Wen, W.-L.; Chen, M.-Y.; Cheng, H.-C.; Salunke, S. B.; Chen, C.-S.; Lin, P.; Chen, C.-T.; Wang, Y.-C., Mitochondrial Apoptosis and FAK Signaling Disruption by a Novel Histone Deacetylase Inhibitor, HTPB, in Antitumor and Antimetastatic Mouse Models. *Plos One* **2012**, **7** (1).
17. Yoon, H.; Choi, Y.-L.; Song, J.-Y.; Do, I.; Kang, S. Y.; Ko, Y.-H.; Song, S.; Kim, B.-G., Targeted Inhibition of FAK, PYK2 and BCL-XL Synergistically Enhances Apoptosis in Ovarian Clear Cell Carcinoma Cell Lines. *Plos One* **2014**, **9** (2).
18. Vanamala, J.; Radhakrishnan, S.; Reddivari, L.; Bhat, V. B.; Pitsyn, A., Resveratrol suppresses human colon cancer cell proliferation and induces apoptosis via targeting the pentose phosphate and the talin-FAK signaling pathways-A proteomic approach. *Proteome Science* **2011**, **9**.
19. Elmore, S., Apoptosis: A review of programmed cell death. *Toxicologic Pathology* **2007**, **35** (4), 495-516.
20. Zhang, L.-L.; Liu, J.; Lei, S.; Zhang, J.; Zhou, W.; Yu, H.-G., PTEN inhibits the invasion and metastasis of gastric cancer via downregulation of FAK expression. *Cellular Signalling* **2014**, **26** (5), 1011-1020.
21. Chen, Q.; Xu, R.; Zeng, C.; Lu, Q.; Huang, D.; Shi, C.; Zhang, W.; Deng, L.; Yan, R.; Rao, H.; Gao, G.; Luo, S., Down-Regulation of Gli Transcription Factor Leads to the Inhibition of Migration and Invasion of Ovarian Cancer Cells via Integrin beta 4-Mediated FAK Signaling. *Plos One* **2014**, **9** (2).
22. Huang, G.; Ho, B.; Conroy, J.; Liu, S.; Qiang, H.; Golubovskaya, V., The Microarray Gene Profiling Analysis of Glioblastoma Cancer Cells Reveals Genes Affected by FAK Inhibitor Y15 and Combination of Y15 and Temozolomide. *Anti-Cancer Agents in Medicinal Chemistry* **2014**, **14** (1), 9-17.
23. Lane, D.; Matte, I.; Laplante, C.; Garde-Granger, P.; Rancourt, C.; Piche, A., Osteoprotegerin (OPG) activates integrin, focal adhesion kinase (FAK), and Akt signaling in ovarian cancer cells to attenuate TRAIL-induced apoptosis. *Journal of Ovarian*

Research 2013, 6.

24. Kong, X.; Li, G.; Yuan, Y.; He, Y.; Wu, X.; Zhang, W.; Wu, Z.; Chen, T.; Wu, W.; Lobie, P. E.; Zhu, T., MicroRNA-7 Inhibits Epithelial-to-Mesenchymal Transition and Metastasis of Breast Cancer Cells via Targeting FAK Expression. *Plos One* 2012, 7 (8).
25. Wan, H.-T.; Mruk, D. D.; Li, S. Y. T.; Mok, K.-W.; Lee, W. M.; Wong, C. K. C.; Cheng, C. Y., p-FAK-Tyr(397) regulates spermatid adhesion in the rat testis via its effects on F-actin organization at the ectoplasmic specialization. *American Journal of Physiology-Endocrinology and Metabolism* **2013**, 305 (6), E687-E699.
26. Jiang, X.; Sinnett-Smith, J.; Rozengurt, E., Differential FAK phosphorylation at Ser-910, Ser-843 and Tyr-397 induced by angiotensin II, LPA and EGF in intestinal epithelial cells. *Cellular Signalling* **2007**, 19 (5), 1000-1010.
27. Mukai, M.; Iwasaki, T.; Tatsuta, M.; Togawa, A.; Nakamura, H.; Murakami-Murofushi, K.; Kobayashi, S.; Imamura, F.; Inoue, M., Cyclic phosphatidic acid inhibits RhoA-mediated autophosphorylation of FAK at Tyr-397 and subsequent tumor-cell invasion. *International Journal of Oncology* **2003**, 22 (6), 1247-1256.
28. Hunger-Glaser, I.; Fan, R. S.; Perez-Salazar, E.; Rozengurt, E., PDGF and FGF induce focal adhesion kinase (FAK) phosphorylation at Ser-910: Dissociation from Tyr-397 phosphorylation and requirement for ERK activation. *Journal of Cellular Physiology* **2004**, 200 (2), 213-222.
29. Jacamo, R.; Jiang, X.; Lunn, J. A.; Rozengurt, E., FAK phosphorylation at Ser-843 inhibits Tyr-397 phosphorylation, cell spreading and migration. *Journal of Cellular Physiology* **2007**, 210 (2), 436-444.
30. Eide, B. L.; Turck, C. W.; Escobedo, J. A., IDENTIFICATION OF TYR-397 AS THE PRIMARY SITE OF TYROSINE PHOSPHORYLATION AND PP60(SRC) ASSOCIATION IN THE FOCAL ADHESION KINASE, PP125(FAK). *Molecular and Cellular Biology* **1995**, 15 (5), 2819-2827.
31. Choi, H. S.; Wang, Z. C.; Richmond, W.; He, X. H.; Yang, K. Y.; Jiang, T.; Sim, T. B.; Karanewsky, D.; Gu, X. J.; Zhou, V.; Liu, Y.; Ohmori, O.; Caldwell, J.; Gray, N.; He, Y., Design and synthesis of 7H-pyrrolo 2,3-d pyrimidines as focal adhesion kinase inhibitors. Part 1. *Bioorganic & Medicinal Chemistry Letters* **2006**, 16 (8), 2173-2176.
32. Choi, H. S.; Wang, Z. C.; Richmond, W.; He, X. H.; Yanga, K. Y.; Jiang, T.; Karanewsky, D.; Gu, X. J.; Zhou, V.; Liu, Y.; Che, J. W.; Lee, C. C.; Caldwell, J.; Kanazawa, T.; Umemura, I.; Matsuura, N.; Ohmori, O.; Honda, T.; Gray, N.; He, Y., Design and synthesis of 7H-pyrrolo 2,3-d pyrimidines as focal adhesion kinase inhibitors. Part 2. *Bioorganic & Medicinal Chemistry Letters* **2006**, 16 (10), 2689-2692.
33. Barra de Oliveira, D. A.; de Oliveira Neto, M.; Martins, J. B. L., Theoretical study of disubstituted pyrrolopyrimidines as focal adhesion kinase inhibitors. *International Journal of Quantum Chemistry* **2012**, 112 (10), 2324-2329.
34. de Courcy, B.; Piquemal, J.-P.; Garbay, C.; Gresh, N., Polarizable Water Molecules in Ligand-Macromolecule Recognition. Impact on the Relative Affinities of Competing Pyrrolopyrimidine Inhibitors for FAK Kinase. *Journal of the American Chemical Society* **2012**, 134 (10), 3312-3320.
35. Moreno Nascimento, E. C.; Martins, J. B. L., Electronic structure and PCA analysis of covalent and non-covalent acetylcholinesterase inhibitors. *Journal of Molecular Modeling* **2011**, 17 (6), 1371-1379.
36. James J. P. Stewart, *Journal of Molecular Modeling*, Optimization of parameters for semiempirical methods V: Modification of NDDO approximations and application to 70 elements December **2007**, Volume 13, Issue 12, pp 1173-1213.
37. Yan Zhao, Oksana Tishchenko, and Donald G. Truhlar. How Well Can Density Functional Methods Describe Hydrogen Bonds to π Acceptors. *The Journal of Physical Chemistry*. 2005, 109 (41), pp 19046-19053. Dario Caccial, Francesca Micciché, Giuliana Cassinelli, Piera Mondellini, Patrizia Casalini and Italia Bongarzone. Dasatinib reduces FAK phosphorylation increasing the effects of RPI-1 inhibition in a RET/PTC1-expressing cell line. *Molecular Cancer* **2010**, 9:278

Daniel A. B. de Oliveira ^{a*} &
João B. L. Martins ^b

^aUFT, Rua Paraguai s,n (esquina com Urixamas)- Setor Cimba-CEP- 77838-824(Araguaína-TO) I

^bUNB, IQ, CP 4478, Asa Norte 70904970 - Brasília, DF - Brasil 2

*E-mail: danielchem@uft.edu.br

Evaluation of the Photophysics of Four Ru(II) Phthalocyanine/TiO₂ (Anatase) Complexes Using DFT Methods

D. M. S. Araújo, L. T. Ueno, A. O. T. Patrocínio & A. E. H. Machado

Introduction

Electron transfer is the most basic form of a chemical reaction: the electron is spontaneously transferred from a donor to an acceptor center^{1,2}. The understanding of the photophysics related to the photoinduced electron transfer is fundamental for the comprehension of certain natural processes, such as light harvesting, making feasible the developing of artificial systems for solar fuel production³.

In the study of photocatalytic processes, computational quantum mechanics has made significant contributions⁴⁻⁷. Jono and coworkers, for example, demonstrated the occurrence of interfacial charge transfer from an organic compound to the surface of titanium dioxide, using visible radiation⁸.

Among the possible applications of such phenomenon stands out the use of solar energy in visible region to trigger photocatalytic processes (solar energy conversion, environmental remediation and photocatalytic production of hydrogen are some examples) since that a large part of the known semiconductor oxides with photocatalytic activity are active only in the ultraviolet. Thus, this has attracted the attention of several researchers around the world⁹⁻²⁰.

Considered as the energy source of the future the hydrogen, in addition of being a renewable font, concentrates a large amount of energy per unit mass (1.0 kilogram of hydrogen contains about the same energy supplied by 2.7 kilograms of gasoline), enabling the portability of energy^{21,22}. Experts have pointed out

three major obstacles to the expansion of hydrogen consumption, taking into account the currently available technology: clean production, low cost and the storage and transportation. As a result, many efforts to expand the use of hydrogen as cheap energy supply has been based on the development of efficient processes free of fossil fuels^{16,19,20}.

The photocatalytic degradation of water to produce hydrogen under the solar irradiation is a promising way to obtain clean and cheap hydrogen. Despite the advances in photocatalysis using ultraviolet radiation, the use of visible radiation is yet a theme of intense studies^{16,20}.

Studies show that the incorporation of photosensitizing dyes to the surface of a photocatalyst is a viable option to increment the H₂ production²³⁻²⁴. TiO₂ is the most studied photocatalyst since it is stable, usually presents photocatalytic activity, of low-cost and versatile. However, this semiconductor has a negligible photocatalytic activity in almost all the visible spectrum. So, much effort has been directed to work around this problem^{16,20}. One of the alternatives found are the dye-sensitized photocatalysts^{16,25}. These systems are capable to minimize the recombination of the charge carriers and the red shift of the absorption spectrum enabling the use of visible radiation¹⁶.

In the present study, we evaluate the role of functional groups on the photoinduced charge transfer in four complexes based on the chemical association between Ru(II) phthalocyanines and a cluster of anatase (TiO₂), continuing the study started by Gomes et al. (2015)²⁶.

Methods

To optimize the structure of the complexes 1-diethyl-1-carboxyl-RuPc-Anatase (1), 2-diethyl-1-carboxyl-RuPc-Anatase (2), 2-diethyl-2-carboxyl-RuPc-Anatase (3), and 3-diethyl-1-carboxyl-RuPc-Anatase (4), and calculate their vibrational frequencies, we used the hybrid functional B3LYP and the basis set LANL2DZ ECP²⁷⁻²⁹ with the corresponding pseudo-potential for Ru and Ti, and the basis set def2-TZVP³⁰ for the other elements. The functional CAM-B3LYP³¹ was used in the TDDFT approaches for predicting the first sixty singlet excited states for the construction of the electronic spectrum of each studied derivative.

The nanocluster of anatase used in the calculation was based in a structure described by Jono and co-workers⁸, being kept frozen in all calculations.

All calculations were done considering the derivatives solvated in acetonitrile. This was done using CPCM (Polarizable Conductor Calculation Model)³².

The contribution of the molecular orbitals on electronic state was calculated using Chemissian³³. GaussSum³⁴ was used to calculate the contribution of the most important electronic transitions and to build energy diagrams and graphs of states densities.

Structural optimizations, infrared frequency calculations and simulations of excited states were done using the software Gaussian 09³⁵.

Results and Discussion

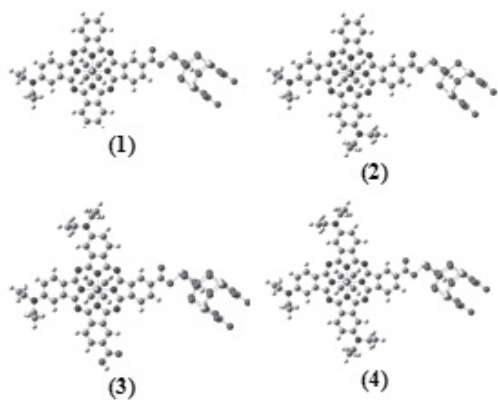


Figure 1. Optimized structures: (1) 1-diethyl-1-carboxyl-RuPc-Anatase (2) 2-diethyl-1-carboxyl-RuPc-Anatase (3) 2-diethyl-2-carboxyl-RuPc-Anatase (4) 3-diethyl-1-carboxyl-RuPc-Anatase

The vibrational spectra calculated for the derivatives did not have imaginary frequencies, indicating that the stationary point found on the optimization corresponds to global minima.

The values of the geometric parameters of each structure show good agreement with typical bonds and angles observed of similar structures³⁶⁻³⁸.

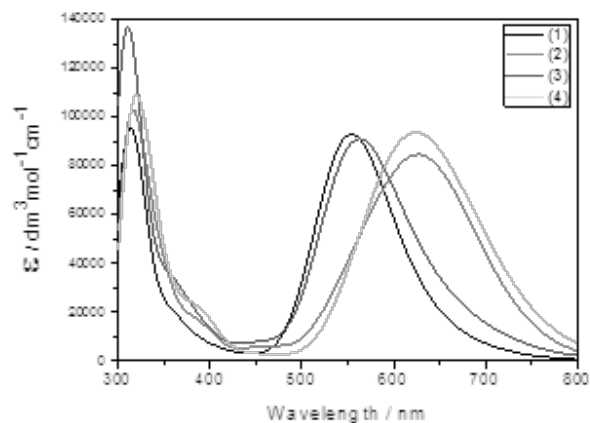


Figure 2. Simulated electronic absorption spectra of the complexes (1) to (4) solvated in acetonitrile.

The simulated spectra of these complexes exhibit the two characteristic absorption bands typical of phthalocyanines³⁹. This suggests that the light absorption properties observed for the ruthenium phthalocyanines under study are preserved in these complexes. The maintenance of these properties may represent a significant advantage for use of these complexes in applications based on sunlight absorption⁴⁰⁻⁴³.

The shifts observed in the Q-bands suggest that the nature, position, number of substituents in the macrocycle, and chemical bonding with TiO₂ exert great influence on the electronic structure of the complexes. The complexes (2) and (4) that have a greater number of donor substituents present a red-shifted Q-band.

Complexes (2) and (4) have both absorption bands red shifted relative to the others. These complexes present in general expressive values of oscillator strength for the first five excited states, typical of electronic transitions of high probability. They are related to photoinduced charge transfer from donor groups, and are in the range of the Q-band. Differently, for complexes (1) and (3) the most

intense electronic transitions are related to states S4 and S5. Different combinations and weights of the molecular orbitals in the range between HOMO-2 and LUMO+3, excluding the LUMO, are involved in the transitions that constitute the five first electronic states of these four complexes.

The Soret (B) band in these complexes is of high probability, involves high electronic states and practically does not suffer electronic shift. However, the intensity of the bands varies, being the most intense related to complex (3). This complex possesses donor and acceptor groups linked to the macrocycle. The analysis of the orbital structure of this band suggests that it is mainly of charge transfer from the macrocycle and metallic center of phthalocyanine to the semiconductor.

Table 1 presents the contribution of main molecular fragments (Ru(II), the TiO₂ cluster - TiO₂, the free base phthalocyanine - Mcycle, the donor groups - Donor, and the axial pyridines - Py) in the molecular orbital composition of each complex.

The data from Table 1 shows that the TiO₂ cluster does not contribute with the occupied orbitals. However, this contribution is very significant in the virtual orbitals, according to the verified in the analysis of the molecular orbitals involved in photoinduced charge transfer.

Ru(II), as well as, the free base phthalocyanine type structure and the donor groups have expressive contribution in the occupied orbitals, mainly HOMO-2 and HOMO-1 in all complexes, and HOMO-4 in the complex (4). Such orbitals are important in the Q-band, as observed in the electronic spectra (Figure 2), and in the electronic delocalization in these phthalocyanines.

The analysis of the DOS (Figure 3) corroborates with the

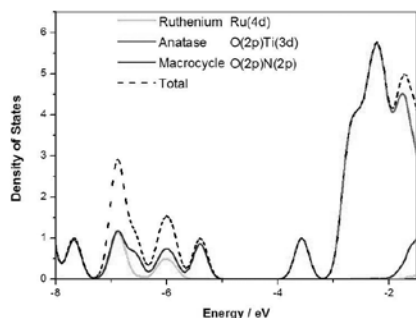


Figure 3. Density of states (DOS) diagram calculated for the complex (4), presenting the partial DOS corresponding to Ru(II), macrocycle and anatase.

Table 1. Contributions of molecular orbitals in the main areas of each complex

	MO	Contribution (%)				
		Ru(II)	TiO ₂	Mcycle	Donor	Py
1	H-5	-	-	98	-	2
	H-2	54	-	41	-	5
	H-1	24	-	70	3	3
	H	10	-	71	18	1
	L+1	-	99	1	-	-
	L+3	-	100	-	-	-
	L+23	8	6	83	-	3
	L+28	-	100	-	-	-
2	H-7	1	-	97	1	1
	H-6	1	-	96	1	2
	H-2	35	-	56	7	2
	H-1	31	-	48	19	2
	H	3	-	85	-	12
	L+1	-	100	-	-	-
	L+3	-	99	1	-	-
	L+23	-	99	1	-	-
	L+24	-	95	5	-	-
3	H-6	-	-	96	4	-
	H-2	34	-	56	7	3
	H-1	30	-	48	19	3
	H	4	-	85	11	-
	L+1	-	100	-	-	-
	L+2	-	100	-	-	-
4	H-7	12	-	82	1	5
	H-4	49	-	51	-	-
	H-2	26	-	51	20	3
	H-1	23	-	50	25	2
	H	2	-	82	16	-
	L+1	-	100	-	-	-
	L+2	-	100	-	-	-
	L+3	-	98	2	-	-
	L+13	-	99	1	-	-
	L+14	-	100	-	-	-
	L+23	-	99	1	-	-
	L+25	-	100	-	-	-

data of Table 1. The partial DOS of anatase predominates above -4 eV, in the range of virtual states, showing that the electronic transitions governed by the Q-band tend to induce electron transfer from phthalocyanine to 3d states of the fivefold coordinated titanium atoms⁴⁴. Additionally, the involvement of 4d orbitals of Ru(II) in these transitions is evidenced by two bands in the DOS diagrams calculated for these complexes.

Conclusions

The photophysical characterization of four complexes formed by chemical association between derivatives of Ru(II) phthalocyanine and anatase nanocluster showed, through electronic structure analysis, that the electronic excitation of the Q-band of such complexes results in the efficient electron transfer from phthalocyanine to TiO₂ (anatase). Also, the number of donor groups, peripheral to the macrocycle, favors this process and is responsible for a red shift of the Q-band, and that this band should occur in the visible, above 500 nm. This opens the possibility of applications of such complexes to enhance photocatalytic processes by sensitization of photosensitizers based on TiO₂ using sunlight.

The DOS diagram shows that the most effective contributions in the sensitization process are due to the macrocycle and Ru(II).

Acknowledgments

The authors are grateful for the support given by FAPEMIG, CNPq and CAPES.

References

- Zhang, M. J., Guo, Y. R., Fang, G. Z., and Pan, Q. J., *Comput. Theor. Chem.*, 1019, 94, (2013).
- Agnihotri, N. and Steer, R. P., *J. Porphyr. Phthalocya.*, 18, 475 (2014).
- Scholes, G. D., Fleming, G. R., Olaya-Castro, A., van Grondelle, R., *Nature Chemistry*, 3, 763 (2011).
- Zhang, C. R., et. al., *Comput. Theor. Chem.*, 1017, 99, (2013).
- Ueno, L. T., et. al., *J. Brazil Chem. Soc.*, 23, 2237, (2012).
- Risplendi, F., Cicero, G., Mallia, G., and Harrison, N. M., *Phys. Chem. Chem. Phys.*, 15, 235, (2013).
- Manzhos, S., et. al., *J. Phys. Chem. C.*, 115, 21487, (2011).
- Jono, R., et. al., *J. Phys. Chem. Lett.*, 2, 1167, (2011).
- Xie, P. H. and Guo, F. Q., *Curr. Org. Chem.*, 11, 1272, (2007).
- Bernede, J. C., *J. Chil. Chem. Soc.*, 53, 1549, (2008).
- Valdes, A., et. al., *Phys. Chem. Chem. Phys.*, 14, 49, (2012).
- Ni, M., et. al., *Renew. Sust. Energ. Rev.*, 11, 401, (2007).
- Patel, M., et. al., *Phys. Rev. B*, 86, (2012).
- de la Calle, et. al., *Int. J. Hydrogen Energ.*, 37, 10549, (2012).
- Yang, H. H., Guo, L. J., Yan, W., and Liu, H. T., *J. Power Sources*, 159, 1305, (2006).
- Machado, A. E. H., et. al., *Solar Radiation*. 2012.
- Hisatomi, T., Kubota, J., and Domen, K., *Chem. Soc. Rev.*, 43, 7520, (2014).
- Liao, C. H., Huang, C. W., and Wu, J. C. S., *Catalysts*, 2, 490, (2012).
- Huang, C. W., et. al., *Sol. Energ. Mat. Sol. C.*, 107, 322, (2012).
- Machado, A. E. H., et. al., A. Méndez-Vilas, Editor., *Formatex*. 867 (2013).
- Smith, B. and Shantha, M. S. *Int. J. Chem. React. Eng.*, 5, 1542, (2007).
- Neto, E.H.G. *Brasil H2 Fuel Cell Energy*, Curitiba. 2005.
- Biswal, N., Das, D. P., Martha, S., and Parida, K. M., *Int. J. Hydrogen Energ.*, 37, 6118, (2012).
- Yang, M., Men, Y., Li, S. L., and Chen, G. W., *App. Catal. a-Gen.*, 433, 26, (2012).
- Pankaj, C., Hassan, G. and Ajay, K. R. *American Chemical Society*, 1124, 231, (2013).
- Gomes, W. R., Ueno, L. T. Cabecione, D. R., Araújo, D. M. S., Patrocínio, A. O. T., Machado, A. E. H., In preparation.
- Wadt, W. R. and Hay, P. J., *J. Chem. Phys.*, 82, 284, (1985).
- Hay, P. J. and Wadt, W. R., *J. Chem. Phys.*, 82, 299, (1985).
- Hay, P. J. and Wadt, W. R., *J. Chem. Phys.*, 82, 270, (1985).
- Rappoport, D. and Furche, F., *J. Chem. Phys.*, 133, 134105 (2010).
- Yanai, T., Tew, D. P., and Handy, N. C., *Chem. Phys. Lett.*, 393, 51(2004).
- Cossi, M., Rega, N., Scalmani, G., and Barone, V., *J. Comp. Chem.*, 24, 669, (2003).
- Chemissian, A Computer Program to Analyse and Visualise Quantum-Chemical Calculations (L. Skripnikov, 2012).
- O'Boyle, N. M., Tenderholt, A. L., Langner, K. M., *J. Comp. Chem.*, 29, 839 (2008).
- Frisch, M. J., et al., *Gaussian 09 Revision D.01*. 2013, Gaussian, Inc.: Wallingford, CT, USA.
- Koppen, S. and Langel, W., *Phys. Chem. Chem. Phys.*, 10, 1907, (2008).

37. Enakieva, et. al., Mendelev Commun., 14, 193, (2004).
 38. Ueno, L. T., Machado, A. E. H., and Machado, F. B. C., THEOCHEM, 899, 71, (2009).
 39. Kobayashi, N., et al., Inorg. Chem., 41, 5350, (2002).
 40. Goncalves, L. M., et al., Energ. Environ. Sci., 1, 655, (2008).
 41. Gratzel, M., Inorg. Chem., 44, 6841, (2005).
 42. Ngoh, S. K. and Njomo, D., Renew. Sust. Energ. Rev., 16, 6782, (2012).
 43. Simon, J. J et al., Int. J. Mater. Prod. Tech., 34, 469, (2009).
 44. Diebold, U., Surf. Sci. Rep., 48, 53, (2003).
-

D. M. S. Araújo^{a*}, L. T. Ueno^b,
A. O. T. Patrocínio^a & A. E. H.
Machado^a

^a Laboratório de Fotoquímica e Ciência de Materiais, Instituto de Química, Universidade Federal de Uberlândia, P.O. Box 593, CEP 38400-902 Uberlândia, MG, Brasil

E-mail address: diesleymartins@yahoo.com.br,

^b Faculdade de Ciências Integradas do Pontal, Universidade Federal de Uberlândia, CEP 38302-074 Ituiutaba, MG, Brasil

*E-mail: diesleymartins@yahoo.com.br

Estudo Teórico de Propriedades Geométricas e Eletrônicas da Nimesulida no Vácuo Utilizando Dinâmica Molecular de Car-Parrinello

Eduardo C. Vaz, Ademir J. Camargo & Solemar S. Oliveira

Introdução

O nimesulida é um fármaco da classe dos anti-inflamatórios não-esteroides (AINES) e atua inibindo a biossíntese de prostaglandinas, através de um bloqueio competitivo da enzima ciclooxigenase (COX) e também diminuindo a formação de radicais livres em nível da cascata do ácido araquidônico, impedindo a formação de eicosanoides, combatendo, assim, os processos inflamatórios, dores e febre^{1,2}.

Realizamos a dinâmica de Car-Parrinello no vácuo objetivando analisar as propriedades geométricas da molécula. Para comparação, também realizamos cálculos de Teoria do Funcional de Densidade (DFT), e analisamos a estrutura eletrônica. Comparamos nossos resultados com dados experimentais obtidos por difração de raios-X.

Modificações em sua estrutura molecular foram listadas na literatura provando um maior efeito anti-inflamatório do nimesulida³⁻⁵. Tais modificações juntamente dos resultados obtidos serão utilizados para estudos de uma dinâmica em sistema aquoso focando melhorias na sua farmacodinâmica.

Metódos

Para os cálculos, a molécula primeiramente foi otimizada geometricamente e minimizada sua função de onda com o auxílio do algoritmo *Steepest Descent*.

A molécula estabilizada foi utilizada como input para os cálculos em todos os métodos. Para Car-Parrinello, utilizou-se o funcional PBE com cálculos realizados com o auxílio do programa *Quantum Espresso*. Para o método de DFT os cálculos com base 6-31+g(d,p) foram realizados com o auxílio do programa Gaussian09.

Resultados e Discussões

Os resultados da dinâmica mostraram-se positivos, confirmando que a molécula possui comportamento estável.

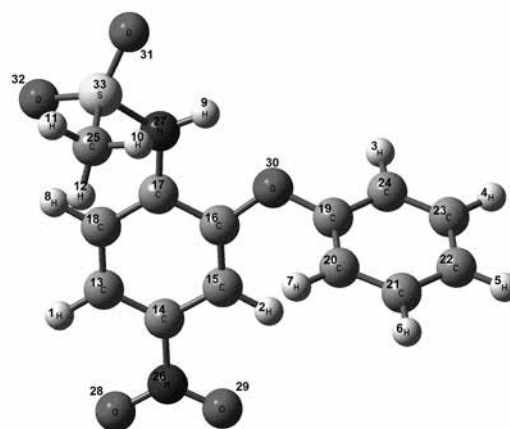


Figura 1: Molécula de Nimesulida com átomos respectivamente enumerados.

Os resultados também mostraram que a molécula manteve a separação energia entre os subníveis eletrônico e iônico durante toda a simulação, como pode ser observado no gráfico:

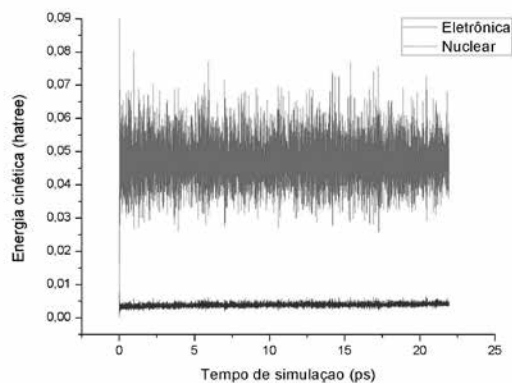


Gráfico 1: Separação adiabática dos subsistemas nuclear e eletrônico para a simulação da molécula de nimesulida.

Por meio de DFT pode-se observar as propriedades eletrônicas do nimesulida, tais como mapa de potencial eletrostático (MEP) e orbitais HOMO-LUMO.



Figura 2: Orbitais HOMO-LUMO.

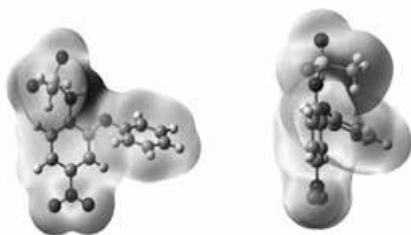


Figura 3: Mapa de potencial eletrostático (MEP).

As comparações dos parâmetros geométricos entre os métodos teóricos e os resultados experimentais estão expressos nos gráficos abaixo:

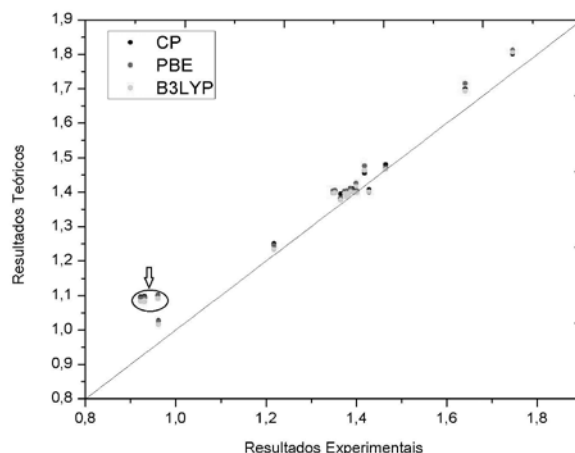


Gráfico 2: Gráfico comparativo de comprimentos de ligação (Å) entre resultados teóricos e experimentais.

Ao observar o gráfico 2, verificamos que havia um grupo de valores que mais se distanciava da reta em relação aos outros (pontos destacados no gráfico). Ao analisarmos esses valores, verificamos que se trata de uma possível repulsão eletrônica H-H, entre H(8)-H(12), H(9)-H(10) e H(2)-H(7). Os demais valores apresentaram um aceitável desvio padrão da reta.

Já ao observarmos o gráfico 3, verificamos que os valores de ângulo de ligação estavam bastante dispersos, mas dois grupos se destacavam mais, em relação aos outros, da reta (pontos destacados no gráfico). Ao analisarmos os valores, percebemos que se trata do efeito de eletropositividade na angulação da molécula, uma vez que os pontos que apresentaram alto desvio padrão correspondem a angulação entre $S_{(33)}-N_{(27)}-H_{(9)}$ e $S_{(33)}-N_{(27)}-C_{(17)}$ (como pode ser observado no MEP).

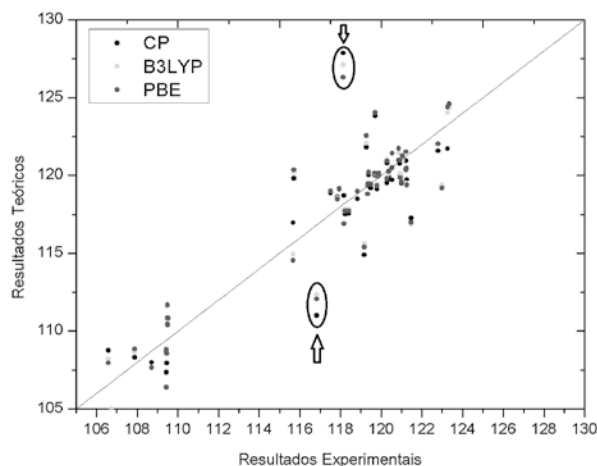


Gráfico 3: Gráfico comparativo de ângulos de ligação (°) entre resultados teóricos e experimentais.

Conclusões

Por meio dos resultados pode-se observar as regiões as quais o solvente provavelmente irá interagir. A probabilidade de interação é maior devido à presença de uma região eletropositiva na molécula e do posicionamento do orbital LUMO. Tal região tem maior facilidade em liberar próton, facilitando também a interação de um solvente com a molécula.

Pode-se também comparar e verificar qual dos métodos possui maior acurácia quando comparado aos resultados experimentais a nível de parâmetros geométricos.

Agradecimentos

Gostaria de agradecer à Universidade Estadual de Goiás (UEG), por meio do Programa de Auxílio-Eventos (Pró-Eventos) pela concessão da bolsa que possibilitou minha participação no evento.

Referências

1. L. Cullen, L. Kelly, S.O. Konnor, D.J. Fitzgerald, J. Pharmacol. Exp. Ther. 287(1998) 578.
2. Dubois R, Abramson S, Crofford L et al - Cyclooxygenase in biology and disease. Faseb J. 1998;12:1063-1088,.
3. Bhattacharya, K. Kankanala, S. Pal, A. K. Mukherjee a, Journal of Molecular Structure. 975 (2010) 40–46.
4. C. Michaux, C. Charlier, F. Julémont, X. de Leval, J. –M. Dogné, B. Pirotte, F. Durant, Eur. J. Med. Chem. 40 (2005) 1316.
5. T. Inaba, K. Tanaka, R. Takeno, H. Nagaki, C. Yoshida, S. Takano, Chem. Pharm. Bull. 48 (2000) 131.
6. CAR & PARRINELLO. Phys. Rev. Lett., v. 55, n. 22, p. 2471-2474, 1985.
7. GAUSSIAN 09, Revision D.01, Frisch M. J. et al. Gaussian, Inc., Wallingford CT, 2009.

Eduardo C. Vaz, Ademir
J. Camargo & Solemar S.
Oliveira*.

Universidade Estadual de Goiás (UEG) – Câmpus de Ciências Exatas e Tecnológicas (CCET)

*E-mail: solemar@ueg.br.

Planejamento Fatorial para a Investigação das Propriedades Espectroscópicas, Efeitos Relativísticos e de Solvatação de Derivados Halogenados da 2-Amino-1,4-Naftoquinona

Eduardo P. Rocha, Livia C. T. Lacerda, Mateus A. Gonçalves, Maíra S. Pires, Telles C. Silva, Henrique A. Rodrigues & Teodorico C. Ramalho

Introdução

Nos últimos anos, o interesse por processos fotoquímicos e fotofísicos tem aumentado.¹ Muitos desses processos apresentam aplicações industriais, como a fotocatalise, ou aplicações biomédicas, como as sondas fluorescentes para o diagnóstico de imagem.² Muitos compostos apresentam características fluorescentes, dentre esses compostos, encontram-se os derivados de naftoquinonas.³ Esses compostos, de origem natural, apresentam diversas aplicações biológicas, como antitumorais, antifúngica, antimalárica, entre outras.⁴ Derivados de naftoquinonas já foram testados por grupos de pesquisa³ como sondas fluorescentes em alguns tipos de câncer, como o câncer de cólon e de boca.^{3,5} Estudos das propriedades desses derivados apresentam, dessa forma, grande importância, uma vez que alterações estruturais podem fornecer sondas fluorescentes mais eficientes, seletivas e com um maior precisão.¹

Modificações estruturais, como adição de halogênios em determinadas posições da molécula pode promover alterações das propriedades espectroscópicas, o que possibilita a geração de novas regiões de absorção e emissões.⁶ Estudos de derivados halogenados de naftoquinonas empregam a espectroscopia de fluorescência⁷, Raman⁸, UV-VIS⁹, entre outras análises para a avaliação dos padrões de emissão e absorção desses compostos, bem como, por estudos teóricos, que envolvem a análise das energias de absorção, de emissão, a análise da diferença entre os orbitais homo-lumo, entre outras características.⁷

Recentes estudos teóricos envolvem, também, a análise dos diferentes mecanismos de emissão de fluorescência apresentado por esses compostos.^{1,10}

Dentre os estudos teóricos existem diferentes métodos que permitem a análise de processos de absorção e emissão, como os métodos Multi-Referenciais CASSCF, CASPT2, entre outros⁹. Nos últimos anos, o emprego da teoria do funcional de Densidade (DFT) tem se tornado importante por permitir a análise de diferentes sistemas químicos com tamanhos diferenciados, como para a análise de complexos metálicos e sistemas biológicos.¹¹ A análise de propriedades de absorção e emissão é realizada com o emprego da Teoria do Funcional de Densidade dependente do tempo (TD-DFT), que permite a análise das transições verticais de compostos diversos, bem como a análise da diferença entre os orbitais homo-lumo e pode ser aplicada aos estudos dos mecanismos de fluorescência de inúmeras moléculas.¹²

Dentre os diversos aspectos relacionados ao processo de emissão e absorção, os efeitos relativísticos têm sido considerados importantes para o estudo de átomos com alta massa molecular, como o Bromo e o Iodo.¹³ Esses efeitos têm sido amplamente estudados para átomos como o ouro¹³, podendo ser negligenciados em compostos orgânicos que envolvam apenas átomos com baixa massa molecular. Entretanto, efeitos relativísticos, como o acoplamento spin-órbita, que está relacionado ao desdobramento dos níveis de energia de átomos pesados, podem influenciar significativamente propriedades eletrônicas de compostos químicos.¹⁴

Desde o enunciado da Equação de Dirac para resolução

dos efeitos relativísticos, diferentes métodos têm sido desenvolvidos, como o método de Douglas-Kroll-Hess, que transforma o hamiltoniano de quatro componentes para duas componentes apenas.¹⁵⁻¹⁷ Ou o método da Aproximação Regular de Ordem Zero (ZORA), que emprega o método de Pauli para a resolução da Equação de Dirac para compostos químicos.^{18,19} Esses métodos modificam o hamiltoniano da Equação de Schrödinger e promovem o cálculo de propriedades relativísticas para sistemas químicos que apresentam grande aplicação a estudos de propriedades espectroscópicas de complexos metálicos e estruturas químicas que envolvam átomos de alto peso molecular.^{20,21}

Desta forma, para compostos com átomos pesados, a incorporação de efeitos relativísticos é essencial para o cálculo acurado de propriedades espectroscópicas. Todavia, a escolha de qual o melhor método relativístico a ser aplicado normalmente requer a avaliação de vários fatores. Dentre esses fatores, encontra-se, por exemplo, a utilização ou não do acoplamento spin-órbita e o emprego de funções de base relativísticas. Neste contexto, o planejamento experimental empregando a metodologia de planejamento fatorial pode auxiliar na escolha das melhores condições para o estudo. O planejamento fatorial é uma abordagem estatística que envolve a construção de uma combinação de fatores, escolhidos dentre os parâmetros que se deseja estudar, para a investigação da significância desses fatores sobre o estudo. Existem diferentes formas de construir o planejamento fatorial (2K, 3K, ...), e com isso diferentes formas de modelar o sistema na busca pela interpretação correta dos resultados.

O presente estudo visa a aplicação da metodologia de planejamento fatorial do tipo 3K para avaliação de métodos relativísticos sobre o processo de absorção de compostos halogenados de 2-amino-1,4-naftoquinona visando avaliar as melhores condições e os fatores significativos para o estudo da propriedade espectroscópica dos derivados halogenados.

Metodologia

O trabalho foi desenvolvido aplicando o método TD-DFT/B3LYP²² para o cálculo das propriedades espectroscópicas dos compostos 2-amino-3-Bromo-1,4-Naftoquinona (ABNQ)²³ e 2-amino-3-Iodo-1,4-Naftoquinona (AINQ), conforme estruturas químicas apresentadas na Figura 1. Os 8 primeiros estados excitados foram avaliados com

o programa ORCA²⁴ empregando o método COSMO^{7,19} para simular o efeito do solvente metanol,²³ o qual foi empregado como solvente nos estudos experimentais para o composto ABNQ. O método de Tamm-Dancoff (TDA)²⁵ foi empregado para simular o efeito de relaxação do solvente no estado excitado dentro do método TD-DFT.

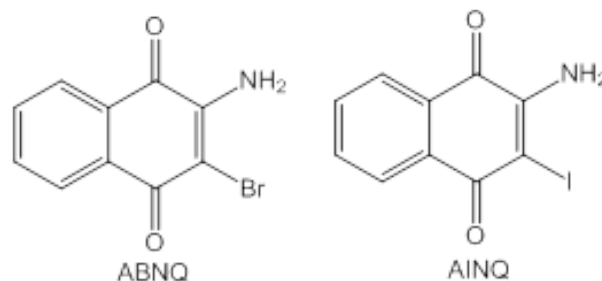


Figura 1. Estrutura química dos compostos halogenados da 3-amino-1,4-naftoquinona.

O planejamento fatorial foi executado dentro do programa Statistica®, empregando metodologia tipo 3K, conforme descrito na Tabela 1. Os parâmetros do planejamento fatorial foram a presença do acoplamento spin-órbita (sem o acoplamento, o acoplamento spin-órbita apenas utilizando a carga nuclear efetiva (SO (1)) e o acoplamento spin-órbita com aproximação de campo e potencial efetivo (SO (3))), a função de onda (TVZ, TVZ_ZORA e TVZ_DKH)²⁴ implementada no programa ORCA para avaliação das funções de onda relativísticas e o hamiltoniano (não relativístico, ZORA e DKH2).²⁶ A variável resposta para o composto ABNQ foi a diferença entre o valor calculado e o valor experimental²³, já para o composto AINQ a variável resposta foi apenas o valor calculado, uma vez que para esse composto não há valor experimental reportado na literatura é o presente momento. A estimativa dos efeitos foram realizados com o auxílio do programa Statistica® e descritos na Tabela 2, bem como a análise ANOVA, descrita na Tabela 3. Para critério de aceitação foi empregado, juntamente com a ANOVA, o Teste t a 5% de probabilidade.

Resultados e Discussão

O planejamento Fatorial do tipo 3K para o composto 2-amino-3-Bromo-1,4-Naftoquinona (ABNQ) seguiu os parâmetros estipulados na Tabela 1. Nesse planejamento, avaliou-se no parâmetro A o efeito do acoplamento spin-órbita, no parâmetro B a função de base e no parâmetro C o método relativístico. Os níveis de cada parâmetro foram estipulados desde o método sem efeitos relativísticos (sem o acoplamento spin-órbita, função de base não relativística e o hamiltoniano não

relativístico), passando pelo nível médio (adição do efeito spin-órbita, função de base com implementação ZORA, e método ZORA), até o nível alto (adição do efeito spin-órbita, função de base com implementação DKH e método DKH2). Avaliou-se, também, a interação dos fatores entre si. Como resposta, os valores de absorção empregando o método TD-DFT e o modelo COSMO, para simular o efeito do solvente metanol, foram calculados. O valor experimental²³ foi comparado aos ²⁷ ensaios calculados e representados na Tabela 1.

Tabela 1. Planejamento Fatorial do tipo 3³ com os níveis e fatores avaliados no planejamento.

Nível	-1	0	+1	
(A) Acoplamento Spin-Órbita	Sem	SO (1)	SO (3)	
(B) Função de base	TVZ	TVZ_ZORA	TVZ_DKH	
(C) Método Relativístico	Não-Rel.	ZORA	DKH2	
A	B	C	R (Metanol) ABNQ	R(Metanol) AINQ
-1	-1	-1	458,7 (+ 6,7)*	461
-1	-1	0	457,2 (+5,2)	460,8
-1	-1	1	457,7 (+5,7)	462,9
-1	0	-1	457,1 (+5,1)	463,2
-1	0	0	458,4 (+6,4)	460,8
-1	0	1	454,2 (+2,2)	460,6
-1	1	-1	459,4 (+7,4)	463,4
-1	1	0	459,4 (+7,4)	461
-1	1	1	452,7 (+0,7)	460,6
0	-1	-1	458,7 (+6,7)	461
0	-1	0	457,2 (+5,2)	460,8
0	-1	1	457,7 (+5,7)	462,9
0	0	-1	457,1 (+5,1)	463,2
0	0	0	458,4 (+6,4)	460,8
0	0	1	454,2 (+2,2)	460,6
0	1	-1	459,4 (+7,4)	463,4
0	1	0	459,4 (+7,4)	461
0	1	1	452,7 (+0,7)	460,6
1	-1	-1	458,7 (+6,7)	461
1	-1	0	457,2 (+5,2)	460,8
1	-1	1	457,7 (+5,7)	462,9
1	0	-1	457,1 (+5,1)	463,2
1	0	0	458,4 (+6,4)	460,8
1	0	1	454,2 (+2,2)	460,6
1	1	-1	459,4 (+7,4)	463,4
1	1	0	459,4 (+7,4)	461
1	1	1	452,7 (+0,7)	460,6

* Valores em parênteses são referentes ao erro comparado ao valor experimental de 452 nm.²³

O modelo quadrático empregado para a análise do planejamento fatorial possui a forma descrita na Equação 1. O planejamento fatorial deste estudo busca encontrar os melhores fatores em relação aos parâmetros que gerem os menores erros, buscando uma minimização dos resultados. Pode-se notar que os fatores que se mostraram significativos foram com relação ao fator C, ou seja, ao método relativístico adotado. E a interação entre a função de base e o método relativístico também se mostraram importantes para o composto avaliado.

As Equações 1 e 2 são geradas pelos valores significativos descritos na Tabela 2 e 3, para os compostos ABNQ e AINQ, respectivamente. Para o ABNQ, a equação é referente ao erro absoluto gerado pela comparação do valor calculado com o

experimental. Para o composto AINQ, a equação foi gerada com o valor bruto do comprimento de onda obtido pelo cálculo. A análise da Equação 1, que representa o modelo quadrático para o fatorial 3^K , mostrou que o fator A não é significativo para a construção das respostas, ou seja, a adição do acoplamento spin-órbita para o composto ABNQ. O fator B, apesar de estar dentro do modelo, também não foi significativo para o estudo. Dessa forma, as funções de base estudada, com a adição dos efeitos relativísticos, não produziram efeitos sobre a resposta. O parâmetro C foi significativo para o estudo, destacando um valor de -3,53% para a análise linear, o que indica que ao passar do nível baixo (-1) para o nível médio ou alto (0, +1) a resposta diminui em 3,53%.

Tabela 2 - Estimativa dos efeitos para o modelo quadrático do planejamento fatorial 3^3 para o composto ABNQ baseado nos valores de Erro.

Fator	Efeito	Erro padrão	t(17)	p	-95% Limite de confiança	+95% Limite de Confiança
Média	5,20	0,22	23,16	0,00	4,72	5,67
A	0,00	0,54	0,00	1,00	-1,16	1,16
A2	0,00	0,47	0,00	1,00	-1,00	1,00
B	-0,70	0,54	-1,27	0,22	-1,86	0,46
B2	-0,95	0,47	-1,99	0,06	-1,95	0,05
C	-3,53	0,54	-6,42	0,00	-4,69	-2,37
C2	+1,7	0,47	3,56	0,00	0,69	2,70
A*B	0,00	0,67	0,00	1,00	-1,42	1,42
A*C	0,00	0,67	0,00	1,00	-1,42	1,42
B*C	-2,85	0,67	-4,23	0,00	-4,27	-1,42

De acordo com o modelo, a variação do hamiltoniano sem efeito relativístico para o método de Douglas-Kroll-Hess de segunda ordem (DKH2) diminuiu o erro estimado para a resposta. Isso significa que o método DKH2 se mostra mais acurado para o estudo dos valores de absorção e do comprimento de onda para a molécula ABNQ. A estimativa do efeito mostrou um valor de -2,85% para a interação entre a função de base e o método relativístico, demonstrando que a resposta diminui

quando passa do nível baixo para o médio ou alto em 2,85%. Novamente, a união dos métodos sem os efeitos relativísticos gerou os maiores erros, indicando que a associação do método DKH2 com a função de base TZV_DKH é mais acurada no estudo do comprimento de onda e dos valores de absorção para a molécula ABNQ. Todos os valores calculados para a estimativa dos efeitos estão detalhados na Tabela 2 e na Tabela 3 apresenta-se a ANOVA do planejamento fatorial.

Tabela 3. ANOVA para os planejamentos fatoriais dos compostos ABNQ e AINQ.

Composto	ABNQ					AINQ					
Fator	SS	df	MS	F	P	Fator	SS	df	MS	F	P
A	0,00	1	0,00	0,00	1,00	A	0,00	1	0,00	0,00	1,00
A2	0,00	1	0,00	0,00	1,00	A^2	0,00	1	0,00	0,00	1,00
B	2,20	1	2,20	1,62	0,22	B	0,04	1	0,04	0,16	0,68
B2	5,41	1	5,41	3,97	0,06	B^2	0,04	1	0,04	0,15	0,70
C	56,18	1	56,18	41,28	0,00	C	6,12	1	6,12	22,41	0,00
C2	17,34	1	17,34	12,74	0,00	C^2	7,04	1	7,04	25,76	0,00
A*B	0,00	1	0,00	0,00	1,00	A*B	0,00	1	0,00	0,00	1,00
A*C	0,00	1	0,00	0,00	1,00	A*C	0,00	1	0,00	0,00	1,00
B*C	24,36	1	24,36	17,90	0,00	B*C	16,56	1	16,56	60,62	0,00
Erro	23,13	17	1,36	-	-	Erro	4,64	17	0,27	-	-
Total SS	128,64	26	-	-	-	Total SS	34,46	26	-	-	-

A análise fatorial empregando os valores calculados de comprimento de onda (Equação 2) ou o erro gerado ao se comparar com o valor experimental (Equação 1) produzem equações quadráticas semelhantes. Isto demonstra que nas duas ocasiões, o modelo se aplica, porém, ao se comparar ao valor experimental pode-se decidir melhor como interpretar cada modelo de acordo com o objetivo do estudo, que é de minimizar o erro em relação ao valor de comprimento de onda calculado.

$$Y = 5,20 - 0,70B - 0,95B^2 - 3,53C + 1,70C^2 - 2,85B^*C$$

Equação 1

$$Y = 457,2 - 0,70B - 0,95B^2 - 3,53C + 1,70C^2 - 2,85B^*C$$

Equação 2

A análise dos gráficos mostrados na Figura 2A e 2B apresentam todos os valores dos efeitos estimados para os dois modelos quadráticos e o valor de corte para o teste F a 0,5% de probabilidade, mostrando que os parâmetros são semelhantes e que os modelos se equiparam.

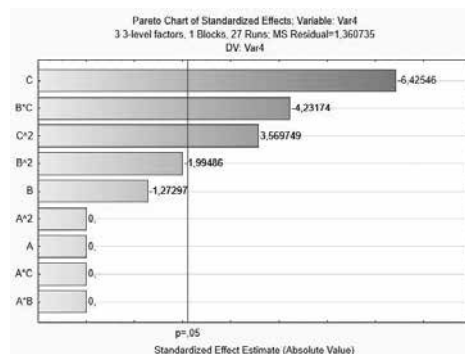


Figura 2A. Efeitos padronizados de Pareto para o planejamento fatorial 3K baseado nos valores de comprimento de onda.

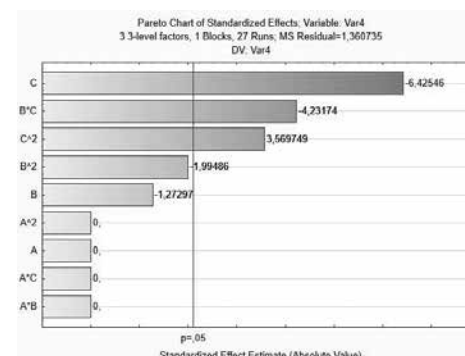


Figura 2B. Efeitos padronizados de Pareto para o planejamento fatorial 3K baseado nos valores do erro.

Baseado no modelo de planejamento fatorial apresentado para o ABNQ, pode-se construir um modelo semelhante para o 2-amino-3-Iodo-1,4-Naftoquinona (ver Figura 1) e comparar os dois modelos baseado na importância dos efeitos relativísticos para o cálculo de energia de absorção e do comprimento de onda desses compostos. Para o composto AINQ, os cálculos dos 27 ensaios foram realizados conforme

descrito na Tabela 1. Os comprimentos de onda e a energia de absorção foram calculados empregando o método TD-DFT juntamente com o modelo COSMO para simular o solvente metanol. Comparativamente ao composto ABNQ, o AINQ apresentou apenas o fator C como significativo, possuindo valor de -1,16% enquanto o ABNQ apresentou o valor de -3,53%.

Tabela 4 - Estimativa dos efeitos para o modelo quadrático do planejamento fatorial 33 para o composto AINQ baseado nos valores de comprimento de onda.

Fator	Efeito	Erro padrão	t(17)	P	-95% Limite de confiança	+95% Limite de Confiança
Média	461,58	0,10	4588,06	0,00	461,37	461,80
A	0,00	0,24	0,00	1,00	-0,51	0,51
A2	0,00	0,21	0,00	1,00	-0,45	0,45
B	0,10	0,24	0,40	0,68	-0,41	0,61
B2	-0,08	0,21	-0,39	0,70	-0,53	0,36
C	-1,16	0,24	-4,73	0,00	-1,68	-0,64
C2	-1,08	0,21	-5,07	0,00	-1,53	-0,63
A*B	0,00	0,30	0,00	1,00	-0,63	0,63
A*C	0,00	0,30	0,00	1,00	-0,63	0,63
B*C	-2,35	0,30	-7,78	0,00	-2,98	-1,71

A análise das interações se mostrou significativa apenas entre os fatores B e C, mostrando valor de -2,35% para o AINQ enquanto que para o ABNQ apresentou o valor de -2,85%, mostrando que para todos os efeitos que se mostraram significativos nesse estudo a resposta diminui quando sai do nível baixo (-1) para o nível médio (0) ou alto (+1), conforme descrito na Tabela 4. Novamente, pela análise da estimativa dos efeitos, pode-se observar que o método relativístico e a função de onda são significativos para estes estudos. O modelo apresentado para o composto ABNQ apresentou maior erro relativo ao valor experimental seguindo a orientação das estimativas dos efeitos, por comparação. O mesmo aconteceu com a estimativa dos efeitos para o AINQ, portanto, seguindo a mesma tendência, os fatores de menor nível apresentarão os maiores erros, ou seja, sem o acoplamento spin-órbita, com a função de base TVZ e com o hamiltoniano não relativístico. Assim, o melhor método para o estudo, ou seja, o método que apresenta os menores erros comparados ao valor experimental será,

novamente, é o método de DKH2 e sua combinação com a função de base TZV_DKH.

Conclusão

O planejamento fatorial 3k para os compostos ABNQ e AINQ se mostrou satisfatório, revelando que para o cálculo TD-DFT do comprimento de onda e das energias de absorção utilizando o método COSMO para avaliar o solvente, apenas o hamiltoniano relativístico foi significativo para o cálculo, sendo o método DKH2 apresentou os menores erros. Mostrou, também, que na fase gás a função de onda é significativa para o cálculo. Em ambos os casos, a interação da função de onda com o método se mostrou significativo, sendo que o método DKH2 com a função de base TVZ_DKH geraram os menores erros para a propriedade observada. Com base no experimento avaliado para o ABNQ, pode ser desenvolvido método semelhante para o AINQ (ver Figura 1) comparando os parâmetros dos planejamentos fatoriais e definindo os melhores fatores para o cálculo das propriedades espectroscópicas.

Referências Bibliográficas

1. Zhao, J.; Ji, S.; Chen, Y.; Guo, H.; Yang, P. **2012**, 8803–8817.
2. Dugave, C.; Demange, L. **2003**.
3. Laurieri, N.; Eggleton, J. E.; Varney, A.; Thinnies, C. C.; Quevedo, C. E.; Seden, P. T.; Thompson, S.; Rodrigues-Lima, F.; Dairou, J.; Dupret, J. M.; Russell, A. J.; Sim, E. *PLoS ONE* **2013**, 8.
4. Ferreira, V. F.; Jorquera, A.; Souza, A. M. T.; Da Silva, M. N.; De Souza, M. C. B. V.; Gouvêa, R. M.; Rodrigues, C. R.; Pinto, A. V.; Castro, H. C.; Santos, D. O.; Araújo, H. P.; Bourguignon, S. C. *Bioorganic and Medicinal Chemistry* **2006**, 14, 5459–5466.
5. Luo, Y.; Li, Y.; Qiu, K. M.; Lu, X.; Fu, J.; Zhu, H. L. *Bioorganic and Medicinal Chemistry* **2011**, 19, 6069–6076.
6. Bermejo-Bescós, P.; Martín-Aragón, S.; Jiménez-Aliaga, Karim L. *BERMEJO-BESCÓS, P. et al. In vitro antiamyloidogenic properties of 1,4-naphthoquinones. Biochemical and Biophysical Research Communications*, v. 400, n. 1, p. 169–174, 2010.; Ortega, A.; Molina, M. T.; Buxaderas, E.; Orellana, G.; Csáky, A. G. *Biochemical and Biophysical Research Communications* **2010**, 400, 169–174.
7. Guzow, K.; Milewska, M.; Czaplowski, C.; Wicz, W. *Spectrochimica Acta - Part A: Molecular and Biomolecular Spectroscopy* **2010**, 75, 773–781.
8. Tucker, S. C.; Honn, K. V. *Biochemical Pharmacology* **2013**, 85, 676–688.
9. Levine, B. G.; Mart, T. J. **2007**.
10. Il'ichev, Y. V.; Kühnle, W.; Zachariasse, K. a *Journal of Physical Chemistry A* **1998**, 102, 5670–5680.
11. Alam, M. J.; Ahmad, S. *Spectrochimica Acta Part A: Molecular and Biomolecular Spectroscopy* **2012**, 96, 992–1004.
12. Jana, S.; Dalapati, S.; Ghosh, S.; Guchhait, N. *Journal of Photochemistry and Photobiology A: Chemistry* **2013**, 261, 31–40.
13. Gorin, D. J.; Toste, F. D. *Nature* **2007**, 446, 395–403.
14. Arumugam, K.; Becker, U. *Computational Redox Potential Predictions: Applications to Inorganic and Organic Aqueous Complexes, and Complexes Adsorbed to Mineral Surfaces*; **2014**; Vol. 4.
15. Kutzelnigg, W. *Chemical Physics* **1997**, 225, 203–222.
16. Cheng, L.; Stopkowicz, S.; Gauss, J. *International Journal of Quantum Chemistry* **2014**, 114, 1108–1127.
17. Bu, M.; Reimann, C.; Pantazis, D. A.; Bredow, T. **2008**, 1449–1459.
18. Wolff, S. K.; Ziegler, T.; Van Lenthe, E.; Baerends, E. J. *The Journal of Chemical Physics* **1999**, 110, 7689.
19. Green, T. F. G.; Yates, J. R. *The Journal of chemical physics* **2014**, 140, 234106.
20. Vaara, J.; Pyykkö, P. *Journal of Chemical Physics* **2003**, 118, 2973–2976.
21. Pyykkö, P. *Annual review of physical chemistry* **2012**, 63, 45–64.
22. Pyykkö, P. *Angewandte Chemie (International ed. in English)* **2004**, 43, 4412–56.
23. Pushpam, S.; Kottaisamy, M.; Ramakrishnan, V. *Spectrochimica Acta - Part A: Molecular and Biomolecular Spectroscopy* **2013**, 114, 272–276.
24. Neese, F. *Wiley Interdisciplinary Reviews: Computational Molecular Science* **2012**, 2, 73–78.
25. Roemelt, M.; Beckwith, M. a; Duboc, C.; Collomb, M.-N.; Neese, F.; DeBeer, S. *Inorganic chemistry* **2012**, 51, 680–7.
26. Haiduke, R. L. a.; Comar, M.; Da Silva, A. B. F. *Chemical Physics* **2006**, 331, 173–177.

Eduardo P. Rocha, Lívia
C. T. Lacerda, Mateus A.
Gonçalves, Maíra S. Pires,
Telles C. Silva, Henrique A.
Rodrigues & Teodorico C.
Ramalho*

Departamento de Química, Universidade Federal de Lavras, Minas Gerais, Brasil.

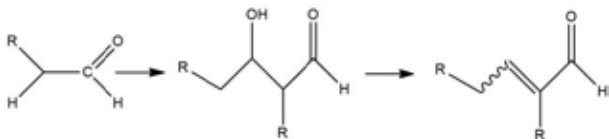
*E-mail: teo@dqf.ufla.br

Investigação Teórica de Adições Aldólicas de Monocarbonilas e β -Dicarbonilas Catalisadas

Ellen V. D'Alessandro & Josefredo R. Pliego Jr.

Introduction

As reações aldólicas são conhecidas há mais de um século e estão entre as mais úteis em química orgânica, sendo um tópico clássico.¹ Parte de sua importância reside na habilidade de formação de ligações carbono-carbono (Esquema 1).



Esquema 1. Adição e condensação aldólica.

A reação pode ser via catálise ácida ou básica. Também pode ocorrer catálise via formação de enamina, um mecanismo de grande interesse em organocatálise. Apesar do tempo que esta reação é conhecida, e dos vários estudos teóricos e experimentais já realizados, ainda existem muitos aspectos não bem esclarecidos desta reação.² Soma-se a isso o fato de que muitos estudos abordam aspectos específicos, faltando uma visão mais ampla da reação em todas suas etapas. Baseado nestas considerações, iniciamos estudos teóricos/computacionais desta classe de reações com o objetivo

de montar o perfil de energia livre global, analisando os vários equilíbrios, etapas de ativação (estados de transição), e efeito do solvente.

Neste trabalho, abordaremos a catálise básica com piperidina em metanol como solvente. Como sistemas modelo, estudamos a reação de acetona com benzaldeído, que é uma reação aldólica clássica. Estudamos também a reação aldólica envolvendo um composto β -dicarbonílico, a aceto-acetona, mais ativado em relação a desprotonação, com o benzaldeído. Esta última reação recebe o nome de Knoevenagel. A etapa estudada até o momento é a adição aldólica, que consiste da formação do ceto-álcool.

Metodologia

Otimização de geometria para obter os mínimos e estados de transição foram realizados em nível CPCM/X3LYP/6-31(+)G(d), de forma a incluir o solvente na otimização de geometria. Este nível de teoria foi utilizado também para realizar o cálculo de frequências harmônicas, de forma obter a energia livre em fase gasosa. Uma vez obtido os pontos estacionários, realizamos cálculos da energia em nível M08-HX com bases TZVPP aumentadas com funções difusas sp sobre o oxigênio e nitrogênio. Por fim, a energia livre de solvatação foi calculada em nível SMD, com densidade X3LYP/6-31(+)G(d).

Resultados e Discussões

O trabalho envolveu duas reações: (a) acetona com benzaldeído e (b) aceto-acetona com benzaldeído, ambas catalisadas pela piperidina, atuando como catalisador básico.

No primeiro sistema investigado, acetona mais benzaldeído, a primeira etapa da reação é a desprotonação da acetona pela piperidina, formando um enolato (MS1). Para calcular a energia livre deste processo, utilizamos a reação de troca de próton da acetona com fenóxido (pKa de 14,0 em metanol) e determinamos que o pKa da acetona é 25,0 em metanol. Com base neste valor e no pKa da piperidina protonada (11,7), a primeira etapa de reação tem uma energia livre de 19,2 kcal/mol, como mostrado no diagrama da Figura 1. Na etapa seguinte, o enolato formado atua como um nucleófilo e ataca o benzaldeído via um estado de transição TS1, formando o intermediário MS2. A barreira de energia livre para esta etapa é de 16,1 kcal/mol, que somada a etapa anterior, leva a uma barreira global de 35,3 kcal/mol. O intermediário formado, MS2, é essencialmente um alcóxido, que pode pegar um próton do meio e gerar o produto final MS3, um ceto-álcool. Como podemos notar, a piperidina não é uma base forte o suficiente para desprotonar favoravelmente a acetona, tornando o mecanismo inviável com esta base.

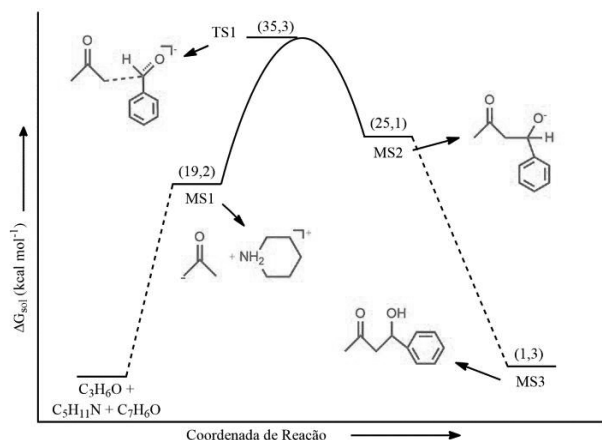


Figura 1. Diagrama de energia livre para a reação de acetona com benzaldeído.

Na segunda reação, envolvendo a aceto-acetona, a etapa de desprotonação é muito favorável, com uma energia livre de apenas 0,8 kcal/mol (Figura 2). Na etapa de ataque do enolato ao benzaldeído, a barreira é mais alta do que a anterior, 21,0 kcal/mol. Isto se deve ao maior impedimento espacial da aceto-acetona desprotonada. A barreira final de 21,8 kcal/mol torna este mecanismo viável, apesar do valor levemente positivo da energia livre do produto final de 2,6 kcal/mol.

Há na literatura alguns dados de substratos parecidos que podemos comparar valores cinéticos. Medien reportou a cinética da reação de ácido de Meldrum com benzaldeído em DMSO a temperatura ambiente.³ Com base em seus dados, podemos estimar uma barreira de energia livre de 19,7 kcal/mol. Rodriguez et al.⁴ utilizaram esponja de próton como catalisador da reação de acetoacetato de etila com benzaldeído em DMSO a 80 oC, e seus dados de conversão nos permite estimar uma barreira de 28 kcal/mol. A temperatura mais alta eleva a energia livre, de modo que um valor de 26 kcal/mol seria razoável a 25 oC. Estas comparações indicam que a barreira obtida neste trabalho está dentro da faixa de valores experimentais.

Conclusões

Os altos valores de ΔG_{sol}^\ddagger na reação (a) mostram o quanto é desfavorável esta reação via catálise com

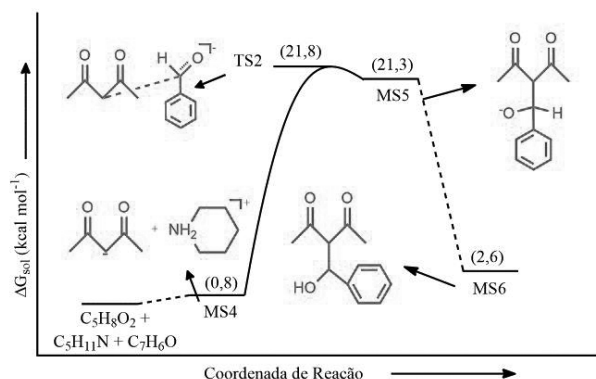


Figura 1. Diagrama de energia livre para a reação de acetona com benzaldeído.

piperidina. Seria necessário metóxido ($\text{pK}_a(\text{CH}_3\text{OH}) = 18,3$) para desprotonar a acetona em metanol numa extensão apreciável. Já a reação (b), de Knoevenagel, a acetoacetona é bem mais facilmente desprotonada, e a reação seria observada, mesmo que a etapa de adição tenha uma barreira maior devido a repulsão espacial. Os resultados obtidos estão em concordância com as observações experimentais para ambos os sistemas.

Agradecimentos

Os autores agradecem ao suporte das agências CNPQ e FAPEMIG

Referências

1. Carey, F.; Sundberg, R. J., *Advanced Organic Chemistry. Part B: Reactions and Synthesis*. 4 ed.; Kluwer Academic/ Plenum Publishers: New York, **2000**;
2. Zhang, X.; Houk, K. N., *Acid/Base Catalysis by Pure Water: The Aldol Reaction*. *J. Org. Chem.* **2005**, 70, 9712-9716;
3. Medien, H. A. A., *Kinetic Studies of Condensation of Aromatic Aldehydes with Meldrum's Acid*. *Zeitschrift für Naturforschung B* **2002**, 57, 1320-1326;
4. Rodriguez, I.; Sastre, G.; Corma, A.; Iborra, S., *Catalytic Activity of Proton Sponge: Application to Knoevenagel Condensation Reactions*. *J Catal* **1999**, 183, 14-23.

Ellen V. D'Alessandro* &
Josefredo R. Pliego Jr.

Departamento de Ciências Naturais, Universidade Federal de São João del Rei

*E-mail: dalessandroellen@gmail.com

An improved Method of ^{13}C NMR Chemical Shift by GIAO-DFT Calculations in the Study of a Synthetic Prenylated Chalcone

Fabio L. P. Costa & Gunar V. S. Mota

Introduction

Chalcones (1,3-diaryl-2-propen-1-ones) (Fig. 1) are important intermediates for the synthesis of biologically active compounds such as flavonoid and isoflavonoid and their derivatives.¹ Due to their bio-physico-chemical properties, the chalcones have been the focus of experimental and theoretical investigations.^{1,2} The large numbers of publications concerning the synthesis and biological evaluation of chalcone and your derivatives have shown the increase of the interest in these compounds, and in their potential for medicinal applications.³

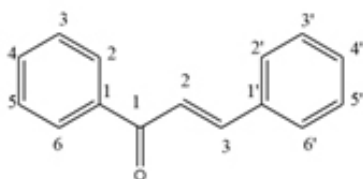


Figure 1. Structure of chalcone

In this work, we intent to investigate the ability of two different approaches in order to determine the ^{13}C NMR chemical shifts (δ) for the prenylated chalcone (PC) (2E)-1-(3,4-dimethoxyphenyl)-3-{3-methoxy-4-[(3-methylbut-2-en-1-yl)oxy]phenyl}prop-2-en-1-one, by use GIAO-DFT and GIAO-HF, to achieve a high cost-effectiveness ratio. In the first one, the calculated δ (δ_{cal})

will be scaled (δ_{sca} , where $\delta_{\text{sca}} = \delta_{\text{cal}} * 1.05 - 1.22$)⁴ at the mPW1PW91/6-31G(d)//mPW1PW91/6-31G(d) level of theory. In the second one, the δ_{cal} will not be scaled, the calculations will be performed using DFT methods (B3LYP, PBE1PBE, TPSS, M05-2X and M06-2X) and the HF method, all calculations will be performed using 6-311++G(d,p) basis set.⁵

Methods

A randomized conformational search of the chalcone molecule 3 (fig. 1) using the Monte Carlo (MC) method with a search limit of 200 structures, and employing the Merck molecular force field (MMFF) as implemented in the Spartan'08 software package⁶ considering an initial energy cutoff of 10 kcal.mol⁻¹ was performed. The lowest energetic conformer was selected to energy minimization calculations carried out at the mPW1PW91/6-31G(d) (fig. 2). Frequency calculations confirmed that the optimized geometries corresponds to a true minima on the potential-energy surfaces and delivered values of free energy at 298 K and 1 atm. ^{13}C atomic chemical shielding tensors (σ) and isotopic atomic δ were calculated from gauge including atomic orbitals (GIAO) theory with for same level theory and basis set used in the optimization molecular. Both in relation at the tetramethylsilane (TMS). these calculation were performed using the Gaussian 09 W software package.⁷

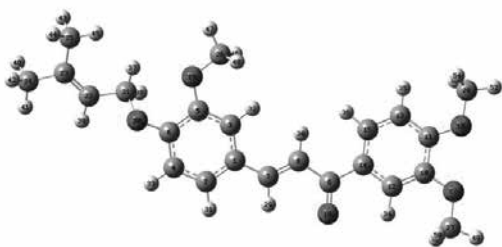


Figure 2. Optimized structure of PC at the mPW1PW91/6-31G(d) level of theory.

Results and Discussion

The major differences between our geometry calculations results and those obtained by Espinoza-Hicks *et al.*,⁵ carried out at the M06-2X/6-311++G(d,p) level of theory, was noticed in the central zone, here described as a practically flat region with a maximal deviation from total planarity of 2.87°, while Espinoza-Hicks *et al.*⁵ point out 16°, approximately. Moreover, the methoxy groups at 18O and 17O are located in neighboring carbon atoms. Regarding the plane of the benzene A-ring, due to the steric hindrance, the methoxy groups are oriented at opposite sides, maintaining dihedral angle of 179.73° (176.46°, for Espinoza-Hicks *et al.* results)(10C–11C–18O–28C). For the other methoxy group, dihedral angle (11C–10C–17O–27C), we found -179.31° while Espinoza-Hicks *et al.* found -81.43°. In view of this difference in behavior, one would expect some discrepancy between the Espinoza-Hicks *et al.* calculated NMR ¹³C chemical shift for C12 and ours. Indeed, it was observed that our error was significantly smaller than the Espinoza-Hicks *et al.* error, 2.17 ppm and 10.32 ppm (for their the best result, see table 3), respectively.

The comparisons shown in Table 1 indicate that all DFT methods predict good results when these are compared to experimental values. It is important to point out that, after using the scaling factor our result at the mPW1PW91/6-31G(d)// mPW1PW91/6-31G(d) level of theory presents the smaller MAD (mean absolute deviation) and RMS (root mean square) errors, in despite

of its less computational demanding. On the other hand, before using the scaling factor MAD and RMS errors were higher than those obtained at the GIAO-TPSS/6-11++G(d,p)//M06-2X/6-311++G(d,p) level of theory, which was the Espinoza-Hicks *et al.* best results. It shows how important is to apply scaling factors in order to improve the ¹³C NMR chemical shift calculations results, in spite of the use of small basis set as.

Table 1. Statistical data illustrating the performance of various methods for the GIAO calculation of ¹³C NMR chemical shifts (δ , in ppm) for the PC molecule.

Level	MAD	RMS
B3LYP/6-311++G(d,p)//M06-2X/6-311++G(d,p)	7.38	9.45
PBE1PBE/6-311++G(d,p)//M06-2X/6-311++G(d,p)	6.91	9.04
TPSS/6-311++G(d,p)//M06-2X/6-311++G(d,p)	4.44	5.92
M05-2X/6-311++G(d,p)//M06-2X/6-311++G(d,p)	19.35	22.35
M06-2X/6-311++G(d,p)//M06-2X/6-311++G(d,p)	17.28	20.23
HF/6-311++G(d,p)//M06-2X/6-311++G(d,p)	7.18	10.08
mPW1PW91/6-31G(d)//mPW1PW91/6-31G(d) (in this work)	6.26**	7.47**
mPW1PW91/6-31G(d)	3.97*	5.35*

* from δ_{scal} , **from δ_{calc}

Conclusions

Despite the calculation approximations, such as a truncated basis set, as well as the non-considered effects, such as solvent and rovibrational effects, the chemical shifts calculated at the mPW1PW91/6-31G(d)//mPW1PW91/6-31G(d) using a simple relationship (δ_{scale})

$=1.05 \delta_{\text{calc}} - 1.22$ where δ_{calc} and δ_{scale} are the calculated and the linearly scaled values of the ^{13}C chemical shifts, respectively) were able to yield MAD and RMS errors as small as those obtained with all DFT methods using bigger basis sets, 6-311++G(d,p). A good agreement between the generated universal scaling factor and the simple linear regression (obtained by using the experimental and the calculated ^{13}C NMR chemical shift) results was observed. Thus, its high cost-effectiveness ratio scaling factor, as well as its successful applicability to a real problem, was confirmed. In conclusion, mPW1PW91/6-31G(d)//mPW1PW91/6-31G(d) linear regression obtained by using the experimental and the calculated data, is a very attractive tool as an alternative to more computationally demanding approaches, which are usually applied in order to achieve ^{13}C NMR chemical shift calculations.

Acknowledgments

The authors are grateful for the support given from the FAPEG, CAPES, and CNPQ. We also would like to thank to CENAPAD-SP for the computational facilities (proj616).

References

1. A. Crozier, I. B. Jaganath, M. N. Clifford, (Eds: A. Crozier, M. N. Clifford, H. Ashihara), Blackwell Publishing Ltd, Oxford, pp. 1–21 (2006).
2. R. Dimmock, D. W. Elias, M. A. Beazely, N. M. Kandepu, *Curr. Med. Chem.* 6, 1125 (1999).
3. P. Singha, A. Anandb, V. Kumarc, *Eur. J. Med. Chem.* 85, 758 (2014).
4. L. P. Costa, A. C. F. de Albuquerque, F. M. dos Santos Jr., M. B. de Amorim, *J. Phys. Org. Chem.* 23, 972 (2010).
5. J. C. Espinoza-Hicks, A. A. Camacho-Dávila, N. R. Flores-Holguín, G. V. Nevárez-Moorillón, D. Glossman-Mitnik and L. M. Rodríguez-Valdez, *Chem. Cent. J.* 7, 17 (2013).
6. Sparta'08, Wavefunction, Inc., Irvine California, USA.
7. Gaussian 09, Revision A.01, M. J. Frisch, G. W. Trucks, H. B. Schlegel, G. E. Scuseria, M. A. Robb, J. R. Cheeseman, G. Scalmani, V. Barone, B. Mennucci, G. A. Petersson, H. Nakatsuji, M. Caricato, X. Li, H. P. Hratchian, A. F. Izmaylov, J. Bloino, G. Zheng, J. L. Sonnenberg, M. Hada, M. Ehara, K. Toyota, R. Fukuda, J. Hasegawa, M. Ishida, T. Nakajima, Y. Honda, O. Kitao, H. Nakai, T. Vreven, J. A. Montgomery, Jr., J. E. Peralta, F. Ogliaro, M. Bearpark, J. J. Heyd, E. Brothers, K. N. Kudin, V. N. Staroverov, R. Kobayashi, J. Normand, K. Raghavachari, A. Rendell, J. C. Burant, S. S. Iyengar, J. Tomasi, M. Cossi, N. Rega, J. M. Millam, M. Klene, J. E. Knox, J. B. Cross, V. Bakken, C. Adamo, J. Jaramillo, R. Gomperts, R. E. Stratmann, O. Yazyev, A. J. Austin, R. Cammi, C. Pomelli, J. W. Ochterski, R. L. Martin, K. Morokuma, V. G. Zakrzewski, G. A. Voth, P. Salvador, J. J. Dannenberg, S. Dapprich, A. D. Daniels, O. Farkas, J. B. Foresman, J. V. Ortiz, J. Cioslowski, and D. J. Fox, Gaussian, Inc., Wallingford CT, 2009.

Fabio L. P. Costa^a & Gunar V. S. Mota^b

^a CIEXA – IAT Universidade Federal de Goiás, GO, Brasil. BR 364, km 195, nº 3800 CEP 75801-615 – Jataí -GO 1

^b Natural Science Faculty, Federal University of Pará, ICEN, UFPA, 66075-110, Belém, PA, Brasil 2

Modeling Polymer/Fullerene Heterojunctions: a Case Study for the Interfaces PTPD3T/PCBM and PBTI3T/PCBM

Rodrigo M. D. Ledo, Luciano A. Leal, Luiz A. R. Juniora & Antônio L. A. Fonseca

Introduction

Due to increased energy demand, one of the great current global problems is to promote the generation of energy to supply the industrial sector, the higher energy consumer. Each year it needs more and more energy to increase production and maintain the current supplies. However, in the current social conjuncture, humankind faces a dilemma: how to continue development, minimizing damage to the environment? This fact takes greater proportions when you consider that the traditional sources of energy resources, such as minerals, organic compounds and water resources are limited and exhaustible. In this sense, science seeks the development and improvement of alternative means of power generation, we can emphasize mainly the use of solar energy based on photovoltaic effect - conversion of sunlight into electrical energy - which is characterized by being a clean and sustainable energy source¹.

In recent decades, studies related to the construction of organic solar cells (OSCs) have gained prominence, because they combine very important features for the productive sector: the low environmental impact and the potential of cost-effectiveness that can lead to the development and overcoming model inorganic cells. The photon absorption mechanism in organic compounds leads to the formation of the exciton, a bonded pair of electron-hole that is electrically neutral, due to the strong electron-lattice interaction. Due to this reason, the optical

absorption in organic materials does not lead directly to free electrons and holes carries to generate electric current, first the exciton must be dissociated, which is why the charge transport mechanism in heterojunction donor-acceptor polymer (D-A)². Studies to investigate the exciton dissociation modes are crucial to describe the principles of operation of OSCs.

In this work, using an ideal organic system of isolated molecules (model dimer), computational methods of molecular dynamics and DFT were applied on it, being possible to characterize the molecular structures, energy band gaps, and charge separation states. Furthermore, understanding the excitonic character by analyzing the electric dipole properties is crucial to establish new ways to study the exciton dissociation³⁻⁶. Such characteristics can serve as a guidance for further studies aimed at increasing the energy conversion efficiency of the photovoltaic effect applied on OSCs.

Methods

Model dimers of increasing complexity have been considered. However, the starting point of the computational simulation methods presents an ideal configuration of a D-A interface compounded by PTPD3T and PBTI3T molecules and a tailed C60 and C70 (PCBM) to investigate the energy variations in a less degree of details. The polymers were submitted to validation tests of the force-field. Molecular dynamics

calculations were performed on Materials Studio.

In a second moment, using Gaussian, the induced molecular dipole momentum was evaluated in isolated systems of the polymers appraise the levels of theory by quantum-chemical calculations using DFT method (B3LYP functional). The same procedure was applied on the tailed C60 and C70.

Results and Discussion

Experimental results show that the π -stacking phenomenon occurs in regions formed by similar structures to those studied polymers⁷. First, two isolated polymer systems (PTPD3T and PTBI3T) were built. Figure 1 provides a view them in two thin films. The structures were submitted to geometry optimization procedures (parameters).

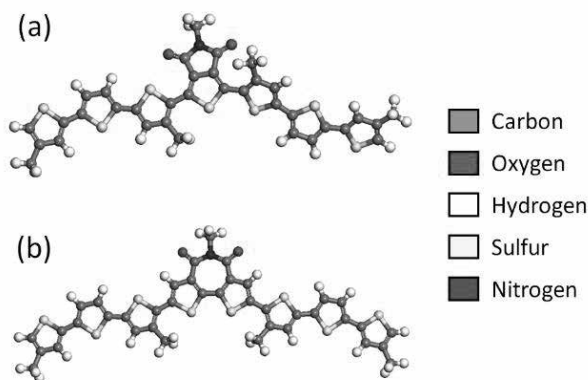


Figure 1 – Polymers PTPD3T (a) and PTBI3T (b).

For purposes of force field and model validation, a micro-region of PTBD3T polymer was constructed. It is formed by two sheets of the polymer which were submitted to molecular dynamics for a time of 30ns using the Universal force-field. From the results of molecular dynamics, the two layers remain connected by a long-range interaction between them. This fact is relevant, because it validates the use of the system and the force-field, showing that the π -stacking phenomenon also occurs process simulation. Figure 2 refers to the last snapshot of the molecular dynamics method and model validation.

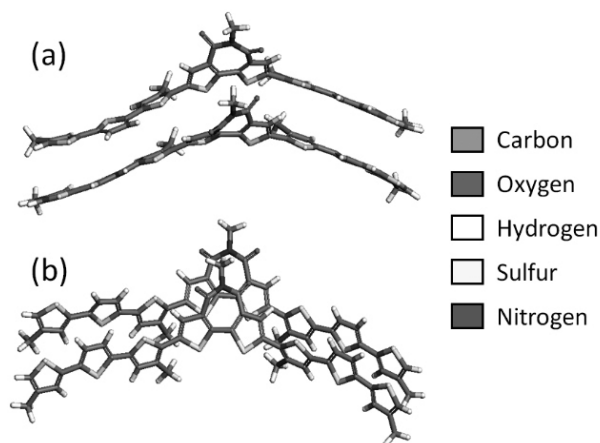


Figure 2 – Different views of the micro-regions Pentacenes after the molecular dynamics process.

After this validation, two other structures were also constructed, PC60BM and PC70BM, which can be seen in Figure 3. They also were submitted to geometry optimization processes. In the four raised structures, computer calculations and simulations were performed in the DFT (using B3LYP functional) that allowed obtaining the dipole moments of each unit, which are shown in Table 1.

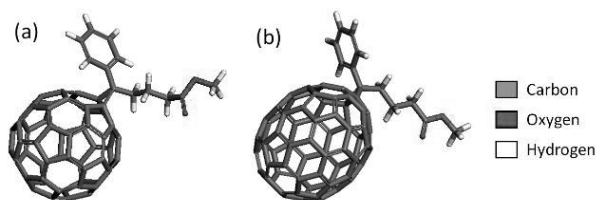


Figure 3 – PC60BM (a) and PC70BM (b) structures.

Table 1. Dipole Moments for the structures after DFT calculations.

Structure	Dipole Moment		
	μ_x	μ_y	μ_z
PTPD3T	-0.5987251	1.1092229	-0.2560705
PTBI3T	-0.0072081	2.5723123	0.187208
PC60BM	1.3026876	0.2402921	-0.0795589
PC70BM	1.1435207	1.3755452	1.0676037

Conclusions

For a first study, the computational procedures and methods used showed results consistent with empirical observations. Knowing the molecular behaviors separately contribute to a future analysis of a D-A system, when polymers are interacting with PCBM.

For future works, the PCBM molecules can be set to float on a parallel plane to the surface of polymers. Variations in the magnitude and direction of the induced dipole moment can be evaluated. To characterize the electronic structure of the molecules at the interfaces performing quantum-chemical calculations on small- and medium-size system. Also, it is possible to evaluate some properties to analyze the interface dipole, the Millikan net charge and the levels of energy of the molecular orbitals.

Acknowledgments

The authors are grateful for the support given from the IFB, UnB, FAPEG, CAPES, CNPQ and FINATEC.

References

1. B. Kippelen, J.-L. Brédas. *Energy Environ. Sci.*, **2009**, 2, 251-261.
2. J.-L. Brédas, J. Norton, J. Cornil, V. Coropceanu. *Accounts of Chemical Research*, 2009, 42, 11, 1691-1699.
3. M. Linares, D. Beljonne, J. Cornil, K. Lancaster, J.-L. Brédas, S. Verlaak, A. Mityashin, P. Heremans, A. Fuchs, C. Lennartz, J. Idé, R. Méreau, P. Aural, L. Ducasse, F. Castet. *J. Phys. Chem. C*, **2010**, 114, 3215-3224.
4. J.-L. Brédas, *Science* 343, 492 (**2014**).
5. J.-L. Brédas and G. B. Street, *Acc. Chem. Res.* 18, 309 (**1985**). 12.
6. J.-L. Brédas, *AIP Conference Proceedings* 1419, 55 (**2013**).
7. X. Guo, N. Zhou, S. J. Lou, J. Smith, D. B. Tice, J. W. Hennek, R. P. Ortiz, J. T. L. Navarrete, S. Li, J. Strzalka, L. X. Chen, R. P. H. Chang, A. Facchetti and T. J. Marks, *Nature Photonics*, **2013**, 7, 825-833.

Rodrigo M. D. Ledo^{a,b},
Luciano A. Leal^a, Luiz
Antônio R. Junior^{a,c} &
Antônio L. A. Fonseca^{a,c}

^aInstitute of Physics, University of Brasília, 70.919-970, Brasília, Brazil

^bFederal Institute of Education, Science and Technology of Brasília, 70.830-450, Brasília, Brazil

^cUniversity of Brasília, UnB Faculty of Planaltina, 73.345-010, Brasília, Brazil

Impact of Coulomb Interactions on the Exciton Dissociation in Polymer Heterojunctions

Gesiel G. Silva, Luiz A. R. Junior & Antonio L. A. Fonseca

Introduction

Organic Solar Cells (OSCs) have attracted considerable interest currently by combining features that make them amenable to manufacturing with low environmental impact and potentially cost-effective to promising new photovoltaic technologies than their inorganic counterparts¹⁻³. In these devices, the charge transport is one of the most important physical processes that should be intensively investigated in order to improve the power energy conversion efficiency^{4,5}. The charge transport mechanism in polymer-based materials are generally dominated by hopping (nonadiabatic) process of charge carriers between localized electronic states⁶. Due to the strong electron-lattice interactions in these materials, the conventional self-localized charge carriers are polarons which possess spin $\pm 1/2$ and charge $\pm e$ ⁷. However, when the photoexcitation process results in a large concentration of polarons, two acoustic polarons of same charge and antiparallel spins, for example, can recombine to form an bipolaron, that are spinless structures with charge $\pm 2e$ ⁸. An exciton, in its turn, is a bound electron-hole pair structure, which can be accomplished by charge injection or photoexcitation mechanisms resulting on the emergence of self-localized electronic states. The photoexcitation mechanism in OSCs leads primarily to the formation

of excitons and consequently, to generate current, the excitons must first dissociate into free charges. Once that these structures are the main responsible by the charge transport mechanism in donor-acceptor (D-A) polymer heterojunctions, studies considering channels for their interaction in these materials, although crucial to a more detailed description of the charge transport, lacking theoretically and are also very few experimentally.

From the theoretical point of view, the generation of charge carriers in conjugated polymers was numerically investigated using an extended version of the Su-Schrieffer-Heeger (SSH) model that includes inter-chain interaction. It was obtained that the recombination between a polaron and an exciton can generate four kind of products, i. e., a triplet exciton, a singlet exciton, an excited polaron, and a bipolaron depending on the inter-chain coupling strength. However, one of the most relevant molecular parameters which may affect the rate of the exciton dissociation and, consequently, the recombination between the structures present in a photovoltaic interface is the band widths (ΔE) of the donor and acceptor materials, as shown in Figure 1. From these results, one can see that further detailed investigations about the possible channels for the charge carrier formation mechanism in polymer D-A heterojunctions and its impact on the charge transport can be a key

to enhance the power energy conversion efficiency in OSCs being of major interest.

Sun and Stafstrom recently investigated how exciton dissociation is affected for temperature effects, intensity of the external electric field and inter-chain interaction strenght⁹. For the Coulomb interaction (U), they adopted 4.1 eV for interaction between the sites. In this scope, our goal was to investigate the influence of Coulomb interaction for different distances (d) inter-chain, or to vary Coulomb interaction for different distances. In this sense, we vary d from 1 to 10 Å and, for each d, varies U between 0.5 and 4.5 eV with increase of 0.5 eV.

The starting point for the simulations present a configuration in which one exciton lies in the donor chain while the acceptor chain contains an electron–polaron. In this case, the negatively charged polaron is represented by the doubly occupied HOMO-1 and the solely occupied LUMO levels. On the other hand, the exciton is denoted by electrons with parallel spin orientation in the HOMO and LUMO+1 levels, as shown in Figure 1.

Methods

The overall Hamiltonian of our model is $H = H_{\text{intra}} + H_{\text{inter}} + H_{\text{latt}}$. The term $H_{\text{intra}} = H_{\text{elec}} + H_{\text{ee}}$ represents the intra-chain electronic part.

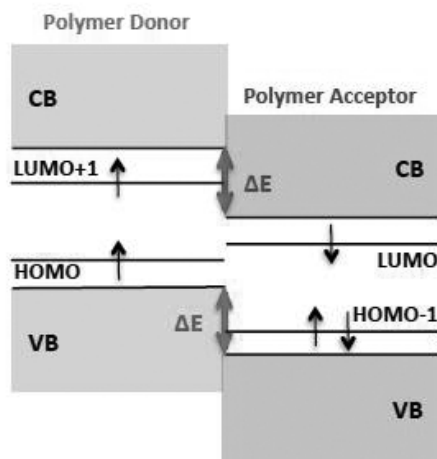


Figure 1. Schematic diagram of the energy levels for a D–A polymer heterojunction. Here, CB represents the conduction band whereas VB denotes the valence band.

In this way, H_{elec} can be expressed in the following form

$$H_{\text{elec}} = \sum_{i,s} \Delta_n C_{n,s}^\dagger C_{n,s} - \sum_{i,s} t_{n,n+1} (C_{n,s}^\dagger C_{n+1,s} + C_{n+1,s}^\dagger C_{n,s})$$

in which Δ_n denotes the on-site energy of site n. Here, the label n runs over the sites off both donor and acceptor chains without a specific index for the two different chains. In order to implement the D–A polymer heterojunction, the on-site energy for all sites of the donor chain is settled as $\Delta_n = \Delta E$ whereas for the sites of the acceptor chain $\Delta_n = 0$. The operator $C_{n,s}^\dagger$ ($C_{n,s}$) creates (annihilates) a π -electron state at a particular site n with spin s. $t_{n+1,n} = e^{-i\gamma A(t)} [(1+(-1)^i \delta_0) t_0 - \alpha(u_{n+1} - u_n)]$ is the intra-chain transfer integral where t_0 is the transfer integral between nearest neighboring sites in a dimerized lattice, α the electron-phonon coupling constant, u_n the displacement of a site from its equilibrium position, and δ_0 the Brazovskii-Kirova symmetry-breaking term that is introduced in order to lift the ground-state degeneracy for non-degenerated polymers¹⁰. $\gamma = ea\hbar/c$, with a is the lattice parameter, e the absolute value of the electronic charge, and c is the speed of light. The external electric field is introduced in the model through the time-dependent vector potential, in which $E = -(1/c) \dot{A}$.

The contribution of the electron-electron interactions (H_{ee}) to the model Hamiltonian can be placed as in which U is the screened on-site Coulomb interactions,

$$H_{\text{inter}} = - \sum_{\langle i,j \rangle, s} t_{i,j}^\dagger (C_{i,s}^\dagger C_{j,s} + C_{j,s}^\dagger C_{i,s}) + \frac{1}{2} \sum_{i,j} V_{i,j} (n_i - 1)(n_j - 1)$$

$n_i = \sum_s C_{i,s}^\dagger C_{i,s}$ and $V_{i,j}$ denotes the Ohno potential¹¹ defined as for i and j running over the sites of the same chain. $V_{i,j}$

$$V_{i,j} = \frac{U}{\sqrt{1 + (\beta r_{ij}/r_0)}}$$

defines the long-range electron–electron interactions, in which β denotes screening factor, r_{ij} is the distance between sites i and j , and r_0 the average bond length.

The inter-chain interactions (H_{inter}) has the form

$$H_{inter} = - \sum_{(i,j)s} t_{i,j}^{\perp} (c_{is}^{\dagger} c_{js} + c_{js}^{\dagger} c_{is}) + \frac{1}{2} \sum_{i,j} V_{i,j} (n_i - 1)(n_j - 1)$$

where $\sum_{(i,j)s}$ establishes that the sum is restricted to pairs of nearest and next nearest neighboring sites at different chains, i and j are the sites index of opposite chains, and $t_{i,j}^{\perp}$ represents the interchain hopping integral as a function of the inter-chain distance d and has the form of

$$t_{i,j}^{\perp} = \frac{t_0}{10} \exp(1 - d/5)$$

where $\sum_{(i,j)s}$ establishes that the sum is restricted to pairs of nearest and next nearest neighboring sites at different chains, i and j are the sites index of opposite chains, and $t_{i,j}^{\perp}$ represents the interchain hopping integral as a function of the inter-chain distance d and has the form of

$$t_{i,j}^{\perp} = \frac{t_0}{10} \exp\left(1 - \frac{\sqrt{d^2 + r_0^2}}{5}\right)$$

for the next nearest hopping. Here, $V_{i,j}$ denotes the inter-chain Coulomb interactions.

The last term in our model Hamiltonian describes the lattice backbone where K is the harmonic constant of a σ

bond, M is the mass of a CH group, and i runs over the sites of both chains¹². Recently, Miranda et al. developed a set of parameters to use when Coulomb interactions are considered^{13,14}. Thus, we adopt this parameters developed by them: $t_0=2.1$ eV, $\alpha=3.2$ eV/Å, $\delta_0=0.05$ eV, $K=21.0$ eV/Å², $M=1349.14$ eV fs² / Å², $r_0=1.22$ Å, $\beta=3.4$.

$$H_{latt} = \frac{K}{2} \sum_i (u_{i+1} - u_i)^2 + \frac{M}{2} \sum_i \dot{u}_i^2$$

Results and Discussion

As we can see in Figure 2(a), two similar lattice distortions appears in the acceptor layer, which depicts the time evolution of the staggered order parameter for the bond length. These well localized lattice structures denote the presence of two negative polarons in the acceptor layer whereas the donor layer contains only one localized lattice structure with similar degree of distortion, which denotes the presence of a negative polaron. It is easy to conjecture that, due to the parallel spin configuration presented by the electrons in the LUMO and LUMO+1 levels (two spin up electrons), the bipolaron formation can not takes place. Moreover, one can see from Figure 2(b), which displays the time evolution of the mean charge density, that a positive amount of charge rises in the polymer donor coupled to the shallower lattice deformation, whereas two negative structures appears in the polymer acceptor, which indicates that the former neutral excited structure is now a positively charged polaron and the two structures present in the acceptor layer are negatively charged polarons.

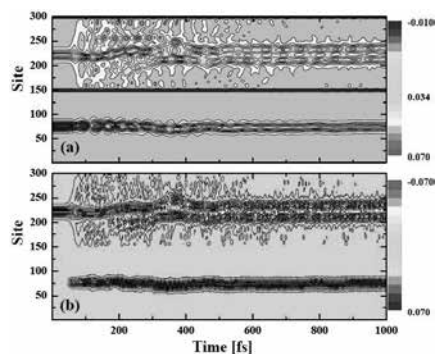


Figure 2. Time evolution (a) of the staggered order parameter of the bond length and (b) the mean charge density for a system with inter-chain distance (d) of 5 Å and band offset strength (ΔE) of 0.8 eV.

Acknowledgments

The authors are grateful for the support given from the FAPEG, CAPES, CNPQ and FINATEC.

References

1. R. Shivanna, S. Shoaie, S. Dimitrov, S. K. Kandappa, S. Rajaram, J. R. Durrant, and K. S. Narayan, *Energy. Environ. Sci.* 7, 435 (2014).
2. D. J. Burke and D. J. Lipomi, *Energy. Environ. Sci.* 6, 2053 (2013).
3. B. Kippelen and J.-L. Brédas, *Energy. Environ. Sci.* 2, 251 (2008).
4. J.-L. Brédas, *Science* 343, 492 (2014).
5. J.-L. Brédas, *AIP Conference Proceedings* 1519, 55 (2013).
6. S. Stafström, *Chem. Soc. Rev.* 39, 2484 (2010).
7. J.-L. Brédas and G. B. Street, *Acc. Chem. Res.* 18, 309 (1985).
8. B. Di, Y. Meng, Y. D. Wang, X. J. Liu, and Z. An, *J. Phys. Chem. B.* 115, 964 (2011).
9. Z. Sun and S. Stafström, *J. Chem. Phys.* 138, 164905 (2013).
10. A. J. Heeger, *Rev. Mod. Phys.* 73, 681 (2001).
11. K. Ohno, *Theoret. Chim. Acta.* 2, 219 (1964).
12. W. P. Su, J. R. Schrieffer, and A. J. Heeger, *Phys. Rev. Lett.* 42, 1698 (1979).
13. R. P. Miranda, A. J. Fisher, L. Stella, and A. P. Horsfield, *J. Chem. Phys.* 134, 244101 (2011).
14. R. P. Miranda, A. J. Fisher, L. Stella, and A. P. Horsfield, *J. Chem. Phys.* 134, 244102 (2011).

Gesiel G. Silva^a, Luiz A.
R. Junior^b & Antonio L. A.
Fonseca

^aInstitute of Physics, University of Brasília, 70.919-970, Brasília, Brazil.

^bUniversity of Brasília, UnB Faculty Planaltina, 73.345-010, Brasília, Brazil.

^cFederal Institute of Education, Science and Technology of Goiás, 72.811-580, Luziânia, Brazil.

*E-mail: geisel.silva@ifg.edu.br

An Experimental Spectroscopic and Theoretic Study of Acetylbergenin

Gisele F. de Castro, Diego dos S. Freitas, Alberto S Marques & YujiTakahata.

Introduction

The acetylbergenin was synthesized from bergenin extracted from the bark of *Endopleura uchi*, which extract is used by Amazonian community to treat infections¹, and various biological activities have been proven, among them: anti-ulcerogenic, hepatoprotection, anti-HIV, obesity inhibitor, antioxidant, antimicrobial, etc^{2,3,4,5,6}. However, bergenin is (a little) lipophilicity, and is poorly absorbed by the human gastrointestinal tract⁷. The study of acetylbergenin showed greater biological effect and greater efficacy in relation to bergenin^{2,3,4,5}. This study expands the information on the molecule 3, 4, 8, 10, 11-penta-ortho-acetylbergenin through theoretical calculations and UV/Visible spectroscopy.

Methods

The sample of acetylbergenin was synthesized from the acetylation of bergenin as described in⁸. The molecular geometry optimization as crystallography⁹, was performed using the Hartree - Fock method with base function 6-31G*, simulating the molecule in three different (environments settings): vacuum, ethanol and water. Subsequently, the excitation energies were calculated using the Time Dependent Density Functional Theory (TD-DFT) using functional B3LYP and base function 6-31G*.The sample[2] was subjected to crystallization procedure in methanol at 40 °C for

purification. Spectra UV /Visible impure sample and sample recrystallized, (both in ethanol) at a concentration of 1x10⁻⁴M, were recorded on a spectrophotometer UV absorption /Visible New 2102 UV PC. In this way it intends to study the solvent effect mainly in the UV spectrum of the molecule, and analyze in detail the nature of the electronic transitions by comparing the theoretical and experimental spectra.

Results and Discussion

UV ABSORPTION SPECTRUM

Vacuum simulation

The theoretical spectrum of UV-Visible absorption acetilbergenin in vacuum (Figure 1.a) was obtained from the data of the DFT B3LYP calculation DT / 6-31G*. It was observed that it had, three bands A, B, C in the simulated spectra in vacuum. The energies (nm) and f-values of peaks of the three bands are: A(257 nm, F = 0.0159), B (238 nm f = 0.11689), and C (223 nm f = 0.0488), respectively .

The band B is the most intense and the band A is of lower intensity. The band B consists of two transitions, S₁ and S₂ of low intensities. S₁ transition is due to transition D (138) (HOMO-3, n carbonyls, → V(1) (LUMO , antibonding (π*), located on the aromatic

where D (138) is random orbital-138 doubly occupied, and V (1) is first virtual orbit. S2 is due to transition D(140) (HOMO-1 (orbital (π) located on the aromatic ring)) to the LUMO+1 (antibonding (π^*) of the aromatic ring). The band B is composed of two transitions, S₃ and S₄, high intensities. S₃ transition occurs from the HOMO-2 orbital, (ring D-glucopyranose, n) to the orbital V (1), LUMO. The transition S₄ of the HOMO orbital (π located on the aromatic ring) to the LUMO. The C band is composed of two transitions, S₅ and S₆ average intensities. S₅ transition is due to a transition part of the HOMO-6 orbital (n, located on the aromatic ring) to the LUMO.

The S6 transition is due a transition orbital D (134) HOMO-7 (n, with major contribution in orbital n located in the δ -lactone ring V (1) (LUMO).

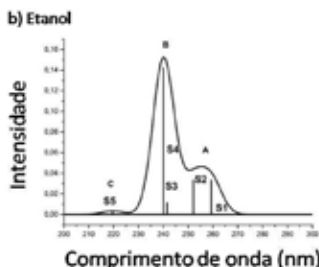
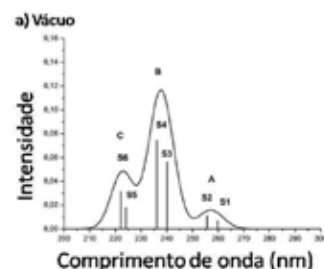
Ethanol simulation

The UV-Vis spectrum experimental compound in ethanol solution 10⁻⁴M presented three bands with peaks at 219nm (B'), 259nm (A') and 309nm (X') (Figure 1d) and the experimental spectrum of recrystallized acetilbergenin presented four bands with maxima at 205nm (C'), 225nm (B'), 255nm (A') and 304nm (X') (Figure 1.e).

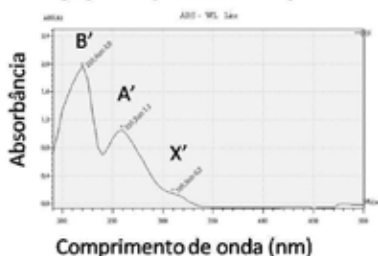
The two experimental spectra are similar in bands B' and A'. However, there are some differences between the two spectra. First, the presence of the small band C', which is on the left shoulder of the intense band B'. In Figure 1.e spectrum as the spectrum in Figure 1.d, both do not have a band C'. It is very likely that the band C' did not appear in the compound spectrum before recrystallization (Figure 1.d), because of impurity. Second, the presence of the band X' is sharp in Figure 1.d, whereas in Figure 1.e, the band X' is not well defined. In the spectrum of the compound crystallized in Figure 1.e, the band X', or does not exist or the intensity of the band is so weak that it is hidden in the right side of the band. It is very likely that the band X' in the sample spectrum before recrystallization (Figure 1.d), is due to impurity. In the compound crystallized, the amount of impurity has been reduced. Therefore, the spectrum of the recrystallized compound (Figure 1.e), the intensity of X' band significantly decreased and was almost invisible.

The theoretical spectrum of UV-Vis absorption acetilbergenin based on the result of the calculation by the B3LYP DFT DT / 6-31G* in ethanol for three bands, A, B, C (Figure 1.b) where the band B is the more intense, and then the band A and band C have lower intensity. The

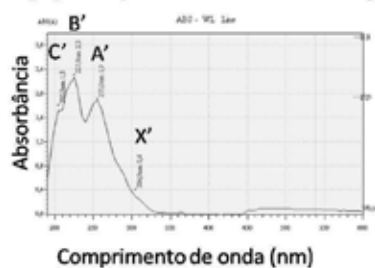
Espectros Teóricos; a),b),c)



d) Espectro Experimental do composto em etanol



e) Espectro Experimental em etanol da Acetilbergenina recrystalizada



c) Água

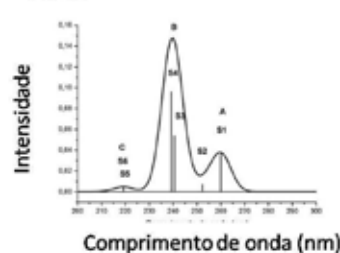


Figure 1. Theoretical Absorption Spectrum; a) vacuum, b) ethanol, c) water, d) UV-Visible Experimental Absorption Spectrum, all in ethanol concentration 10⁻⁴ M before crystallize, e) and recrystallized.

energies (nm) and f-values of peaks are the three bands A (255 nm $f = 0.0464$), B (240 nm $f = 0.152947$) and C (220 nm $f = 0.0033$) respectively.

The experimental absorption spectrum of the UV-VIS acetilbergenin in ethanol (Figure 1e) is similar to the theoretical spectrum (Figure 1.b). The bands A, B, C of the theoretical spectrum corresponding to bands A', B', C' respectively of the experimental spectrum. In the theoretical spectrum (Figure 1.b) there is a band on the right side of the band corresponding to the band X' of the experimental spectrum. We conclude that the band X' in the experimental spectrum in Figure 1.d and Figure 1.e is probably due to impurity. The band A of the theoretical spectrum consists of two transitions, S₁ and S₂ of medium intensity. The S₁ transition is due to D(140) (HOMO-1, orbital π) \rightarrow V(1) (LUMO, antibonding orbital (π^*) of aromatic ring). The S₂ transition is due to a transition from D(139) (HOMO-2, n located on orbital D- glucopiranosse ring) to the orbital V (1) (LUMO, π^*).

The band B is composed of two transitions, S₃ and S₄, high intensities. S₃ transition occurs a transition orbital D (135) (HOMO-6, n acetyl group of the aromatic ring) to the orbital V (1) (LUMO). The S₄ transition is the transition part of the orbital D (141) (HOMO, π located on the aromatic ring) to the orbital V (1) (LUMO).

The C band is composed of a transition, S₅, low intensity. S₅ transition is due to a transition of the orbital D (139) (HOMO-2, n) located on the aromatic for the orbital V (2) (LUMO + 1, antibonding π^*) located on the aromatic ring. The photoactive region of the molecule are located on the aromatic ring region, where transitions occur between the HOMO, LUMO, HOMO-2 and LUMO+1. Comparing the two theoretical spectra, one in vacuum (Figure 1.a) and another ethanol (Figure 1.b), it is observed that the relative intensity of the C band from the band B in Figure 1.b is smaller than the same in Figure 1.a.

Water simulation

The theoretical spectrum of the UV-VIS absorption acetilbergenin result of the calculation by DFT B3LYP / 6-31G* in water is shown in Figure 1c. There are three bands, A, B, and C, in a theoretical spectrum, where the peak positions are the wavelengths at 260 nm ($f = 0,03791$, A), 240 nm ($f = 0.1480$, B) and 219 nm ($f = 0.0048$, C). The A band consists of the transitions, S₁ and

S₂ medium intensity. S₁ V (1) (LUMO, π^*) transition is due to transition D(140) (HOMO-1, π) where the orbital are located on the aromatic ring and S₂ refers to transition D(139)(HOMO-2, n) \rightarrow V(1) (LUMO, π^*) leaving the carbonyl of D-glucopyranose ring. The band B is composed of two transitions, S₃ and S₄, high intensities. S₃ transition occurs a transition orbital D(134)(HOMO - 7, n) located on the acetyl group of the aromatic ring to the orbital V (1) (LUMO, π^*). The S₄ transition is the transition part of the orbital D (141) (HOMO, π) for the orbital V (1) LUMO. The C band is composed of two transitions, S₅, and S₆, of low intensity. S₅ transition is due to a transition of the orbital D(140)(HOMO-1, π) to the orbital V(2) (LUMO + 1, π^*). The transition S₆ respect to transition D(134)(HOMO - 7) \rightarrow V(1) LUMO.

Solvent effect

The theoretical analysis of the absorption spectra, in Figure 1, shows that comparatively the bands of simulation in ethanol (Figure 1.b) shifted to longer wavelengths relative to the vacuum spectrum (Figure 1.a), and in the water spectrum (Figure 1.c) it was reversed. This demonstrates that the nature of electronic transitions in bands A and B is predominantly of type $\pi \rightarrow \pi^*$ in vacuum and in water, while band C in the ethanol simulates the transition $n \rightarrow \pi^*$ predominates.

By visualizing the orbital calculated by DFT for acetilbergenin in vacuum, it was observed that the photoactive region of the molecule is located on the aromatic ring, where transitions occur between the HOMO \rightarrow LUMO and HOMO-1 \rightarrow LUMO +1 (Figure 2).

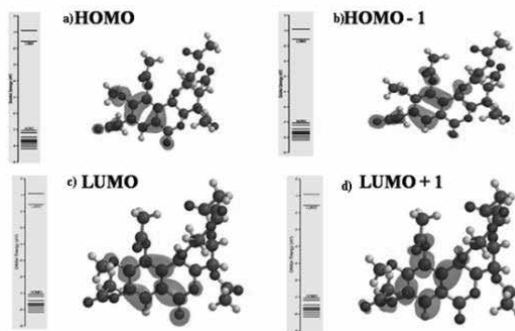


Figure 2. Molecular orbitals of acetilbergenin in vacuum. a)HOMO b) HOMO-1 c) LUMO d) LUMO+1

The solvent change slightly altered the electrostatic potential map both in water (Figure 3.a) and ethanol (Figure 3.b). Probably this change was due to changes in the conformation of the molecule between these the dihedral were highlighted: $C_{24}O_1C_1C_5$ (water= $-43,97^\circ$; ethanol= $-43,45^\circ$; vacuum= $-45,64^\circ$), $C_{15}O_{10}C_{16}C_{17}$ (water= $9,12^\circ$; ethanol= $7,43^\circ$; vacuum= $12,62^\circ$), $C_{13}C_{12}O_8C_{11}$ (water= $-15,90^\circ$; ethanol= $-15,14^\circ$; vacuum = $-17,92^\circ$) and the dihedral $C20O13C21O14$ (water= $-0,33^\circ$; ethanol= $2,39^\circ$; vacuum = $-1,84^\circ$) of the acetyl group of the aromatic ring where there was a change of plan in the middle ethanol.

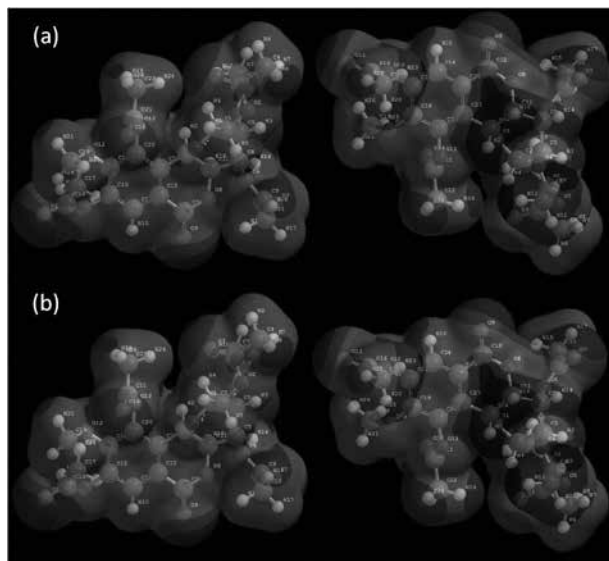


Figure 3: Map of the electrostatic potential of acetilbergenin molecule on a surface of $0.002\text{eV}/\text{ua}^3$. a) water b) ethanol.

The dipole moment of acetilbergenin in water 7,8826 Debye ($26,2931 \cdot 10^{-30} \text{ C.m}$) was larger than 7,57 Debye ($25,2331 \cdot 10^{-30} \text{ C.m}$) in ethanol and in vacuum 6,07 Debye. The increase dipole highlights the transitions $n \rightarrow \pi^*$ with charge transfer character and also the molecular deactivation process in the excited electronic state to another in the ground state via the Forster mechanism¹⁰.

A comparison was made of the HOMO and LUMO energies in the three simulations and it was found that the HOMO energy that has suffered changes with respect to

the vacuum simulation was ethanol and the LUMO energy (-1.64 v) in water. Amid ethanol energy difference between HOMO and LUMO showed lower value indicating higher reactivity¹¹. The change in polarizability, with respect to the vacuum simulation was small in ethanol of 0.07 and 0.08 in water (79.58) (Table 1).

Table 1. Some properties calculated DFT 6-31G*

Acetilbergenin	Vacuum	Ethanol	Water
Log P	-0,76	-0,76	-0,76
Polarizability	79,50	79,57	79,58
Dipole moment (D)	6,07	7,57	7,88
E-HOMO (eV)	-7,06	-6,95	-7,04
E-LUMO (eV)	-1,58	-1,56	-1,64
LUMO-HOMO	5,48	5,39	5,4

Conclusions

The results of the theoretical calculations showed consistency with the experimental data: (1) all three spectra have three bands, A, B, and C; (2) appearance and relative intensity of bands A and B are similar in the three spectra; (3) the relative intensity of band C in ethanol and in water is very weak compared to 1a. The orbitals HOMO and LUMO are localized at the aromatic ring acetilbergenin, this being its most photoactive region.

The calculation showed that ethanol has changed to transition a long distance charge transfer, since in vacuum stemmed orbital (n) of δ -lactone ring to the antibonding orbital (π^*) of the aromatic ring and the orbiting ethanol was (n) the ring D- glucopyranose to the aromatic ring. This type of transition is usually the driving force responsible for the interaction of the molecule with biological material, because of this molecule is shown in more photoactive hydrophilic medium (ethanol, $f = 0.0333$) with oscillator strength greater than simulation vacuum (isolated molecule without interaction, $f = 0.0068$).

Acknowledgments

The authors are grateful for the support given from the CNPQ and MURAKI Foundation.

References

1. CORRÊA, M. P. ; Dictionary of useful plants in Brazil and cultivated exotic in Rio de Janeiro, National Press, V.6; **1984**.
2. BORGES, J. C. Collection and evaluation of antinociceptive and anti-inflammatory activities. Masters dissertation Federal University of Pará. **2010**.
3. JUNG, J. C., LIM, E., KIM, S. H., KIM, S., JUNG, M., & OH, S. Practical synthesis and biological evaluation of bergenin analogs. *Chem Biol, Drug Des*, **2011**, 78:725-729.
4. LIM, H., KIM, H., KIM, S., CHANG, M., RHEE, G. P., CHOI, J. Protective effects of acetylbergenin against carbon tetrachloride-induced hepatotoxicity in rats. *Pharmacology, Toxicology & Pharmaceutic*, 24(2): 114-118, **2001**.
5. LIM, S., KIM, H., CHOI, H., OH, S., JANG, C. G., CHOI, W. J. Effects of acetylbergenin against D- galactosamine induced hepatotoxicity in rats. *Pharmacological Research* , 42 (5): 471-474, **2000**.
6. NAZIR, N., KOUL, S., QURISHI, M. A., NAJAR, M. H., ZARGAR, M. I. . Evaluation of antioxidant and antimicrobial activities of Bergenin and its derivatives obtained by chemoenzymatic synthesis. *European Journal Medicinal Chemistry* , V. 46, p.2415-2420. **2011**.
7. QUIN, X., YANG, Y., FAN, T., GONG, T., ZHANG, X., & HUANG, Y. Preparation, characterization and in vivo evaluation of bergenin phospholipid complex. *Acta Pharmacologica Sinica*, 31:127-136, **2010**.
8. SANTOS, D. R. Biotransformation of bergenin using Amazon fungi as biocatalyst. Masters dissertation UEA, **2012**.
9. FRICK, W., HOFMANN J., FISCHER, H., SCHMIDT, R. R. The structure of bergenin, *Carbohydrate Research*, 210:71-77, 1991.
10. ØBIRKS, J. B.; *Photophysics of Aromatic Molecules*, John Wiley & Sons Ltd., New York, **1970**.
11. FUKUI, K. T., YONEZAWA, T., SHINGU, H. . A Molecular Orbital Theory of Reactivity in Aromatic Hydrocarbons. *J. Chem. Phys* , p.722-725. **1952**

Gisele Franco de Castro^{a*},
Diego dos Santos
Freitas^a, Alberto dos Santos
Marques^b & Yuji Takahata.

^aUniversidade do Estado do Amazonas, Centro de Estudos Superiores de Tefe, AM.

^bUniversidade Federal do Amazonas, Laboratório de Tecnologia com Moléculas Bioativas, LTMB, Departamento de Química.

*E-mail: francogisele@gmail.com

Theoretical Evidence to *Cis* Folding in PhoR Histidine Kinase of *Corynebacterium Pseudotuberculosis*

Gleiciane L. Moraes, Guelber Cardoso, Cláudio N. Alves & Jerônimo Lameira

Introduction

Two-component systems (TCS) are signaling pathways that respond to changes environmental by modifying cellular behaviors. The first component of these systems is a dimeric sensor histidine kinase (HK); the second is its cognate target, termed the response regulator (RR)¹. In bacterias the main signal-transduction mechanism is via TCS systems, in which the signaling process starts by the autophosphorylation of a highly conserved histidine residue in the sensor HK. In response to a signal generated in the N-terminus sensor domain of HK, occur transfer γ -phosphate from ATP bound to the catalytic ATP-binding domain (CA) to conserved histidine residue on the dimerization/histidine phosphorylation (DHp) domain in the C-terminus kinase core (DHp_CA)¹. Depending on the architecture of the DHp domain, the histidine residue is phosphorylated by CA domain of same chain (cis-autophosphorylation) or of the other chain (trans- autophosphorylation)² (Fig.1). This being suggested that autophosphorylation mechanism is determined by the loop at the base of the DHp domain four-helix bundle^{2,3,4}. Surprisingly, Ashenberg and colleagues (2013) found that the mode of autophosphorylation be highly conserved in orthologous sets of histidine kinases, despite the sequence of the DHp domain loop is highly variable, and that orthologs of PhoR with diverse loops autophosphorylated in cis and

orthologs of EnvZ with diverse loops autophosphorylated in trans. Chimeras constructed in which was replaced the loop of EnvZ (trans) by loop of PhoR (cis), change autophosphorylation mechanism from in cis to in trans, indicate that the DHp loop is a functionally important determinant of autophosphorylation mechanism in histidine kinases, supplanting the notion that these loops are simple linkers between helices^{2,4}. Here, we obtained structure 3D by comparative molecular modeling of the phosphate sensor PhoR *Corynebacterium pseudotuberculosis* in folding cis and trans, and carried out a molecular dynamics simulation to finding theoretical evidences of folding in HK.

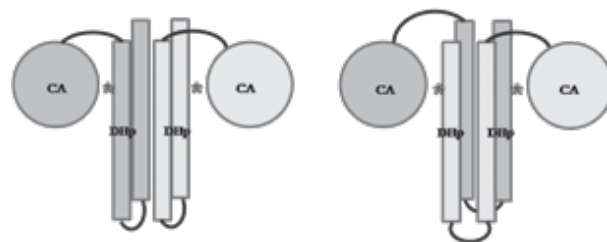


Figure 1. Folding C-terminus kinase core in HK. a) Folding to cis-autophosphorylation and b) Folding to trans-autophosphorylation.

Methods

PROTEIN STRUCTURE MODELING

The amino acid primary sequences enzyme of *M. tuberculosis* FRC41 were obtained from the NCBI (<http://blast.ncbi.nlm.nih.gov/>) under accession number YP_003784140.1. The structures of the enzymes were generated by of SWISS-MODEL Server⁵ and Modeller 9v12⁶ software. Modeling of the folding to cis-autophosphorylation was obtained using osmolarity sensor protein EnvZ chimera *E. coli* (EnvZchim) histidine kinase (PDB code: 4KP4)⁴; and folding to trans-autophosphorylation was obtained using osmolarity sensor protein EnvZ native *E. coli* (EnvZ^{wt}) histidine kinase (PDB code: 4CTI)⁷. ATP and Mg²⁺ were transfer as a rigid body to generated model using the BLK residue type in Modeller 9v12⁶. The structures of each protein modelled were validated using Ramachandran plot,⁸ QMEAN score⁹ (available in SWISS-MODEL Server⁵) and ProQ¹⁰.

MOLECULAR DYNAMICS SIMULATION

The ionization state of ionizable residues was assessed from PROPKA¹¹ calculations, except to catalytic residue histidine (His289), which must be protonated in triphosphate hydrolysis¹².

We carried out molecular dynamics simulations using AMBER 12 software package¹³. The system was immersed in an octahedral box of TIP3P14 water molecules and sodium ions were added to neutralize the system. The parm99SBildn force field parameters in the Amber12¹³ package were used for the protein and ions, the Carlson corrected parameters¹⁵ were used for the ATP molecule and the Sticht parameters¹⁶ for the cofactor ion Mg²⁺. The minimization has been made using multistep protocol, first the adjustment of hydrogens, following water molecules and counterions were refined, and finally the minimization of the whole system. Thermalization of system was performed by heating in 10 steps, initially one step of 20ps from 0 to 100 K at constant volume, 8 steps of 1ns increasing the temperature from 100 to 300 K, and an additional step of 5ns was performed in order to equilibrate the system density at constant pressure (1 bar). The bonds containing hydrogen atoms

were kept at the equilibrium distance using the Shake algorithm¹⁷. Finally, a 50ns trajectory were run in the NTP formalism, the temperature were kept constant Berendsen thermostat¹⁸ using a time step of 2fs, periodic boundary conditions and Ewald sums¹⁹ (grid spacing of 1 Å) for long-range electrostatic interactions.

Results and Discussion

PROTEIN STRUCTURE MODELING

Homology modeling or comparative modeling allows the construction of the tertiary structure of a protein based on the primary structure similarity²⁰. The best structures obtained by comparative molecular modeling of the phosphate sensor PhoR *C. pseudotuberculosis* in folding cis (Fig.2a) and trans (Fig.2b) are presented. The better structure in folding trans was obtained in Modeller 9v12⁶ software. The folding trans structure constructed in SWISS-MODEL Server⁵ had intertwining of DHP loop, because this structural error the model was rejected to continue the work (structure not shown). The better structure in folding cis was obtained in SWISS-MODEL Server⁵.

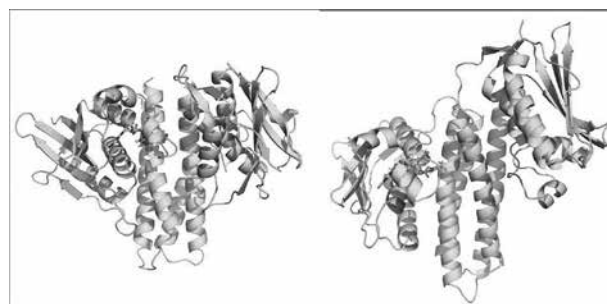


Figure 2. Folding C-terminus kinase core in HK of the *C. pseudotuberculosis*. a) folding cis and b) folding trans.

Table 1 shows a summary of validation results of build 3D structures.

Table 1. Validation proteins modeled.

Folding	Ramachandran plot	LGscore	QMEAN	RMSD
cis	91.9%	5.021	0.614	1.519
trans	94.4%	4.068	0.683	8.681

Based on the parameters shown in Tab.1, both built models show good values Ramachandran plot8 (most favoured regions), QMEAN⁹ and LGscore¹⁰. However, *trans* folding showed high RMSD to the template (8.681). Furthermore, graphical plots of ANOLEA²¹ mean force potential that represents the energy for each amino acid of the protein chain indicates that the packing quality of the 3D structure is better in *cis* folding (Supporting information). In other modeling performed using HK CpxA of *E. coli*²² (32% de identity and 49% de similarity), a folding *trans*, showed 90,8% of the residues are in the most favoured regions of the Ramachandran plot8, QMEAN9 of 0.453, LGscore¹⁰ of 3.76, RMSD of 7.46 Å and very bad packing quality (structure not shown). It is important to note that, despite the low identity between the osmolarity sensor protein EnvZ^{chim} (26% identity and 46% similarity) of *E. coli* and the phosphate sensor PhoR of *C. pseudotuberculosis*, the models obtained from this template were very better including the quality of packaging and RMSD. The superposition of the between target and templates (Fig.3) indicates that all secondary structures in the target protein were conserved in both models, however the model constructed using EnvZ^{chim}, *trans* folding, it does not shows good structural overlap. On the other hand, o model constructed using EnvZ^{wt}, *cis* folding, and the model shows good structural overlap and the generated 3D structure is good according to the parameters analysed.

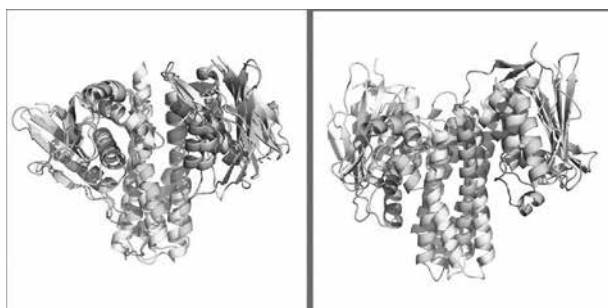


Figure 3. Superposition of the calculated PhoR of *C. pseudotuberculosis* (green) and a) EnvZchim (PDB code: 4KP44), b) EnvZwt (PDB code: 4CTI7) of *E. coli* (yellow).

The catalytic core (DHp_Ca) HK of *C. pseudotuberculosis* N-terminus (DHp) is formed by two long helices ($\alpha 1$ and $\alpha 2$), where $\alpha 1$ contains the phosphorylatable conserved His289 residue, and C-terminus (CA) is formed by an α/β sandwich fold similar to the ATPase domains of the ATPase superfamily²³. This latter domain binds ATP in a pocket covered by a flexible and variable loop named ATP lid²⁴.

MOLECULAR DINAMICS SIMULATION

To explore the implications of folding in the stability of catalytic core PhoR complex (protein+ATP+Mg²⁺), we performed 50 ns of MD simulations at 300 K for structures obtained in the previous step (Fig.4b). Moreover, we carried out molecular dynamics simulations in EnvZ^{chim} (*cis*) and EnvZ^{wt} (*trans*) complex (protein+ATP+Mg²⁺) (Fig.4a)

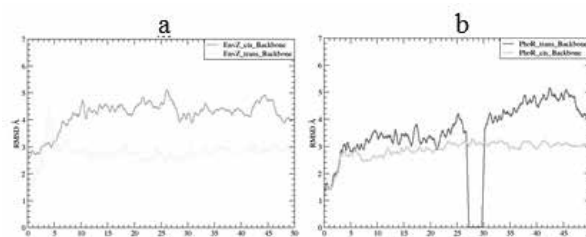


Figure 4. Average RMSD in performed trajectory of 50 ns of MD simulations. a) EnvZchim and EnvZwt of *E. coli* and b) PhoR of *C. pseudotuberculosis* folding *trans* and *cis*.

After the first 5 ns MD, it is observed that the RMSD of EnvZwt stabilizes, as well as the RMSD folding *cis* PhoR. It is important to remind that orthologs of PhoR with diverse loops autophosphorylated in *cis* and orthologs of EnvZ with diverse loops autophosphorylated in *trans*². Interestingly osmolarity sensor protein EnvZ native structure of *E. coli* and the more probable structure folding of phosphate sensor PhoR of *C. pseudotuberculosis* are which present the more stable RMSD during MD simulation trajectory. Even after 50 ns MD simulation the RMSD of chimera EnvZ *cis* and PhoR *trans* folding are less stable. In crystallographic studies by Marina et. al. (2014)⁴ there

was obtained the EnvZ chimera shown that it is possible to change the autophosphorylation mechanism of cis to trans in histidine kinase by changing the connection handle. However, our studies show that during the MD simulation time produced, this folding is less stable. Regarding the PhoR protein, it is important to note that DHp loop connection was not replaced. In our study, the sequence of the native PhoR protein was modeled in folds cis and trans and has been theoretically evaluated the stability of structure in each folding. We also monitored the interactions of the active site of *C. pseudotuberculosis* PhoR (Fig 5). It is expected that a Mg^{2+} ion bridges the three nucleotide phosphates, an invariant Asn and two water molecules complete the octahedral coordination sphere of the Mg^{2+} ion in the structures^{4, 25}.

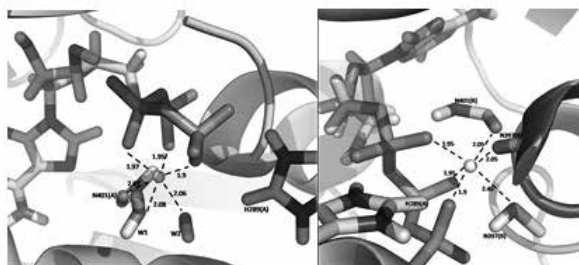


Figure 5. Octahedral coordination sphere of the Mg^{2+} ion in the *C. pseudotuberculosis*. a) folding cis and b) folding trans.

During the MD simulations of the different PhoR system was observed the formation of an octahedral coordination sphere. The octahedral coordination sphere observed in cis folding PhoR showed Mg^{2+} ion bridges with three ATP phosphates, Asn401 carbonyl and two water molecules (W1 and W2) (Fig.5a), as described for other HK^{4, 25}. On the other hand, the octahedral coordination sphere observed in trans folding PhoR showed Mg^{2+} ion bridges with three ATP phosphates of chain A, Asn397 and Asn401 carbonyl and Thr400 amino acid residues (Fig.5b). The latter octahedral coordination sphere is not according to the procedure described for other HK.

Conclusions

The results obtained by comparative modeling and MD simulations indicate the fact that the probable folding to phosphate sensor PhoR of *C. pseudotuberculosis* (based in orthologs of PhoR) is the better structure obtained by comparative modeling and show the more stable RMSD during DM simulations. Therefore, the HK folding can be predicted theoretically.

Acknowledgments

The authors are grateful for the support given from the UFPA and CAPES.

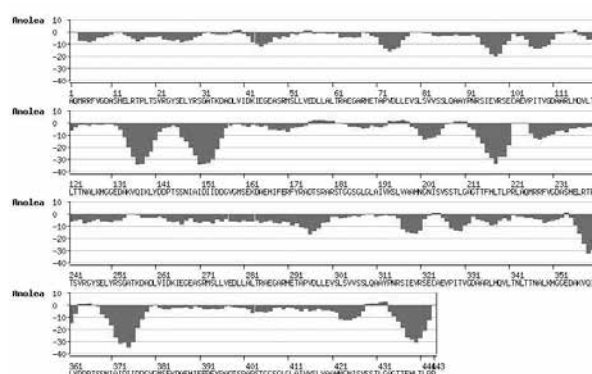
References

1. R. Gao, A. M. Stock, *Annu. Rev. Microbiol.* 63, 133, (2009).
2. O. Ashenberg, A. E. Keating, M. T. Laub, *J. Mol. Biol.* 425, 1198, (2013).
3. P. Casino, V. Rubio, A. Marina, *Cell.* 139, 325, (2009).
4. P. Casino, L. Miguel-Romero, A. Marina, *Nat. Commun.* 5, 3258, (2014).
5. K. Arnold, L. Bordoli, J. Kopp, T. Schwede, *Bioinformatics.* 22, 195, (2006).
6. N. Eswar, B. Webb, M. A. Marti-Renom, M. S. Madhusudhan, D. Eramian, M-Y. Shen, U. Pieper, A. Sali. *Curr. Protoc. Protein Sci / editorial board, J. E. Coligan [et al] Chapter 2, Unit 2.9, (2007).*
7. H. U. Ferris, M. Coles, A. N. Lupas, M. D. Hartmann, *J. Struct. Biol.* 186, 376, (2014).
8. R. A. Laskowski, M. W. Macarthur, D. S. Moss, J. M. Thornton. *J. Appl. Cryst.* 26, 283, (1993).
9. B. Wallner, A. Elofsson, *Prot. Sci.* 12, 1073, (2003).
10. P. Benkert, S. C. E. Tosatto, D. Schomburg, *proteins struct. funct. bioinf.* 71, 261, (2008).
11. M. H. M. Olsson, C. R. Sondergaard, M. Rostkowski, J. H. Jensen, *J. Chem. Theory Comput.* 7, 525, (2011).
12. G. Wallin, S. C. Kamerlin, J. Aqvist, *Nat. Commun.* 4, 1733, (2013).
13. D.A. Case, T.A. Darden, T.E. Cheatham III, C.L. Simmerling, J. Wang, R.E. Duke, R. Luo, R.C. Walker, W. Zhang, K.M. Merz, B. Roberts, S. Hayik, A. Roitberg, G. Seabra, J. Swails, A.W. Götz, I. Kolossváry, K.F. Wong, F. Paesani, J. Vanicek, R.M. Wolf, J. Liu, X. Wu, S.R. Brozell, T. Steinbrecher, H. Gohlke, Q. Cai, X. Ye, J. Wang, M.-J. Hsieh, G. Cui, D.R. Roe, D.H. Mathews, M.G. Seetin, R. Salomon-Ferrer, C. Sagui,

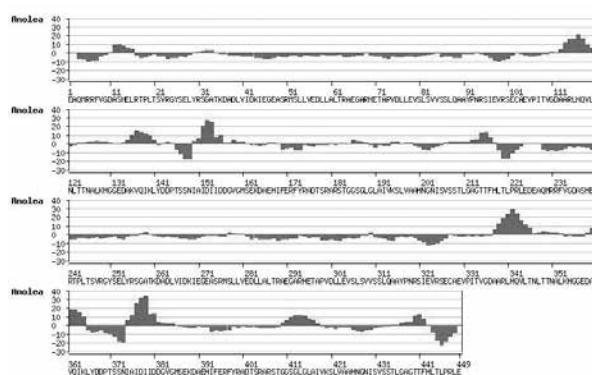
V. Babin, T. Luchko, S. Gusarov, A. Kovalenko, and P.A. Kollman, AMBER 12, University of California, San Francisco, (2012).

14. W.L. Jorgensen, J. Chandrasekhar, J.D. Madura, R.W. Impey, M.L. Klein, J. Chem. Phys. 79, 926, (1983).
15. K.L. Meagher, L.T. Redman, H.A. Carlson, J. Comput. Chem. 24, 1016, (2003).
16. O. Allnér, L. Nilsson, A. Villa, J. Chem. Theory Comput. 8, 1493, (2012).
17. J.P. Ryckaert, G. Ciccotti, H.J.C. Berendsen, J. Comput. Phys. 23, 327, (1977).
18. H.J.C. Berendsen, J.P.M. Postma, W.F. van Gunsteren, A. DiNola, J.R. Haak, J. Chem. Phys. 81, 3684, (1984).
19. D. M. York, T. A. Darden, L. G. Pedersen, J. Chem. Phys. 99, 8345, (1993).
20. H. D. Höltje, W. Sippl, D. Rognan, G. Folkers, Weinheim: Wiley-VCH, (2008).
21. F. Melo, E. Feytmans, J. Mol. Biol. 277, 1141, (1998).
22. A. E. MECHALY, N. SASSOON, J. BETTON, P. M. ALZARI, Plos Bio. 12, 1001776, (2014).
23. R. Dutta, M. Inouye, Trends. Biochem. Sci. 25, 24, (2000).
24. A. Marina, C. Mott, A. Auyzenberg, W. A. Hendrickson, C. D. Waldburger, J. Biol. Chem. 276, 41182, (2001).
25. A. M. Bilwes, C. M. Quezada, L. R. Croall, B. R. Crane, M. I. Simon, Nat. Struct. Biol. 8, 353, (2001).

Supporting information



S1. Plots of ANOLEA1 mean force potential. a) Folding cis PhoR of *C. pseudotuberculosis* and b) Folding trans PhoR of *C. pseudotuberculosis*



1 F. Melo, E. Feytmans, J. Mol. Biol. 277, 1141, (1998).

Gleiciane L. Moraes^a,
Guelber Cardoso^b, Cláudio
Nahum Alves^a & Jerônimo
Lameira^{b*}

^a Laboratório de Planejamento de Fármacos, Instituto de Ciências Exatas e Naturais, Universidade Federal do Pará, CEP 66075-110 Belém, PA, Brazil.

^b Laboratório de Planejamento de Fármacos, Instituto de Ciências Exatas e Naturais, Universidade Federal do Pará, CEP 66075-110 Belém, PA, Brazil; Instituto de Ciências Biológicas, Universidade Federal do Pará, CEP 66075-110 Belém, PA, Brazil

*E-mail: lameira@ufpa.br

Fully Anharmonic Resonance Raman Spectrum of Diatomic Molecules Through Numerical Solution of the Vibrational Schrodinger Equation

Gustavo J. Costa, Rogério Custodio, Pedro A. M. Vazquez & Luciano N. Vidal

Introduction

The molecular contribution to the intensity of the Raman scattering is given by the general polarizability $\alpha_{\rho\sigma}^{fi}$. In the far-from-resonance (FFR) regime, the energy of the excitation radiation ($\hbar\omega_0$) is far from that of any electronic transition and $\alpha_{\rho\sigma}^{fi}$ receives balanced contributions of many excited electronic states, expressed by the well known Placzek's electronic polarizability, whose geometrical derivatives are related to the intensities of FFR Raman.¹ On the other hand, the Resonance Raman (RR) scattering occurs when $\hbar\omega_0$ is close from the energy of an electronic transition. In RR the intensity of the scattered radiation is orders of magnitude stronger than that of FFR regime and $\alpha_{\rho\sigma}^{fi}$ is dominated by one (or few) excited electronic state.¹ Therefore, this form of Raman provides structural and dynamical information of both ground and excited (resonance) electronic states. Within the Born-Oppenheimer (BO) and Frank-Codon (FC) approximations, the corresponding expression for $\alpha_{\rho\sigma}^{fi}$ of RR is given by:

$$\alpha_{\rho\sigma}^{fi} = \frac{1}{\hbar} \langle g | \mu_\rho | e \rangle \langle e | \mu_\sigma | g \rangle \sum_n \frac{\langle v_f | n \rangle \langle n | v_i \rangle}{\omega_{eg} + \omega_{ni} - \omega_0 + i\Gamma_e}$$

This expression involves, among other quantities, FC integrals of the initial (v_i) and final (v_f) vibrational states in the ground electronic state g with vibrational states (n) of the resonance electronic state e . In order to simplify the calculation of FC integrals, the Potential Energy Surface (PES) of g and e states are considered harmonic and those integrals are evaluated analytically from recurrence formulas.² To the best of our knowledge, there is only one article reporting the calculation of FC integrals for anharmonic wave-functions in RR.³ On that pure theoretical work, the RR cross section of diatomic systems is obtained from analytic integration of unidimensional eigenfunctions of the Morse potential. The FC factors were computed for several values of the vibrational quantum numbers v and n of hypothetical molecules, and were compared with those from analytic solution of the harmonic potential. It was shown that FC factors differ only few percent between Morse and harmonic models for $v, n=0, 1$ or 2 , however, for higher values the anharmonic FC factors can be many time greater or lower than the corresponding harmonic data. In the case of RR cross sections, the anharmonic effects can be strong even for fundamental transitions.

In the present study, the FC integrals are numerically evaluated for vibrational states of the true PES obtained from correlated ab initio methods. The vibrational wave-functions are calculated using a version of the Variational Monte Carlo (VMC)

method. Our method is applied to calculate the FC RR spectrum of diatomic molecules. In addition, the Herzberg-Teller (HT) intensity borrowing mechanism is also taken into account in the current model, thus $\alpha_{\rho\sigma}^{\text{fi}}$ can be corrected for the effect of coupling the electronic transition moments with the nuclear motion.

Methods

The electronic structure calculations were performed with Dalton quantum chemistry code⁴ for a single reference (e.g. CCSD) and multi-reference (e.g. NEVPT2) electron correlation *ab initio* methods using correlation consistent basis sets augmented with diffuse functions (aug-cc-pVXZ, X=D,T,Q). The electric dipole transition moment $\langle g | \mu_{\rho} | e \rangle$ and vertical excitation energy $\hbar\omega_{\text{eq}}$ were obtained from the Linear Response of the CCSD wave-function at the ground state equilibrium geometry. HT effects can also be taken into account in our model if the electronic transition moment is expanded in Taylor series of normal coordinate Q :

$$\langle g | \mu_{\rho} | e \rangle = \langle g | \mu_{\rho} | e \rangle_0 + \left(\frac{d\langle g | \mu_{\rho} | e \rangle}{dQ} \right)_0 Q + \dots$$

When the above expansion is used for $\langle g | \mu_{\rho} | e \rangle$, the resulting $\alpha_{\rho\sigma}^{\text{fi}}$ demands the computation of FC and HT integrals of the general form: $\langle v_f | Q^m | n \rangle$ and $\langle n | Q_m | v_i \rangle$, with $m=0,1,2,\dots$. All FC and HT integrals were evaluated by numerical methods. The required geometric derivatives of the electronic transition moments were computed at the ground state equilibrium geometry using central difference formulas. These derivatives, the FC and HT integrals and the RR spectrum were obtained by our code PLACZEK, developed for the calculation of infrared and Raman spectra.⁵ Temperatures effects may be important for those systems with low energy vibrations. In such cases, the RR cross sections of several initial v_i states are calculated and average by their thermal population. From the current approach, any RR fundamental or overtone transition is available. They have quite similar computational costs and depend on the speed of convergence of the cross section with respect to the

number of intermediate vibrational states n .

The vibrational analysis was carried out considering an alternative Quantum Monte Carlo. In this formalism the Hamiltonian is represented as the combination of the well-know kinetic energy operator and the potential energy is selected according to the requirements of system. In this work, the potential energy was taken from *ab initio* calculations described above. The second derivative of the Laplacian is describe by a central difference expression:

$$\left(\frac{\partial^2 \psi}{\partial x^2} \right) = \left(\frac{2}{h_i + h_{i-1}} \right) \left(\frac{\psi_{i+1} - \psi_i}{h_i} - \frac{\psi_i - \psi_{i-1}}{h_{i-1}} \right)$$

where, $h_i = x_{i+1} - x_i$. The initial wave function is described as a set of arbitrary values defined in each particular discretized coordinate. From the discretized mean value theorem, the Hamiltonian and the discretized wave function it is possible to estimate the total energy of the system.⁶ One of the discrete values of the wave function is selected at random and modified by, for example: $\psi_{\text{new}} = \psi_{\text{old}} + (0.5 - \text{rand})\delta$, where rand is a uniform distributed random number and δ is a parameter defining the degree of change in the wave function. From the modified wave function, the total energy is calculated and compared with the precious energy. If the new energy is accepted, the modification in the wave function is preserved. If the new energy increases, the change in the wave function is rejected. The procedure follows the variational principle and the final energy is achieved after a selected degree of convergence of the system is defined.

Results and Discussion

Preliminary results are presented in Figure 1, showing some vibrational wave-functions and their energies for N₂ evaluated at the ground electronic state. The PES was calculated at the NEVPT2(6,6)/aug-cc-pVTZ level. The spectroscopic constants obtained for different sets of vibrational states are shown in Table 1 together with experimental data. They are useful to access the quality of the vibrational wave-functions.

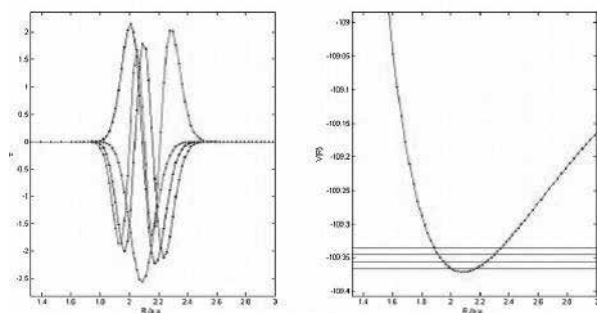


Figure 1. Anharmonic vibrational wave-functions (left) and their energy (right) for the first 4 states of N₂.

Table 1. Spectroscopic constants calculated for the ground electronic state of N₂ at the NEVPT2(6,6)/aug-cc-pVTZ level for several vibrational states (v).

v	ω_e/cm^{-1}	$\omega_e X_e/\text{cm}^{-1}$	$\omega_e Y_e/\text{cm}^{-1}$
5	2344.903	23.335	0.157
8	2346.754	24.503	0.347
10	2323.642	16.111	-0.409
12	2349.555	23.922	0.155
15	2344.457	22.196	0.020
Exp.7	2358.57	14.324	-0.00226

Conclusions

Our method is under final development with the VMC code ready and RR results now being compared with analytical data from the harmonic model to check their accuracy.

Acknowledgments

The authors are grateful for the support given from the CNPQ, FAPESP e FAEPEX-UNICAMP.

References

1. D. A. Long, The Raman Effect; John Wiley & Sons, LTD: Chichester, (2002).
2. F. Santoro, C. Cappelli and V. Barone, J. Chem. Theory Comput., 7, 1824, (2011). F. Egidi, J. Bloino, C. Cappelli and V. Barone, J. Chem. Theory Comput., 10, 346, (2014). F. Santoro, R. Improta, A. Lami, J. Bloino, and V. Barone, J. Chem Phys., 126, 084509, (2007).

3. H. Kono, Z. Z. Ho and S. H. Lin, J. Chem. Phys. 80, 1760, (1984).
4. Dalton, a molecular electronic structure program, Release Dalton2015. (2015), see <http://daltonprogram.org>.
5. O. Beruski and L. N. Vidal, J. Comput. Chem., 35, 290, (2014). L. N. Vidal and P.A. M. Vazquez, Quim. Nova, 35, 2076 (2003).
6. R. Custodio, M. R. Custodio, E. J. Creatto, Quim. Nova, 35, 2076 (2014).
7. K. Huber and G. Herzberg, Molecular Spectra and Molecular Structure. IV. Constants of Diatomic Molecules, 2nd ed., Van Nostrand Reinhold: New York, (1979).

Gustavo Juliani Costa^a,
Rogério Custodio^b, Pedro
A. M. Vazquez^b & Luciano
Nassif Vidal^a

^a Universidade Tecnológica Federal do Paraná, DAQBI, Curitiba/PR, Brazil.

^b Universidade Estadual de Campinas, IQ-DFQ, Campinas/SP, Brasil.

Analysis of Titanium Dioxide Nanotubes, Rutile (110) and Anatase (101)

G. O. Silva, J. D. Santos, J. B. L. Martins, C. A. Taft & E. Longo

Introduction

The experimental and theoretical studies of nanotubes have increased over the past decade¹⁻³. Nanostructured compounds containing Ti oxides are fairly investigated due to their electronic properties and the application possibilities in areas such as medicine^{4,5}, molecular biology⁶, solar^{7,8}, photocatalytic processes^{9,10}. It is also the subject of study in the application as gas sensor¹¹⁻¹³. Theoretical investigations are carried out on different materials (nanotube surfaces) formed of various compounds (TiO_2 , ZnO , SnO_2 , C, GaAs,). From quantum mechanical calculations, it is possible to access the energy parameters (the interaction and surface energy, gap) and compare these results with experimental data. Among the structures that have interest due to their potential applicability in the experimental and theoretical studies, titanium dioxide nanotubes¹⁴⁻¹⁸ is widely used.

In the present work, using a programming language, we selected the atoms of specific crystal planes of both the anatase and rutile faces to yield several nanotubes of different diameters and lengths, depending on the number of TiO_2 units. This methodology seeks nanotubes formed by basic units having the same geometry of the source structure. Models with geometries of the armchair and zig-zag¹⁹⁻²² were generated.

Computational Details

The simulations was conducted with small tubes of rutile and anatase titanium dioxide structures. The entire process is carried out through algorithms created in bash shell language in the Linux system, to obtain the structures of surfaces and nanotubes of TiO_2 , of rutile and anatase using their experimental lattice parameters²³. From the crystal lattice parameters of rutile and anatase, a basic unit was formed for the nanotubes. In the case of anatase crystal, we selected the (101) plane, and for the rutile crystal the (110) plane was investigated. The choice for these planes is due to these planes were well known in the literature for their properties and potential applications²⁴⁻²⁹. Figures 1 and 2 show a representation of the structures and sequence of the formation of anatase and rutile nanotubes, respectively:

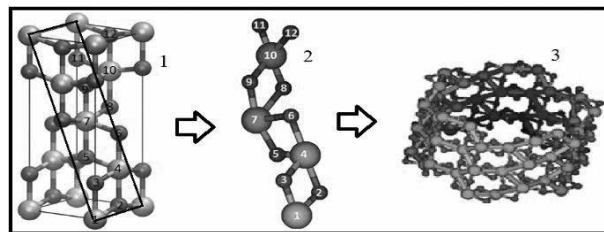


Figure 1. Representation of the following structures for (101) anatase nanotubes. 1 – Unit Cell (Anatase); 2 – Monomer for anatase; 3 – Nanotube TiO_2 (Anatase).

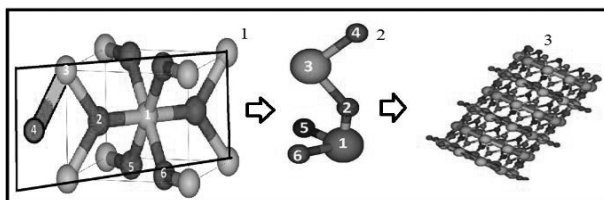
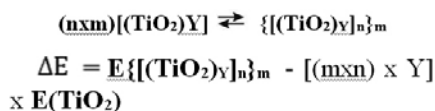


Figure 2 - Representation of the following structures for (110) rutile nanotubes. 1-Unit Cell (Rutile); 2-Monomer for rutile; 3- TiO_2 nanotube (Rutile).

The models were subjected to the energy calculation with semi-empirical method based on PM7 and abinitio HF and DFT, with 6-31G and 6-311G basis functions. MOPAC2012 software was used for the semi-empirical method, while the RHF and DFT the Gaussian 03 was used. The models were generated from the experimental cell parameters crystals of rutile and anatase, in the cartesian coordinate system. The optimization was performed in all structures with semi-empirical PM7. The RHF and DFT calculations were performed using the optimized coordinates from semi-empirical method.

The energy values variation was obtained from the chemical equation (1.1):



Y is the index the TiO_2 units and is related to the structure, rutile ($Y=2$) and anatase ($Y=4$). 47 models were obtained of anatase nanotubes with 1, 2 and 3 layers, while for rutile 31 models were obtained. Only the results for the variation energy of anatase are shown in Figure 3. The results of rutile presents the same behavior. A decrease of energy variation follows the stability of increasing nanotube length.

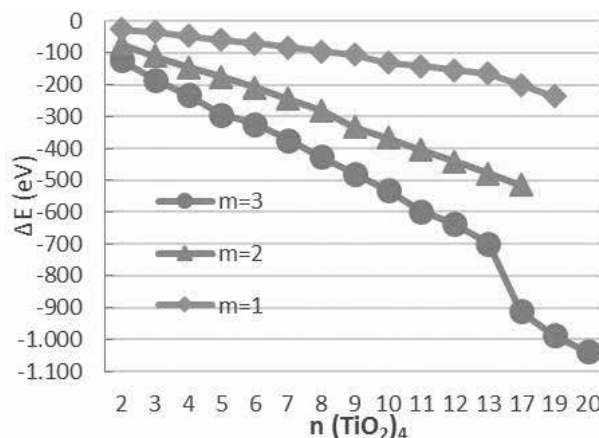


Figure 2. a – PM7 ΔE in relation to the number of units ($n [(\text{TiO}_2)_4]$) of anatase.

DFT and RHF (Table 3) result were performed and show the same trend for the variation energy. The results of anatase nanotubes demonstrate that increasing the length and diameter not contribute significantly in changing the gap values, without changing the conductivity properties thereof. Anatase nanotubes kept the gap values in the range between 6.00 eV and 8.00 eV, behaving as an insulator material.

Table 3 - Comparison between the calculations of the semi-empirical method and ab initio calculations.

	ΔE (eV)				PM7
	DFT/B3LYP		HF		
	6-31G	6-311G	6-31G	6-311G	
$\{[(\text{TiO}_2)_4]_2\}_1$	-34.8674	-34.6987	-35.0023	-35.1008	-26.5585
$\{[(\text{TiO}_2)_4]_3\}_2$	-125.6752	-125.7489	-123.9780	-124.0187	-109.9690
$\{[(\text{TiO}_2)_4]_6\}_3$	-372.6210	-372.9514	-370.9832	-371.1296	-323.1400

The DOS results demonstrate that nanotubes valence band of anatase concentrated in the range between -15.00 -10.00 eV to eV, while the conduction band had values in the range from -2.50 eV to 5.00 eV. In the case of rutile nanotubes, the results show that the valence band are concentrated in the range of -16.00 eV to -6.00 eV, and the conduction band showed values ranging from -3.00 eV to 5.00 eV.

Table 4 - Comparison between the calculations of the semi-empirical method and ab initio calculations of gap (eV).

Structure	Gap (eV)				
	DFT/B3LYP		HF		PM7
	6-31G	6-311G	6-31G	6-311G	
{[(TiO ₂) ₄] ₂ 1	2.47	2.46	9.43	9.70	8.46
{[(TiO ₂) ₄] ₃ 2	2.03	2.05	8.95	-	7.69
{[(TiO ₂) ₄] ₆ 3	2.29	2.29	9.28	9.48	7.00

The results showed in Table 4 a large difference between the results of the HF and DFT method. The HF method overestimated values of the gap compared with the semi-empirical method, since the values of the DFT method gave values below compared with the semi-empirical and HF. In comparing the 6-31G and 6-311G bases, considerable variation between their values was not found. Compared to experimental and theoretical results in the literature, the values found by the DFT method with values between 2.00 eV to 2.50 eV, are the closest.

Conclusions

The energy variation analysis with the length of 3 levels of anatase and rutile nanotubes have shown that stability is achieved with increasing the diameter. RHF and DFT results showed the same trend.

The rutile nanotubes had a gap values of about 2.00 to 4.00 eV, while anatase nanotubes had values in the range of 6.00 eV to 8.00 eV, for the calculation PM7; The results of the gap calculations with the DFT method for anatase nanotubes (2.00 eV to 2.50 eV) underestimated values found with the semi-empirical method.

Acknowledgments

The authors are grateful for the support given from the FAPEG, CAPES and CNPQ.

References

- Moraes, E., Gargano, R., Politi, J. R. S., Castro, E. A. S., Santos, J. D., Longo, E., Martins, J. B. L. 2014, v. 3, n. 4, p. 400-407.
- Santos, J. D., Ferreira, M. D., Martins, J. B. L., Taft, C. A., & Longo, E. Current Physical Chemistry, 2014 v. 3, n. 4, p. 451-476.
- Ferreira, M. D., Santos, J. D., Taft, C. A., Longo, E. Computational Materials Science, 2009, v. 46, n. 1, p. 233-238.
- Ganguly, D.; Zhao, Y. Fabrication of TiO₂ Nanotube Arrays Using 1, 2 Propanediol Electrolyte for Application in Biomedical Implants. In: TMS 2014 143rd Annual Meeting & Exhibition, Annual Meeting Supplemental Proceedings. John Wiley & Sons, 2014 p.191.
- Li, Z.; Ding, D.; Liu, Q.; Ning, C.; & Wang, X. Nanoscale research letters, 2014, v. 9, n. 1, p. 118.
- Schweicher, J.; Desai, T. A. Journal of applied electrochemistry, 2014, v. 44, n. 3, p. 411-418.
- Kim, W. R.; Park, H.; Choi, W. Y. Nanoscale research letters, 2014, v. 9, n. 1, p. 1-10.
- Schmuki, P.; Roy, P.; Kim, D.; Lee, K.; Spiecker, E. et al. Nanoscale, 2010 v. 2, n. 1, p. 45-59.
- Costa, L. Aplicação de nanotubos de titânia na fotodegradação de corantes. Doutorado em Química – Instituto de Química, Universidade de Brasília, Brasília, 2009.
- Thomas, J.; Chitra, K.; R. Materials Focus, 2014 v. 3, n. 3, p. 233-238.
- Tian, W. C.; Ho, Y. H.; Chen, C. H.; Kuo, C. Y. Sensors, 2013, 13, 865–874.
- Zhang, X. X.; Zhang, J. B.; Jia, Y. C.; Xiao, P.; Tang, J. Sensors, 2012, 12, p. 3302–3313.
- Galstyan, V.; Comini, E.; Faglia, G.; & Sberveglieri, G. Sensors, 2013, v. 13, n. 11, p. 14813-14838.
- Guo, Z.; Prezhd, O. V.; Hou, T.; Chen, X.; Lee, S. T.; & Li, The Journal of Physical Chemistry Letters, 2014.
- Nuzzi, F.; Angelis, D. F. The Journal of Physical Chemistry C, 2010, v. 115, n. 5, p. 2179-2186.
- Yu, Y.; Zhang, P.; Guo, L.; Chen, Z.; Wu, Q.; Ding, Y.; & Cao, Y. The Journal of Physical Chemistry C, 2014.
- Li, Z.; Ding, D.; Liu, Q.; Ning, C.; & Wang, X. Nanoscale research letters, 2014, v. 9, n. 1, p. 118.
- Song, T.; Han, H.; Choi, H.; Lee, J. W.; Park, H.; Lee, S., ... & Paik, U. Nano Research, 2014, v. 7, n. 4, p. 1-11.
- He, T.; Zhao, M.; Zhang, X.; Zhang, H.; Wang, Z.; XI, Z.; Mei, L. The Journal of Physical Chemistry C, 2009, v. 113, p. 13610-13615.
- Wang, J.; Wang, L.; Ma, L.; Zhao, J.; Wang, B.; Wang, G. Physica E, 2009, v. 41, p. 838-842.
- Hart, J. N.; Parker, S. C.; Lapkin, A. A. ACSNANO, 2009, v. 11, p. 3401-3412.
- Ivanovskaya, V. V.; Enyashin, A. N.; Medvedeva, N. I.; & Ivanovskii, A. L. Condensed Matter - Material Science, 2002.
- Howard, C. J.; Sabine, T. M.; Dickson, Fiona. Acta

Crystallographica Section B: Structural Science, **1991**, v. 47, n. 4, p. 462-468.

24. Shklover, V.; Nazeeruddin, M. K.; Zakeeruddin, S. M.; Barbe, C.; KAY, A.; Haibach, T.; & Gratzel, M. Chemistry of materials, **1997** v. 9, n. 2, p. 430-439.
 25. Gong, X. Q.; Selloni, A.; Batzil, M.; & Diebold, U. Nature materials, **2006**, v. 5, n. 8, p. 665-670.
 26. Diebold, U.; Ruzycski, N.; Herman, G. S.; & Selloni, A. Catalysis Today, **2003**, v. 85, n. 2, p. 93-100.
 27. Beltran, A.; Andres, J.; Sambrano, J. R.; & Longo, E. The Journal of Physical Chemistry A, **2008**, v. 112, n. 38, p. 8943-8952.
 28. Kowalski, P. M.; Meyer, B.; Marx, D. Physical Review B, **2009** v. 79, n. 11, p. 115410.
 29. Ramamoorthy, M.; Vanderbilt, D.; King-Smith, R. D. Physical Review B, **1994** v. 49, n. 23, p. 16721.
-

G.O. Silva^{2*}, J.D Santos¹,
J.B.L Martins², C.A. Taft³, E.
Longo⁴.

¹ Universidade Estadual de Goiás, UEG, UnUCET, Anápolis/GO, Brazil.

² Universidade de Brasília, UNB, LQC, CP 4478, Brasília/DF, Brazil.

³ Centro Brasileiro de Pesquisas Físicas, CBPF, Rio de Janeiro/RJ, Brazil.

⁴ Universidade Estadual Paulista, UNESP, LIEC, Araraquara/SP, Brazil.

*E-mail: gustavo_olinto@hotmail.com

Proposal of Calculation Protocols for Implicit Solvation Methods in Conformational Analysis Involving the Gauche Effect

Filipe B. de Lima, Carlos R. M. Cavalcante, Keyla M. N. de Souza,
Juliana A. B. da Silva & Hécio J. Batista

Introduction

Conformational analyzes in solution media still present many challenges in computational chemistry and one of the main reasons is the little magnitude of interaction energies involved.¹ In order to diminish the arising relative errors very often costly computations are required, with sophisticated methods. One example of such methods is to take into account explicitly the solvent molecular structure, by modeling the solute or the solute supermolecule via quantum methods and the bulk structure via classical approaches. One low cost alternative method is the implicit solvent model, where the solvent bulk is represented by a continuum dielectric medium and the solute is immersed in an arbitrary cavity in the dielectric. This is the case of the PCM¹ (Polarizable Continuum Model), based on Onsager theory of Self-consistent Reaction Field (SCRF). Today, modern versions of this theory are implemented in many computational chemistry programs like Gaussian, Orca, ADF, among others, like the PCM model of Tomasi¹ and more recently the Truhlar SMD model.² Given the empirical fashion of the PCM model and its large number of parameters, mainly related to the cavity definition, there are a lot of protocols available in different programs, especially in Gaussian,³ and a proper and conscious choice usually is a difficult task. Our group is interested in conformational

analysis of systems where a suitable prediction of the rotamers distribution is of importance. Directly related to this problem is the well known gauche effect (GE) or generalized anomeric effect,⁴ which consists of a stabilizing electronic interaction between a bonding and a nonbonding vicinal orbitals, very common in aliphatic compounds which present conformational equilibrium between gauche (G) and trans (T) rotamers. In order to investigate the performance of PCM protocols in this subject, we choose 1,2-dihaloethanes ($\text{CH}_2\text{X}-\text{CH}_2\text{X}$, where $\text{X}=\text{F}$, Cl , Br and I) as model compounds for a GE analysis in polar and non-polar solvents (CHCl_3 , C_6H_{12} , CCl_4 , DMSO). As it is well known, the 1,2-difluoroethane is the only dihaloethane where the GE is dominant over the Pauli repulsion between the halogen vicinal atoms, thus causing the G form (the polar conformer) to stabilize more than the T one. However, the more polar the solvent is the more stable the G form is, and in the case of dichloroethane, very polar media favor the G isomer. This can be clearly seen in Fig. 1, where experimental results for the free energy difference (ΔG^{GT}) between the G and T rotamers of the dihalothanes are depicted^{5,6} (question marks are written where there is experimental uncertainty). In this work, theoretical estimates (ΔE^{GT}) of ΔG^{GT} with different combinations of methods are obtained.

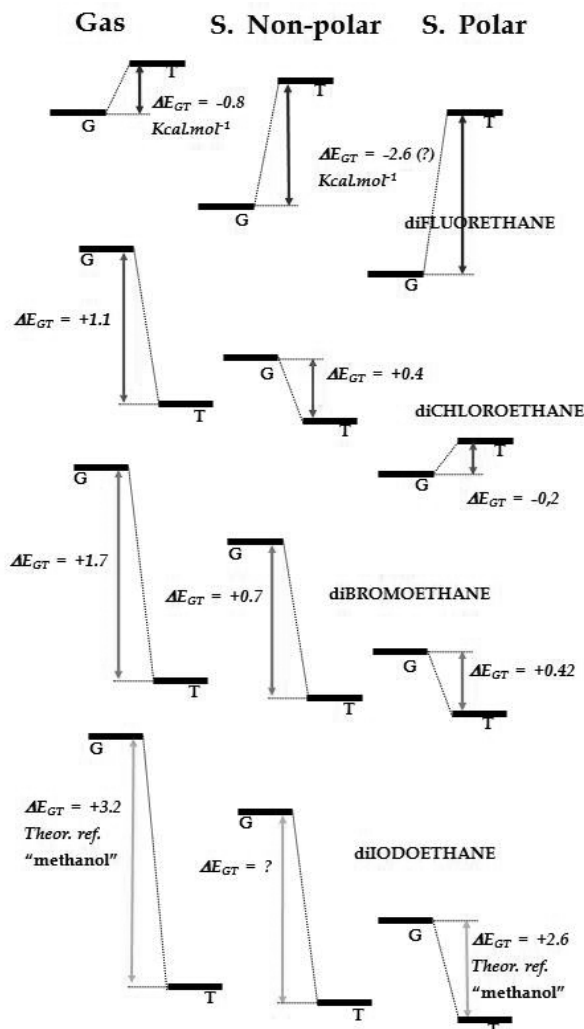


Figure 1. Experimental ΔE_{GT} values for dihalo-ethanes $\text{CH}_2\text{X}-\text{CH}_2\text{X}$.

Methods

The PCM models used in this work, based on the apparent surface of charges (ASC) concept and on the resolution of the nonhomogeneous Poisson equation, split in two classes concerning the building method for the cavity, namely: (i) by superposition of atomic spheres (IEFPCM-“integral equation formalism-PCM”, CPCM-“conductor like model-PCM”, SMD-“Density-based solvation model”) and (ii) from the solute electronic

density (IPCM e SCIPCM). For the IEFPCM and CPCM there are different radii models for the atomic spheres: UFF (Universal force field-based model), UA0, UAHF, UAKS (the last three are “United-Atom”-based models), Pauling and Bondi. After geometry optimizations with frequency determinations for minimum state characterization, single point calculations were done in the G and T forms. The quantum methods were DFT with the functionals B3LYP and M05-2X, with the following basis sets: 6-31G*, 6-31+G*, 6-311G*, 6-311+G*, CCPVTZ, CCPVTZ-PP for bromine, Def2TZVP. For iodine atom, the following effective core potentials were adopted: CRENBL, LanL2DZ, Stuttgart (StuttgartRLC). For the light atoms in diiodoethane, the same above basis sets were used, when applied the SMD, while for the PCMs, only the 6-31+g* basis was used. For SMD method, the cavity-atoms radii model used was the default (similar to Bondi model with a scale factor²). Two versions of Gaussian Program were employed, G03 and G09, but only the results for the latter will be shown here, and a comparison with several experimental works was made^{5,6}.

Results and Discussion

For all the adopted calculation protocols and solvents (only results for CHCl_3 and DMSO will be shown here), for difluoroethane molecule, the GE was confirmed to be dominant ($\Delta E_{GT} = E^G - E^T < 0$) and, for the other dihaloethanes, the T form was found to be the most stable ($\Delta E_{GT} > 0$), revealing the dominance of the Pauli repulsion, as expected. For the B3LYP functional, the best averaged result was obtained with the 6-31+g* basis set combined with the CPCM/Pauling model, that is, the more balanced choice basis for F, Cl, Br and I compounds. The IEFPCM as well as the 6-311+g* basis, although a little bit worse, yield similar results as the above protocol. As expected, a more pronounced stabilization of the G (polar) form with respect to the T (non-polar) form was observed in all the solvents owing to the dipole-induce dipole attractive interactions, and with a much greater extent in polar ones, owing to higher-magnitude dipole-dipole forces. Also, the stabilization of the T form is observed for polar solvents (dipole-induce dipole) and even for non-polar solvents, due to the presence of dispersion interaction, as a non electrostatic term of the PCM calculation.

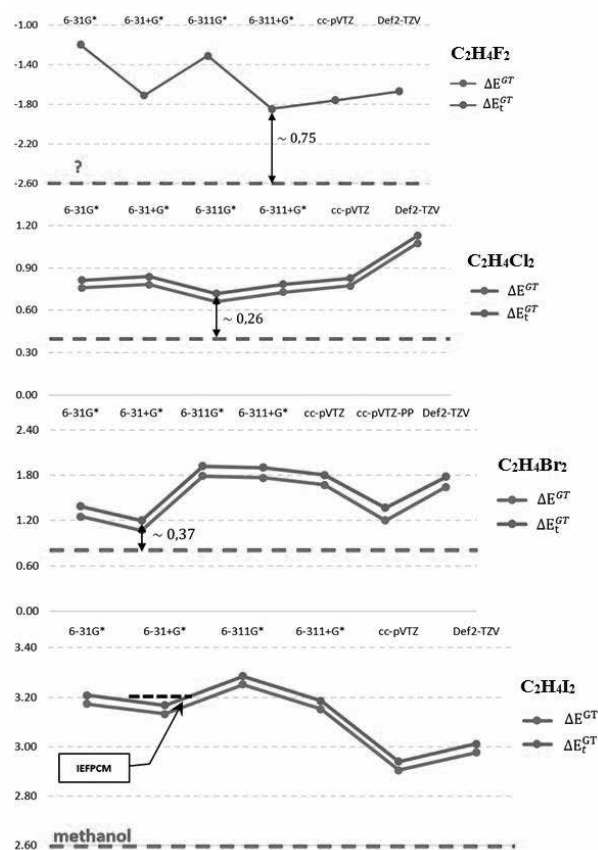


Figure 2. B3LYP/SMD (LanL2DZ for iodine) ΔE_t^{GT} and ΔE^{GT} values in CHCl_3 solvent for the dihalo-ethanes $\text{C}_2\text{H}_4\text{X}_2$ ($\text{X} = \text{F}, \text{Cl}, \text{Br}$ and I). The red dashed lines correspond to the experimental values, for comparison.

Using the B3LYP/6-31+g* recipe, but with the SMD solvation method instead of the CPCM one, we rather obtain the opposite performance. In fact, this protocol yields poor results, especially for light halogen atoms, F and Cl. In this regard, the 6-311+g*, 6-311g* and 6-31+g* basis sets yielded better results for F, Cl and Br, respectively. As can be seen, the lighter the halogen is the higher the basis set level is necessary to get a balanced result. In Fig. 2, we can observe the B3LYP/SMD results for the ΔE^{GT} (electrostatic part of solvation) and ΔE_t^{GT} (estimate for total free energy of solvation = electrostatic plus non-electrostatic component) in CHCl_3 for $\text{CH}_2\text{X}-\text{CH}_2\text{X}$ ($\text{X} = \text{F}, \text{Cl}, \text{Br}$ and I). Since the cavitation energy is positive and of high magnitude, this term dominates the non electrostatic part of solvation energy and the

ΔE_t^{GT} is invariably above the ΔE^{GT} for all the basis sets. However, we can observe that the energy difference between the two curves for all the $\text{C}_2\text{H}_4\text{X}_2$ compounds is entirely systematic, that is, the non electrostatic contribution. Another interesting aspect is that this term increases as the halogen atomic mass increases, as expected. Furthermore, we can see an alternate pattern in account to the quality of the results among the basis sets, especially the lighter the halogen. Very similar results were obtained for the DMSO solvent, but in this case, as expected, the magnitude of solvation energies in this highly polar solvent are larger than in chloroform. For the other non-polar solvents, C_6H_{12} and CCl_4 , the results are similar, but the stabilization of the G form, as expected, is less pronounced because of the lack of dipole-dipole interaction, producing higher ΔE_t^{GT} values. It is important to emphasize the lack of a consistent and more complete experimental data. Finally, comparing between the B3LYP and M05-2X functionals, in general the latter gives better results for whole the halogen series. Particularly for diiodoethane, the protocol M05-2X/SMD yields the best results, associated with the use of LanL2DZ effective core potential. We must stress that the experimental result for $\text{C}_2\text{H}_4\text{I}_2$ is only qualitative.

Conclusions

As preliminary results for ΔE_t^{GT} values, the B3LYP/6-31+g* furnish the best average results when combined with the CPCM/Pauling model, that is, this is the more balanced choice basis for F, Cl, Br and I. For SMD method, using the B3LYP functional, we rather obtain the opposite behavior with the basis 6-31+g*, since it yields poor results, especially for lighter halogen atoms, F and Cl. In this respect, the 6-311+g*, 6-311g* and 6-31+g* basis yielded better results for the F, Cl and Br, in the respective order. In short, the lighter the halogen is the higher level of the basis set is needed. As a general result, we obtain that the electrostatic interactions are dominant and are sufficient to explain qualitatively the experimental values for ΔE^{GT} . Finally, for the SMD method, since it was optimized for Truhlar density functionals, in general we obtain better results with the M05-2X against the B3LYP. Calculations with this functional for the PCM models used in this work are in progress, for a more complete comparison.

Acknowledgments

The authors acknowledge for the support given from the FACEPE, CAPES, CNPQ.

References

1. J. Tomasi, B. Mennucci, R. Cammi, Chem. Rev., 105, 2999 (2005).
2. A. V. Marenich, C. J. Cramer, D. G. J. Truhlar, Phys. Chem. B 113, 6378 (2009).
3. <http://www.gaussian.com>.
4. K. B. Wiberg, T. A. Keith, M. J. Frish, M. Murcko, J. Phys. Chem. 99, 9072 (1995).
5. R. K. Sreeruttun e P. Ramasami, Phys. Chem. Liquids 44, 315 (2006).
6. Q. Kong, J. Kim, M. Lorec, T. K. Kim, H. Ihee e M. Wulff, J. Phys. Chem. 109, 10451 (2005).

Filipe B. de Lima^a, Carlos R. M. Cavalcante^b, Keyla M. N. de Souza^c, Juliana A. B. da Silva^d & Hécio J. Batista^{*a}

^aDepartamento de Química. Universidade Federal Rural de Pernambuco

^bDepartamento de Física. Universidade Federal Rural de Pernambuco

^cDepartamento de Química Fundamental. Universidade Federal de Pernambuco

^dCentro Acadêmico do Agreste. Universidade Federal de Pernambuco

*E-mail: helciojb@gmail.com

A Theoretical Kinetic and Thermodynamics Study about the Effect of Substituents in the Synthesis of Chalcones

H. G. Machado, H. C. B. Oliveira, G. R. Oliveira, W. A. Silva & V. H. Carvalho

Introduction

Chalcones are natural compounds found in plants with two aromatic rings united by a fragment of three α,β -unsaturated carbons with one carbonyl. They can be formed by the chemical modification of several precursors. The most common path of synthesizing this compound is from aldol condensation of aromatic ketones and aromatic aldehydes – Claisen-Schmidt mechanism⁴ (Figure 1).

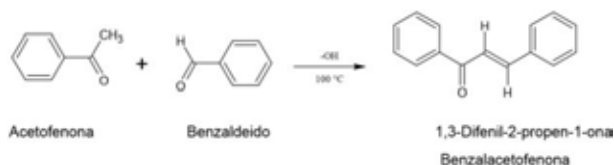


Figure 1. Generic Claisen-Schmidt reaction

Some chalcones are biologically active, and among these activities we can mention the following characteristics: cytotoxicity, antimicrobial, anti-inflammatory and antimalarial. Sofalcone, for example, was approved for clinical trials of anti-*Helicobacter pylori* (*H. pylori* activity)⁶. An essential aspect of chalcone studies is understanding their reaction mechanisms; the kinetic

study of this reaction is very important for the elucidation of the step-by-step synthesis of these molecules.

Although there are several experimental works that estimated the kinetic rate constant^{1,2,5,7} and proposed mechanisms^{1,2} for this reaction, there are few theoretical studies⁴ in this reaction.

In this paper, we reported an understanding of the effect of the different substituents on these reactions and an estimative of the kinetic rate constant. It was characterized by the main reactive channels of the studied reactions. Then, we predicted if the condensation is viable, if it is energetically favorable, and what more stable compound among the studied.

Methods

To develop this work, we characterized the transition states with the Density Functional Theory (DFT) from the existence of only one negative frequency for each substituent. The quantum calculations were performed at the B3LYP /6-311++G** level of calculation as implemented in the GAUSSIAN09 suit of programs.

The transition states were located using the ‘Synchronous transit-guided quasi-Newton’ method. The transition states were used to estimate the activation energies and build an energetic profile of these reactions using different substituents - NO₂, Cl, OH, H, NH₂ and

CH₃O (MeO). The Zero Point of Energy (ZPE) was used to correct the activation energies.

The estimative of the rate constant considered only the first step (abstraction of hydrogen of ketone molecule by anion hydroxyl) of the reaction (hypothesis of the rate determining step, see Figure 2). The rate constant was calculated using the Transition State Theory (TST)³ including Wigner correction tunneling.⁸

Results and Discussion

In the first step of the Claisen-Schmidt mechanism for the formation of a generic chalcone, the anion hydroxyl OH⁻, a basic catalyst, abstracts hydrogen of ketone molecule. The first transition state, which was found, and the mechanism of the first step of chalcone synthesis are represented in Figure 2.

With the description of the first step study of these reactions using DFT and QST2 methodology, it was possible to estimate the rate constant. This kinetic data is temperature dependent and was fitted with models of Arrhenius law, obtaining values for the activation energy (E_a) for each substituent in meta position of the aromatic ring of the ketones, as can be seen in Table 1.

Table 1. Values of barrier height and activation energy (Arrhenius law) in the first step of synthesis of chalcones. Units are in kJ.mol⁻¹.

Chalcones	Barrier Height	Activation Energy	Literature
Chalc-NO ₂	8.0	16.5	-
Chalc-Cl	15.3	22.7	-
Chalc-OH	17.9	24.8	-
Chalc-H	18.2	25.1	32,61
Chalc-NH ₂	20.4	27.3	-
Chalc-MeO	23.5	30.5	41,02

Based on the analysis of the first step of the formation mechanisms of chalcones in Table 1, it was perceived that the barrier height and the activation energy tend to be smaller when the substituents are withdrawing groups and to favor the reaction, making it faster.

Thermodynamic parameters of energy variation between products and reactants have been calculated for the first step of the reaction (Table 2). All of the process is exothermic and spontaneous.

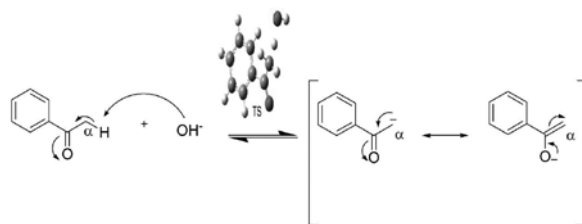


Figure 2. First step of Claisen-Schmidt mechanism for the formation of a generic chalcone, and the transition state which been found

Table 2. Enthalpy and Gibbs free variation energy for first step of synthesis of chalcone. Units are in kJ.mol⁻¹.

Chalcones	ΔH	ΔG
Chalc-NO ₂	-45.9	-46.1
Chalc-Cl	-26.8	-28.5
Chalc-OH	-23.2	-25.6
Chalc-H	-22.1	-25.3
Chalc-NH ₂	-18.3	-25.5
Chalc-MeO	-14.3	-17.2

Conclusions

The preliminary results show that the use of aromatic ketones substituted at the meta position by withdrawing groups favors the reaction, making it faster, because they reduce the activation energy. The complete study of the reaction becomes necessary once the remaining steps of the reaction can be more decisive in the kinetics of this reaction. We expect that these results will orient futures experimental works.

Acknowledgments

The authors are grateful for the support given from FAPEG, CAPES, CNPQ and FINATEC.

References

- AGUILERA, A. et al. Ba(OH)₂ as the catalyst in organic reactions. Part XIV. Mechanism of Claisen-Schmidt condensation in solid-liquid conditions: Spain, **1986**.
- COOMBS, E.; EVANS, D. P.; Condensation of Carbonyl Compounds. A kinetic Study of the Reaction of Acetophenone

with Benzaldehyde, **1940**.

3. EYRING, H. The Activated Complex in Chemical Reactions. The Journal of Chemical Physics, v. 3, n. 2, p. 107–115, **1935**.
4. GASULL, E. I. et al. A theoretical and experimental study of the formation mechanism of 4-X-chalcones by the Claisen–Schmidt reaction. Journal of Molecular Structure: THEOCHEM, v. 503, n. 3, p. 131–144, **2000**.
5. GUIDA, A. et al. Hydrotalcites as base catalysts. Kinetics of Claisen-Schmidt condensation, intramolecular condensation of acetonylacetone and synthesis of chalcone. Applied Catalysis A: General, v. 164, n. 1-2, p. 251–264, **1997**.
6. ISOMOTO, H. et al. Sofalcone, a mucoprotective agent, increases the cure rate of *Helicobacter pylori* infection when combined with rabeprazole, amoxicillin and clarithromycin. World Journal of Gastroenterology, v. 11, n. 11, p. 1629–1633, **2005**.
7. GETTLER, J. D.; HAMMETT, L. P. Rates and temperature Coefficients of the hydroxyl ion catalyzed aldol condensation of benzaldehyde with methyl ethyl ketone and acetone: New York, **1943**.
8. WIGNER, Phys. Rev. 40 (**1932**) 74

H. G. Machado^{a*}; H.C.B. Oliveira^b; G.R. Oliveira^c, W.A. Silva^b & V.H.Carvalho^{a*}

^aGrupo de Química Teórica e Estrutural de Anápolis, Campus de Ciências Exatas e Tecnológicas, Universidade Estadual de Goiás, 75001-970, Anápolis, Brasil

^bInstituto de Química, Universidade de Brasília, 70904-970, Brasília, Brasil.

^cInstituto de Química, Universidade Federal de Goiás, 74001-970, Goiânia, Brasil.

*E-mail: hugogontijomachado@gmail.com

Electronic Spectra of Nitrosyl Chloride: A Reinvestigation Using Coupled Cluster and DFT Calculations

Iran da Luz Sousa, Pedro A. M. Vazquez & Nelson H. Morgon

Introduction

Nitrosyl chloride ($\text{Cl} - \text{N} = \text{O}$) can be observed at the stratosphere and troposphere of the earth, being of interest in atmospheric chemistry.^{1,2} In particular, CINO can efficiently be photolyzed by ultraviolet (UV) radiation, releasing atomic chlorine radicals which are harmful for the ozone layer.³ The structure of nitrosyl chloride has been identified by various methods, including microwave, infrared, Raman and photochemistry spectroscopies.

CINO in the ground state has a bent molecular geometry and C_s symmetry. The valence electronic structure of CINO was investigated in early studies by photoelectron spectroscopy and theoretical calculations.⁴⁻⁷ The CINO electronic configuration of the frontier MOs is... $(3a'')(12a')(13a')(4a'')(14')...$, where single and double prime denote orbitals that are symmetric and anti-symmetric with regard to the molecular plane, respectively. This system can be studied by rigorous computational methods because it has "only" 32 electrons.⁸

The elucidation of the decomposition process can be studied using molecular electronic spectra. The spectrum of nitrosyl chloride in gas phase was obtained by Goodeve and Katz.⁹ The UV/Vis region (2-7 eV) CINO exhibits a strong broad absorption band consisting of three contributions, where the most intense of them has a maximum at 6.3 eV.

The purpose of this work is to carry out calculations of the UV spectrum of nitrosyl chloride, based on current state-of-the-art methods. These methods include the approximate equation-of-motion coupled cluster with single-and-double excitations (EOM-CCSD).

Methods

The molecular structure of the NOCl system was optimized using program GAUSSIAN 09 program¹⁰ at the CCSD or DFT levels. In the last case were employed B3LYP, CAM-B3LYP and PBE0 exchange/correlation functionals. The following basis sets were used: Dunning triple ζ aug-cc-pVTZ (ACCT) and quadruple ζ aug-cc-pVQZ (ACCq).

Calculations of the vertical excited states were carried out at EOM-CCSD and TDDFT/CAM-B3LYP levels of theory. The CAM-B3LYP functional showed better performance than others conventional functional when applied for the excited electronic states.

Results and Discussion

In Table 1, the molecular structure of NOCl, showing calculated and experimental values

Table 1. Geometrical parameters molecular structure of NOCl.

	NO (Å)	NCI (Å)	NOC (°)
CCSD/ACCt	1.135	1.942	113.1
CCSD/ACCq	1.131	1.934	113.1
CCSD(T)/ACCt	1.141	1.979	113.4
CCSD(T)/ACCq	1.138	1.967	113.3
B3LYP/ACCt	1.127	1.997	114.1
CAMB3LYP/ACCt	1.125	1.952	113.4
PBE0/ACCt	1.126	1.952	113.8
Exp. ¹¹	1.14	1.97	113.3

All theoretical results give geometrical parameters closer to experimental values. The CCSD(T)/ACCT results provided a better performance and these results are in Fig. 1.

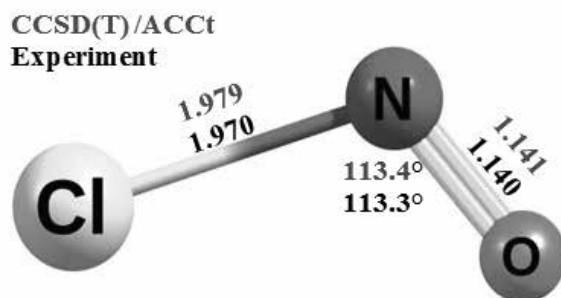


Figure 1. Molecular structure of nitrosyl chloride.

The result of the UV spectrum for singlet and triplet states is summarized in Table 2. The UV spectrum of NOCl in the gas phase shows a two very weak bands at 2.06 eV (oscillator strength $f = 10^{-5}$), 2.64 eV ($f = 9 \times 10^{-5}$), a shoulder at 3.72 eV ($f = 10^{-3}$) and a very strong band at 6.30 eV ($f = 0.5$).

Table 2. Computed transition energies (in eV) and oscillator strength of NOCl employed different methodologies.

State	EOM-CCSD/ aug-cc-pVQZ			CAM-B3LYP/ aug-cc-pVQZ	
	ΔE	f		ΔE	f
13A"	2.19 (2.06) ^a	0 (10^{-5}) ^a		1.76	0
11A"	2.77 (2.64)	10^{-4} (9×10^{-5})		2.71	10^{-4}
21A"	4.49 (3.72)	7×10^{-4} (10^{-3})		4.05	0
21A'	4.77	3×10^{-4}		4.23	4×10^{-4}
31A'	4.87	6×10^{-4}		4.99	1.4×10^{-4}
31A"	4.93	3×10^{-4}		5.07	3×10^{-4}
41A'	6.49 (6.30)	0.57 (5×10^{-1})		6.61	0.45
51A'	8.51 (8.26)	5×10^{-2}		8.14	6.8×10^{-2}

^a Experimental results (in parentheses)⁹.

The calculations EOM-CCSD/ACCq overestimates of excitation energy experimental. This methodology produced intensities comparable to the experiment. The energy of the bands in the CAM-B3LYP/ACCt simulation agrees quite well with experiment, although it overestimates at first and last excitation energy.

The calculated 41A' state, probably correspond to the most intense component of the experimental band. The functional CAM-B3LYP estimates this energy 6.61 eV ($f = 0.45$) and the energy transition calculated using equation-of-motion coupled cluster is 6.49 eV ($f = 0.57$). Both methods describe this electronic transition.

The best description for an electronic state few studies in literature, 51A' state, also computed in this study. The experimental vertical excitation energy is 8.26 eV (51A' state). The energy calculated we found this transition is: 8.51 eV ($f = 5 \times 10^{-2}$) with EOM-CCSD/ACCq method and 8.14 eV ($f = 6.8 \times 10^{-2}$) using CAM-B3LYP functional.

Conclusions

The molecular and electronic structure of the nitrosyl chloride was investigated using density functional and coupled cluster methodologies. A good agreement was observed between CCSD(T)/ACCT calculations and experimental results.

The calculations EOM-CCSD/ACCq overestimates of excitation energy experimental. The CAM-B3LYP/ACCq provides the best results of excitation energy for the second and last bands. Both methods describe well at the experimental intensities

Acknowledgments

The authors are grateful for the support given from the CAPES, FAPESP, CNPq and FAEPEX-UNICAMP.

References

1. T. J. Luick, R. W. Heckert, K. Schulz and R. S. Disselkamp, J. Atmos. Chem. 32, 315, (1999).
2. P. Q. Wang, Modern Physics Letters., B, 26, 1250065, (2012).
3. S. Luca et al, Phys. Chem. Chem. Phys., 17, 9040, (2015).
4. D. C. Frost, S. T. Lee, C. A. McDowell, N. P. C. Westwood, J. Electron Spectrosc. Relat. Phenom., 7, 331, (1975).
5. M. I. Abbas, J. M. Dyke, A. Morris, J. Chem. Soc., Faraday Trans., 72, 814, (1976).

6. E. Gilberg, W. Schatzl, H. W. Schrenk, Chem. Phys., 13, 115, (1976).
 7. T. Yamashita, S. Kato. J. Chem. Ph., 121, 2105, (2004).
 8. J. M. Kiera, J. A. Milkiewicz, B. J. Whitaker, A. G. Sage, Alan, A. G. Worth. ChemPhysChem, 14, 1439, (2013).
 9. C. F. Goodeve, S. Katz, Proc. Roy. Soc. A., 172, 432, (1939).
 10. <http://www.gaussian.com>
 11. G. Cazzoli, C. Degli Esposti, P. Palmieri and S. Simeone, J. Mol. Spectrosc., 97, 165 (1983).
-

Iran L. Sousa^{*a}, Pedro A.
M. Vazquez^a & Nelson H.
Morgon^a

^aInstituto de Química, Universidade Estadual de Campinas, CP 6154,
13084-862 Campinas-SP, Brasil

*E-mail: iran.sousa@iqm.inicamp.br

Construction of Brn² Protein in Complex with MORE DNA Through *In Silico* Methods

Ivan E. V. Coelho, Denise C. A. & Alex G. Taranto

Introduction

The incidence of non-melanoma (basal cell and squamous cell carcinoma) and melanoma skin cancers has increased in last decades. In three diagnosed cancers, one is skin cancer. More rare and lethal, melanoma is the most aggressive type of skin cancer. Currently, 132000 cases occur worldwide each year.¹ However, if detected early, the cure chances are more than 90%. Metastatic melanoma cases have a worse prognosis, which in most cases has no cure and have a limited number of therapeutic options.² Therefore, prevention campaigns and early diagnosis are very important. Typically, melanoma arises in areas of the body most exposed to solar radiation, especially people with pale skin.³ In recent years, some new drugs have improved the survival of patients with melanoma. However, this increase in survival is modest and most patients with metastatic melanoma are not cured.² Thus, studies should be conducted to search for new molecular targets and more effective treatment options for melanoma skin cancer.

In this context, Brn2 transcription factor has been studied due its relationship with melanoma development. High levels of this protein expression, compared to the low levels found in differentiated melanocytes, have been found in melanoma cell lines.^{4,5,6,7,8} The Brn2 protein, codified by POU3F2 gene and known as N-Oct-3

when complexed with DNA target site, is a member of transcription factor family, which has conserved POU domain.⁹ Melanocyte precursors also express Brn2, but express lower levels with the differentiation of these cells. This protein can coordinate the normal development of melanocytic lineage or can reactivate signals to an abnormal growth as in malignant melanoma.¹⁰ Moreover, there is evidence that BRN2 overexpression is regulated by the major signaling pathways in melanoma: Wnt/b-catenin, MAPK/BRAF e PI3K/AKT.^{8,11,12}

The Brn2 structure can interact with distinct types of DNA targets: the more palindromic Oct recognition element (MORE), palindromic Oct recognition element (PORE) and N-Oct-3 recognition element (NORE) as a monomer but also as a dimer.¹³ Similar to POU proteins, Brn2 can interact with several DNA sequences, with different orientations and spacing between its POU-specific subdomain (POUs) and POU-homeodomain (POUh) subdomains because of subdomains are bonded by flexible linker. This protein, constituted of 443 amino acids (47 kDa), has both transactivation N-terminal domain (local of interactions with co-regulatory proteins) and DNA-binding C-terminal domain.¹⁴ The conserved DNA-binding domain consists of N-terminal POU of approximately 75 amino acids and C-terminal POUh of 60 amino acids joined by a less conserved linker.⁹

The POU domain-DNA interaction occurs primarily on 5'-ATGCAAAT-3' octameric sequence. Both POU_s and POU_h subdomains form a helix-turn-helix motif using the second and third helices of each subdomain.¹⁵ However, neither the Brn2 three-dimensional structure nor its POU domain are available in the Protein Data Bank (PDB).¹⁶ Only part of the structure (POU domain) of several POU proteins can be found in PDB, and no complete structure is available. The Brn2 DNA-binding domain was constructed through homology modeling using as template the Oct-1 protein (PDB code: 1OCT).¹⁷ However, the construction of full-length Brn2 model and molecular dynamics (MD) simulation of this protein in complex with MORE DNA provide knowledge of its structure and function. This studies can contribute for the development of selective inhibitors against this protein or DNA target site.

In this work, we construct the full-length three-dimensional structure of Brn2 bound to MORE half-site (5'-ATGCATGAGGA-3'). The MD simulation of Brn2-MORE complex is in progress.

Methods

The primary sequence of Brn2 was retrieved from NCBI's protein database,¹⁸ access code NP_005595.2.19 Currently, there is no template available in PDB for full Brn2 protein. Thus, this protein was built using PHYRE2 program.²⁰ This built model was improved using Swiss-Model program,²¹ which built a new brn2 model using the previous model generated by PHYRE2 and Oct-6 (POU3F1) POU domain available in PDB (2XSD) as templates. The model was evaluated to structural quality using PROCHECK 3.5.4,²² Verify 3D,^{23,24} ANOLEA25 and structural features obtained from circular dichroism spectra of full-length Brn2 protein.¹⁴ The DNA-target structure which has the 5'-ATGCATGAGGA-3' sequence was retrieved from PDB (2XSD). This complex was submitted to 20000 steps of energy minimization under conjugated gradient using NAMD program²⁶ and the CHARMM36 all-atom force field.^{27,28,29,30} The explicit solvent model with water box (TIP3P water model)^{31,32} and periodic boundary conditions were used. The protein-DNA complex was immersed in a water box and solvent molecules closer than 2.4 Å to the solute were eliminated. The dimensions of box sides were 79, 90

and 104 Å whereas the water box had at least 12 Å of extension between any protein-DNA atom and the edge of the box. Counter ions Na⁺ were added to neutralize the system before simulation. Electrostatic interactions were calculated using the Particle Mesh Ewald method³³ with real-space cutoff of 12 Å and 1 Å between grid points. The Lennard-Jones interactions were included with force switching from 10 Å to 12 Å. The list of nonbonded atoms was kept for interatomic distances of 14 Å.

Results and Discussion

The full three-dimensional structure of the Brn2 protein was obtained by comparative modeling method. This protein was bound to an 11 base pair oligonucleotide containing the half-site of the MORE motif (ATGCAT) and optimized through energy minimization. The stereochemical quality of the Brn2 model, was evaluated using the PROCHECK 3.5.4 software after energy minimization. The model showed 76.5% of its amino acid residues in favourable regions, 17.9% in allowed regions, 2.7% in generously allowed regions and 3.0% in disallowed regions (except glycine and proline residues). Moreover, the POU domain, which interact with DNA, has 92.7% of your amino acid residues in favourable regions and 5.8% in allowed regions. This region (both POU_s and POU_h subdomains) has 95.31% of sequence identity with the same Oct-6 region available in PDB which was also used for model building. High sequence similarity level (greater than 30%) confers reliability to built model.³⁴ The model analysis through Verify 3D showed that 85.78% of the residues had an averaged 3D-1D score ≥ 0.2 (threshold value is 80%)^{23,24} (figure 1). The model showed compatibility of its atomic model (3D) with its own amino acid sequence (1D) when comparing the results to good structures. The figure 2 shows the energy estimation of Brn2 model through non-local atomic interaction energy assessment using ANOLEA before and after energy minimization. The model quality was improved after energy minimization. As can be seen, the number and energy value of high-energy amino acid residues decrease after the process. The POU domain of this protein is constituted mainly of helices and transactivation domain of loop regions. As shown in figure 3, the model has 9 α -helices without β -sheet. The POU_s subdomain consists of 4 α -helices

and POUh of 3 α -helices. Both subdomains have helix-turn-helix motif using the second and third helices of each subdomain, similar to other POU proteins. The protein remaining is mainly constituted of loop regions and two short helices (figure 3). The Brn2 structure was compared with structural features data obtained from circular dichroism spectra of full-length Brn2 reported by Cabos-Siguier and collaborators.¹⁴ The structure of Brn2 model was similar to circular dichroism data which suggested the presence of α -helical secondary structures. The location of trypto-phan residues was also in agreement with the circular dichroism spectra mentioned above. The side chains of the three trypto-phan residues located in the transactivation domain were more exposed to the solvent than those two trypto-phan residues found in the POU subdomains, which was buried inside the three-dimensional structure of the protein. Thus, the model showed good quality for further MD simulation in complex with MORE half-site which is in progress. This studies can contribute to describe the structural properties of full Brn2 protein and the mechanism of its interaction with specific DNA target site.

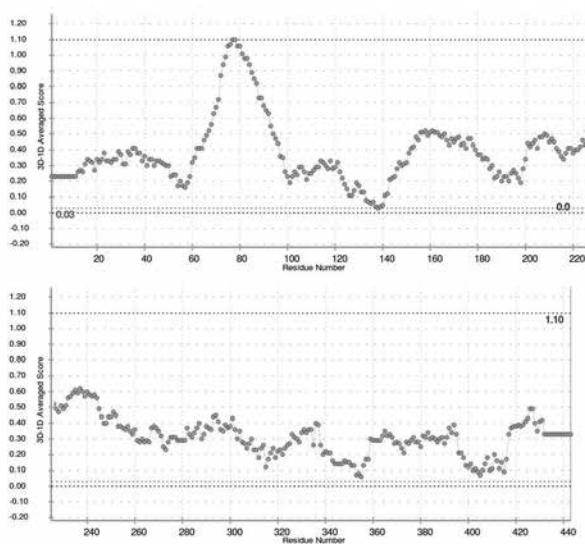


Figure 1. Analysis of Brn2 model using Verify 3D. The model has 85.78% of the residues with averaged 3D-1D score ≥ 0.2 (threshold value is 80%).

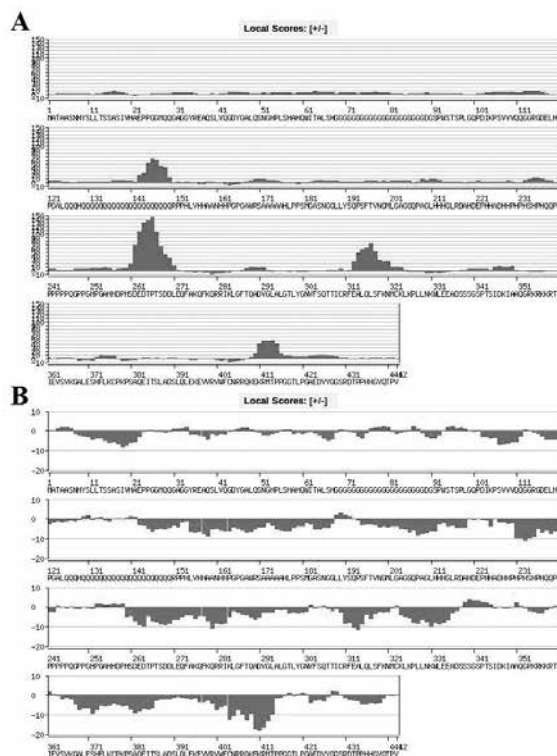


Figure 2. Energy estimation of Brn2 model using ANOLEA before (A) and after (B) energy minimization. The plot shows a detailed energy analysis along the sequence.

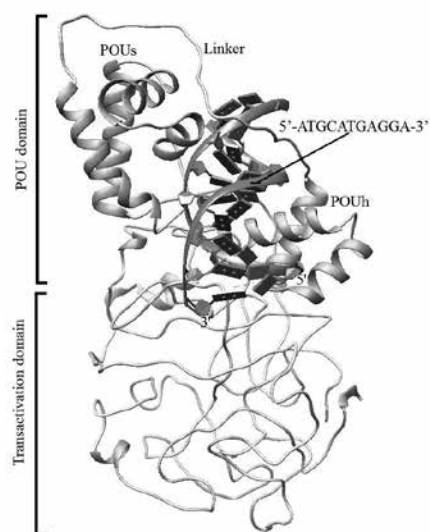


Figure 3. Three-dimensional structure of full-length Brn2 model in complex with MORE half-site. The recognition helices of Brn2 POUh and Brn2 POUu are inserted within the major groove of the DNA (red). The model is constituted mainly of helices (blue) and loop (white) regions.

Conclusions

The model showed good quality verified through evaluation by PROCHECK 3.5.4, Verify 3D, ANOLEA and structural features obtained from circular dichroism spectra of Brn2 protein. The POU domain of Brn2 model shared structural similarity to other members of transcription factor family. This Brn2 domain is also very similar to Oct-6 POU domain available in PDB, which the regions share high sequence similarity. The MD simulation of Brn2-DNA target site is in progress. This simulation will allow to refine this protein structure, and understand its specific interactions with MORE DNA. Knowledge about these interactions will also provide information to contribute for the development of specific inhibitors against Brn2 or DNA target site.

Acknowledgments

The authors are grateful for the support given from the CAPES, PPGBiotec/UFSJ, FAPEMIG and FAEP.

References

1. World Health Organization (WHO), 2015. Skin Cancers. Retrieved from <http://www.who.int/uv/faq/skincancer/en/>.
2. C. Karimkhani, R. Gonzalez, R. P. Dellavalle, *Am. J. Clin. Dermatol.*, 15, 323 (2014).
3. U. Leiter and C. Garbe, *Adv. Exp. Med. Biol.*, 624, 89, (2008).
4. R. A. Sturm, B. J. O'Sullivan, J. A. Thomson, N. Jamshidi, J. Pedley, P. G. Parsons, *Pigment Cell Res.*, 7, 235, (1994).
5. J. A. Thomson, K. Murphy, E. Baker, G. R. Sutherland, P. G. Parsons, R. A. Sturm, *F. Thomson, Oncogene*, 11, 691, (1995).
6. T. Eisen, D. J. Easty, D. C. Bennett, C. R. Goding, *Oncogene*, 11, 2157, (1995).
7. A. Flammiger, R. Besch, A. L. Cook, T. Maier, R. A. Sturm, C. Berking, *J. Invest. Dermatol.*, 129, 945, (2009).
8. J. Goodall, C. Wellbrock, T. J. Dexter, K. Roberts, R. Marais, C. R. Goding, *Mol. Cell Biol.*, 24, 2923, (2004).
9. A. K. Ryan and M. G. Rosenfeld, *Genes Dev.*, 11, 1207, (1997).
10. R. Besch and C. Berking, *Eur. J. Cell Biol.*, 93, 55, (2014).
11. J. Goodall, S. Martinozzi, T. J. Dexter, D. Champeval, S. Carreira, L. Larue, C. R. Goding, *Mol. Cell Biol.*, 24, 2915, (2004).
12. E. Bonvin, P. Falletta, H. Shaw, V. Delmas, C. R. Goding, *Mol. Cell Biol.*, 32, 4674, (2012).
13. L. Nieto, G. Joseph, A. Stella, P. Henri,
14. O. Burlet-Schiltz, B. Monsarrat, E. Clottes, M. Erard, *J. Mol. Biol.*, 370, 687 (2007).
15. B. Cabos-Siguier, A. L. Steunou, G. Joseph, R. Alazard, M. Ducoux-Petit, L. Nieto, B. Monsarrat, M. Erard, E. Clottes. *Protein Express. Purif.*, 64, 39, (2009).
16. A. L. Cook and R. A. Sturm, *Pigment Cell Melanoma Res.*, 21, 611, (2008).
17. H. M. Berman, J. Westbrook, Z. Feng, G. Gilliland, T. N. Bhat, H. Weissig, I. N. Shindyalov, P. E. Bourne, *Nucl. Acids Res.*, 28, 235, (2000). Available in www.rcsb.org.
18. S. Millevoi, L. Thion, G. Joseph, C. Vossen, L. Ghisolfi-Nieto, M. Erard, *Eur. J. Biochem.*, 268, 781 (2001).
19. K. D. Pruitt, G. R. Brown, S. M. Hiatt, F. Thibaud-Nissen, A. Astashyn, O. Ermolaeva, C. M. Farrell, J. Hart, M. J. Landrum, K. M. McGarvey, M. R. Murphy, N. A. O'Leary, S. Pujar, B. Rajput, S. H. Rangwala, L. D. Riddick, A. Shkeda, H. Sun, P. Tamez, R. E. Tully, C. Wallin, D. Webb, J. Weber, W. Wu, M. Dicuccio, P. Kitts, D. R. Maglott, T. D. Murphy, J. M. Ostell, *Nucleic Acids Res.*, 42, 756, (2014).
20. C. L. Avery, C. M. Sitlani, D. E. Arking, D. K. Arnett, J. C. Bis, E. Boerwinkle, B. M. Buckley, Y. D. Ida Chen, A. J. de Craen, M. Eijgelsheim, D. Enquobahrie, D. S. Evans, I. Ford, M. E. Garcia, V. Gudnason, T. B. Harris, S. R. Heckbert, H. Hochner, A. Hofman, W. C. Hsueh, A. Isaacs, J. W. Jukema, P. Knekt, J. A. Kors, B. P. Krijthe, K. Kristiansson, M. Laaksonen, Y. Liu, X. Li, P. W. Macfarlane, C. Newton-Cheh, M. S. Nieminen, B. A. Oostra, G. M. Peloso, K. Porthan, K. Rice, F. F. Rivadeneira, J. I. Rotter, V. Salomaa, N. Sattar, D. S. Siscovick, P. E. Slagboom, A. V. Smith, N. Sotoodehnia, D. J. Stott, B. H. Stricker, T. Stürmer, S. Trompet, A. G. Uitterlinden, C. van Duijn, R. G. Westendorp, J. C. Witteman, E. A. Whitsel, B. M. Psaty, *Pharmacogenomics J.*, 14, 6, (2014).
21. L. A. Kelley, S. Mezulis, C. M. Yates, M. N. Wass, M. J. Sternberg, *Nat. Protoc.*, 10, 845, (2015).
22. M. Biasini, S. Bienert, A. Waterhouse, K. Arnold, G. Studer, T. Schmidt, F. Kiefer, T. G. Cassarino, M. Bertoni, L. Bordoli, T. Schwede, *Nucleic Acids Res.*, 42, 252, (2014).
23. R. A. Laskowski, M. W. MacArthur, D. S. Moss, J. M. Thornton, *J. App. Cryst.*, 26, 283, (1993).
24. J. U. Bowie, R. Lüthy, D. Eisenberg, *Science*, 253, 164, (1991).
25. R. Lüthy, J. U. Bowie, D. Eisenberg, *Nature*, 356, 83, (1992).
26. F. Melo and E. Feytmans, *J. Mol. Biol.*, 277, 1141, (1998).
27. J. C. Phillips, R. Braun, W. Wang, J. Gumbart, E. Tajkhorshid, E. Villa, C. Chipot, R. D. Skeel, L. Kalé, K. Schulten, *J. Comput. Chem.*, 26, 1781 (2005).
28. R. B. Best, X. Zhu, J. Shim, P. E. Lopes, J. Mittal, M. Feig, A. D. MacKerell Jr., *J. Chem. Theory Comput.*, 8, 3257, (2012).
29. A. D. MacKerell Jr., M. Feig, C. L. III. Brooks, *J. Am. Chem. Soc.*, 126, 698, (2004).

30. K. Hart, N. Foloppe, C. M. Baker, E. J. Denning, L. Nilsson, A. D. MacKerell Jr., *J. Chem. Theory Comput.*, 8, 348, **(2012)**.
31. A. D. MacKerell Jr. and N. K. Banavali, *J. Comput. Chem.*, 21, 105, **(2000)**.
32. M. W. Mahoney and W. L. Jorgensen, *J. Chem. Phys.*, 112, 8910, **(2000)**.
33. W. L. Jorgensen, J. Chandrasekhar, J. D. Madura, R. W. Impey, M. L. Klein, *J. Chem. Phys.*, 79, 926, **(1983)**.
34. T. Darden, D. York, L. Pedersen, *J. Chem. Phys.*, 98, 10089, **(1993)**.
35. L. Bordoli, F. Kiefer, K. Arnold, P. Benkert, J. Battey, T. Schwede, *Nat. Protoc.*, 4, 1, **(2009)**.

Ivan E. V. Coelho^{*a}, Denise
Costa Arruda^b & Alex G.
Taranto^a

^aFederal University of São João del-Rei, Campus Centro-Oeste Dona Lindu, Divinópolis/MG, Brazil.

^bUniversity of Mogi das Cruzes, Mogi das Cruzes/SP, Brazil

*E-mail: ivanglista2009@yahoo.com.br

Estudo QTAIM/NBO das Interações Estabilizante do Empacotamento do (E)-1,1,1-Tricloro-5,5-Difenil-4-Metoxipent-3-en-2-ona (CL₃ONA)

José A. S. de Freitas, Mariano A. Pereira, Alex F. C. Flores, Davi A. C. Ferreira & Tatiane L. Balliano

Introdução

O estudo espectroscópico com a finalidade de investigar as organizações intrínsecas da matéria foi um marco para a ciência moderna, pois ampliou os horizontes da aplicação dos modelos matemáticos do comportamento da matéria¹. Dentre estas técnicas, a Difração de Raios-X se destaca na determinação estrutural. Esta se baseia na interação da densidade eletrônica com um campo externo incidente, resultando em padrões de difração, concentração pontual das flutuações eletrônicas². Assim, a densidade eletrônica é o parâmetro experimental que determina a propriedade do material.

Mesmo assim, a densidade eletrônica é considerada um parâmetro físico-químico polêmico, devido às flutuações na descrição da densidade de carga^{3,4}. Informação importante na descrição das interações em sistemas cristalinos e transferência de carga no seio do cristal o que determinam a topologia eletrônica do sistema. Para tratar deste problema, Bader desenvolveu uma teoria que descreve o comportamento atômico em uma molécula, ligação química estabilidade e estrutura molecular a partir das propriedades topológicas da densidade monoelétrica ρ . Ou seja, as propriedades topológicas de ρ adquirem um significado físico^{5,6}. Desta forma, a Teoria Quântica de Átomos em Moléculas (QTAIM) descreve o comportamento da matéria mediante da descrição das propriedades contida na densidade eletrônica; onde define a ligação química como “caminho de ligação” (bond path

- BP) onde a distribuição da densidade eletrônica no ponto crítico (critical point - CP) – região onde há mudança abrupta da densidade eletrônica – é um mínimo entre atratores e máximo na direção perpendicular ao BP, tendo o gradiente da densidade eletrônica o agente determinante da topologia molecular⁷. Atribuindo ao sistema uma aparência de “grafo” molecular.

A abordagem de grafo molecular, formado pelos atratores a partir de caminho de ligação, para definir a ligação química de um sistema apresenta corroboração experimental na análise de densidade em cristais⁸⁻¹⁰. A QTAIM se apresenta como uma poderosa ferramenta para a investigação das interações estabilizantes de sistemas moleculares¹¹ e cristalinos¹². Neste trabalho, aplicamos o modelo QTAIM¹³ de descrição de estrutura eletrônica para compreender as interações intermoleculares no empacotamento molecular no cristal de CL3ONA.

Métodos

Neste estudo, as estruturas determinadas pela caracterização de difração de Raios-X foram eletronicamente analisadas pela aplicação da Teoria do Funcional de Densidade, através do funcional PBE1PBE e base atômica cc-pVDZ implementados no pacote de programas Gaussian09. A análise QTAIM das interações do cristal foi realizada usando o pacote de programa AIMAll. A análise NBO para as interações estabilizadoras ainda se encontra em fase de finalização.

Resultados e Discussão

O sistema molecular CL3ONA apresenta um arranjo cristalino monoclinico com grupo de simetria P 21/n. Cujos dados da cela unitária (Figura 1) é: $a = 6,0493(2)$ Å, $b = 12,3443(5)$ Å e $c = 23,4876(9)$ Å; $\beta = 95,654(3)^\circ$; $Z = 4$ moléculas/cela unitária; $V = 1745,39(3)$ Å³; $F(000) = 759,9$. E, o experimento apresentou os seguintes dados: 11935 reflexões coletadas; 3683 reflexões independentes; 208 parâmetros refinados; $S = 0,9330$; $R(\text{int}) = 0,0711$, $R_{\text{obs}} = 0,0529$ e $R_{\text{all}} = 0,1163$.

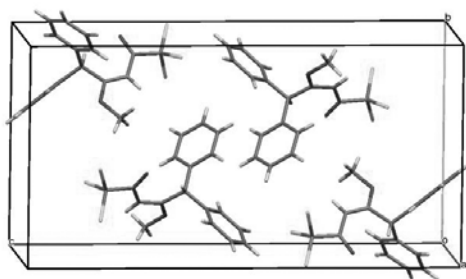


Figura 1. Cella unitária da CL3ONA.

A análise da topologia da densidade eletrônica da cela unitária do cristal de CL3ONA mostrou duas regiões intermoleculares, região formada pela interação de quatro moléculas de CL3ONA no empacotamento (Figura 2). Onde cada grupo R é uma molécula de CL3ONA distinta no empacotamento.

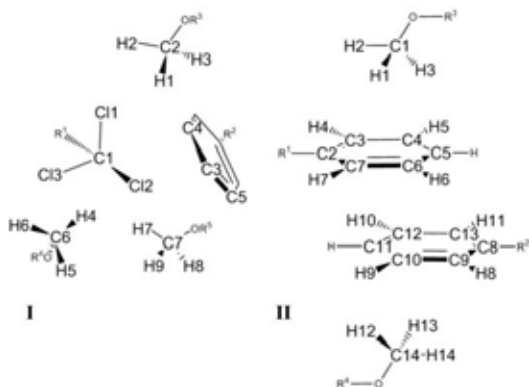


Figura 2. Interações estabilizadoras no cristal de CL3ONA: I) vizinhança da região tri-halogenada do CL3ONA; II) empilhamento- π .

Numa tentativa de compreender a natureza das interações estabelecidas entre as moléculas no empacotamento, realizamos análises QTAIM para extração de propriedades topológicas da densidade eletrônica nos pontos críticos de ligação (BCP) destacados na Figura 3.

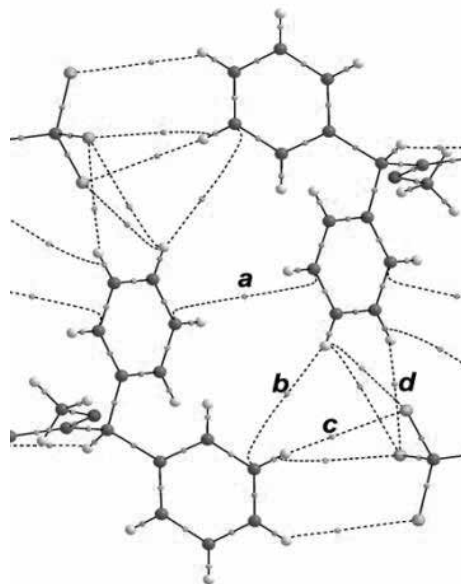


Figure 3. BCP's na cela unitária CL3ONA

Nesta análise, verificamos que há uma rede de interações não-convencionais que auxiliam no empacotamento da CL3ONA. Esta rede de interações foi caracterizada através da determinação de densidade eletrônica (ρ), laplaciana de densidade eletrônica ($\nabla^2 \rho$), elipticidade da densidade eletrônica no ponto crítico (ϵ), e densidade de energia potencial (V); estas propriedades foram catalogadas (em a.u.) na Tabela 1.

Tabela 1. Propriedades QTAIM da cela da CL3ONA.

BCP	ρ	$\nabla^2 \rho$	ϵ	V
a	0.001107	+0.003285	5.519133	-0.000456
b	0.001000	+0.003244	2.777557	-0.000367
c	0.004218	+0.013040	0.040367	-0.002158
d	0.003961	+0.013848	0.111278	-0.001998

Como pode ser observado na Figura 3, a existência do BP, com CP a, indica a ocorrência de uma interação do tipo empilhamento- π , de magnitude semelhante à da interação delineada pelo BP e CP b. As interações descritas pelos CP's a e b são topologicamente correspondentes à uma interação fraca, cada uma equivalente à metade da força de uma ligação de hidrogênio convencional ($\rho = 0.002$ a.u. a 0.035 a.u.; $\nabla^2 \rho = +0.024$ a.u. a -0.139 a.u.). Já as interações descritas por c e d são expressivas o suficiente para entrar na classificação de ligação de hidrogênio segundo a QTAIM, além de apresentar valores de V que indicam pontos de maior estabilização eletrônica com relação aos pontos *a* e *b*.

Conclusão

Cálculos QTAIM indicaram que as interações responsáveis pelo empacotamento molecular da CL3ONA se baseiam em sucessivos empilhamentos- π e ligações de hidrogênio não convencionais, topologicamente caracterizadas, envolvendo fragmentos moleculares do tipo C-H...Cl-C.

Agradecimentos

CAPES e CNPq.

Referências

1. A. Messiah, Quantum Mechanics, Dover Publications Inc. (1999).
2. B. E. Warren, X-ray diffraction, Dover Publications Inc. (1969).
3. R. G. Parr, P. W. Ayers, R. F. Nalewajski, J. Phys. Chem. A, 110F, W. Bader, T. T. Nguyen-Dang, Y. Tal, Rep. Prog. Phys., 44, 893 (1981).
4. R. F. W. Bader, M. T. Carroll, J. R. Cheeseman, C. Chang, J. Am. Chem. Soc., 109, 7968 (1987).
5. R. F. W. Bader, T. T. Nguyen-Dang, Y. Tal, Rep. Prog. Phys., 44, 893 (1981).
6. R. F. W. Bader, M. T. Carroll, J. R. Cheeseman, C. Chang, J. Am. Chem. Soc., 109, 7968 (1987).
7. P. L. A. Popelier, Coord. Chem. Rev., 197, 169 (2000).
8. T. S. Koritsanszky, P. Coppens, Chem. Rev., 101, 1583 (2001).
9. R. Flaig, T. Koritsanszky, B. Dittrich, A. Wagner, P. Luger, J. Am. Chem. Soc., 124, 3407 (2002).
10. E. Espinosa, E. Molins, C. Leconte, Chem. Phys. Lett., 285, 170 (1998).
11. P. L. A. Popelier, J. Phys. Chem. A, 102, 1873, (1998).
12. G. V. Gibbs, R. T. Downs, D. F. Cox, K. M. Rosso, N. L. Ross, A. Kirfel, T. Lippmann, W. Morgenroth, T. D. Crawford, J. Phys. Chem. A, 112, 8811, (2008).
13. R. F. W. Bader, Chem. Rev., 1991, 91, 893–928

José A. S. de Freitas^{1*},
Mariano A. Pereira¹, Alex
F. C. Flores³, Daví A. C.
Ferreira², Tatiane L. Balliano¹

¹Laboratório de Cristalografia e Modelagem Molecular - LabCriMM, Instituto de Química e Biotecnologia, Universidade Federal de Alagoas, Av. Lourival Melo Mota, s/n, Cidade Universitária, Maceió - Al, CEP: 57072-900.

²Laboratório de Modelagem de Sistemas Complexos - LMSC, Instituto de Química, Universidade de Brasília, Campus Darcy Ribeiro, Asa Norte, Brasília-DF, CP: 04478, CEP: 70910-000

³Laboratório de Química Orgânica, Escola de Química e Alimento, Universidade Federal do Rio Grande, Av. Itália s/n Carreiros, Rio Grande-RS, CEP: 96203-900.

*E-mail: anderson_jasf@hotmail.com

Adsorption of Atoms on Cubic β -MoC (001) Surface

José R. S. Politi & Alanna P. C. Dantas

Introdução

O metano é um dos principais poluentes industriais e tem várias aplicações nas mais diversas áreas, sendo alvo de inúmeros estudos. Um dos processos mais utilizados para o uso racional desse gás é a reforma à vapor. Nesse processo o metano é convertido em uma mistura de hidrogênio e monóxido de carbono. Essa mistura é conhecida como gás de síntese e é muito utilizada como insumo em várias indústrias de transformação, como, por exemplo na produção de amônia e síntese de hidrocarbonetos via processos Fischer-Tropsch. Contudo, a reforma à vapor é um processo caro industrialmente principalmente pelo uso de metais nobres como catalisadores. Por isso há grande interesse no estudo de catalisadores mais baratos para essa reação.

A adsorção é uma das principais etapas na catálise heterogênea, pois é através da formação de novas estruturas, resultantes da adsorção das moléculas do meio sobre o catalisador, que ocorrem as modificações nos mecanismos que promovem o aumento da taxa de reação. a demanda por tecnologias mais econômicas e com menor impacto ambiental vem crescendo, e segundo Basta et al (1994), esse é um dos fatores que mais contribuem para o desenvolvimento da técnica de adsorção química^{1,2}.

Os carbetos de metais de transição (TMC) têm se mostrado catalisadores promissores em diversas reações estudadas. Estudos publicados na literatura de nanopartículas de ouro suportadas em TiC se mostraram

excelentes catalisadores para a dissociação de oxigênio³ e a dessulfuração do tiofeno.⁴

A extensão desse estudo para nanopartículas de prata e cobre mostrou que essas estruturas têm propriedades catalíticas ainda melhores para a dissociação de compostos contendo enxofre orgânico.⁵ A atividade catalítica de superfícies de nanopartículas metálicas é bem conhecida, mas a importância do suporte de carbetos no processo catalítico também foi recentemente provada, devido ao processo de polarização.⁶

Nesse contexto, define-se o objetivo desse trabalho que é estudar a adsorção dos átomos de níquel, rutênio, platina e paládio na superfície do δ -MoC (001).

Metodologia

Nesse estudo foi utilizado o método periódico para representar o sistema sólido e evitar o efeito de borda existente nos estudos de sólidos. Em particular, modelos periódicos de representação de sólidos associados a níveis sofisticados de aproximação são potencialmente úteis para descrever e interpretar aspectos dos fenômenos regidos pelas características eletrônicas, estruturais e de reatividade de sólidos. Os cálculos foram realizados com a teoria do funcional densidade (DFT), dentro da aproximação GGA. Foram utilizados os funcionais PBE e PW91, implementados no programa VASP. Nessa estratégia, a densidade dos elétrons de valência são expandidas em um conjunto de bases de ondas planas e o efeito provocado pelos elétrons internos é descrito pelo

método PAW (projector augmented wave) de Blöch. O método DFT empregado nesse projeto tem se mostrado o método *ab initio* mais adequado para esse tipo de estudo, apresentando uma boa acurácia quando comparado a dados experimentais e teóricos.

Resultados e Discussão

Foram propostos diferentes sítios de adsorção, com o intuito de determinar em qual deles ocorre a interação mais favorável. A adsorção de um único átomo na estrutura cúbica do δ -MoC foi provada nos sítios bridge, hollow, topC e topM, mostrados na figura a seguir.

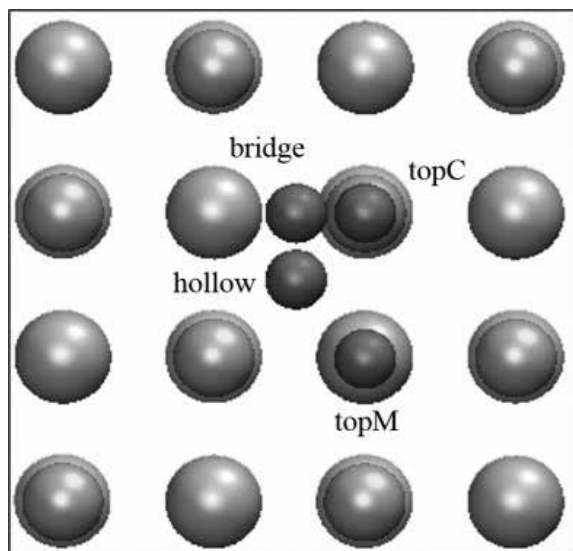


Figura 1. Sítios de adsorção na superfície δ -MoC

O sítio hollow foi o que apresentou a menor energia de adsorção para os adátomos (ad) selecionados. Na tabela a seguir, são apresentadas essas energias de adsorção.

Energia de adsorção (ev) dos adátomos (ad) na posição hollow

Ad	Ni	Pd	Pt	Ru
Eads(ev)	4,9292	4,4067	4,9575	7,0247

Ao serem adsorvidos, todos os átomos promoveram uma reconstrução da superfície (001) do δ -MoC. Os átomos de carbono se deslocam na direção do metal adsorvido e os de molibdênio se afastam (figura 2).

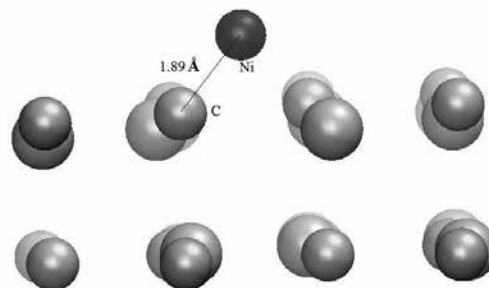


Figura 2. Átomo de Ni adsorvido na superfície 001 do δ -MoC

A carga sobre o Ni varia em +0,1 na adsorção. Variação semelhante ocorre com os demais átomos.

Conclusão

Os átomos de níquel, paládio, platina e rutênio foram adsorvidos pela superfície. É possível observar a ocorrência de reconstrução na superfície com a adsorção desses átomos. O comprimento de ligação e as energias envolvidas indicam que essas adsorções são químicas. Há um leve aumento da carga dos átomos quando ocorre a adsorção, significando uma transferência de carga do adátomo para a superfície. Essa transferência torna a superfície ligeiramente mais oxidativa, o que sugere que esses adátomos favorecem a ação catalítica da superfície.

Agradecimentos

Os autores agradecem o suporte fornecido para a realização deste trabalho: UnB; CENAPAD SP; FAP-DF; CNPq e CAPES.

Referências

1. J. A. Rodriguez, L. Feria, T. Jirsak, Y. Takahashi, K. Nakamura, and F. Illas, J. Am. Chem. Soc. 132 (9), 3177(2010).
2. J. A. Rodriguez, P. Liu, Y. Takahashi, K. Nakamura, F. Vines, and F. Illas, J. Am. Chem. Soc. 131 (24), 8595 (2009); Rodriguez, JA

, Liu, P., Takahashi, Y., Vines, F., Feria, L., Florez, E., Nakamura, K., Illas, F., Catalysis Today 166 (1), 2 (2011)

3. Lee, J., S. Oyama, and M. Boudart, Molybdenum carbide catalysts: I. Synthesis of unsupported powders. Journal of Catalysis, **1987**. 106(1): p. 125-133.
4. Leclercq, G., et al., Treatment of bulk group VI transition metal carbides with hydrogen and oxygen. Applied Catalysis A: General, **1995**. 121(2): p. 169-190.

José R. S. Politi* & Alanna de Pádua Carieli Dantas

Universidade de Brasília, Instituto de Química, Campus Universitário
Darcy Ribeiro, Brasília - BRAZIL

*E-mail: politi@unb.br

Synthetic Routes of the Fundamental Building Blocks of Life: Computational Study of The Reaction Free Energy

Kelson M. T. Oliveira & Elaine Harada

Introduction

In recent years, theoretical and experimental studies have made efforts to understand the origin of the building blocks that gave rise to life, generating a lot of discussion about abiogenesis theme¹⁻³. The idea most widely widespread, known as “the RNA World”⁴⁻⁵, maintains that life arose spontaneously through five main stages: (1) prebiotic synthesis of nucleotides; (2) prebiotic formation of polynucleotides from the nucleotides; (3) emergence of special RNA molecules catalyzing its own replication; (4) evolution of the primordial replicases towards more efficient ones; (5) emergence and evolution of other and better catalytic RNA molecules⁶⁻⁷. All stages are target of much speculation and discussion as it can not be replicated faithfully the original conditions in the laboratory, and there is no guarantee that will be performed in the future⁸. This work, from a semi-empirical theoretical approach, investigates some aspects of the two first stages by means of thermochemical data from the prebiotic nucleotide synthesis reactions, and short sequences of DNA and RNA. The objective was to verify that various abiotic reactions identified in the literature⁹⁻¹⁰ as natural precursor in the formation of life blocks can occur spontaneously in abiotic environment. It was used as a criterion calculating the Gibbs free energy, since the thermodynamic parameters calculated by semi-empirical methods such

as AM1 and PM3 has shown a good correlation with experimental data¹¹.

Methods

The theoretical quantum chemical calculations were performed in an INTEL Quadcore™ PC (8 GB RAM), on the Debian LINUX (5.0 version) by Gaussian 03 Program (Revision E.01). In the optimization geometry and energy routines, the AM1 and PM3 methods were used. Molecular geometries were fully optimized by the force gradient method using Berny's algorithm, and potential energy surfaces were characterized using standard analytical harmonic vibrational analysis to confirm that the stationary points corresponded to minima of the potential energy surfaces (no imaginary frequencies or negative eigenvalues were found). The thermochemical parameters ΔH_r and ΔS_r for each compound were obtained from vibrational analysis (T=298.15K), allowing the calculation of ΔG_r . The methodology consisted of modeling of reactional systems in two distinct stages: 1. Abiotic synthesis reactions of nucleic acids; 2. Formation reactions of short sequences of nucleotides. For this purpose the optimized geometries were obtained as well as the calculation of the energies, frequencies and thermochemical data of each participant's reaction compound. The nucleotide sequences used, are for a single helix conformation, as Table 1.

Table 1. Conformational data from a single helix sequence.

Single Helix β	
α	-39,17
β	-151,44
γ	30,89
χ	-95,44
δ	156,56
ϵ	159,19
ζ	-98,97
Sugar form	3' Endo

Table 2. Thermochemical Data of compounds necessary for the abiotic synthesis reactions of nucleic acids, nucleotides and sequences.

Compounds	ΔH (Kcal/mol)	ΔS (Cal/mol)	ΔG^* (Kcal/mol)
C-Diaminomaleonitrile	136.575669	87.49	110.4905255
T-Diaminofumaritrile	137.0281037	87.35	110.9847012
Aminoimidazol Carbonitrile	143.6157037	81.11	119.4327572
HCN	44.00288373	47.89	29.72448023
HCN dimer	82.05885519	63.89	63.00885909
Aminomaleonitrile	110.2911576	76.81	87.3896598
Formamidine	55.92557373	61.35	37.63228233
Adenine	163.2818671	86.24	137.5694111
Thymine	17.07517461	84.59	-8.14533389
Gtosine	69.92092926	78.88	46.40285726
Guanine	129.5707748	89.54	102.8744238
Uracil	6.44703774	79.56	-17.27377626
Deoxyribose	-101.4005959	91.61	-128.7141174
H ₃ PO ₄	-252.5621073	77.99	-275.8148258
NH ₂ CONHCHCHN	73.8830274	90.05	47.0346199
PO ₄	-57.79178847	74.71	-80.06776757
dAdenine	120.3156299	129.89	81.58892635
dGtosine	28.44314577	125.81	-9.06710573
dGuanine	86.9979864	133.73	47.1263869
dTIMINA	-25.51518411	131.41	-64.69507561
HCCCN	107.2251437	57.67	90.03083324
HOCHCHN	38.33019333	71.48	17.01843133
NH ₂ CONH ₂	-1.44390051	65.95	-21.10689301
Thiocyanate	13.1588847	47.63	-1.0419998
H ₂ CO ₃	-122.1824721	64.00	-141.2640721
H ₂	3.09613434	30.76	-6.07525781
O ₂	5.75803176	46.38	-8.07016524
H ₂ O	-44.05496706	45.09	-57.49855056
NH ₄ OH	-28.76192085	78.46	-52.15476985
NH ₃	16.7168664	45.84	3.0365518
AT	-117.1605096	222.92	-183.6241076
CT	-208.5400	212.75	-271.9772667
ATC	-40.72853	284.05	-107.1921346
ATCG	-231.2606529	398.96	-350.2105769
ATCGA	-69.66929775	485.23	-214.3406223
AUCG	-312.8915462	426.92	-440.1777442
dAPO ₂	107.5150534	121.98	71.14671636
dTPO ₂	-43.41678939	125.04	-80.69746539
dCPO ₂	3.79267044	118.24	-31.46058556
dGPO ₂	70.75740009	120.5	34.83032509
dPO ₄	-301.1972699	117.78	-336.3142713

Table 3. Free energy (in Kcal/mol) of routes of synthesis of nucleic acids.

Reaction	ΔG_1	ΔG_2	ΔG_3	ΔG_4	ΔG_5	ΔG_6
R 01	3.54	-5.33	-6.62	0.49	8.45	-11.58
R 02	3.54	-5.33	-6.62	8.49	-16.46	
R 03	-15.51	51.12	56.87			
R 04	-68.22	56.87				
R 05	56.87	-0.82				

Results and Discussion

1. REACTIONS FROM NUCLEIC ACID SYNTHESIS

The estimation of the free energies of formation of each compound (Table 2) allowed the calculation of ΔG_r of each reaction (Table 3). The more traditional reactional routes were chosen (Figure 1). In the case of adenine and cytosine, two main routes have been calculated. The abiotic synthesis of thymine and guanine are the subject of discussion, and have not been investigated in this work ¹².

Results showed that all the nucleic base synthesis routes are energetically unfavorable and may not spontaneously occur in the way it has been proposed. Reactions 01 and 02 had more than one intermediate step thermodynamically unfavorable. The second step of the reaction 03 presents a large ΔG_r , which makes it impossible to produce cytosine. There is a similar argument to reaction 04. Reaction 05, as proposed by Luisi¹⁵ depends on the spontaneous formation of cytosine by other mechanisms, especially thiocyanate and urea routes, which proved to be energetically unfavorable. In this case, with the formation of cytosine, uracil spontaneous generation is possible, a basic component for RNA.

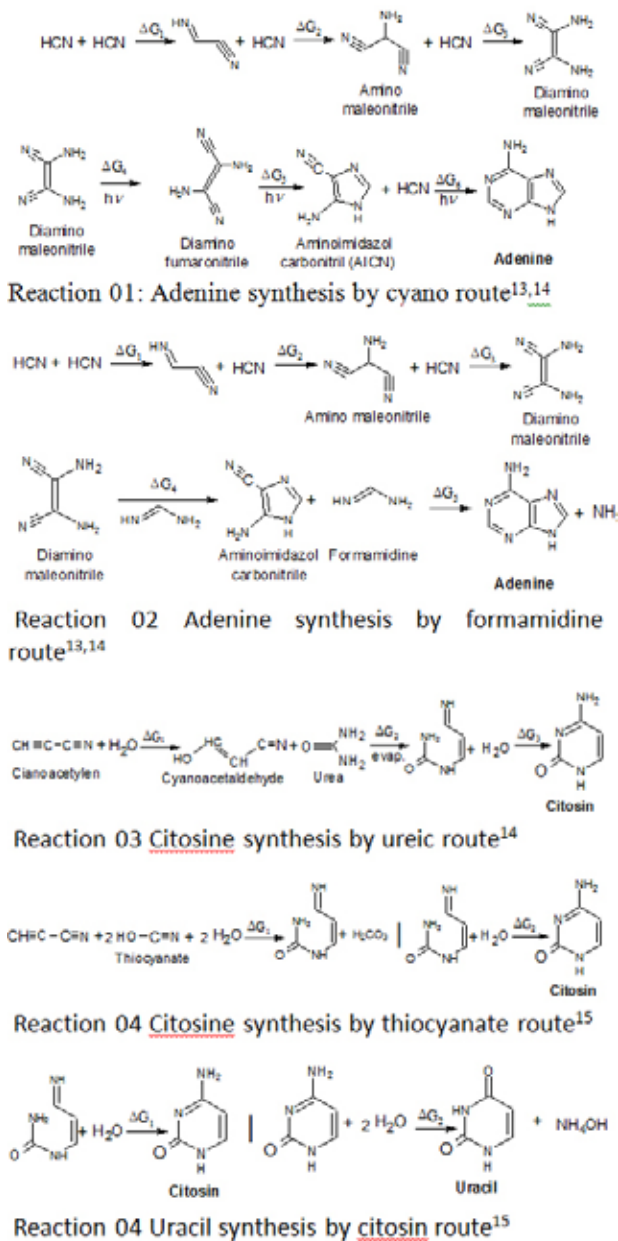


Figure 1. Abiotic routes of synthesis of Adenine, Cytosine, Uracil nucleic acids.

2. REACTIONS FROM FORMATION OF SHORT SEQUENCES OF DNA AND RNA

The abiotic mechanism of simple sequences of nucleotides formation has never been adequately and sufficiently demonstrated. There are at least three possible

suggestions of formation: (a) reaction from the individual components present in the environment; (b) nucleosides reaction in environments rich in phosphorus; (c) reaction from pre-existing sequences containing a phosphodiester bridge.

In case (a), free energy was calculated with the thermochemical data of all necessary components to form a single sequence (Table 4). Analysis of the resulting values presents a strong correlation with the size of the sequence. The longer the more positive the value of ΔG_r (Figure 2). Extrapolation to a complete sequence (single helix) with 200x106 nucleotides, as contained in the human genetic code, without any particular order, will result in a DGf of 3.19x1010 Kcal/mol.

Table 4. Free energy (in kcal/mol) of formation of short sequences, from the individual components present in the environment (nitrogen basis, deoxyribose and phosphoric acid).

COMPONENTS	→ SEQUENCE	ΔG_r
A + T + 2DEOXY + 1 H ₃ PO ₄	→ AT + 2H ₂ O	105.18
A + T + C + 3DEOXY + 2 H ₃ PO ₄	→ ATC + 4H ₂ O	424.74
A + T + C + G + 4DEOXY + 3 H ₃ PO ₄	→ ATCG + 6H ₂ O	368.37
A + T + C + G + A + 5DEOXY + 4 H ₃ PO ₄	→ ATCGA + 8H ₂ O	656.18
A + U + C + G + 4DEOXY + 3 H ₃ PO ₄	→ AUCG + 6H ₂ O	287.52

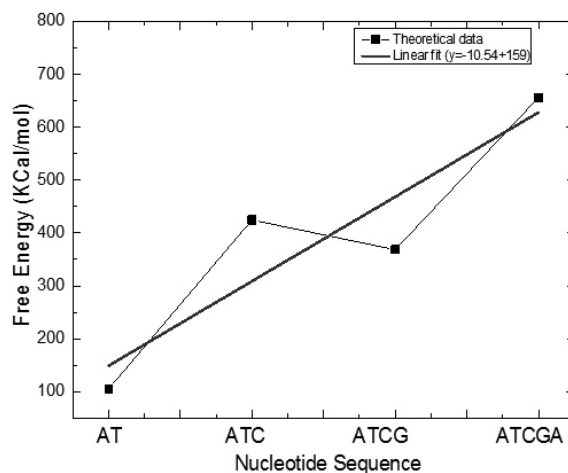


Figure 2. DG_r formation of random nucleotide sequences according to the size of the sequence. In blue, the linear fit.

For case (b), some longer sequences were shown to be energetically favorable to spontaneous formation, if complete nucleosides are available in the environment in the presence of anion of phosphoric acid (Table 5). However, the formation deoxynucleotides (dA, dC, dG and dT) proved to be energetically unfavorable.

Table 5. Free energies (in kcal/mol) of d-nucleosides complete reactions in the presence of phosphorus.

COMPONENTS → NUCLEOSIDES/SEQUENCES	ΔG_r
d + A → dA + H ₂ O	15.13
d + T → dT + H ₂ O	14.66
d + C → dC + H ₂ O	15.74
d + G → dG + H ₂ O	15.46
dC + dT + PO ₄ → CT	-118.15
dA + dT + PO ₄ → AT	-120.45
dA + dT + dC + 2PO ₄ → ATC	45.12
dA + dT + dC + dG + 3PO ₄ → ATCG	-164.95
dA + dT + dC + dG + dA + 4PO ₄ → ATCGA	-30.61

The latter case (c) investigated the formation of new sequences from other smaller d-nucleosides sequences containing a phosphodiester bridge (see Figure 3). The results showed that some sequences may have negative DGr, but the data are not sufficient to set as a rule. Once the first sequence is not energetically favored (107.89 Kcal/mol), the next cannot be formed therefrom (Table 6).

Table 6. Formation free energy (in kcal/mol) of new sequences from pre-existing sequences and d-nucleosides with phosphodiester bridge.

SEQUENCE PREEXISTING → RESULTING SEQUENCE	ΔG_r
AT + dCPO ₂ → ATC	107.89
ATC + dGPO ₂ → ATCG	-277.85
ATCG + dAPO ₂ → ATCGA	64.72

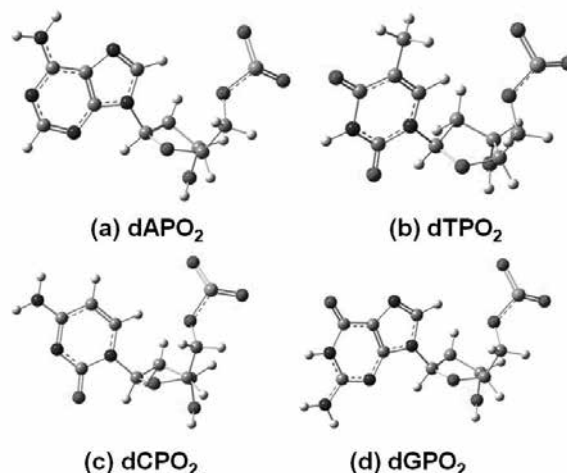


Figure 3. Deoxyribonucleosides containing a phosphodiester bridge.

Conclusions

None of the investigated abiotic reactions of nucleic acids synthesis showed positive DGr in all their stages. Calculated values do not contemplate a spontaneous occurrence of these reactions in an abiotic way. The formation of sequences of nucleotides, considering the presence of all components in an abiotic reaction environment also resulted in positive values. In this case, even with all components present, there is no formation of nucleotides sequences. In the presence of complete deoxynucleotides there is the possibility of spontaneous formation of larger sequences. However, the formation of these deoxynucleotides remains not spontaneous, which prevents the generation of longer sequences. Finally, reactions with complete nucleosides which exhibit a phosphodiester bridge, do not guarantee that larger DNA sequences can be formed continuously. Therefore, it is suggested that other reactions and proposals should be exhaustively investigated before giving a final word on the appearance of bases of life from an abiotic environment.

Acknowledgments

The authors are grateful for the support given from the FAPEAM and PPGQ/UFAM.

References

1. B.S. Palmer, *Int. J. of Astrobio.*, 12, 39 (2013).
2. L. Li, C.Francklyn, C.W. Carter Jr, *J. Biol. Chem.*, 288, 26856 (2013).
3. W. Ma, C. Yu, W. Zhang, *Biosystems* 90, 28 (2007).
4. W. Gilbert, *Nature* 319, 618 (1986).
5. L.E. Orgel, *Crit. Rev. Biochem. Mol. Biol.* 39, 99 (2004).
6. G.F. Joyce, L.E. Orgel. *The RNA World*. Cold Spring Harbor Laboratory Press, NY, 49–77 (1999)
7. G.F. Joyce, *Nature*, 418, 214 (2002)
8. J.L. Bada, *Earth and Planet. Sc. Letters* 226, 1 (2004).
9. S.A. Miller, *Science*. 117, 528 (1953)
10. S.A. Miller, A. Lazcano (78-109); J. Ferris (113-135); L. Orgel (140-154) . In: *Life's Origin: The Beginnings of Biological Evolution*. J. William Schopf (Ed). University of California Press, 78 (2002).
11. . Ma, H.H. Schobert. *J. Phys. Chem. A* 104, 1064(2000).
12. S.G. Trevino, N. Zhang, M.P. Elenko, A. Lupták, J.W. Szostak. *PNAS*, 108, 13492 (2011)
13. J.P. Ferris, A.R. Hill, R. Liu, L.E. Orgel. *Nature*, 381, 59 (1996).
14. S.A. Miller, A. Lazcano. *Formation of the Building Blocks of Life*. W. Schopf, ed. (2002)
15. P.L. Luisi. *The Emergence of Life: From Chemical Origins to Synthetic Biology*. Cambridge University Press (2006).

Kelson Mota T. Oliveira^a &
Elaine Harada^b

^aLaboratório de Química Teórica e Computacional, LQTC/DQ-ICE.

^bInstituto de Computação, IComp. Av Rodrigo Otávio 3000, Setor Norte. Manaus-AM. Universidade Federal do Amazonas

*E-mail: kelsonmota@ufam.edu.br,

Conformational Analysis, MC Simulation, Experimental and GIAO-DFT ^{13}C NMR Calculation on 2'-Hydroxy-3,4,5-Trimethoxy-Chalcone

Leandro O. Duarte, Paulo G. Freitas, Andressa K. Silva, Luciano M. Lião & Fabio L. P. Costa

Introduction

Chalcones (1,3-diaryl-2-propen-1-ones) (Fig. 1) are important intermediates for the synthesis of biologically active compounds such as flavonoids, isoflavonoids and their derivatives.¹ Due to their bio-physico-chemical properties, among which we highlight the antioxidant activity, the chalcones have been the focus of experimental and theoretical investigations.^{1,2} Their properties are related, among other factors, to its great conformational freedom, as well as to the several patterns of substitution of A and B rings.⁴

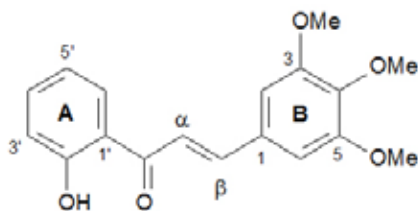


Figure 1. Structure of 2'-hydroxy-3,4,5-trimethoxy-chalcone molecule

The goal of this work is to investigate the ability of the scaling factor protocol at the mPW1PW91/6-31G(d)//mPW1PW91/6-31G(d) level of theory to predict the NMR ^{13}C chemical shifts (δ) of the 2'-hydroxy-3,4,5-

trimethoxy-chalcone (chalcone) molecule. Moreover, it will be compared two different approaches for determining the chemical shift of the chalcone. In the first one (I), the absolute shieldings (σ) for all carbon atoms in each geometrically optimized conformers of the 2'-hydroxy-3,4,5-trimethoxy-chalcone molecule were calculated using the GIAO approximation at the mPW1PW91/6-31G(d)//mPW1PW91/6-31G(d) (NMR//optimization) level of theory, and further used to generate weighted average values for each atom considering the previously obtained conformational distribution, σ_{aver} . In the second one (II), only the σ for the lowest energetic conformer was taken to account, σ_{lowe} .

Methods

A randomized conformational search of the 2'-hydroxy-3,4,5-trimethoxy-chalcone molecule using the Monte Carlo (MC) method with a search limit of 200 structures, and employing the Merck molecular force field (MMFF) as implemented in the Spartan'08 software package⁵ considering an initial energy cutoff of 10 kcal. mol⁻¹ was performed. The conformation preferences of these molecules are ruled mainly by the formation of hydrogen bond interactions between the OH and C=O, see figure 2.

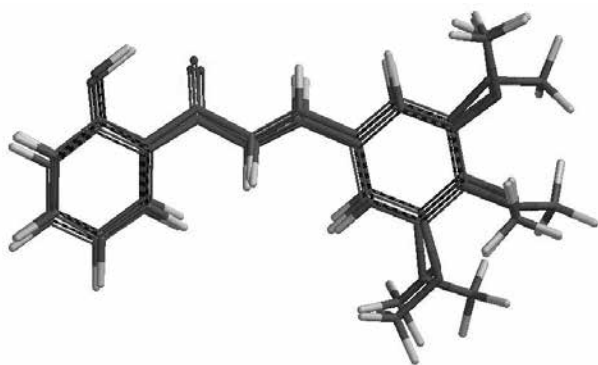


Figure 2. Superposition of the three lowest energy conformations of the chalcone molecule

In the approach (I), for each optimized conformer geometry, ^{13}C atomic chemical shielding tensors (σ) were computed at the mPW1PW91/6-31G(d)//mPW1PW91/6-31G(d) level of theory. Isotropic atomic chemical shifts (δ) in units of ppm were computed as differences between the atomic isotropic shielding of the solutes and corresponding reference atoms in tetramethylsilane (TMS). So, the Population-averaged chemical shifts for the selected conformers were computed assuming Boltzmann statistics, see equation 1, based on mPW1PW91/6-31G(d) free energies. Finally, the ^{13}C NMR chemical shifts were scaled according to Costa *et al*⁷. Protocols.

$$\langle \delta \rangle = \frac{\sum_i \delta_i e^{-\Delta E_i / kT}}{\sum_i e^{-\Delta E_i / kT}} \quad (1)$$

In the approach (I), only the lowest-energetic conformer was used to obtain the scaled chemical shifts. The chalcone was obtained from Sigma Aldrich Chemical Co, ^{13}C NMR assignments are based on ^1H and ^1H - ^{13}C HSQC / HMBC spectra at 500 MHz and 125 MHz, using CDCl_3 .

Results and Discussion

Our results are in very good agreement with empirical data. Indeed, ^{13}C chemical shifts calculated at the mPW1PW91/6-31G(d)//mPW1PW91/6-31G(d) level of theory reproduce the chalcone experimental data with small mean deviation (MD), see equation 2, and mean square deviation (MSD), see equation 3 error (see Table 1).

$$MD = \frac{\sum_{i=1}^n (\delta_{i\text{exp}} - \delta_{i\text{theor}})}{n} \quad (2)$$

where $\{\delta_{i\text{exp}}\}$ and $\{\delta_{i\text{theor}}\}$ are ^{13}C NMR experimental and theoretical (δ_{calc} and δ_{scal}) chemical shifts of the chalcone.

$$MSD = \sqrt{\frac{\sum_{i=1}^n (\delta_{i\text{exp}} - \delta_{i\text{theor}})^2}{n}} \quad (3)$$

Table I. Statistical data illustrating the performance of various methods for the GIAO calculation of ^{13}C NMR chemical shifts (δ , in ppm) for the chalcone

Level	MD MSD)a	MD (MSD)b
(I)	0.63 (1.80)	-1.43 (2.14)
(II)	-3.10 (3.45)	1.10 (1.81)

aCalculated chemical shifts ($\delta_{\text{calc}} = \text{TMS} - \delta$) obtained by TMS subtraction; bScaled chemical shifts ($\delta_{\text{scal}} = 1.05\delta_{\text{calc}} - 1.22$) obtained by the generated universal scaling factors.

The main differences between experimental and scaled δ , level (I) and (II), were observed in carbons C4, OMe-3, OMe-4 and OMe-5. These differences are consistent with the 3 selected conformers (see fig. 2) to obtain the δ at the level (I). The reason is that they have different orientations of the OCH_3 group (atoms C3, C4 and C5) with respect to the aromatic ring and the their δ_{are} systematically dependent on the orientation of the methoxy group.

Table II. Differences between scaled and experimental ^{13}C NMR chemical shifts (in ppm) in the chalcone relative to TMS.

Nuclei	Level (I)	Level (II)
C1	0.61	0.90
C2	1.00	0.50
C3	-0.77	-0.68
C4	-6.56	-1.12
C5	-1.45	-0.48
C6	1.00	0.50
α	-3.03	-3.57
β	3.72	3.75
C9	2.39	2.38
C1'	0.62	0.63
C2'	-2.52	-2.48
C3'	0.02	0.08
C4'	0.62	0.62
C5'	3.35	3.30
C6'	0.45	0.38
OMe-3	-2.86	1.89
OMe-4	6.71	1.96
OMe-5	-3.32	1.90

Conclusions

We investigated the ability of the scaling factor protocol at the mPW1PW91/6-31G(d)//mPW1PW91/6-31G(d) level of theory to predict the NMR ^{13}C δ of the 2'-hydroxy-3,4,5-trimethoxy-chalcone molecule. Although, the two approaches were able to reproduce the δ of the chalcone, significant differences in the calculated δ of the carbons C4, OMe3, OMe4 and OMe5 were observed. The best results were obtained at the level (II), where only the σ lowe were taken to account to obtain in order to the δ_{calc} . These findings suggest that, in this case, the level (II) is that best approach and that further analysis of the methoxychalcones is therefore justified.

Acknowledgments

The authors are grateful for the support given from the FAPEG, CAPES, and CNPQ.

References

1. A. Crozier, I. B. Jaganath, M. N. Clifford, (Eds: A. Crozier, M. N. Clifford, H. Ashihara), Blackwell Publishing Ltd, Oxford, pp. 1–21 (2006).
2. J.R. Dimmock, D.W. Elias, M.A. Beazely, N.M. Kandepu, *Curr. Med. Chem.* 6, 1125 (1999).
3. D. Kozłowski, P. Trouillas, C. Calliste, P. Marsal, R. Lazzaroni, J.-L. Duroux, *J. Phys. Chem. A* 111, 1138 (2007).
4. M. Larsen, H. Kromann, A. Kharazmi, S.F. Nielsen, *Bioorg. Med. Chem. Lett.*, 15, 4858 (2005).
5. Sparta'08, Wavefunction, Inc., Irvine California, USA.
6. Gaussian 09, Revision A.01, M. J. Frisch, G. W. Trucks, H. B. Schlegel, G. E. Scuseria, M. A. Robb, J. R. Cheeseman, G. Scalmani, V. Barone, B. Mennucci, G. A. Petersson, H. Nakatsuji, M. Caricato, X. Li, H. P. Hratchian, A. F. Izmaylov, J. Bloino, G. Zheng, J. L. Sonnenberg, M. Hada, M. Ehara, K. Toyota, R. Fukuda, J. Hasegawa, M. Ishida, T. Nakajima, Y. Honda, O. Kitao, H. Nakai, T. Vreven, J. A. Montgomery, Jr., J. E. Peralta, F. Ogliaro, M. Bearpark, J. J. Heyd, E. Brothers, K. N. Kudin, V. N. Staroverov, R. Kobayashi, J. Normand, K. Raghavachari, A. Rendell, J. C. Burant, S. S. Iyengar, J. Tomasi, M. Cossi, N. Rega, J. M. Millam, M. Klene, J. E. Knox, J. B. Cross, V. Bakken, C. Adamo, J. Jaramillo, R. Gomperts, R. E. Stratmann, O. Yazyev, A. J. Austin, R. Cammi, C. Pomelli, J. W. Ochterski, R. L. Martin, K. Morokuma, V. G. Zakrzewski, G. A. Voth, P. Salvador, J. J. Dannenberg, S. Dapprich, A. D. Daniels, O. Farkas, J. B. Foresman, J. V. Ortiz, J. Cioslowski, and D. J. Fox, Gaussian, Inc., Wallingford CT, 2009.
7. F.L.P Costa, A.C.F. de Albuquerque, F.M. dos Santos Jr., M. B. de Amorim, *J. Phys. Org. Chem.* 23, 972 (2010).

Leandro O. Duarte^a, Paulo Gomes Freitas^a, Andressa Kuhnen Silva^b, Luciano Moraes Lião^b & Fabio Luiz Paranhos Costa^{a,*}

^aInstituto de Ciências de Exatas e Tecnológicas - ICET, UFG, Jataí-GO, Brazil.

^bLaboratório de RMN - Instituto de Química, UFG, Goiânia-GO, Brazil

*E-mail: flpcosta@ufg.br

Proposta para o Cálculo do Coeficiente de Partição Gás/Aerossol de Compostos Orgânicos Voláteis Utilizando Métodos DFT Associados ao Modelo IEFPCM

Leonardo Baptista & Lillian L. Castilho

Introdução

Já é bem aceito na literatura o fato da composição do aerossol orgânico secundário (SOA) ser composto majoritariamente pelos produtos de oxidação de compostos orgânicos voláteis, como os terpenos emitidos pelas plantas. Por este motivo, encontra-se uma série de trabalhos que tentam caracterizar a composição do SOA, suas fontes, velocidade de particionamento dos compostos entre a fase gasosa e o aerossol líquido e elaboração de modelos para o cálculo dos coeficientes de partição gás/aerossol. Devido a importância do tema para qualidade do ar e saúde dos seres vivos, o presente trabalho propõe uma alternativa para o cálculo dos coeficientes de partição gás/aerossol pelo cálculo da energia livre de Gibbs de solvatação usando métodos DFT associados ao modelo IEFPCM para inclusão do efeito do solvente

Metodologia

O processo estudado no presente trabalho é o particionamento dos produtos de oxidação de terpenos no aerossol atmosférico, como está ilustrado na Figura 1. O parâmetro K_p é o coeficiente de partição gás/aerossol dos produtos de oxidação.

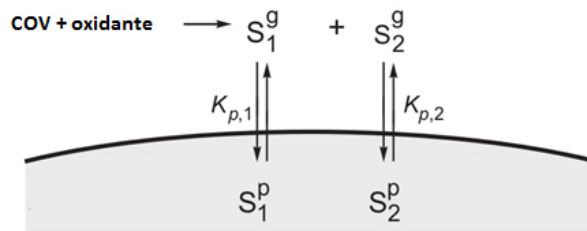


Figura 1: Esquema do particionamento dos produtos de oxidação no aerossol atmosférico e formação do SOA. Adaptado da referência [1].

Os produtos de oxidação do d-limoneno e Δ^3 -careno² foram escolhidos como o caso de estudo. Inicialmente, uma busca conformacional em fase gasosa foi realizada de para fornecer o conjunto de estruturas possíveis para cada produto de oxidação em fase gasosa. Esta etapa foi feita utilizando dinâmica molecular e o campo de força AMBER. A partir das estruturas iniciais, cada conformação foi completamente otimizada com os funcionais PBE1PBE e M06-2x na base 6-311G*.

Em seguida, todas as conformações foram otimizadas na presença do solvente (água) utilizando o modelo IEFPCM para inclusão do efeito do solvente. A energia livre de Gibbs de solvatação média,

$\Delta G_{av}(\text{solv})$, foi calculada via uma média ponderada da energia eletrônica corrigida por ZPE de todas conformações em fase gasosa, considerando que as estruturas obedecem a distribuição de Boltzmann.

O coeficiente de partição gás/aerossol foi calculado segundo um modelo de rede simples

$$\ln K_{ar}^{\text{aerossol}} = \frac{\mu^0(\text{aerossol}) - \mu^0(ar)}{RT} - \ln \left(\frac{\gamma_{\text{aerossol}}}{\gamma_{ar}} \right) \quad (1)$$

onde μ^0 é o potencial químico do soluto em cada fase e γ é o coeficiente de atividade do soluto em cada fase.

Resultados e discussão

A Tabela 1 apresenta os valores para $\Delta G_{av}(\text{solv})$ e $\ln K_{ar}^{\text{aerossol}}$ para alguns produtos de oxidação de terpenos. Em uma primeira aproximação foi considerado $\gamma_{\text{aerossol}} = 1$. Nesta aproximação, o coeficiente de partição calculado se assemelha ao cálculo da constante da Lei de Henry para os solutos.

Como era de se esperar, devido a formação de compostos oxigenados, todos os compostos são altamente solúveis em água. Logo, espera-se que em uma primeira aproximação, estes compostos sejam encontrados principalmente no aerossol atmosférico ao invés da fase gasosa.

Tabela 1: Energia livre de Gibbs de solvatação média ($\Delta G_{av}(\text{solv})$) e $\ln K_{ar}^{\text{aerossol}}$ calculado em nível PBE1PBE/6-311G**.

	$\Delta G_{av}(\text{solv})$ kcal mol ⁻¹	$\ln K_{ar}^{\text{aerossol}}$
Ácido cárico	-15,46	26,19
Caronaldeído	-8,77	14,86
Ácido carônico	-14,91	25,26
Ácido limônico	-8,30	14,06
Ácido limononico	-7,92	13,42

O efeito da inclusão da força iônica do aerossol está mostrado na Figura 2. Foram utilizados valores médios da força iônica medida para cada tipo de aerossol³. O efeito da concentração de eletrólitos reflete na solubilidade de cada produto de oxidação, diminuindo de forma drástica a solubilidade de cada espécie. O mesmo efeito é observado para os produtos de oxidação do limoneno. Logo, apesar da baixa volatilidade destas espécies, deve-se esperar que estas espécies sejam encontradas em concentração apreciável no aerossol troposférico no aerossol e em fase gasosa.

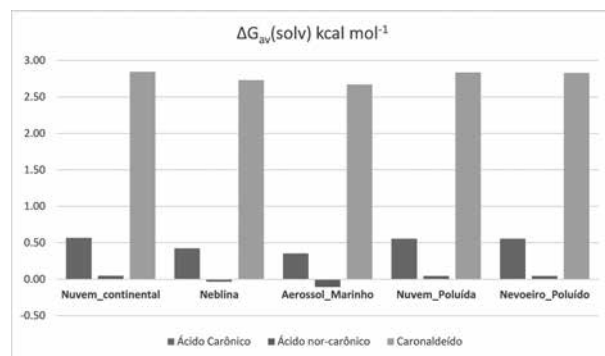


Figura 2: Valores de $\Delta G_{av}(\text{solv})$ para os produtos de oxidação do 3-careno calculados em nível PBE1PBE/6-311G**. O efeito do solvente foi incluído por meio do modelo IEFPCM.

O coeficiente de partição para ácido cárico foi calculado por meio da equação (1), considerando $\gamma_{\text{aerossol}} = 1$, por se tratar de um gás ideal e γ_{ar} utilizando o modelo AIOMFAC⁴. Para o cálculo foi considerado um intervalo de valores para a fração molar do ácido e as propriedades experimentais do aerossol foram retiradas da referência³. A Tabela 2 apresenta os resultados para $\ln K_{ar}^{\text{aerossol}}$ do ácido cárico quando a fração molar deste composto no aerossol é 10⁻² em função do tipo de aerossol. Apesar do processo de solvatação ser espontâneo ($\Delta G_{av}(\text{solv}) < 0$) para todos os tipos de aerossol considerados, $\ln K_{ar}^{\text{aerossol}}$ é negativo. Estes resultados indicam que a presença de íons em solução dificulta a migração do ácido da fase

gasosa para a fase aquosa. É possível perceber, que a energia livre de solvatação diminui a metade quando é considerado o efeito de eletrólitos em solução aquosa.

Tabela 2: $\ln K_{ar}^{aerosol}$ calculado para o ácido cárico utilizando a equação (1) e $\Delta G_{av}(solv)$ em nível PBE1PBE/6-311G**. O efeito do solvente foi incluído por meio do modelo IEFPCM.

	$\Delta G_{av}(solv)$ kcal mol ⁻¹	$\ln K_{ar}^{aerosol}$
Nuvem continental	-7,70	-16,40
Aerossol marinho	-7,95	-16,47
Nuvem poluída	-7,71	-16,09
Neblina poluída	-7,72	-16,13
Chuva	-7,70	-16,07

3. H. Herrmann, Chem. Rev., 103 4691 (2003)
4. <http://www.aiomfac.caltech.edu/model.html> acessado em 5 de outubro de 2015

Leonardo Baptista* & Lillian Lopes Castilho

Universidade do Estado do Rio de Janeiro, CEP 27537-000, Resende, Brasil

*E-mail: leobap@gmail.com

Conclusões e Perspectivas Futuras

O cálculo da energia livre de solvatação associados ao cálculo de $\ln K_{ar}^{aerosol}$, negligenciando o coeficiente de atividade da fase condensada, para produtos de oxidação de terpenos indicam que estas espécies devem se encontrar majoritariamente no aerossol atmosférico. No entanto, quando se inclui o efeito dos eletrólitos dissolvidos no aerossol, a solubilidade destas espécies é alterada significativamente. Este efeito mostra que as espécies consideradas podem ser encontradas tanto no aerossol atmosférico aquoso, quanto em fase gasosa. No presente momento, cálculo dos coeficientes de atividade para fase aquosa, utilizando o modelo AIOMFAC, estão em andamento. Estes coeficientes possibilitarão o cálculo dos coeficientes de partição para sistemas que emulam condições mais próximas as observadas no aerossol atmosférico.

Agradecimentos

Os autores agradecem o suporte financeiro do CNPQ e FAPERJ.

1. J. H. Kroll, J. H. Seinfeld, Atmos. Environ. 42 3593 (2008)
2. a) S. Leungsakul et al, Environ. Sci. Technol., 39, 9583 (2005);
b) C. S. Gibson, J. L., J. Simonsen, Chem. Soc., 0, 305 (929)

Análise termodinâmica e cinética de reações de mecanismo de ação para Compostos de Platina (II) Análogos a cisplatina com ligantes derivados de terpenos.

Lucas C. Santana & Juliana F. Lopes

Introdução

A cisplatina é uma das drogas mais eficientes e utilizadas para o tratamento do câncer¹. Entretanto oferece alguns problemas, sendo baixa solubilidade e efeitos colaterais indesejados como: nefrotoxicidade, cardiotoxicidade, ototoxicidade, toxidez ao trato intestinal, entre outros². Atualmente há mais de 3000 complexos análogos a cisplatina, porém nenhum está à altura da cisplatina³. Por esse motivo há uma busca por complexos de platina (II), a fim de que suas propriedades sejam melhoradas em relação à cisplatina e nesse contexto o estudo tem como principal objetivo utilizar a química computacional para determinar propriedades como: geometria, estabilidade energética, lipofilicidade e barreira de ativação na reação de substituição dos ligantes cloro por ligantes aquo de 12 complexos análogos a cisplatina.

Metodologia

Todos os cálculos foram realizados nos computadores do LaQC, através do software Gaussian 09, com a metodologia DFT, funcional M062X, função de base para os átomos leves 6,31g(d,p) e pseudo potencial LanL2DZ para o átomo de platina. Os 12 complexos estudados foram divididos em três modelos para a facilitação em sua identificação. De acordo com a Fig. 1.

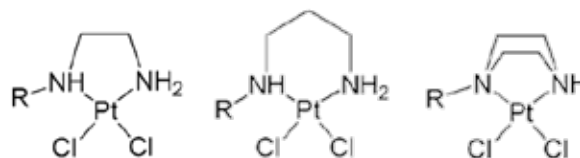


Figura 1 – Representação simplificada dos 12 complexos estudados em três modelos base ($R=C_5H_9$, $C_{15}H_{25}$, $C_{10}H_{17}$).

A partir dos modelos representados na Fig. 1, altera-se a ramificação lateral, por quatro derivados de óleos essenciais: Prenila, Farnesila, Geranila e seu isômero Nerila.

Resultados e Discussão

Neste trabalho são apresentados os resultados para somente um dos doze complexos, cuja estrutura é a mais simples (MOD1- $R=C_5H_9$), os outros complexos seguem o mesmo comportamento. Os complexos estudados apresentam estrutura quadrático plana, os ligantes cloro e amino ligados diretamente ao átomo de platina de forma análoga a cisplatina, conforme ilustra a Fig. 2.

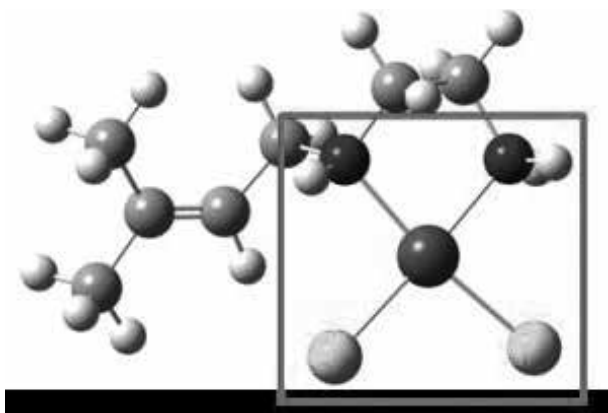


Figura 2 – Representação da estrutura de mínimo local para o complexo (MOD1-R=C₅H₉).

Os processos reacionais dos complexos apresentam uma etapa de substituição a mais (em relação à cisplatina) devido a não simetria destes complexos. Assim a entrada do ligante aquo fornece propriedades diferentes ao complexo, conforme a posição que este ligante ocupa no lugar do cloro. As reações envolvidas estão descritas pela Fig. 3.

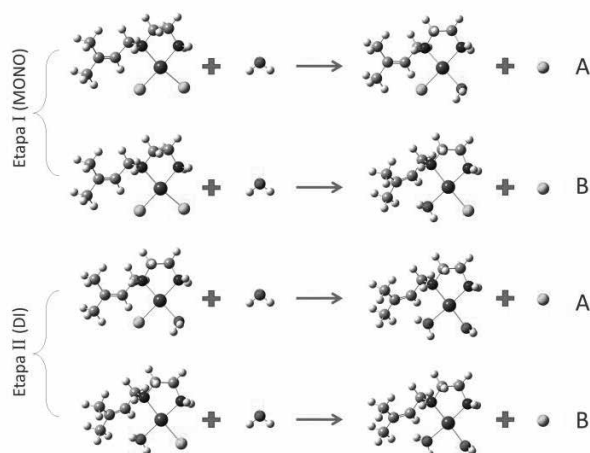


Figura 3 – Equação representante da substituição dos ligantes cloro por ligantes aquo. Observa-se que os complexos não são simétricos como a cisplatina o que realiza a adição da etapa B ao processo, sendo que a cisplatina segue apenas a etapa A.

Após a obtenção dos parâmetros termodinâmicos dos complexos de forma isolada, identificou os estados de transição para cada reação. Os estados de transição obtidos possuem estrutura bipirâmide trigonal, assim como o TS da cisplatina e como esperado para compostos quadráticos planos. Os TS estão ilustrados pela Fig. 4.

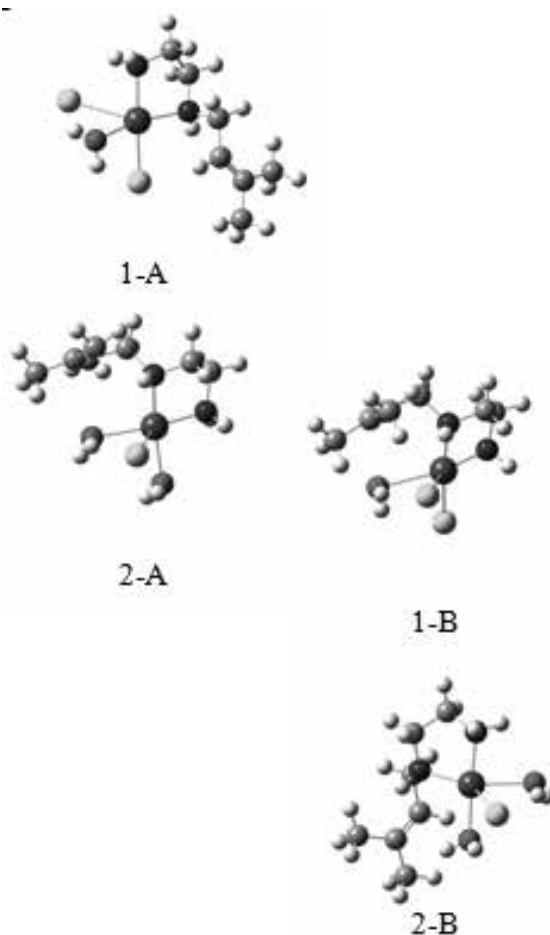


Figura 4 - Estruturas do estados de transição do modelo 1 com ramificação R= C₅H₉, cuja estrutura é bipirâmide trigonal nas quatro etapas reacionais.

Em seguida com os cálculos de IRC, verificou-se como ocorreu a substituição dos ligantes, ou seja, o caminho percorrido por cada ligante. Confirmando que os TS pertencem às reações descritas, fornecendo a estrutura dos reagentes e produtos intermediários. Os cálculos de IRC estão demonstrados pela Fig. 5.

Por fim, otimizando os produtos e reagentes obtidos pelo IRC determinou os parâmetros termodinâmicos e cinéticos envolvidos na reação com reagente e produtos intermediários. A energia de ativação possui um módulo inferior ao da cisplatina, assim como a energia livre de Gibbs. Verifica-se que para o caso dos reagentes e produtos isolados tem-se um absurdo, isto porque os produtos possuem energia superior ao estado de transição, devido ao desbalanceamento de cargas da reação, fato também observado para o processo reacional da cisplatina. Outro fator é não ter adicionado o efeito solvente para descrever melhor o sistema biológico.

As barreiras de energia para as etapas estão ilustradas pela Fig. 6. Para os 12 complexos analisados, tem-se uma energia de ativação em torno de 15 kcal.mol⁻¹ e cerca de 3 kcal.mol⁻¹ a menos que a cisplatina, sendo um fator signficante na velocidade de reação, pois a velocidade de reação é descrita pela equação de Arrhenius⁵, ou seja, esta descrita por uma exponencial, logo torna a velocidade de reação mais sensível a qualquer variação na energia de ativação.

É observado para alguns complexos (etapa 2-A da Fig. 6) uma energia de ativação superior a da cisplatina, com 1,7 kcal.mol⁻¹, no entanto em sua maioria os complexos apresentam menor energia de ativação, ou seja, maior velocidade de substituição que a cisplatina.

Um exemplo é o complexo apresentado ao longo do trabalho (MOD1 R=C₅H₉) que apresenta a menor energia de ativação para a primeira etapa de substituição (monoaquo) com energia de 11,9 kcal.mol⁻¹.

Para a segunda etapa de substituição o complexo com maior velocidade de substituição é o complexo MOD3 R=C₁₅H₂₅.

Em relação a variação da energia livre de Gibbs observa-se que o complexo MOD3 R=C₁₅H₂₅ é o mais espontâneo (mais negativo) e para a segunda etapa, tem-se o MOD3 R=C₁₀H₁₇, com energia de 88,77 kcal.mol⁻¹ e 168,63 kcal.mol⁻¹ respectivamente.

Reforçando o fato de que a análise com os reagentes e produtos intermediários descrevem melhor a reação, por eliminar o desbalanceamento de cargas, entretanto a otimização e análise vibracional dos reagentes e produtos do IRC ainda estão em andamento.

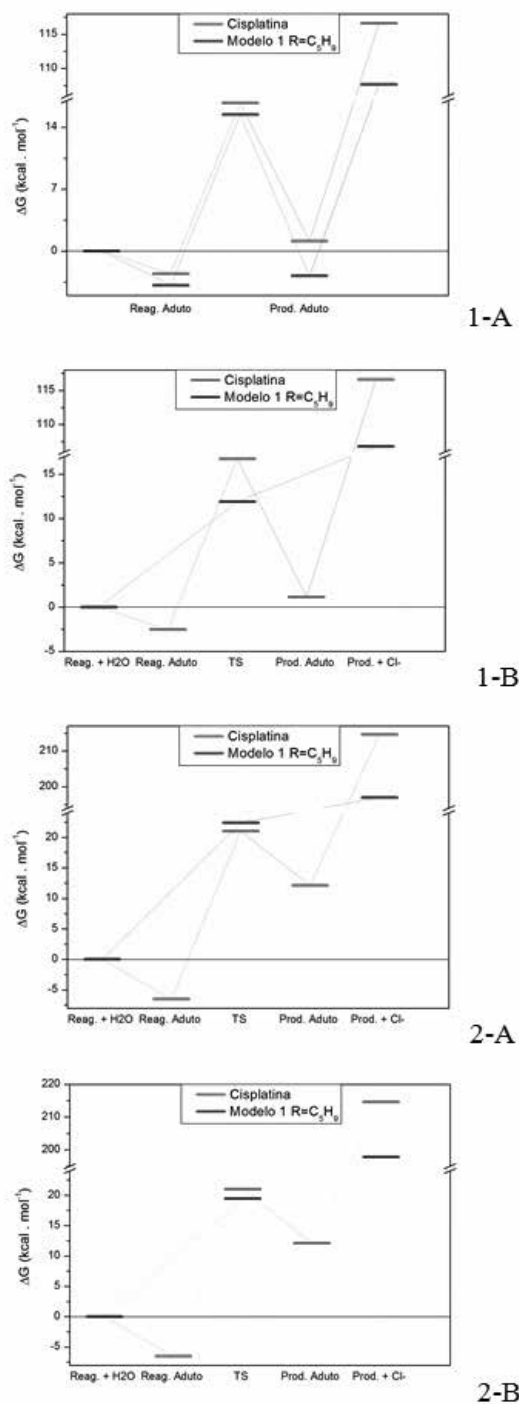


Figura 6. Comparação dos parâmetros termodinâmicos da cisplatina4 (vermelho) com os complexos (azul), em específico para o modelo 1 R= C5H9.

Conclusão

Os parâmetros termodinâmicos para os reagentes e produtos intermediários descrevem melhor a reação, por não possuírem o desbalanceamento de carga.

Os parâmetros termodinâmicos dos complexos estão melhorados em relação a cisplatina, pois a energia de ativação é menor e a energia livre de Gibbs mais negativa, o que fornece uma reação mais rápida e mais espontânea.

Agradecimentos

Os autores são gratos ao suporte dado pelas agencias de fomento FAPEMIG, CNPQ e RQ-MG.

Referências

1. Lopes, J.F., et al., Theoretical study of the potential energy surface for the interaction of cisplatin and their aquated species with water. *Journal of Chemical Physics*, **2008**. 128(16): p. 14.
2. Lippard, E.R.J.a.S.J., Structure, Recognition, and Processing of Cisplatin-DNA Adducts. *Chem. Rev*, **1999**. 99: p. 2467-2498.
3. Wilson, J.J., J.F. Lopes, and S.J. Lippard, Synthesis, Characterization, and Photophysical Properties of Three Platinum(II) Complexes Bearing Fluorescent Analogues of the Di-2-pyridylmethane Ligand. *Inorganic Chemistry*, **2010**. 49(11): p. 5303-5315.
4. Kai-Chi Lau, J. and Deubel, D. V., Hydrolysis of the Anticancer Drug Cisplatin: Pitfalls in the Interpretation os Quantum Chemical Calculations . *Journal of Computational Chemistry*. **2005**, 2, p. 103-106.
5. Cramer, C., J., *Essentials of Computational Chemistry: theories and models*. 2ª edition. England: John Wiley & Sons Ltd, **2004**.

Lucas Chuman Santan &
Juliana Fedoce Lopes

LaQC- Laboratório de Química Computacional, Universidade Federal de Itajubá, Av. BPS nº1303, Bairro: Pinheirinho, 37500-903, Itajubá, MG, Brasil

Multiple Hartree-Fock Solutions of Systems Constituted with First Line Atoms: BH and FH molecules using the Double Zeta Base

L. A. C. Malbouisson, A. M. de C. Sobrinho & M. D. de Andrade

Introduction

In the study of atoms, molecules and aggregates, the Hartree-Fock (HF) approximation is a start point to determine the energy and properties. A central aspect of this method is that the basic equation, the HF equation, is not linear¹. Thus, in principle, these equations have multiple solutions and consequently the HF functional has multiple extremes.

The absolute minimum is, among the extreme HF, the one that best represents the ground state, in this approach, with regard to energy. The determination of the absolute minimum HF, however, is still an open problem. There is no resolution method of HF equation ensuring their achievement. Direct minimization of the HF functional have been employed in this absolute minimum search process².

In addition to the absolute minimum HF, the others extreme of the functional HF have been used in the calculation of non-variational properties. For instance, in the calculations of permanent electrical dipole and quadrupole moments using the Multi-Reference Configuration Interaction method based on multiple HF references (MRHFCI)³.

The usual procedure for solving the HF equations is the self-consistent field (SCF) method⁴ and its extensions⁵.

Another method for solving the HF equations is the algebraic method (AM) [1c,d].

In this work it is presented two sets of HF solutions (the HF energies), obtained using a combination of the SCF and AM procedures, for the BH and FH systems using the double zeta (DZ) base.

Theroy

Since the Roothaan and Pople-Nesbet problems are very well known and documented in the literature⁴, only the closed-shell HF-Roothaan real equations will be presented. The HF equations for a system with 2n electrons constitute a system of integro-differential equations,

$$\hat{F}(\varphi_1, \dots, \varphi_n) \varphi_i = \epsilon_i \varphi_i \quad ; \quad i = 1, \dots, n, \quad (1)$$

where \hat{F} is the HF operator, φ_i is the molecular orbitals (MO) and ϵ_i are the orbital energies [4a]. The equations (1) can be expanded in a linear combination of atomic orbitals (LCAO), and are written in matrix form [4a]

$$F(c_1, \dots, c_n) c_i = \epsilon_i S c_i \quad ; \quad i = 1, \dots, n. \quad (2)$$

The usual method to solve the HF-Roothaan equations is the self-consistent field (SCF) method ^{4a}. The SCF method is an iterative algorithm based on an occupation orbital rule (aufbau usually). This procedure is one of trial and error. One assumes a set of c_i 's, calculates the F matrix, solves equation (2) for the ϵ_i lowest eigenvalues, and compares the resulting c_i 's with the assumed ones until to obtain the convergence. This procedure has been improved by several investigators, in particular by Pulay [5a-b] and Kudin et al. [5c]. The aufbau rule is a sufficient [6a], but not necessary, condition [6b] to find a minimum.

Another method for solving the HF equations is the algebraic method (AM) [1c,d]. In the AM, the HF integro-differential equations are rewritten as a infinite nonlinear system of polynomial equations. For the HF-Roothaan real problem the AM method is formulated as follows. The eigenvectors φ_i , $i=1, \dots, \infty$ of the \hat{F} operator that define the pseudo-eigenvalue problem of the SCF algorithm are orthonormal and form a base of the one particle space. The matrix representation of \hat{F} on its own base of eigenvectors is diagonal. So, the eigenvectors φ_i must to satisfy the following equations, in the real case:

$$F_{ij} = \langle \varphi_i | \hat{F} | \varphi_j \rangle = 0, \quad i < j = 1, \dots, \infty \quad (3)$$

$$S_{ij} = \langle \varphi_i | \varphi_j \rangle = \delta_{ij}, \quad i \leq j = 1, \dots, \infty \quad (4)$$

we obtain a algebraic system of polynomial equations in the LCAO coefficients, $c_{\mu i}$. For the restricted closed-shell HF real problem we have the following equations:

$$\varphi_i = \sum_{\mu} c_{\mu i} \xi_{\mu} \quad , \quad (5)$$

In the above equations, $\langle \xi_{\mu} | \xi_{\nu} \rangle$, $\langle \xi_{\mu} | \hat{h} | \xi_{\nu} \rangle$ and $\langle \xi_{\mu} \xi_{\lambda} | \xi_{\nu} \xi_{\sigma} \rangle$ are the overlap, core and correlation integrals, respectively. The index k indicates the occupied molecular orbitals (MO), μ, ν, λ and σ indicates the atomic orbitals (AO), and $i, j=n+1, \dots, \infty$ indicates the virtual MOs.

In the Roothaan approximation of the closed-shell HF real problem with a atomic base $\xi = [\xi_1$

$$F_{ij} = \sum_{\mu\nu} c_{\mu i} c_{\nu j} \langle \xi_{\mu} | \hat{h} | \xi_{\nu} \rangle + \sum_k^n \sum_{\mu\nu\lambda\sigma} c_{\mu i} c_{\lambda k} c_{\nu j} c_{\sigma k} [2 \langle \xi_{\mu} \xi_{\lambda} | \xi_{\nu} \xi_{\sigma} \rangle - \langle \xi_{\mu} \xi_{\lambda} | \xi_{\sigma} \xi_{\nu} \rangle] = 0, \quad i < j \quad (6)$$

$$S_{ij} = \sum_{\mu\nu} c_{\mu i} c_{\nu j} \langle \xi_{\mu} | \xi_{\nu} \rangle - \delta_{ij} = 0, \quad i \leq j \quad (7)$$

$\{\dots, \xi_m\}$, the AM equations is a system of m^2 nonlinear polynomials algebraic equations in the m^2 coefficients LCAO $c_{\mu i}$. In the base ξ , the ω^{th} HF solution is a set of functions $\{ \varphi_i^{\omega} = \xi c_i^{\omega}; i=1, \dots, n \}$ where c_i^{ω} is a column vector with components $c_{1i}^{\omega}, \dots, c_{mi}^{\omega}$. The functions φ_i^{ω} are called occupied LCAO-MO. Both algorithm SCF and AM generate a additional set of functions $\{ \varphi_a^{\omega} = \xi c_a^{\omega}; a=n+1, \dots, m \}$ called virtual LCAO-MO orbitals of the ω^{th} solution. After solve the AM equations, we can calculate the associated orbital energies of the ω^{th} solution, ϵ_i^{ω} , $i=1, \dots, n, n+1, \dots, m$, calculating the diagonal elements F_{ii} , using the set $\{ \varphi_i^{\omega} = \xi c_i^{\omega}; i=1, \dots, n, n+1, \dots, m \}$, i.e.,

Table I. Multiples HF energies (hartree) for the BH molecule in DZ basis set.

Nº	Energy	Nº	Energy
01	-25.11339530	11	-8.22439472
02	-24.28664301	12	-7.87053289
03	-23.75420066	13	-7.73994180
04	-23.18328731	14	-6.51796174
05	-22.83648699	15	-6.27733084
06	-22.36169840	16	-6.06047772
07	-22.31472311	17	-4.44263542
08	-21.86719149	18	-4.34199043
09	-21.03503117	19	-3.91640233
10	-20.85752741		

Interatomic distance: 2.329 bohr; Symmetry of the solutions (1) Σ^+ .

Table II. Multiples HF energies (hartree) for the FH molecule in DZ basis set.

Nº	Energy	Nº	Energy
01	-100.02189594	18	-90.71852225
02	-99.01552707	19	-89.55574937
03	-97.79015093	20	-89.53665280
04	-97.41570193	21	-89.25579499
05	-97.22026796	22	-89.14047913
06	-97.06425308	23	-87.70156966
07	-96.39560029	24	-85.79229772
08	-95.52923980	25	-82.74910380
09	-94.74488707	26	-45.49958845
10	-94.01348082	27	-44.35475371
11	-93.99396778	28	-43.60336904
12	-93.68292526	29	-35.15266557
13	-93.08505171	30	-33.21222009
14	-92.48397594	31	-29.47566301
15	-91.27628076	32	-26.24509634
16	-91.00880325	33	-18.49652725
17	-90.94870392		

Interatomic distance: 1.7334 bohr; Symmetry of the solutions $(1)\Sigma^+$.

Conclusões

The determination of all extremes of the HFR functional can be a complicated algebraic-geometry problem. To ensure the achievement of the HF ground state by solving the HF equations, it is necessary to search all the solutions, which are minimal points. Consequently, it becomes clear that obtaining the HF ground state may not be an easy task.

For any Hartree–Fock problem, it is possible, in principle, to obtain several HF extremes in the symmetry class of interest, in our case $(1)\Sigma^+$. These extremes correspond to minimum, maxima and saddle points of the HF functional and correspond to different orbital occupations.

With each HF solution and its respective virtual orbitals, it is possible to construct a basis of the full Configuration Interaction (CI) space. These HF extremes can be used in a multi-reference HF CI method for energy and properties calculations³.

The number of solutions of a HF problem is an open problem too. In our two examples we present here, we have obtained, beyond of the usual HF solution, more eighteen and the thirty two unpublished HF solutions, for the BH and FH molecules, respectively, using the DZ base.

The calculations of sets of HF solutions, using several bases for the systems H_2 , LiH, BH, CH⁺, Li₂, OH[−], FH, CO, N₂, BeH₂, CH₂, H₂O, NH₃, CH₄, HCHO, CH, NH, NH₂, OH and O₂ are now in progress.

Referências

- (a) W. H. Adams. Phys. Rev., 127, 1650 (1962); (b) R. E. Stanton. J. Chem. Phys., 48, 258 (1968); (c) L. A. C. Malbouisson, J. D. M. Vianna. J. Chim. Phys., 87, 2017 (1990); (d) R. M. Teixeira Filho, L. A. C. Malbouisson and J. D. M. Vianna. J. Chim. Phys., 90, 1999 (1993).
- M. D. de Andrade, K. C. Mundim and L. A. C. Malbouisson. Int. J. of Quantum Chem. 103, 493 (2005); M. D. de Andrade, M. A. C. Nascimento, K. C. Mundim and L. A. C. Malbouisson. Int. J. of Quantum Chem. 106, 2700 (2006);
- (a) L. A. C. Malbouisson, M. G. R. Martins and N. Makiuchi, Int. J. Quantum Chem., 106, 2772 (2006); (b) A. M. C. Sobrinho, M. A. C. Nascimento, M. D. de Andrade and L. A. C. Malbouisson. Int. J. of Quantum Chem., 108, 2595 (2008); (c) L. A. C. Malbouisson, M. D. de Andrade and A. M. de C. Sobrinho. Int. J. of Quantum Chem., 112, 3409 (2012); (d) A. M. de C. Sobrinho, M. D. de Andrade, M. A. C. Nascimento, L. A. C. Malbouisson. J. Mol. Model., 20, 2382 (2014).
- (a) C. C. Roothaan. J. Rev. Mod. Phys., 23, 69 (1951); (b) J. A. Pople, R. K. Nesbet. J. Chem. Phys., 22, 571 (1954).
- (a) P. Pulay. Chem. Phys. Lett., 73, 393 (1980); (b) P. Pulay. J. Comput. Chem., 3, 556 (1982); (c) K. N. Kudin, G. E. Scuseria, E. Cancès. J. Chem. Phys., 116, 8255 (2002).
- (a) J. C. Facelli and R. H. Contreras. J. Chem. Phys., 79, 342 (1983); (b) Stanton, R. E. J. Chem. Phys., 48, 258 (1968).
- J. E. Dardenne, N. Makiuchi, L. A. C. Malbouisson, J. D. M. Vianna. Int. J. Quantum Chem., 76, 600 (2000).
- K. M. Brown. SIAM J. Numer. Anal., 6, 560 (1969).

L. A. C. Malbouisson*, A. M. de C. Sobrinho & M. D. de Andrade

Instituto de Física da UFBA – Depto. de Física do Estado Sólido, Salvador – Ba, Brasil

*E-mail: lmalbou@ufba.br

The Confined Helium Atom in Hyperspherical Coordinates

M. N. Guimarães & F. V. Prudente

Introduction

This work aims to develop and implement an efficient theoretical and computational method for the non-relativistic quantum study of spatially confined two electrons atoms. Especially, in recent decades, studies on simply and doubly excited states of helium atom have attracted considerable attention in atomic physics.¹ Additionally, advances in semiconductor technology have increasingly attracting the interest of physicists and chemists for investigating new quantum objects obtained by the confinement of electrons, atoms or molecules by potential models.²

Methods

Our methodology is based on the variational formalism and hyperspherical coordinates fixed in space,¹ consisting of one hyperradius, ρ , and five hyperangles, Ω , being applied to study the helium atom whose Hamiltonian operator for the time-independent Schrödinger equation in this coordinate system is given by where μ depends on

$$\hat{H} = -\frac{\hbar^2}{2\mu} \left(\frac{\partial^2}{\partial \rho^2} + \frac{5}{\rho} \frac{\partial}{\partial \rho} \right) + \frac{\hbar^2}{2\mu\rho^2} \Lambda^2 + V,$$

the masses, Λ is the hyperangular momentum operator containing all the angular variables³ and the confinement potential is given by the expression

$$V(\rho, \Omega) = \frac{1}{4\pi\epsilon_0} \frac{C(\Omega)}{\rho} + \phi(\rho)$$

with the first term representing the Coulomb interaction and the second term representing a harmonic isotropic confinement:

$$V(\rho, \Omega) = \frac{1}{4\pi\epsilon_0} \frac{C(\Omega)}{\rho} + \phi(\rho)$$

Also we employed the finite element method for expansion of the wave function in terms of a finite set of local basis functions. In particular, we propose a modification in its p-version (p-FEM) assuming that the Hamiltonian is invariant under a reflection around a midpoint, then the parity is preserved. In this case, we propose to use the p-FEM to build, in a simple way, basis functions adapted to the parity of the wave function. In Figure 1 we show, as an example, the eigenfunction of the seventh excited state of one-dimensional harmonic oscillator problem together with the basis functions utilized to expand an even function. Also we utilize the self-consistent finite element method⁴ to optimize the elements mesh, which, among other things, provide a reduction in the matricial dimensions of the problem.

with the first term representing the Coulomb interaction and the second term representing a harmonic isotropic confinement:

$$\phi(\rho) = \frac{1}{2} \omega^2 \rho^2.$$

Also we employed the finite element method for expansion of the wave function in terms of a finite set of local basis functions. In particular, we propose a modification in its p-version (p-FEM) assuming that the Hamiltonian is invariant under a reflection around a midpoint, then the parity is preserved. In this case, we propose to use the p-FEM to build, in a simple way, basis functions adapted to the parity of the wave function. In Figure 1 we show, as an example, the eigenfunction of the seventh excited state of one-dimensional harmonic oscillator problem together with the basis functions utilized to expand an even function. Also we utilize the self-consistent finite element method⁴ to optimize the elements mesh, which, among other things, provide a reduction in the matricial dimensions of the problem.

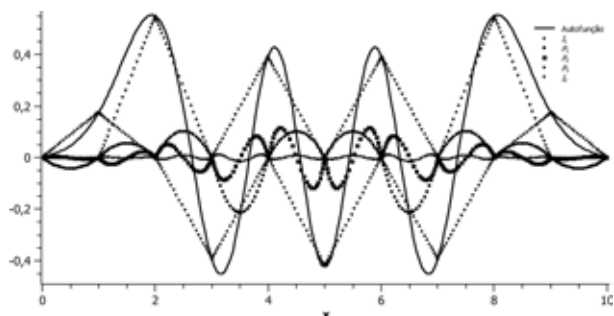


Figure 1. Eigenfunction of seventh excited state of the one-dimensional harmonic oscillator and their symmetry-adapted basis functions using the FEM.

Results and Discussion

Our emphasis is given to the calculation of the energy levels in atomic units. All calculations were made using a computational implementation in Fortran. Because

of the symmetry of the Hamiltonian solutions of the hyperangular equation can be divided into even and odd. Therefore, we can apply the finite element method with basis functions appropriate to symmetry of the problem in which we had argued in the previous section. Examining the singlet states, $S = 0$, of helium atom with total angular momentum $L = 0$ it is possible to note that the conditions given by problem equations determine that only even solutions will exist.

The use of hyperspherical coordinates enables propose an adiabatic separation between the hyperradius and hyperangles in the same sense as the usual adiabatic model for a molecule. In Figure 2 are shown the potential curves for the first eigenvalues obtained from the solution of hyperangular part considering $\omega = 0$, corresponding to free helium atom, and $\omega = 0.1$ a.u., corresponding to the harmonic confinement. We note that the potential curve of Figure 2 for $\omega = 0$ are compatible with the graphics in the literature.⁵ On the other hand, in the confinement situation, we note that as the hyperradius increases the angular eigenvalues tend to feel more the influence of the confinement potential increasing rapidly its value as compared to the free situation.

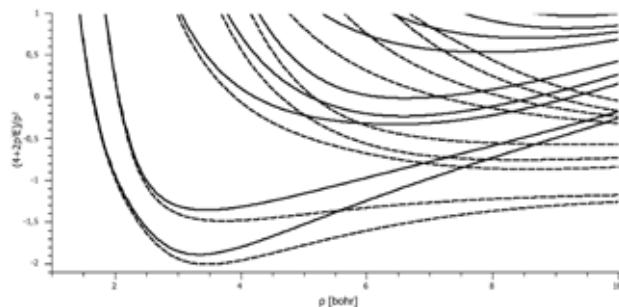


Figure 2. Potential curves of the solution the hyperangular part of the problem of harmonically confined helium atom. Dashed line corresponds to $\omega = 0$ a.u. and solid line corresponds $\omega = 0.1$ a.u..

In the Table 1 we show some energy values of singlet states with $L = 0$ for two confinement intensities, ω . We note that even in a weak confinement the levels are already significantly different from the free helium atom presented in literature⁵. Although we have no numerical data for comparison we note that our results have values

consistent with those presented in Figure 6 of the Sako and Diercksen paper⁶.

Also in Figure 3, we show the energy spectrum, E , depending on the intensity of confinement, ω . In this figure it can clearly be observed split between the levels with $L = 0$ when ω increases in value which becomes more evident as the confinement is getting stronger. Indeed, for large values of ω , the influence of Coulomb repulsion on the correlation of electrons is smaller and its movements become mostly governed by the harmonic potential of confinement that affects the state with higher energies.

Table 1. Energy levels of helium atom, with $L = 0$, confined by a harmonic isotropic potential obtained by p-FEM.

State	Energy [a.u.]	
	$\omega = 0.1$	$\omega = 0.5$
1S	-2.892146	-2.655916
2S	-2.048908	-1.006816
3S	-1.756004	0.115915

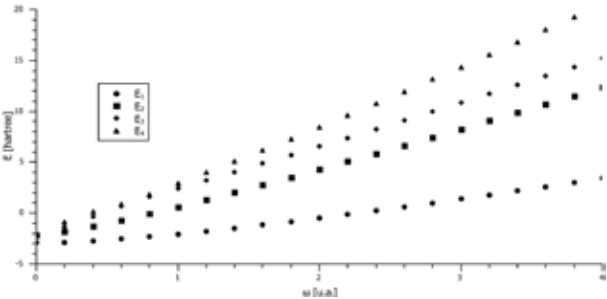


Figure 3. Energy spectrum, E , depending on the intensity of the confinement, ω , for the helium atom confined by an isotropic harmonic potential.

Conclusions

We conclude that the procedure focused on p-FEM was overall quite efficient. We believe that the realization of this work represents a starting point to achieving our primary goal in this research field: the building of

computer codes based on new variational methods for solving the time-independent Schrödinger equation which are capable of performing extensive calculations of spatially confined atomic systems.

Acknowledgments

The authors are grateful for the support given from the CNPq.

References

1. C. D. Lin, Phys. Rep., 257, 1, **1995**.
2. W. Jaskólski, Phys. Rep., 271, 1, **1996**.
3. F. T. Smith, Phys. Rev., 120, 1058, 1960.
4. E. M. Nascimento, F. V. Prudente, M. N. Guimarães and A. M. Maniero, J. Phys. B: At. Mol. Opt. Phys., 44, 015003, **2011**.
5. J. J. De Groote, M. Masili and J. E. Hornos, J. Phys. B: At. Mol. Opt. Phys., 31, 4755, **1998**.
6. T. Sako and H. F. Diercksen, J. Phys. B: At. Mol. Opt. Phys., 36, 1681, **2003**.

M. N. Guimarães* & F. V. Prudente

Instituto de Física. Universidade Federal da Bahia. Salvador, BA.
*mng@ufba.br

Quasiperiodic CH_2/SiH_2 Molecular Nanowires

David L. Azevedo, M.S. Vasconcelos, Marco A. de Andrade, Kleber A. T. da Silva,
Fábio F. Monteiroa & Antonio L. A. Fonseca

Introduction

Nanotechnology is a fast growing researcher field [1]. With their application, it promises a new industrial revolution, giving us the understanding, production, control, and use of structured matter at the atomic and molecular level, i. e., objects with dimensions from 1 to 100 nanometers, where the physics laws that govern this world is quantum mechanics. Thus, the study of quantum mechanics applied to these miniature systems enables us to discover new and revolutionary directions in science, and the development of new technologies associated with this miniature world, called nanotechnology. Various scientific groups are keen about this technology and are devoting themselves to the development of more, new, and better nanomaterials [2, 3, 4]. In the next decade, the expectation is that no field will be left untouched by the incredible benefits available through application of nanotechnology. Between these news developments, we detach the one-dimensional nanowire [5, 6, 7, 8]. The complete understanding of these nanowires is one important key to further applications in nanotechnology.

In this paper we address to theoretical calculations of the electronic spectra of molecular nanowire where its molecular components are arranged in a Fibonacci quasiperiodic sequence. This nanowire is formed by CH_2 and SiH_2 radicals. We have used molecular mechanics with universal force field(UFF) for obtain the optimized relaxed structures, and semi-empirical quantum method based on Hückel extended model to obtain the electronic spectra. In our calculations we use only a single point which is the sufficient condition

to consider all the orbitals and charge distribution across the entire system. Although the calculations presented here are more complete than the models adopted in the literature which take into account the electronic interaction, up to the second and third neighbors, an interesting property remains in their electronic spectra: the fractality (which is the main signature of this kind of system). We make some preliminarily considerations about the electronic gap decreasing with the increasing of the nanowire. Furthermore, we discuss the fractality trends of the spectra.

Methods

Consider a straight line of radicals (CH_2 and SiH_2) obeying a Fibonacci sequence rule. The Fibonacci chain can be obtained by an inflation rule or recursive sequence, forming a binary string that can be grown by juxtaposing two building blocks A (CH_2) and B (SiH_2). The n-th stage S_n of Fibonacci chain is generated by: $S_n = S_{n-1}S_{n-2}$ ($n \geq 2$), with $S_0 = B$ and $S_1 = A$. Another way to obtain a GFS is through the recurrence relation $A \rightarrow AB$ and $B \rightarrow A$. The total number of blocks A and B in S_n is equal to the Fibonacci number F_n , and is given by the recurrence relation $F_n = F_{n-1} + F_{n-2}$, with $F_1 = F_0 = 1$. The first terms of the sequence are : A, AB, ABA, ABAAB,..., where A and B are building blocks of the sequence, i. e., CH_2 and SiH_2 radicals, respectively. We adopted an initial bond length of 1.5 Å between Si – C and C – C. After a complete optimization, the final bond length found for Si–C, and C–C were around 1.87Å, and 1.53Å respectively. In the Figure 1 we show a 3D representation of the fifth generation molecule.

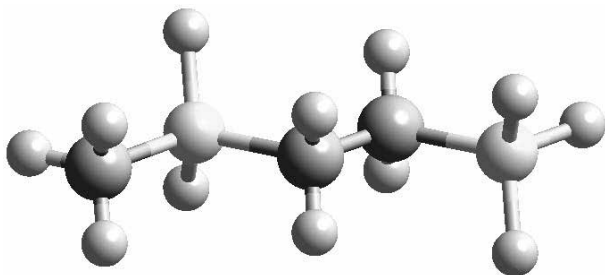


Figure 1. Atoms disposition in a CH₂-SiH₂. The atom number one is at the origin, while the atom number two is at 1.6 Å to the right of the atom one, and the same rule we apply to others terms of the Fibonacci sequence. This figure is equivalent to the ABAAB term.

Results and Discussion

In the Fig. 2, we show results obtained for the spectra of eigenenergies for each generation, and the corresponding density of states for the whole spectrum. The DOS indicates a fractal trends on the bands structures.

In the Fig. 3 we show the band gap variation with length of the chain or nanowire Fibonacci generation. There is a decreasing of the gap with the chain increasing, which is awaited property in a typical polymer. Although we have just quantum mechanics qualitative results, we can infer from the observed results, that for quasiperiodic chain, in general the gap is lower than the periodic chain for same generation, which is surprising interesting, the order of chain growth could influence the gap behavior. Further investigation with a more robust quantum mechanics method would provide a better understanding of this behavior.

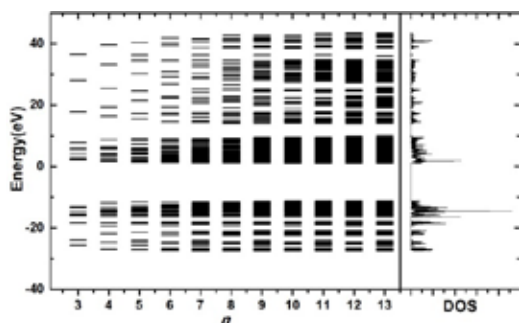


Figure 2. Energy levels in function of the generation number for Fibonacci nanowire, and the corresponding to the entire density of states (DOS) for the whole spectrum.

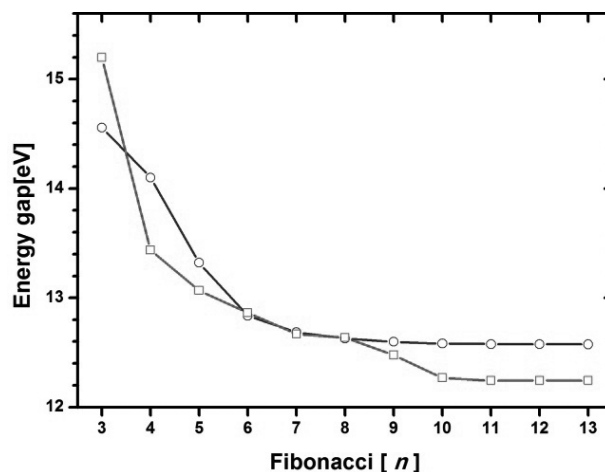


Figure 3. Gap energy behavior for each Fibonacci generation n. Open blue circle corresponds to periodic nanowire. Open red square corresponds to Fibonacci nanowire. Figure 3. Gap energy behavior for each Fibonacci generation n. Open blue circle corresponds to periodic nanowire. Open red square corresponds to Fibonacci nanowire.

Conclusions

In summary, we investigated the Quasiperiodic CH₂/SiH₂ atomic nanowire with extended Hückel methodology. Our calculations show clearly a fractal aspect in the eigenenergies distribution with the increasing of the Fibonacci generation, i.e. the inclusion of more complex structure with four orbitals per atom does not break the main property of this system: the multifractality. Curiously there is an electronic gap reduction with the introduction of disorder through quasiperiodicity along the nanowire. Maybe this could happen due of some above mentioned Hückel method limitations. Further investigations with more precise methods would clarify this aspect.

If we compare with others models, the method applied here are more complete and could give more physical information not explored yet in the literature. We hope that the present findings described in this paper may stimulate further investigations in the quasiperiodic molecular nanowires.

Acknowledgments

The authors are grateful for the support given from the CNPq, CAPES, FINATEC, FAP-DF and FAPEMA.

References

1. W. Lu1 and C. M. Lieber, J. Phys. D: Appl. Phys. 39, R387 (2006).
2. V. Kumar and S.K. Yadav, J. Chem. Technol. Biotechnol. 84, 151 (2009).
3. P. Mohanpuria, N.K. Rana, and S.K. Yadav, J. Nanopart. Res. 10, 507 (2008)
4. J.K. Jaiswal and S.M. Simon, Trends Cell. Biol. 14, 497 (2004).
5. C. O'Regan, S. Biswas, N. Petkovab and J. D. Holmes, J. Mater. Chem. C 2, 14 (2014).
6. Y. Cui and C. Lieber, Science 291, 851 (2001).
7. M. Hocevar, G. Immink, M. Verheijen, N. Akopian, V. Zwiller, L.Kouwenhoven, and E. Bakkers, Nature Commun. 3, 1266 (2012).
8. M. Amato, M. Palummo, R. Ruruli and S. Ossicini, Chem. Rev. 114, 1371 (2014).

David L. Azevedo^{a,b}, M.S. Vasconcelos^c, Marco A. de Andrade^{a,b}, Kleber A. T. da Silva^d, Fábio F. Monteiro^a & Antonio L. A. Fonseca^{a,b}

^aInstitute of Physics, University of Brasília, 70.919-970, Brasília, Brazil

^bUniversity of Brasília, UnB Planaltina Faculty, 73.345-010, Brasília, Brazil

^cECT, Federal University of Rio Grande do Norte, 59072-970, Natal- RN, Brazil

^dDepartment of Physics, Federal University of Maranhão, São Luís, Brazil

A Theoretical Study of CCD4a Dioxygenase of Citrus, a Cleavage Enzyme of Carotenoids in Plants

Mauricio Vega-Tejido, Margot P. Zunini, Carolina López & Maria J. Rodrigo

Introduction

The coloration in citrus and other plants is due the accumulation of carotenoids, which are isoprenoid pigments of 40 carbon atoms (C40) and its derivatives. The enzymatic function of CCD4a has been associated previously with the metabolism of carotenoids in *Chrysanthemum morifolium* [1]. The flowers with white petals showed a high expression of CCD4a in contrast with those with yellow petals that showed a low expression. The interpretation was that the synthesized carotenoids are degraded by CCD4a to produce colorless petals [1]. In saffron stigmas (*Crocus sativus*) CCD4a and CCD4b were associated with the transformation of zeaxanthin in the apocarotenoids responsible by the color, taste and aroma of this so appreciated spice [2].

Recently, Rodrigo et al. [3], reported a series of CCD4-type citrus dioxygenases involved in the generation of C30 apocarotenoids. These natural compounds provide an attractive reddish-orange pigmentation to the peel of many sweet oranges and mandarins, which is associated with its perception of quality. Among them, CCD4b1 is the first reported case of dioxygenase that cleaves double bonds of carotenoids C40 in the position 7,8 or 7'-8', generating the corresponding C30 derivative. In this case, the possible products are β -citraurin or 8- β -apocarotenal depending on the carotenoid used as substrate, that is, zeaxanthin or β -carotene, respectively. β -cryptoxanthin substrate can derivate in one or other product depending on the ring

cleaved. Still remains unclear the specific position where CCD4a enzymes can cleave a carotenoid double bond. Two possible double bonds could be cleaved, 7-8/7'-8' as CCD4b1 or 9-10/9'-10' as has been previously reported by Rubio et al. [2] for CCDD4a of *Crocus sativus* with zeaxanthin and β -carotene as substrates. In the case of CCD4a of citrus the specific position is not confirmed yet and this is one of the aims of our studies (Figure 1).

Here we report a new tridimensional model of CCD4a and their complexes with a series of 3 carotenoids (4 different complexes). The structure of CCD4a was optimized and stabilized in an explicit water box using Molecular Dynamics (MD). The complexes with the ligands were constructed by means Docking. Finally, MD was used to optimize, and then, simulate and study these molecular systems.

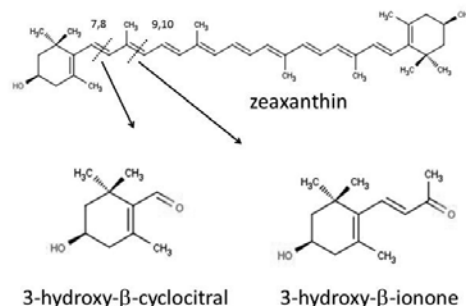


Figure 1. Schematic representation of zeaxanthin and both possible subproducts of cleavage.

Methods

The structures were modeled by sequence homology (2biw, PDB code [4]) and Molecular Dynamics (MD). After this, Docking calculations [5] were performed in CCD4a receptor with thousands of initial ligand conformations, in order to find all the possible poses in the active site. The evaluation of the interaction energy was done by means of ASE scoring posing, an Amber99 refinement and LondonDG rescoring. The force field used in MD was Amber99, with a 0.002ps time-step using the NPA algorithm. The water box was constructed orthorhombic with 6 nm distances to the faces. The MD procedure was implemented by heating of 100ps from 0 to 300K, 100ps of equilibration and 5ns of simulation at 300K, in order to obtain values with statistical significance.

Results and Discussion

The docking results are presented in two tables, one for the all-trans ligands (Table 1) and other for the 9-10-Z isomers (Table 2). All-trans ligands are known as substrates of CCD enzymes in general. In docking results we observed that ligands adopt a curvature in the active site, so we tested ligands with a trans-cis transformation of the 9-10 double bond. Some examples, as CCD8, can cleave cis isomers [6]. Even we can mention that in the 2biw crystallographic structure, used as template for our model, the soaking procedure of the crystal without Fe(2+) (inactive enzyme) were done with the all-trans substrate. Despite this, the final structure of the ligand showed an isomerization when the active form with Fe(2+) was obtained [4]. The authors suggest that some members of the CCD family can act as isomerases.

Table 1. LondonDG scores for the best five solutions. In β -cryptoxanthin column two solutions correspond to the conformation with the OH moiety out of the active site.

	zeaxanthin	β -crptoxanthin	β -carotene
1	-20.91	-19.94 (out)	-16.43
2	-20.62	-19.93	-16.25
3	-20.6	-19.67	-16.13
4	-20.54	-19.63(out)	-16.04
5	-20.53	-19.41	-15.83

The results of docking (Table 1) show LondonDG score of -20, -19 and -16 kcal/mol, for all-trans zeaxanthin, β -cryptoxanthin and β -carotene, respectively (Figure 2). The correlation can be associated with the number of hydroxylic moieties (two, one or none), this correlation were experimentally observed in CCD4b1 for these substrates [3]. The same correlation was observed with the 9-10-Z isomers with slightly more favorable scores and only one solution with the OH moiety out of the active site.

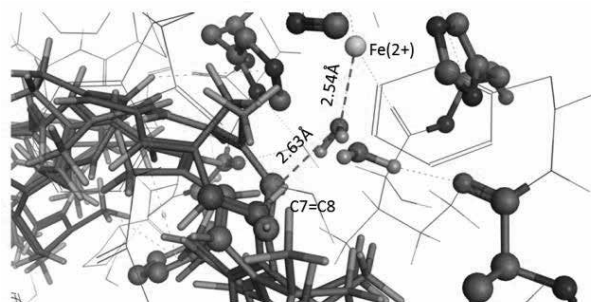


Figure 2. Ligands docked in the active site of CCD4a. One water molecule occupies one coordination site of Fe(2+). This site is occupied by a reactive oxygen molecule during the catalysis.

Table 2. LondonDG scores for the best five 9-10-Z isomers solutions. In β -cryptoxanthin column one solution corresponds to the conformation with the OH moiety out of the active site.

	zeaxanthin	β -crptoxanthin	β -carotene
1	-21.85	-19.85	-16.53
2	-21.67	-19.65 (out)	-16.48
3	-21.13	-19.50	-16.42
4	-20.55	-19.49	-16.37
5	-20.16	-19.39	-16.35

All the molecular complexes showed a stable behavior when were simulated by MD (Figure 3). The interaction of the ligands with the actives site of CCD4a was estimated by the Uab value that is the potential energy of interaction between the ligand and all the surrounding. The same sequence in the estimated interaction strength (Uab) was obtained for the three ligands using MD [5] (Table 3). Very similar values were observed for the two

possible orientations of β -cryptoxanthin in the active site, so it is hard to say if one or other is a preferential substrate for CCD4a.

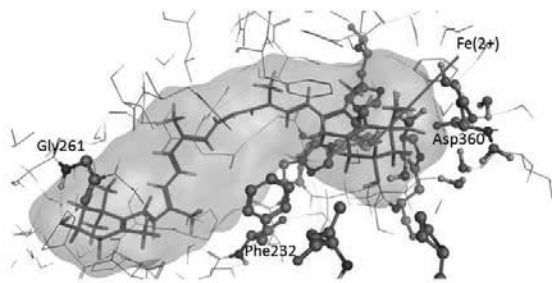


Figure 3. Zeaxanthin ligand in the active site of CCD4a.

Table 3. Average values for the Uab (kcal/mol) and standard deviation for MD calculations.

Uab	Average (Std. Dev)
zeaxanthin	-126.0 (4.2)
β -crtptoxanthin (OH out)	-110.8 (4.5)
β -cryptoxanthin	-107.0 (5.0)
β -carotene	-87.5 (4.3)

The distance between the water molecule coordinated with Fe(2+) and C8 is in a range of 2-4Å, the same occurs for C9 (Figure 2). Both distances are alternative one shorter than the other during all the MD simulations, so, depending on this parameter both double bonds can be aim of the cleavage when an O2 molecule is the one coordinated to Fe(2+). All the process may involve other parameters influencing the selective cleavage or unselective, these questions are those we hope could be clarified in next steps of our work.

Conclusions

These findings will be discussed considering the potential in vivo substrates and products, and the physiological role in citrus fruits.

Acknowledgments

The authors are grateful for the support given for PEDECIBA, CSIC, ANII and IBERCAROT.

References

1. Ohmiya, A., Kishimoto, S., Aida, R., Yoshioka, S., and Sumitomo, K. (2006) *Plant Physiol.* 142, 1193–1201.
2. Rubio-Moraga, A., Rambla, J.L., Fernández de Carmen, A., Traper-Mozos, A., Ahrazem, O., Orzáez, D., Granell, A., Gómez-Gómez, L. (2008) *J Biol Chem* 283(36): 24816–24825.
3. Rodrigo, M.J., Alquézar, B., Alós, E., Medina, V., Carmona, L., Bruno, M., Al-Babili, S., Zacarías, L. (2013) *Journal of Experimental Botany* 64(14): 4461–4478.
4. Kloer, D.P., Ruch, S., Al-Babili, S., Beyer, P., Schulz, G.E. (2005) *Science*. 308, 267-269.
5. MOE. Molecular Operating Environment (MOE 2007.09), Chemical Computing Group, Inc., Montreal, Quebec, Canada.
6. Harrison, P.J., Bugg, T.H.D. (2014) *Arch. Biochem. Biophys.* 554, 105-111.

Mauricio Vega-Teijido^{a,b},
Margot Paulino Zunini^a,
Carolina López^a & Maria J. Rodrigo^c

^aCeBioinfo, DETEMA, Facultad de Química, UdelAR

^bCCBG, DETEMA, Facultad de Química, UdelAR

^cLaboratorio Fisiología y Biotecnología Postcosecha Instituto de Agroquímica y Tecnología de Alimentos IATA-CSIC, Valencia, España.

Solving the Schrödinger Equation Using Anharmonic Potentials and a Variational Quantum Monte Carlo Method

Maurício G. Rodrigues, Régis C. Leal & Rogério Custodio

Introduction

Oscillators are important models in quantum systems because they are good approximation for different problems. The harmonic oscillator is the first approximation used for the vibrational spectroscopy models.^{1,2} In this model, Hooke's law defines the potential energy operator:

$$\hat{V}(x) = \frac{1}{2} kx^2 \quad (1)$$

where k is the force constant and depends on the nature of the bonded atoms and x is the vibration coordinate.

A more realistic model to describe molecular vibrations is given by the anharmonic oscillator. In this case, many different forms of analytical operators have been proposed. One of the most popular is the well-known Morse potential,¹

$$\hat{V}(x) = D_e(1 - e^{-\beta x})^2 \quad (2)$$

where D_e is the molecular dissociation energy and β is a parameter associated with the curvature of $V(x)$.

The potential operator can also be described from accurate quantum mechanical calculations. MRCI is among the quantum mechanical calculations able to describe the dissociation process as well as other spectroscopic constants in a very high level of accuracy. However, such methods are limited to be used in relatively small molecules. An interesting alternative to be applied in large system are the composite

methods. Such alternative correspond to a combination of well-defined ab initio calculations to achieve an accurate total energy at a low computational cost when compared to high level calculations. These methods have been applied successfully in the calculation of thermochemical properties.³⁻⁵ However, potential energy curves provided by such accurate methods have not been used to estimate spectroscopic properties.

The objective of this work is to explore potential curves of some diatomic molecules from a composite method to estimate spectroscopic constants. The composite method to be explored will be the Gaussian 3 theory or simply G3.6 In order to obtain the spectroscopic constants a new variational numerical procedure will be presented to solve the Schrödinger equation.

Methods

The general G3 energy is defined as:

$$E_{G3} = E[MP4/6-31G(d)] + \Delta E(+) + \Delta E(2df,p) + \Delta E(QCI) + \Delta E(G3large) + \Delta E(SO) + E(HLC) + E(ZPE) \quad (3)$$

Where the correction are: $\Delta E(+)$ for diffuse functions; $\Delta E(2df,p)$ for polarization functions; $\Delta E(QCI)$ for electronic correlation effects beyond fourth order perturbation theory using the method of quadratic configuration interaction; $\Delta E(G3large)$ for larger basis set effects and for the non-additivity caused by the assumption of basis set extensions for diffuse functions and higher polarization functions; spin-

orbit correction, $\Delta E(\text{SO})$, for atomic species only; E(HLC), higher level correction, added to take into account remaining deficiencies in the energy calculations and finally E(ZPE) the zero-point energy at 0 K and thermal effects. In the present work, E(ZPE) is not being included to describe the potential curves. All the calculations were performed by using Gaussian09 software⁷.

From the G3 potential curves the time independent Schrödinger equation was solved using a form of variational quantum Monte Carlo (VQMC) method. The one-dimension mean value energy of a system is described as:

$$E = \frac{\langle \psi | \hat{H} | \psi \rangle}{\langle \psi | \psi \rangle} = \frac{\langle \psi(x) | \hat{T}(x) + \hat{V}(x) | \psi(x) \rangle}{\langle \psi(x) | \psi(x) \rangle} \quad (4)$$

where the right side of Eq.(4) contains the kinetic (T) and potential operators (V).

The kinetic energy operator is a second order derivative which can be described numerically by⁸

$$\hat{T}\psi = \frac{1}{2\mu} \frac{d^2\psi}{dx^2} \cong \frac{1}{2\mu} \left[\frac{2}{h_i - h_{i-1}} \right] \left[\frac{\psi(x_{i+1}) - \psi(x_i)}{h_i} - \frac{\psi(x_i) - \psi(x_{i-1}))}{h_{i-1}} \right] \quad (5)$$

where i is the i-th component of a discretized wavefunction vector, μ is the reduced mass of the system and $h_i = x_{(i+1)} - x_i$. The potential energy operator will be described as set of discretized points obtained from the G3 calculation. After the application of the operators in an arbitrary and discretized wave function, Eq. (5) gives the energy of the system.

The systematic to get the result by VQMC is:⁹

- i. Generates a random vector to be the initial wave function.
- ii. Calculate the average energy using a discretized version of Eq.(4), Eq.(5) and the desired potential function.
- iii. Select at random a single point of the vector and modify its value according to the equation:

$$\psi(x_{i-1}) = \psi(x_i) + (1 - \text{rand})\delta \quad (6)$$

where rand is a random number generator with uniform distribution between zero and 1, and δ is a number which defines the range of change of the selected wave function.

- iv. Recalculate the energy with the modified wave function using Eq. (4). If the new energy is lower than the first one, the modification is accepted. If it is not, the previous

wave function is restored.

- v. The procedure is repeated until determined number of steps and/or the convergence factor is reached.

After the optimization of the ground state wave function, the first excited states can be obtained using the same procedure but preserving the orthogonality of the system. In this work the Gram-Schmidt method was used.¹⁰ The procedure is repeated to provide as many excited states as necessary.

After 106 steps of VQMC, an extra optimization of the meshes was carried out using the modified Simplex algorithm of Nelder and Mead¹¹.

Results and Discussion

The harmonic oscillator, which has the potential energy operator shown in Eq. (1), was used as an initial test case. The boundaries of the domains have been defined between ± 5 atomic units. The mass of the particle and the force constant have been set to 1 a.u. Table 1 shows ten states of the harmonic oscillators with 50, 125 and 200 points.

Table 1. The tenth firsts states for the harmonic oscillator. Energies are in atomic units.

State	50pts	125pts	200pts	Exact
E0	0.4987	0.4998	0.4999	0.5
E1	1.4934	1.4990	1.4996	1.5
E2	2.4823	2.4974	2.4990	2.5
E3	3.4672	3.4949	3.4982	3.5
E4	4.4463	4.4920	4.4981	4.5
E5	5.4196	5.4876	5.4972	5.5
E6	6.3896	6.4851	6.4981	6.5
E7	7.3582	7.4833	7.5021	7.5
E8	8.3347	8.4987	8.5240	8.5
E9	9.3420	9.5225	9.6037	9.5

As expected, increasing the number of the points yield more accurate energies which tends to the exact value. The accuracy is reduced for higher excited states. The more orthogonal functions are required from the calculations, the more pronounced is the error propagation.

Figure 1 shows the first three harmonic wave functions.

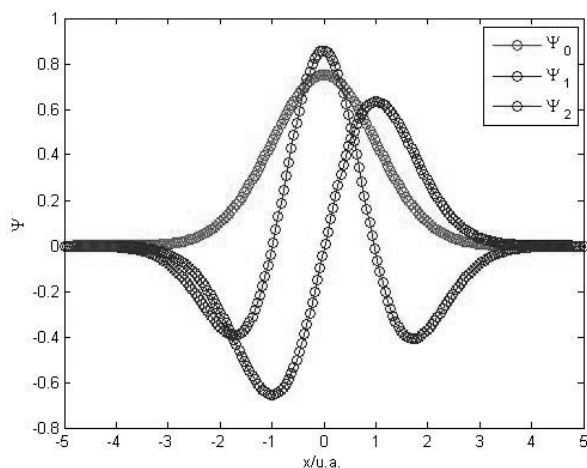


Figure 1. The three firsts wavefunctions of the harmonic oscillator.

The method generates not only accurate energies, but also well behaved wave functions as shown in Fig.1.

From the present uncertainty for harmonic oscillator, a mesh of 200 points will be used for the calculations involving the Morse and the G3 potentials. The reduced mass, dissociation energy and curvature for Morse's potential were taken from Herzberg,¹² as well as the experimental energies. The same domain of the Morse's potential has been used to calculate the energies from the G3 theory. All meshes were constructed firstly with few points which were increased by spline interpolation. Table 3 shows the vibrational energies for LiH, H₂, HF, HCl, HBr, O₂ and Cl₂ by Morse's potential, G3 energies and experimental results. All the data are in atomic units.

Table 2 shows that the error in energy increases with the increases of the state of energy. By comparison, the error of the zero-th state of the H₂ molecule, in Morse's potential, is 0.23%, while the fourth state is 3.0%. This enlargement of the error is explained by an error accumulation.

Some spectroscopic parameters were estimated by the equation:

$$E(n) = \tilde{\nu}_e \left(n + \frac{1}{2} \right) - \tilde{x}_e \tilde{\nu}_e \left(n + \frac{1}{2} \right)^2 \quad (7)$$

where $\tilde{\nu}_e$ is the fundamental frequency and $\tilde{x}_e \tilde{\nu}_e$ is the anharmonic constant. Table 3 shows the values of $\tilde{\nu}_e$ and $\tilde{x}_e \tilde{\nu}_e$ from the calculations using the Morse and G3 potential, plus the experimental value.

Table 2. The first five vibrational energies calculated from the Morse and G3 potentials and experimental results. The simulation were carried out with discretized wave functions containing 200 points. Energies are in atomic units.

	State	Morse	G3	Exp.12
LiH	E0	0.00317	0.00298	0.00317
	E1	0.00934	0.00880	0.00937
	E2	0.01528	0.01443	0.01535
	E3	0.02109	0.01985	0.02112
	E4	0.02720	0.02506	0.02668
H2	E0	0.00986	0.00990	0.00989
	E1	0.02871	0.02901	0.02884
	E2	0.04642	0.04688	0.04668
	E3	0.06297	0.06361	0.06341
	E4	0.08145	0.07921	0.07904
HF	E0	0.00931	0.00936	0.00932
	E1	0.03000	0.02744	0.02736
	E2	0.04443	0.04468	0.04458
	E3	0.06072	0.06111	0.06098
	E4	0.07614	0.07672	0.07656
HCl	E0	0.00674	0.00672	0.00675
	E1	0.01977	0.01972	0.01990
	E2	0.03222	0.03218	0.03256
	E3	0.04408	0.04409	0.04475
	E4	0.05554	0.05530	0.07365
HBr	E0	0.00596	0.00599	0.00598
	E1	0.01749	0.01762	0.01764
	E2	0.02847	0.02880	0.02889
	E3	0.03893	0.03953	0.03972
	E4	0.04889	0.04978	0.05014
O2	E0	0.00357	0.00356	0.00359
	E1	0.01057	0.01061	0.01067
	E2	0.01738	0.01756	0.01765
	E3	0.02402	0.02438	0.02453
	E4	0.03046	0.03108	0.03129
Cl2	E0	0.00127	0.00122	0.00128
	E1	0.00375	0.00363	0.00382
	E2	0.00616	0.00600	0.00638
	E3	0.00852	0.00834	0.00892
	E4	0.01174	0.01063	0.01148

Table 3. Numerical and experimental values of vibrational parameters, in cm⁻¹.

	$\tilde{\nu}_e$			$\tilde{x}_e \tilde{\nu}_e$		
	Morse	G3	Exp. ¹²	Morse	G3	Exp. ¹²
LiH	1342.9	1317.9	1405.6	19.12	42.92	23.20
H ₂	4406.6	4431.9	4401.2	132.2	129.1	121.3
HF	4132.7	4157.5	4138.3	94.45	95.43	91.68
HCl	2972.5	2978.8	2990.9	59.17	62.64	52.82
HBr	2642.0	2650.4	2649.0	57.41	48.44	45.22
O ₂	1577.8	1573.6	1580.2	20.40	12.44	11.98
Cl ₂	535.15	538.24	559.72	0.183	4.422	2.675

The calculated constants show that the errors do not follow a regular behavior. It implies that there are some situations that the Morse's potential fits better than G3, but this is not a rule.

Conclusions

The simulations performed in this work reveal that the present version of the variational principle associated with a Monte Carlo search is an accurate method to generate vibrational energies and well-behaved wave functions. The calculated spectroscopic parameters were usually considerably close to the experimental data with a small error. The approximate nature of both potentials tested may be pointed out as responsible for the deviations. Tests considering rigorous potential curves are under progress.

Acknowledgments

The authors are grateful for the financial support given from CAPES, CNPQ, FAPESP and FAEPEX-UNICAMP.

References

1. F.L. Pilar. Elementary Quantum Chemistry. Mineola: Dover Publications SA, 2nd edition, **2001**.
2. D.A. McQuarrie, J.D.Simon. Physical Chemistry: A Molecular Approach. New Delhi: Viva Books, **2013**.
3. D. H. Pereira, A. F. Ramos, N. H. Morgon, and R. Custodio, J. Chem. Phys. 135, 034106 (**2011**).
4. D. H. Pereira, A. F. Ramos, N. H. Morgon, and R. Custodio, J.

Chem. Phys. 135, 219901 (**2011**).

5. C. M. R. Rocha, D. H. Pereira, N. H. Morgon, and R. Custodio, J. Chem. Phys. 139, 184108 (**2013**).
6. Larry A. Curtiss, Krishnan Raghavachari, Paul C. Redfern, Vitaly Rassolov, and John A. Pople. Journal Chemical Physics 109, 7764 (**1998**).
7. M. J. Frisch, G. W. Trucks, H. B. Schlegel, G. E. Scuseria, M. A. Robb, J. R. Cheeseman, G. Scalmani, V. Barone, B. Mennucci, G. A. Petersson, H. Nakatsuji, M. Caricato, X. Li, H. P. Hratchian, A. F. Izmaylov, J. Bloino, G. Zheng, J. L. Sonnenberg, M. Hada, M. Ehara, K. Toyota, R. Fukuda, J. Hasegawa, M. Ishida, T. Nakajima, Y. Honda, O. Kitao, H. Nakai, T. Vreven, J. A. Montgomery, Jr., J. E. Peralta, F. Ogliaro, M. Bearpark, J. J. Heyd, E. Brothers, K. N. Kudin, V. N. Staroverov, T. Keith, R. Kobayashi, J. Normand, K. Raghavachari, A. Rendell, J. C. Burant, S. S. Iyengar, J. Tomasi, M. Cossi, N. Rega, J. M. Millam, M. Klene, J. E. Knox, J. B. Cross, V. Bakken, C. Adamo, J. Jaramillo, R. Gomperts, R. E. Stratmann, O. Yazyev, A. J. Austin, R. Cammi, C. Pomelli, J. W. Ochterski, R. L. Martin, K. Morokuma, V. G. Zakrzewski, G. A. Voth, P. Salvador, J. J. Dannenberg, S. Dapprich, A. D. Daniels, O. Farkas, J. B. Foresman, J. V. Ortiz, J. Cioslowski, and D. J. Fox, Gaussian 09, Revision B.01, Gaussian, Inc., Wallingford CT, (2010).
8. B. Carnahan, H.A. Luther, J.O. Wikes. Applied Numerical Methods. New York: John Wiley & Sons, **1969**.
9. R. Custodio, M.R. Custodio, E.J. Creatto. Quim. Nova, 35, 2076, (**2012**).
10. R. Custodio. Quim. Nova, 9, 89, (**1987**).
11. J. A. Nelder and R. Mead, Comput. J. 7, 308 (**1965**).
12. K.P. Huber, G. Herzberg. Molecular Spectra and Molecular Structure IV. New York: Van Nostrand Reinhold Company, **1978**.

Maurício G. Rodrigues^a,
Régis C. Leal^{a,b} & Rogério
Custodio^a

^aUniversidade Estadual de Campinas (UNICAMP), 13083-970, Campinas – SP, Brazil.

^bInstituto Federal de Educação, Ciência e Tecnologia do Rio Grande do Norte (IFRN), Campus Nova Cruz, 59215-000, Nova Cruz-RN, Brazil.

Estudo de Acoplamento Molecular e NBO das Interações entre a Molécula 5-FU e o Alvo Biológico HER-2

Michell O. Almeida, Daiane A. S. Barros, Sheila C. Araújo,
Sergio H. D. M. Faria & Kathia Maria Honório

Introdução

O câncer é uma doença que atualmente afeta grande parte da população. Essa doença crônica tem como características a proliferação e o crescimento celular rápido e descontrolado. A cada ano, o número de casos de câncer aumenta e devido a este fato, diversos estudos vêm sendo realizados com o intuito de tratar o câncer¹. Alguns estudos mostram que existem diversos alvos biológicos relacionados a essa enfermidade. Um desses alvos é o receptor tipo 2 do fator de crescimento epidérmico humano (HER-2), sendo que a amplificação do gene faz com que haja produção excessiva da proteína contribuindo, assim, para a progressão do câncer². Desta forma, busca-se inibir essa proteína. Uma molécula utilizada em estudos sobre o câncer é a 5-FU (5-fluorouracil)³. Desta forma, neste trabalho foram utilizados os seguintes métodos computacionais: acoplamento molecular, cálculos quânticos em meio solvatado (para validar os métodos teóricos) e cálculos NBO⁴ (orbitais naturais de ligação), tendo como objetivo estudar as possíveis interações que ocorrem entre a molécula 5-FU e sítio ativo de HER-2.

Método

O acoplamento molecular foi realizado utilizando o programa GOLD, tendo como intuito inserir a molécula 5-FU no sítio ativo de HER-2 (PDB 3PP0) e analisar as interações intermoleculares entre 5-FU e HER-2. Após a análise do acoplamento, foram realizados cálculos da molécula 5-FU em solvente dioxano (métodos IEFPCM e Osanger), pois a comparação dos valores dos momentos de dipolo teóricos e experimentais ($4,11 \pm 0,5$ Debye, D⁵) é utilizada para

escolher e validar as funções de bases a serem selecionadas (B3LYP/6-31G (2d,2p) e B3LYP/cc-pVDZ) para o cálculo dos orbitais naturais de ligação (NBO). O cálculo NBO teve o intuito de analisar as interações de orbitais aceptores e doadores da molécula 5-FU e dos resíduos ASP-863 e PHE-864 (resíduos que fazem interações de ligação de hidrogênio com 5-FU, mostradas pelo acoplamento molecular).

Resultados e Discussão

A Figura 1 ilustra a interação intermolecular (ligação de hidrogênio) entre 5-FU e o sítio ativo de HER-2 (resíduos ASP-863 e PHE-864).

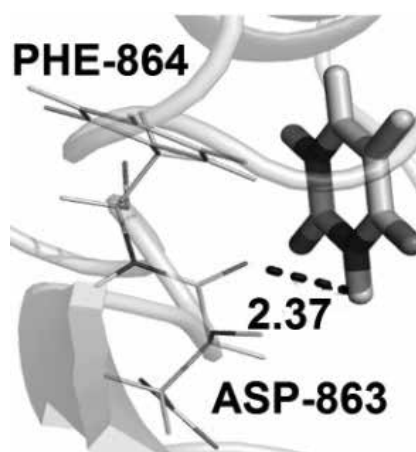


Figura 1. Análise do acoplamento molecular da estrutura 5-FU no sítio ativo de HER-2 (PDB 3PP0).

Após as análises do acoplamento, foram realizadas comparações dos valores de momento de dipolo teórico e experimental (Tabela 1).

Tabela 1. Valores teóricos de momento de dipolo para 5-FU em solvente dioxano, comparados com o valor experimental ($4,11 \pm 0,5$ D)

B3LYP	PCM	Osanger
6-31G(2,2p)	4,35	4,17
cc-pVDZ	4,35	4,15

Os resultados mostram que ambas as funções de base são válidas para cálculos computacionais, sendo que a próxima etapa foi a realização da análise NBO, que se encontra na Figura 2 e Tabela 2.



Figura 2. Estruturas de 5-FU, ASP-863 e PHE-864 utilizadas na análise NBO.

Tabela 2. Análise NBO para a molécula 5-FU*

NBO Doador	NBO Aceitador	ΔE^2 (kcal/mol)	
5-FU para ASP-863 e PHE-864			
LP N1	RY* O16	0,84	cc-pVDZ
LP N1	RY* O16	1,17	6-31G(2d,2p)
ASP-863 e PHE-864 para 5-FU			
LP O16	BD*(π) C3-O9	5,43	cc-pVDZ
LP O16	BD*(π) C3-O9	4,47	6-31G(2d,2p)

BD (Ligante), BD (Anti-ligante), LP (Lone Pair, par solitário) e RY* (Rydberg anti-ligante).

A Tabela 2 apresenta as interações de transições eletrônicas que ocorrem entre os orbitais aceptores e doadores NBO de 5-FU e dos resíduos ASP-863 e PHE-864 e também mostra o valor da energia perturbativa de segunda ordem, a qual estabiliza esse sistema doador-aceitador. Nota-se que para ambas as funções de base, o maior valor de transição eletrônica que ocorre é entre os resíduos ASP-863 e a molécula 5-FU. Sendo assim, os resultados apresentados sugerem uma transferência do par de elétrons do átomo O16 para os orbitais anti-ligantes BD*(π) C4-O7, indicando um mecanismo de reação entre ASP-863 e 5-FU.

Conclusões

Os métodos empregados neste estudo de modelagem molecular, tais como cálculo teórico da molécula 5-FU em solvente, acoplamento molecular e a análise dos orbitais de naturais de ligação (NBO), fornecem dados significativos para o planejamento de novas substâncias, candidatas ao tratamento do câncer. Os resultados obtidos no acoplamento molecular indicam possíveis interações que podem ocorrer entre o composto 5-FU e resíduos do sítio ativo de HER-2, onde se notou que o composto interage com o resíduo de aminoácido ASP-863. Os resultados obtidos dos cálculos de 5-FU em solvente se mostraram próximos dos valores experimentais, sendo que os métodos escolhidos para o cálculo NBO são válidos. Por fim, os resultados obtidos pela técnica NBO foram capazes de indicar a interação intermolecular que ocorre entre os orbitais aceptores e doadores de elétrons do composto 5-FU e dos resíduos de aminoácido ASP-863 e PHE-864, sendo que essas informações são de extrema importância no estudo das interações desses compostos com o sítio ativo de HER-2.

Agradecimentos

Os autores são gratos pelo apoio dado pela FAPESP, UFABC, CAPES e CNPq.

Referências

1. T. L. Lemke, D. A. Williams, V. F. Roche, S. W. Zito. Foye's principles of medicinal chemistry. 6 ed.; Lippincott Williams & Wilkins (2008).
2. I. Kümler, M. K. Tuxen, D. L. Nielsen. Cancer Treat. Rev. 40 (2), 259, (2014).

3. E. T. H. Yeh, C. L. Bickford. J. Am. Coll. Cardiol, 53 (24), 2231, (2009).
4. J. P. Foster, F. Weinhold, J. Am. Chem. Soc, 102, 7211, (1980).
5. I. Kulakowska, M. Geller, B. Lesyng, K. L. Wierzchowski. Dipole moments of 2,4-diketopyrimidines: Biochim. Biophys. Acta, 361 (2), 119 (1974).

Michell O. Almeida^a, Daiane
A. S. Barros^b, Sheila C.
Araújo^a, Sergio H. D. M.
Faria^{c,d} & Kathia Maria
Honório^{a,b}

^aCentro de Ciências Naturais e Humanas - UFABC

^bEscola de Artes, Ciências e Humanidades – USP

^cInstituto de Química, Universidade Estadual de Campinas

^dInstituto de Ciências da Saúde, Universidade Paulista, Campinas-SP

Effect of the Methyl Group on the Stability and Twisting of Flavonoids

Milene A. R. de Oliveira, Keylla U. Bicalho & João B. Fernandes

Introduction

Flavonoids is a class of phytochemicals/phytonutrients originated from polyphenols of low molecular weight found in several plants¹. They present good effects on human health such as active role on sickness healing. These compounds are classified as the most important natural colorants and flavors besides presenting a wide range of biological activities, highlighting the anti-inflammatory² and antioxidant³ properties. They are found in hydro and liposoluble forms, and as aglycones (without sugar units) or glycosides flavonoids^{4,5,6}.

Some great sources of flavonoids are the seeds and fruits of plants from the Leguminosae and Compositae families⁷. More than 5000 flavonoids have been identified in the nature and classified according to their chemical structure. This class of compounds is subdivided in 9 subgroups: flavones, flavonols, flavanones, flavanes, isoflavones, anthocyanins, flavanonols (flavan-3-ol or catechins), chalcones and dihydrochalcones

The computational chemistry is a powerful tool that can help better understanding some of the doubts questioned in this work. With the advance of the computational chemistry, is even more needed and easy to explain some experimental observations based on the quantic chemistry⁸ from many studies found on literature^{9,10,11-14}. This kind of study provides valuable information at low costs, that allows to understand the effect of the different structural features of the compounds. Some theoretical studies about a great variety of flavonoids were published¹², where some of them

focus on the energetic properties of these compounds and the effect of the hydroxyl groups on the structure.

In this perspective, this work presents the results from a study of four glycoside flavones. Figure 1 shows the representation of the general structure for flavonoids, including the ones discussed in this research. This molecular structure is characterized by charge delocalization on the studied molecules from ring A to B trough C due to the double bond C2-C3. Then, the main question of this work is to understand how the presence of the methyl group affects the charge delocalization and how it is related to the geometrical and molecular parameters and the molecular energy, as well as the twisting profiles around the C2-C1' bond and its effect on rotation properties of cathecol (ring B). The intramolecular hydrogen bonds will also be studied. Density Functional Theory (DFT) was applied in this work since it provides confident results between the precision and computational requirements, considering the compounds studied and its properties.

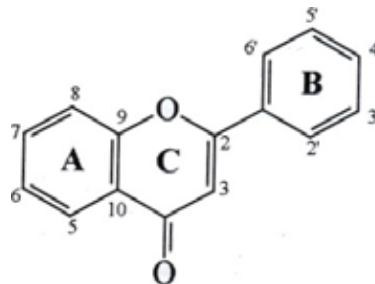


Figura 1. Molecula skeleton of flavone showing atoms numeration and named rings.

The flavones have the same basic structure derived from the original molecule presented in Figure 1 and the optimized structures for the compounds I-IV studied in this work are presented in Figure 2. In these compounds, the methyl, glucosyl and hydroxyl groups are alternating in the positions 3 and 7.

Computational Methods

DFT calculations were performed with the Gaussian 0515 pack according to the Density Functional Theory, using the exchange of corrected functional gradient of Becke16 and Lee-Tang-Parr functional correlations17. For these parameters, the B3LYP method was used18. The set of bases 6-311 ++G ** was used for the calculations presented in this work. The atomic charges, bonds length and dihedral angles were calculated for the optimized structures in gas phase and in vacuum.

Results and Discussion

STRUCTURAL FEATURES

The optimizations of the four structures presented in Figure 2 were performed and the intramolecular hydrogen bonds in the structures and the main molecular parameters are showed in Table 1.

As discussed in Santiago Aparício work20, the dihedral angle between ring B and the plane formed by rings A and C is about 20° for flavones without the hydroxyl group and 0° for the ones with hydroxyl group at position 3. In our results is observed that both structures with the methyl group presented a dihedral angle, between the plane of the rings A-C and B (C3-C2-C1'-C2') of -71,36° (Structure I) e 0,49° (Structure II), and the structures with the hydroxyl, -23,18° (Structure III) and -0,05° (Structure IV).

The values obtained indicate that the glucosyl group present on structures at position 3, confirms the significant change in the dihedral angle. This observation can also be explained by the intramolecular hydrogen bonds present in these molecules. On structure I, the hydrogen bond between the hydroxyl hydrogen 7 at the glucosyl group with the oxygen at position 2' from ring B, can justify the non-coplanarity between these rings, once this bond is 1.85341 Å, which is considered as strong bond21. On structure II

the rings are almost coplanar and that is explained by the hydrogen bond between the oxygen bonded to methyl at position 3 and the hydrogen at position 2' from B ring, where the distance is 2.29746 Å

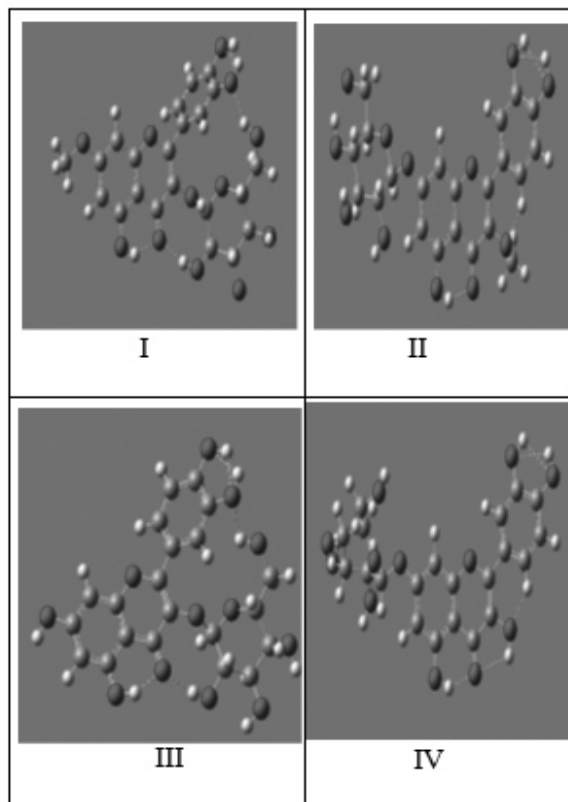


Figure 2 – Optimized structures of the studied flavones I-IV from the calculation in gas phase on B3LYP//6-311 ++ G ** theoretical level, with indication of the hydrogen bonds. Atom Colour code: Oxygen (red), carbon (grey) and hydrogen (white).

For structures III and IV, that have the hydroxyl changing by glucosyl, follows the same tendency of III that has the sugar unit at position 3, the B ring has a small rotation due to the hydrogen bond between the hydroxyl hydrogen 7 at glucosyl unit with the oxygen at position 2' at B (1.91915 Å), and for structure IV, the rings can be considered coplanar, where the intramolecular bond between the hydrogen at position 2' and the oxygen at position 3 is considered strong (1.79635 Å). Table 2 shows

the intramolecular hydrogen bonds on these structures.

In terms of stability, is observed that when the glucosyl in the molecule is at position 3, it is more stable than its correspondent at position 7. Since the atom of C, O and H has a contribution of -38.2792077 a.u., -74.46309364 a.u and -0.56119365 a.u, respectively, for the stabilization energy of a molecule (not considering the contributions from hydrogen bonds, radicals and ions), it is possible to compare the stabilization of the four structures (I-IV).

Atom numeration as Figure 1. Interatomic distances, r in Å; dihedral angles, τ , in degrees; energy E in a.u.; dipole moment, μ , in D.

Table 1. Main geometrical and energetic parameters from the studied flavones I-IV in gas phase calculated in the B3LYP / 6-311 ++ G ** theoretical level.

Structure	r C4=O	r 3-OH	r 5-OH	r 3'-OH	r 4'-OH
I	1.235	--	0.975	0.961	0.959
II	1.230	--	0.965	0.961	0.941
III	1.263	--	0.994	0.966	0.969
IV	1.234	0.951	0.985	0.963	0.968

Table 2 – Intramolecular hydrogen bonds in Å.

Structures	C2'H-O3	O3'H-O4'	O4'H-O3'	O5H-O4
I	3.30500	2.50884	2.50348	1.81243
II	1.80116	2.49596	2.49636	1.81245
III	3.17287	2.15164	2.18359	1.691006
IV	1.79594	2.49790	2.49531	1.82113

Table 3 - Huckel charge calculated by the B3LYP method with base 6-311 ++ G ** for I-IV

Structures	C4=O	C3-O	C5-O	C7-O	C4'-O
I	0.602	0.556	0.554	0.516	0.547
II	0.571	0.544	0.558	0.527	0.549
III	0.609	0.550	0.557	0.542	0.568
IV	0.594	0.544	0.559	0.531	0.550

Therefore, removing one CH₂ group from the structures I and II, it is obtained an energy of -1714.90063333 a.u and -1714.8854695 a.u, respectively. The comparison of the four calculated energies for I-IV, we can conclude that having a hydroxyl group (structure III) instead of a methyl group results in a more stable molecule, which agrees with the lower dipole moment for this structure. The Table 3 shows the Hückel charges, and it can be observed that the most electronegative atom is the carbonyl oxygen and that on the structure III the charge is bigger. The crescent order for these oxygens from the structures would be III>I>IV>II. This crescent order for the Hückell charge on the carbonyl oxygen is equivalent to the crescent order of the stability of the studied structures, confirming that the structures with the glucosyl at position 3 is more stable than when it is at position 7, regardless if they have hydroxyl or an methyl group at position 7.

Conclusions

It can be concluded from this work that the methyl group decreases the stability on the studied structures, either if they are at 3 or 7 position, but the structures with the glucosyl at position 3 are more stable than when the glucosyl is at position 7, no matter if it has a hydroxyl or a methyl group. It can also be concluded that the methyl group does not influence on the ring B twisting, once it is connected with an oxygen that has an intramolecular bond with the hydrogen at position 1' at ring B. On the other hand, when the flavone has the glucosyl unit at position 3, the tendency is that the planarity of ring B in relation to the ring A-C does not occurs. The Hückel charge has a linear relationship with the stability of the studied structures.

Acknowledgments

The authors are grateful for the support given from the FAPEG, CAPES, CNPQ and FINATEC.

References

- SIMÕES, C. M. O. (organizadora). Farmacognosia: da planta ao medicamento. Porto Alegre/Florianópolis: Ed. Universidade / UFRGS/Ed. da UFSC (2000).
- PATHAK, D.; PATHAK, K.; SINGLA, A.K. Flavonoids as

- medicinal agents: recent advances. *Fitoterapia*, 57, 371(1991).
3. RICE-EVANS, C.A.; MILLER, N.J.; BOLWELL, G.P.; BRAMLEY, P.M.; PRIDHAM, J.B. The relative antioxidant activities of plant derived polyphenolic flavonoids. *Free Radical Res.* 22, 375 (1995).
 4. TREASE, G.E.; EVANS, W.C. Phenols and phenolic glycosides. In: *Pharmacognosy* 14.ed. London: W.B. Saunders, 218 (1996)
 5. YAO, L.H.; JIANG, Y.M.; SHI, J.; TOMÁS-BARBERÁN, F.A.; DATTA, N.; SINGANUSONG, R.; CHEN, S.S. Flavonoids in food and their health benefits. *Plant Foods Hum. Nutr.* 59, 113(2004)
 6. Acker, S.A.B.E.V.; Berg, D.J.V.B.; Tromp, M.N.J.L.; Griffioen, Bennekom, W.P.V.; Vijgh, W.J.F.V.D.; Bast, A. Structural aspects of antioxidant activity of flavonoids. *Free Radical Biol. Med.* 20, 331(1996).
 7. Cramer, C. J.; *Essentials of Computational Chemistry: Theories and Models*, 2a ed., Wiley: Chichester, (2004).
 8. van Acker, S.A.B.; de Groot, M.J.; van der Berg, D.J.; Tromp, M.N.; Donne, G.; Wim, F.J.; van der Vijgh, W.J.F.; Bast, A. A quantum chemical explanation of the antioxidant activity of flavonoids. *Chem. Res. Toxicol.* 9, 1305(1996).
 9. van Acker, S.A.B.; de Groot, M.J.; van der Berg, D.J.; Tromp, M.N.; Griffen, D.H.; van Bennekom, W.P.; van der Vijgh, W.J.F.; Bast, A. Structural aspects of antioxidant activity of flavonoids. *Free Radical Biol. Med.* 20, 331(1996).
 10. Antonczak, S. Electronic description of four flavonoids revisited by DFT method. *J. Mol. Struc. Theochem.* 856, 38(2008).
 11. Lameira, J.; Alves, C.N.; Moliner, V.; Silla, E. A density functional study of flavonoid compounds with anti-HIV activity. *Eur. J. Med. Chem.* 41, 616(2006).
 12. Leopoldini, M.; Marino, T.; Russo, N.; Toscano, M. Density functional computations of the energetic and spectroscopic parameters of quercetin and its radicals in the gas phase and in solvent. *Theor. Chem. Acc.* 111, 210(2004).
 13. Mendoza, A.M.; Glossman, D. CHIH-DFT determination of the molecular structure; infrared and ultraviolet spectra of the flavonoid querdetin. *J. Mol. Struc.-Theochem.*, 681, 71 (2004).
 14. Olejniczak, S.; Potrzebowski, M.J. Solid state NMR studies and density functional theory (DFT) calculations of conformers of quercetin. *Org. Biomol. Chem.*, 2, 2315(2004).
 15. Frisch, M.J.; Trucks, G.W.; Schlegel, H.B.; Scuseria, G.E.; Robb, M.A.; Cheeseman, J.R.; Montgomery, J.A., Jr.; Vreven, T.; Kudin, K.N.; et al. *Gaussian 03 (Revision C.02)*; Gaussian Inc.: Wallingford, CT, USA, (2004).
 16. Becke, A.D. Density-functional exchange-energy approximation with correct asymptotic behavior. *Phys. Rev. A*, 38, 3098(1988).
 17. Lee, C.; Yang, W.; Parr, R.G. Development of the Colle-Salvetti correlation-energy formula into a functional of the electron density. *Phys. Rev. B*, 37, 785(1988).
 18. Becke, A.D. Density-functional thermochemistry. III. The role of exact exchange. *J. Chem. Phys.*, 98, 5648(1993).
 19. Besler, B.H.; Merz, K.M.; Kollman, P.A. Atomic charges derived from semiempirical methods. *J. Comput. Chem.*, 11, 431–439 (1990).
 20. Aparicio, S.; A Systematic Computational Study on Flavonoids. *Int. J. Mol. Sci.*, 11, 2017(2010).
 21. Rodrigues, J.A.R.; Ligações Hidrogênio fortes em ácidos dicarboxílicos e diaminas aromáticas. *Quím. Nova* 23, 812, (2000).

Milene A. R. de Oliveira*,
Keylla U. Bicalho & João B.
Fernandes

Departamento de Química. Universidade Federal de São Carlos. São Carlos, SP.

*E-mail: mileneoli1@hotmail.com

Aspectos Moleculares da Solvatação do Íon Fluoreto em Água e DMSO

Natália M. Silva & Josefredo R. Pliego Jr.

Introdução

O efeito do solvente é essencial na descrição de reações em solução, principalmente reações iônicas. No caso de reações do tipo ion-molécula, é necessário a solubilização de ambos o substrato orgânico e o íon inorgânico. Solventes como água e metanol usualmente tem uma forte solvatação de ânions, tornando sua reatividade muito baixa. A introdução dos solventes apróticos dipolares há mais de 50 anos atrás permitiu a solubilização de sais inorgânicos e dos compostos orgânicos simultaneamente. Ao mesmo tempo, a menor solvatação dos ânions nestes solventes levou a uma maior reatividade destes.¹

Apesar da importância deste efeito bem conhecido dos solventes apróticos dipolares, com sua larga aplicação em química orgânica sintética, e da publicação de escalas de solvatação,^{2,3} os aspectos moleculares da diferença de solvatação de ânions pequenos como o fluoreto em água e DMSO não foi investigada ainda. Neste trabalho foram feitos cálculos de energia em nível MP2 utilizando moléculas de água como solvente prótico e moléculas de dimetilsulfóxido (DMSO) como solvente aprótico dipolar para solvatar o íon fluoreto. Nosso objetivo foi entender a primeira camada de solvatação, que é essencial para descrever reatividade química em solução.⁴

Metodologia

Os complexos formados pelo íon fluoreto e moléculas de água ou DMSO foram investigados em nível ab initio. As geometrias foram otimizadas utilizando o método

MP2 com bases aug-cc-pVDZ. Após otimização de geometria, foram feitos cálculos da energia no ponto, também em nível MP2, mas utilizando uma base mais estendida, aug-cc-pVTZ.

Resultados e Discussões

A energia de interação do íon fluoreto com uma molécula de água é de -31,88 kcal/mol. Com adição de mais moléculas de água, a energia de formação do cluster vai se tornando mais negativa, apesar de que a cada nova molécula adicionada, a energia diminui menos, o que já era esperado. Com 4 moléculas de água, o cluster é estável por -85,05 kcal/mol. As estruturas estão mostradas na Figura 1. Como podemos observar, metade do íon fluoreto fica completamente solvatado por 4 moléculas de água.

Tabela 1: Dados de energia para formação dos clusters do íon Fluoreto com solvente prótico H₂O, e aprótico DMSO, em nível de cálculo MP2/aug-cc-pVTZ//MP2/aug-cc-pVDZ.*

	□E
F ⁻ (H ₂ O)	-31,88
F ⁻ (H ₂ O) ₂	-52,34
F ⁻ (H ₂ O) ₃	-69,27
F ⁻ (H ₂ O) ₄	-85,05
F ⁻ (CH ₃ SOCH ₃)	-32,79
F ⁻ (CH ₃ SOCH ₃) ₂	-55,72

*Valores em kcal/mol

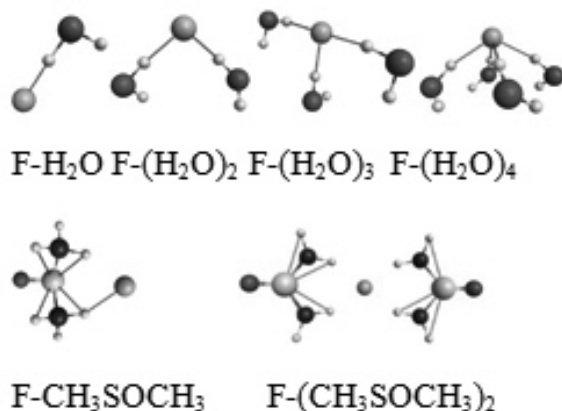


Figura 1: Complexos do íon fluoreto com água e DMSO.

Para complementar a argumentação de que o tamanho das moléculas do solvente tem um papel importante na energia livre de solvatação, observamos que cada um dos clusters com 2 DMSO e 4 águas terão ainda de ser solvatados pelo restante do solvente. Considerando o modelo de Born, cuja energia livre de solvatação por um dielétrico é dada por:

$$\Delta G_{\text{sol}} = -\frac{1}{2} \frac{1}{4\pi\epsilon_0} \frac{q^2}{R} \left(1 - \frac{1}{\epsilon}\right)$$

notamos que a energia livre de solvatação é inversamente proporcional ao tamanho do íon (R , raio do íon). Ou seja, o cluster de fluoreto com 4 moléculas de água deveria ser melhor solvatado do que com 2 moléculas de DMSO.

Tabela 2: Dados da Análise da Decomposição de Energia (EDA) para os complexos, em nível de cálculo MP2, todos calculados com conjunto de função de base aug-cc-pVTZ.*

	Eletrostática	Troca-Repulsão	Polarização	Dispersão
$(\text{H}_2\text{O}) \text{F}^-$	-44,02	40,91	-26,99	-1,78
$(\text{H}_2\text{O})_2 \text{F}^-$	-72,46	57,41	-33,39	-3,90
$(\text{H}_2\text{O})_3 \text{F}^-$	-96,05	67,63	-35,07	-5,78
$(\text{H}_2\text{O})_4 \text{F}^-$	-117,32	74,9	-32,53	-10,10
$\text{F}^-(\text{CH}_3\text{SOCH}_3)$	-40,51	33,97	-22,92	-3,33
$\text{F}^-(\text{CH}_3\text{SOCH}_3)_2$	-67,11	48,25	-31,04	-5,82

Com o intuito de compreender melhor a natureza das interações moleculares nestes complexos, fizemos também cálculos EDA (Energy Decomposition Analysis).⁵ A energia eletrostática para o cluster do fluoreto com moléculas de água torna-se cada vez mais negativa ao se adicionar mais moléculas de água, ao passo que sua energia de troca-repulsão torna-se cada vez mais positiva. Entretanto, enquanto a energia eletrostática aumenta por um fator de 2,7, a contribuição de troca-repulsão aumenta por um fator de apenas 1,8. Isto pode ser explicado pelo aumento da distância entre o fluoreto e os hidrogênios, que inicia em 1,414 Å com uma água até 1,713 Å com quatro águas, aliviando assim o termo de troca-repulsão, de curto alcance.

No caso do termo de polarização, que chega a ser 61% da interação eletrostática com uma molécula de água, é evidente a forte polarização da água pelo pequeno íon fluoreto. Este termo apresenta uma variação pequena com o aumento das águas, indo de -27,0 kcal/mol com uma água e atingindo um valor mais negativo com três moléculas de água, -35,07 kcal/mol. Esta contribuição se torna -32,53 kcal/mol com quatro águas. Este mínimo pode ser explicado pelo arranjo das moléculas de água, onde a simetria de quatro águas em torno do fluoreto inibe a polarização maior em uma direção. Além disso, o aumento da distância das moléculas de água ao fluoreto gera um campo elétrico menor nas águas, e portanto, menor polarização. A energia de dispersão segue a tendência esperada de aumentar (mais negativa) com a quantidade de elétrons no sistema.

Nos clusters do fluoreto com moléculas de DMSO, a tendência nas energias é bem mais previsível. Comparando com o cluster de água, vemos que as energias eletrostática e de polarização são de menor magnitude com DMSO, mas os termos de troca-repulsão também. Isto ocorre pelo fato do DMSO ficar bem mais distante do fluoreto do que a água. Por exemplo, no complexo do fluoreto com apenas uma molécula de DMSO a distância hidrogênio-fluoreto é de 1,821 Å e com duas moléculas de DMSO é de 1,929 Å. Como consequência, o termo de troca-repulsão é menor, e os termos eletrostáticos e de polarização são menos negativos.

Conclusão

A interação do íon fluoreto com uma ou duas moléculas de DMSO é mais negativa do que sua interação com uma ou duas moléculas de água, desafiando a visão de que ânions interagem fracamente com DMSO. Entretanto, o fato de a molécula de DMSO ser bem maior do que a molécula de água leva a uma interação mais forte do F⁻ com a primeira camada de solvatação de água do que com a primeira camada de solvatação de DMSO. Como consequência, o fluoreto é muito mais solvatado em meio aquoso do que em DMSO, levando a sua maior reatividade em DMSO.

Agradecimentos

Os autores agradecem ao CNPq e a FAPEMIG.

Referências

1. A.J. Parker, Chem. Rev. 69 (1969) 1.
2. J.R. Pliego, E.L.M. Miguel, J. Phys. Chem. B 117 (2013) 5129.
3. .R. Pliego Jr, J.M. Riveros, Phys. Chem. Chem. Phys. 4 (2002) 1622.
4. .R. Pliego Jr, J. Phys. Chem. B 113 (2009) 505.
5. P. Su, H. Li, J. Chem. Phys. 131 (2009) 014102.

Natália M. Silva* & Josefredo
R. Pliego Jr.

Departamento de Ciências Naturais, Universidade Federal de São João
del-Rei

*E-mail: natalia.more.silva@gmail.com

Glucose-6-Phosphate Dehydrogenase as Potential and Selective Target Against Malaria

Nelson A. N. de Alencara, Jordi Jimenez Juarez, Jeronimo Lameira Silva & Javier Luque Garriga

Introduction

Science does not have a magic formula for malaria, *Plasmodium* parasites are developing unacceptable levels of resistance and many insecticides are no longer useful against mosquitoes that transmit the disease. Years of vaccine research have produced few hopeful candidates and although scientists are redoubling the search, an effective vaccine is years away.¹ In response to this difficult situation, which in this study, we explored the pentose phosphate pathway of the malaria parasite *Plasmodium falciparum* (pf), in particular the Glucose-6-Phosphate Dehydrogenase enzyme (G6PD), in order to find a new potential therapeutic target and new alternative drugs.²

Methods

Was constructed the three dimensional structure of the enzyme pfG6PD using molecular homology modeling, with the MODELLER³ program and human enzyme in the same structure as a mold.

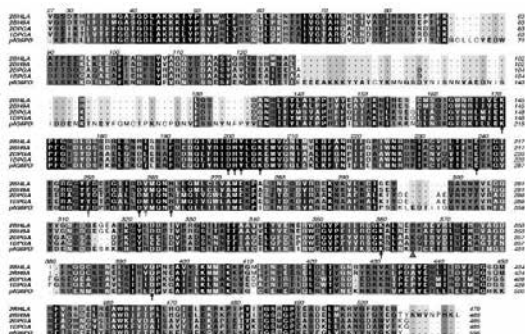


Figure 1. Multiple Align between pfG6PD and templates. Arrows show the active site. The red triangle presents most important residue for this study. The accentuated residues with blue were cut off for humanize the plasmodium.

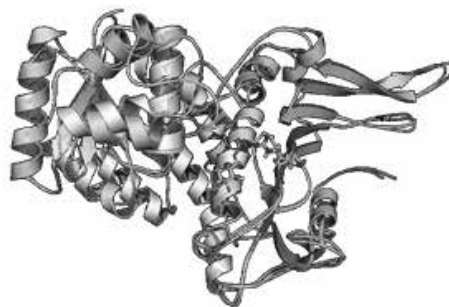


Figure 2. 3D Alignment between hG6PD and pfG6PD humanized hG6PD in Green cartoon, pfG6PD in yellow Cartoon and G6P in stick white. The key residue in this study is displayed under stick.

From the structural change of a single residue of the active site between the two enzymes (Arg365-h/Asp575-pf), were proposed and complexed six selective inhibitors of the pfG6PD enzyme. Then studies of molecular dynamics (MD) using the method of molecular mechanics (MM) via the program AMBER⁴ and binding free energy calculations using the SIE⁵ method (solvated interaction energy). Time of Dynamic was 100 ns.

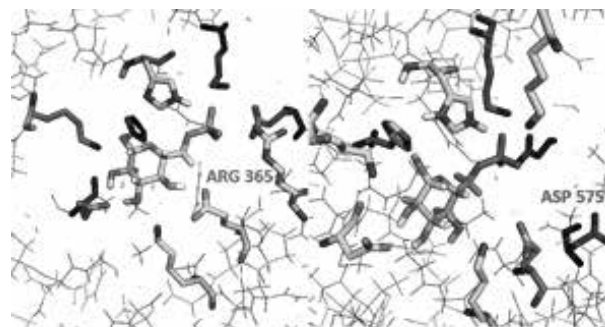


Figure 3. Active site of hG6PD and pfG6PD models complexed with G6P ligand, Show the structural change of a single residue of the active site Arg365-h (in Blue) and Asp575-pf (in Red)

Results and Discussion

Results showed that the proposed model is satisfactory, both structurally and energetically, the mean values of free energy (SIE) for hG6PD and pfG6PD were -7.46 and -7.71 kcal/mol, respectively, compatible with the literature,² and site active well maintained with RMSD never exceeding 3 Å for pfG6PD.

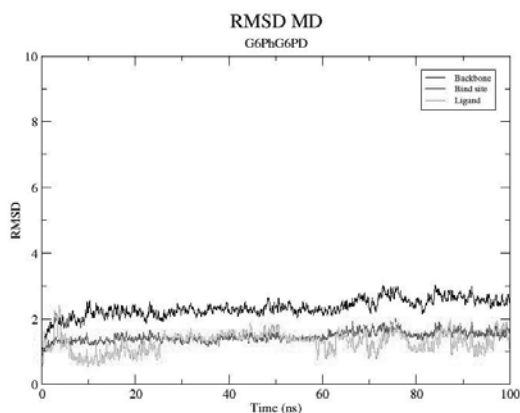


Figure 4. RMSD of hG6PD (black) complexed with the substrate G6P (green), red shows the RMSD of the active site, for a time of 100 ns.

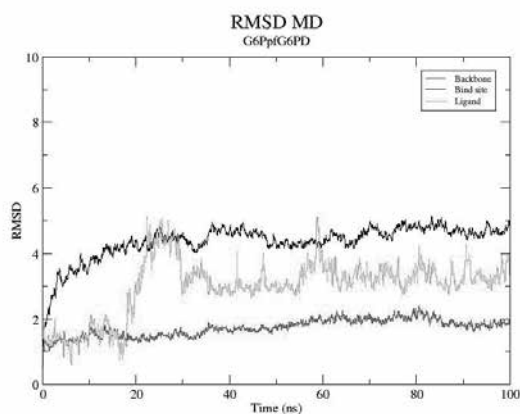


Figure 5. RMSD of pfG6PD (black) complexed with the substrate G6P (green), red shows the RMSD of the active site, for a time of 100 ns.

The SIE results presented next to the values found in G6P-pfG6PD complex, with values below -6kcal/mol for the proposed inhibitors LIG3 and LIG6, values close to those found in the interaction of the enzyme with G6

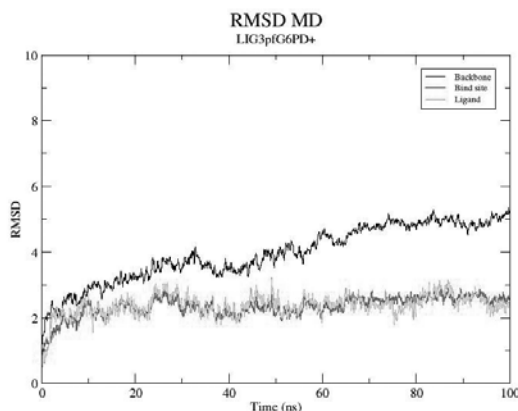


Figure 6. RMSD of pfG6PD (black) complexed with the ligand 3 (green), red shows the RMSD of the active site, for a time of 100 ns.

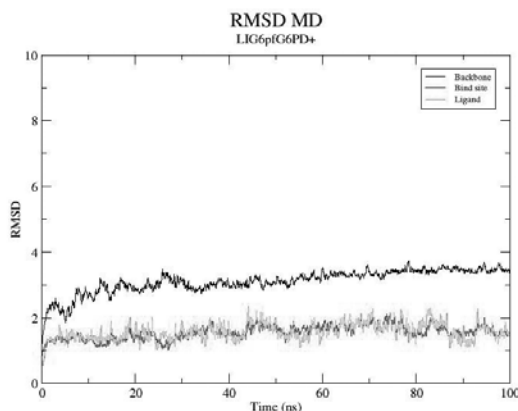


Figure 7. RMSD of pfG6PD (black) complexed with the ligand 3 (green), red shows the RMSD of the active site, for a time of 100 ns.

Conclusions

In this study was constructed the 3D structure of Glucose-6-Phosphate Dehydrogenase enzyme of the plasmodium falciparum pfG6PD, that presented a significantly mutation in one residue in the active

site, compared with the similar human enzyme. Were proposed six ligands for inhibit the pfG6PD enzyme. The best ligands were LIG 3 and 6, based with SIE method. The mutation of this single residue found in active site of pfG6PD can open a new path in search of the Plasmodium falciparum selective inhibitors and drug candidates against malaria. These binders are being synthesized and applied in studies of biological assay in vitro to confirm the possibility of inhibition, results will be presented in a next opportunity.

Acknowledgments

The authors acknowledge the financial support given by CAPES, FIBRA e UFPA

References

1. WHO, (2012). World Health Organization: Geneva, Switzerland.
2. PREUSS, J., E. JORTZIK (2012). IUBMB Life 64(7): 603-611.
3. SALI, A., T. L. BLUNDELL (1993). J Mol Biol 234(3): 779-815
4. CASE, D. A., ET AL (2005). J Comput Chem 26(16): 1668-1688
5. SULEA, T., PURISIMA E. (2012) Methods Mol Biol, 819, 295-303.

Nelson A. N. de Alencar^{a,b},
Jordi Jimenez Juarez^c,
Jeronimo Lameira Silva^a &
Javier Luque Garriga^c.

^a Universidade Federal do Pará- UFPA

^b Faculdade Integrada Brasil Amazônia (FIBRA)

^c Universitat de Barcelona, Barcelona - Espanha.

Modelagem do Equilíbrio de Fases do Pentano e da Mistura de Pentano e CO₂

Patrícia B. Gusmão, Leonardo Baptista & Márcio Paredes

Introdução

A descrição precisa do comportamento de fases da mistura de hidrocarbonetos e dióxido de carbono não é apenas um problema acadêmico, mas também é fundamental em muitos campos industriais e tecnológicos, tais como a concepção de equipamentos de separação nas indústrias química e de energia, recuperação avançada de petróleo, e sistemas geotérmicos avançados com presença de CO₂.

O sistema tem recebido maior atenção devido ao crescente interesse na captura e armazenamento geológico do dióxido de carbono. O equilíbrio de fases da mistura em questão desempenha um papel importante na avaliação do comportamento em longo prazo do dióxido de carbono em reservatórios subterrâneos profundos.

Este trabalho tem como objetivo investigar o equilíbrio de fases de hidrocarbonetos e da mistura de hidrocarbonetos e dióxido de carbono através de simulação molecular utilizando o método de Monte Carlo.

Métodos

O método de Monte Carlo (MC) foi utilizado para simular o equilíbrio de fases do pentano puro e da mistura binária de pentano e dióxido de carbono. As simulações foram realizadas nas temperaturas 343k, 350k, 400k, 410k, 420k, 430k, 440k e 450k, considerando um total de 1000 moléculas no sistema. Aplicou-se o campo de força Trappe em conjunto ao ensemble de Gibbs NVT. O programa utilizado foi o MCCCCS Towhee¹.

Resultados e discussões

Os resultados obtidos por simulação foram comparados com os valores estimados por interpolação nas curvas

experimentais encontradas na literatura.^{2,3}

Para as simulações com o pentano puro, o modelo demonstrou ser representativo na predição da entalpia de vaporização. Pode se observar que a curva simulada se aproxima da curva experimental à medida que a temperatura se aproxima da temperatura crítica do pentano, 469K. O maior desvio encontrado foi na temperatura de 343k, que apresentou um erro próximo a 8%; e o menor desvio encontrado foi na temperatura de 440k, que apresentou um erro de 0,8%. Os dados podem ser observados na Tabela e Figura 1. Os dados estimados por interpolação na curva experimental estão em vermelho. É possível observar pelos gráficos que o acordo entre os dados teóricos e experimentais aumenta à medida que a temperatura aumenta.

Tabela 1: Dados teóricos e experimentais de $\Delta H(\text{vap})$ do pentano. Resultados teóricos obtidos com o campo de força Trappe. Valores em kJ mol⁻¹.

Entalpia de vaporização			
		Dados simulados	
Temperatura	Experimental	Teórico	Desvio padrão
310	25,5	-	-
343	23,4	21,6	0,215
350	23	21,2	0,222
390	19,7	-	-
400	18,6	17,3	0,176
410	17,4	16,4	0,344
420	16,3	15,2	0,315
430	15,1	14,1	0,391
440	12,9	12,8	0,468
450	10,7	11,2	0,564
460	8,5	-	-

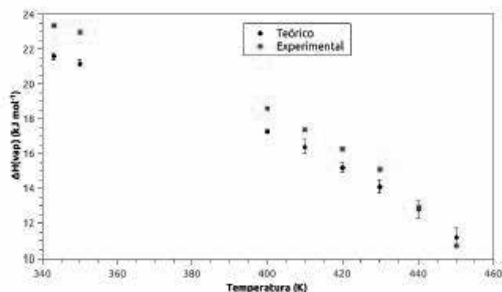


Figura 1: Comparação entre dados teóricos e dados experimentais.

Os valores teóricos para a densidade da fase líquida apresentam um bom acordo com os dados experimentais para o pentano puro, porém os desvios dos valores teóricos foram elevados, indicando que a simulação necessita ser refinada.

Todas as simulações anteriores negligenciaram o termo eletrostático do campo de força, visto que a molécula é apolar e não apresenta carga. Foi realizada uma simulação a 343K contabilizando o termo eletrostático, porém o mesmo não se mostrou vantajoso. O valor de entalpia de vaporização obtido foi similar ao calculado sem a contribuição eletrostática e com um desvio padrão menor, porém o tempo de simulação praticamente dobrou.

Outros campos de força também foram testados, entre eles o SKS. O equilíbrio de fases do pentano puro foi modelado também a 343K utilizando o campo de força SKS nas mesmas condições anteriores. O erro relativo observado neste campo de força foi de aproximadamente 9%, próximo ao erro indicado pelo campo de força Trappe, que ficou em torno de 8%. Os desvios observados foram baixos em ambos os campos de força.

Outras temperaturas precisam ser avaliadas para uma melhor análise. Os dados mencionados podem ser observados na Tabela 2.

Tabela 2. Comparação entre dados teóricos. Valores em kJ mol⁻¹.

$\Delta H(\text{vap}) - 343\text{K}$						
Modelo						Experimental
Trappe com termo eletrostático	Desvio pad.	Trappe sem termo eletrostático	Desvio pad.	SKS	Desvio pad.	
21,5	0,08	21,6	0,2	25,5	0,5	

Para as simulações com a mistura pentano e dióxido de carbono, o modelo demonstrou ser representativo na predição da fração molar dos componentes na fase vapor. Foram encontrados dados experimentais para fração molar em função da temperatura e pressão nas temperaturas de 408,15K e 438,15K. Estes dados foram comparados com os dados teóricos obtidos a 410K e 440K, assumindo que a diferença entre estes valores de temperaturas pode ser negligenciada. Pode-se observar uma boa aproximação entre os valores interpolados a partir dos dados experimentais e os valores obtidos por simulação. O erro em ambas as temperaturas foi menor que 2,5%. Estes dados podem ser observados na Tabela 3.

Tabela 3. Dados experimentais e dados simulados da fração molar de CO₂. Os dados em vermelho foram obtidos por extrapolação dos dados experimentais.

Fração Molar 408,15k			Fração Molar 438,15k		
P kPa	Exp.	Simulação	P kPa	Exp.	Simulação
1400	0,114	-	-	-	-
1779	0,264	-	2206	0,113	-
1908	0,299	0,305	2800	0,19	0,186
2413	0,439	-	2820	0,193	-

Conclusão

Os sistemas estudados via método de Monte Carlo no ensemble de Gibbs NVT demonstraram boa confiabilidade na predição das entalpias de vaporização do pentano e das frações molares na fase vapor da mistura de pentano e dióxido de carbono. Entretanto o modelo e a metodologia aplicada ainda precisam ser melhorados e aplicados a outros hidrocarbonetos e suas misturas com CO₂, assim como o cálculo de outras propriedades termodinâmicas do sistema em equilíbrio, como densidade e pressão. A próxima etapa é simular o equilíbrio de fases para hidrocarbonetos de maior ordem e suas misturas com CO₂.

Agradecimento

CAPES, CNPq e FAPERJ.

Referências

1. <http://towhee.sourceforge.net>, acessado em 14/11/2015.
 2. Leu, A. D.; Robinson, D. B. J. Chem. Eng. Data **1987**, 32, 447-450.
 3. <http://webbook.nist.gov/cgi/cbook.cgi?ID=C109660&Mask=4#Thermo-Phase>, acessado em 14/11/2015.
-

Patrícia B. Gusmão^{1*},
Leonardo Baptista² & Márcio
Paredes¹

¹ Universidade Estadual do Rio de Janeiro, Instituto de Química, Rio de Janeiro - RJ

² Universidade Estadual do Rio de Janeiro, Faculdade de Tecnologia, Resende - RJ

*pbgusmao@gmail.com

Cooperativity Effects on the Hydrogen Bonds Within HCN and HNC Complexes

Paulo M. C. de Oliveira, Juliana A. B. Silva & Ricardo L. Longo

Introduction

Hydrogen bonding (H-bond) remains relevant because of its importance in Chemistry, Biology and Materials Science. The diversity and peculiarities of H-bonds still cause debates regarding, for instance, the behavior and properties simple liquids such methanol and water. Another aspect is the relationships between the topological and statistical mechanics descriptors of complex H-bond networks and the properties of liquids and mixtures.¹⁻³ For instance, the presence of small-world patterns in H-bond networks of aqueous mixtures may be related to special behavior of these networks, such as resilience and rapid response to perturbation.¹⁻³ These characteristics may be helpful to explain and interpret various physical chemistry properties of aqueous solutions. Thus, it is important to extend these statistical mechanics analyses to more diverse H-bond networks, such as pure HCN and HNC liquids and their mixtures. The H-bond networks used in these analyses are obtained from computer simulations employing classical intermolecular interaction potentials, usually obtained by parametrization from the liquid experimental properties. However, these potentials are not available for HCN/HNC systems, which leads to their parametrization with respect to high-level quantum chemical calculations or to quantum computer simulations such as the Born-Oppenheimer Molecular Dynamics (BOMD) method.

HCN was chosen because it is a polar compound that may form H-bond networks containing linear, branched

and cyclic aggregates.^{4,5} In addition, HCN may be a relevant prebiotic and extraterrestrial species related to the origin of life.⁶ Thus, the topological properties of the H-bond bond networks in liquid HCN and HCN-HNC mixtures could be relevant in understanding their thermodynamics and structural properties. In addition, it has shown that the H-bond cooperativity effects are important for several properties.⁷⁻⁹ Computer simulation methods such as Monte Carlo and molecular dynamics do capture many-body effects on the H-bonds. However, these H-bond cooperativity effects require specialized intermolecular potentials or the use of quantum methods that describe these effects properly.

Thus, the quantitative properties of the H-bonds in HCN-HNC dimeric and trimeric complexes are investigated in detail by electronic structure methods. This aims at providing a benchmark for selecting density-functionals to be employed in BOMD simulations or a database for parametrization of the intermolecular interaction potentials for HCN/HNC systems.

Methods

All possible dimeric and trimeric HCN-HNC complexes were fully optimized with the MP2/6-311++G(d,p) method without symmetry constraints. Energy (single-point) calculations were performed with global-hybrid (B3LYP, BP86 and PBE) and meta-GGA (TPSS) density functionals, with long-range and

Table 1. Interaction energies (kJ mol⁻¹) calculated for a set of density functionals, with dispersion (GD3) and long-range (LR) corrections, using the cc-pVDZ basis set and BSSE corrected values are in parenthesis.

	HCN-HCN	HCN-HNC	HNC-HCN	HNC-HNC
B3LYP	21.63 (16.69)	31.71 (25.48)	20.92 (17.74)	33.14 (28.49)
B3LYP-GD3	24.64 (19.71)	35.27 (29.00)	23.05 (19.87)	36.69 (32.05)
B3LYP-LR	24.10 (18.95)	34.85 (28.28)	22.80 (19.41)	35.40 (30.46)
TPSS	20.59 (16.36)	31.13 (25.73)	20.59 (18.12)	33.60 (29.96)
TPSS-GD3	23.60 (19.37)	34.64 (29.25)	22.72 (20.25)	37.15 (33.51)
TPSS-LR	23.97 (19.79)	34.52 (29.12)	22.13 (19.66)	34.02 (30.33)
BP86	19.33 (14.56)	29.87 (23.85)	19.62 (16.57)	32.68 (28.28)
BP86-GD3	22.34 (17.57)	33.39 (27.41)	21.76 (18.70)	36.23 (31.88)
BP86-LR	26.53 (22.01)	38.16 (32.34)	24.77 (21.92)	37.82 (33.68)
PBE	22.72 (17.61)	33.56 (27.15)	23.05 (19.75)	36.61 (31.92)
PBE-GD3	25.73 (20.63)	37.07 (30.71)	25.15 (21.84)	40.17 (35.48)
PBE-LR	24.60 (20.21)	35.61 (29.96)	22.89 (20.21)	35.35 (31.42)
CCSD(T)/CBS	19.76	29.92	19.93	30.98

dispersion corrections. The following basis sets were employed: cc-pVXZ with X = D, T and Q. The basis-set superposition error (BSSE) in the interaction energies were corrected using the counterpoise method.

As reference, the H-bond energies were calculated with the ab initio correlated CCSD(T) method extrapolated to the complete basis-set (CBS) limit. This extrapolation was performed by applying the Eqs. 1 and 2 to evaluate the corresponding correlation (corr) and Hartree-Fock (HF) energies:^{10,11}

$$E^{corr}(X) = E^{corr}(\infty) + A^{corr}X^{-\alpha} \quad (\text{Eq. 1})$$

$$E^{HF}(X) = E^{HF}(\infty) + A^{HF}X^{-\beta} \quad (\text{Eq. 2})$$

where X = 2 for the cc-pVDZ basis and X = 3 for the cc-pVTZ basis set, and α and β are optimized exponents.^{10,11}

Results and Discussion

The reported experimental binding energy for the HCN-HCN dimer the gas-phase is 15.9 ± 0.67 kJ mol⁻¹.¹² There is also an older reported value of 10.88 kJ mol⁻¹ obtained from vapor density data.¹³ The binding

energy calculated in this work for CCSD(T)/CBS for HCN dimer is 19.8 kJ mol⁻¹. Employing the zero-point vibrational energy (ZPE) contribution (5.1 kJ mol⁻¹) calculated with the MP2/cc-pVTZ method, provides a corrected ZPE value (14.7 kJ mol⁻¹) in excellent agreement with the experiment based on spectroscopic data.¹² The binding energies calculated for the HCN/HNC dimers are summarized on Table 1 and consider the BSSE, dispersion and long-range contributions separately employing density-functionals available in the CP2K program.

Regardless of the method or the corrections employed, the H-bonds with HNC as donor (e.g., HCN-HNC and HNC-HNC) are at least 10 kJ mol⁻¹ stronger than the H-bonds with HCN as donor. This behavior is due to the larger positive charge density at the hydrogen in the HNC molecule compared to the HCN. For instance, the calculated (B3LYP/cc-pVDZ) APT atomic charges at the hydrogen are +0.25 and +0.40 in HCN and HNC, respectively. In addition, the intermolecular charge transfer in the HCN-HNC and HNC-HNC dimers are larger than those in HCN-HCN and HNC-HCN ones, which can be correlated to the strengthen of the H-bond.¹⁴ These observations can also be used to explain the differences on the binding energies for the trimeric species. Noteworthy

that the dispersion and long-range corrections shown in Table 1 lead to overestimation the binding energies. In fact, the results obtained with the BP86 functional without any of these corrections are in very good agreement with the reference (CCSD(T)/CBS) data. The trend observed by including the dispersion correction corroborates recent analysis of a set of small H-bonded complexes.¹⁵ In this analysis, the electrostatic contributions are the determining factor in the intermolecular interactions and the inclusion of dispersion corrections in the most density functionals leads large errors. Notice that this situation changes when the BSSE correction is taken in account. However, because the interest is to perform BOMD simulations during which the BSSE correction is not considered, the best compromise (error cancelation) is the BP86/cc-pVDZ method for describing the H-bond energy in dimers. This is quite fortunate because this method does not present a high computational demand and provides results at the CCSD(T)/CBS quality. A quantitative analysis can be ascertained from Table 2, which presents the mean absolute error on the energies for the 12 investigated species: HCN-HCN, HCN-HNC, HNC-HCN, HNC-HNC, HCN-HCN-HCN, HCN-HCN-HNC, HCN-HNC-HCN, HCN-HNC-HNC, HNC-HCN-HCN, HNC-HCN-HNC, HNC-HNC-HCN, and HNC-HNC-HNC, taking the CCSD(T)/CBS results as reference. The qualitative analysis observed for the binding energies of the dimers is quantitatively corroborated.

Table 2. Mean absolute error (kJ mol⁻¹) for the binding energy with respect to CCSD(T)/CBS.

	cc-pVDZ	cc-pVTZ	cc-pVQZ
B3LYP	3.65	2.79	4.07
B3LYP-GD3	8.16	1.72	0.49
B3LYP-LR	7.90	0.95	0.61
TPSS	3.18	2.25	3.02
TPSS-GD3	7.69	2.37	1.59
TPSS-LR	6.90	1.07	0.56
BP86	1.63	4.74	5.88
BP86-GD3	5.98	1.41	2.09
BP86-LR	12.61	6.13	5.32
PBE	7.58	1.49	1.35
PBE-GD3	12.08	5.62	4.57
PBE-LR	8.67	2.26	1.42

Namely, the inclusion of dispersion and long-range corrections lead to overestimated results for the smaller basis set (cc-pVDZ). For triple and quadruple-zeta quality basis sets these corrections become relevant and errors decrease, except for the PBE density-functional. In fact, for this functional, the dispersion correction is a problem because it causes significant overestimation even for large basis set. Whereas, the B3LYP results improve with dispersion and long-range corrections for cc-pVXZ X = T and Q basis sets. For the smaller basis set, the BP86 functional, without any correction, provided the best results. This very fortunate cancelation of errors allows the application of the BP86/cc-pVDZ method within BOMD simulations because the inclusion of BSSE and long-range corrections are very troublesome.

An important characteristic of H-bonds is their cooperative enhancement when the number of hydrogen bonds increases. For the trimeric H-bonded complexes (see Table 3), there are cooperativity effects, in addition to the observed influence of the nature of the donor in the H-bond: HCN X HNC. The cooperative energy for the trimeric complexes was obtained by subtracting from their binding energy, the respective energies from the dimeric species that form the H-bonds. In the Table 3, the cooperative energies calculated for all possible trimeric species of HCN/HNC are presented. It can be noticed that the cooperative energy increases as the number of HNC molecule increases in the complex. This increase of the cooperative energy is roughly 2 kJ mol⁻¹ per unit of HNC moiety that is a donor in the H-bond. Because the minimum cooperative energy is ca. 5 kJ mol⁻¹ (HCN-HCN-HCN) it almost double when the number of HNC donors doubles (HCN-HNC-HNC and HNC-HNC-HNC). Noteworthy that the DFT/cc-pVDZ methods provide similar results for the H-bond cooperative energy and they systematically overestimate this quantity compared to the CCSD(T)/CBS calculations. This is probably due to the basis set effects.

These findings suggest that the liquid mixtures of these HCN/HNC molecules should have distinct topological behavior depending upon the mole fraction of each species. For instance, in a 50:50 mixture, the H-bond networked system most likely would prefer to make intercalated bonds of HCN and HNC instead of bonds between molecules of the same type. However, the large differences between the pure HCN and HNC networks also suggest that phase separation

Table 3. Cooperative energies (kJ mol⁻¹) for HCN/HNC trimers calculated with the DFT/cc-pVDZ methods and CCSD(T)/CBS.

Complex	B3LYP	TPSS	BP86	PBE	CCSD(T)/CBS
HCN-HCN-HCN	5.31	5.31	5.48	5.65	4.78
HCN-HCN-HNC	7.20	7.36	7.45	7.53	6.44
HCN-HNC-HCN	6.86	6.90	7.07	7.15	5.96
HCN-HNC-HNC	9.96	10.33	10.59	10.67	8.03
HNC-HCN-HCN	5.44	5.52	5.61	5.73	4.81
HNC-HCN-HNC	7.91	5.44	5.27	5.19	6.94
HNC-HNC-HCN	7.41	7.61	7.87	8.03	6.07
HNC-HNC-HNC	10.84	11.51	11.80	12.01	8.20

at particular thermodynamics situation may occur. In fact, these cooperativity effects can have considerable influence upon the topological structures of these networks in the liquid phase. As a perspective, topological studies of these liquid systems may provide relevant information on how these molecules interact in a complex network and how this network behave upon external perturbations.

Conclusions

CCSD(T)/CBS//MP2/6-311++G(d,p) calculations provided a benchmark to ascertain the reliability of density functionals, basis sets, BSSE, dispersion and long-range corrections for determining H-bond energies in dimeric and trimeric species of HCN/HNC and the cooperative energies in the trimeric complexes. One of the most reliable and precise method was the BP86/cc-pVDZ without any correction. This is very fortunate because it is the simplest and the least demanding method to perform BOMD simulations of liquid HCN/HNC mixtures. In addition, the cooperative effects of the H-bonds may significantly affect the topological behavior of the H-bond networks in these mixtures.

Because the H-bond networks in liquids can be large, we are currently investigating these cooperativity effects within the H-bonds of larger (tetramer and pentamer) HCN/HNC complexes with the BP86/cc-pVDZ method.

Acknowledgments

The authors are grateful for the support given from CAPES, CNPq, FACEPE, FINEP and inct-INAMI.

1. Silva, J. A. B.; Moreira, F. G. B.; dos Santos, V. M. L.; Longo, R. L.,

Phys. Chem. Chem. Phys., 13, 593 (2011).

2. Silva, J. A. B.; Moreira, F. G. B.; dos Santos, V. M. L.; Longo, R. L., Phys. Chem. Chem. Phys., 13, 6452 (2011).
3. Silva, J. A. B.; Moreira, F. G. B.; dos Santos, V. M. L.; Longo, R. L., Phys. Chem. Chem. Phys., 16, 19479 (2014).
4. Mamajanov, I.; Herzfeld, J.; J. Chem. Phys., 130, 134503 (2009).
5. Matthews, C. N., Orig. Life Evol. Biosphere, 21, 421 (1991).
6. Martiniano, H. F. M. C.; Cabral, B. J. C.; Chem. Phys. Lett., 555, 119 (2013).
7. Del Bene, J. E.; Alkorta, I.; Elguero, J., J. Phys. Chem. A., 114, 8463 (2010).
8. Provasi, P. F.; et al., J. Phys. Chem. A., 109, 6555 (2005).
9. Adrian-Scotto, M.; Vasilescu, D., J. Mol. Struct. (Theochem), 803, 45 (2007).
10. Truhlar, D. G., Chem. Phys. Lett., 294, 45 (1998).
11. Huh, S. B.; Lee, J. S., J. Chem. Phys., 118, 7 3035 (2003).
12. Mettee, H. D., J. Phys. Chem., 77, 14 (1973).
13. Giaque, W. F.; Ruehrwein, R. A., J. Am. Chem. Soc., 61, 2626 (1939).
14. Araújo, R. C. M. U.; Ramos M. N.; J. Braz. Chem. Soc., 9, 499 (1998).
15. Boese, D. A.; ChemPhysChem, 16, 978 (2015).

Paulo McMiller C. de Oliveira^{a*}, Juliana A. B. Silva^b & Ricardo L. Longo^a

^a Departamento de Química Fundamental, Universidade Federal de Pernambuco, 50740-540, Recife, PE, Brazil,

^b Centro Acadêmico do Agreste, Universidade Federal de Pernambuco, 55002-970, Caruaru, PE, Brazil

*E-mail: mcmiller@live.nl

Application of the G3(MP2)-CEP Theory in Understanding Diels-Alder Mechanism

Régis C. Leal, Douglas H. Pereira & Rogério Custodio

Introduction

Even 80 years after the formulation of the “endo rule” proposed by Alder and Stein in 1934,¹ the factors controlling the formation of endo product in [4+2] cycloaddition reactions are still not completely understood.² In the context of organic synthetic chemistry, the Diels–Alder reaction is among the most powerful and well-known mainly due to the facility of generating two carbon-carbon bonds simultaneously.³

There are at least three points in an attempt to explain the preference that leads to the formation of a given product in this type of reaction. The first one is the Secondary Orbital Interactions (SOI) proposed by Hoffmann and Woodward⁴ to rationalize the empirical endo rule formulated by Alder and Stein, as previously mentioned. Arrieta and Cossio⁵ studying the classical Diels-Alder reaction between cyclopentadiene (CP) and maleic anhydride (MA), claim that SOI do exist and are responsible for at least an important part of the observed stereo control.

An opposite tendency is defended by García, Mayoral and Salvatella⁶ which justify that the SOI concept was based on the assumption that closed-shell repulsions were identical in endo and exo approximations. Therefore, the SOI concept is unnecessary and should be abandoned by chemists as a general explanation for the endo preference in Diels-Alder reactions. The study by Ogawa and Fujimoto based on the reaction between

maleic anhydride and butadiene has shown that the endo preference is not due to SOIs, but to a balance of several energy terms, including electrostatic attractions and closed-shell repulsions.^{6,7} As a logical conclusion, the endo preference of the cyclopentadiene and maleic anhydride reaction should be essentially attributed to the steric repulsion induced by the methylene group in the exo approach, although other interaction mechanisms (such as dispersion forces) may also play a role.^{6,7} Fernández and Bickelhaupt have also confirmed that neither the orbital interactions nor the total interaction between the deformed reactants contributes to the endo selectivity. They believe that the selectivity is mainly caused by an unfavorable steric arrangement in the transition-state region of the exo pathway which translates into a more destabilizing activation strain.¹

Another relevant question is the solvent effect that seems to have certain influence in some properties depending on the system. The classical work of Cativiela et al.⁸ illustrates examples in which the polarity of the solvent changes the selectivity endo/exo in Diels-Alder reactions. However, overall donor properties of the solvent are not important, although in some reactions a solvent with high donation ability may reduce the reaction rate. On the other hand, Tuvi-Arad and Avnir⁹ studying the classical reaction of [4 + 2] cycloaddition of (E,E)-1,4-dimethoxy-1,3-butadiene (DMB) with tetracyanoethylene (TCNE), show that the reactivity increases with the polarity of the solvent used.

Independent of the hypothesis being analyzed, the alliance between computation and experimental results has been increasingly used with the goal to provide subsidies for the discussion on the clarification of structural and/or electronic properties of various types of reactions, including the cycloaddition reactions [4+2] as is the case of Diels-Alder reactions.

Significant advances in reducing the computational cost while preserving the accuracy was recently developed by Pereira et al.^{10,11} combining a Compact Effective Pseudopotential (CEP) of Stevens, Bash and Krauss^{12,13} in the G3 theory, referred to as G3CEP theory. The theory reduces the CPU time between 7 and 60% without losing quality of the results obtained. The mean absolute deviation for the theory is 1.29 kcal mol⁻¹ compared to 1.16 kcal mol⁻¹ from the original all-electron theory for the test set G3/05.

Rocha et al. similarly developed G3(MP2)//B3-CEP theory adapting the CEP in G3(MP2)//B3 theory.¹⁴ The mean absolute deviation compared to the experimental data for all thermochemical results was 1.60 kcal mol⁻¹ and 1.41 kcal mol⁻¹ for theories G3(MP2)//B3-CEP and G3(MP2)//B3, respectively, with CPU time reduction between 10% and 40% using pseudopotential.

The success of these new theories developed with respect to their original all-electron methodologies, mainly due to the accuracy of results and reduced computational time, led to the implementation of CEP in the G3(MP2) reduced order theory¹⁵, which led to the G3(MP2)-CEP theory¹⁶. The objective of this study is to evaluate the performance of this new method to study the mechanism of a set of selected some Diels-Alder reactions.

Method

The G3(MP2)-CEP theory is characterized by the same sequence of calculations of the G3(MP2) original theory with the replacement of core electrons by pseudopotential CEP. The procedure for obtaining the final G3(MP2)-CEP energy is also similar and are described in the literature.¹⁶ All maximums (TS, Transition State) were characterized by frequency calculation and then undergoing the IRC (Intrinsic Coordinate Reaction) procedure with the MP2/CEP-P31G(d) methodology. All calculations were carried out with Gaussian 09W software.¹⁷

Four cases were selected where the reactions have different endo/exo yields in order to evaluate the behavior

of G3(MP2)-CEP theory relative to experimental results and the other calculations from the literature.

Results and Discussion

It is known that the experimental ratio of endo/exo adducts is greatly changed when the cyclopropene is replaced by cyclopentene in a reaction with cyclopentadiene, and this was the reason for the choice of these particular mechanisms.

REACTION 1: CYCLOPROPENE AND CYCLOPENTADIENE^{18,19}

This reaction provides an endo/exo ratio of 97:3. Figure 1 shows the energy profile calculated with: (a) G3(MP2)-CEP and (b) IRC obtained at MP2/CEP-P31G(d) level indicating a kinetic preference for endo adduct, because the barrier is 4.5 kcal mol⁻¹ lower compared to the analogue which leads to the exo TS. However, the exo adduct is still the product thermodynamically more stable, which is in agreement with the endo rule proposed by Alder and Steinl.

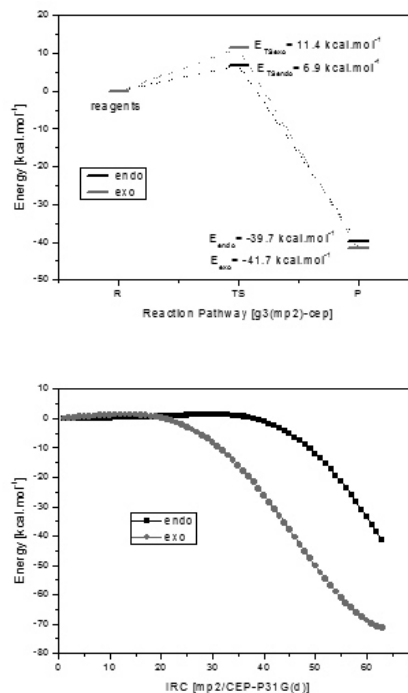


Figure 1. Energy profile (a) and IRC (b) for the reaction between cyclopropene and cyclopentadiene.

REACTION 2: CYCLOPENTENE AND CYCLOPENTADIENE 19,20

The reaction between cyclopentene and cyclopentadiene provides a kinetic preference for the exo adduct formation. It can be seen that the difference between both barriers is approximately $2.5 \text{ kcal mol}^{-1}$. The exo adduct also is the thermodynamic product. The results once again may justify the 20:80 (endo/exo) ratio found in the literature. In this case the kinetic and thermodynamic preferences point to the exo adduct (see Figure 2).

According to Liu et al.¹⁹ the reactivity of cycloalkenes as dienophiles are controlled by distortion energies from the reactants into the transition-state geometries. The distortion energies increase from cyclopropene to cyclohexene resulting in a decrease in the Diels-Alder reactivity resulting in an enlargement of the activation barrier. Observe that the TSendo energy of the reaction 2 is practically the triple compared to reaction 1, 21.0 and $6.9 \text{ kcal mol}^{-1}$, respectively.

On the other hand the dienes reactivities are controlled by both distortion and interaction energies. Interaction energy is the difference between the activation energy and the total energy of distortion.

The energy difference between the endo/exo stereoisomers, in reactions 1 and 2 do not exceed 2 kcal mol^{-1} . The barrier height can justify well the experimental

yield in these two situations.

REACTION 3: CYCLOHEXADIENE AND ACRYLONITRILE

Tuvi-Arad and Avnir²¹ studied the symmetry-enthalpy correlations in Diels-Alder reactions with three cyclic dienes: cyclopentadiene, cyclohexadiene and cycloheptadiene, beyond acyclic butadiene, and three dienophiles: cyanoethylene (acrylonitrile), 1,1-dicyanoethylene and 1,1,2-tricyanoethylene. Cyanoethylene derivatives are widely studied due to their known ability to accelerate cycloaddition reactions.²² In particular, cyanoethylene (acrylonitrile) is a reactive dienophile in DA reactions with cyclopentadienes, cyclohexadienes, and cycloheptadienes²³. In general, the reactivity decreases as the ring size increases²⁴.

Takakis et al.²⁵ showed that the reactions of cyclohexadiene and cycloheptadiene with acrylonitrile are exceptions to the Alder-Stein rules regarding the exo/endo ratio of 40:60 for cyclohexadiene (Reaction 3) and 35:65 for cycloheptadiene (Reaction 4).

Figure 3 shows results found by G3(MP2)-CEP for the reaction between cyclohexadiene and acrylonitrile. The small energy difference between the transition states and products shows a balance between both adducts agreeing with the experimental yield.

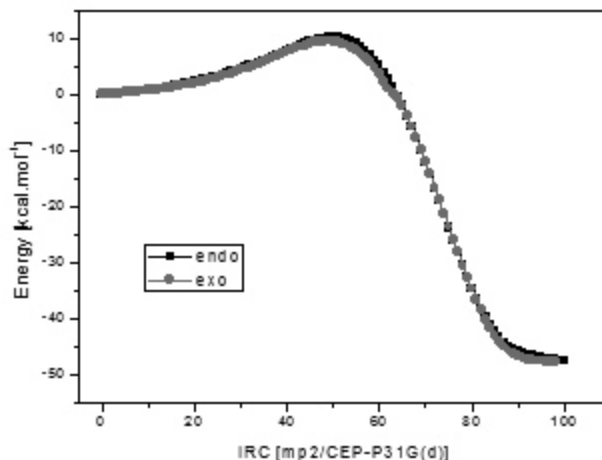
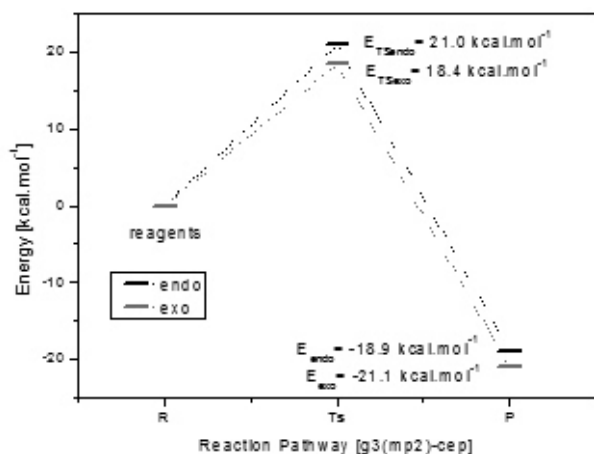


Figure 2. Energy profile (a) and IRC (b) for the reaction between cyclopentene and cyclopentadiene.

REACTION 4: CYCLOHEPTADIENE AND ACRYLONITRILE

The small energy difference, either between TSs or products, does not allow state a high selectivity for a particular stereoisomer, agreeing therefore once again with the experimental yield 35:65 (endo/exo).

It is observed in reactions 3 and 4 that the difference of energy between TSs and reaction products do not exceed 0.5 kcal mol⁻¹. IRC profiles are also practically overlapped showing no significant difference in energy between both paths.

Conclusions

In the Diels-Alder reactions studied one cannot reach a general conclusion to explain the preference for a particular endo/exo product from the reactants. The four mechanisms analyzed show kinetic preference for the endo stereoisomer in Reaction 1, exo in Reaction 2, and balance between both products in Reactions 3 and 4. The thermodynamic preference points to the exo product in Reactions 1 and 2, and balance between both products in Reactions 3 and 4.

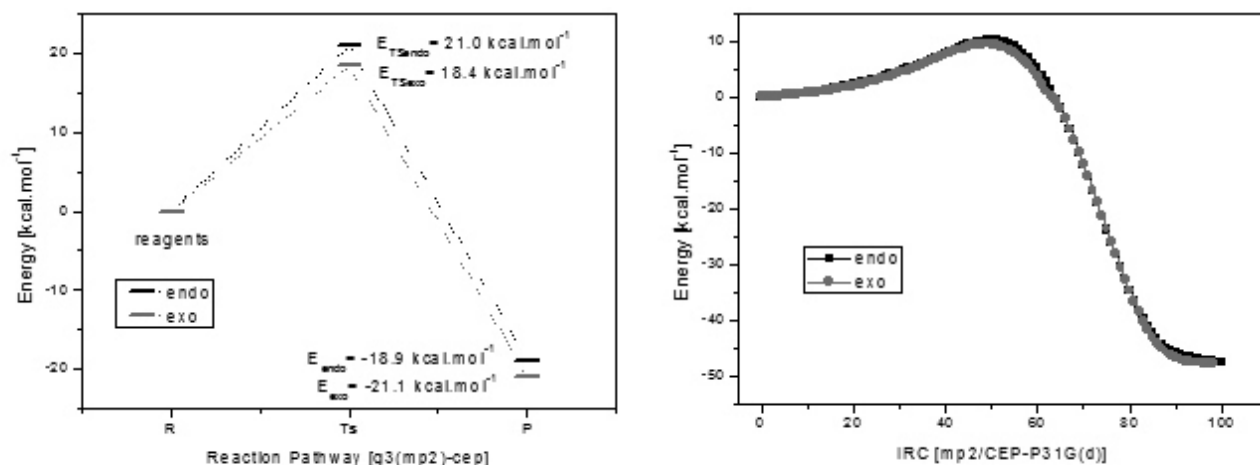


Figure 3. Energy profile (a) and IRC (b) for the reaction between cyclohexadiene and acrylonitrile.

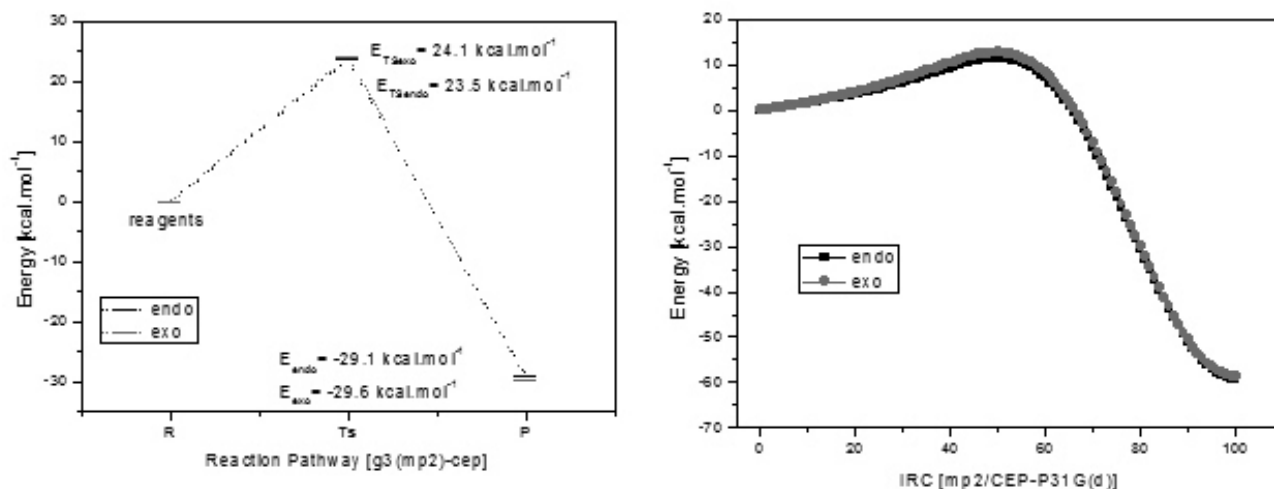


Figure 4. Energy profile (a) and IRC (b) for the reaction between cycloheptadiene and acrylonitrile.

The endo rule cannot be followed in many cases, as shown in some of the reactions discussed here. Though often the experimental yield point out to high selectivity for the endo or exo product, theoretically it is not verified large differences in energy between the products formed independent of the methodology used.

The G3(MP2)-CEP theory agrees with the experimental data in all analyzed reactions, although in some cases (Reactions 3 and 4) the energy difference is very small (~0,5 kcal/mol). Worth remembering that the solvent effect has little influence in most Diels-Alder reactions. The question of SOI likewise cannot be taken into account to explain alone the selection by either adduct, as some authors claim.

The interaction and distortion energy seems the best way to explain the cases studied in this work. The G3(MP2)-CEP theory performed well in all cases tested and will be used in other situations in order to attempt to elucidate the Diels-Alder reaction yields.

Acknowledgments

The authors are grateful for the support given from the CAPES, FAPESP (Center for Computational Engineering and Sciences, Grant 2013/08293-7), CNPq, FAEPEX-UNICAMP.

References

1. Fernández, I.; Bickelhaupt, F. M.; *J. Comput. Chem.*, **35**, 371, (2014).
2. Alder, K.; Stein, G.; *Justus Liebigs Ann. Chem.*, **514**, 1, (1934).
3. Moody, C. J.; Nawrat, C. C.; *Angew. Chem. Int. Ed.*, **53**, 2056, (2014).
4. Hoffmann, R.; Woodward, R. B.; *J. Am. Chem. Soc.*, **87**, 4388, (1965).
5. Arrieta, A.; Cossio, F. P.; *J. Org. Chem.*, **66**, 6178, (2001).
6. García, J. I.; Mayoral, J. A.; Salvatella, L. *Eur. J. Org. Chem.*, **85**, (2005).
7. Ogawa, A.; Fujimoto, H.; *Tetrahedron Lett.*, **43**, 2055, (2002).
8. Cativiela, C.; García, J. I.; Mayoral, J. A.; Salvatella, L.; *Chem. Soc. Reviews*, **25**, 209, (1996).
9. Tuvi-Arad, I.; Avnir, D.; *J. Org. Chem.*, **76**, 4973, (2011).
10. D. H. Pereira, A. F. Ramos, N. H. Morgon, and R. Custodio, *J. Chem. Phys.*, **135**, 034106, (2011).
11. D. H. Pereira, A. F. Ramos, N. H. Morgon, and R. Custodio, *J. Chem. Phys.*, **135**, 219901, (2011).
12. W. J. Stevens, H. Basch, and M. Krauss, *J. Chem. Phys.*, **81**, 6026, (1984).
13. W. J. Stevens, M. Krauss, H. Basch, and P. G. Jasien, *Can. J. Chem.*, **70**, 612, (1992).
14. C. M. R. Rocha, D. H. Pereira, N. H. Morgon, and R. Custodio, *J. Chem. Phys.*, **139**, 184108, (2013).
15. Curtiss, L. A.; Redfern, P. C.; Raghavachari, K.; Rassolov, V.; Pople, J. A.; *J. Chem. Phys.*, **110**, 4703, (1999).
16. Pereira, D. H. Modification and application of Gaussian 3 theory for studies of electronic and structural properties of atoms and molecules. 2014. 157 p. Phd thesis - State University of Campinas, Institute of Chemistry, Campinas, SP. In: Capítulo 4. Pseudopotential implementation in the reduced order G3(MP2) theory for molecules containing atoms of the 1st, 2nd and representative of the third period of the periodic table.
17. M. J. Frisch, G. W. Trucks, H. B. Schlegel, G. E. Scuseria, M. A. Robb, J. R. Cheeseman, G. Scalmani, V. Barone, B. Mennucci, G. A. Petersson, H. Nakatsuji, M. Caricato, X. Li, H. P. Hratchian, A. F. Izmaylov, J. Bloino, G. Zheng, J. L. Sonnenberg, M. Hada, M. Ehara, K. Toyota, R. Fukuda, J. Hasegawa, M. Ishida, T. Nakajima, Y. Honda, O. Kitao, H. Nakai, T. Vreven, J. A. Montgomery, Jr., J. E. Peralta, F. Ogliaro, M. Bearpark, J. J. Heyd, E. Brothers, K. N. Kudin, V. N. Staroverov, T. Keith, R. Kobayashi, J. Normand, K. Raghavachari, A. Rendell, J. C. Burant, S. S. Iyengar, J. Tomasi, M. Cossi, N. Rega, J. M. Millam, M. Klene, J. E. Knox, J. B. Cross, V. Bakken, C. Adamo, J. Jaramillo, R. Gomperts, R. E. Stratmann, O. Yazyev, A. J. Austin, R. Cammi, C. Pomelli, J. W. Ochterski, R. L. Martin, K. Morokuma, V. G. Zakrzewski, G. A. Voth, P. Salvador, J. J. Dannenberg, S. Dapprich, A. D. Daniels, O. Farkas, J. B. Foresman, J. V. Ortiz, J. Cioslowski, and D. J. Fox, Gaussian 09, Revision B.01, Gaussian, Inc., Wallingford CT, (2010).
18. Wiberg, K. B.; Bartley, W. J. J.; *J. Am. Chem. Soc.*, **82**, 6375, (1960).
19. Fang Liu, Robert S. Paton, Seonah Kim, Yong Liang, and K. N. Houk, *J. Am. Chem. Soc.*, **135**, 15642, (2013).
20. Brúson, H. A.; Riener, T. W. *J. Am. Chem. Soc.*, **67**, 723, (1945).
21. Tuvi-Arad, I.; Avnir, D. *Chem. Eur. J.*, **18**, 10014, (2012).
22. J. Sauer, *Chem. Ber. Recl.*, **97**, 3183, (1964); b) G. O. Jones, V. A. Guner, K. N. Houk, *J. Phys. Chem. A*, **110**, 1216, (2006).
23. F. F. Fleming, Z. Y. Zhang, *Tetrahedron*, **61**, 747, (2005).
24. T. L. Gilchrist, R. C. Storr, *Organic Reactions and Orbital Symmetry*. 2nd Ed, Cambridge University Press, (1979).
25. I. M. Takakis, W. C. Agosta, *J. Org. Chem.*, **43**, 1952, (1978).

Régis Casimiro Leal^{a,c,*},
Douglas Henrique Pereira^b &
Rogério Custodio^a

^aUniversidade Estadual de Campinas, Instituto de Química, 13083-970, Campinas-SP, Brazil.

^bUniversidade Federal do Tocantins, Departamento de Ciências Exatas

^cBioteecnológicas, Campus Gurupi, 77410-530, Gurupi-TO, Brazil.

^eInstituto Federal de Educação, Ciência e Tecnologia do Rio Grande do Norte, Campus Nova Cruz, 59215-000, Nova Cruz-RN, Brazil.

*E-mail: regis.cassimiro@ifrn.edu.br

Interplay Between Interatomic Distance and Orbital Overlap at Control of Magnetism in FeBO_3 (B = Ti, Ge, Zr, Sn) Ilmenites

Renan A. P. Ribeiro, Ageo M. de Andrade, Luis H. S. Lacerda, Alexandre C. Jr. & Sergio R. de Lázaro

Introduction

Perovskites oxides, which have the general formula ABO_3 , are widely studied by theoretical or experimental means due to the large variety of intriguing properties, such as ferroelectricity, piezoelectricity, multiferroicity and others.¹⁻³ One fascinating feature for this structure is the capability to control the existence of different properties from chemical substitution and doping at A- and B-sites.⁴ For example, the ilmenite structure based on very common mineral of earth surface (FeTiO_3), allows a high compositional diversity of A^{2+} and B^{4+} cations that occupy alternate basal-planes along the [001] hexagonal axis of a ordered corundum structure.⁵ The most studied ilmenite materials are Ti-based compounds with different A^{2+} (A = Mn, Fe, Ni, Co) cations, although other materials are found in this symmetry.⁶⁻⁹ In relation to the magnetic ordering of ilmenite materials, mainly ATiO_3 (A = Mn, Fe, Ni, Co), Goodenough and Stickler proved that such materials are antiferromagnetic insulators and have two different magnetic couplings constants: Intralayer (J_1) and Interlayers (J_2), as shown in Figure 1. For J_1 , the magnetic exchange happens between A-O-A atoms and is dominated by the coupling of a t_{2g} orbital in one cation with an e_g orbital in other. Thus, the signal for exchange parameter depends upon the occupancies of the interacting orbitals making MnTiO_3 antiferromagnetic and FeTiO_3 , CoTiO_3 , NiTiO_3 ferromagnetic for intralayer coupling (J_1). The J_2 interactions are mediated by the BO_6

clusters in the intermetallic connection A-O-B-O-A with a less contribution of a direct overlap in [001] direction due to the vacancy in cationic sublattice (Figure 1) with opposite magnetization directions between adjacent A layers (antiferromagnetic).^{5,10}

In Fe-based ilmenite materials, aim of this study, the antiferromagnetic ordering is stabilized by the long-range exchange coupling (J_2). Therefore, J_2 is the responsible for magnetic ordering control of these materials. As previously discussed, J_2 depends of intermetallic connection Fe-O-B-O-Fe suggesting that the non-magnetic B-site replacement can control the magnetism for such materials.

Other kind of materials show superexchange interactions (A-O-B-O-A) as the key for magnetic ordering control, for instance, A_2BO_6 and $\text{AA}'\text{B}_4\text{O}_{12}$ compounds.¹¹ Shiraki and co-workers reported that A-site ordered perovskites $\text{CaCu}_3\text{Ge}_4\text{O}_{12}$ and $\text{CaCu}_3\text{Sn}_4\text{O}_{12}$, which are isostructural to antiferromagnetic $\text{CaCu}_3\text{Ti}_4\text{O}_{12}$, are ferromagnets.¹² Mizumaki and co-authors using X-ray absorption spectroscopy (XAS) for such materials proved that the antiferromagnetism in $\text{CaCu}_3\text{Ti}_4\text{O}_{12}$ can be explained by strong hybridization of the Cu 3d, Ti 3d and O 2p orbitals, while $\text{CaCu}_3\text{Ge}_4\text{O}_{12}$ and $\text{CaCu}_3\text{Sn}_4\text{O}_{12}$ spectra shows hybridization only for Cu 3d and O 2p orbitals.¹³ Similar results are found in ab initio predictions performed by Toyoda and co-workers to investigate the magnetic coupling constants of $\text{CaCu}_3\text{B}_4\text{O}_{12}$ (B = Ti, Ge, Zr and Sn) from energetic and Density of States calculations.¹⁴ Such simulations clarify the magnetic

ordering for $\text{CaCu}_3\text{B}_4\text{O}_{12}$ materials proving that long-range superexchange interaction can turn the magnetic orientation through orbital hybridization.

From this point of view, Shimakawa and Saito synthesized solid solutions based on the mixing of non-magnetic B-cations ($\text{B} = \text{Ge}, \text{Ti}, \text{Sn}$) in $\text{CaCu}_3\text{B}_4\text{O}_{12}$ materials and shown that the magnetic orientation depends of Ti concentration in ferromagnetic $\text{CaCu}_3\text{B}_4\text{-xTi}_x\text{O}_{12}$ ($\text{B} = \text{Ge}, \text{Sn}$) compounds.¹⁵ In other hand, Zhu and co-author investigating $\text{Cr}_2(\text{Te}_{1-x}\text{W}_x)\text{O}_6$ solid solutions found that magnetic interactions are controlled by tuning the orbital hybridization between Cr 3d and O 2p orbitals through W 5d. In this case the authors argue that W d and O p coupling creates a virtual hole which mediates ferromagnetic interactions between Cr atoms.¹⁶ Such experimental and theoretical observations lead us to the following question: Is possible to control the magnetic ordering of Fe-based ilmenite materials by non-magnetic B-site cation replacement?

In this study, we investigate the interlayers exchange coupling of FeBO_3 ($\text{B} = \text{Ti}, \text{Ge}, \text{Zr}, \text{Sn}$) ilmenite materials by DFT periodic calculations. Our results proved that the orbital hybridization between B-O atoms and Fe^{2+} interlayers distances controls the magnetism of ilmenite materials making FeTiO_3 and FeGeO_3 antiferromagnetic, while FeZrO_3 and FeSnO_3 are ferromagnetic.

Methods

Electronic and Magnetic properties of FeBO_3 ($\text{B} = \text{Ti}, \text{Ge}, \text{Zr}, \text{Sn}$) ilmenite materials were investigated by means of periodic DFT calculations within a hybrid functional consisting of a non-local exchange functional developed by Becke¹⁷ combined with a correlation functional based on gradient of electronic density (GGA) developed by Lee, Yang and Parr¹⁸, using CRYSTAL09 code.^{19,20} The R-3 ($n^\circ 148$) ilmenite structure (Fig. 1) is based on experimental lattice parameters $a = b = 5.0875 \text{ \AA}$ and $c = 14.0827 \text{ \AA}$ and internal coordinates: Fe (0, 0, 0.3536), B (0, 0, 0.1446) and (0.3172, 0.0234, 0.2450).²¹ All FeBO_3 ($\text{B} = \text{Ti}, \text{Ge}, \text{Zr}, \text{Sn}$) materials were full-relaxed (lattice parameters and atomic coordinates) in relation to system total energy of Ferromagnetic (FEM) state (Fig. 2a).

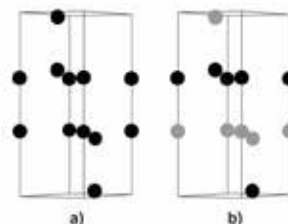


Figure 2. Magnetic configurations for FeBO_3 ($\text{B} = \text{Ti}, \text{Ge}, \text{Zr}, \text{Sn}$) ilmenite materials: a) FEM and b) AFM. The up and down-spin sites are represented by black and gray balls, respectively.

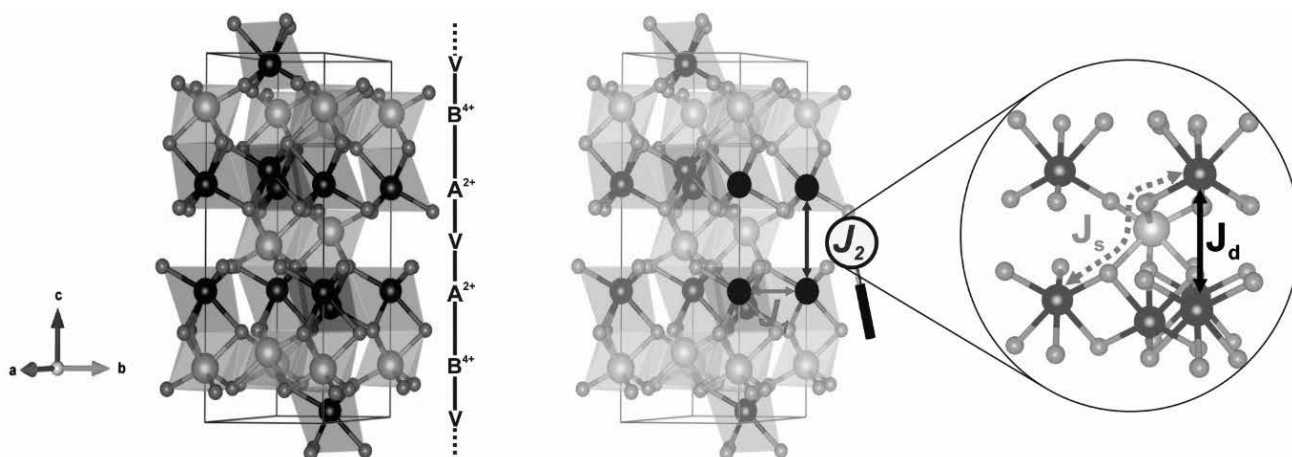


Figure 1. Ilmenite-type conventional unit cell and their exchange coupling constants. Black, orange and red balls represent A^{2+} , B^{4+} and O^{2-} ions, respectively.

The antiferromagnetic (AFM) model (Fig. 2b) refers to the FEM optimized geometry and their energy is obtained by a single-point calculation as performed by Chartier and co-workers for Mn_3O_4 .²² All-electron atom-centered Gaussian-type-function (GTF) basis sets of triple-zeta valence quality, augmented by a polarization function (TZVP) are adopted for Fe, Ti, Si, Ge, Zr e O atoms,²³ while Sn atoms are described by pseudopotential basis set (Sn_DURAND-21G*); where the core electrons are described by an effective potential defined by Durand and Barthelat.²⁴ Infinite Coloumb and exchange sums are truncated by five thresholds set to 10^{-7} , 10^{-7} , 10^{-7} , 10^{-7} and 10^{-14} . The shrinking factor (Pack–Monkhorst and Gilat net)²⁵ was set to $6 \times 6 \times 6$, corresponding to 40 independent k points in the irreducible part of the Brillouin zone integration. The convergence threshold for SCF energy calculation on optimization process was set to 10^{-8} Hartree.

Results and Discussion

The optimized structural parameters of FeBO_3 (B = Ti, Ge, Zr, Sn) in FEM state are presented in Table 1. The results obtained for FeTiO_3 show good agreement with experimental one.²¹ In relation to the other materials, was observed that the lattice parameters and unit cell volume were modified in accordance with the ionic radius for B-site cation. A more detailed discussion about structural properties of ilmenite materials can be found in our previous work.²⁶

In order to analyze the magnetic properties for such materials, we used a magnetic ordering stability criteria

that was derived from comparison between the calculated total energies at FEM and AFM spin configurations. This scheme has been successfully used in a lot of theoretical studies.^{14,27-29} In FEM configuration the spin orientation within the Fe^{2+} layers and in adjacent layers is parallel (Fig. 2a); whereas, for AFM state the Fe^{2+} magnetic moments are ferromagnetic coupled in a [001] plane but, they have opposite orientation for adjacent layers in c axis (Fig. 2b). The energy results indicate that FeTiO_3 and FeGeO_3 are AFM materials, while FeZrO_3 and FeSnO_3 are FEM. In the following subsections, we will discuss the interlayers magnetic ordering for FeBO_3 ilmenite materials considering the existence of both direct (J_d) and superexchange (J_s) couplings between adjacent Fe^{2+} layers, as shown in Figure 1.

As previously discussed, the ilmenite structure arrangement enables a vacancy formation between adjacent Fe^{2+} layers separated by a B-site plane. From this, the interlayer magnetic coupling integral can be visualized as a direct coupling between 3d orbitals of adjacent Fe^{2+} cations. Once the vacancy formation occurs in cationic (B) sublattice and the direct exchange coupling depends on the distance, the non-magnetic B-site cation modification can affect the magnetic ordering in such direction. To investigate such hypothesis, the energy difference (ΔE) between FEM and AFM states was plotted against the interatomic distance for Fe^{2+} layers, as shown in Figure 3. From these results, it was observed that the FEM state is stabilized for ilmenite materials with large B-site metals (Sn, Zr), whereas, contracted ilmenite cells (Ge, Ti) exhibit an AFM behavior.

Table 1. Theoretical and Experimental results for structural parameters and Energy Difference (ΔE) between magnetic configurations for FeBO_3 (B = Ti, Ge, Zr, Sn) ilmenite materials.

Models	Lattice Parameters (Å)		Bond distance (Å)				Fe-Fe (Å)	$\Phi\text{O-B-O}$ (degrees)	ΔE (meV)
			Fe-Oax	Fe-Oeq	B-Oax	B-Oeq			
FeTiO3	5.093	14.226	2.180	2.100	2.120	1.860	4.158	160.43	-45.8
FeGeO3	4.762	14.191	2.243	2.075	1.978	1.882	4.056	165.00	-17.0
FeZrO3	5.453	14.242	2.216	2.152	2.223	2.057	4.193	161.50	63.3
FeSnO3	5.275	14.437	2.263	2.139	2.162	2.046	4.111	166.81	94.8
Exp.21	5.087	14.083	2.200	2.080	2.090	1.870	-	-	-

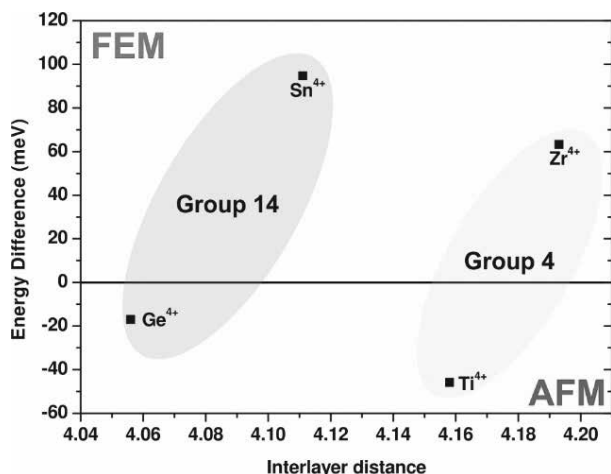


Figure 3. Energy difference (in meV) between AFM and FEM configuration as function of Fe-Fe interlayer distance (in Å).

This result can be discussed as function of electronic repulsion between Fe^{2+} atoms 3d orbitals in different layers, as presented in Figure 4. In this case, we use the c-axis oriented 3d orbital ($3d_{z^2}$), once the cationic vacancy induces a coupling in such direction. In Figure 4 is possible to see that B-cation volume control the distance between different Fe^{2+} layers in accordance with the results presented in Table 1 and Figure 3. For instance, from periodic Group 14 (Sn, Ge), the increase in B-site cation ionic radius (Ge = 0.53 Å; Sn = 0.69 Å) induces an angular distortion in O-B-O bonds in axial plane, which causes an increase in bond distances allowing a bigger spacing between Fe^{2+} layers (Table 1). The same behavior was observed when we compare the FeBO_3 (B=Ti, Zr) ilmenite materials from periodic Group 4 (Table 1 and Figure 3).

In these different periodic Groups (4 and 14), such O-B-O angular distortion induces a decrease of direct overlap between $3d_{z^2}$ orbitals from different layers enabling a FEM ground-state due to the control of smaller electronic repulsion between the unpaired electrons. On the other hand, for smaller cations the proximity between Fe^{2+} layers increase the overlap between $3d_{z^2}$ orbitals stabilizing an AFM ground-state, once the higher electronic repulsion induces a pairing of electrons in agreement with the Pauli Exclusion Principle.

Regarding the results presented in Figure 3, was noted that the last discussion is not valid if we compare B-site cation from different periodic groups. For instance, the expected result for FeTiO_3 (Group 4) from the interlayer distance (Figure 3) suggests a FEM ordering due to the larger spacing in comparison to the FeSnO_3 material (Group 14), which can be attributed to the chemical differences between such metals, for instance, valence orbitals, ionization potential, ionic radius and others.

As previously cited in the introduction section is know that the B-site cations for ilmenite materials enables a connection between different Fe^{2+} layers, which is denominated intermetallic connection Fe-O-B-O-Fe. Goodenough and Stickler argue that this kind of interaction originates a long-range coupling, which is the most fundamental reason to the AFM arrangement observed in ilmenite materials.⁵ However, this kind of long-range coupling is also observed in other materials that exhibit variations of the magnetic ordering as function of valence orbitals from “atom-bridge”.¹²⁻¹⁴

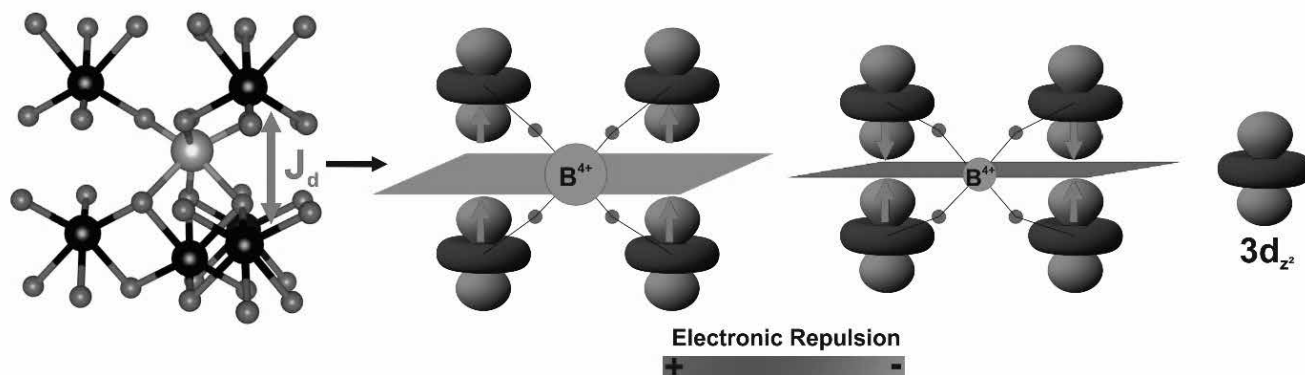


Figure 4. Representation of electronic repulsion between adjacent Fe^{2+} layer in FeBO_3 (B = Ti, Ge, Zr, Sn) as function of ionic radius of B-site cation and its influence on magnetic ordering.

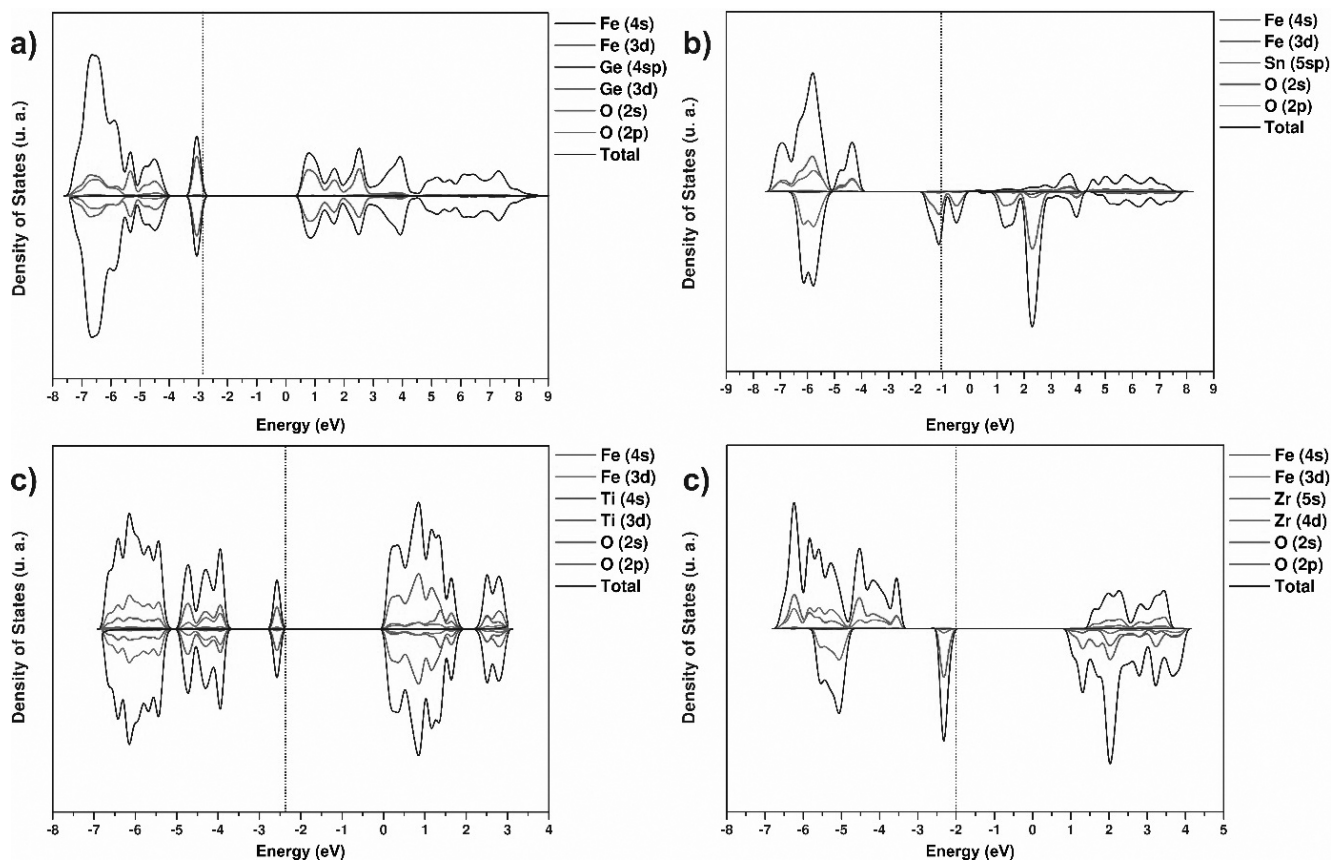


Figure 5. Spin-polarized Density of States for a) FeGeO_3 , b) FeSnO_3 , c) FeTiO_3 , d) FeZrO_3 ilmenite materials

In order to investigate the orbital overlap effect on magnetic ordering of ilmenite materials, the spin-polarized Density of States was evaluated as presented in Figure 5. From this result is clearly shown that the Valence Band (VB) exhibits the same pattern of orbitals distribution for all investigated ilmenite materials: Fe 3d orbitals are always overlapped with O 2p orbitals in VB. However, for Conduction Band (CB) were observed different compositions as function of valence orbitals from B-site metals. For FeGeO_3 and FeSnO_3 materials (Figure 5a, b), the CB is mainly composed by 4sp and 5sp of the Ge and Sn atoms, respectively; whereas, for FeTiO_3 and FeZrO_3 the 3d and 4d orbitals of the Ti and Zr atoms are superposed with O 2p orbitals, respectively (Figure 5a, b).

Following the same discussion addressed by Toyoda and co-workers for $\text{CaCu}_3\text{B}_4\text{O}_{12}$ ($\text{B} = \text{Ti, Ge, Zr, Sn}$) materials, the expected behavior suggest a FEM ordering for B-site cations without d valence orbitals; whereas, the AFM ground state is stabilized for transitions metals from d valence orbitals. Such expected result can be related to the large overlap between d and 2p oxygen orbitals, which strengthen the intermetallic connection and, consequently, induces a large electronic repulsion among unpaired electrons stabilizing the AFM configuration from Pauli Exclusion Principle.^{13,14} However, the comparison between the ground-states for FeTiO_3 and FeZrO_3 materials indicates that only Ti-based ilmenite (Figure 5c) has an AFM ordering, while FeZrO_3 (Figure 5d) is a FEM semiconductor. This result can be attributed to the contribution of d valence orbitals in CB observed from

DOS results. For FeTiO_3 (Figure 5c), a large contribution of 3d overlapped with O 2p orbital was observed between 0 to 2 eV suggesting a bigger overlap between these states providing strengthens in intermetallic connection. On the other hand, the smaller overlap between Zr(4d) and O(2p) orbitals added large Zr-O bond distances enabling a smaller interlayer electronic repulsion, which is responsible by FEM ordering.

Similarly, the FeBO_3 (B=Ge, Sn) ilmenite materials are expected to be FEM due to the absence of d valence orbitals (Figure 5a, b). However, only Sn-based ilmenite has this configuration suggesting a large effect of ionic radius and interlayer distance of the FeO_6 clusters. Comparing the ionic radius and bond distance for FeBO_3 (B=Ge, Sn) materials was observed that the increase in ionic radius from Ge^{4+} to Sn^{4+} induces a large spacing among Fe^{2+} layers in intermetallic connection that drastically reduce the electronic repulsion and stabilize the FEM configuration. The summation of these theoretical results demonstrates that the magnetic ordering of ilmenite materials can be controlled from a complex relation between ionic radius and valence orbitals of non-magnetic metals occupying B-site.

Conclusions

From theoretical results obtained through DFT/B3LYP theory applied to the ilmenite structure of FeBO_3 (B = Ti, Ge, Zr, Sn) materials, it was observed that structural parameters were calculated with good agreement to experimental results and describe very well the B-site effect on such parameters. Furthermore, the simulations performed in this work reveal the effect of non-magnetic B-site cations at control of magnetic ordering of ilmenite materials from a complex relation between interlayer distance, valence orbital and intermetallic connection. In particular, FeSnO_3 and FeZrO_3 materials exhibit ferromagnetic ground state due to the large spacing among Fe^{2+} layers and the weak intermetallic connections; whereas, FeGeO_3 and FeTiO_3 materials are antiferromagnetic for the opposite reasons.

Acknowledgments

The authors are grateful for the support given from the CAPES, UEPG and Fundação Araucária.

References

- Bhalla, A. S.; Guo, R. Y.; Roy, R. *Materials Research Innovations*, 4, 3, (2000).
- Wu, H.; Li, L.; Liang, L.-Z.; Liang, S.; Zhu, Y.-Y.; Zhu, X.-H. *Journal of the European Ceramic Society*, 35, 411, (2015).
- Zhu, X. *Recent Patents on Nanotechnology*, 3, 42, (2009).
- King, G.; Woodward, P. M. *Journal of Materials Chemistry*, 20, 5785, (2010).
- Goodenough, J. B. *Physical Review B*, 164, 768, (1967).
- Abrahams, S. C. *Acta Crystallographica Section B-Structural Science*, 63, 257, (2007).
- Gou, H.; Zhang, J.; Li, Z.; Wang, G.; Gao, F.; Ewing, R. C.; Lian, J. *Applied Physics Letters*, 98, (2011).
- Okada, T.; Narita, T.; Nagai, T.; Yamanaka, T. *American Mineralogist*, 93, 39, (2008).
- Zhang, T. S.; Shen, Y. S.; Zhang, R. F. *Materials Letters*, 23, 69, (1995).
- Kato, H.; Yamada, M.; Yamauchi, H.; Hiroyoshi, H.; Takei, H.; Watanabe, H. *Journal of the Physical Society of Japan*, 51, 1769, (1982).
- Shimakawa, Y.; Mizumaki, M. *Journal of Physics-Condensed Matter*, 26, (2014).
- Shiraki, H.; Saito, T.; Yamada, T.; Tsujimoto, M.; Azuma, M.; Kurata, H.; Isoda, S.; Takano, M.; Shimakawa, Y. *Physical Review B*, 76, (2007).
- Mizumaki, M.; Saito, T.; Shiraki, H.; Shimakawa, Y. *Inorganic Chemistry*, 48, 3499, (2009).
- Toyoda, M.; Yamauchi, K.; Oguchi, T. *Physical Review B*, 87, (2013).
- Shimakawa, Y.; Saito, T. *Physica Status Solidi B-Basic Solid State Physics*, 249, 423, (2012).
- Zhu, M.; Do, D.; Dela Cruz, C. R.; Dun, Z.; Zhou, H. D.; Mahanti, S. D.; Ke, X. *Physical Review Letters*, 113, (2014).
- Becke, A. D. *J. Chem. Phys.*, 98, 5648, (1993).
- Lee, C.; Yang, W.; Parr, R. G. *Physical Review B*, 37, 785, (1988).
- Dovesi, R.; Orlando, R.; Civalleri, B.; Roetti, C.; Saunders, V. R.; Zicovich-Wilson, C. M. *Z. Kristallogr*, 220, 571, (2005).
- Dovesi, R.; Saunders, V. R.; Roetti, C.; Orlando, R.; Zicovich-Wilson, C. M.; Pascale, F.; Civalleri, B.; Doll, K.; Harrison, N. M.; Bush, I. J.; D'Arco, P.; Llunell, M. *CRYSTAL09 User's Manual*; University of Torino: Torino, 2009.
- Wechsler, B. A.; Prewitt, C. T. *American Mineralogist*, 69, 176, (1984).
- Chartier, A.; D'Arco, P.; Dovesi, R.; Saunders, V. R. *Physical Review B*, 60, 14042, (1999).

23. Peintinger, M. F.; Oliveira, D. V.; Bredow, T. J. *Comput. Chem.*, 34, 451, (2013).
 24. Durand, P.; Barthelat, J.-C. *Theoret. Chim. Acta*, 38, 283, (1975).
 25. Monkhorst, H. J.; Pack, J. D. *Physical Review B*, 13, 5188, (1976).
 26. Ribeiro, R. A. P.; de Lazaro, S. R. *Rsc Advances*, 4, 59839, (2014).
 27. Lebernegg, S.; Schmitt, M.; Tsirlin, A. A.; Janson, O.; Rosner, H. *Physical Review B*, 87, (2013).
 28. Liu, Y. P.; Fuh, H. R.; Wang, Y. K. *Computational Materials Science*, 92, 63, (2014).
 29. Liu, M.; Lv, Z.-L.; Cheng, Y.; Ji, G.-F.; Gong, M. *Computational Materials Science*, 79, 811, (2013).
-

Renan A. P. Ribeiro^{a*}, Ageo
Meier de Andrade^a, Luis H.
S. Lacerda^a, Alexandre C.
Jr.^b & Sergio R. de Lázaro^a

^a Department of Chemistry, State University of Ponta Grossa, Av. General Carlos Cavalcanti, 4748, 84030-900, Ponta Grossa, PR, Brazil

^b Department of Physics, State University of Ponta Grossa, Av. General Carlos Cavalcanti, 4748, 84030-900, Ponta Grossa, PR, Brazil

*E-mail: ribeiroapr@gmail.com

Success Case of the Application of Virtual High Throughput Screening Against Molecular Antimalarial Targets

Renata R. Nunes, Rafael C. R. Chagas, Fernando P. Varotti & Alex G. Taranto

Introduction

Malaria is an infectious disease caused by parasites belonging to the genus *Plasmodium*, having five species which infect humans: *Plasmodium falciparum*, *P. vivax*, *P. malariae*, *P. ovale* and *P. knowlesi*.¹

The main symptoms presented by the disease are fever, chills, headache, vomiting, anemia, diarrhea, anorexia, fatigue. The untreated malaria can evolve to pulmonary edema, renal complications, obstructive jaundice, causing the death of infected individual.²

According to the World Health Organization (WHO), about three billion people are exposed to the risk of having malaria, of these, 216 million are affected by the disease and 655,000 die from it. In Brazil, the most important species are *P. vivax*, responsible for 90% of the cases, and *P. falciparum*, responsible for the most serious cases and for the mortality increase. A major factor contributing to the spread of the disease is the resistance of parasites to current antimalarial drugs used in therapy.³

In this context, new groups started to develop strategies to search for new antimalarial drugs. Based on molecular biology techniques and high throughput screening.⁴

Although many studies have focused on the screening of new molecules with *in vitro* and *in vivo* antimalarial activity, few compounds reached the stage of clinical trials. Therefore, it is of fundamental importance to focus

efforts to find new molecules with potential antimalarial activity to create a therapeutic arsenal.³

A major factor contributing to the spread of the disease is the resistance of parasites to current antimalarial drugs used in therapy.³ In addition, the *plasmodium* resistance to commercially available drugs for antimalarial therapy is a threatening factor in controlling the disease worldwide.⁵

One strategy used for the development of new drugs is the use of *in silico* techniques due to high experimental costs such as X-ray crystallography and *in vivo* biological assay for few molecular targets. Hence, molecular modeling techniques, such as comparative modeling⁶, docking⁷, molecular dynamics⁸ and virtual screening⁹, have been used as a tool to development of new drugs. Such techniques allow researchers to build molecular target scaffolds to simulate and predict toxicity, activity, bioavailability and effectiveness. Therefore this rational drug design project, reduces the time and the costs to develop a new drug, wherein, virtual screening approaches, consists in the identification of novel molecules against specific molecular targets.¹⁰ It has been largely used to obtain the pharmacoforic conformation and the binding energy, of a set of compounds against a biological receptor.¹¹

In this context, our research group has studied specific targets building a database denoted by Our Own Molecular Targets (OOMT)¹² with 40 structures

from Protein Data Bank (PDB)¹³ and built by comparative homology modeling.⁶

In a previous study, we performed virtual screening process on 10 compounds using OOMT database. Following, the compound I showed specificity for the malaria targets. Hence, this compound was addressed for antimalarial assay. As a result of experimental work, the compound I had a satisfactory antimalarial activity. In this study, we described a success case of a hit compound obtained from virtual High Throughput Screening (vHTS). This process consisted the use of docking approach between the compound I and specific *P. falciparum* molecular targets, such as plasmepsin IV, plasmepsin II, falcipain II14 and PfATP6.¹⁵

All these proteins are present in the digestive vacuole of *P. falciparum*, except PfATP6 present in membrane. Additionally, the digestive vacuole enzymes work with optimum pH of 4-5.¹⁶

Methods

The previous results of virtual screening using OOMT database motivated us to study new molecular targets against selected *P. falciparum* targets. The molecular targets plasmepsin IV plasmepsin II, falcipain II, which were obtained from PDB under codes 2ANL, 1LF3, 3BPF, respectively,¹³ while PfATP6 was obtained by previous comparative modeling methodology.¹⁵

The promising compound was designed in MarvinSketch program where its protonation was adjusted to pH 4.5. Next, it was refined in the MOPAC17 program using the semi-empirical parametric method 7 (PM7).¹⁸

The compound was oriented toward the binding site through a grid box with dimensions of 20 Å covering all binding site. The coordinates X, Y and Z were defined according to table 1 with spaced points of 1 Å centered in the ligand. Following, crystallographic ligands were re-docked into the targets to evaluate the docking methodology, obtaining the root mean square deviation (RMSD) values for heavy atoms. Two distinct approaches were used, rigid and flexible docking using programa AutoDock Vina7. After the rigid docking, the binding site amino acid residues were chosen for flexible docking (table 2).

Table1. Grid box size and position for all molecular targets.

Coordinates (Å)			
	x	y	z
2ANL	54.924	13.448	25.686
1LF3	16.215	6.850	27.605
3BPF	-36.87	31.066	-47.069
PfATP6	-5.142	-48.212	8.979

In addition, the targets state of protonation was adjusted to acid pH using PROPKA from Maestro software¹⁹.

All docking simulations were carried using AutoDock vina⁷, DockThor²⁰ and SwissDock²¹ softwares. The exhaustiveness was set to 8 to improve the docking search.

Finally, DS Visualizer v.4.0 (Accelrys Software

Table 2. Flexible residues in the binding sites of molecular targets

2ANL	1LF3	3BPF	PfATP6
ASP34	ILE14	GLN36	ILE251
GLY36	MET15	CYS42	LEU253
ILE75	ILE32	TRP43	PHE254
TYR77	ASP34	LEU72	GLN257
GLY78	GLY36	ASN81	LEU258
LEU131	TYR77	GLY82	ILE261
ASP214	VAL78	GLY83	ILE748
THR217	SER79	LEU84	ILE752
VAL292	ILE123	HIS174	ASN 755
ILE300	TYR192		ILE756
	ASP214		VAL759
	SER218		PHE763
			LEU815
			ILE816
			LEU821
			TYR824
			ILE825

Inc, USA) was used to show the docking results of the binding conformations; thereby establishing the best molecular target for the compound. Moreover, logP, Molecular Weight (MW), number of hydrogen atoms acceptors and donor, Log S, Druglikeness, properties were calculated using DataWarrior program.

Results and discussion

Initially, the re-docking using AutoDock Vina process showed that the crystallographic and docked ligand shared the same conformation into the binding site. The RMSD values are represented in table 3.

Table 3. Root mean square deviation (RMSD)

Software	Molecular targets - RMSD values (Å)			
	2ANL	1LF3	3BPF	PfTP6
AutoDockVina	0.25	0.40	1.51	1.12
DockThor	7.09	2.37	1.59	3.46
SwissDock	9.16	2.94	1.89	3.04

values found after crystallographic ligands were re-docked into the targets to evaluate the docking methodology

These results evaluated the docking methodology considering the RMSD value less 2.0 Å. In this context, the AutoDock Vina program showed the best RMSD results compared with SwissDock and DockThor softwares⁷.

The AutoDock Vina⁷, DockThor²⁰ and SwissDock²¹ software were used to generate the binding energy of compound for four enzymes. Table 4 shows the binding energies between the promise ligand and all targets for rigid and flexible approach.

Table 4. Binding energy (Kcal/mol) between the compound and binder crystallographic against Plasmeptin IV, Plasmeptin II, Falcipain II and PfATP6, using the software AutoDock Vina (Flexible and rigid), DockThor and SwissDock. Table A, B, C and D, respectively

(A)

Flexible Docking using AutoDock Vina				
	2ANL	1LF3	3BPF	PfATP
Compound	-10.1	-10.4	-8.0	-12.2
Crystal	-12.7	-12.1	-8.1	-6.8

(B)

Rigid Docking using AutoDock Vina				
	2ANL	1LF3	3BPF	PfATP
Compound	-8.1	-8.6	-6.7	-8.6
Crystal	-12.5	-17.9	-6.8	-7.7

(C)

Using Docking DockThor				
	2ANL	1LF3	3BPF	PfATP
Compound	-30.96	-47.08	-23.38	-16.39
Crystal	-31.22	-37.96	-31.79	-20.84

(D)

Using Docking SwissDock				
	2ANL	1LF3	3BPF	PfATP
Compound	-8.18	-8.36	7.50	-6.62
Crystal	-9.16	-11.33	-7.25	-6.98

As can be seen, the Autodock Vina program obtained more accuracy results than other softwares. In addition, both rigid and flexible approaches through AutoDock Vina suggested the 3BPF and PfATP6 as molecular targets for compound I.

The compound could perform electrostatic, van der Waals and Pi interaction. Fig. 1 shows the interaction of compound with 3BPF3 and PfATP6 into the binding site. The crystallographic ligand and compound shared the same amino acids in the binding site Fig.2.

In addition, the compound was evaluated against Lipinski rule ($\log P < 5$, number of hydrogen bond groups acceptors (HBA) < 10 ,

number of hydrogen bonds groups donors (HBD) (< 5 and $MW < 500$)²² using Data Warrior software.

As a result, the compound respects the Lipinski rule having MW, HBA, HBD, and logP of 291.377 g/mol, 4, 2 and 3.33, respectively. Moreover, this molecule has aqueous solubility and druglikeness of -3.205 mol/liter and 2.76, respectively. These results are close with antimalarial drugs, like chloroquine. Furthermore, Datawarrior could not estimate any mutagenic, tumorigenic, irritant activity.

Figure 1. Electrostatic interactions, van der Waals and Pi interaction between target and compound. a) falcipaina II. b) PfTPA6. Green and pink show van der Waals interactions and electrostatic, respectively.

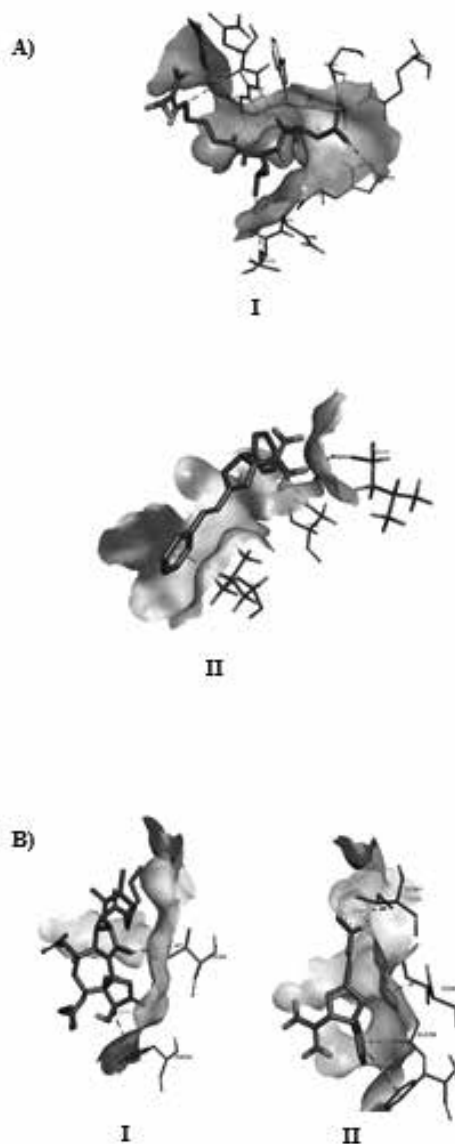
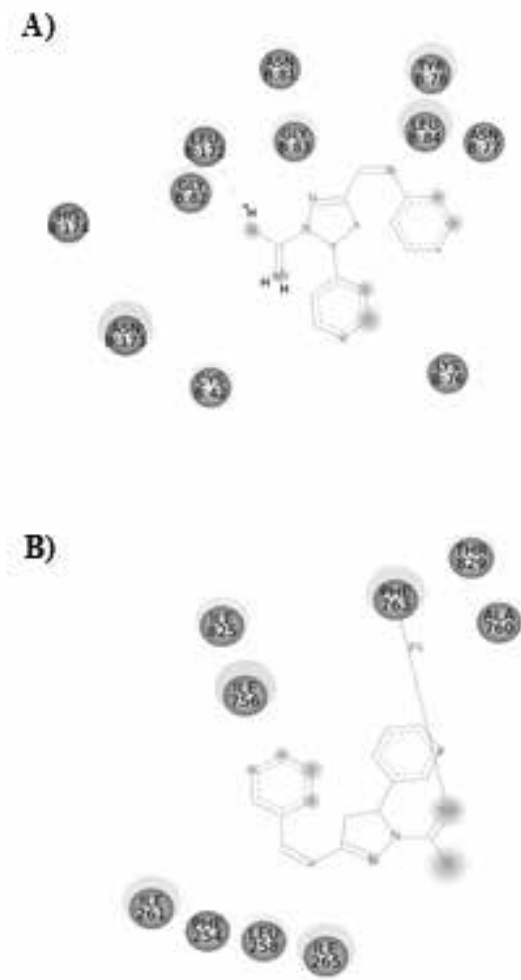


Figure 2. Binding site kept a) falcipaina II; I – Crystallographic ligand and II - compound b) PfATP6; I - crystallographic ligand and II -compound.

Conclusions

This work evaluated the accuracy among three different docking methodologies, which AutoDock Vina showed more suitable results for our system.

The data addressed PfATP6 and falcipaina II as a

potential molecular target for this synthetic compound. In addition, this compound fits into Lipinski rule with acceptable values of Log S and druglikeness, suggestion it as a potential new antimalarial drug. Noteworthy, after docking studies, this compound was addressed to antimalarial assay. As a result, this compound was able to kill 78% of parasites in vitro test. Further ligand optimization cycle had begun generating new hit for docking and biological assay.

Acknowledgments

The authors are grateful for the support given from FAPEMIG (APQ-00557-14), CAPES, CNPq (UNIVERSAL 449984/2014-1) and PPGCF/UFSJ.

References

- Lamikanra, A. A. et al. *Blood* 110, 18–28 (2007).
- Leite, F. H. A. et al. *BBR - Biochem. Biotechnol. Reports* 2, 59 (2013).
- Ferreira, M. U., M. D. S.-N. & Silva-Nunes, M. Da. *Journal of Infection in Developing Countries* 4, 533–545 (2010).
- Sahu, N. K., Sahu, S. & Kohli, D. V. *Chem. Biol. Drug Des.* 71, 287–297 (2008).
- Melo, G. C. et al. *PLoS One*. 9, e105922 (2014).
- Bordoli, L. et al. *Nat. Protoc.* 4, 1–13 (2009).
- Trott, O. & Olson, A. J. *J. Comput. Chem.* 31, 455–461 (2010).
- Fonseca, A. L., Nunes, R. R., Ricardo José Alves, R. J. et al. *BBR - Biochem. Biotechnol. Reports* 2, 111–113 (2013).
- Westermaier, Y., Barril, X. & Scapozza, L. *Methods* 71, 44–57 (2015).
- Irwin, J. J., Sterling, T., Mysinger, M. M., Bolstad, E. S. & Coleman, R. G. *Journal of Chemical Information and Modeling* (2012).
- Andricopulo, A. & Ferreira, L. *Medicinal J. Mod. Med. Chem.* 2, 20–31 (2014).
- Carregal, A. P., Jr, M. C. & Taranto, A. G. *BBR - Biochem. Biotechnol. Reports* 2, 14–16 (2013).
- Berman, H. M. et al. *Nucleic Acids Res.* 28, 235–242 (2000).
- De Oliveira, M. E. et al. *Molecules* 18, 15276–15287 (2013).
- Guimarães, D. S. M. et al. *Mem. Inst. Oswaldo Cruz* 110, 255–8 (2015).
- Kuhn, Y., Rohrbach, P. & Lanzer, M.. *Cell. Microbiol.* 9, 1004–1013 (2007).
- Stewart, J.J.P., S. C. C. MOPAC2012. (2012). at <HTTP://openmopac.net>
- Stewart, J. J. P.. *J. Mol. Model.* 19, 1–32 (2013).
- Salam, N. K., Adzhigirey, M., Sherman, W. & Pearlman, D. A. *Protein Eng. Des. Sel.* 27, 365–374 (2014).
- De Magalhães, C. S., Almeida, D. M., Barbosa, H. J. C. & Dardenne, L. E. *Inf. Sci. (Ny)*. 289, 206–224 (2014).
- Grosdidier, A., Zoete, V. & Michielin, O. *Nucleic Acids Res.* 39, 270–277 (2011).
- Jorgensen, W. L. *Science* 303, 1813–1818 (2004).

Renata R. Nunes*, Rafael C. R. Chagas, Fernando de P. Varotti & Alex G. Taranto

Universidade Federal de São João del Rei - Campus CCO - Rua Sebastião Gonçalves Coelho, 400 - Chanadour - MG - CEP 35.501-296

*E-mail: renata.rachidee@gmail.com

Theoretical Quantum Study of the Molecular System XLi_2 , with $\text{X}=\text{D}, \text{T}$, and Mu

Ricardo Gargano, Thiago F. da Cunha, Henrique V. R. Vila, Wiliam F. da Cunha, Luciano A. Leal & Geraldo M. e Silva

Introduction

This work presents an exact quantum investigation of the reactive scattering process $\text{X}+\text{Li}_2 \rightarrow \text{LiX}+\text{Li}$, with $\text{X}=\text{D}, \text{T}$, and Mu in the fundamental state with total angular momentum equal zero. The study has been carried out with a recently developed potential energy surface (PES) [1], which has been fitted from the ab initio energies determined through a full CI calculation for the 6-311G (2df, 2pd) basis set and also through a pseudo potential representing the Li.

Methods

Analytical representations of the $\text{X}+\text{Li}_2$ PES, with $\text{X}=\text{D}, \text{T}$ and Mu , were obtained using a Bond Order (BO) polynomial expansion for both two and three-body terms, in agreement with the standard many-body method. Due to the fact that the considered reaction is highly exothermic (yielding an amount of energy of about 33.66 kcal/mol), a great number of rovibrational states and quadratures has been taken into account (even for low energies) in order to accurately describe its dynamical properties. The time-independent nuclear Schrödinger equation has been solved by means of the ABC program [2]. This code is ideally suited to calculating detailed state-to-state quantities - such as the state-resolved differential crosssections - in which the quantum states of the reactants, as well as those of the products, are specified at the same time. ABC simultaneously expands the wave functions of all three possible chemical arrangements in the Delves hyper-spherical coordinate system.

Results and Discussion

The obtained results show the isotope effects in promoting the reactivity of the $\text{H}+\text{Li}_2$ reaction and the reproduction of the physical behavior expected by the eigenvalues of the adiabatic vibrational functions to demonstrate the reliability of the expansion of the nuclear wave function. In both purely excitation rotational and vibrational, the system reactivity is higher when the translational energy of the reagent and low. The isotopic systems follow the trend of the studies for the hydrogen atom and also, the studies by da Cunha et. al [3] on the HLi_2 system and its isotopic variants, ie, both the vibrational excitation as the rotational influence the reactivity XLi_2 the system.

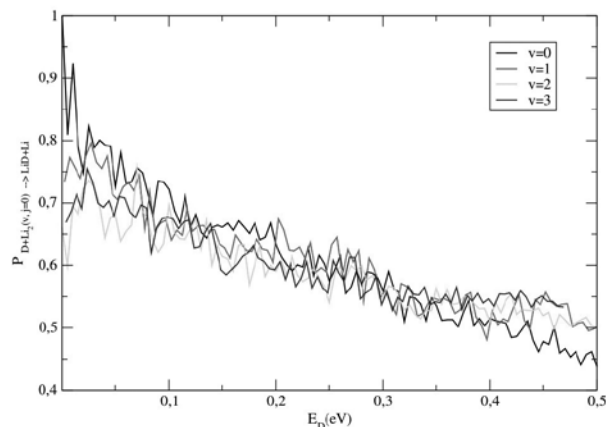


Figure 1. Reaction probabilities as a function of the translational energy of reactant Deuterium for the purely rotational excitation of the molecule Li_2 .

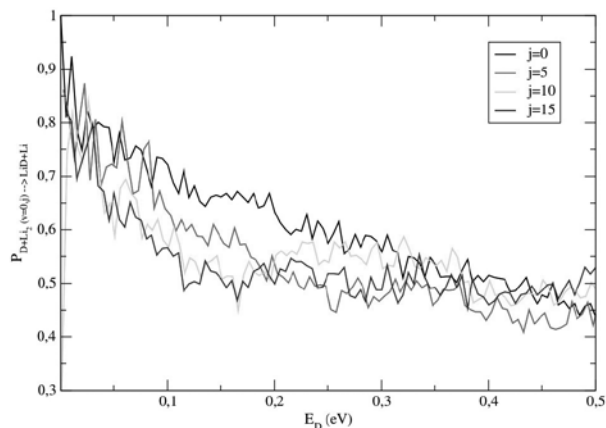


Figure 2. Reaction probabilities as a function of the translational energy of reactant Deuterium for the purely vibrational excitation of the molecule Li_2 .

On analysis of the energy distribution is observed that for higher values of total energy E there are more ro-vibrational states of products, but with lower probability of reaction in these cases.

Conclusions

These results show us that the probability of reaction of $\text{D}+\text{Li}_2$ and $\text{T}+\text{Li}_2$ systems is greater at low translational energies of the reactant and also, when the reagent Li_2 is in the fundamental state ro-vibrational.

From these results, we conclude also higher reduced mass of the reaction diatoms ($\text{T}+\text{Li}_2 \rightarrow \text{LT}+\text{Li}$), the greater the reactivity of the system. This result is consistent with the fact that the greater the mass of the system, the greater the coupling and the bonding of ro-vibracionais states of reactant and product participating in the reaction.

This has also influence in energy distribution. It is observed in energy distribution of the products that the energy yield of the product is greater when the molecules products are more massive, or in isotopic systems with more massive nuclei.

Acknowledgments

The authors thank CNPq and CAPES received by holders.

1. Maniero A. M., Acioli P. H., e Silva G. M., Gargano R. *Chemical Physics Letters*, v.490, p.123-126, (2010).
2. D., Castillo J. F., Manolopoulos D. E. *Computer Physics Communications*, v.133, p.128, (2000).
3. Da Cunha W. F., Leal L. A., Da Cunha T. F., E Silva G. M., Martins J. B. L., Gargano R. *Journal of Molecular Modeling*, v.20, p.2315, (2014).

Ricardo Gargano*, Thiago F. da Cunha, Henrique V. R. Vila, Wiliam F. da Cunha, Luciano A. Leal & Geraldo M. e Silva

Instituto de Física, Universidade de Brasília. CP04455, Brasília, DF, CEP 70919-970, Brazil

*E-mail: Gargano@Unb.Br

Angular Momentum Coupling and Discrete Quantum Mechanics: the 10-Spin Network, the Pentagonal Relationship, an Eigenvalue Equation and Semiclassical Limits

Robenilson F. dos Santos, Mirco Ragni, Ana Carla P. Bitencourt,
Frederico V. Prudente & Vincenzo Aquilanti

Introduction

Remarkable advances in quantum angular momentum theory and related spin network approaches are of relevance not only to the traditional fields of atomic, molecular and nuclear spectroscopy and dynamics, but also to recent developments in quantum information and quantum relativity [1]. Applications are being developed also for imaging reconstruction, particularly in tomography.

An icosahedral “abacus” representation combines pentagonal and hexagonal relationships. The latter has been recently reconsidered in [2], the pentagonal one is the subject of this work.

Another aspect considered is the relationship with the classification of continuous and discrete polynomials within semiclassical limit illustrated in Figure 1.

Methods

Recoupling schemes [3,4] can be arranged in pentagonal relationships, allowing to illustrate properties of Wigner $6j$ symbols or Racah coefficients [5], Wigner $3j$ symbols or Clebsch-Gordan coefficients [6]. Wigner $d_{jm}^j(b)$ rotation matrices or symmetric-top wavefunctions. As an important alternative to the generality of treatments, the asymptotic or semiclassical limit connecting $6j$ to $3j$ and $d_{jm}^j(b)$ permits a unifying vision, also to be connected to the modern theory of

orthogonal polynomials and the sets of Sturmian orbitals of applied quantum mechanics. Importantly, it generates uniformly the recurrence relationships permitting calculations and asymptotic analysis [2,5,6].

The $6j$ symbols relate to the $3j$ symbols by a semiclassical limit procedure, illustrated graphically by the downward arrow in Fig 1, can be simply written as follows, without specifying the phase and the normalization factor:

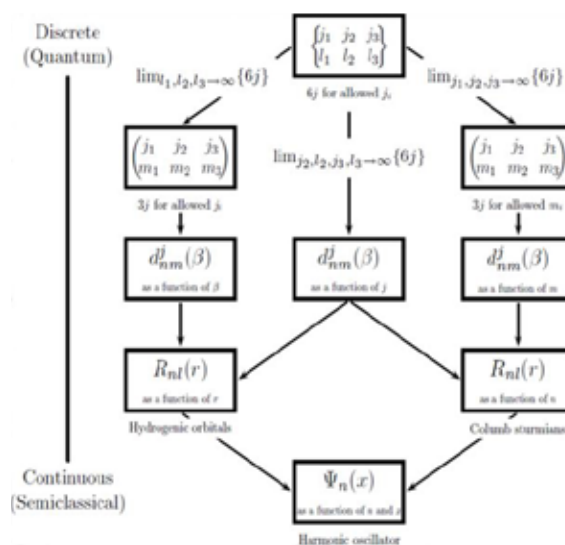


Figure 1. Quantum angular momentum and wavefunctions.

$$\left\{ \begin{matrix} a & b & x \\ C & D & Y \end{matrix} \right\} \rightarrow \left(\begin{matrix} a & b & x \\ D - Y & Y - C & C - D \end{matrix} \right)$$

From the viewpoint of interpreting the coupling of two angular momenta, we have the Clebsch-Gordan coefficients relating to the symbols $3j$ (Figure 2):

$$C_{j_1 j_2 m_1 m_2}^{j m} \equiv C(j_1 j_2 j_3 m_1 m_2 m_3)$$

$$\left(\begin{matrix} j_1 & j_2 & j_3 \\ m_1 & m_2 & m_3 \end{matrix} \right) = (-1)^{j_1 - j_2 - m_3} \frac{1}{\sqrt{2j_3 + 1}} C_{j_1 j_2 m_1 m_2}^{j m}$$

$$C_{j_1 j_2 m_1 m_2}^{j m} = (-1)^{j_1 - j_2 + m_3} \sqrt{2j_3 + 1} \left(\begin{matrix} j_1 & j_2 & j_3 \\ m_1 & m_2 & -m_3 \end{matrix} \right)$$

- j_1, j_2 e j_3 inteiros ou semi-inteiros não negativos;
- m_1, m_2 e m_3 inteiros ou semi-inteiros;
- $-j_1 \leq m_1 \leq j_1, -j_2 \leq m_2 \leq j_2$;
- $|j_1 - j_2| \leq j_3 \leq j_1 + j_2$;
- $m_1 + m_2 = m_3$.

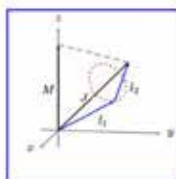


Figure 2. Illustration of the coupling of two angular momenta giving a third one and of the associated projections, as they occur in the Clebsch-Gordan coefficient or equivalently in Wigner $3j$ symbols.

Results and discussion

THE PENTAGONAL RELATIONSHIP

Making use of the tree structures, several relationships between $3nj$ symbols can be graph. If we consider relationships involving only different tree structures, i.e. without any permutation in the order of the labels a, b, c and d, so that only recoupling operations are considered, we obtain the pentagonal scheme. Figure 3 illustrates graphically the origin of the pentagonal relationships in angular momentum theory known as the Biedenharn-Elliott identity, that we write in a rearranged form as follows and illustrate in Fig 3:

$$\left\{ \begin{matrix} j_a & j_b & j_{ab} \\ j_c & j_{abc} & j_{bc} \end{matrix} \right\} = \sum_{jcd} (-1)^x (2j_{abc} + 1)(2j_{cd} + 1)(2j_{bcd} + 1)$$

$$\left\{ \begin{matrix} j_a & j_{bc} & j_{abc} \\ j_d & j & j_{bcd} \end{matrix} \right\} \left\{ \begin{matrix} j_b & j_c & j_{bc} \\ j_d & j_{bcd} & j_{cd} \end{matrix} \right\}$$

$$\left\{ \begin{matrix} j_a & j_b & j_{ab} \\ j_{cd} & j & j_{cd} \end{matrix} \right\} \left\{ \begin{matrix} j_{ab} & j_c & j_{abc} \\ j_d & j & j_{cd} \end{matrix} \right\}$$

$$x = j_a + j_b + j_c + j_{ab} + j_{bc} + j_{bcd} + j_{cd} - j_{abc} - j_d - j$$

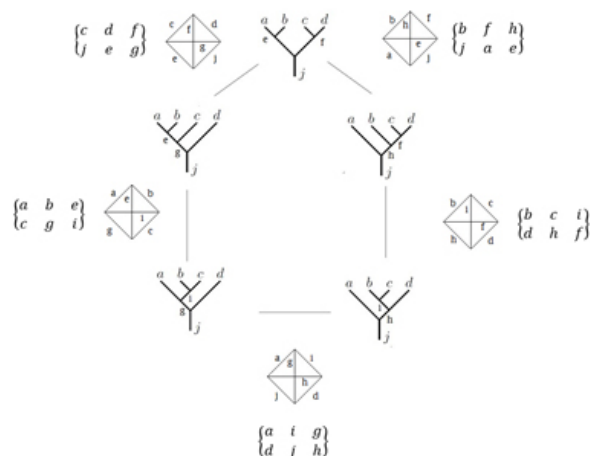


Figure 3. Illustration of the pentagonal relationship, exhibiting the coupling scheme trees, their representation as tetrahedra and the associated $6j$ symbols.

RECURRENCE RELATIONSHIPS AS EIGENVALUE EQUATIONS

The three-term relationship for $6j$ symbols can be obtained by specializing to specific values entries in the above equations and imposing increase of one of the angular momenta in unity steps. A way of writing here, useful for computation and semiclassical analysis, is:

$$j_{bc} E(j_{bc} + 1) \left\{ \begin{matrix} j_a & j_b & j_{ab} \\ j_c & j & j_{bc} + 1 \end{matrix} \right\} + F(j_{bc}) \left\{ \begin{matrix} j_a & j_b & j_{ab} \\ j_c & j & j_{bc} \end{matrix} \right\} + (j_{bc} + 1) E(j_{bc}) \left\{ \begin{matrix} j_a & j_b & j_{ab} \\ j_c & j & j_{bc} - 1 \end{matrix} \right\} = 0$$

where

$$E(j_{bc}) = \left[\left(j_{bc}^2 - (j - j_a)^2 \right) \left[(j + j_a + 1)^2 - j_{bc}^2 \right] \left[j_{bc}^2 - (j - j_b)^2 \right] \left[(j + j_c + 1)^2 - j_{bc}^2 \right] \right]^{1/2}$$

$$F(j_{bc}) = (2j_{bc} + 1) \{ j_{bc}(j_{bc} + 1) [-j_{bc}(j_{bc} + 1) + j_b(j_b + 1) + j_c(j_c + 1)] + j_a(j_a + 1) [j_{bc}(j_{bc} + 1) - j_b(j_b + 1) + j_c(j_c + 1)] + j(j + 1) [j_{bc}(j_{bc} + 1) + j_b(j_b + 1) - j_c(j_c + 1)] - 2j_{bc}(j_{bc} + 1) j_{ab}(j_{ab} + 1) \}$$

When rearranged as an eigenvalue equation, this relationship can be interpreted as a second order finite difference equation, and therefore as a discrete Schrödinger equation of interest for applied quantum mechanics.

QUANTUM AND SEMICLASSICAL SPIN NETWORKS:

Spin networks are illustrated here for the case of two quantum systems, as described by coupling schemes associated to tree-like structures, each endowed with angular momenta, which can assume in usual cases integer or half-integer values in terms of reduced Planck's constant. In practice, they actually can be not only an electronic or nuclear spin but also e.g. rotational and orbital, giving a state with total angular momentum j (coupling described by e.g. spin-orbit terms in the Hamiltonian).

Figure 4 illustrates schematically the combination of pentagonal and hexagonal relationships of these angular momenta. Representations of couplings as trees extend those in Fig 3 to an additional angular momentum and permit the introduction of the $9j$ coupling scheme as a combination of intermediate coupling along a path on the abacus.

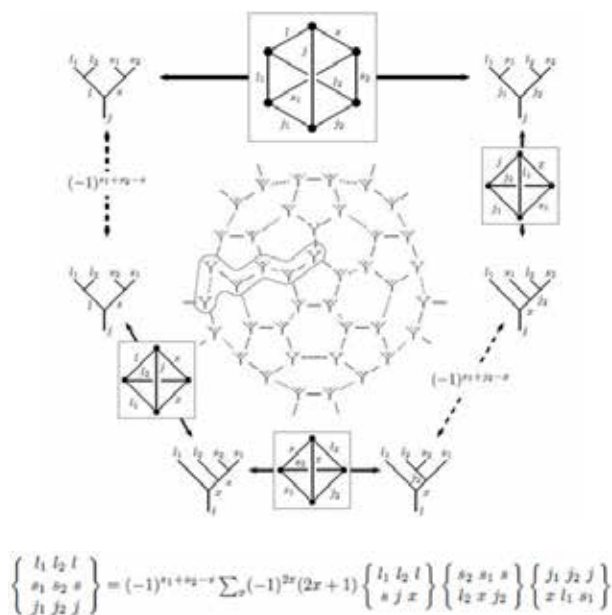


Figure 4. Icosahedral "abacus" representation, combining the hexagonal relationship rediscussed in Ref 2, and the pentagonal relationship reconsidered in this work.

Conclusions

Numerical exact and approximate calculations can be explicitly carried out following the techniques developed previously [7]. Besides general use in the contexts mentioned, the results are of perspective use in solutions of quantum mechanical problems by discretization algorithms. In general relativity, spacetime is discretized by Regge calculus; spin-networks originated from Ponzano-Regge asymptotics; Regge symmetries are crucial for our developments: we dedicate this modest contribution to the memory of Professor Tullio Regge (Torino, 1931-2014).

Acknowledgments

The authors are grateful for the support given from the CAPES and CNPQ. Also, V.A. thanks CAPES for a PVE position at UFBA.

References

1. V. Aquilanti, A.C.P. Bitencourt, C. da S. Ferreira, A. Marzuoli, M. Ragni, Quantum and semiclassical spin networks: from atomic and molecular physics to quantum computing and gravity, *Physica Scripta*, **2008**, 78, 058103.
2. D. Marinelli, A. Marzuoli, V. Aquilanti, R. Anderson, A.C.P. Bitencourt, M. Ragni, Symmetric Angular Momentum Coupling, the Quantum Volume Operator and the 7-spin Network: A Computational Perspective, *Lecture Notes in Computer Science*, **2014**, 8579, 508
3. V. Aquilanti, G. Grossi, Angular momentum coupling schemes in the quantum mechanical treatment of P-state atom collisions, *J. Chem. Phys.* **1980**, 73, 11654.
4. V. Aquilanti, S. Cavalli, G. Grossi, Hund's cases for rotating diatomic molecules and atomic collisions: angular momentum couplings and orbital alignment, *Z. Phys. D.* **1996**, 36, 215.
5. R.W. Anderson, V. Aquilanti, A.C.P. Bitencourt, D. Marinelli, M. Ragni, The Screen Representation of Spin Networks: 2D Recurrence, Eigenvalue Equation for $6j$ Symbols, Geometric Interpretation and Hamiltonian Dynamics, *Lecture Notes in Computer Science*. **2013**, 7972, 46.
6. A.C.P. Bitencourt, M. Ragni, R.G. Littlejohn, R. Anderson, V. Aquilanti, The Screen Representation of Vector Coupling Coefficients or Wigner $3j$ Symbols: Exact Computation and Illustration of the Asymptotic Behavior, *Lecture Notes in Computer Science*. **2014**, 8579, 468.
7. M. Ragni, A.C.P. Bitencourt, C.S. Ferreira, V. Aquilanti, R.W. Anderson, R.G. Littlejohn, Exact computation and asymptotic approximations of $6j$ symbols: Illustration of their semiclassical limits, *Int. J. Q. Chem.* **2010**, 110, 731

Robenilson F. dos Santos^{1,2*},
Mirco Ragni³, Ana Carla
P. Bitencourt³, Frederico
V. Prudente¹ & Vincenzo
Aquilanti^{1,4}

¹Instituto de Física, Universidade Federal da Bahia, Brasil;

²Instituto Federal de Alagoas, Campus Piranhas, Brasil;

³Departamento de Física, Universidade Estadual de Feira de Santana, Brasil;

⁴Departamento de Química, Biologia e Biotecnologia, Universidade de Perugia, Itália

*E-mail: roferreirafs@gmail.com

Cálculo da Segunda Hiperpolarizabilidade da L-arginina Fosfatada Monohidratada Considerando o Efeito do Ambiente Cristalino

Rosemberg Fortes Nunes Rodrigues, Clodoaldo Valverde, Basílio Baseia & Heibbe C. B. de Oliveira

Introdução

Para uma classe de matérias com alta aplicabilidade em óptica moderna estão os materiais com características Óptica não Linear (ONL), no qual os cristais híbridos orgânicos-inorgânicos se mostraram excelentes candidatos para a sua confecção [1]. Estes sistemas podem exibir elevado comportamento óptico não linear na região do visível e boa estabilidade térmica e mecânica, quando comparados com os cristais orgânicos. Um típico cristal orgânico-inorgânico ONL é a L-arginina fosfatada monohidratada ($C_6H_{14}N_4O_2H_3PO_4H_2O$), mais conhecida pela sigla (LAP) [2,3]. A sua unidade cristalográfica assimétrica é composta por uma molécula orgânica quirál [L-arginina]⁺, uma molécula inorgânica [H_2PO_4]⁻, e uma molécula de água.[3].

A estrutura cristalina da LAP pode ser descrita como camadas alternadas de íons de fosfato, íons L-arginina e moléculas de água presas por ligações intermoleculares de hidrogênio de uma forma rígida não-centrossimétrica [2]. A estrutura molecular da LAP é mostrada na figura 13.

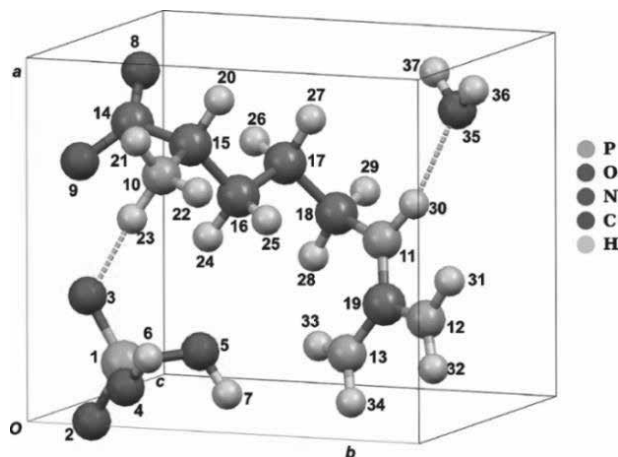


Figura 1. Estrutura molecular da unidade assimétrica da LAP4)

No estado sólido, a LAP se cristaliza no sistema monoclinico, que pertence ao grupo de simetria espacial $P2_1$, e os parâmetros da cela unitária são $a = 7,319 \text{ \AA}$, $b = 7,912 \text{ \AA}$, $c = 10,779 \text{ \AA}$, $\beta = 98,05^\circ$ (ângulo cristalográfico entre os eixos a e c) [3]. Observa-se ainda a existência de duas unidades assimétricas por cela unitária. No presente

trabalho empregamos um modelo teórico proposto por Fonseca et al. [4] para explorar as propriedades cristalinas da L-arginina fosfatada monohidratada. O objetivo é obter a segunda hiperpolarizabilidade dessa molécula envolvida em um ambiente cristalino, para este fim, utilizou-se a teoria do funcional da densidade (DFT-Density Functional Theory).

Métodos

Nesse trabalho foi feita uma abordagem supramolecular através da qual é possível detectar os efeitos da polarização do meio sobre as propriedades elétricas da LAP. Nesse aspecto, as moléculas vizinhas são vistas como cargas pontuais. Esta aproximação se baseia no fato de que as interações entre moléculas são, predominantemente, de natureza eletrostática e leva em conta os efeitos eletrostáticos de longo alcance [5].

A figura 2 mostra uma molécula de LAP envolvida por outras iguais. Nesse trabalho foi considerado um número próximo de 249 unidades assimétricas como cargas pontuais, constituindo um conjunto de celas unitárias 5X5X5, e cada cela unitária contendo duas unidades assimétricas.

Os cálculos foram feitos nos nível DFT usando o conjunto de funções base 6-311+G(d), para os seguintes funcionais de densidade: B3LYP, B2PLYP, CAM-B3LYP.

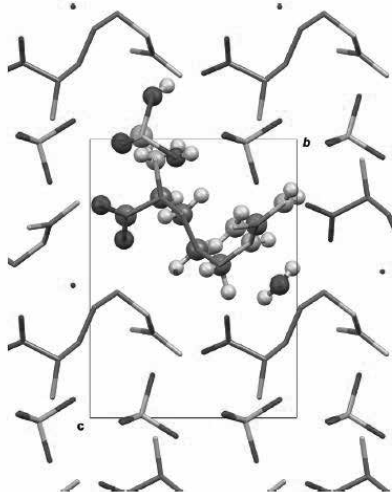


Figura 2. Projeção ao longo do eixo a do cristal mostrando a unidade assimétrica de LAP envolvida no campo de polarização das moléculas das unidades envolvidas tratadas como cargas pontuais4.

Resultados e Discussão

Inicialmente o cálculo das propriedades elétricas do cristal de LAP foi efetuado por Fonseca et al. [4], no nível MP2 utilizado o conjunto de funções base 6-311+G(d). Nesse trabalho as propriedades elétricas calculadas foram momento de dipolo, polarizabilidade linear e primeira hiperpolarizabilidade.

No presente trabalho, realizamos os cálculos das propriedades elétricas do cristal de LAP em nível DFT utilizando os funcionais, CAM-B3LYP, B3LYP e B2PLYP, e com o conjunto de funções base 6-311+G(d).

Ao comparar os valores do momento de dipolo elétricos da molécula envolvida no nível DFT, utilizando diferentes funcionais, com o valor invariável de 33,26 D (MP2), obtêm-se percentuais variados. Desse modo o CAM-B3LYP, nota-se uma diferença de 0,21%. Assim, seguindo o mesmo raciocínio comparativo, verificam-se que, para B3LYP, tem-se 0,75% e por último, B2PLYP uma diferença de 0,45%.

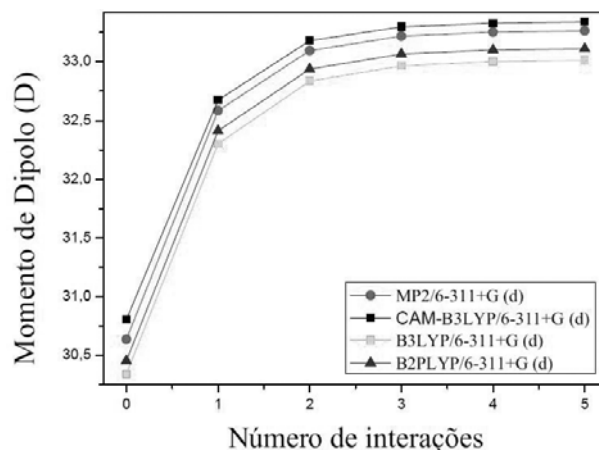


Figura 3. Evolução dos valores do momento de dipolo da LAP com os respectivos números de interação (conjunto cela unitária 5X5X5)

Para o cálculo da segunda hiperpolarizabilidade utilizou-se o funcional CAM-B3LYP e B2PLYP, pois ambos representaram valores próximos ao MP2 no cálculo do momento de dipolo, com o objetivo de mostrar os valores de (γ) , notando uma rápida convergência assim como para o momento de dipolo.

A tabela 1 mostram os resultados das componentes e resultante para segunda hiperpolarizabilidade (γ) da LAP com os respectivos números de interação e uma visualização alternativa dessa convergência fica evidente através de gráficos da figura 3

Tabela 1. CAM-B3LYP/6-311+G(d) Resultados das componentes da segunda hiperpolarizabilidade e sua resultante (10-36esu)

Número de Interações	0	1	2	3	4	5
γ_{xxxx}	25,97	18,65	18,13	18,65	18,68	11,36
γ_{yyyy}	29,60	17,27	16,98	17,02	17,05	18,58
γ_{zzzz}	20,70	8,93	7,92	7,72	7,70	12,06
γ_{xxyy}	9,00	6,11	5,96	6,11	6,14	5,49
γ_{xxzz}	6,63	4,25	4,12	4,14	4,15	4,08
γ_{yyzz}	-4,44	-0,66	-0,59	-0,47	-0,48	2,64
γ_{total}	25,10	14,75	14,21	14,33	14,35	14,37

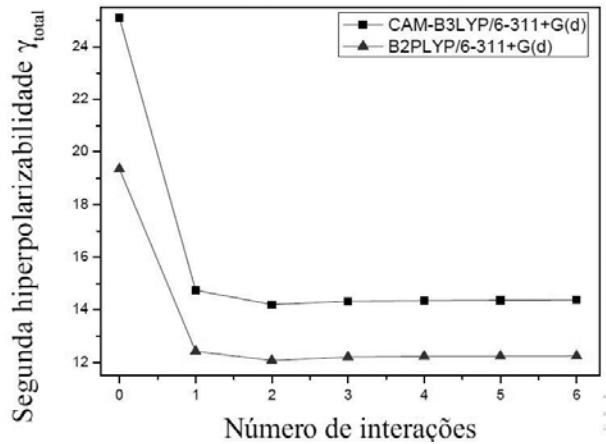


Figura 2. CAM-B3LYP e

Conclusões

Dessa forma os resultados apresentados para (γ) serão de fundamental importância para o meio científico, pois o entendimento das propriedades ópticas dos materiais propicia a obtenção das maneiras de manipulação da luz. As investigações sobre essas propriedades e esse tipo material são vitais à aplicação da óptica moderna.

Agradecimentos

Os autores são gratos pelo apoio dado por FAPEG, CAPES e CNPQ.

Referências

1. S. Manivannan, S. Dhanuskodi, K. Kirschbaum; S. K. Tiwari, Cryst. Growth Des. 5, 1463, (2005).
2. K. Aoki, K. Nagano, Y. Litaka, Acta Crystallogr., Sect. B: Struct. Crystallogr. Cryst. Chem. 27, 11, (1971).
3. E. Espinosa, C. Lecomte, E. Molins, S. Veintemillas, A. Cousson, W. Paulus, Acta Crystallogr., Sect. B: Struct. Sci. 52, 519, (1996).
4. T. L. Fonseca, J.R. Sabino, M. A. Castro, H. C. Georg, J. Chem. Phys. 133, 144103, (2010).
5. M. B. Kanoun, E. Botek, B. Champagne, Chem. Phys. Lett. 487, 256, (2010).

Rosemberg Fortes Nunes
Rodrigues^{a,b}, Clodoaldo
Valverde^{a,b*}, Basílio Baseia^c,
Heibbe Crithian Benedito de
Oliveira^d

^a Campus Henrique Santillo, Universidade Estadual de Goiás, Rod. BR 153, km 98, 75.132-903 Anápolis, GO, Brasil.

^b Universidade Paulista (UNIP), Rod. BR 153, km 7, 74.845-090 Goiânia, GO, Brasil

^c Instituto de Física, Universidade Federal de Goiás, 74.001-970 Goiânia, GO, Brasil.

^d Laboratório de Modelagem de Sistemas Complexos, Instituto de Química, Universidade de Brasília, 70904-970 Brasília, Brasil.

*E-mail: valverde@ueg.br

The Charge Carrier Density Influence and Thermal Effects on Charge Transport in Organic Semiconductors

Sara Santiago de Brito, Wiliam Ferreira da Cunha, Demétrio Antônio da Silva Filho & Pedro Henrique de Oliveira Neto

Introduction

Conjugated polymers have optical and electronic properties presenting semiconductor characteristics that make them ideal for manufacture of solar cells and electronic devices. These organic materials may be similar to the metals and semiconductors. Peculiar qualities are related to processes involved in interchain charge transport. In this sense, a phenomenological description involving temperature, different types of charge carriers, as well as, the influence of charge carriers density is fundamental to the understanding and eventual improvement of these devices. Usually, the creation of charge carriers in organic conductors is connected to photon absorption or injection of electrons in gaps, due to the large electron-phonon interaction, which leads to creation of quasiparticles. These particles are responsible for the charge transport in conjugated polymers. Recently, in a theoretical study, it was observed the temperature effect on interchain polarons dynamics. The results suggest a charge transfer increase due to the thermal effects leading to greater mobility of the carriers¹. In another study, the effect of charge carriers density was studied, showing that charge density increase leads to a nonlinear carrier mobility growth². However, both studies take into account only polarons. Therefore, the thermal effect on interchain charge transport remains poorly described.

In this research, we study the charge transport between two polyacetylene molecules in the presence of external electric field. We take into account several

temperature regimes, electric field and charge density. We have investigated the both polarons and bipolarons quasiparticles and the influence of intermolecular interaction for transportation of charge in coupled chains. This study deals with the improvement of interchain charge transport.

Methods

We use a modified version of model Su-Schrieffer-Heeger (SSH). The model is a semi-empirical tight-binding which considers the interactions between the nearest neighboring sites where the network potential are weakly overlapping. The dynamic of the system was solved on a numerical approach in the context of Hartree-Fock approximation. The SSH model was modified to include the effects of temperature, the term of Brazovskii-Kirova symmetry breaking, external electric field and interaction between chains. We use the following Hamiltonian:

$$H = H_1 + H_2 + H_{int},$$

with j indexing the chain, and:

$$H_j = \sum_{n,s} t_{jn,n+1} (C_{jn+1,s}^\dagger C_{jn,s} + H. c.) + \sum_n \frac{K}{2} y_{jn}^2 + \sum_n \frac{p_{jn}^2}{2M'}$$

The operator $C_{jn,s}$ is the annihilation operator of an π electron with spin s at the n -th site of the j -th chain, K is the harmonic constant and M is the mass of a CH group. The Hopping term is $t_{jn,n+1} = [1 + (-1)^n \delta_0](t_0 + y_{jn})$, where α is the electron-phonon coupling constant, t_0 is the transfer integral between the nearest neighboring sites in an undimerized chain and δ_0 is the Brazovskii-Kirova symmetry breaking parameter.

Results and Discussion

The simulations in this study describe two coupled cis-polyacetylene chains with 80 sites each³.

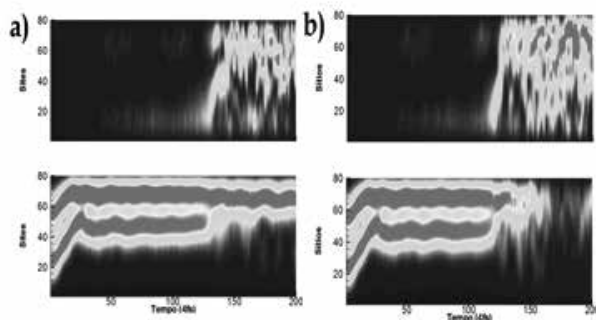


Figure 1: Temporal evolution of charge density for two polarons for an electric field of $-0,0195 \text{ mV/\AA}$: (a) $T = 0 \text{ K}$, (b) $T = 4,7 \text{ K}$.

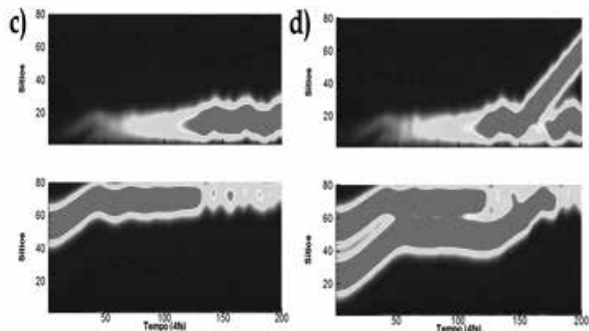


Figure 2: Temporal evolution of charge density for two bipolarons for an electric field of $-0,013 \text{ mV/\AA}$: (c) $T = 50 \text{ K}$, (d) $T = 100 \text{ K}$.

The temperature regime ranged from 0 to 100 K. The results are shown respectively in the graphs of Figures 1(a), 1(b) and 2(c), 2(d). In the first set of simulations figure 1.a) shows two polarons in the presence of an external electric field at $T = 0 \text{ K}$. Eventually, these quasiparticles reach the end of the chain where there is the interaction between the molecules. Due to the strong electrical field, one of the quasiparticles moves to the next chain. However, the charge density profile suggests the degradation of the polaron. Here, the external electric field provides energy in order to dissociate the charge from the phonons. Figure 1.b) shows the $4,7 \text{ K}$ temperature regime. It is noted that, in the presence of thermal effects, the charge transfer occurs faster than in the absence of temperature, however both quasiparticles have degraded. The figure 2 shows the interchain charge transport with bipolarons. 2-c) shows one bipolaron in the interface when thermal effects are taken into account. With this charge carrier, the energy provided by the electric field and the temperature were not enough to overcome the barrier between the two molecules. In 2-d) it is presented a simulation with two bipolarons. Note that the increase in charge density initiates the interchain charge carrier transport mechanism. Also, we find that an increase in the temperature do not change this mechanism.

Conclusions

It was investigated the interchain charge transport in polyacetylene molecules. In order to do this, it was used o modified version of SSH model. Both temperature and carriers density play an important role on charge transport in conjugated polymers.

In this study we analyzed different charge carriers. We simulated conjugated-polymer chains with polarons and bipolarons under the presence of an external electric field and thermal effects. The simulations investigated the interchain charge transport. The results of simulations performed in this study reveal for two polarons the effect of interaction between quasiparticles affects the charge transport. The interaction between two bipolarons results in charge transportation between chains and effective untrapping area of interaction interchain. It is possible to visualize how the thermal effects provide charge carrier mobility gain. We observed that the perturbation provided by thermal effects improves the charge delocalization.

Besides, in a interchain process the results suggest that the polaron transfer is enhanced by thermal perturbation.

In this study, it is presented the temperature increase raises the delocalization of the charge carrier, fastening the transport and, thus, leading to a mobility increase. It was shown that temperature effects give rise to systems with an improved of charge carriers and higher mobility especially through untrapping mechanisms.

Acknowledgments

The authors thank the funding agencies CNPq, CAPES and Finatec.

References

1. P. H. D. Neto, W. F. Cunha and G. M. e Silva. Europhys. Lett. 88, 67006 (2009).
2. P. H. D. Neto, W. F. Cunha , R. Gargano and et. al.. J. Phys. Chem. A. 113, 14975 (2009).
3. S.S. Brito, Influência da Densidade de Portadores e de Efeitos Térmicos no Transporte de Carga em Semicondutores Orgânicos. Dissertação de mestrado, Brasília, 2014.

Sara S. de Brito*, Wiliam F. da Cunha, Demétrio A. da Silva Filho & Pedro H. de Oliveira Neto

Instituto de Física, Universidade de Brasília. CP04455, Brasília, DF, CEP 70919-970, Brasil.

*E-mail: sarahsantiagobrito@gmail.com

Estudo Termodinâmico e Cinético da Formação de Modelos Químicos Derivados de Adamantano para a Interação com Ciclodextrinas

Selma F. Bazan, Clara H. S. Braga, Frederico B. de Sousa & Juliana F. Lopes

Introdução

Complexos de inclusão são objetos de estudos da química supramolecular, sendo que uma das moléculas mais estudadas para criar estes sistemas são as ciclodextrinas (CDs). A partir da formação de um composto de inclusão é possível, por exemplo, modular a liberação de um fármaco.¹ Também é possível aperfeiçoar a eficiência e diminuir os efeitos colaterais já apresentados pelo fármaco, quando incluídos na cavidade das CDs.² O adamantano (Ad) é uma molécula que quando interage com ciclodextrinas, produz complexos de estabilidade alta,³ isso faz com que seja possível modificar a cadeia lateral desta molécula e estudar a estabilidade de diferentes complexos de inclusão modelos.² Diante disso, pretendia-se realizar os estudos termodinâmicos de equilíbrio entre os complexos de inclusão, formados por ciclodextrinas e os modelos de adamantano, porém a dificuldade experimental na síntese de tais derivados de adamantano exigiu a mudança no foco do objetivo inicial. As reações a serem estudadas seguem na Figura 1 e 2:

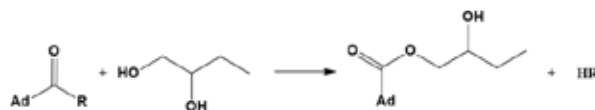


Figura 1. Primeira reação de esterificação (R = OH ou Cl)

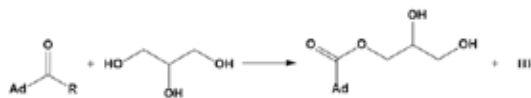


Figura 2. Primeira reação de esterificação (R = OH ou Cl)

Os cálculos com a reação do Modelo 1, (R = OH) apresentaram resultados termodinâmicos e cinéticos insatisfatórios ($\Delta G > 0$ ou próximo de 0 e $\Delta G^\ddagger > 50$ kcal/mol), o que foi observado experimentalmente, mesmo na presença de catalisadores como as carbodiimidas, esses resultados já foram apresentados em outro trabalho. Assim, os resultados que serão apresentados neste trabalho referem-se apenas ao estudo termodinâmico e

cinético das reações do Modelo 2 ($R = Cl$), que tem como produtos as espécies a serem incluídas na cavidade da ciclodextrina.

Metodologia

Todos os cálculos foram realizados utilizando o programa Gaussian 09. Realizando otimização de geometria e análise vibracional com o nível de teoria DFT (M062x), funções de base 6-31g(d,p) para todos os átomos. Realizaram-se cálculos com o efeito do solvente utilizando o modelo contínuo (SMD). A obtenção dos derivados de Ad como descrito na Figura 1 foi realizada de acordo com metodologia adaptada da literatura, pela reação do derivado ácido do Ad com cloreto de tionila, para formação cloreto de do Ad e posterior reação em solvente anidro (CH_2Cl_2) com o álcool da para obtenção do éster, Figura 1.⁴

Resultados e Discussão

Com o objetivo de estudar a estabilidade termodinâmica e cinética das reações em questão, cálculos foram realizados (reação Figura 1) para reagentes e produtos intermediários e isolados, como mostrado na Figura 3:

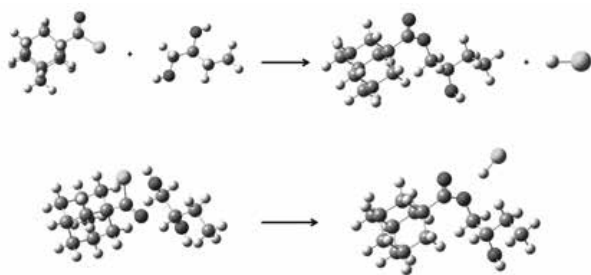


Figura 3. Estruturas otimizadas dos reagentes e produtos isolados e intermediários.

Também foi possível encontrar o estado de transição com o efeito do solvente da primeira reação. Sua estrutura apresenta-se na Figura 4 e a respectiva coordenada intrínseca da reação (IRC) é apresentada na Figura 5:

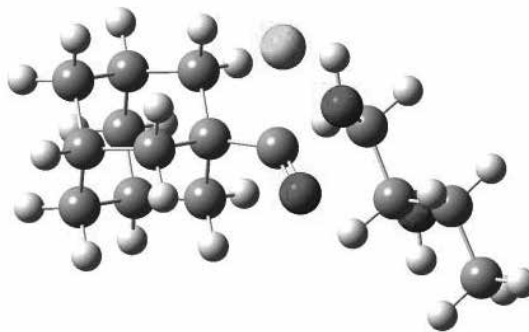


Figura 4. Estado de transição da primeira reação (M062x/SMD/196,12i)

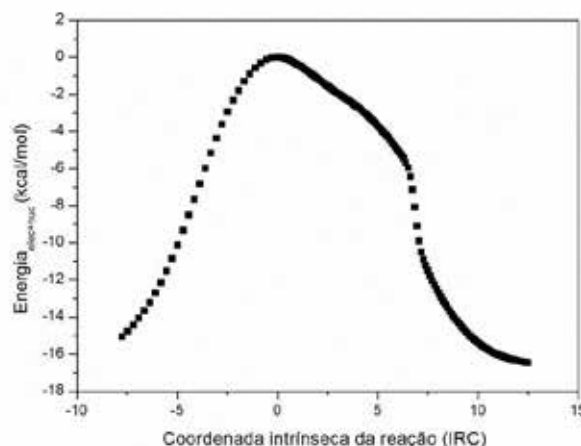


Figura 5. Gráfico da coordenada intrínseca da reação (IRC) para a primeira reação

Os cálculos foram iniciados com o efeito do solvente (água), pois as tentativas em fase gás não possibilitaram caracterizar o estado de transição. Porém após obter a estrutura em solução aquosa, os cálculos em fase gás foram feitos, tomando como a base a estrutura do estado de transição com solvente, assim como com o solvente utilizado na parte experimental (diclorometano).

Na Tabela 1 apresentam-se os resultados termodinâmicos e cinéticos obtidos:

Tabela 1. Dados termodinâmicos e cinéticos dos cálculos descritos anteriormente (kcal/mol):

	ΔG	ΔH	$T\Delta S$	ΔG^\ddagger
FG – isolados	-1,16	-3,55	-2,38	29,70
FG – intermediários	-2,32	-3,44	-1,12	27,27
SMD (H ₂ O) – isolados	-1,38	-4,10	-2,71	25,59
SMD (H ₂ O) – intermediários	-4,10	-3,95	0,16	19,67
SMD (CH ₂ Cl ₂) – Isolados	-2,43	-3,66	-1,22	24,16
SMD (CH ₂ Cl ₂) – Intermediários	-2,70	-2,68	0,02	21,56

FG – fase gasosa / SMD – modelo de solvente

Com os resultados obtidos pode-se esperar uma reação espontânea com energia de ativação relativamente baixa. Comparando a energia livre de Gibbs com as reações realizadas para a hidroxila, tem-se os dados termodinâmicos apresentados na Tabela 2 e cinéticos na Tabela 3:

Tabela 2. Dados termodinâmicos para as duas reações (kcal/mol):

	ΔG (R = OH)	ΔG (R = Cl)
FG – Isolados	-0,04	-1,16
FG – Intermediários	6,44	-2,32

Tabela 3. Dados cinéticos para as duas reações (kcal/mol)

	ΔG^\ddagger (R=OH)	ΔG^\ddagger (R=Cl)
FG – Isolados	66,89	29,70
FG – Intermediários	73,30	27,27

A reação referente ao Modelo 2 mostrou-se possivelmente espontânea, tanto para a reação considerando as moléculas isoladas e intermediários, o que não é visto para a reação referente ao Modelo 1. Isso pode ser explicado pelo fato de que o cloro é um grupo abandonador melhor do que a hidroxila, já que o cloro comporta melhor a carga negativa (mais

esférico). Observa-se também uma energia de ativação relativamente baixa para o Modelo 2 e alta para o Modelo 1, pode-se afirmar, portanto, que a reação é cineticamente favorável somente para o Modelo 2.

Os resultados experimentais por espectroscopia de absorção na região do infravermelho (FTIR-ATR) indicaram que a formação do cloreto do ácido e sua posterior esterificação com o butano-1,2,diol foram viáveis através da metodologia utilizada. As principais evidências são as variações nos estiramentos C=O ($V_{C=O}$ Ad-COOH 1687, Ad-COCl 1785 e Ad-COOR 1724 cm^{-1}). Para o cloreto do ácido é observado o estiramento V_{C-Cl} em 749 cm^{-1} e para o produto da esterificação com o butano-1,2,diol são verificados os V_{C-O} em 1224 e o V_{C-O-C} em 1070 cm^{-1} . Mais ainda, não são observados os V_{OH} em 3600 e 1049 cm^{-1} referentes ao diol, o que sugere a esterificação nas duas hidroxilas, primária e secundária, Figura 6.

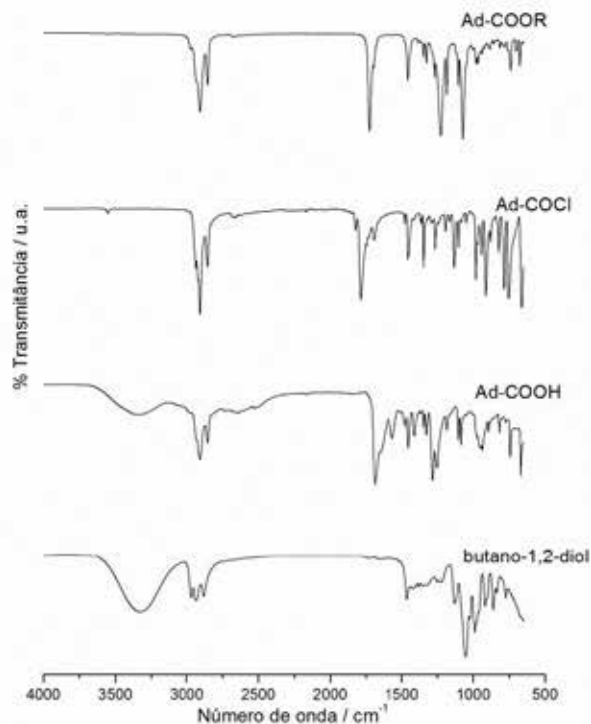


Figura 6. FTIR-ATR dos reagentes utilizados e produto obtido.

Realizando os cálculos para a segunda reação de esterificação (Figura 2), sendo $R = Cl$, foi possível encontrar o estado de transição, apresentado na Figura 7, e seu respectivo gráfico de IRC na Figura 8.

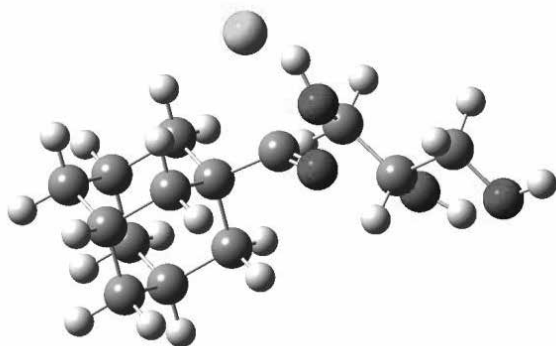


Figura 7. Estado de transição da segunda reação (M062x/SMD/289,39i)

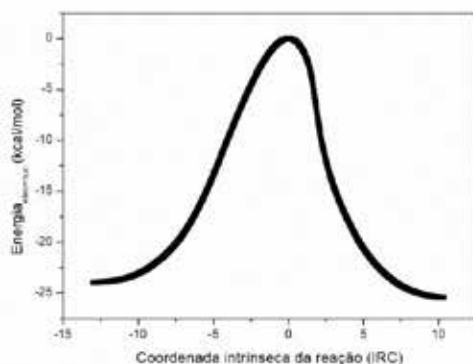


Figura 8. Gráfico da coordenada intrínseca da reação (IRC) para a segunda reação.

Espera-se concluir todos os cálculos para cada um dos modelos descritos, para que se possa realizar o estudo termodinâmico de equilíbrio entre a ciclodextrina e os modelos de adamantano.

Conclusão

É possível concluir que a reação descrita pelo Modelo 2 tem dados termodinâmicos favoráveis a uma reação espontânea e dados cinéticos relativamente baixos para

que a reação ocorra. Comparando os resultados entre os modelos, com o cloro (Modelo 2), têm-se melhores resultados, sendo, portanto preferíveis para os estudos que serão realizados com as ciclodextrinas.

Agradecimentos

Os autores agradecem o suporte oferecido pela CNPq, FAPEMIG e RQ-MG.

1. D. Thassu, et al. *Nanoparticulate Drug Delivery Systems*. 1ª ed. New York: Informa HealthCare, **2007**.
2. F. B. De Sousa, et al. *Phys. Chem. Chem. Phys.* 14, 1934, **(2012)**.
3. D. Harries, et al. *J. Am. Chem. Soc.*, 127, 2184, **(2005)**.
4. T. Liu, et al. *ACS Macro Lett.*, 4, 357, **(2015)**.

Selma Fabiana Bazan¹, Clara H. S. Braga², Frederico B. De Sousa² & Juliana Fedoce Lopes¹

¹ Universidade Federal de Itajubá, LaQC – Laboratório de Química Computacional, Av. BPS nº1303, Bairro: Pinheirinho, 37500-903, Itajubá, MG, Brasil;

² Universidade Federal de Itajubá, LSPS – Laboratório de Sistemas Poliméricos e Supramoleculares, Av. BPS nº1303, Bairro: Pinheirinho, 37500-903, Itajubá, MG, Brasil

*E-mail: sfbazan@hotmail.com -

N-Deethylation Process of Rhodamine B in Aluminum Polyphosphate Gel: Theoretical and Experimental Study

Sheila C. S. Costa, Paula A. Jaramillo, Rodrigo J. Oliveira & Marcos S. Amaral

Introduction

Rhodamine B (RhB) is a xanthene dye, whose optical properties depend of several factors, such as solvents, concentration, pH, etc. The carboxyl group present on structure participates in acid-base balance, giving rise to acidic and basic structural forms [1]. This compound is widely used in textile industries, ink and cosmetics, among others [2]. However, it was proved experimentally the carcinogenicity of Rhodamine B and its high toxicity[3], such as most of non-biodegradable coloring agents [4], the RhB remain in waste waters of industrial handling, and an improper discharge of these wastes in urban storm water systems can cause adverse effects, harmful to the aquatic ecosystem and to human life. Several techniques have been employed for the removal of dyes from wastewater [5]. Currently, a great interest has been concentrated on the incorporation of organic dyes in solid matrices using the sol-gel technique as a photocatalyst of noxious compounds to the environment [6]. The Rhodamine B may suffer several degradation pathways, one such process is the de-N-ethylation under irradiation of visible light [7]. With this end, we propose the entrapment of Rhodamine B in Aluminum Polyphosphate Gel (APP/Gel) as a photocatalytic precursor and we associate theoretical simulation to investigate the type of degradation process that occurs with the RhB within

the APP/Gel [8]. We used a combination of sequential Monte Carlo/quantum mechanics (MC/QM) to describe the absorption bands of two forms of Rhodamine B (RhB⁺) and Rh⁺ (Figure 1). Time-dependent density-functional theory (TD-DFT) [9] using three functional (B3LYP, CAM-B3LYP, BP86) [9] was also used in the theoretical description. All calculations were carried out using Gaussian 09 suite program [9] and DICE [10].

Methods

In experimental procedure, the synthesis of the Aluminum Polyphosphate/RhB (APP/RhB) was prepared using $2.0 \text{ mol} \times \text{L}^{-1}$ of sodium polyphosphate and $1.0 \text{ mol} \times \text{L}^{-1}$ of aluminum nitrate in aqueous solution[8]. An aqueous solution of RhB using $1.0 \times 10^{-3} \text{ mol} \times \text{L}^{-1}$ was prepared and added in the sodium polyphosphate solution and mixed at room temperature ($\sim 25^\circ \text{C}$) under mechanical stirring. From of the experimental absorption data of the (APP/RhB), we simulate the N-Deethylation process of Rhodamine B. We optimized the structures of RhB⁺ in cationic form (Figure 1-a), and Rh⁺ (Figure 1-c) using DFT (B3LYP, CAM-B3LYP, PB86) methods and [6-311+(d,p)] basis set. sequentially, was used the Monte Carlo method to simulate both RhB⁺ and Rh⁺ molecules plus 1500 water molecules in the NPT ensemble in a cube box of lengths of

35.7 (Å). The average calculated density was 1.024 g/cm³ and average specific molar heat was 0.02130 kcal/mol·K. After calculating the statistical correlation interval [11], a total of 75 uncorrelated configurations were selected with less than 15% of statistical correlation, for both Rhodamine B systems. TDDFT (B3LYP, BP86)//6-31+G(d, p) in PCM [9] level, were performed on each solute-solvent structure selected, which included the molecules of water explicit in hydrogen bond (HB).

Results and Discussion

Samples of APP/RhB were monitored via UV-vis absorption (Figure 2), the normalized absorption spectra exhibited an hypsochromic shift of 57 nm between the absorption bands from APP/RhB initially formed (559 nm) up to N-deethylated product (502 nm) measured after 308 hours. The maximum absorption for initial time (just after preparing sample), is ~559 nm; after 308 hours, the maximum absorption is ~502 nm. The normalized absorption spectra for RhB⁺ and Rh⁺ in water (Figure 3) correspond to excited states calculated to 75 solute-solvent configurations from MC simulation. Theoretically was found a blue shift of ~ 54 nm approximately between the absorption bands of the RhB systems added in H₂O with.

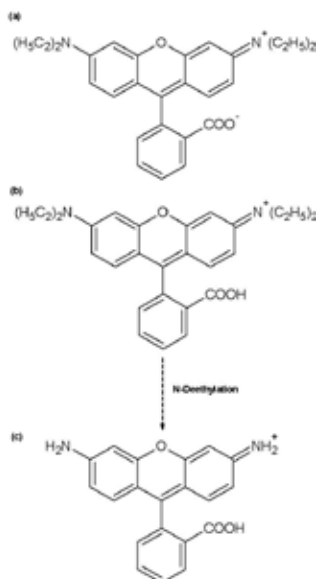


Figure 1. Schematic description of the Rhodamine B conformations. (a) Zwitterion form (RhB[±]), (b) Cationic form (RhB⁺) and (c) N-Deethylated (Rh⁺) product (Rhodamine-110).

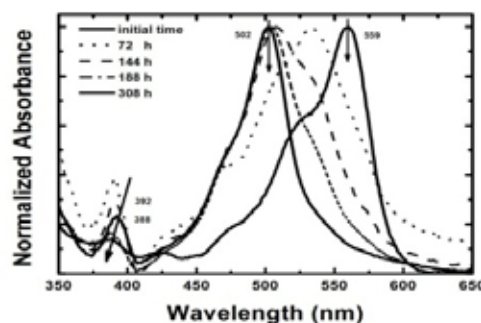


Figure 2 – Normalized UV-vis absorption spectra for Aluminum Polyphosphate and Rhodamine B (prepared from 2.0 mol×L⁻¹ of sodium polyphosphate, 1.0 mol×L⁻¹ of aluminum nitrate and 1.0×10⁻³ mol×L⁻¹ of Rhodamine B, in aqueous solution) in room temperature (~25 °C) at different degradation instants. The maximum absorption for initial time (just after preparing sample), is centered at ~559 nm; after 308 hours, the maximum absorption band is centered at ~502 nm. The intermediate absorption spectra carry the hypsochromic shift signature of the main band.

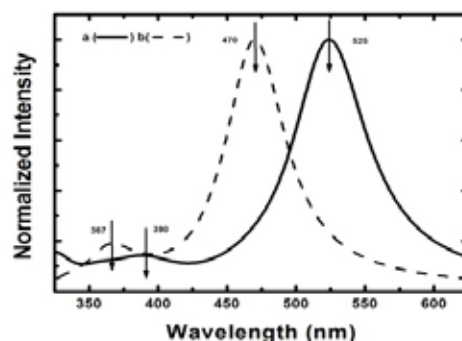


Figure 3. Normalized absorption spectra for RhB⁺ and Rh⁺ in water with hydrogen bond (HB) calculated with TD-BP86/6-31+G(d,p) method. These spectra correspond to excited states calculated on 75 solute-solvent configurations from MC simulation. In the simulation of the N-deethylation process of RhB⁺ (a) the maximum absorption peak at ~525 nm undergoes a blue shift of ~ 55 nm compared to Rh⁺ (b).

Conclusions

In this work, we propose to identify the type of degradation of Rhodamine B in the sol-gel matrix polyphosphate of aluminum. Through theoretical simulation we describe the gel of the internal environment where the Rhodamine B has been encapsulated, as well to study the occurrence of the N-ethylation process via absorption spectrum. Experimentally verified

by absorption spectra of the APP / RhB undergoes a hypsochromic shift characteristic of the process of de-N-ethylation of RhB. Considering that the theoretical and experimental results are in good agreement we propose that the matrix APP / Gel is a good fotocatalizador precursor and can be used for removal of dyes from wastewater.

Acknowledgments

The authors are grateful for the support given from the FUNDECT, UFMS, CNPQ and INCT-FCx-USP.

References

1. J. Jorge, G. R. Castro, M. A. U. Martines, *Orbital Elec. J. Chem.* **5** (2013) 23-29.
2. T. A. Khan, S. Sharma, I. Ali, J. *Toxicology and Environ. Health Sciences* **3** (2011) 286-297.
3. H. Lee, S. H. Park, Y.-K. Park, B. H. Kim, S.-J. Kim, S.-C. Jung. *Chem. Central Journal* **7** (2013) 156-161.
4. A.E. Ghaly, R. Ananthashankar, M. Alhattab, V. V. Ramakrishnan, *J. Chem Eng Process Technol* **5** (2014) 1-19.
5. T. A. Khan, V. V. Singh, D. Kumar, *J. Scientific & Ind. Research* **63** (2004) 355-364.
6. S. Wahyuningsih, C. Purnawan, P. A. Kartikasari, N. Praistia, *Chem. Papers* **68** (2014) 1248-1256.
7. F. Chen, J. Zhao, H. Hidaka, *Int. Journal of Photoenergy*, **5** (2003) 209-217.
8. E. C. O. Lima, F. Galembeck, *J. Colloid Interf. Sci.* **166** (1994) 309-315.
9. M. J. Frisch, *Gaussian 09*, Revision A.02 Gaussian, Inc.: Wallingford, CT, **2009**.
10. K. Coutinho, S. Canuto, *DICE: A Monte Carlo Program for Molecular Liquid Simulation*, v. 2.9, University of São Paulo, São Paulo. **2009**.
11. P. Jaramillo, K. Coutinho, S. Canuto. *Int. J. Quantum. Chem.* **110** (2010) 2371-2377.

Sheila C.S. Costa^{a*}, Paula A. Jaramillo^b, Rodrigo J. Oliveira^c & Marcos S. Amaral^a.

^a Universidade Federal do Mato Grosso do Sul, INFI, 79070-900, Campo Grande, MS – Brasil.

^b Universidade Federal da Integração Latino-Americana, ILACVN, 85867-970, Foz do Iguaçu, PR – Brasil.

^c Universidade Estadual da Paraíba, DQ, 58109-790, Campina Grande, PB – Brasil.

*E-mail: sheila.costa@ufms.br

Deformed Transition State Theory: Inclusion of the Tunneling Effect by Euler Exponential, Limit of Validity and Description of Bimolecular Reactions

V. H. Carvalho, V. Aquilanti, H. C. B. Oliveira & K.C. Mundim

Introduction

Aiming to understand reaction mechanisms presenting non-Arrhenius behavior, studies over a wide range of temperature reactions become a tool of great importance¹⁻⁴. An interesting formulation for this problem was proposed by Eyring, named Transition State Theory (TST). A recent paper⁵ generalized the Transition State Theory by Tsallis Distribution⁶, adding non-equilibrium effect in the description of the kinetic rate constant. However, this formulation depends on the deformation parameter that has no well-defined physical meaning.

Focused in the possibility of providing a meaning to the deformed parameter, we proposed a comparison between d-Arrhenius and Bell models, and we found that the deformation parameter is put into relationship with the height of the energy barrier (E_0) and the negative frequency (ν^\ddagger)⁷ (see Figure 1a). This parameter tends to zero for high values of the E_0 and ν^\ddagger , and the usual Arrhenius law is recovered. However, significant values of d implies in the tunneling contributions and consequently Sub-Arrhenius behavior (concave curve at Arrhenius plot, see Figure 1b). This result makes the extension of TST by Tsallis Distribution (d-TST) possible as following:

1b). This result makes the extension of TST by Tsallis Distribution (d-TST) possible as following:

$$k_{d-TST}(T) = \frac{k_B T}{h} \frac{Q^{[TS]^\ddagger}}{Q^{[Reactant]}} \left(1 - d \frac{E_0}{RT} \right)^{\frac{1}{d}} \quad (1)$$

where k is the kinetic rate constant, E_0 is the barrier energy, Q is the partition function and d is the deformed parameter.

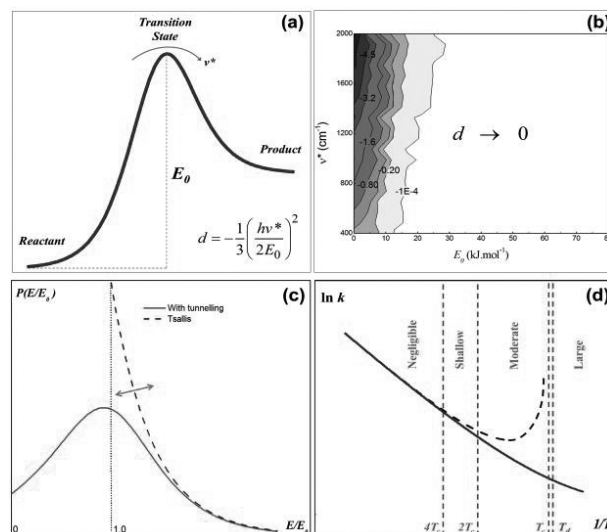


Figure 1. (a) Definition of deformation parameter, d . (b) Dependence of deformation parameter with E_0 and ν^\ddagger . (c) Comparison of Tsallis and Tunneling distributions. The deformation parameter controls the flexibility of Tsallis distribution, represented by the green arrow. (d) d-TST limit of validity considering T_d .

The d-TST formulation presents validity limits in the description of tunnelling, since the Tsallis distribution (the hypothesis used to describe the Sub-Arrhenius behaviour) does not describe particles whose energy is less or equal to the height barrier. However, the flexibility of this distribution implies in a better description compared with Boltzmann distribution (Figure 1c). Again, comparing d-Arrhenius and Bell models, we propose a validity temperature (T_d) that ensures the description of d-TST formula:

$$T_d = T_c + \frac{dE_0}{2k_B} \quad (2)$$

where T_c is the crossover temperature^{4,8}. At temperatures below the T_d , there is no way to ensure the d-TST description, i.e., this model neglects large tunneling contributions (Figure 1d).

Methods

The alternative approach, Equation 1, was implemented in the source code of the program developed by Gargano and co-authors⁹. This program provides information about the kinetic rate constant by TST with Wigner¹⁰, Bell corrections⁴ and d-TST. To validate this formalism we chose the gas-phase bimolecular reaction: $\text{CH}_4 + \text{OH} \rightarrow \text{CH}_3 + \text{H}_2\text{O}$,¹¹ $\text{CH}_3\text{Cl} + \text{OH} \rightarrow \text{CH}_2\text{Cl} + \text{H}_2\text{O}$,¹² and $\text{H}_2 + \text{CN} \rightarrow \text{H} + \text{HCN}$.¹³ The properties (geometry, frequency and energy) of the reactants, products and TS were calculated at the MP2/6-311++G** and DFT level using the Gaussian 03 program suite. We have tested several DFT functionals.

Results and Discussion

Figure 2 presents the results of the Arrhenius plot for the three reactions. From this figure, it can be seen that the conventional models for calculating the kinetic rate constant reasonably agree with experimental data. However, it can be seen that the d-TST model agrees well with experimental data, compared to conventional models, proving itself to be a very robust option to study non-Arrhenius behavior in

chemical kinetics. However, the quality of the estimative of the rate constants is dependent on the electronic structure method. The rate constant of proton transfer reactions with hydroxyl radical are well described by the MP2 method and fail with the M062X functional. Already, the proton transfer reaction with H_2 molecules agrees with experimental data when calculated with the FHB functional. There is no protocol for the method chosen. It is an empirical process. The kinetic of the $\text{H}_2 + \text{CN} \rightarrow \text{H} + \text{HCN}$ reaction was previously described in Ref 5 using a non-equilibrium formulation. However, this formulation is not predictive because the deformation parameter is fitted to the rate constant experimental. In addition, the deformation parameter proposed in this work is positive, in disagreement with our formulation that only allows negative values for Sub-Arrhenius behavior, in the spirit of our previous report⁷.

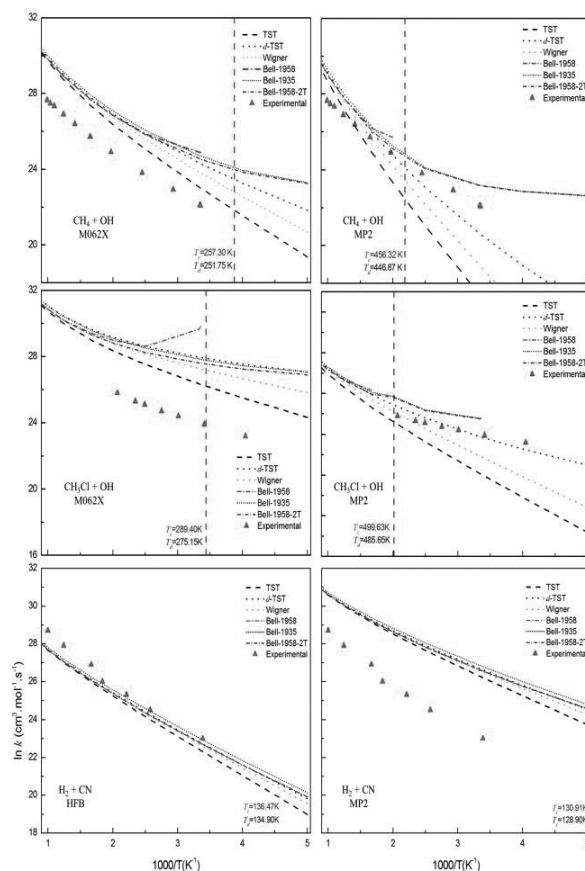


Figure 2. Arrhenius plot for $\text{CH}_4 + \text{OH} \rightarrow \text{CH}_3 + \text{H}_2\text{O}$,¹¹ $\text{CH}_3\text{Cl} + \text{OH} \rightarrow \text{CH}_2\text{Cl} + \text{H}_2\text{O}$,¹² and $\text{H}_2 + \text{CN} \rightarrow \text{H} + \text{HCN}$,¹³ reactions by TST with Wigner, Bell corrections and d-TST. The vertical lilac line defines validity temperature, T_d .

Molecular properties are strongly influenced by the electronic structure method, specifically, the DFT functional. In Figure 3, we present a comparison between rate constants at different DFT functionals with experimental data for the $\text{CH}_3\text{Cl} + \text{OH} \rightarrow \text{CH}_2\text{Cl} + \text{H}_2\text{O}$ reaction. The rate constant dependence with the DFT functional is clear.

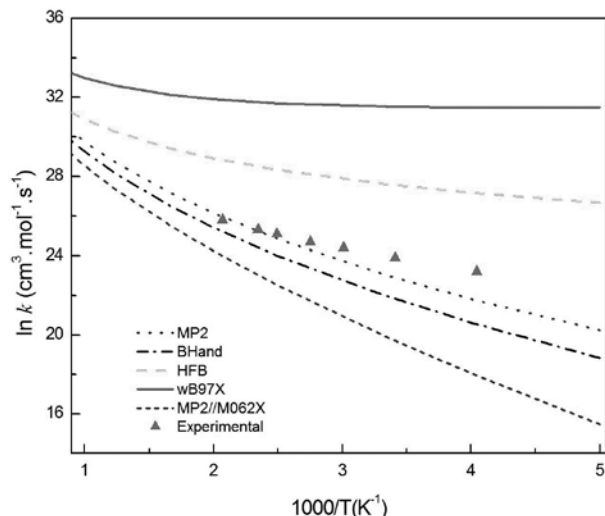


Figure 3. Comparison among rate constants at different DFT functional with experimental data for the $\text{CH}_3\text{Cl} + \text{OH} \rightarrow \text{CH}_2\text{Cl} + \text{H}_2\text{O}$ reaction.

Conclusion

In summary, the d-TST is a good alternative for describing systems with moderate tunneling contribution. The rate constant of the proton transfer reaction is in agreement with experimental data. This formulation is electronic structure method dependent, specifically with DFT functional.

Since the estimative of proton transfer in several systems chemistry are very important, this model becomes a robust option for describing Sub-Arrhenius behavior.

Acknowledgments

The authors are grateful for the support given from FAPEG, CAPES, CNPQ and FINATEC. V. Aquilanti thanks CAPES for the appointment as Special Visiting Professor (Professor Visitante Especial) at the Institute of Physics, Federal University of Bahia, Salvador (Brazil)

References

1. Limbach, H.-H., Miguel Lopez, J. & Kohen, A. *Philos. Trans. R. Soc. B Biol. Sci.* 361, 1399–1415 (2006).
2. Benderskii, V. A., Goldanskii, V. I. & Makarov, D. E. *Phys. Rep.* 233, 195–339 (1993).
3. Caldin, E. F. *Chem. Rev.* 69, 135–156 (1969).
4. Bell, R. P. *The Tunnel Effect in Chemistry*. (Chapman and Hall, 1980).
5. Quapp, W. & Zech, A. *J. Comput. Chem.* 31, 573–585 (2009).
6. Tsallis, C. *Introduction to Nonextensive Statistical Mechanics: Approaching a Complex World*. (Springer, 2009).
7. Silva, V. H. C., Aquilanti, V., de Oliveira, H. C. B. & Mundim, K. C. *Chem. Phys. Lett.* 590, 201–207 (2013).
8. Christov, S. G. *Mol. Eng.* 7, 109–147.
9. Barreto, P. R. P., Vilela, A. F. A. & Gargano, R. J. *Mol. Struct.* 639, 167 – 176 (2003).
10. Wigner, *Phys. Rev.* 40, 749–759 (1932).
11. Jeong, K. M. & Kaufman, F. J. *Phys. Chem.* 86, 1808–1815 (1982).
12. Bryukov, M. G., Knyazev, V. D., Lomnicki, S. M., McFerrin, C. A. & Dellinger, B. *J. Phys. Chem. A* 108, 10464–10472 (2004).
13. Sun, Q., Yang, D. L., Wang, N. S., Bowman, J. M. & Lin, M. C. J. *Chem. Phys.* 93, 4730–4739 (1990).

V. H. Carvalho^{a,*}, V. Aquilanti^b, H. C. B. Oliveira^c & K. C. Mundim^c

^aGrupo de Química Teórica e Estrutural de Anápolis, Campus de Ciências Exatas e Tecnológicas, Universidade Estadual de Goiás, 75001-970, Anápolis, Brasil

^bUniversità di Perugia, Via Elce di Sotto 8, 06123 Perugia, Italy. Instituto de Física, Universidade Federal da Bahia, 40210 Salvador, Brazil. Istituto di Struttura della Materia, Consiglio Nazionale delle Ricerche, 00185 Rome, Italy.

^cInstituto de Química, Universidade de Brasília, 70904-970, Brasília, Brasil.

*E-mail: fatioleg@gmail.com

Inverse Virtual Screening of Bradyoxetin and a Synthetic Intermediate using OOMD as a Source Database

Vanildo M. L. Braga & Alex Taranto

Introduction

Quorum sensing bacteria produce and release chemical signal molecules (like N-acyl homoserine, AHL1) that increase in concentration as a function of cell density. The responses cover a large spectrum of process such as the virulence in *Staphylococcus aureus*², competence for DNA-uptake in *Bacillus subtilis*³ and *Streptococcus pneumoniae*, sporulation in *Bacillus subtilis*⁴, conjugal plasmid transfer in *Enterococcus faecalis*⁵, and bacteriocin production in lactic acid bacteria. The collapse of (AHL) signaling system in bacteria represents an attractive therapeutic approach towards the development of new antibiotics. Recently, a new extracellular modulator was isolated from a symbiotic bacterium (*Bradyrhizobium japonicum*)⁵ that nodulates soybean. This quorum sensing molecule, containing a novel oxetane ring, was partially characterized and named bradyoxetin (2-{4-[[4-(3-aminooxetan-2-yl)phenyl](imino)methyl]phenyl}oxetan-3-ylamine)(Figure 1). Since there's a lack of information (other than the nodulation of soy bean) it seemed extremely appropriate to investigate this unique organic scaffold using in silico techniques such as Inverse Virtual Screening (IVS)⁶ using our own molecular database (OOMD). IVS should provide us initial information on the biological profile of this molecule, as well as other synthetic intermediate, 3-azido-2-phenyl oxetane (Figure 1).

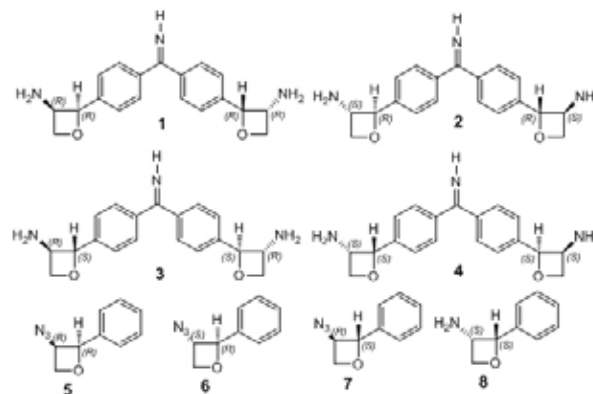


Figure 1. Structural formula and synthetic intermediate of 3-azido-2-phenyl oxetane

Experimental Procedures

The molecules were entered using Marvin Sketch (ChemAxon, version 14.7.7). During this process the molecules were also protonated accordingly to its structure. The bradyoxetin series were able to accommodate three protons, one in the imine functionality, and other two on the amino groups attached to the oxetanes rings. The pH during protonation was set to be 7.4. The phenyl azido oxetanes were not protonated. During this process Geisteiger charges were also added. The ligand was set to be torsion free and the remaining structures were checked for incongruities in 3D. After this protocol the

molecules had their energy minimized by MOPAC using pm⁷. The molecules were then opened in Auto Dock Tolls and were saved in pdbqt and in smiles for the purpose of expansion of a database of ligands.

The docking studies were performed using Vina1.0.27. The data for the conf.txt files were extracted

from the ligand present in the original pdb file (location of the binding site). Exhaustiveness was set to 8 and the grid box set to 20 Å on each side.

With the docking finished, next step was to verify the graphical results. For this, we've used Discovery Studio v4.1.0.14169 (Accelrys Software Inc.).

Table 1. The expressed results

Mol. Target	1AGW	1DDX	1GKC	1GMY	1LD8	1LF3	1LRH	1QIB	1QJA
Lig. Crist.	-8.1	-9.2	-6.6	-7.7	-13.2	-10.0	-7.7	-9.3	-11.0
5	-5.6	-7.5	-6.9	-5.6	-5.6	-5.9	-6.2	-6.8	-5
6	-5.7	-7.6	-6.9	-5.5	-5.7	-5.5	-6	-6.8	-4.9
7	-5.6	-7.8	-7.2	-5.8	-5.6	-5.4	-6.5	-7.1	-5.5
8	-5.4	-7.4	-6.9	-5.4	-5.6	-5.5	-6.3	-6.5	-4.8
1	-7.8	-9.3	-9.4	-7	-7.8	-7.6	-4.9	-9.3	-6.2
2	-8.1	-9.1	-9.6	-7.2	-8.1	-7.7	-4.7	-9.4	-6.3
3	-8.2	-9.4	-9.5	-7.1	-8.2	-7.7	-4.9	-9.4	-6.4
4	-7.7	-9.0	-9.5	-7.0	-7.7	-7.6	-4.2	-9.7	-6.1
Mol. Target	1W6M	1W22	1Z57	1ZZ1	2ANL	2HYY	2K05	2QHN	2VV9
Lig. Crist.	-4.3	-9.0	-9.5	-7.6	-10.0	-12.6	-33.3	-7.4	-9.1
5	-4.9	-5.3	-8.7	-8.7	-8.1	-7.1	-4.8	-5.6	-6.4
6	-4.6	-5.2	-8.8	-8.6	-7.7	-7.2	-4.7	-5.7	-6.5
7	-4.8	-5.3	-9.3	-8.6	-7.7	-7.4	-5.1	-5.7	-6.8
8	-5.0	-5.3	-8.8	-8.7	-8.2	-7.0	-4.7	-5.6	-6.3
1	-6.2	-7.8	-7.8	-8.7	-8.1	-9.7	-6.9	-7.7	-8.8
2	-6.2	-8.1	-8.1	-8.6	-7.7	-10.2	-7.2	-7.7	-8.8
3	-6.2	-8.2	-8.2	-8.6	-7.7	-10.4	-7.2	-7.7	-8.8
4	-6.2	-7.7	0.0	-8.7	-8.1	-10.0	-6.7	-7.7	-9.1
Mol. Target	2YOE	2ZOQ	3BKY	3BPF	3BZ3	3C4C	3DV3	3EDQ	3ENE
Lig. Crist.	-5.4	-7.8	-9.1	-6.7	-11.1	-10.4	-9.4	-10.7	-9.8
5	-5.7	-6	-5.5	-4.9	-6	-6.2	-5.6	-5.2	-6.1
6	-5.5	-6.1	-5.4	-5.0	-6.1	-6.3	-6.1	-5.5	-6.3
7	-5.8	-6.3	-6	-5.1	-6.1	-6.6	-6.2	-5.8	-6.5
8	-5.5	-6.0	-5.4	-5.1	-6.4	-6.3	-6.0	-5.3	-5.9
1	-8.1	-8.2	-7.1	-6.9	-8.2	-9.3	-9.1	-7.3	-8.2
2	-7.8	-8.6	-6.8	-6.9	-8.6	-9.5	-9.6	-7.4	-8.1
3	-8.0	-8.6	-7.3	-6.8	-8.7	-9.8	-9.6	-7.4	-8.0
4	-8.1	-8.2	-7.1	-6.9	-8.2	-9.3	-9.1	-7.3	-8.5
Mol. Target	3FAP	3FL5	3G0E	3HIG	3JYA	3N8Z	3U1I	4AGN	4EY7
Lig. Crist.	-19.4	-11.5	-10.4	-9.1	-8.4	-9.3	-9.6 ou -7.4	-6.5	-12.7
5	-6.8	-7.7	-6.3	-7.1	-6.1	-6.4	-4.9	-4.8	-7.4
6	-6.4	-7.2	-6.2	-7.1	-6.2	-6.1	-5.6	-4.9	-7.3
7	-6.6	-8.0	-6.5	-6.6	-6.9	-6.4	-5.8	-5.1	-7.8
8	-6.9	-7.5	-6.2	-5.5	-6.2	-5.8	-5.3	-6.5	-7.2
1	-9.1	-6.9	-8.9	-10.2	-8.2	-5.9	-7	-6.6	-10.1
2	-9.4	-6.8	-8.7	-9.9	-8.2	-5.6	-7.3	-6.4	-10.4
3	-9.3	-7.0	-8.6	-9.9	-8.2	-5.9	-7.3	-6.1	-10.6
4	-9.2	-7.5	-9.1	-9.8	-8.2	-5.9	-6.9	-6.5	-10.2
Mol. Target	PFATP	PFHT							
Lig. Crist.	-8.5	-5.4							
5	-6	-5							
6	-6.0	-5.7							
7	-6.1	-5.7							
8	-6.0	-5							
1	-8.5	-7.4							
2	-8.3	-7.8							
3	-8.3	-7.7							
4	-8.5	-7.4							

Legenda:

cancer

dengue

malária

ativo

inativo

Results and Discussion

The most significant results were found in 1GKC8, 1W6M9, 2YOE10. In these cases the difference between the natural complex (ligand plus receptor) and the created complex generated through docking was more expressive. In most cases, the targets are involved with cancer. 1GKC is part of the Matrix metalloproteinases (MMPs), the class of enzymes involved in the degradation of extra cellular matrix and surrounding cells are known to be expressed during cancer cell invasion, arthritis and metastasis and MMP-9, in particular seems to be a key protease associated with tumor progression. 1W6M is equally involved with cancer although through a different mode of action. It's presence is associated with cell migration and with tumor malignancy. 2YOE is a GABA receptor modulated by benzodiazepines.

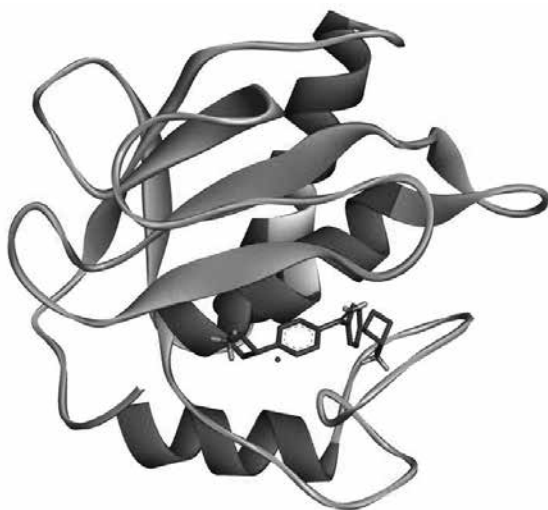


Figure 2. ligand 2 complexed with GKC

As it can be seen, looking to the pharmacophore map on figure 3, Pi interactions play a major role in binding process of ligand 2. In one of the rings there is a Pi stack created by a Zn atom and His 401. The zinc atom also interacts with the second ring increasing the stability of the complex. The amino groups also play a pivotal role having also Pi interactions with Phe 110, His 405 and Tyr 423. The imine bridge also interacts with His 401 contributing for the low energy of the complex.

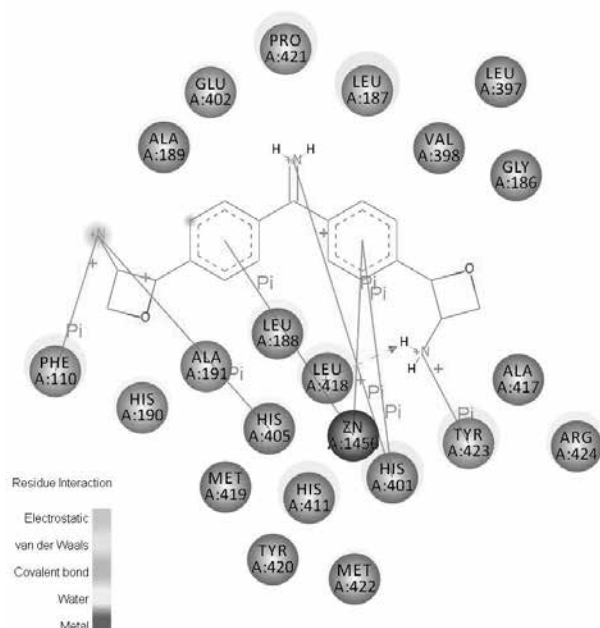


Figure 3. Pharmacophoric map of GKC complexed with ligand 2.

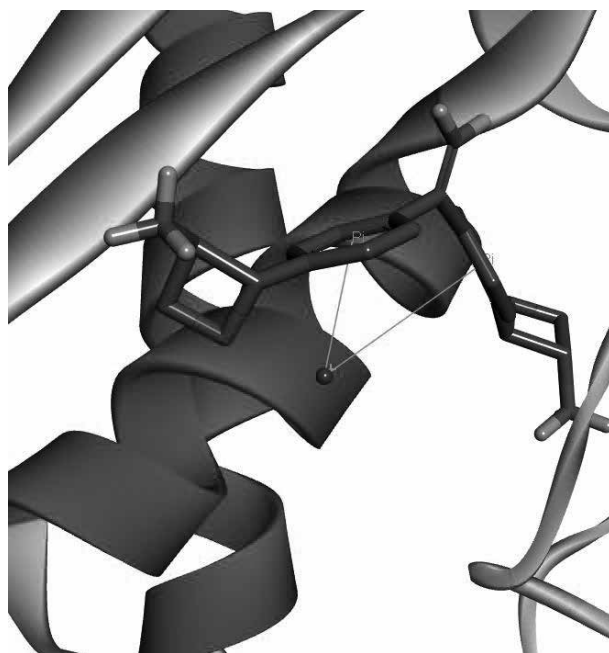


Figure 4. Pi interactions between Zn and aromatic rings of ligand 2



Figure 4. ligand 1 complexed with 1W6M

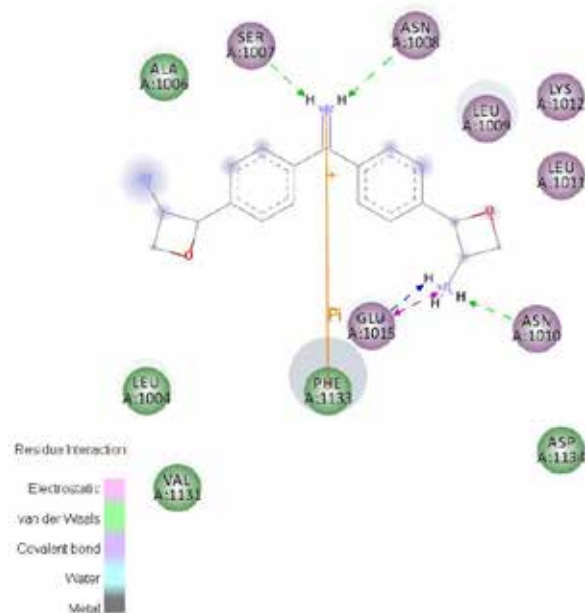


Figure 5. Pharmacophoric map of ligand 2 and 1W6M

As it can be seen in the figure above the number of interactions is much smaller than the previous example. Even so, it is enough to have a better value than the crystallographic complex. The key interactions are a Pi interaction between Phe 1133 and the imine moiety and hydrogen bonds between one of the amine groups and Glu 1015 and Asn 1010.



Figure 6. ligand 4 complexed with 2YOE. The ligand is highlighted in yellow.

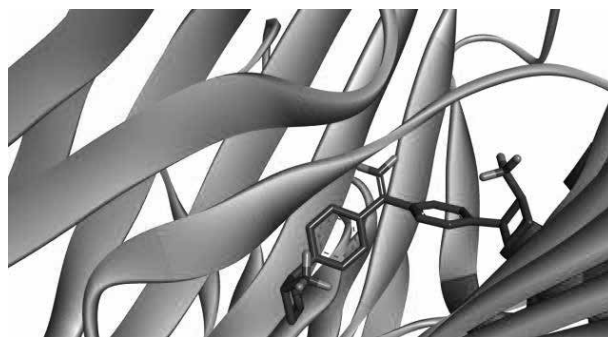


Figure7. A zoom taken off from Figure 6

Phe 78 and Tyr 102 interact with 2YOE through Pi bonds with the aromatic ring and with the imine. Other interactions seen before are the hydrogen bonds between the protonated amines and the surrounding residues such as Val73, Glu59 and Leu 76.

Conclusions

The sources for therapeutic molecules seem to be infinite. What were the odds of a symbiotic bacterium that helps nodulation and therefore with nitrogen fixation on soy display good results in an in silico screening against cancer mainly. Although the results look promising, a biological study is mandatory to validate the in silico results.

The next step should be a refinement docking followed by molecular dynamics.

Acknowledgments

The authors are grateful for the support given from the FAPEMIG, CAPES and CNPQ.

References

1. Parsek, M. R. and E. P. Greenberg (2000). "Acyl-homoserine lactone quorum sensing in Gram-negative bacteria: A signaling mechanism involved in associations with higher organisms." *PNAS* 97(16): 8789-8793.
2. Johnson, Jeffrey G.; Wang, Boyuan; Debelouchina, Galia T.; Novick, Richard P.; Muir, Tom W. "Increasing AIP Macrocyclic Size Reveals Key Features of agr Activation in *Staphylococcus aureus*" *ChemBioChem* (2015), 16(7), 1093-1100
3. Vidal, Jorge E.; Ludewick, Herbert P.; Kunkel, Rebekah M.; Zahner, Dorothea; Klugman, Keith P. "The LuxS-dependent quorum sensing system regulates early biofilm formation by *Streptococcus pneumoniae* strain D39" *Infection and Immunity* (2011), 79(10), 4050-4060.
4. Higgins, Douglas; Dworkin, Jonathan. "Recent progress in *Bacillus subtilis* sporulation", *FEMS Microbiology Reviews* (2012), 36(1), 131-148.
5. Dunny, Gary M. "Enterococcal sex pheromones: signaling, social behavior, and evolution." *Annual Review of Genetics* (2013), 47, 457-482.
6. Loh, John; Carlson, Russell W.; York, William S.; Stacey, Gary. "Bradyoxetin, a unique chemical signal involved in symbiotic gene regulation." *Proceedings of the National Academy of Sciences of the United States of America* (2002), 99(22), 14446-14451.
7. Schomburg, Karen T.; Bietz, Stefan; Briem, Hans; Henzler, Angela M.; Urbaczek, Sascha; Rarey, Matthias. "Facing the Challenges of Structure-Based Target Prediction by Inverse Virtual Screening." *Journal of Chemical Information and Modeling* (2014), 54(6), 1676-1686.
8. Polikanov, Y.S., Melnikov, S.V., Soll, D., Steitz, T.A. "Structural insights into the role of rRNA modifications in protein synthesis and ribosome assembly." (2015) *Nat.Struct.Mol.Biol.* 22: 342-344.
9. Lopez-Lucendo, M.I.F., Solis, D., Andre, S., Hirabayashi, J., Kasai, K., Kaltner, H., Gabius, H.J., Romero, A. "Structural insights into the role of rRNA modifications in protein synthesis and ribosome assembly." (2015) *Nat.Struct.Mol.Biol.* 22: 342-344.
10. Spurny, R., Ramerstorfer, J., Price, K., Brams, M., Ernst, M., Nury, H., Verheij, M., Legrand, P., Bertrand, D., Bertrand, S., Dougherty, D.A., De Esch, I.J.P., Corringer, P., Sieghart, W., Lummis, S.C.R., Ulens, C. "Pentameric ligand-gated ion channel ELIC is activated by GABA and modulated by benzodiazepines." (2012) *Proc. Natl. Acad. Sci. USA* 109: E3028.

Vanildo M. L. Braga & Alex Taranto

Universidade Federal de São João Del Rei – Centro-Oeste campus 35501-296, Chanadour, Divinópolis-MG.

Conjugation and Hyperconjugation Effects: Comparative Studies Through Localized Molecular Orbitals Energy Decomposition Analysis (LMO-EDA) and Natural Bond Orbitals (NBO)

V. A. V. Ferreira, V. G. do Nascimento & M. B. de Amorim

Introduction

Delocalized chemical bonds are those that are not localized between two atoms only, but three or more atoms.¹ An example of delocalized chemical bonds is the conjugation effect, measured by energy of delocalization.² In these systems $n \rightarrow \pi^*$, $\pi \rightarrow \pi^*$ or $\pi \rightarrow p$ (where n is a lone pair and p is vacant p orbital) interactions occur.³

Another kind of electronic delocalization is represented by hyperconjugation, which was proposed by Mulliken, and consists on interactions of the σ , π or n orbitals and a σ^* orbital.² The hyperconjugation effect is most often overlooked or disregarded by authors, although it is almost ubiquitous.⁴ The most known hyperconjugative effect in the literature is the anomeric effect (negative hyperconjugation $n \rightarrow \sigma^*$) which is commonly observed in carbohydrates, and whose definition can be extended to structures with a C-X-C-Y pattern (where X = N, O or S and Y = Br, Cl, F, N, O or S), and the generalized prefix is added to the effect name.^{5,6}

These concepts are important to explain properties, stabilization and reactivities of chemical structures,^{7,8,9} and primarily has its application in organic chemistry and natural products research.

In order to better understand these effects and to apply them in the analysis of chemical and biological properties of natural products, we started the study of methods of analysis of delocalized electron densities.

One of these approaches, the LMO-EDA,¹⁰ is an variational energy decomposition analysis method based on Morokuma and Kitaura,^{11,12} and Hayes and Stone procedures.¹³ This method uses the localized molecular orbitals of Edmiston and Ruedenberg, which are based on maximum intraorbital repulsion,¹⁴ for analysis of both covalent bonds and intermolecular interactions. The method decomposes the bond/interaction in contributing terms,

$$\Delta E^{\text{Total}} = \Delta E^{\text{Elect}} + \Delta E^{\text{Ex}} + \Delta E^{\text{Rep}} + E^{\text{Pol}} + \Delta E^{\text{Disp}} \quad (1)$$

whose sum results in the total bond/interaction energy. The first term is related to electrostatic energy, or Coulomb interactions; the second is related to Pauli exchange energy; the third is the Pauli repulsion, caused by orbital superposition; the fourth term is related to polarization energy, and is the sum of charge transfer and bond polarization; and the last term is related to dispersion energy, relative to the difference of the Hartree-Fock (HF) energy and the perturbational methods energy (MPn or CC) obtained for the supermolecule.¹⁰

Another widely and more reliably method for the study of these effects is NBO, which uses the HF delocalized wave function and the non-orthogonal atomic orbitals (AOs) to obtain the natural atomic orbitals

(NAOs), the natural hybrid orbitals (NHOs), the natural bond orbitals (NBOs) and the natural localized molecular orbitals (NLMOs),^{15,16}



The NBO analysis is based on the natural orbitals of Löwdin (Θ_i), which have a eigenvalue (n_i) correspondent to the maximum occupation of these natural orbitals ($0 \leq n_i \leq 2$, respecting the Pauli exclusive principle), which guarantee the maximum orbital occupation.¹⁷

An important difference between these methods is the initial orbital set used to the description of the electronic delocalization.⁴ NBO method initially uses orthogonal orbitals, while the LMO-EDA method uses non-orthogonal orbitals that necessarily orthogonalized by the combination of occupied and (higher energy) virtual orbitals, resulting in a exacerbation of the repulsion energy.^{13,18}

In order to investigate the usefulness and suitability of the LMO-EDA method in the analysis of the influence of conjugation and hyperconjugation phenomena on chemical structures and to better understand their importance in chemical and biological properties of natural products, herein we started a comparative analysis of the LMO-EDA method with the more reliable NBO method, whose first results are herein reported.

Methods

The evaluation of the effects previously described made use of appropriate structural models, namely: methoxybenzene (1), where only conjugation effect is found; dimethoxymethane (2), where only hyperconjugation effect exists (Fig. 1).

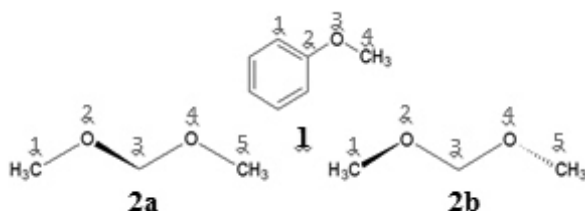


Figure 1: Structures used as appropriate models in this study: 1 – methoxybenzene, 2 – dimethoxymethane (a - C1 and b - C2).

The geometries were optimized and submitted to conformational searches around the C-O bonds at the MP2/CC-pVTZ level of theory, both in GAMESS19 and Gaussian0920 packages. The dihedral angles were varied from 0 to 180°, in steps of 10°. The dihedral angles chosen for variation were (Fig.1): C1-C2-O3-C4, for 1 and 2a (the last one had its C2-O3-O4-C5 dihedral kept fixed at 180° in order to guarantee the presence of only one generalized hyperconjugative effect), and C1-O2-C3-O4 and O2-C3-O4-C5 for 2b in order to maintain C2 symmetry and observe the effect of two concurrent hyperconjugative effects. The treatments of wave functions used, LMO-EDA and NBO, were made in the same level theory of the optimization in all conformers obtained in conformational searches.

Energy decomposition analyses were performed using the GAMESS package, while for NBO analysis the ORCA21 package was used.

Results and Discussion

To analyze how the conjugation and hyperconjugation effects vary and when they occurs we used the models previously shown, methoxybenzene (1) and dimethoxymethane (2) (Fig. 1). As model 2 may have two possibilities of hiperconjugation effect, we locked the O2-C3-O4-C5 dihedral angle in 180° of 2a structure (C1 point group), in order to guarantee the presence of only one generalized hyperconjugative effect.

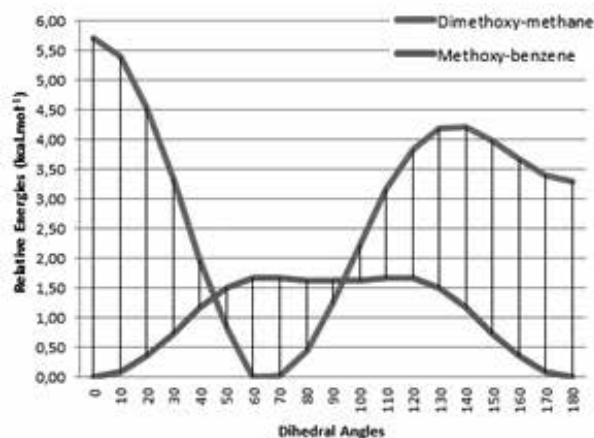


Figure 2: Energy profile of dimethoxymethane and methoxybenzene conformations.

Figure 2 shows the energy profile of conformational search around the chosen dihedral angle (C1-C2-O3-C4) for 1 and its equivalent dihedral angle for 2a. For 1, the most pronounced conjugation interaction occurs in 0° and 180° dihedral angles, when the aromatic ring and methoxy group remain in the same plane, allowing a greater orbital overlapping and conjugation effect. For 2a, we notice a greater interaction between 60 - 70° dihedral angles ($66,98^\circ$ with the relaxed geometry), where the orientation of oxygen's lone pair is eclipsed with the σ^*C-O , generating an expected greater orbital overlapping and consequent hyperconjugative effect. These hypothesis are evaluated in next steps of this study, where the EDA and NBO analysis are performed.

The LMO-EDA data for 1 and 2a are shown in figure 3 and 4, respectively.

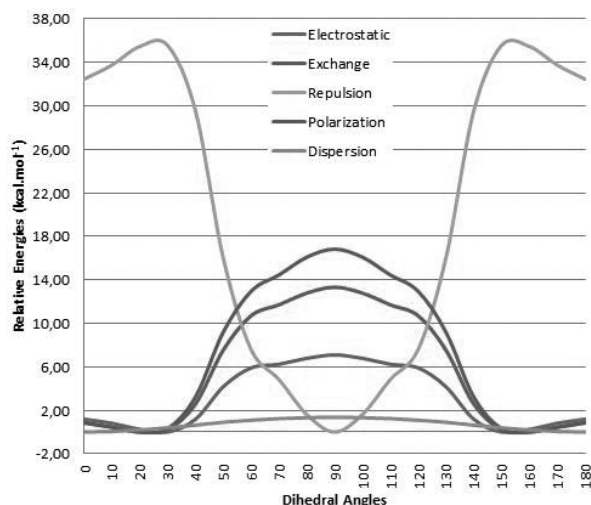


Figure 3: Energy profile of LMO-EDA terms for conformations of 1.

The LMO-EDA profile of 1 (figure 3) shows that in the range of 20 - 30° the electrostatic, exchange and polarization terms are stabilizing ones, while the repulsive term is a maximum in energy. At 90° the repulsive term reaches its global minimum. According to NBO data, conformers shows an interaction between the oxygen's lone pairs (one of the pairs are hybridized sp and the other is purely p) with both adjacent aromatic π^* orbitals which is greater in planar conformation and can probably

explains the stabilizing exchange and polarization terms forecasted by LMO-EDA in small dihedral angles.

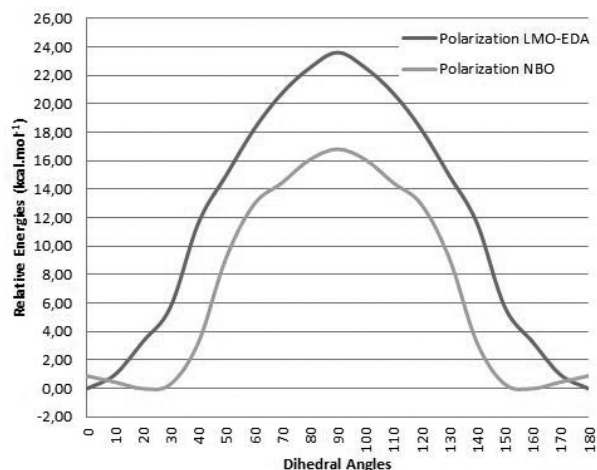


Figure 4. Energy comparative profile of polarization term obtained in LMO-EDA and NBO methods for conformations of 1.

Figure 4 shows the correlation of the polarization terms obtained by both methods for 1. Within the LMO-EDA method the polarization term is obtained by the sum of charge transfer and bond polarization, while for NBO method it was considered by us as the sum of all orbital interaction relative to the analyzed bond. Figure 4 shows a good correlation between them, with exception of the conformers in the range of 20 - 30° . Nevertheless, an inflexion point is shown in the NBO's profile, indicating a polarization disturb in this range of angles, whose origin we don't know yet.

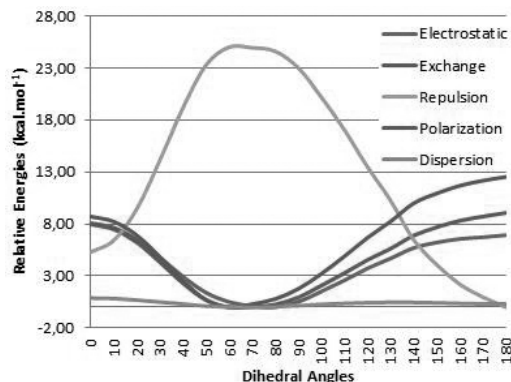


Figure 5. Energy profile of LMO-EDA terms for conformations of 2a.

For 2a, as shown in figure 5, the LMO-EDA's exchange and polarization terms are stabilizing at 60°, and the electrostatic term has its minimum at 80°. The Pauli repulsion term shows máxima two maxima in energy at this range of dihedral angles.

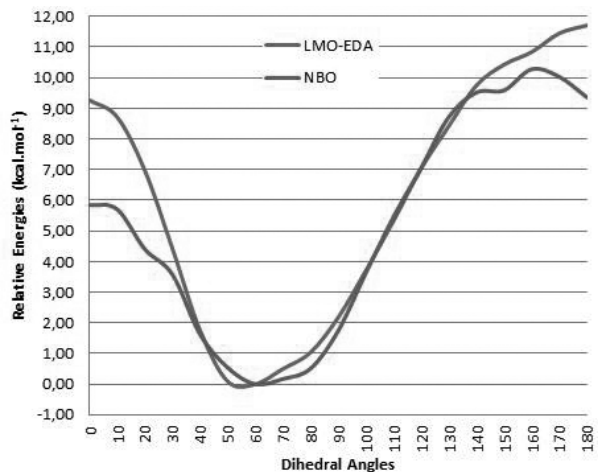


Figure 6. Energy comparative profile of polarization term in LMO-EDA and NBO methods for conformations of 2a.

Figure 6 shows the correlation of the polarization terms provided by both methods for 2a, where we can see a good correlation between them, except for the values next to planar configuration (0° and 180°). It must be stressed, however, that the trends are the same for both methods.

The C2 symmetry of dimethoxymethane (2b) may be able to present a second generalized anomeric effect, and therefore important energetic differences (Fig. 7).

Figure 7 shows that the energy profile of 2b (C2 point group) and of 2a (C1 point group) are very similar, except for the fact that the later has a much more stable gauche (near 60°) conformation relative to plane (C2v) ones (0° and 180°), an indication that both hyperconjugative effects are acting in a cooperative stabilizing way in this C2 conformer. However, the energy profile obtained by the LMO-EDA method

(Fig. 8) is completely different in comparison with the energy profile of 2a (C1 point group) obtained on the same level. The electrostatic, exchange and polarization terms have an energy minimum near to 40°; while the Pauli repulsion term has a maximum in this same dihedral angle, and a minimum in the opposite situation. Nevertheless, the sum of the contributing terms (including the dispersion one) shows that the bond on the conformer with 60° dihedral angle is stronger than the conformer with 40°.

The comparative profile of polarization terms for 2b conformers are shown in figure 9. A great distortion between the conformers on the range of 20-50° dihedral angle is clearly shown. However, for the others conformers, a good correlations is seen. We believe that this discrepancy occurs due to the presence of a second generalized anomeric effect of same magnitude, but opposite sign, which influences in the bond stabilization, affecting the contributing terms (mainly in the polarization one).

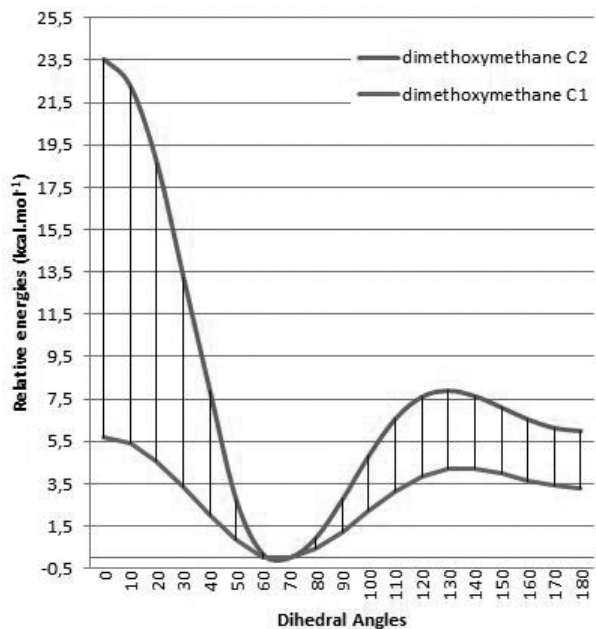


Figure 7. Energy profile of conformations of 2a (C1 point group) and 2b (C2 point group). Note that in the dihedral angle of 0° and 180° the symmetry group of 2b becomes C2v.

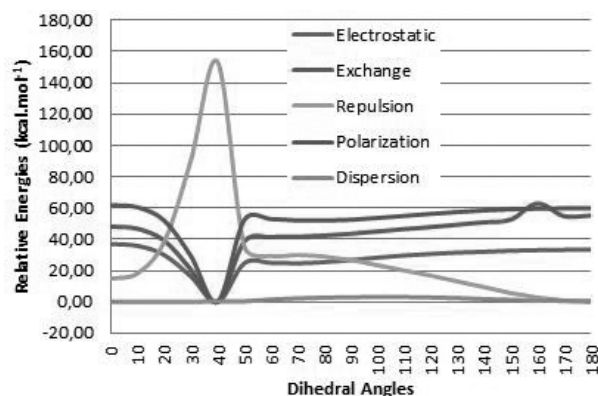


Figure 8. Energy profile of conformations of 2b (C2 point group) using the LMO-EDA method.

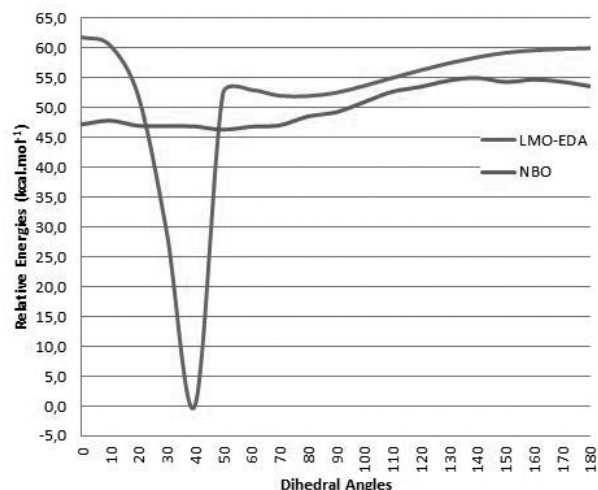


Figure 9. Energy comparative profile of LMO-EDA polarization term and NBO for 2b conformers.

Conclusions

Despite the Pauli repulsive exacerbation of LMO-EDA method, caused by the initial non-orthogonalized orbitals set, the polarization term shows a very good correlation with the NBO polarization, except for the 2b structure, which we believe is due to the presence of a second generalized hyperconjugative anomeric effect.

We also believe that LMO-EDA method has a very good description of energies terms involved in bonds, and has proved to be reliable in analyzes of short-range effects.

In order to do a better comparison of that delocalized effects, we will make the same analysis with the diphenoxymethane structure (same point groups of dimethoxymethane), where the two effects (conjugation and anomeric hyperconjugation) coexist. And then extend that analysis to commonly seen natural products nuclei, 1,2-dimethoxybenzene (competitive conjugative effects) and 1,3-benzodioxole (competitive anomeric hyperconjugative and conjugative effect against each other).

Acknowledgments

The authors are grateful for the financial support given from the CAPES and CNPQ.

References

1. M. B. Smith, *March's Advanced Organic Chemistry: Reactions, Mechanisms, and Structure*, 7th ed., Wiley, (2013).
2. R. S. Mulliken, C. A. Rieke, W. G. Brown, *J. Am. Chem. Soc.*, 63, 41, (1941).
3. IUPAC, *The Gold Book*, 2nd ed., (2006).
4. I. V. Alabugin, K. M. Gilmore, P. W. Peterson, *WIREs Comput. Mol. Sci.*, 1, 109, (2011).
5. J. T. Edward, *Chem. Ind. - London*, 1102, (1955).
6. I. Tvaroska & T. Bleha, *Adv. Carbohydr. Chem. Bi.*, 47, 45, (1989).
7. B. Milián-Medina & J. Gierschner, *WIREs Comput. Mol. Sci.*, 2, 513, (2012).
8. H Hopf, *Wiley-VCH*, (2000); R. P. Orenha, R. Vessecchi, S. E. Galembeck, *Struct. Chem.*, 26, 365, (2015).
9. M. Flister & Q. K. Timerghazin, *J. Phys. Chem. A*, 118, 9914, (2014).
10. P. Su & H. Li, *J. Chem. Phys.*, 131, 014102, (2009).
11. K. Kitaura & K. Morokuma, *Int. J. Quantum Chem.*, 10, 325, (1976).
12. K. Morokuma, *J. Chem. Phys.*, 55, 1236, (1971).
13. I. C. Hayes & A. J. Stone, *Mol. Phys.*, 53, 83, (1984).
14. C. Edmiston & K. Ruedenberg, *Rev. Mod. Phys.*, 35, 457, (1963).
15. J. P. Foster & F. Weinhold, *J. Am. Chem. Soc.*, 102, 7211, (1980).

16. A. E. Reed, R. B. Weinstock, F. Weinhold, J. Chem. Phys., 83, 735, (1985).
 17. P. Löwdin, Phys. Rev., 97, 1474, (1955).
 18. F. Weinhold & J. Carpenter, J. Mol. Struct. THEOCHEM, 165, 189, (1988).
 19. M.W. Schmidt, et al., J. Comput. Chem., 14, 1347, (1993).
 20. M. J. Frisch, et al., Gaussian, Inc., Wallingford CT, (2009).
 21. F. Neese, WIREs Comput. Mol. Sci., 2, 73, (2012).
-

V. A. V. Ferreira*,
V. G. do Nascimento &
M. B. de Amorim

Walter Mors Institute of Research on Natural Products (IPPN), Federal University of Rio de Janeiro (UFRJ).

*E-mail:ferreiravav@correio.nppn.ufrj.br

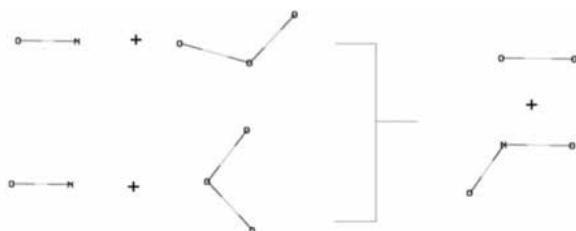
Unconventional Channel of Atmospheric Reaction $\text{NO} + \text{O}_3 \rightarrow \text{NO}_2 + \text{O}_2$: a Mechanistic Study Using Born-Oppenheimer Molecular Dynamics

Yago S. de Sousa; Ademir J. Camargo; Heibbe C. Oliveira; Valter H. Carvalho

Introduction

Given the importance of the ozone in the stratosphere against harmful radiation, the understanding of the ozone depletion process become mandatory¹⁻³.

There are several compounds involved in the degradation of ozone and specifically in the stratosphere exist a significant amount of NOx compounds⁴. Knowledge of these mechanisms has been responsible by a relative abundance of experimental and theoretical work⁴⁻⁸. However, the mechanism involving the NO compound still remains unclear since the experiments observe two different mechanisms (abstracts an end-O-atom and a central-O-atom) by nitric oxide⁷ and just the first possibility has been elucidated theoretically.



Scheme1. The two mechanism involved in the reaction of $\text{NO} + \text{O}_3$.

In this paper, inspired by cross section experimental data, we reported the nonconventional mechanism for the abstraction of central-O-atom using Born-Oppenheimer Molecular Dynamics.

Methods

The structures of all reactive components have been built in the GaussView⁵ program and all theoretical calculations were carried out using the G09⁹ program suite. The proposed reaction pathway has been guided by a centralized attack the N atom to ozone to produce effective collisions reagents for the formation of the desired product. We used the Bohr-Oppenheimer Molecular Dynamics (BOMD)¹⁰ approach to simulate the mechanism. A specified temperature of 0.65eV was adopted. The electronic structure was treated with B3LYP/3-21G. The lower level of these calculations is admittedly, but it is compromise, initially, with the description of the process. The system was built with one NO molecule and one O₃ molecule in the vacuum. A reaction coordinate (Δr) was defined as the difference between lengths of the bond that is progressively broken, r_2 and of one which is concertedly formed, r_1 (see, Figure 1). At $\Delta\gamma < 0$, the condition given by the reagents, such that it, $\Delta\gamma > 0$, it evidences the formation of the product.

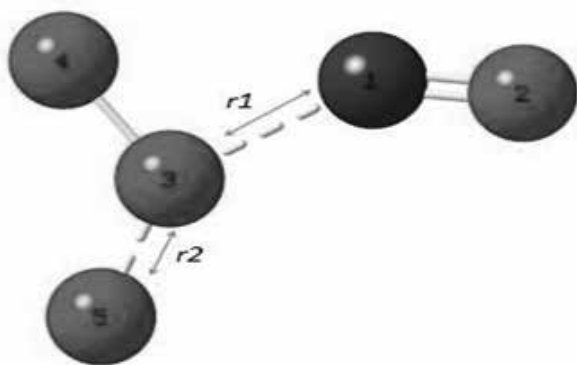


Figure 1. Reaction coordinates used to describe the mechanism.

Results and Discussion

During the numerous simulations, there were certain discrepancies with the abstraction of the central oxygen ozone carried by nitric oxide. Working with STQN method (Synchronous Transit-Guided Quasi-Newton)¹¹, in an attempt of found a stationay transition state involved in the process, this procedure has been ineffective.

The BOMD procedure showed trajectories able to describe the interest mechanism. It was observed a binding between the molecule of NO and O₃. In the Figure 2, it is showed specifics configuration of the trajectories, point out reactants (A panel), transition state (B panel) and products (C and D panels) with temporal scale of the event.

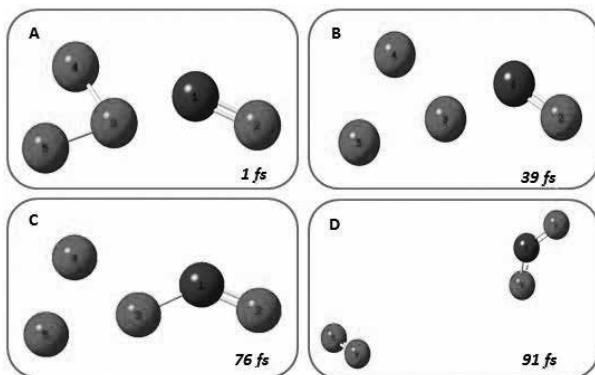


Figure 2. Temporal evolution of the NO + O₃ reaction using BOMD at B3LYP/3-21G level.

A potential energy profile of the reaction is presented in the Figure 3. The stationary points in the potential curve satisfactorily characterized (A – D configurations. Transition state is well characterized in the B point, however, there is a unconvention profile in the potential curve: flat region. The shape can explain the inefficiency of the STQN method, a gradient method that demands well defined stationary point.

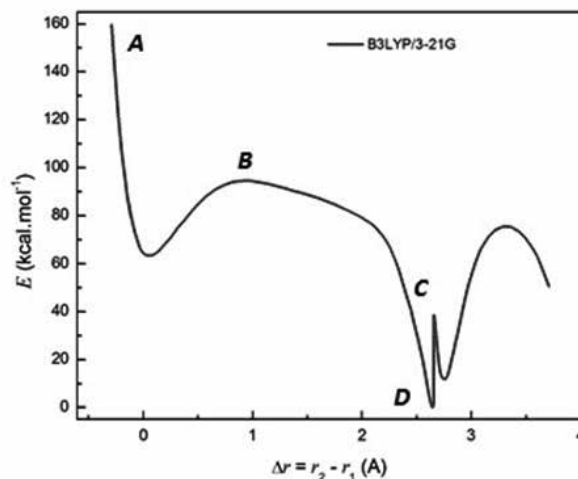


Figure 3. Potential energy profile for the NO + O₃ → NO₂ + O₂ reaction.

As discussed, the flat region represented by B indicates the noticeable maximum value, which, this point corresponds to the transition state, with 5 kcal. mol⁻¹ barrier height, approximately. The minimum stationary point (A and D) in the potential curve defined the reactants and products, respectively.

Conclusion

In summary, the BOMD procedure was able to describe the unconventional mechanism for the NO + O₃ reaction. The main stationay points were observed in the calculated trajectory. The transition state is localized in the flat region on the potential curve, this result explain the inefficacy of the STQN method. The understanding of this mechanism can be guide the comprehension of the dynamics and kinetics parameters involved in the depletion of the ozone in the stratosphere. In addition,

other trajectories are being calculated with high level ab initio methods.

Acknowledgments

The authors are grateful for the support given from the FAPEG, CAPES, CNPQ and FINATEC.

References

1. Heinhorst, S. & Cannon, G. C. J. Chem. Educ. 86, 150 (2009).
2. Read, K. A. et al. Nature 453, 1232–5 (2008).
3. Savarino, J., Bhattacharya, S. K., Morin, S., Baroni, M. & Doussin, J.-F. J. Chem. Phys. 128, 194303 (2008).
4. Dutta, A. K., Vaval, N. & Pal, S. J. Chem Theory Comput. 8, 1895–1901 (2012).
5. Kahler, C. C., Ansell, E., Upshur, C. M. & Green, W. H. J. Chem. Phys. 80, 3644 (1984).
6. Kahler, C. C. & Kowalczyk, M. J. Chem. Phys. 84, 1946 (1986).
7. Ende, D. van den. J. Chem. Phys. 77, 2206 (1982).
8. Jaroszyńska-Wolińska, J. J. Mol. Struct. THEOCHEM 952, 74–83 (2010).
9. Frisch, M. J. et al. Gaussian 09 Revision D.01. (2009).
10. Marx, D. & Hutter, J. Mod. methods algorithms quantum Chem. 1, 301–449 (2000).
11. Peng, C. & Bernhard Schlegel, H.. Isr.J. Chem. 33, 449–454 (1993).

Yago S. de Sousa¹; Ademir
J. Camargo¹; Heibbe
C. Oliveira² & Valter H.
Carvalho^{1,*}

^aGrupo de Química Teórica e Estrutural de Anápolis, Campus de Ciências Exatas e Tecnológicas, Universidade Estadual de Goiás, 75001-970, Anápolis, Brasil

^bInstituto de Química, Universidade de Brasília, 70904-970, Brasília, Brasil.

*fatioleg@gmail.com

Theoretical Study of the Mechanism and Rate Constant Calculations of the Reaction of Carbon Monoxide with Ethylene

Washington B. Silva & Alessandra F. Albernaz

Introduction

The CO + ethylene (C₂H₄) reaction participate as product in important chemical processes of class of fuels in combustion.^{1,2} Investigation on the reactions of hydrocarbons with some atmospheric species can provide significant insights into combustion, hydrocarbon synthesis, interstellar space and atmospheric chemistry. Ethylene is one of the highest volume chemicals produced globally.^{3,4} In addition, ethylene is an important element in petrochemical industry.⁵ The study of reaction CO + C₂H₄ give support to understanding the whole combustion mechanism and is useful for establishing appropriate models for combustion simulations under the atmospheric condition.¹ In this work we investigated the pathways reaction of the CO + ethylene reaction. Initial

equilibrium geometries of the reactions, intermediate reactions, transitions states, and product were optimized at density functional CBS-QB3⁶ to all species involved in the reaction. The rate constant has been calculated using transition state theory⁷ and Wigner, Eckart tunneling correction factor^{7,8,9} and writing down in the Arrhenius form for temperature range of 100 – 4000 K.

Methods

TRANSITION STATE THEORY

Based on the transition state theory, the thermal rate

constant (TRC) of a bimolecular reaction, A+BC →TS → C+AB can be written as⁸:

$$k^{\text{TST}} = \frac{\kappa_B T}{h} \frac{Q^{\text{TS}}}{Q^R} \exp\left(-\frac{V}{RT}\right) \quad (7)$$

where KB and h are Boltzmann and Planck constants, while T is the temperature and R is the universal gas constant. Q^{TS} and Q^R (Q^AQ^{BC}) are the partition functions of transition state (TS) and reactant (R=A+BC), respectively. In this work, we have considered two corrections for the tunneling effect: Wigner (KW(T)) and Eckart (K_E(T)). The Wigner transmission coefficient is given by^{7,8}

$$\kappa_W(T) = 1 + \frac{1}{24} \left| \frac{\hbar \omega^\ddagger}{k_B T} \right|^2 \quad (8)$$

and the Eckart tunneling correction (K_E(T)) is obtained solving the Schrödinger equation for the *V*:

$$\kappa_E(T) = \frac{\exp(\Delta V^{TS}/RT)}{RT} \int_0^\infty \exp(-E/RT) \Gamma(E) dE \quad (9)$$

here the transmission probability ($\Gamma(E)$) is given by:

$$\Gamma(E) = 1 - \frac{\cosh[2\pi(\alpha-\beta)] + \cosh[2\pi\gamma]}{\cosh[2\pi(\alpha+\beta)] + \cosh[2\pi\gamma]}, \quad (10)$$

with

$$\alpha = \frac{1}{2}(E/c)^{1/2}, \quad \beta = \frac{1}{2}\left(\frac{E-a}{c}\right)^{1/2}, \\ \gamma = \frac{1}{2}\left(\frac{b-c}{c}\right)^{1/2} \quad \text{and} \quad c = \frac{(\hbar\omega^{TS})^2 B}{16\Delta V^{TS}(\Delta V^{TS}-a)}.$$

The TRC were then written in the Arrhenius form as:

$$k(T) = AT^n \exp\left(-\frac{E_a}{RT}\right) \quad (11)$$

where A is the pre-exponential factor, n is the temperature power factor and E_a is the activation energy.

AB INITIO CALCULATIONS

The CBS-QB3 method⁶ encompasses the so called complete basis set model chemistries originally developed by Peterson and coworkers. CBS models involve low-level (SCF and ZPE) calculations on large basis sets, mid-sized sets for second-order corrections, and small sets for high-level corrections. They include extrapolation to the complete basis sets to correct Møller–Plesset second-order energies in addition to empirical and spin-orbit interaction corrections.¹⁰⁻¹⁶ Specifically, the CBSQB3 method involves the following steps:

- i. B3LYP/6-311G(2d,d,p) geometry optimization.
- ii. B3LYP/6-311G(2d,d,p) frequencies with a 0.99 scale factor for the ZPE.
- iii. UMP2/6-311+G(3d2f,2df,2p) energy and CBS extrapolation.
- iv. MP4(SDQ)/6-31+G(d(f),p) energy.
- v. CCSD(T)/6-31+G* energy. Finally, the total and free energy are calculated from the following:

$$E_{\text{CBS-QB3}} = E_{\text{MP2}} + \Delta E_{\text{MP4}} + \Delta E_{\text{CCSD(T)}} + \Delta E_{\text{ZPE}} + \Delta E_{\text{CBS}} + \Delta E_{\text{emp}} + \Delta E_{\text{int}}, \quad (1)$$

$$G_{\text{CBS-QB3}} = E_{\text{MP2}} + \Delta E_{\text{MP4}} + \Delta E_{\text{CCSD(T)}} + \Delta E_{\text{thermalcorrection}} + \Delta E_{\text{CBS}} + \Delta E_{\text{emp}} + \Delta E_{\text{int}}, \quad (2)$$

where ΔE_{CBS} is the term correcting the basis set truncation error in the second-order energies, and the energy terms ΔE_{MP4} , $\Delta E_{\text{CCSD(T)}}$, ΔE_{emp} , and ΔE_{int} are calculated from the following respective equations:

$$\Delta E_{\text{MP4}} = \frac{E_{\text{MP4(SDQ)}}/6-31+G(d(f),p) - E_{\text{MP2}}/6-31+G(d(f),p)}{6-31+G(d(f),p)} \quad (3)$$

$$\Delta E_{\text{CCSD(T)}} = \frac{E_{\text{CCSD(T)}/6-31+G*} - E_{\text{MP4(SDQ)}/6-31+G*}}{6-31+G*} \quad (4)$$

$$\Delta E_{\text{emp}} = -0.00579 \sum_{i=1}^{N\beta} (\sum_{\mu=1}^{N_{\text{virt}}+1} c_{\mu i})^2 |S|_{ii}^2 \quad (5)$$

$$\Delta E_{\text{int}} = -0.00954 [(S^2) - S_z(S_z - 1)]. \quad (6)$$

The CBS-QB3 method has been employed in our work to optimize the geometries of the reactant, complex reactants, transition states, complex products and products of the reaction of carbon monoxide with ethylene ($\text{CO} + \text{C}_2\text{H}_4$). Vibrational frequencies calculated at CBS-QB3 levels were used for characterization of stationary points as minima and transition states, for zero-point energy (ZPE) corrections, because it is known that the ZPE value is significant in hydrogen-bonded systems.¹⁷ The number of imaginary frequencies (0 or 1) indicates whether a minimum or a transition state has been located. To confirm that the transition state really connects with designated intermediates along the reaction path, the intrinsic reaction coordinate (IRC)¹⁸ calculations were performed. Also, the IRC calculations were used to confirm the connection between the designated transition states and the reactants or products. All quantum chemistry calculations were performed with Gaussian 09 program.¹⁹

Results and Discussion

The relative energies (the total energy of the reactants is set to zero for reference) of all species involved at the CBS-QB3 level are summarized in Figure 1.

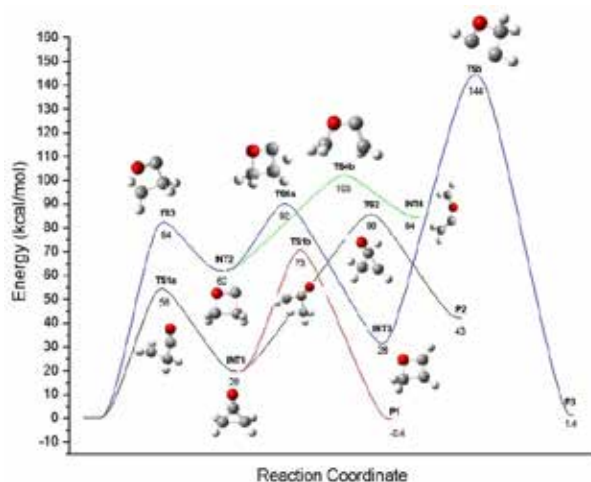


Figure 1. Potential energy diagram for decomposition of $\text{CO} + \text{C}_2\text{H}_4$ reaction at the CBS-QB3 level.

During the simulations, we found four pathways for the Potential Surface Energy - SEP. We found some pathways that were proposed by Karami and Vahedpour¹ and we found two new pathways. Our results for the reactants, intermediates and products are in good agreement compared with results obtained by Karami and Vahedpour, and all real frequencies and any transition state has only one imaginary frequency.

In Table 1 we display the rate constant for the $\text{CO} + \text{C}_2\text{H}_4 \rightarrow \text{C}_2\text{H}_3\text{COH}$ reaction to temperature of 250K.

Table 1: Conventional (k^{TST}), Wigner (k^{TST}), and Eckart (k^{TST}) thermal rate constants calculated for the $\text{CO} + \text{C}_2\text{H}_4 \rightarrow \text{C}_2\text{H}_3\text{COH}$ reaction at 250 K.

T(K)	k^{TST} [cm ³ .molecule ⁻¹ .s ⁻¹]
250	1.57×10^7 (k^{TST})
	3.99×10^7 (k^{TST})
	3.46×10^{128} (k^{TST})

Conclusions

In this work, the $\text{CO} + \text{C}_2\text{H}_4$ reaction potential energy profiles were determined based on the geometrical optimization, frequency and energy calculations at the CBS-QB3 level. Our simulations for the SEP predicted two new pathways for the $\text{CO} + \text{C}_2\text{H}_4$ reaction and for the others paths presented in good concordance with SEP investigated by Karami and Vahedpour. The thermal rate constants showed high possibility of occurrence at room temperature for the pathway studied.

Acknowledgments

The authors are grateful for the support given from the Instituto Federal de Educação, Ciência e Tecnologia do Goiás - IFG.

References

1. F. Karami and M. Vahedpour, J. Iran Chem Soc., 11, 781, (2014).
2. H. Hua, B. Ruscic, B. Wang, Chem. Phys., 311, 335, (2005).
3. Assessment report on ethylene for developing ambient air quality objectives, <http://gov.ab.ca/env/protenf/standards/index.html>. Alberta Environ (2003).
4. Production: Growth is the Norm//Chemical and Engineering News, 84, 28 (2006). <http://pubs.acs.org/cen/coverstory/84/pdf/8428production.pdf>
5. A. Lifshitz, H. Ben-Hamou, J. Phys. Chem., 87, 1782 (1983).
6. J. A. Montgomery, M. J. Frisch, J. W. Ochterski, G.A. Petersson., J. Chem. Phys., 110, 2822 (1999).
7. E. Henon, F. Bohr, Journal of Molecular Structure (Theochem), 531, 283 (2000).
8. D. G. Truhlar, A. D. Isaacson, B. C. Garrett, Generalized Transition State Theory, Series: Theory of Chemical Reaction Dynamics. CRC Press, Inc., vol. 4, p. 65, (1985).
9. C. Eckart, Phys. Rev. 35, 1303 (1930).
10. Ochterski, J. W.; Petersson, G. A.; Montgomery, J. A., Jr. J Chem Phys, 104, 2598 (1996).
11. Nyden, M. R.; Petersson, G. A. J Chem Phys, 75, 1843 (1981).
12. Petersson, G. A.; Bennett, A.; Tensfeld, T. G.; Al-Laham, M. A.; Shirley, W.; Matzaris, J. J Chem Phys, 89, 2193 (1988).
13. Petersson, G. A.; Al-Laham, M. A. J Chem Phys, 94, 6081 (1991).
14. Petersson, G. A.; Yee, A. K.; Bennett, A. J Chem Phys, 83, 5105 (1983).
15. Montgomery, J. A., Jr.; Ochterski, J. W.; Petersson, G. A. J Chem

Phys, 101, 5900 (1994).

16. Montgomery, J. A., Jr.; Frisch M. J.; Ochterski, J. W.; Petersson, G. A. J Chem Phys, 112, 6532 (2000).
17. O. Mó, M. Elguero Yáñez, J. Chem. Phys. 97, 6628 (1992).
18. K. Raghavachari, G. W. Trucks, J. A. Pople, M. Head-Gordon, Chem. Phys. Lett. 157, 479 (1989).
19. Frisch, M. J. et al. Official Gaussian 09 Literature Citation. Gaussian, Inc.: Pittsburgh PA (2009).
20. http://www.gaussian.com/g_tech/g_ur/m_citation.htm

Washington Barbosa da
Silva^{a,b} & Alessandra F.
Albernaz^a

^aInstituto de Física, Universidade de Brasília, Brasília, DF, Brazil

^bInstituto Federal de Educação, Ciência e Tecnologia do Goiás- IFG, GO, Brazil

Anacardic Acid Derivatives as Potential Acetylcholinesterase Inhibitors

A. S. Kiametis, M. Abreu, R. Gargano & L. A. S. Romeiro

Introduction

Alzheimer's disease is the leading cause of dementia among people over 65 years of age. Although its etiology is not fully known, the decreased levels of acetylcholine (ACh) has been linked to the pathophysiology of the disease [1]. The cholinergic hypothesis is a line therapy based on increasing the level of acetylcholine by reversible inhibition of the enzyme acetylcholinesterase (AChE) therefore promoting an improvement in the patient's cognitive profile. This paper aims to propose possible candidates to AChE inhibitors, designed from the lipid phenolic derivatives of cashew, more specifically the anacardic acid, the most abundant phenolic lipid derivative extracted from the cashew nutshell liquid, which is a natural resin found in the honeycomb structure of the cashew (*Anacardium occidentale*) nutshell.

Methodos

AChE structure looks like a deep narrow gorge (figure 1), with about 20Å length, lined by 14 conserved aromatic residues [2]. Among these residues, several functional amino acids have been identified such those in the catalytic triad where AChE hydrolyses ACh. After being recognized by the residues localized among

the peripheral anionic site and the aromatic site (a hydrophobic subunit), ACh reaches deep into the protein binding to the catalytic triad and the aromatic site. The ACh's amino group binds to the aromatic Trp84 by cation- π interactions while Tyr70, Tyr121 and Phe330 residues act on ACh through hydrophobic-aromatic interactions with methylene spacers containing up to 8 carbons.

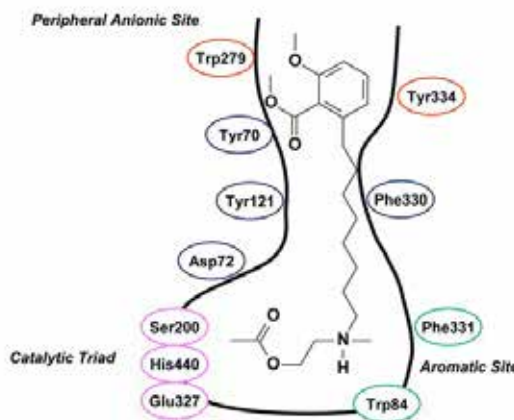


Figure 1. Acetylcholinesterase - a schematic representation of the inhibitor candidate interaction with the residues of electrophorus electricus AChE.

Our compounds were designed to mimics ACh behavior so they were divided in two pharmacophoric subunits (figure 2), according to the respectively site in which may occur a interaction (peripheral or catalytic). A hydrophobic spacer sufficiently long was inserted between the two subunits thus the drug occupies the whole gorge and the expected interactions becomes possible.

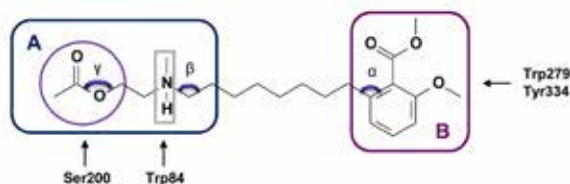


Figure 2. Design of our inhibitor candidates of AChE.

In total, twenty molecular structures with different functional groups were designed taking into account the possible interactions between these functional groups and enzyme active sites. For each molecule, a conformational analysis was done in a way to identify the more stable conformers. The geometries were first optimized by semiempirical method and then optimized again, for greater accuracy, by using the hybrid functional B3LYP and basis set 6-311+G(2d,p). A single point was taken for the equilibrium geometry for each compound and several electronic properties important for the molecular recognition by the enzyme, like HOMO, HOMO-1, LUMO, LUMO+1, GAP and atomic charges, were calculated for the compounds studied. The polarizable continuum model has been implemented in the ab initio calculations to simulate solvating. Geometric and lipophilicity properties were also determined for each candidate using quantitative structure activity relationship

Results and Discussion

The descriptors for this group of molecules are strongly correlated so we have used the Principal Component Analysis (PCA) to treat the initial data set. This technique has been successfully used before to predict the most relevant descriptors to correlate inhibitors and active drugs

[3]. Here, we tried to correlate our candidates with donepezil. To ensure accurate results, the PCA was performed taking into account all possible linear combinations of the variables (descriptors). For a cluster analysis, only those combinations in which the PC1 variance showed equal or greater than 75% were selected. After systematic analysis, for the case where the PCM solvating model was not used in electronic structure calculations, in general, the molecules number 5 and 7 remained near the drug for the first two principal components. Others like number 1-10, 14 and 16 remained near the drug for PC1 but not for PC2. The descriptors identified as the most suitable for the correlation are Mulliken charge of the nitrogen belonging to amino group (N), log P, polarizability and molecular mass, whereas the latter two contribute more effectively to the PC1, accounting 79% of the information about the correlation. Including the PCM solvating model in electronic structure calculations, the distribution of molecules in the first two principal components is expressively affected. In this situation, molecules 5 and 7 still remain close to donepezil for PC1 but deviate considerably for PC2. Molecule 16, which was far from the drug for PC2, now is the most correlated with donepezil, according to figure 6. The score plot of PC1 versus PC2 (figure 3) shows how remarkably close molecule 16 is to donepezil for both components. The acid character of the carboxyl group of the anacardic acid is possibly influencing the ligand-receptor interactions in the presence of solvent, leading to this result.

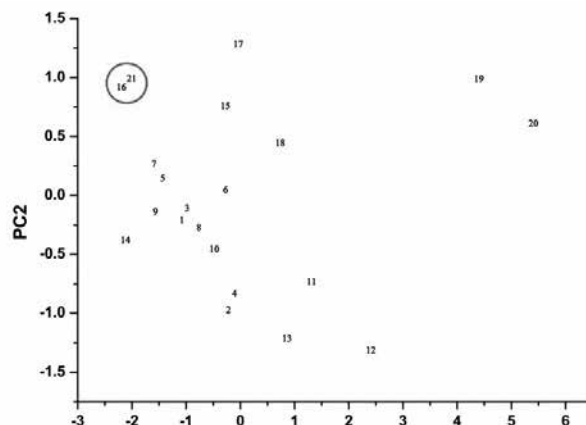


Figure 3. Score plot of PC1 versus PC2 in a solvating model. The cluster involving donepezil and molecule 16 is shown.

In structural terms, molecule 16 is more similar to donepezil than the others. The molecule has a benzene heterocyclic ring bonded to an amine group where is concentrated the HOMO orbital, showing the electron donor character of the compound in this region. The HOMO energy for molecule 16 was -8.797eV . In this case, the benzene group is possibly interacting with Trp84 residue through cation- π . The LUMO orbital is concentrated at the dimethoxy-phenyl ring, showing the electron acceptor character of the compound in this region. So this group is possibly interacting with the aromatic residues of the peripheral site through π -stacking. The LUMO energy for molecule 16 was -0.263eV . The electrostatic potential map (figure 4) for compound 16 indicates that a hydrogen bond type occurs between the oxygen of the acetyl group belonging to dimetoxi-phenil ring and the peripheral anionic site (attractive region, reddish) and also between the nitrogen of the enzene heterocyclic ring and the catalytic site (attractive region, reddish).

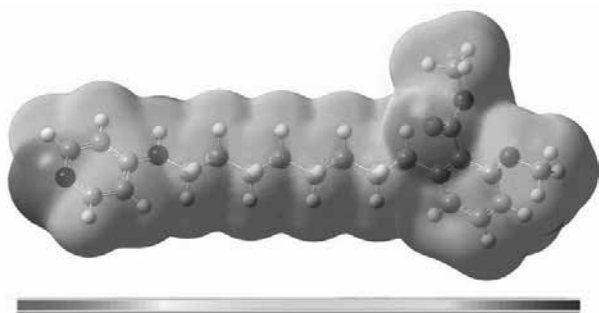


Figure 4: Molecular electrostatic potential for molecule 16.

Conclusions

This work proposes possible new inhibitor candidates of AChE designed from the anacardic acid. Based on electronic properties and also on the expected binding sites between the receptor and the ligands we concluded that molecule 16 plays the role of inhibitor better than the other structures, once PCA and HCA methods revealed that molecule 16 is very correlated to the donepezil.

Actually, one can find in the literature studies of biological activity with purified AChE, derived from the electrophorus electricus [3], indicating the therapeutic action of cholinergic compounds designed from another kind of phenolic lipid derivative. So we hope to find satisfactory experimental results of inhibition activity for our candidate.

Acknowledgments

The authors are grateful for the support given from the CAPES and CNPQ.

References

1. J. L. Cummings, *Rev. Neurol. Dis.* **2004**, 1, 60.
2. H. Dvira, I. Silmanb, M. Harela, T. L. Rosenberryc, J. L. Sussman, *Chemico-Biol Interact.* **2010**, 10, 187. J. L. Cummings, *Rev. Neurol. Dis.* **2004**, 1, 60.
3. A. A. N. De Paula, J. B. L. Martins, M. L. dos Santos, L. C. Nascente, L. A. S. Romeiro, T. F. M. A. Areas, K. S. T. Vieira, N. F. Gambo, N. G. Castro, R. Gargano, *Eur. J. Med. Chem.* **2009**, 44, 3754

A. S. Kiametis^a, M. Abreu^a,
R. Gargano^a & L. A. S.
Romeiro^b

^a University of Brasilia, Institute of Physics, CP 04454 Brasilia, Brazil

^b University of Brasilia, Department of Pharmacology, CP 04454 Brasilia, Brazil

The NH^{2+} and Be_2^{2+} Vibrational Spectroscopic Constants From use of the New Analytical Potential Energy Function

Ana Paula de Oliveira, Valter Henrique Carvalho Silva, Kleber C. Mundim, Ricardo Gargano, Heibbe Cristhian B. de Oliveira & Luciano Ribeiro

Introduction

Experimental and computational studies of charged molecules are the great interest in chemistry, physical and biological systems, and the description of their properties are essential for understanding of fundamental mechanism¹⁻³. Diatomic dications are interesting ions because they can be generated as a long-lived molecule in the gas phase. The study of potential energy curves (PECs) for small dications has received growing attention in recently papers because these can provide several spectroscopic properties^{1,4,5}, however, the behavior of the PEC is very different when compared with neutral and singly charged diatomic molecules: these kinds of molecules have some new features that the potential curves may have both potential minimum and maximum or singly repulsive branch (Figure 1).

Methods

In previous paper Wang and co-authors⁶ proposed a new analytical PEC including an ionic Coulomb repulsion term and the Varandas potential term, as follow,

$$V(R) = \left(\sum_{n=0}^3 a_n R^n \right) e^{-a_4 R} + \frac{C}{R}, \quad (1)$$

which can be used to describe the diatomic ions with both potential minimum and maximum or without any stationary point.

In this work we propose a new analytical PEC for doubly charged diatomic ions. These functions are based on the deformed exponential function (d-Exponential), defined as:

$$e_d^{-x} = [1 - dx]^{\frac{1}{d}}. \quad (2)$$

In this way, we proposed a new analytical PEC, as follow:

$$V_d(R) = \left(\sum_{n=0}^3 a_n R^n \right) e_d^{-a_4 R} + \frac{C}{R}. \quad (3)$$

The new function, eq. 3 is most flexible to build up the PEC due to the inclusion of an additional parameter (parameter). The d-Exponential function has been applied successfully to a variety of problems in electronic structure⁷⁻¹⁰, where and are adjustable parameters. All coefficients were optimized using a hybrid procedure based on the global optimization method known as Generalized Simulated Annealing (GSA)^{11,12}, the simplex

gradient and Levenberg-Marquardt 13 methods.

We evaluated the spectroscopic constants using the Dunham's method 14, which is obtained by comparing Eq.(4) and the PEC written with a Taylor expansion around the equilibrium distances. The Dunham's method needs force constants at minimum. From the new function (equation 3) it is easy to derive quadratic, cubic and quadratic terms, as follows:

$$f_2 = \sum_{n=0}^3 a_n n(n-1) R^{n-2} [e_d^{-a_4 R}] + \sum_{n=0}^3 a_n (-2a_4 n R^{n-1} + a_4^2 d R^n) [e_d^{-a_4 R}] + 2C/R^3 \quad (4)$$

$$f_3 = \sum_{n=0}^3 a_n n(n-1)(n-2) R^{n-3} [e_d^{-a_4 R}] + \sum_{n=0}^3 a_n (-3a_4 n(n-1) R^{n-2} + 3a_4^2 d n R^{n-1} - a_4^3 d^2 R^n) [e_d^{-a_4 R}]^d - 6C/R^4, \quad (5)$$

and

$$f_4 = \sum_{n=0}^3 a_n n(n-1)(n-2)(n-3) R^{n-4} [e_d^{-a_4 R}] + \sum_{n=0}^3 a_n \left(-4a_4 n(n-1)(n-2) R^{n-3} + 6a_4^2 d n(n-1) R^{n-2} - 4a_4^3 d^2 n R^{n-1} + a_4^4 d^3 R^n \right) [e_d^{-a_4 R}]^d + 24C/R^5. \quad (6)$$

Results and Discussions

In this section we present results of dynamics properties of the and NH_2^+ system using the new analytical PECs proposed in this work. The PECs for are shown in Figure 1, and for NH_2^+ are shown in Figure 2, where, in both cases, the red solid line represent the fitted line and the black circles re the ab initio calculated values.

The results of the maximum (minimum) deviation and the error found between values for the ab initio and fitted energies were: 1.21×10^{-3} (1.30×10^{-5}) and 1.19×10^{-6} and 8.28×10^{-4} (2.52×10^{-5}) and 1.12×10^{-5} , for the deformed PEC and the usual one, respectively. From these results we can see close agreement between the ab initio and fitted energies. It is important to point out that the success of the fitting procedure is, in part, due to the d-Exponential function's flexibility.

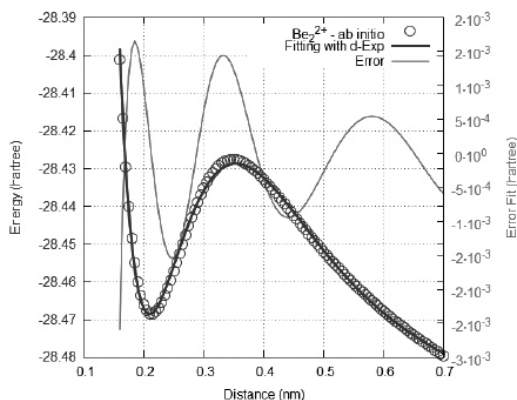


Figure 1 - The fitted potential energy curves for $\text{Be}^{22+}(\text{X1 } \Sigma_g^+)$

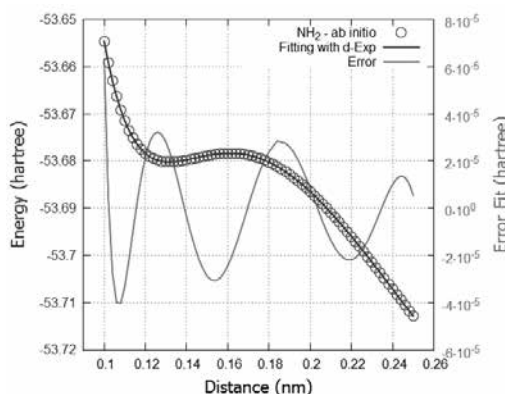


Figure 2 - The fitted potential energy curves for $\text{NH}_2^+(\text{X1 } \Sigma_g^+)$

The results of calculated spectroscopic constants for Be_2^{2+} molecular system are show in the Table 1. From this Table we can see a good agreement with reference 6.

All values of ω_e , $\omega_e x_e$ and B_e are in excellent agreement with experimental data ⁶.

Table 1: The calculated potential minima and maxima for the ground state of Be_2^{2+} , BH^{2+} , CH^{2+} , NH^{2+} molecules.

Molecules	Rmin(nm)	Rmax(nm)	$\Delta E(\text{Hartree})$
Be22+	0.215	0.350	0.0453
NH2+	0.132	0.163	0.0012

Table 2: The parameters of the analytic potential function for Be_2^{2+} .

Molecules	$\text{Be22+}(X^1\Sigma_g^+)$	
	PEC	qPEC
a0 (eV)	165.987	-166.063
a1 (eV)	351.774	351.681
a2 (eV)	-588.099	-587.7244
a3 (eV)	-7200.8517	-7205.404
a4 (eV)	260.0921	260.078
C	6.0118	6.015
q	-	-5.92450E-012
X^2	4.524E-010	3.37282E-010

Table 3: The derived force constant for Be_2^{2+} and NH^{2+} molecules.

$\text{Be22+}(X^1\Sigma_g^+) \rightarrow 2\text{Be}^+(^1S_g)$		
$f_2(\text{eV nm}^{-2})$	PEC	4080.8
	d-PEC	4079.97
$f_3(\text{eV nm}^{-3})$	PEC	-56941.8
	d-PEC	-56929.9
$f_4(\text{eV nm}^{-4})$	PEC	1059383.0
	d-PEC	1059161.2
$\text{NH2+}(X^2\Sigma^+) \rightarrow \text{H}^+(^1S_g) + \text{N}^+(^1D_g)$		
$f_2(\text{eV nm}^{-2})$	PEC	5227.7
	d-PEC	5229.0
$f_3(\text{eV nm}^{-3})$	PEC	-118812.6
	d-PEC	-118841.5
$f_4(\text{eV nm}^{-4})$	PEC	3600384.4
	d-PEC	3601258.1

Table 4: The derived spectroscopic constants for Be_2^{2+} and NH^{2+} molecules.

		$\text{Be22+}(X^1\Sigma_g^+)$	$\text{NH2+}(X^2\Sigma^+)$
B_e	PEC	0.809	10.29
	d-PEC	0.809	10.29
ω_e	PEC	1569.2	3888.8
	d-PEC	1568.7	3889.1
$\omega_e x_e$	PEC	0.3034	3.8594
	d-PEC	0.3034	3.8594
α_e	PEC	-7.3732E-016	-3.9251E-012
	d-PEC	-1.2356E-020	3.34854E-016

Conclusions

In this paper we have proposed a new alternative analytical function aiming to better describe the potential energies curves of the doubly charged diatomic molecules. To this end, we used the new PEC obtained by included the deformed exponential function (d-Exponential function). To test the new function, we also calculated the force constant, spectroscopic constants and the rovibrational spectra for the Be22+ . The calculated values of equilibrium vibrational frequency (ω_e), anharmonic constant ($\omega_e x_e$) and rotational constant (B_e) are very close to experimental data available in the literature. This fact suggests that the results of other spectroscopic constants and rovibrational energies presented in this work have the same accuracy. The results presented in this work show that the new PEC is sufficiently better when compared with the usual analytical.

Acknowledgments

The authors gratefully acknowledge the support given to this work by from UEG, CNPq and FAPEG.

References

1. A.G.S. De Oliveira-Filho and F.R. Ornellas, J. Chem. Phys. 138, (2013).
2. D. Schröder and H. Schwarz, J. Phys. Chem. A 103, 7385 (1999).
3. B. Shepperson, J. Liu, A.M. Ellis, and S. Yang, J. Phys. Chem. A 115, 7010 (2011).
4. T.V. Alves, W. Hermoso, K. Franzreb, and F.R. Ornellas, Phys. Chem. Chem. Phys. 13, 18297 (2011).

5. R. Linguerri, M. Hochlaf, M.-C. Bacchus-Montabonel, and M. Desouter-Lecomte, *Phys. Chem. Chem. Phys.* 15, 824 (2013).
 6. F. Wang, C. Yang, and Z. Zhu, *J. Mol. Struct. THEOCHEM* 684, 9 (2004).
 7. C.S. Esteves, H.C.B. de Oliveira, L. Ribeiro, R. Gargano, and K.C. Mundim, *Chem. Phys. Lett.* 427, 10 (2006).
 8. L.R. Salviano, C.S. Esteves, H.C.B. de Oliveira, K.C. Mundim, L. Ribeiro, and R. Gargano, *Phys. A Stat. Mech. Its Appl.* 389, 3604 (2010).
 9. H.C.B. de Oliveira, F.C. Rangel, C.S. Esteves, F.M.C. Vieira, and K.C. Mundim, *J. Phys. Chem. A* 113, 14691 (2009).
 10. F.C. Rangel, H.C.B. de Oliveira, A.L.B. Montel, and K.C. Mundim, *Phys. A Stat. Mech. Its Appl.* 389, 5208 (2010).
 11. K.C. Mundim and C. Tsallis, *Int. J. Quantum Chem.* 58, 373 (1996).
 12. M.D. de Andrade, K.C. Mundim, and L.A.C. Malbouisson, *Int. J. Quantum Chem.* 103, 493 (2005).
 13. D.W. Marquardt, *J. Soc. Ind. Appl. Math.* 11, 431 (1963).
 14. J.L. Dunham, *Phys. Rev.* 41, 721 (1932).
-

Ana Paula de Oliveira^a, Valter
Henrique Carvalho Silva^a,
Kleber C. Mundim^b, Ricardo
Gargano^c, Heibbe Cristhian
B. de Oliveira^b & Luciano
Ribeiro^a

^aUnidade Universitária de Ciências Exatas de Anápolis – Universidade Estadual de Goiás, CP 459, Anápolis, GO, Brasil

^bInstituto de Química, Universidade de Brasília, CP 4478, 70919-970, Brasília, DF, Brasil

^cInstituto de Física, Universidade de Brasília, CP 4478, 70919-970, Brasília, DF, Brasil

Width Influence on the Polaron Dynamics in Graphene Nanoribbons

Ana V. P. Abreu, Luiz A. R. Junior & Antonio L. A. Fonseca

Introduction

Carbon-based nanomaterials¹⁻⁴ are recognized as promising solutions to the development of novel electronic devices that present smaller environmental impact when compared to its inorganic counterparts. Due to unique features such as easy of synthesis, strict two-dimensionality, low cost, and high mechanical strength graphene has attracted huge interest to the design of photovoltaic⁵, energy storage⁶, and field-effect transistor applications. Significant efforts have been performed theoretically⁷ and experimentally⁸ in order to understand the charge transport mechanism in graphene sheets and nanoribbons. Importantly, these works have investigated the charge transport from the framework of metallic-like behavior⁸⁻¹². Nonetheless, theoretical studies considering the semiconducting-like physical picture for charge transport mechanism, to describe the system features which may affect the polaron dynamics, are still insufficient.

In this work, the influence of the nanoribbon width on the dynamics of polarons in armchair graphene nanoribbons (GNRs) is numerically investigated in the scope of a two-dimensional Su-Schrieffer-Heeger model

with lattice relaxation. The results show that the polaron dynamics changes substantially varying the nanoribbon width. Moreover, the interplay between external electric field and the electron-phonon coupling plays the role of drastically modifying the charge localization through the nanoribbon and, consequently, the polaron dynamics. This investigation may enlighten the understanding of the charge transport mechanism in graphene-based nanomaterials.

Methods

In order to describe the charge transport in GNRs we developed a two-dimensional version of the Su-Schrieffer-Heeger (SSH) model¹², modified to include an external electric as follows

$$H_{elec} = - \sum_{\langle i,j \rangle, s} (t_{i,j} C_{i,s}^{\dagger} C_{j,s} + h.c.) + \sum_{\langle i,j \rangle} \frac{K}{2} y_{i,j}^2 + \sum_{\langle i,j \rangle} \frac{p_i^2}{2M}$$

where $\langle i,j \rangle$ denotes summing over nearest neighbor sites i and j . For the electronic part, the operator $C_{j,s}(C_{j,s}^\dagger)$ creates (annihilates) a π -electron with spin s at the i th site. $t_{ij} = \exp[-i\gamma A(t)\delta](t_0 - \alpha y_{ij})$ is the hopping integral, where δ denotes the hopping of a π -electron between neighboring sites with no field present in an evenly spaced lattice, α is the e-ph coupling constant, and y_{ij} is the relative displacement coordinate between neighboring sites. The electric field $E(t)$, which was turned on adiabatically according to reference¹³ in order to avoid numerical errors, is included in our model by means of the time-dependent vector potential $A(t)$ through a Peierls substitution of the phase factor to the hopping integral. This is the simplest way of implementing electric fields consistently with periodic boundary conditions. $\gamma \equiv ea/(\hbar c)$, with a being the lattice parameter, e the absolute value of the electronic charge, and c the speed of light.

The lattice backbone dynamics is treated with a classical approach by means of a Newtonian equation $M\ddot{u}_n = F_n(t)$. Here, $F_n(t)$ represents the force experienced by a particular carbon atom n . The force expression is analogous to that originally developed by Silva and co-workers¹³. Moreover, this equation can be numerically integrated according to the methodology described in reference¹³. The electron dynamics is obtained by solving the Schrödinger equation (TDSE). The wave functions are constructed by means of a linear combination of instantaneous eigenstates. Thus, the solutions of the TDSE can be expressed as

$$\psi_{k,i}(t + dt) = \sum_l \left[\sum_m \phi_{l,m}^*(t) \psi_{k,m}(t) \right] \times \exp(-i\varepsilon_l dt/\hbar) \phi_{l,i}(t)$$

in which $\{\phi_{l,i}(t)\}$ and $\{\varepsilon_l\}$ are the eigenfunctions and the eigenvalues of the Hamiltonian at a given time t , respectively. In this work, we have adopted the following values for the constants, $t_0 = 2.7$ eV and $K = 57$ eV/Å². The e-ph coupling α is in the range from 3.5 to 10 eV/Å, which according to the literature corresponds to suitable values for GNRs. This range for α is in very good agreement with values obtained in experimental studies for graphene^{8,10,12}, which are 6.0 eV/Å, if the e-ph coupling mechanisms other than the bond stretching can be neglected. Moreover, the energy band gaps obtained in our study are also in agreement with the band gap energies for GNRs obtained through electronic structure calculations.

Results and Discussions

As a starting point of our investigations, we have studied the behavior of the band gap value as a function of the e-ph constant and the GNR width. The results presented in Figure 1 are in very good agreement with earlier studies, which justifies the method used in this work. In the following, we restrict our studies of the features of the polarons to the parameter space that gives finite band gaps. In particular, from the two possible families of GNR widths, that is, $2p$ and $2p+1$, we limit the discussion here to the $2p$ family ($n = 4, 6, 8, \text{ and } 10$) because the band gap of the $2p+1$ family is essentially zero and no polaron solution is possible.

We now turn to results concerning the polaron dynamics in GNRs. Figure 2 shows the actual path of a polaron through an armchair GNR with width $n = 4$ and with periodic boundary conditions. The e-ph coupling constant is set to 5.0 eV/Å, and the external electric field is 1.0 mV/Å, applied in the direction along the nanoribbon. It is important to note that the hexagonal grid presented in the figure is a mere representation of the GNR structure. Therefore, one should take the charge disposition over bondless regions of the ribbon as a qualitative pattern. Two interesting properties stand out in the polarons

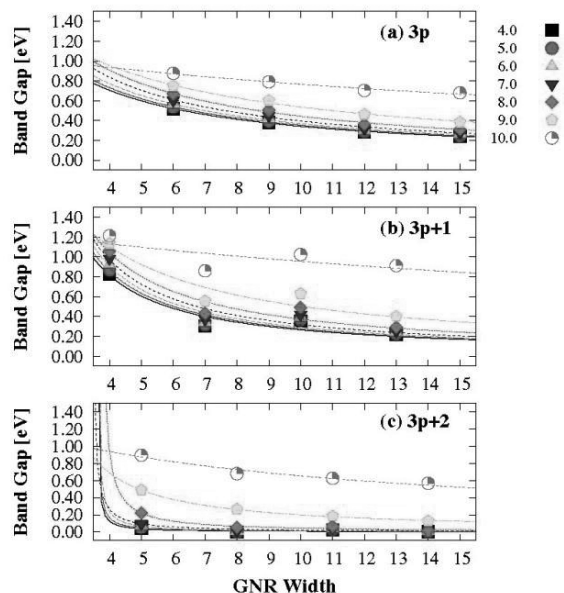


Figure 1. Different band gap regimes as a function of the GNR widths for several different electron–phonon coupling strengths considering the (a) $3p$, (b) $3p+1$, and (c) $3p+2$ families.

dynamics of Figure 4. First is the delay in the polaron response to the applied electric field, and second is the difference between the initial and the steady-state extension of the polaron. Naturally, these two features are connected and have to do with the aforementioned two-fold role the electric field plays in polaron dynamics for GNRs. The electric field initially plays the role of assisting the charge localization in order to create a stable polaron; it is only after this task is accomplished that the collective behavior is fully manifested as the movement through the lattice. Therefore, we can conclude that the applied electric field favors the polaronic charge density profile presented in Figure 2.

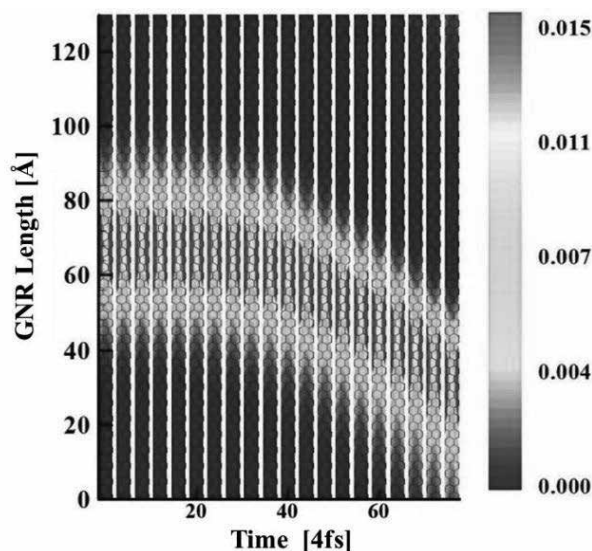


Figure 2. Polaron dynamics in an $n = 4$ width armchair nanoribbon subjected to an electric field of $1.0 \text{ mV}/\text{\AA}$.

Conclusions

In summary, we have performed a systematic numerical study on the polaron dynamics in armchair GNRs by means of a two-dimensional tight-binding model with lattice relaxation. By comparing different GNR widths, we could determine the critical conditions for a polaron transport to take place. Moreover, our methodology was able to accurately predict the band gap dependence on the width of the GNRs as well as their values. A careful investigation on the velocity regimes of

polarons was also performed. We observed that electric fields favor the occurrence of supersonic polarons.

Acknowledgments

The authors are grateful for the support given from the FAPEG, FAPDF, CAPES, CNPQ, and FINATEC.

References

1. Novoselov, K. S.; Geim, A. K.; Morozov, S. V.; Jiang, D.; Zhang, Y.; Dubonos, S. V.; Grigorieva, I. V.; Firsov, A. A. Electric Field Effect in Atomically Thin Carbon Films. *Science* **2004**, 306, 666–669.
2. Stankovich, S.; Dikin, D. A.; Dommett, G. H. B.; Kohlhaas, K. M.; Zimney, E. J.; Stach, E. A.; Piner, R. D.; Nguyen, S. T.; Ruoff, R. S. Graphene-Based.
3. Composite Materials. *Nat. Lett.* **2006**, 442, 282–286. Geim, A. K.; Novoselov, K. S. The Rise of Graphene. *Nat. Mater.* **2007**, 6, 183–191.
4. Li, X.; Wang, X.; Zhang, L.; Lee, S.; Dai, H. Chemically Derived, Ultrasoft Graphene Nanoribbon Semiconductors. *Science* **2008**, 319, 1229–1231.
5. Yip, H.-L.; Jen, A. K. Y. Recent Advances in Solutions-Processed Materials for Efficient and Stable Polymer Solar Cells. *Energy Environ. Sci.* **2012**, 5, 5994–6011.
6. Pumera, M. Graphene-Based Nanomaterials for Energy Storage. *Energy Environ. Sci.* **2011**, 4, 668–674.
7. Son, Y. W.; Cohen, M. L.; Louie, S. G. Half-Metallic Graphene Nanoribbons. *Nat. Lett.* **2006**, 444, 347–342.
8. Baringhaus, J.; Ruan, M.; Edler, F.; Tejada, A.; Sicot, M.; Taleb-Ibrahimi, A.; Li, A.-P.; Jiang, Z.; Conrad, E. H.; Berger, C.; et al. Exceptional Ballistic Transport in Epitaxial Graphene Nanoribbons. *Nat. Lett.* **2014**, 506, 349–354.
9. Mak, K. F.; Lui, C. H.; Shan, J.; Heinz, T. F. Observation of an Electric-Field-Induced Band Gap in Bilayer Graphene by Infrared Spectroscopy. *Phys. Rev. Lett.* **2009**, 102, 256405–256409.
10. Han, M. Y.; Brant, J. C.; Kim, P. Electron Transport in Disordered Graphene Nanoribbons. *Phys. Rev. Lett.* **2010**, 104, 056801–056805.
11. Martins, T. B.; Miwa, R. H.; da Silva, A. J. R.; Fazzio, A. Electronic and Transport Properties of Boron-Doped Graphene Nanoribbons. *Phys. Rev. Lett.* **2007**, 98, 196803–196807.
12. Han, M. Y.; Ozyilmaz, B.; Zhang, Y.; Kim, P. Energy Band-Gap Engineering of Graphene Nanoribbons. *Phys. Rev. Lett.* **2007**, 98, 206805–206809.
13. Su, W. P.; Schrieffer, J. R.; Heeger, A. J. Solitons in Polyacetylene. *Phys. Rev. Lett.* **1979**, 42, 1698–1701.

14. Oliveira Neto, P. H.; Teixeira, J. F.; da Cunha, W. F.; Gargano, R.; e Silva, G. M. Electron–Lattice Coupling in Armchair Graphene Nanoribbons. *J. Phys. Chem. Lett.* **2012**, 3, 3039–3042.
-

Ana Virgínia Passos Abreu^a,
Luiz Antonio Ribeiro Junior^{a,b}
& Antonio Luciano de
Almeida Fonseca

^aInstitute of Physics, University of Brasília, 70.919-970, Brasília, Brazil

^bUniversity of Brasília, UnB Faculty Planaltina, 73.345-010, Brasília, Brazil

Parameterization Study of LRC Functional Applied to Optical Properties of Carotenoids

Andriele S. Prado, Luiz A. R. Júnior & Wiliam F. da Cunha

Introduction

Solar energy is considered the most promising renewable energy source to attend the increasing global demand in green energy applications^{1,2}. Nowadays, dye-sensitized solar cells (DSSCs), pioneering developed by Grätzel³⁻⁵, are recognized as excellent candidates to replace the current silicon-based photocell technology. Advantages such as relatively high light-harvesting efficiency, low cost, simple synthesis process, and large-scale production make the DSSCs attractive for both academic and industrial applications. The working principle of a DSSC involves the optical absorption and charge separation processes by the association of a sensitizer as a light-absorbing material with a wide band-gap semiconductor⁶. In this sense, the carotenoids (polyene-like molecules), which are natural pigments in plants and animals, can be employed as sensitizers by presenting interesting characteristics for photonics applications as, for example, ultrafast optical response^{7,8}. In order to improve the efficiency of DSSCs, the optoelectronic properties of dye molecules, such as the energy gap, should be carefully investigated. It is known that the energy gap of molecular systems calculated by solving the Kohn-Sham equation, with conventional Density

Functional Theory functional (DFT), is usually small compared to the gap values obtained experimentally. These errors indicate a clear failure of the approximated functional often used in DFT, and can often lead to misinterpretations regarding the optical properties of these systems. This work

proposes a new methodology for functional parameterization that includes longrange corrections, dedicated to the molecules of the main carotenoids present in the Buriti oil (see Figure 1). Such functional contains 100% of the exact Hartree-Fock exchange, a non-local operator extremely important for a realistic description of the Highest Occupied Molecular Orbital (HOMO) and Lowest Unoccupied Molecular Orbital (LUMO) energies and other properties of the excited state. The group of carotenoids investigated has high potential for application in organic photovoltaic devices and has been extensively explored both theoretically and experimentally.

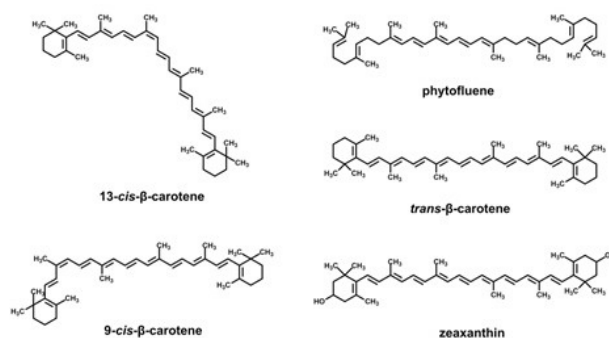


Figure 1. The carotenoid molecules investigated in this work. As a common trait, we can see that all molecules possess isoprene groups - that could act as an electron acceptor in an organic electronic device - and a backbone bridge - a possible donor.

Methods

In this work, we investigate the optoelectronic properties of a group of carotenoids derivatives contained in the Buriti oil (*Mauritia flexuosa* L.), which presents interesting optical properties for applications in optoelectronic devices based on organic materials. In order to do so, the DFT and Time Dependent DFT (TDDFT) approaches are used considering the functionals B3LYP, LC-BLYP and ω B97. The B3LYP functional is traditionally used in DFT calculations. However, it is well known that this functional causes the delocalization of the wave function. This is a huge challenge in the modeling of organic semiconductor materials, as localized quasiparticles are responsible for the charge transport mechanism in these systems. On the other hand, the LC-BLYP and ω B97 functionals already include a parameter for long-range corrections.

The central idea in the conception of these functionals is the separation of the Coulomb operator into two terms that take into account the short-range (SR) and long range (LR) interactions, considering the standard error function (erf):

$$\frac{1}{r} = \text{erf}\left(\frac{\omega r}{r}\right) + \text{erfc}\left(\frac{\omega r}{r}\right)$$

Thus the Hartree-Fock contribution of long-range, which is essential to maintain the correct description of the system, can be obtained completely. Moreover, the optimization of the correction parameter (ω) for long-range interactions can provide better results for excited state properties when compared to the usual approach.

Optical excitations in molecular dyes can be computed within the TDDFT formalism. Nevertheless, the use of conventional semi-local and standard hybrid DFT functionals (such as the popular B3LYP functional) can lead to poor descriptions of charge-transfer like excitations due to limitations associated with multi-electron selfinteraction errors. To overcome these limitations, we have used the functional LRC where the tuning of the range-separation parameter is based on gap fitting^{9,10}

$$J_{IP}(\omega) = \left| \varepsilon_H^\omega(N) + E_{gs}^\omega(N-1) - E_{gs}^\omega(N) \right|$$

$$J_{EA}(\omega) = \left| \varepsilon_H^\omega(N+1) + E_{gs}^\omega(N) - E_{gs}^\omega(N+1) \right|$$

$$J_{gap}(\omega) = J_{IP}(\omega) + J_{EA}(\omega) \quad ,$$

where $\varepsilon_H^\omega(N)$ is the HOMO energy for the Nelectron system and $E_{gs}^\omega(N)$ is the corresponding ground state energy. The ω optimization through these equations can lead to an improvement of the description of the properties calculated using LRC functionals. For each system, with its optimized geometry, and for each functional, the ω value that minimized J_{gap} is chosen as the optimum value. All excited states are evaluated at TDDFT level using functional LC-BLYP and ω B97 (with both default and tuned ω values) as well as with B3LYP and basis set 6-31G(d,p). Optical absorption spectra were simulated through convolution of the vertical transitions (characterized by a given wavelength and oscillator strength) with Gaussian functions with a full width at half-maximum (FWHM) of 30nm. All calculations were performed with Gaussian 09 (Rev.D.01) software.

Results and Discussion

In this study, we performed a theoretical investigation concerning the properties of the five main carotenoids present in Buriti oil, namely 13- cis- β -carotene, 9-cis- β -carotene, phytofluene, trans- β -carotene and zeaxanthin. The main goal of our work consists in evaluating whether this specific tuning for each system provides better qualitative results than the usual approach. The optimization procedure of the five structures was initially done with the B3LYP functional and the basis set 6-31G (d,p). The carbon atoms are moved until they are in a situation of equilibrium in which the total energy is minimized.

The optimization of the geometry was performed by establishing some important considerations, such as the molecules are in gas phase and in the ground state. The new positions of the atoms are then the primary source of information that we have used as parameters for subsequent calculations. A complete investigation of the optimized geometrical parameters, including the angles was also performed.

After perform a pre-optimization with the usual B3LYP functional and the 6-31G (d,p) basis set, we begin the search for the optimal longrange parameter ω . The ω minimization procedure was performed systematically and iteratively. Our aim was to clarify the requirement for a parameter that is totally dependent on the system. The adjustment procedure is classified as ab-initio, since the results are obtained through the own calculations, without any reference to other computations or experimental results. The ω parameter is chosen initially as imposed by the Koopman's theorem, i. e., the first ionization energy should be equal to $-\epsilon_{\text{HOMO}}$. Thus, we conducted a survey of the curves of the ionization potential and electron affinity making single point calculations of molecules in its neutral state and the corresponding cation and anion. Figure 2 present the curves for the functional LC-BLYP considering the molecule 13-cis- β -carotene. As a result, the optimized values for ω , considering each system with functional LC-BLYP and ω B97, are presented in the following table. We realized that the optimal values of the parameter ω for both functional are very close, with the exception of phytofluene. The value found for this molecule deviates significantly from the others. The evolution of the ω parameter suggests that the characteristic length ($1/\omega$) depends directly on the chemical nature, structure and system size.

The main goal of the present work, however, is to investigate the absorption spectra of the carotenoids. Since it is known that the number of conjugated bonds as well as the end groups influence on the absorption spectra of carotenoids. We expect a large deviation of the phytofluene peak from that of the other molecules.

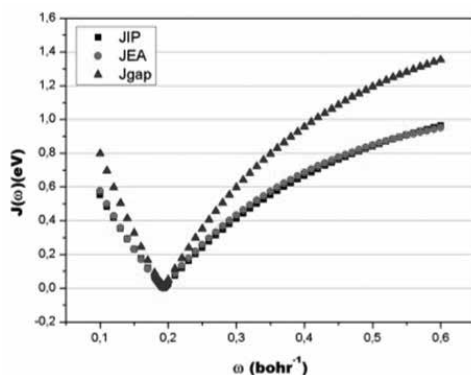


Figure 2. Curves J_{IP} , J_{EA} , and J_{gap} obtained by the optimization process.

Table 1. Optimized ω values for both functionals for the five carotenoids.

Molecule	tuned LC-BLYP	tuned ω B97
13-cis- β -carotene	0.152	0.150
9-cis- β -carotene	0.152	0.150
phytofluene	0.193	0.187
trans- β -carotene	0.151	0.149
zeaxanthin	0.149	0.147

Figure 3 presents a comparison of the absorption spectra for the five molecules at the B3LYP/6-31G(d,p) level of theory (up) together with the results obtained with the tuned LC-BLYP/6-31G(d,p) (down). For sake of succinctness, we omitted the tuned ω B97 spectra, as the results were similar to those shown in figure 3 for the LC-BLYP functional. One important feature of this work is to improve the description of the absorption spectra, with respect to the experimental result, when compared to what was obtained using the B3LYP. We can observe the red shift of the tuned spectra when compared to the regular B3LYP. Indeed, the general trend is to obtain the main peaks nearer to the experimentally expected, i.e., associated to smaller wave-length.

While for the functional optimized LC-BLYP, the wavelength difference obtained for trans- β -carotene compared to the experimental was 68 nm, not optimized for this functional difference reaches 99 nm, which is very significant. The amount of wavelength closest to the experimental value was calculated for phytofluene with the functional optimized LC-BLYP where we obtained a difference of only 8 nm, against 57 nm obtained via LC-BLYP with the default value of β to this functional. In all the cases the accordance between the values obtained through our methodology was better than 87% against 72% of the standard technique. At this point we should emphasize that the success of the results presented so far is not due to the mere use of some ω parameter. Rather, it is the very specific tuning of this parameter for each molecule, which allows this methodology to achieve such improvement as far as experimental accordance is considered. This can be confirmed by the use of the standard values of the ω parameter for the used orbitals. Therefore, it is clear that the long-range ω correction parameter tuning technique is a crucial procedure to

obtain the excited state properties more accurately. The methodology, in fact, was superior in the description of the properties of the studied systems.

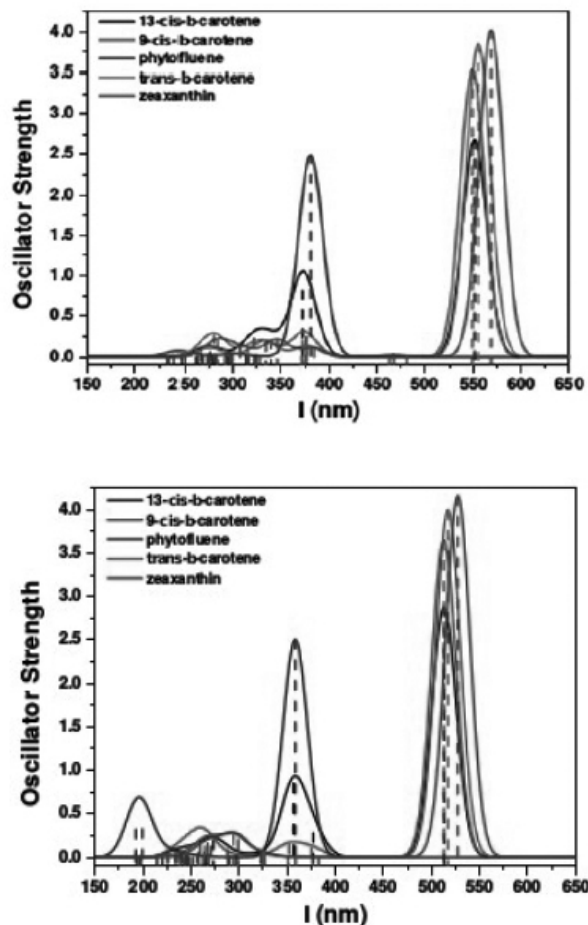


Figure 3. Absorption spectra for the five molecules computed at B3LYP (up) and LCBLYP (down).

Conclusions

In summary, we have demonstrated the importance of using a systematic way of refinement for determining the optimal ω parameter. The procedure is necessary because as there is no single ω value that is ideally universal, optimization gives us a natural way to find a parameter that is dependent on the system, maintaining a correct

balance between the exchange and the correlation.

The method to provide a more localized description and, consequently, better donor-acceptor character of low band gap copolymers optical reference, shows that the optical and electronic properties of systems covered here are in good agreement with the which is experimentally expected. It was observed that ω parameter to be sensitive to the system under consideration. The ω a optimized values generally decrease with increasing chain length, whatever the nature of the functional. As the electronic delocalization increases with system size, it is necessary that the exact exchange has lower weight; thus we have an ω optimally adjusted should exceed a fixed amount. Here, it was found that the values of ω parameter have total dependence on the degree of system combination.

Finally, we can state that here explored approach offers a much more accurate alternative to evaluate electronic and optical properties of such a system, since the use of conventional hybrid functional underestimate the orbital energies and the calculations with functional including long range, using the default values for each functional ω lead to an overestimation of the orbital energies.

Acknowledgments

The authors are grateful for the support given from the FAPEG, FAPDF, CAPES, CNPQ, and FINATEC.

References

- 1B. C. Thompson, J. M. J. Frechet, *Angew. Chemie Inter.* 47, 58, (2008).
- 2S. Gunes, H. Neugebauer, N. S. Sariciftci. *Chem. Rev.* 107,1324, (2007).
- 3M. Gratzel. *J. Photochem. Photobio. C.* 4, 255, (2003).
- 4M. Gratzel. *Inorg. Chem.* 44, 6841, (2005).
- 5A. Hagfeldt, M. Gratzel. *Acc. Chem. Res.* 33, 269, (2000).
- 6A. Hagfeldt, G. Boschloo, L. Sun, L. Kloo, H. Pettersson. *Chem. Rev.* 110, 6595, (2010).
- 7A. J. Heeger, D. Moses, M. Sinclair. *Shynt. Metals* 15, 95, (1986).
- 8D. Polli, G. Cerullo, G. Lanzani, S. de Silvestri, K. Yanagi, H. Hashimoto, R. J. Cogdell. *Phys. Rev. Lett.* 93, 163002, (2004).
- 9 L. Kronik, T. Stein, S. Rafaely-Abramson, R. Baer, *J. Chem. Theory Comput.* 8(5), 1515, (2012).

10. N. Kuritz, T. Stein, R. Baer, L. Kronik, J.Chem.
 11. Theory Comput, 7(8), 2408, (2011).
-

Andriele da Silva Prado^a, Luiz
Antônio Ribeiro Júnior^{a,b} &
Wiliam Ferreira da Cunha^a

^aInstitute of Physics, University of Brasília, 70.919-970, Brasília, Brazil

^b University of Brasília, UnB Faculty of Planaltina, 73.345-010, Brasília, Brazil

Theoretical Characterization of the Resonance-Energy Transfer Between Organic Molecules

Demétrio A. S. Filho

Introduction

One of the most interesting processes that occur in organic materials is the resonance-energy transfer. This process can be useful to further enhance the efficiency of devices based on organic molecules. Here we will investigate theoretically the resonance-energy transfer (RET) process between a para-hexaphenyl (p6P) unit and a α -sexithiophene (6T) unit.

Methods

Theoretical calculations using Density Functional Theory (DFT) and its Time-Dependent approach (TDDFT) were also carried out in order to obtain equilibrium energies, geometries and frequencies for both ground (S_0) and first excited (S_1) states of p6P and 6T. These properties allow us to better understand the mechanisms behind the absorption and emission processes involved in the isolated molecules and to build a qualitative model to understand the energy transfer in the p6P/6T complex.

Geometries, frontier orbitals and total energies of ground state (S_0) and first excited state (S_1) of p6P and 6T were obtained using DFT. We make use of two different DFT functionals: i) the M06-2X functional, [1,2] which has proven to properly describe the spectroscopic properties of these type of systems[2,3] and ii) the CAM-B3YP functional, that has a good track record in the description of the electronic processes in organic molecules.[4,5]

The 6-31G(d) basis set was used for all calculations presented here. This basis set was chosen due to the relative large size of the systems under investigation in addition to the successful reproduction of the absorption and emission data of short oligomers.[5,6] All simulations were carried out using the Gaussian'09 program suite.[7]

Results and Discussion

Figure 1 shows the ground state (S_0) HOMO (highest occupied molecular orbital) and LUMO (lowest unoccupied molecular orbitals) wavefunction for both p6P and 6T.

In solid state, both p6P and 6T are observed to be linear and planar molecules, in both ground and excited states. Thus, in order to better compare the experimental results with our calculations, we also optimized p6P and 6T subjected to the constraint of being planar, and evaluated the impact of this constraint in the $S_0 \rightarrow S_1$ transition energy, which is also included in Figure 1b.

The impact of planarization is larger on p6P than on 6T, as expected from the larger deviation from planarity presented by the former oligomer. A comparison between the HOMO-LUMO gap of the two planar structures shows that p6P has still a larger gap compared to 6T, but the difference between the two has reduced from 1.39 eV, in the twisted form, to 0.46 eV in the planar (solid-state like) form.

The results for M06-2X shows a similar trend, although the mismatches between the gap of p6P and 6T were computed to be 1.37 eV and 0.837 eV, respectively.

This small difference (on the order of tenths of eV) in the HOMO-LUMO gap and the fact that p6P has a larger gap compared to 6T already suggests that p6P can absorb a higher energy photon and transfer this energy to 6T, as it was observed for other thiophene-based systems.

To further characterize this energy transfer, a simulation of the vibronic resolved absorption spectrum of 6T together with the counterpart emission spectrum of p6P must be carried out.

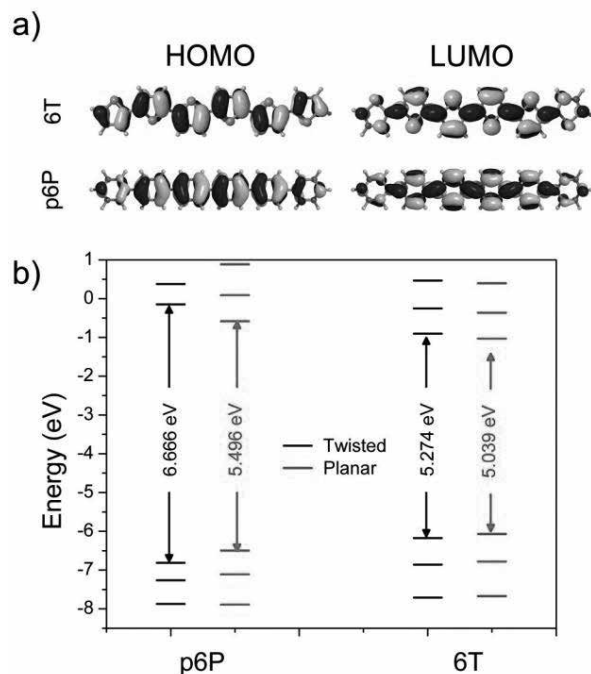


Figure 1. a) 6T (top) and p6P (bottom) ground state HOMO (left) and LUMO (right) wavefunctions. (b) CAM-B3LYP ground state (S0) frontier orbital energies and HOMO-LUMO gap for p6P (left) and 6T (right). Both fully optimized (twisted) and optimized under the planarity constraint (planar) are presented.

Conclusions

Theoretical calculations in the framework of Density Functional Theory were used to characterize the potential energy surfaces of the ground (S0) and first excited (S1) states of p6P and 6T. By a comparison between the energy gap related to the emission of p6P and the absorption of 6T from their lowest vibronic state, we determined a mismatch of 0.2 eV of the order of the vibrational relaxation energy of the molecules, resulting in a high

probability for resonance-energy transfer between the two molecules.

Acknowledgments

D. A. S. Filho gratefully acknowledges the financial support from the Brazilian Research Councils: CAPES, CNPq (grant 306968/2013-4) and FAP-DF (Fundação de Apoio à Pesquisa do Distrito Federal).

References

1. Zhao, Y.; Truhlar, D. G. The M06 Suite of Density Functionals for Main Group Thermochemistry, Thermochemical Kinetics, Noncovalent Interactions, Excited States, and Transition Elements: Two New Functionals and Systematic Testing of Four M06-Class Functionals and 12 Other Function. *Theor. Chem. Acc.* **2008**, 120, 215–241.
2. Zhao, Y.; Truhlar, D. G. The M06 Suite of Density Functionals for Main Group Thermochemistry, Thermochemical Kinetics, Noncovalent Interactions, Excited States, and Transition Elements: Two New Functionals and Systematic Testing of Four M06-Class Functionals and 12 Other Function. *Theor. Chem. Acc.* **2008**, 119, 525.
3. Lumpi, D.; Horkel, E.; Plasser, F.; Lischka, H.; Fröhlich, J. Synthesis, Spectroscopy, and Computational Analysis of Photoluminescent Bis(aminophenyl)-Substituted Thiophene Derivatives. *ChemPhysChem* **2013**, 14, 1016–1024.
4. Charaf-Eddin, A.; Planchat, A.; Mennucci, B.; Adamo, C.; Jacquemin, D. Choosing a Functional for Computing Absorption and Fluorescence Band Shapes with TD-DFT. *J. Chem. Theory Comput.* **2013**, 9, 2749–2760.
5. Jacquemin, D.; Planchat, A.; Adamo, C.; Mennucci, B. TD-DFT Assessment of Functionals for Optical 0-0 Transitions in Solvated Dyes. *J. Chem. Theory Comput.* **2012**, 8, 2359–2372.
6. Da Silva Filho, D. A.; Friedlein, R.; Coropceanu, V.; Ohrwall, G.; Osikowicz, W.; Suess, C.; Sorensen, S. L.; Svensson, S.; Salaneck, W. R.; Brédas, J.-L. Vibronic Coupling in the Ground and Excited States of the Naphthalene Cation. *Chem. Commun. (Camb.)* **2004**, 1702–1703.
7. Frisch, M. J.; Trucks, G. W.; Schlegel, H. B.; Scuseria, G. E.; Robb, M. A.; Cheeseman, J. R.; Scalmani, G.; Barone, V.; Mennucci, B.; Petersson, G. A.; et al. Gaussian 09, Revision A.02, 2009S. W.Benson and O. Dobis, *J. Phys. Chem. A*, 102, 5175, (1998).

Demétrio A. S. Filho

Institute of Physics, University of Brasília, 04455, DF, 70919-970, Brazil

Evaluation of the Best Theoretic Approach DFT Based for Indirect Spin-Spin Coupling Constants of 3-Ishwarone

Eduardo da Conceição & Mauro B. de Amorim

Introduction

The indirect spin-spin coupling constants (SSCC) along with chemical shifts are the most important parameters given by NMR spectroscopy.¹ In this work the study focus is the calculation of indirect nuclear spin-spin coupling constants with originates in the interactions with the surrounding electrons and does not disappear in isotropic media.²

The SSCCs are very sensitive to any variation in molecular geometric structure and provides information about the arrangement and the connectivity of atoms in a molecule.³ The use of DFT based calculations are an efficient approach in the description of indirect SSCCs for various molecular models of in organic chemistry. Given at same time accuracy and lower computational costs.^{2,4}

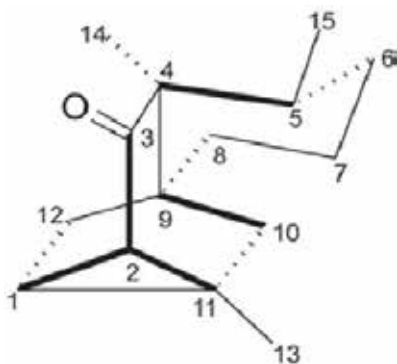


Figure 1. 3-ishwarone.

Methods

In this work we calculated the SSCCs for the molecular model of a sesquiterpene, the 3- ishwarone (Figure 1), using the Gaussian 09 package for optimization at the theoretical level B3LYP/6-31G(d,p). For the calculations of SSCCs it were used three different functionals: B3LYP, B972 and mPW1PW91 5 combined with the basis set: 6-31G, 6-31G(d,p), cc-pVTZ, cc-PCVTZ and basis sets specifically designed for coupling constants calculation: aug-cc-pVTZ-J, pcJ-2 and ccJ-pVTZ.^{6,7,8} The calculated results were compared with experimental data.

Results and Discussion

The results obtained in different theoretical levels demonstrated reproduce satisfactorily the experimental data, MAD and RMSD values (Figure 2) show acceptable calculated values. In the study model, the increased level of theory was not a great advantage leading to large increases in computation time without leading to significant improvements in the accuracy, like showed in other previous studies.⁹

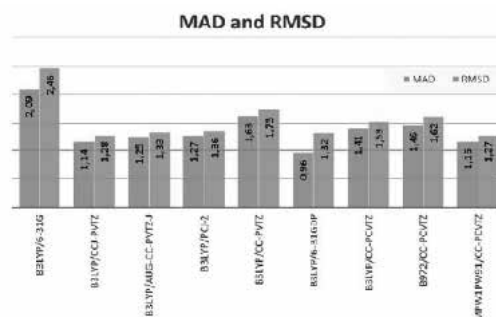


Figure 2. MAD and RMSD values.

Calculated values of geminal couplings: $^2J_{H10aH10b}$ e $^2J_{H12aH12b}$ (Figure 3) showed similar behavior with all the different levels of theory used. The basis set cc-pCVTZ and cc-pVTZ gave lower values than the experimental values. And upper values with 6-31-G, 6-31G(d,p) and specifically designed basis sets for coupling constants calculation.

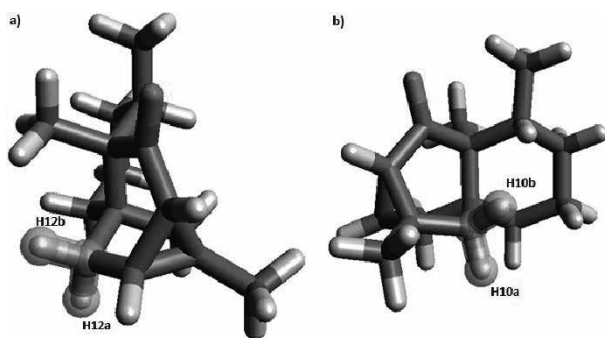


Figure 3. Geminal coupling protons: a) $^2J_{H12aH12b}$ and b) $^2J_{H10aH10b}$.

The calculated values for vicinal couplings: $^3J_{H1H2}$ e $^3J_{H1H12b}$ (Figure 4) although underestimate the experimental values were those who had lower standard deviation.

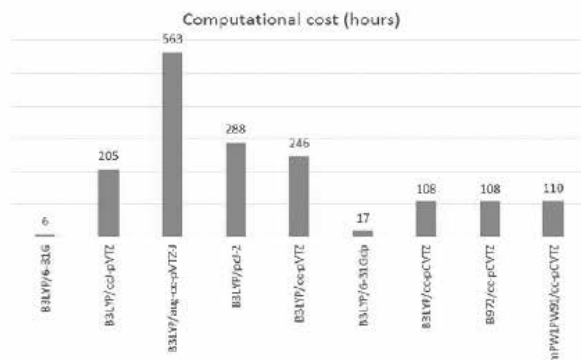


Figure 4 - Computational cost in hours.

Another important point is to know the contribution of each Ramsey's terms, which varies depending on the model under study. In the case of 3-isowarone the fermi contact (FC) is the main contributor, suggesting that a precise determination of the FC is essential for reliable results. Tables 1 and 2 are shown the values of each term for vicinal ($^3J_{H1H2}$) and geminal ($^2J_{H10aH10b}$) couplings.

Table 1 – Absolute values of total and separate contributions to indirect spin-spin coupling (in Hz) for the vicinal coupling ($^3J_{H1H2}$).

Coupling	Theory level	Total	FC	SD	PSO	DSO
$^3J_{H1H2}$	B3LYP/6-31G	7,73	7,35	0,15	0,18	0,41
	B3LYP/cc-pVTZ	8,30	8,10	0,14	0,33	0,39
	B3LYP/aug-cc-pVTZ-J	8,41	8,22	0,14	0,35	0,39
	B3LYP/pcl-2	8,30	8,12	0,15	0,35	0,39
	B3LYP/cc-pVTZ	6,70	6,40	0,15	0,26	0,41
	B3LYP/6-31Gdp	7,31	6,96	0,14	0,19	0,40
	B3LYP/cc-pCVTZ	8,81	8,41	0,18	0,60	0,82
	B972/cc-pCVTZ	8,06	7,67	0,17	0,61	0,83
	mPW1PW91/cc-pCVTZ	8,80	8,39	0,18	0,61	0,83

Table 2 – Absolute values of total and separate contributions to indirect spin-spin coupling (in Hz) for the geminal coupling ($^2J_{H10aH10b}$).

Coupling	Theory level	Total	FC	SD	PSO	DSO
$^2J_{H10aH10b}$	B3LYP/6-31G	16,20	16,30	0,52	0,39	0,81
	B3LYP/cc-pVTZ	12,96	13,73	0,44	1,33	1,01
	B3LYP/aug-cc-pVTZ-J	13,31	13,96	0,41	1,23	0,99
	B3LYP/pcl-2	13,46	14,22	0,41	1,35	1,01
	B3LYP/cc-pVTZ	10,59	11,20	0,41	1,21	1,01
	B3LYP/6-31Gdp	13,17	13,51	0,32	0,97	0,96
	B3LYP/cc-pCVTZ	10,65	11,29	0,39	1,00	0,75
	B972/cc-pCVTZ	10,64	11,27	0,39	0,98	0,73
	mPW1PW91/cc-pCVTZ	11,56	12,21	0,41	0,96	0,71

Acknowledgments

The authors are grateful for the support given from the CAPES.

References

1. J. San Fabian, J. M. García de la Vega, E. San Fabian, J. Chem. Theory Comput. 10, 4938-4949, (2014).
2. T. Helgaker et al. Prog. in NMR Spec., 53, 249- 268 (2008).
3. L. J. Smith. J. Mol. Biol., 255, 494-506 (1996)
4. R. Rittner et al. Chem. Phys. Let., 454, 129-132 (2008).
5. T. Kupka et al. J. Phys. Chem. A, 116, 3728- 3738 (2012).
6. S. P. A. Sauer et al. Theor. Chem. Acc. 100, 275- 284 (1998).
7. F. Jensen. Theor. Chem. Acc. 126, 371 (2009).
8. U. Benedikt, A. A. Auer, F. Jensen. J. Chem. Phys. 129, 064111 (2008).
9. M. Alipour. RSC Adv. 5, 4737-4746 (2015).

Eduardo da Conceição^{a,*} & Mauro Barbosa de Amorim^b

^a, ^bWalter Mors institute of Research on Natural Products (IPPN), Federal University of Rio de Janeiro (UFRJ)

*E-mail: eduardodcon@gmail.com

H₂O₂ + Ng Excited Electronic State Description

Luciano Almeida Leal, Jonathan Teixeira, Luiz Fernando Roncaratti, Geraldo Magela e Silva, Ricardo Gargano

Introduction

Hydrogen peroxide (H₂O₂) plays an important role in several chemical and physical processes, evidenced in astronomy, medicine, and chemical reactions. Due its importance and diversity of applications, this molecule has been subject of several studies^{1,2}. Recently, our research group has developed an analytical interpretation of noble-gases influence on hydrogen peroxide by means of a potential energy surface that involves angular and radial coordinates of noble gases. The Improved Lennard Jones (ILJ) analytical form², widely applied in this kind of systems, was used in order to represent the Van der Waals interaction of noble gas and O-H bound. In this work, we present the H₂O₂-Ng (with Ng=He,Ne, Ar, and Kr) potential energy curves (PEC) in the excited electronic states. Furthermore, these new PEC are exploited to describe the dynamical properties (rovibrational energies and spectroscopic constants) of the H₂O₂-Ng systems.

Methods and Discussion

It is large known that the study of excited states is not an easy task. It request a long computational simulation time and depending on electrons quantity it may be not viable. Considering this facts, it becomes crucial cost-benefits considerations. By these assumptions, we considered H₂O₂ + He, H₂O₂ + Ne, H₂O₂ + Ar, H₂O₂ + Kr on equilibrium geometries given by Table below (geometrical definition are shown in Figure 1).

Ng	$\alpha = \alpha_{eq}$	θ_1	θ_2
He	0°	30°	217°
Ne	0°	32°	215°
Ar	0°	38°	209°
Kr	0°	47°	200°

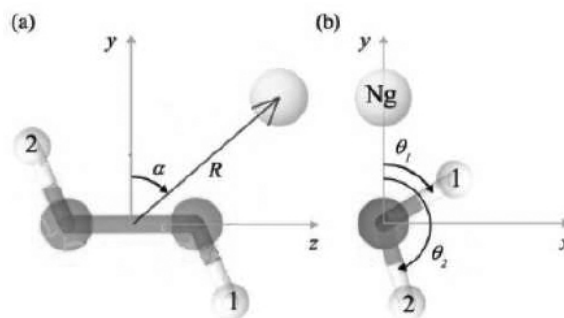


Figure 1: H₂O₂-Ng geometrical representation. (a) R is the distance from noble-gas and center of O-O bond. (b) θ_1 and θ_2 are the angles between O-H bond and y axis.

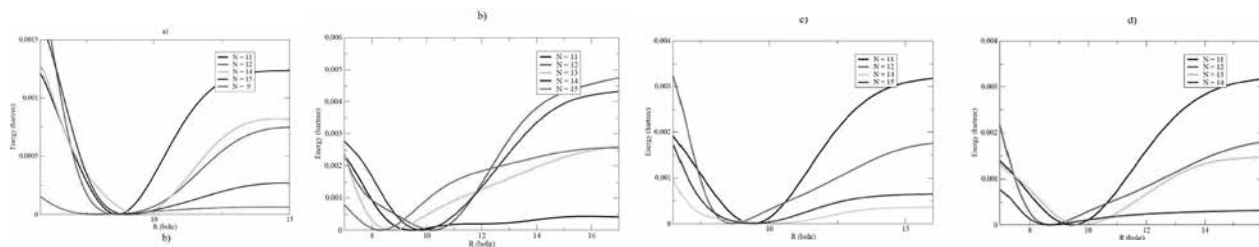


Figure 2: Potential Energy Curves of (a) $\text{H}_2\text{O}_2 + \text{Ne}$, (b) $\text{H}_2\text{O}_2 + \text{Kr}$, (c) $\text{H}_2\text{O}_2 + \text{He}$, (d) $\text{H}_2\text{O}_2 + \text{Ar}$ systems for different excited states ($n = 9, 15$).

For all complexes, we calculated the electronic energies as a function of R (from 3\AA to 10\AA , with 0.2\AA of step) considering 15 excited states. All these calculations were performed using the TDDFT method (implemented in the NWChem code³), with the cam-qtP-00 functional and the aug-cc-pVTZ basis set. These excited electronic energies were adjusted by generalized rydberg functions, as shown in Figure 2. Then, these analytical PEC were used to determine the rovibrational energies and spectroscopic constants. for all studied systems. These properties were calculated by two different methods: Solving the nuclear Schrodinger's equation (by Discrete Variable Representation 4) and Dunham⁵ method. The results obtained through Dunham and DVR methodologies are in an excellent agreement. This fact demonstrates the reliability of our study.

Conclusions

In this work, we have presented a study of the interaction among the H_2O_2 molecule with noble gases (He, Ne, Ar, and Kr) on the excited electronic states. Analytical PEC, ro-vibrational energies and spectroscopic constants were determined considering fifteen electronic states for each system. These kind of results represent the main novelty of this work, since they are presented for first time in the literature.

Acknowledgments

The authors are grateful for the support given by the CNPq, and SEE-DF.

1. L.F. Roncaratti, L. A. Leal, F. Pirani, V. Aquilanti, G.M. e Silva, R. Gargano, *The Journal of Chemical Physics*, 141, 134309, (2014);
2. F. Pirani, S. Brizi, L. F. Roncaratti, P. Casavecchia, D. Cappelletti, and F. Vecchiocattivi, *Phys. Chem. Chem. Phys.* 10, 5489 (2008);
3. M. Valiev, E.J. Bylaska, N. Govind, K. Kowalski, T.P. Straatsma, H.J.J. van Dam, D. Wang, J. Nieplocha, E. Apra, T.L. Windus, W.A. de Jong, "NWChem: a comprehensive and scalable open-source solution for large scale molecular simulations" *Comput. Phys. Commun.* 181, 1477 (2010);
4. Whitnell RM, Light JC (1932) Symmetry-adapted discrete variable representations. *The Journal of chemical physics* 89(6):376-385;
5. J. L. Dunham, *Physical Review* 41, 721 (1931).

Luciano Almeida Leal,
Jonathan Teixeira, Luiz
Fernando Roncaratti,
Geraldo Magela & Silva,
Ricardo Gargano

Institute of Physics, University of Brasília, Brazil

Cálculo do Fator de Debye-Waller na Níquel-Fluorohectorita por EXAFS

Matheus N. Jácome & Luciano Ribeiro

Introdução

Nenhum outro material foi e continua a ser tão importante para a história da humanidade como a argila, devido as suas propriedades: de plasticidade, ou seja, grande maleabilidade, afinidade pela água e aderência a certas superfícies. Estas e outras características das argilas podem ser explicadas e compreendidas pelo conhecimento de sua composição química, estrutura e propriedades moleculares.

A hectorita é uma argila mineral muito usado na atualidade, é possível encontrá-la em esmaltes cerâmicos, colas e adesivos, produtos de limpeza doméstica e entre outros. A fluorohectorita é um tipo de hectorita, uma argila mineral sintetizada quimicamente, possui fórmula química, pela semi-cela unitária, como $M_x - (Mg_{3-x}Li_x)Si_4O_{10}F_2$, onde, M se refere ao cátion entremeado por camadas e x é a proporção dos átomos de lítio.

A Figura 1 mostra sua distribuição espacial e sua estrutura molecular formada pelos tetraedros e octaedros, com o cátion o níquel entremeado entre duas camadas.

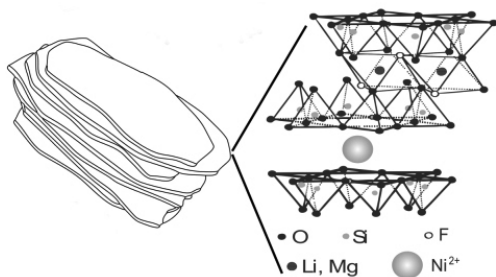


Figura 1. A distribuição espacial de uma níquel-fluorohectorita (Ni-FHT).

O fator de Debye-Waller (DW), também chamado de fator de temperatura, é um termo utilizado para descrever a atenuação do espalhamento de raios X causado pela vibração térmica. Quando se trata da estrutura fina de absorção de raios X (EXAFS), o fator de Debye-Waller está relacionado com as flutuações quadráticas médias das distâncias interatômicas entre os átomos. Para obter o fator DW esse trabalho analisou dados de EXAFS realizados no LNLS, Campinas –SP, na amostra Ni-FHT em função da temperatura e umidade relativa.

Métodos

O fator de temperatura é possível ser obtido através do método da razão ¹, que é uma técnica muito usada na literatura. Ela traz informações sobre o termo que representa a agitação térmica do sistema na equação de EXAFS². A técnica usa por meio de uma relação entre os sinais de EXAFS de duas temperaturas diferentes para fornecer o fator Debye-Waller relativo a uma dessas temperaturas.

Recentemente foi publicado um artigo onde os autores obtiveram o fator Debye-Waller da argila sintética Ni-FHT. Os valores apresentados possuíam uma dependência crescente com a temperatura da argila³. Por outro lado, essa informação, se faz necessária no momento, para corroborar com a possibilidade de que as reduções das intensidades dos picos nas transformadas de Fourier das oscilações de EXAFS (ver Fig.2) seja realizada pela mudança do fator de Debye-Waller devido as mudanças de temperatura e umidades na amostra.

Resultados e Discussões

A partir da transformada inversa de Fourier no intervalo de $\Delta R = 1,2 - 2,2 \text{ \AA}$, da Fig. 2, foi selecionada a primeira esfera de coordenação níquel – oxigênio.

Por meio do método da razão o comportamento da curva $\ln[x(20^\circ \text{C})/X(T)]$ versus K^2 foi obtido. A Fig. 3 descreve as curvas obtidas e estas se mostraram ser aproximadamente linear na região estudada para todas as temperaturas.

Para a obtenção da Fig. 3, a temperatura 20°C foi usada como referência.

Para a transformada de Fourier inversa foi usado o intervalo de $\Delta R = 1,0 - 2,4 \text{ \AA}$, nas oscilações de EXAFS da Fig. 2.

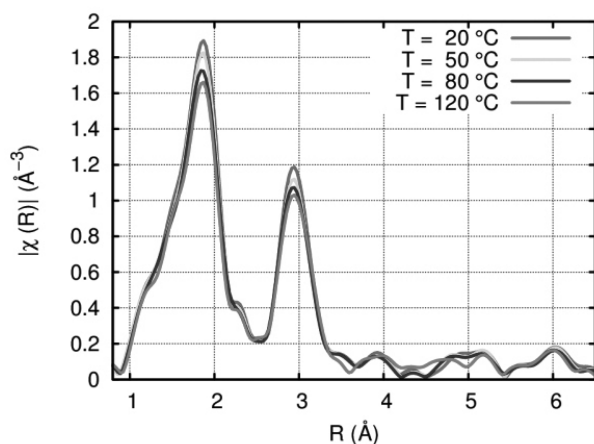


Figura 2. Transformada de Fourier das oscilações de EXAFS, para a Ni-FHT em função da temperatura.

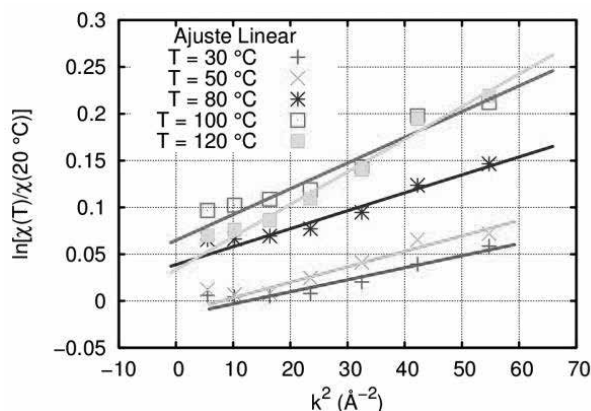


Figura 3. A figura apresenta o comportamento esperado $\ln[x(20^\circ \text{C})/X(T)]$ no intervalo de $\Delta k^2 = 5,5 - 55 \text{ \AA}^{-2}$.

A Fig. 4 ilustra comportamento do fator de Debye-Waller em função da temperatura, encontrado através do coeficiente linear da reta, obtidas em cada uma das temperaturas da Fig. 3.

Cada ponto, presente na Fig. 4 representa o valor do coeficiente linear das retas ajustadas na Fig. 3.

Conclusões

OS resultados do método da razão, Fig. 3 mostrou que o comportamento obtido para a curva versus está aproximadamente linear na região estudada, como era esperado para este método^{1,4,5}. Figura 4 – O gráfico apresenta o fator de Debye-Waller relativo à temperatura de 20°C versus o intervalos de temperatura da Fig. 3. Em termo da Fig. 4 ilustrou o comportamento do fator de Debye-Waller relativo a temperatura de 20°C , encontrado através do coeficiente linear da reta de cada temperatura na Fig. 3. O gráfico confirmou o aumento da desordem diante da elevação da temperatura.

Agradecimentos

Os autores agradecem ao apoio financeiro da CAPES, pela bolsa de iniciação científica, a FAPEG pelos recursos concedidos para a apresentação desse trabalho e a UEG pela estrutura de trabalho.

Referências

1. E.A. Stern, D.E. Sayers, and F.W. Lytle, Phys. Rev. B 11, 4836 (1975).
2. J.J. Rehr and R.C. Albers, Rev. Mod. Phys. 72, 621 (2000).
3. L. Michels, L. Ribeiro, M.S.P. Mundim, M.H. Sousa, R. Droppa, J.O. Fossom, G.J. da Silva, and K.C. Mundim, Appl. Clay Sci. 96, 60 (2014).
4. S.M. Heald and E.A. Stern, Phys. Rev. B 17, 4069 (1978).
5. R.B. Gregor and F.W. Lytle, Phys. Rev. B 20, 4902 (1979).

Matheus Norberto Jácome & Luciano Ribeiro*

Câmpus de Ciências Exatas e Tecnológicas - Henrique Santillo – Universidade Estadual de Goiás, CP 459, Anápolis, GO, Brasil

*E-mail: lribeiro@ueg.br

Theoretical Study of Thermodynamic Properties of Liquid Methyl Tert-Butyl Ether (MTBE) Using Ab Initio Calculations and Monte Carlo Simulation

Luciene B. Silva & Luiz C. G. Freitas

Introduction

Fuel oxygenates are special types of organic compounds blended with gasoline to improve its quality. These compounds raise the oxygen content of gasoline which enhances the combustion process. As a result, the harmful vehicular emissions are reduced.^{1a} MTBE is an ether wherein the oxygen atom is bonded to two alkyl groups (Figure 1). The particular geometry around the oxygen atom and the nature of the C—O bond make MTBE a polar molecule.^{1,2} The polarity leads to a high water solubility that combined to MTBE's high vapor pressure and its widespread use in the fuels, causes additional pollution of the urban storm water, the groundwater and the surface water.³

Thus in spite of the air quality benefits, there are concerns with the use of MTBE. A growing number of studies have detected MTBE in ground water. In some instances, these contaminated waters are sources of drinking water. Low levels of MTBE can make drinking water supplies undrinkable due to its offensive taste and odor.^{1b} There are opportunities for MTBE to leak into the environment and potentially get in drinking water sources wherever gasoline is stored. There are also opportunities for it to be spilled whenever fuel is transported or transferred. Contamination of drinking water sources can occur from leaking underground and above ground fuel storage tanks, pipelines, refueling spills, automobile accidents damaging the fuel tank, consumer disposal of old gasoline, emissions from older marine engines and

to a lesser degree, storm water runoff, and precipitation mixed with MTBE in the air.^{1c}

Several studies have been performed in order to provide developments in technologies for MTBE removal from water.⁴ The gas phase structures and properties of MTBE have been calculated using a variety of ab initio methods.⁵ The structure and energetics of neutral, ionized and protonated MTBE clusters were investigated by vacuum ultraviolet photoionization and ab initio investigations.⁶ Nevertheless, in spite of the great interest in MTBE, the nature and extension of its molecular properties in the condensed phase remain unclear.

Computer simulations methods such as Monte Carlo (MC) are suitable tools for investigations of liquid properties from an atomic level.^{7,8} This methodology provides a direct link between the microscopic details of the system and its macroscopic properties. A key component in simulations is the quality of the force field used to describe the molecular interactions.⁹ Starting from geometries and electrostatic potentials obtained using quantum chemistry methods, force fields for liquid simulations are usually optimized to reproduce experimental pure liquid properties, such as density and heat of vaporization at a given temperature. Typically, intermolecular interactions in force fields are represented by effective pair potentials consisting of Lennard-Jones and Coulomb terms.⁷ Standard Lennard-Jones parameters are available for all common functional groups found in organic liquid. The starting parameters can be further

optimized to reproduce experimental properties of the liquid phase. The assignment of the partial charges used to describe the coulombic potential is critical in force field development. An approach that has been pursued is to fit the charges to reproduce electronic properties, such as dipole moment and electrostatic potentials.¹⁰ The most common alternative in liquid simulation has focused on partial charges from fitting to the electrostatic potential surface (EPS) using ab initio calculations.¹¹

The present work presents an investigation of the thermodynamic properties of liquid MTBE using Monte Carlo simulation technique. For this purpose a force field has been developed in order to reproduce accurate results for available experimental pure liquid properties.

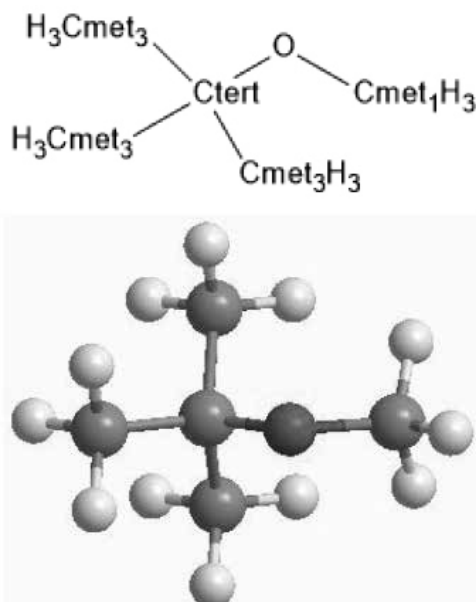


Figure 1: MTBE molecule

Computacional Details

Consistently with the usual procedure in liquid simulations,⁹ the MTBE monomer was described as a set of interaction sites distributed along of the molecular structure (Figure 1). Standard Lennard-Jones plus Coulomb potentials, as shown in Equation (1), were used to calculate the intermolecular interaction energy between two MTBE monomers.

$$E = E_{LJ} + E_{Coulomb} \quad (1)$$

Where:

$$E_{LJ} = \sum_{i < j} 4\epsilon_{ij} \left[\left(\frac{\sigma_{ij}}{r_{ij}} \right)^{12} - \left(\frac{\sigma_{ij}}{r_{ij}} \right)^6 \right]$$

$$E_{Coulomb} = \sum_{i < j} \frac{q_i q_j}{r_{ij}}$$

The parametrization of the force field for liquid MTBE was performed as follows: (i) The geometry of the MTBE molecule was obtained using the BP86 functional and Def-Bas6 basis set implemented in the ORCA quantum chemistry program;¹² (ii) Point charges for each site of the MTBE molecule were calculated using the same functional and basis set above and the CHELPG procedure¹¹ in ORCA program; (iii) The Lennard-Jones parameters were empirically optimized from a series of liquid phase simulations in the NPT ensemble at the temperature of 298K and pressure of 1 atm; (iv) The geometric parameters of the MTBE monomers were considered rigid through the optimization process.

Monte Carlo simulations using the Metropolis algorithm⁷ were performed with the DIADORIM program.¹³ An initial box containing 500 MTBE monomers was generated and periodic boundary conditions were applied through the simulations.

Results and Discussion

Table 1 presents the optimized Lennard-Jones parameters and charges for the MTBE liquid simulations. The sites are named according to Figure 1.

Table 1: Lennard-Jones parameters and charges for MTBE simulations

Site	$\sigma / \text{\AA}$	$\epsilon / \text{kcal mol}^{-1}$	q
O	2.929	0.1260	-0.48818
Ctert	3.535	0.0594	1.05161
Cmet1	3.535	0.0594	-0.14319
Cmet3	3.535	0.0594	-0.55700
H	2.525	0.027	0.10423

Using the parameters set listed in Table 1, the simulations yielded the thermodynamic properties shown in Table 2. The results were obtained with the MC method in the isotherm-isobaric ensemble with T=298 K and p=1.0 atm, with 0.202 x 10⁸ configurations for averaging.

Table 2: Heats of vaporization, ΔH_{vap} , density, expansibilities (α) and compressibilities (κ) for MTBE liquid simulation

	This work
$\Delta H_{\text{vap}} / \text{kcal mol}^{-1}$	6.739 +/- (0.005) ^a
Density / g cm ⁻³	0.703 +/- (0.002) ^b
$\alpha / 10^{-5} \text{ deg}^{-1}$	17.741 +/- (8)
$\kappa / 10^{-6} \text{ atm}^{-1}$	20.30 +/- (2)

Conclusion

Monte Carlo simulations have been used to investigate thermodynamic properties of liquid MTBE. For this purpose, a force field has been developed. An approach of combining charges from fitting to the EPS using the CHELPG procedure and Lennard-Jones parameters empirically optimized provided a proper reproduction of the experimental heat of vaporization and density of the MTBE pure liquid. The force field achieved in this work suggests further studies including the structural characterization of the condensed phase liquid.

Acknowledgments

The authors acknowledge financial support from FAPESP, CNPq and CAPES.

References

1. The U.S. Environmental Protection Agency. (a) MTBE in Fuels. Available from: <http://www.epa.gov/mtbe/gas.htm>; (b) Concerns about MTBE. Available from: <http://www.epa.gov/mtbe/water.htm#concerns>; (c) Occurrence. Available from: <http://www.epa.gov/mtbe/water.htm#occurrence>. 2012. [2013].
2. R. D. Suenram, F. J. Lovas, W. Pereyra, G. T. Fraser and A. R. H. Walker, J. Mol. Spectrosc. 181, 167 (1997).
3. O. C. Braids, Environ. Forensics, 2, 189 (2001).
4. I. Levchuk, A. Bhatnagar and M. Sillanpää, Science of the Total Environment, 415, 476 (2014).
5. L. N. Gregerson, J. S. Siegel and K. K. Baldrige, J. Phys. Chem. A, 104, 11106 (2000).
6. T. M. Di Palma and A. Bende, Chem. Phys. Letters, 18, 561 (2013).
7. M. P. Allen and D. J. Tildesley, Computer Simulations of Liquids, Clarendon Press, Oxford (1987).
8. A. R. Leach, Molecular Modelling: Principles and Applications, Pearson Education (2001).
9. (a) W. F. van Gunsteren and H. J. C. Berendsen, Angew. Chem. Int. Ed. Engl., 29, 992 (1990); (b) W. D. Cornell, P. Cieplak, C. I. Bayly, I. R. Gould, K. M. Merz Jr., D. M. Ferguson, D. C. Spellmeyer, T. Fox, J. W. Caldwell and P. A. Kollman, J. Am. Chem. Soc., 117, 5179 (1995); (c) W. L. Jorgensen, D. S. Maxwell and J. Tirado-Rives, J. Am. Chem. Soc., 118, 11225 (1996).
10. M.M. Francel and L. E. Chirlian, Ver. Comput. Chem., 1, 14 (2001).
11. (a) C. M. Breneman and K. B. Wiberg, J. Comp. Chem. 11, 361, (1990); (b) H. A. Carlson, T. B. Nguyen, M. Orozco and W. L. Jorgensen, J. Comp. Chem. 14, 1240 (1993).
12. F. Neese. The ORCA Program System, Wiley Interdiscip. Rev., Comput. Mol. Sci., 2, 73 (2012).
13. L. C. G. Freitas, J. Braz. Chem. Soc., 20, 1541–1548 (2009).
14. The U.S. Environmental Protection Agency. Available from: http://www.epa.gov/chemfact/s_mtbe.txt. 1994.

Luciene Borges Silva^a & Luiz Carlos Gomide Freitas^{b,*}

^a Departamento de Física, Química e Matemática, Universidade Federal de São Carlos, Campus de Sorocaba, Rod. João Lemes dos Santos, km 110, CEP 18052-780, Sorocaba, São Paulo, Brazil

^b Departamento de Química, Universidade Federal de São Carlos, Caixa Postal 676, CEP 13565-950, São Carlos, São Paulo, Brazil

*E-mail: luizcarlosgomidefreitas@gmail.com

Zn-doped BaTiO_3 Materials: A DFT Investigation for Optoelectronic and Ferroelectric Properties Improvement

Luis H. S. Lacerda, Renan A. P. Ribeiro, Ageo M. de Andrade & Sérgio R. de Lazaro

Introduction

Theoretical methods based on quantum mechanical simulations are an important tool to study material properties. Such methodologies are used for analyzing the electronic, optical, structural, pyro-, piezo- and ferroelectric properties of any materials. In case of crystalline semiconductor materials, these properties are highly dependent on chemical composition due to chemical bond character. Among the crystalline materials, the semiconductor materials stand out once are largely employed to develop electronic, optical devices, piezoelectric and memory devices because of its spontaneous polarization¹⁻¹². Then, the perovskite materials are an important group of materials since are the most abundant minerals in Earth.¹³ This material has ABX_3 stoichiometry since A is a mono or bivalent cation; B is tetra or pentavalent cation and X is a non-metallic element, in most cases oxygen. As well as the other semiconductor materials, the properties of perovskite materials are dependent of chemical bonds and symmetry of crystalline structure.

Among the perovskite materials, a most important is BaTiO_3 material (BTO). This material is a solid that can be found in five crystalline structures which differ according to central atom (Ti) in unit cell. The stability of each crystalline structure of BTO is dependent of temperature variation as showed in

Figure 1. At room temperature (298 K), the BTO has tetragonal structure. Such structure is characterized by Ti position out of symmetric center of unit cell resulting in properties, such as: optical, electronic, pyro-, piezo- and ferroelectric properties.¹⁴⁻¹⁶

In this work, the tetragonal phase was investigated. This material has a band gap of 3.30 eV and is employed to development of integrated circuits, energy storage device, temperature coefficient resistance thermistor, piezoelectric sensors, sensing and monitoring devices, thin films, optoelectronic devices, actuators and others.¹⁶⁻²¹

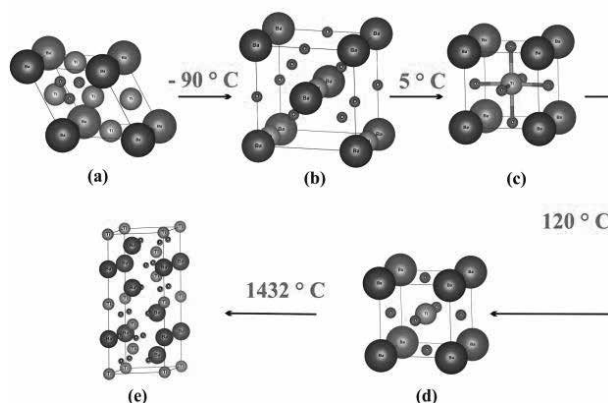


Figure 1. Crystalline Structures of barium titanate. a) Rhombohedra, b) Orthorhombic, c) Tetrahedral, d) Cubic and e) Hexagonal.

Although BTO is a not a recent discovery, such material still is largely studied in order to improve innumerable devices, once its properties can be improved through of doping process. This process consists in adding a controlled amount of impurities in semiconductor structure that changes drastically the properties of a semiconductor material without changing its crystalline structure and controlling their properties.^{22, 23} In case of BTO, the doping process is possible by substitution of Ba, Ti or O atoms.²⁴⁻²⁸ Among these substitutions, the replacement of Ba atoms for Zn atoms (BZTO) was not largely analyzed due to few works focused in this system. Such manuscripts evaluated only the structural, optical, electronic properties, the grain growth and photocatalysis application of Zn-doped BTO.^{24-26, 29, 30} Therefore, we propose a BZTO theoretical investigation based on DFT/B3LYP to evaluate the effects of Zn-doping in different amounts on BTO structural, electronic, optical and ferroelectric properties.

Methods

BTO material simulation was performed based on a tetragonal structure. This structure is composed by one Ba atom, one Ti atom and two O atoms arranged on P4mm (99) space group with lattice parameters $a = b = 3.98601 \text{ \AA}$, $c = 4.0259 \text{ \AA}$ and angles $\alpha = \beta = \gamma = 90^\circ$.¹⁶ The BZTO models was developed from unit cell expansion in the direction of axes a and b resulting at 25-100% doping (Table 1). For all models, the TZVP³¹ basis set was employed to describe the Ti, O and Zn atoms; whereas, the Ba atoms were described by Zagorac³² basis set employing the HAYWSC³³ pseudopotential.

Table 1. Description of the unit cells used for simulating the Zn-doping on BaTiO₃ material.

Doped amount (%)	Unit cell expansion	Ba atoms replaced
0	2x2x1	0
25	2x2x1	1
50	2x2x1	2
75	2x2x1	3
100	2x2x1	4

The calculation level applied was based on the Density Functional Theory (DFT) at set B3LYP hybrid functional^{34, 35}; SCF convergence was truncated in 10-8 Hartree and Mohnkhost-Pach³⁶ method defined as 8x8 using CRYSTAL09^{37, 38} software. Vibrational calculations were also performed using optimized results for all models to evaluation of thermodynamic stability at room temperature (298.5 K) and 1 atm. The theoretical results discussed in this manuscript are Density of States (DOS) Projections and Band Structure analysis. XCrysden^{39, 40} Software was used for structural analysis. Personal computer using Ubuntu Linux operational system made up by quad-core AMD processor with 32 GB of RAM and data storage capability of 3.5 TB was used in all simulations.

Results and Discussion

STRUCTURAL PROPERTIES

The evaluation of Zn influence on structural properties of BTO material (Table 2) was performed through lattice parameters, unit cell angles, tetragonality factor (c/a) and μ structural coefficient (Equation 1). Such results indicate that unit cell symmetry was not affected by Zn-doping. While Zn-doping amount increases, a , b and c lattice parameters decrease linearly (Figures 2). The linear variation of lattice parameters was evaluated based on Vegard's Law^{41, 42} that provides a linear relationship between lattice parameters and impurity amount. According to this empirical rule the linear variation of lattice parameters with dopant amount variation indicates an ideal behavior for solid solution. Then, the Zn insertion in the BTO structure is characterized by an ideal behaviour indicating the possible formation of solid solution. The stability of BZTO materials are better discussed in Thermodynamic Stability Evaluation Section. For 50 % model, the lattice parameter c are bigger than for BTO model due to the equal amount of Ba and Zn in crystalline structure which causes the perturbation through of replaced atoms distribution. However, the tetragonality index and μ values indicate that the tetragonal symmetry of unit cell is kept.

The lattice parameters are changed due to bond length decrease in crystalline structure, once for BTO model the average bond length for Ba – O and Ti – O are 2.865 Å

and 2.033 Å, respectively. As the Zn quantity increases, these values are reduced. Thus, for Zn-doped BTO at 100 % such bonds have average bond length of 2.685 Å and 1.928 Å, respectively. Although Ti – O bonds were changed, the μ coefficient structural evaluation indicates that the Ti position is slightly modified; therefore, it is expected the arising of ferroelectric and piezoelectric properties for BZTO materials are not smaller regarding to BTO.

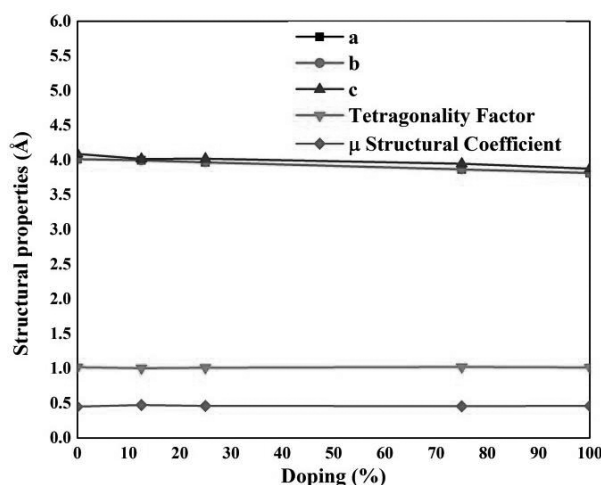


Figure 2. Variation of Lattice parameters (in Å), unit cell angles (in degrees), Tetragonal factor (a/c) and structural coefficient μ for BTO and BZTO models according to dopant amount.

ELECTRONIC PROPERTIES

The electronic properties of BTO and BZTO materials were evaluated through the projected Density of States (DOS) for analysing models, evaluated from last five energy bands of the Valence Band (VB) and the first five energy bands of the Conduction Band (CB) featuring the band gap region (E_g). For BTO model, the O atoms largely contribute to the composition on all VB and for lower energy levels of CB through 2s and 2p orbitals; whereas, Ti atoms have low contribution for VB through 3d and 3p orbitals and compose majority in CB through 3d orbitals. In turn, Ba atoms lightly contribute for VB through 5sp and 6sp orbitals; while, its 3d orbitals contributed for CB. The doping process has showed

low influence on O and Ba contributions in VB and CB. Nevertheless, the Ti contribution in CB was observed in a higher energy level than in BTO model. Zn contribution was made by 4s orbitals that has low contribution in VB and average contribution in CB. This insertion of Zn atoms shows a strong effect on the energy at the top of the VB in relation to the BTO material, causing degeneration of such energy levels, as well as reducing the contribution of the Ti atoms in CB.

OPTICAL PROPERTIES

The optical property of a solid is defined as the interaction between a solid and electromagnetic radiation. In case of semiconductor materials, the interaction only occurs with electromagnetic energy equal to or higher than $E_g^{22, 43}$. The optical property of BTO and BZTO material were evaluated through of E_g values (Table 3) showing that a decrease linearly with the Zn doping. Therefore, the presence of Zn atoms in the crystalline structure cause changes in the electronic structure from Zn orbitals insertion energy lower than Ti orbitals in the CB. The band gap change after doping process is large, once for BTO the characteristic wavelength is located on Ultraviolet-Visible (UV-Vis); whereas, for BZTO at 100 % the radiation characteristic is observed on Infrared region. As shown on Table 3, all the E_g are referred to an indirect excitation, except for 75 % model that present a direct excitation along the G symmetry points.

Table 3. Theoretical results calculated for indirect and direct band gaps (E_g in eV), wavelength (in nm), electromagnetic radiation range in relation to doping amount (in %).

Doping %	E_g (eV)	λ (nm)	Radiation
0	3.28 (M – G)	377.91	UV-Visible
25	2.89 (R – M)	429.33	Visible
50	2.21 (Λ – G)	561.40	Visible
75	1.62 (G – G)	764.53	Infrared
100	0.75 (A – G)	1656.50	Infrared

The Figure 3 shows the band-gap variation ΔE_g for BZTO models in relation to BTO indicating a linear decrease. Then, all BZTO models have band-gap below to of BTO material. Such variation is caused by displacement of bottom of CB to a lower energy level than in BTO material due to Zn orbitals contribution. Figure 4 shows the results for top of VB and bottom of CB energy levels for all models investigated. These results indicate that the VB level for Zn-doped models is slightly different of the energy level observed in BTO material. In order hand, the influence of Zn-doping process on CB energy level is strong, since the energy level is reduced largely.

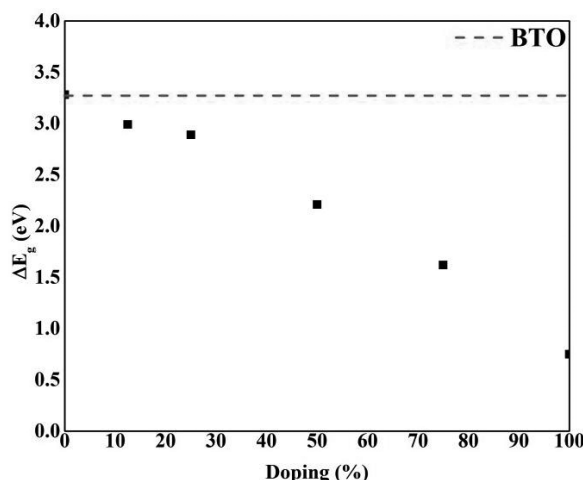


Figure 3. Theoretical results for BTO band gap according to Zn-dopant amount.

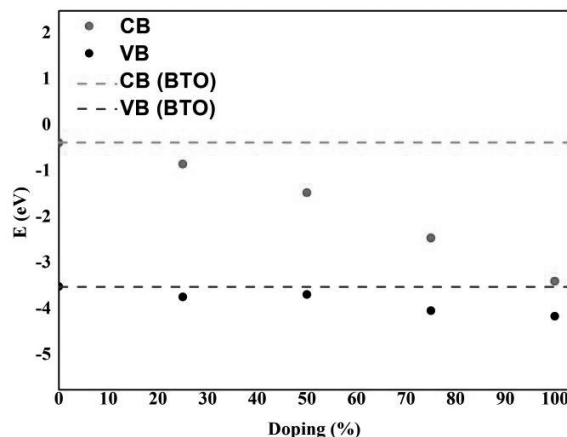


Figure 4. Energy levels calculated from DFT/B3LYP at the top of Valence Band (VB) and the bottom of Conduction Band (CB) according to Zn-doping amount.

FERROELECTRIC PROPERTIES

Nowadays, the perovskite-type materials have been largely applied in the development of ferroelectric memories and charge storage devices because of high values for polarizability and dielectric constants presented by these materials.⁴⁴⁻⁴⁹ In a ferroelectric material the direction of charge polarization can be reverted applying an external electrical field, which is very important to the charge storage property.

In general, the dielectric constant (ϵ) determines the charge storage capacity; whereas, the polarizability (α) describes how much a material is polarizable under an electrical field.⁴³ These measures were developed by solid state theory, in order to better understand the ferroelectric property of the materials and they are dependent on the tensor matrix, which is directed similarly to the Cartesian coordinates system. For BTO and BZTO materials, the ϵ and α amount were investigated based on components presented in Figure 5.

The ϵ and α results for BTO and BZTO models are shown in the Table 4 and indicate that doping process improves largely the ferroelectric property because theoretically there is an increase in all tensor matrix components in relation to BTO; except for BZTO at 100 % model, which shows a decrease for both ϵ and α regarding to pure material. Thus, the higher values for ϵ and α were observed to BZTO at 75 % doping. The increase observed in relation to Zn-doping, can be understood because the octahedron distortion in the crystalline structure that are responsible for the increase of the dielectric constants and polarizability. Another point is associated to the atoms random distribution in crystalline structure causing a lower symmetry in relation to BTO; consequently, the electronic density is randomly distributed providing ferroelectric and dielectric properties higher than those in the BTO.

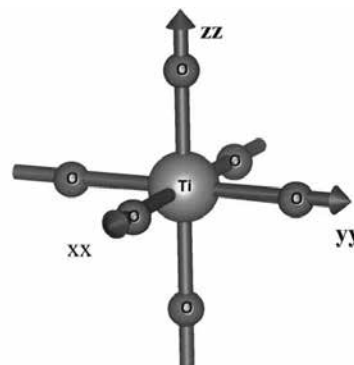


Figure 5. Octahedral sites for tetragonal-BTO and xx, yy and zz components used for calculating dielectric constants and polarizability.

Table 4. Polarizability (α) and dielectric constants (ϵ) for BTO and BZTO models.

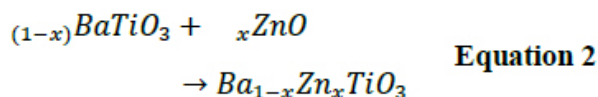
Dopagem (%)	α			ϵ		
	Componente			Componente		
	xx	yy	zz	xx	yy	zz
0	154,1379	-	6216,2654	5,3564		176,6886
25	320,0193	-	8975,2729	5,7011		66,9239
50	295,1744	298,6174	$301,6386 \cdot 10^5$	5,3724	5,4234	$223,41 \cdot 10^3$
75	333,3171	331,4823	$474,9845 \cdot 10^7$	6,2531	6,2241	$374,29 \cdot 10^5$
100	162,264	-	150,181	6,359		5,960

Table 5. Theoretical values for mixing Gibbs Free Energy variation (ΔG_{mix}) and Gibbs Free Energy variation in relation to pure BTO ($\Delta\Delta G$) for BZTO materials

Modelo (%)	ΔG (kJ.mol ⁻¹)	$\Delta\Delta G$ (kJ.mol ⁻¹)
0	0	0
25	-68.8969	-51.4552
50	-41.6027	-24.1609
100	0	-45.7471

THERMODYNAMIC STABILITY EVALUATION

According to Vegard's law, the structural results for BZTO models indicate that this solid solution shows an ideal character; then, it is expected that these materials can be obtained by experimental techniques, once the crystalline structure is linearly changed from dopant amount. In literature, BZTO materials were synthesized from 0 to 10 %. In manuscript of Caballero and coauthors³⁰ is not founded information of Zn solubility limit on BTO crystalline structure. Assuming that the Vegard's law prevision is not enough to determines the stability of BZTO materials, vibrational calculations were performed. Such vibrational calculations were based on DFT/B3LYP and we calculate the mixing Gibbs Free Energy (ΔG_{mix} – Equation 2) and Gibbs Free Energy in relation to BTO material ($\Delta\Delta G$ – Equation 3).



$$\Delta\Delta G = \Delta G_{mix} - \Delta G_{BTO} \quad \text{Equation 3}$$

The positive value for $\Delta\Delta G$ indicates that these models are not favorable thermodynamically to be obtained the crystalline structure; while, the negative values suggest a thermodynamically factor favorable obtained the crystalline structure. The thermodynamically stability results for BTO and BZTO are present on Table 5. For all BZTO models, the $\Delta\Delta G_{mix}$ results are negatives in relation to BTO suggesting that such models are stable at room conditions. Then, these results corroborate with structural results provided by Vegard's law discussed before and they strongly suggest that BZTO materials a viable alternative to development of electronic, optical and ferroelectric devices and they are expected to show excellent fluorescence properties.⁵⁰⁻⁵²

Conclusions

We used DFT with periodic model to evaluate the structure, electronic, optical and ferroelectric properties for Zn-doping in barium titanate. Electronic and optical properties showed that Zn-doping are potential alternatives to be employed in electronic and optical devices, once the band-gap decrease changes the profile wavelength to the visible and infrared range of electromagnetic spectrum. The band-gap variation is caused by Zn atoms influencing as Valence Band as Conduction Band of BaTiO₃ material. The ferroelectric property was evaluated for all models and presented that Zn atoms insertion is a good alternative to improve the ferroelectric properties of BaTiO₃ materials. The vibrational frequencies and structure results for BZTO materials indicates that all models investigated are stable at room condition.

Then, it is concluded that the Zn-doping on BaTiO₃ crystalline structure improves electronic, optical and ferroelectric properties and it is a potential alternative to application in ferroelectric devices employed in several electronic and optical devices, solar cells, and photocatalysis processes.

Acknowledgments

The authors acknowledge support from CNPq, CAPES and Fundação Araucária.

References

1. Z. J. Chew and L. Li, *Materials Letters*, 91, (2013).
2. C. Xun, L. Xiaomin, G. Xiangdong, L. Xinjun, Y. Chang, Y. Rui and J. Ping, *Journal of Physics D: Applied Physics*, 44, (2011).
3. M. K. Gupta, N. Sinha and B. Kumar, *Journal of Applied Physics*, 112, (2012).
4. F. Zhang, X. Li, X. Gao, L. Wu, F. Zhuge, Q. Wang, X. Liu, R. Yang and Y. He, *Solid State Communications*, 152, (2012).
5. S. Nedic, Y. Tea Chun, W.-K. Hong, D. Chu and M. Welland, *Applied Physics Letters*, 104, (2014).
6. M. K. Gupta and B. Kumar, *Journal of Materials Chemistry*, 21, (2011).
7. T. Qiuhong, W. Jinbin, Z. Xiangli, Z. Yichun, W. Qianjin, Z. Yi, X. Zhang and S. Huang, *Electron Devices, IEEE Transactions on*, 58, (2011).
8. J. I. Sohn, S. S. Choi, S. M. Morris, J. S. Bendall, H. J. Coles, W.-K. Hong, G. Jo, T. Lee and M. E. Welland, *Nano Letters*, 10, (2010).
9. S. Lee, H. Kim, D.-J. Yun, S.-W. Rhee and K. Yong, *Applied Physics Letters*, 95, (2009).
10. D. U. Lee, E. K. Kim, W.-J. Cho, Y.-H. Kim and H. Im, *Thin Solid Films*, 521, (2012).
11. J.-W. Zhao, F.-J. Liu, H.-Q. Huang, Z.-F. Hu and X.-Q. Zhang, *Chinese Physics B*, 21, (2012).
12. Y. H. Kang, J.-H. Choi, T. I. Lee, W. Lee and J.-M. Myoung, *Solid State Communications*, 151, (2011).
13. M. W. Davidson and G. E. Lofgren, *Journal of Geological Education*, 39, (1991).
14. P. Erhart and K. Albe, *Journal of Applied Physics*, 102, (2007).
15. M. Yashima, T. Hoshina, D. Ishimura, S. Kobayashi, W. Nakamura, T. Tsurumi and S. Wada, *Journal of Applied Physics*, 98, (2005).
16. R. A. Evarestov and A. V. Bandura, *Journal of Computational Chemistry*, 33, (2012).
17. P. Kumar, S. Singh, M. Spah, J. K. Juneja, C. Prakash and K. K. Raina, *Journal of Alloys and Compounds*, 489, (2010).
18. S.-H. Yao, J.-K. Yuan, P. Gonon, J. Bai, S. Pairis and A. Sylvestre, *Journal of Applied Physics*, 111, (2012).
19. Z.-X. Chen, Y. Chen and Y.-S. Jiang, *The Journal of Physical Chemistry B*, 105, (2001).
20. B. Wodecka-Dus and D. Czekaj, *Archives of Metallurgy and Materials*, 54, (2009).
21. J. A. Dawson, J. H. Harding, H. Chen and D. C. Sinclair, *Journal of Applied Physics*, 111, (2012).
22. H. L. Kwok, *Electronic Materials* (PWS Publishing Company, Boston, 1997).
23. A. R. West, *Basic solid state chemistry* (John Wiley & Sons, Chichester, 2006), 2 ed. edn.
24. A. Y. Fasasi, M. Maaza, E. G. Rohwer, D. Knoessen, C. Theron, A. Leitch and U. Buttner, *Thin Solid Films*, 516, (2008).
25. A. Y. Fasasi, M. Maaza, C. Theron, P. Neethling, U. Buttner, A. Leitch and A. K. Chaudhary, *Thin Solid Films*, 516, (2008).
26. J.-P. Zou, L.-Z. Zhang, S.-L. Luo, L.-H. Leng, X.-B. Luo, M.-J. Zhang, Y. Luo and G.-C. Guo, *International Journal of Hydrogen Energy*, 37, (2012).
27. H.-S. Kwon, H.-I. Yoo, C.-H. Kim and K.-H. Hur, *Journal of Applied Physics*, 107, (2010).
28. C. Tian, Z. Yue, Y. Zhou and L. Li, *Journal of Solid State Chemistry*, 197, (2013).
29. A. C. Caballero, J. F. Fernández, C. Moure and P. Durán, *Journal of the European Ceramic Society*, 17, (1997).
30. A. C. Caballero, J. F. Fernández, C. Moure, P. Durán and Y.-M. Chiang, *Journal of the American Ceramic Society*, 81, (1998).
31. M. F. Peintinger, D. V. Oliveira and T. Bredow, *J. Comput. Chem.*, 34, (2013).
32. D. Zagorac, K. Doll, J. C. Schön and M. Jansen, *Chemistry - A European Journal*, 18, (2012).
33. P. J. Hay and W. R. Wadt, *J. Chem. Phys.*, 82, (1985).
34. A. D. Becke, *J. Chem. Phys.*, 98, (1993).
35. A. D. Becke, *Phys. Rev. A*, 38, (1988).
36. C. Pisani, R. Dovesi and C. Roetti, *Hartree-Fock ab initio Treatment of Crystalline Systems*. (Springer Berlin Heidelberg, 1988), *Lecture Notes in Chemistry*, 48.
37. R. Dovesi, R. Orlando, B. Civalleri, C. Roetti, V. R. Saunders and C.-M. Zicovich-Wilson, *Zeitschrift für Kristallographie*, 220, (2005).
38. R. Dovesi, V. R. Saunders, C. Roetti, R. Orlando, C. M. Zicovich-Wilson, F. Pascale, B. Civalleri, K. Doll, N. M. Harrison, I. J. Bush, P. D'Arco and M. Llunell, *CRYSTAL09 User's Manual* (University of Torino, Torino, 2009).

39. A. Kokalj, J. Mol. Graphics Modell., 17, (1999).
40. A. Kokalj, Comput. Mater. Sci., 28, (2003).
41. A. R. Denton and N. W. Ashcroft, Phys. Rev. A, 43, (1991).
42. L. Vegard, Zeitschrift für Physik, 5, (1921).
43. L. E. Smart, Solid state chemistry: an introduction. (Taylor & Francis, Boca Raton, 2005), 3 ed. edn.
44. W. Wang, Q. Zhao, J. Xu and D. Yu, CrystEngComm, 14, (2012).
45. S. Cho, S. Kim, E. Oh, S.-H. Jung and K.-H. Lee, CrystEngComm, 11, (2009).
46. P. Chen, L. Gu and X. Cao, CrystEngComm, 12, (2010).
47. Y. Yang, J. Qi, W. Guo, Q. Liao and Y. Zhang, CrystEngComm, 12, (2010).
48. L. J. Brillson and Y. Lu, Journal of Applied Physics, 109, (2011).
49. Y. Lee, S. Lee, H. T. Ryu and D. Y. Kim, AIP Conference Proceedings, 1399, (2011).
50. J.-Z. Kong, A.-D. Li, H.-F. Zhai, H. Li, Q.-Y. Yan, J. Ma and D. Wu, Journal of Hazardous Materials, 171, (2009).
51. Z. Ali, S. Ali, I. Ahmad, I. Khan and H. A. Rahnamaye Aliabad, Physica B: Condensed Matter, 420, (2013).
52. Q.-J. Liu, N.-C. Zhang, F.-S. Liu, H.-Y. Wang and Z.-T. Liu, physica status solidi (b), 250, (2013).

Luis H. da S. Lacerda*,
Renan Augusto Pontes
Ribeiro, Ageo M. de Andrade
& Sérgio R. de Lazaro

Ponta Grossa State University, Department of Chemistry, PR

*E-mail: lhslacerda1@gmail.com

Polaron Dynamics in Organic Molecular Stacks

Luiz A. R. Júnior

Introduction

Organic semiconductors have emerged as ideal candidates for the design of optoelectronic devices such as photovoltaics¹ and light-emitting² diodes due to present important traits which are required for the development of new green energy solutions. The potential advantages in terms of low cost, flexibility, and low environmental impact make these materials attractive for the electronics industry. In order to increase the device performance, a better understanding at a molecular and even at the atomic scale of the charge transport properties is absolutely required^{3,4}. Particularly, the polaron stability and dynamics are of critical importance for the device performance.

The charge transport in organic materials can be classified in three different processes, considering the temperature dependence: the small polaron model, which is dominated by the nonadiabatic hopping process; the adiabatic (large) polaron model, and the band-like transport³. Organic molecular crystals and stacks, i. e., 2D and 1D systems, respectively, are particularly interesting in this context since they can, depending on preparation techniques and the choice of molecular constituents, exhibit different combinations of these processes.

Semiconducting molecular crystals are recognized to exhibit two types of electron–phonon couplings: the local intra-molecular (Holstein-type) and the non-local inter-molecular (Peierls-type)³. A considerable amount

of theoretical work, focused on understanding the charge transport processes in organic semiconductors, has been performed in the framework of the Holstein–Peierls model in the last few years^{5–9}. Nevertheless, studies that take into account different electronic and lattice parameters to characterize the polaron stability and dynamics for different kind of molecular stacks, are not available in the literature. Furthermore, the role played by the anisotropy in the polaron stability and dynamics (when more than one stack is considered) is not completely understood and requires a more detailed understanding.

In this work, a systematic numerical investigation of the influence of different electronic and lattice parameters on the polaron stability in organic molecular stacks is performed using a semi-empirical Holstein–Peierls model. The approach takes into account both intra- and inter-molecular electron–lattice interactions to describe also the polaron dynamics in the system. These investigations are performed in one-dimensional systems (molecular stacks) by varying relations between the transfer integral (electronic parameter), force constant and the electron-phonon coupling (lattice parameters). The systems investigated here are designed to resemble single stacks in molecular semiconductors such as pentacene, anthracene, or rubrene. An Ehrenfest Molecular Dynamics approach is performed by using a one-dimensional tight-binding model including lattice relaxation. Temperature effects are included by means of a canonical Langevin equation. The aim of this work is to give a physical picture of the polaron stability and

transport in organic molecular stacks contributing to the understanding of these important processes that may provide guidance to improve the charge transport in organic optoelectronic devices.

Methods

In our model, each molecule is represented by a site with index i having two degrees of freedom where v_i^x is the site displacements involved in the antisymmetric non-local vibrational modes and is the single internal phonon mode coupled to the electronic system through of the local e-ph coupling, according as represented in Figure 1. In this way, the combined Holstein-Peierls Hamiltonian is described as $H_{HP} = H_{elec} + H_{latt}$ and can

$$H_{elec} = \sum_i \alpha_1 u_i \hat{c}_i^\dagger \hat{c}_i + \sum_i (J_{i+1,i} \hat{c}_i^\dagger \hat{c}_{i+1} + h.c.)$$

assumes the following form for the first part (electronic Hamiltonian): where $J_{i+1,i}$ is the inter-molecular transfer integral between two neighboring sites and is defined as

$$J_{i+1,i} = J_0 - [\alpha_2^x (v_{i+1}^x - v_i^x)] e^{-i\gamma \Lambda_x(t)}.$$

The operator \hat{c}_i^\dagger (\hat{c}_i) creates (annihilates) a carrier at the i -th lattice site; J_0 is the transfer integral for a pristine lattice; $v = \frac{m}{m_0}$ with e being the absolute value of the electronic charge, c is the speed of light, and a is the lattice constant; α_1 and α_2^x are the e-ph coupling constants for intra-molecular and inter-molecular, and vibrations, respectively. The electric field is assumed to be static and included in the model by means of the time dependent potential vector $\Lambda_x(t) = -cE_x$.

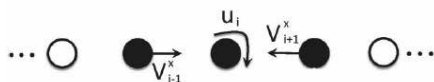


Figure 1. Schematic representation of the one-dimensional Holstein-Peierls System

The last part in is H_{HP} the Hamiltonian of the lattice backbone ($H_{latt} = H_{latt,1} + H_{latt,2}$) which is described by the two separate harmonic oscillators, considering the intra- and inter-molecular modes:

$$H_{latt,1} = \frac{K_1}{2} \sum_i (u_i)^2 + \frac{M_1}{2} \sum_i (\dot{u}_i)^2$$

and

$$H_{latt,2} = \frac{K_2}{2} \sum_i (v_{i+1}^x - v_i^x)^2 + \frac{M_2}{2} \sum_i (\dot{v}_i^x)^2$$

where the force constants and the masses and refer to the intra- and inter- molecular oscillators, respectively. Here, we have used the following values for the above-mentioned parameters: $J_0, \alpha_1, \alpha_2^x, K^1$ and K_2 varying in the range [35-100] meV, [0.5-2.0] eV/Å, [0.5-2.0] eV/Å, [5-10] eV/Å, [1.0-5] eV/Å, respectively, $M_1 = 1.3 \times 10^9$ e² V(as/Å)² M² = 2.6 × 10¹⁰ eV(as/Å)², and $a = 3.5$ Å³⁻⁹. The dynamical simulations are carried out using a particular set of parameters depending on the kind of molecular stack.

The electronic dynamics is performed by means of the time-dependent Schrödinger equation. By introducing instantaneous eigenstates, the solution at each instant of time can be expressed in the form where $\phi_l(m)$ and ϵ_l are the eigenfunctions and eigenvalues

$$\psi(n, t + \Delta t) = \sum_l \left[\sum_m \phi_l^*(m) \psi(m, t) \right] \times e^{-\frac{i\epsilon_l \Delta t}{\hbar}} \phi_l(n)$$

of H_{elec} at time t , respectively. The equations of motion for the lattice backbone are given by the newtonian equations for the intra-molecular displacement and for the antisymmetric inter-molecular vibrations similarly to reported in references^{4,5}.

Results and Discussion

We have mentioned above that our model considers two degrees of freedom. The distortions related to the polaron show a negative value for the intra-site displacements, which denotes a compression of the molecules due to the excess of charge. On the other hand, the inter-molecular distortions show a contraction (negative values) for the two neighboring inter-molecular displacements of the central molecule, where the polaron is initially localized, as represented in Figure 1. These contractions are followed by elongations (positive values) in the displacements of the other molecules. These elongations decrease with increasing numbers of molecules, in order to keep the constraint of fixed total displacements. The lattice geometry of the system is optimized using the resilient backpropagation, RPROP, algorithm. For the charge distribution presented by the optimized geometry, the polaron is localized initially at three molecules with its main contribution residing on a central molecule.

With this geometry configuration and charge localization in mind, we now turn to simulations for the polaron dynamics in a system which resembles a pentacene stack (just to present an overview about the results in this abstract). Figure 2 depicts the results for the polaron dynamics in a one-dimensional system (a molecular stack) consisting of 20 sites. The calculations are carried out considering an adiabatic approximation in which the wavefunction of the charge is assumed to be a single eigenstate (the lowest LUMO) of the total Hamiltonian. In other words, the charge associated with the polaron remains in the same state during transport process and only this state changes its position with time.

After the electric field is applied, it takes a while (about 250fs) for the charge to start moving but then it moves with a constant velocity of about 25 Å/ps. This velocity can be calculated from the molecular charge density (panel (a)) by counting the number of the sites that has been travelled during the simulation time. Beside the charge density, the intra-molecular displacements (u_i) (panel (b)) and intermolecular bond lengths, ($v_{i+1}^x - v_i^x$) (panel (c)) are also demonstrated.

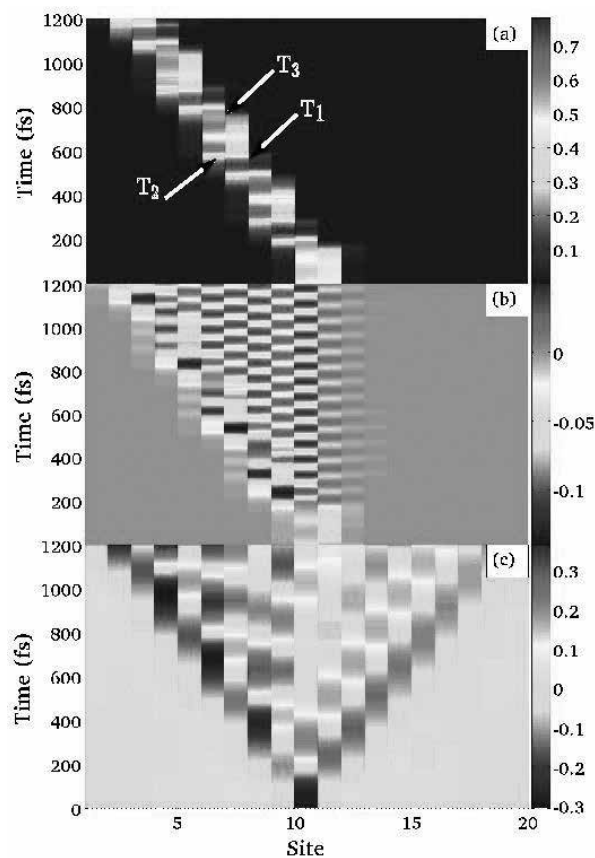


Figure 2. Polaron dynamics in a one-dimensional system (molecular stack): (a) molecular charge distribution, (b) intra-molecular displacement, and (c) inter-molecular bond length for $= 1.5 \text{ eV/\AA}$, $= 10.0 \text{ eV/}$, $= 0.5 \text{ eV/\AA}$, $= 1.5 \text{ eV/}$, $= 50 \text{ meV}$ and $= 2.0 \text{ mV/\AA}$.

Inspite of intra-molecular vibrations, inter-molecular distances, Figure 2(c), form traveling waves in the system which move with approximately the same velocity in the opposite direction of the polaron motion. In summary, when the polaron is situated on site i , the bond length between sites $i-1$ and i (in this case where the polaron moves in the $-x$ direction) will get contracted (blue color in panel (b) and (c)) which in turn will result in an expansion in the bond length between sites i and $i + 1$ (red color in panel (b) and (c)). It should be noted that the oscillatory behavior follows the classical mass-spring oscillator with a frequency $\sqrt{K_2/M_2}$.

It is important to get a view over the polaron transport phenomena according the transport mechanism described in the previous section. In Figure 2(a), it can be seen that the charge is localized on two sites in the beginning. It starts to move due to the applied force of electric field. One can describe the motion as an adiabatic process in which at each instant of time the charge goes from being centered on a single molecule (T1) to being shared equally between two neighboring molecules (T2) and then drifts and gets centered on the next molecule (T3). Obtain more details on this issue and how the transport is affected by changing different parameters is precisely the aim of this work.

Conclusions

In summary, a semi-empirical Holstein–Peierls model was used to study the polaron stability and mobility in crystalline organic semiconductors at a molecular level. The approach takes into account both intra- and intermolecular electron–lattice interactions as well as the effects of an external electric field. Furthermore, we have investigated the effects of the change of parameters on the polaron stability and mobility in order to simulate different kind of molecular stacks.

The results presented above are one of the evidences that the parameters may describe different types of interactions within a molecular crystal and that result in a stable mobile polaron. Nevertheless, the parameters that result in such a mobile polaron agree well with the interaction strengths that we can expect in molecular crystals. It is therefore plausible that the charge transport in terms of large polaron motion occurs in molecular crystals.

Acknowledgments

The authors are grateful for the support given from the FAPDF, CAPES, CNPQ, and FINATEC.

References

1. K. Vandewal et al. *Nat. Mater.*, **2014**, 13, 63.
2. M. S. White et al. *Nat. Photonics*, **2013**, 7, 811
3. S. Stafström, *Chem. Soc. Rev.*, **2010**, 39, 2484.
4. A. Troisi, *Chem. Soc. Rev.*, **2011**, 40, 2347.
5. E. Mozafari and S. Stafström, *Phys. Lett. A*, **2012**, 376, 1807.
6. E. Mozafari and S. Stafström, *J. Chem. Phys.*, **2013**, 138, 184104.
7. K. Hannewald and P. A. Bobbert, *Appl. Phys. Lett.*, **2004**, 85, 1535.
8. F. Ortman, F. Bechstedt and K. Hannewald, *Phys. Rev. B: Condens. Matter Mater. Phys.*, **2009**, 79, 235206.
9. K. Hannewald et al. *Phys. Rev. B: Condens. Matter Mater. Phys.*, **2004**, 69, 075211.

Luiz A. R. Júnior^{a,b}

^aInstitute of Physics, University of Brasília, 70.919-970, Brasília, Brazil

^b University of Brasília, UnB Faculty of Planaltina, 73.345-010, Brasília, Brazil

Desenvolvimento de Ferramenta para a Inserção com Baixa Perturbação de Proteínas de Membrana em Bicamadas Lipídicas para Simulações de Dinâmica Molecular

Luiz F. C. Zonetti & Alexandre S. Araújo

Introdução

Para a melhor compreensão dos fenômenos físicos e químicos observados em sistemas biológicos os métodos de simulação e modelagem computacional são, sem dúvida, uma ferramenta poderosa. Estes métodos de simulação complementam e estreitam a ligação entre a teoria e o experimento, contribuindo significativamente para o melhor entendimento dos sistemas investigados. O método de Dinâmica Molecular tornou-se popular e poderoso para o estudo de bicamadas lipídicas e proteínas de membrana na última década devido aos avanços nas áreas de software e hardware. Entretanto, algumas simulações de Dinâmica Molecular deste tipo de sistema podem envolver um número elevado de átomos, o que resulta em tempos de simulação muito altos, o que é altamente indesejável na fase de equilíbrio do sistema.

Neste trabalho apresentamos o desenvolvimento de um script cuja finalidade é inserir proteínas de membrana em bicamadas lipídicas causando a mínima perturbação possível, de modo a minimizar o tempo de simulação necessário para o reestabelecimento do estado de equilíbrio do sistema. O método foi aplicado na inserção do peptídeo de fusão da proteína E do vírus da dengue em bicamadas puras e mistas. Os resultados obtidos apontam mínima perturbação na bicamada devido ao processo de inserção do peptídeo.

O método desenvolvido foi desenvolvido baseado nas ideias contidas no trabalho de Christian Kandtl,

com a diferença de que em nosso caso não são retiradas moléculas de fosfolípidos da bicamada no processo. Isso é particularmente conveniente em simulações onde é calculado o perfil de energia livre por um caminho de reação usando a técnica de múltiplas janelas, já que as diversas janelas criadas pelo nosso método apresentam o mesmo número de fosfolípidos. São apresentados alguns sistemas gerados e resultados da comparação de propriedades físico-químicas das bicamadas equilibradas usadas como entrada do script e as bicamadas geradas com a proteína já inserida no sistema.

Métodos

Como a finalidade do script é gerar diferentes janelas para simulações de perfil de energia livre por um caminho de reação, a dinâmica de seu funcionamento consiste na geração, a partir de uma configuração inicial, de configurações onde a distância entre dois grupos de átomos assumem diferentes valores consecutivos. No caso do sistema estudado nesse trabalho o caminho de reação é a distância em z entre o centro de massa (CM) do peptídeo e o centro de massa da bicamada. A seguir descrevemos com detalhes cada etapa do método:

1. Movimenta o peptídeo até a posição definida para a janela em questão
2. Verifica se a distância z entre o CM do peptídeo e da bicamada é maior que um

determinado valor definido pelo usuário. Se for, salva a configuração e passa para a próxima janela, se não, segue para as próximas etapas na mesma janela.

3. Calcula a coordenada x do centro geométrico do peptídeo e define duas bandas na bicamada selecionando moléculas de fosfolipídeos cujos átomos de fósforo possuem coordenada x maior ou menor que esse valor.
4. Calcula as dimensões do peptídeo na direção x e desloca as bandas definidas no passo 3 nessa direção de modo a criar uma abertura com o tamanho do peptídeo.
5. Inicia a sequência de “fechamento” da bicamada onde em cada passo a abertura criada é diminuída de uma distância determinada pelo usuário seguida por uma simulação de minimização de energia para dissipar possíveis superposições de átomos.
6. O fechamento para quando o RMSD entre a posição original e atual dos átomos de fósforo é mínima, o que significa que a bicamada retornou à conformação mais próxima da original possível.
7. Salva a configuração obtida e passa para a próxima janela.

Detalhes Computacionais

A linguagem utilizada no script foi o *tel* e sua execução é feita pelo software Visual Molecular Dynamics (VMD)². Como as simulações dos sistemas gerados serão realizadas utilizando o programa NAMD (Nanoscale Molecular Dynamics program)³, o script trabalha com arquivos dos tipos *pdb* e *psf*.

Nos resultados apresentados utilizamos bicamadas lipídicas em solução aquosa compostas por lipídeos de POPC (Palmitoil-Oleil-Fosfatidil-Colina) (bicamada pura) e por lipídeos de POPC e POPG (Palmitoil-Oleil-Fosfatidil-Glicerol) na proporção 4:1 (bicamada mista). Inserimos nessas bicamadas uma sequência de aminoácidos da proteína E do vírus da dengue do resíduo 98 até o resíduo 110, conhecido como peptídeo de fusão, que contem a seguinte sequência de aminoácidos D R G W G N G C G L F G K.

O Perfil de Densidade de Massa fornece informações sobre a espessura da bicamada e a posição média de moléculas específicas como a água, proteína, grupos que compõem os lipídios, etc, para isso usamos o plugin Density Profile do VMD⁴.

Resultados e Discussão

Os arquivos de entrada para o script (bicamadas lipídicas solvatadas) foram gerados no site do CHARMM-GUI^{5,6} com a ferramenta Membrane Builder^{7,8}. Geramos dois sistemas para nossas simulações: a bicamada pura contém 288 moléculas de POPC e a mista contendo 240 moléculas de POPC e 60 moléculas de POPG. As bicamadas foram posicionadas de modo que o eixo normal ao seu plano coincidisse com o eixo z.

As bicamadas foram solvatadas com moléculas de água suficientes para gerar camadas de aproximadamente 80 Å de cada lado. A seguir, foi adicionado ao sistema o peptídeo de modo que a menor distância entre qualquer um de seus átomos e a posição média dos átomos de fósforo dos fosfolipídios mais próximos fosse 20 Å. Esses sistemas contendo a bicamada (pura ou mista), as camadas de água e o peptídeo posicionado na solução foram utilizados como arquivos de entrada para o script. Aplicamos o script para a geração de 60 janelas que diferiram na distância do peptídeo ao centro da bicamada. Selecionamos três dessas configurações, para cada composição da bicamada, para realizarmos as análises apresentadas neste trabalho, sendo que em cada uma delas o peptídeo ocupa ambientes físico-químicos distintos: no sistema 1 o peptídeo está na solução, com seu centro de massa a uma distância em z de aproximadamente 50 Å do centro da bicamada, no sistema 2 o peptídeo se localiza na interface água/bicamada estando seu centro de massa a aproximadamente 20 Å do centro da bicamada e no sistema 3 o peptídeo está completamente inserido na bicamada com o centro de massa coincidindo com o centro da bicamada.

Na figura 1 apresentamos os sistemas gerados com a bicamada pura e na figura 2 os sistemas gerados com a bicamada mista. As moléculas de água estão representadas como uma superfície roxa, o peptídeo representado em licorice e com os resíduos coloridos conforme sua natureza física, em azul e vermelho resíduos com carga positiva ou negativa, respectivamente, em verde os

polares e em branco os hidrofóbicos. Na bicamada, os grupos acílicos das moléculas de POPC estão coloridos em ciano e das de POPG em vermelho, na região polar os átomos de fósforo são as esferas marrons, os nitrogênios esferas azuis e os oxigênios esferas vermelhas. Observamos que em todos os casos o peptídeo está inserido adequadamente na bicamada sem alterações conformacionais significativas tanto no peptídeo como na bicamada. Não observamos superposições severas que podem levar, quando da simulação desses sistemas, a valores de energia que possam desestabiliza-los.

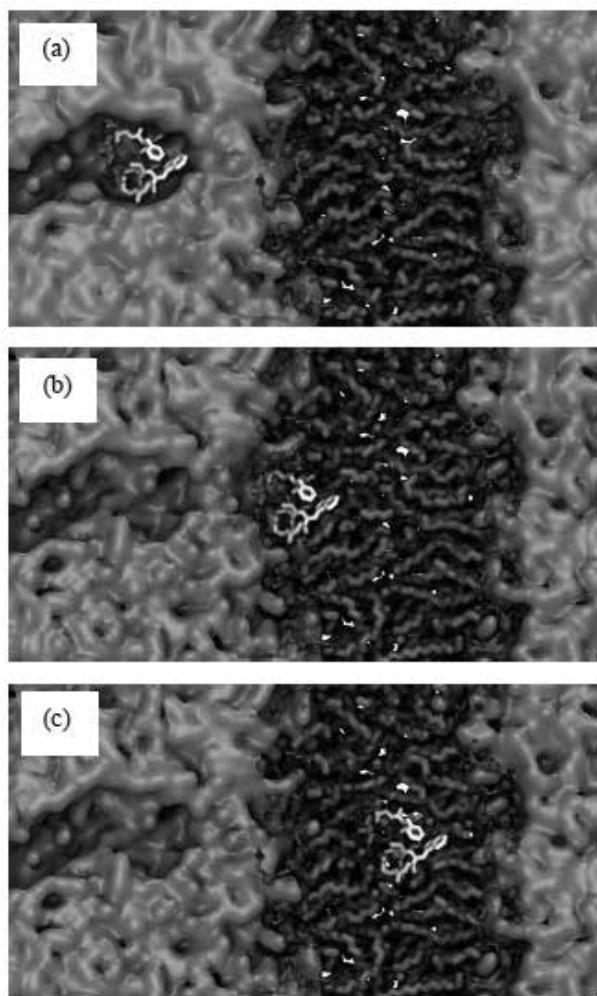


Figura 1. Sistemas gerados com a bicamada de POPC utilizando o método desenvolvido: (a) com o peptídeo localizado na solução. (b) com o peptídeo localizado na interface água/bicamada. (c) com o peptídeo localizado no interior da bicamada.

A figura 3 mostra o RMSD entre as posições dos átomos de fósforo da conformação original e cada etapa do processo de fechamento da bicamada descrito nos itens 5 e 6 da seção de métodos. Nas configurações analisadas nesse trabalho esse processo aconteceu apenas para os sistemas 2 e 3. Observa-se na figura que os sistemas 2 (linha preta) e 3 (linha verde) da bicamada pura apresentam resultados semelhantes com o valor mínimo para o RMSD por volta de 0,5 Å. O mesmo acontece para os sistemas contendo a bicamada mista, como podemos verificar na figura, os

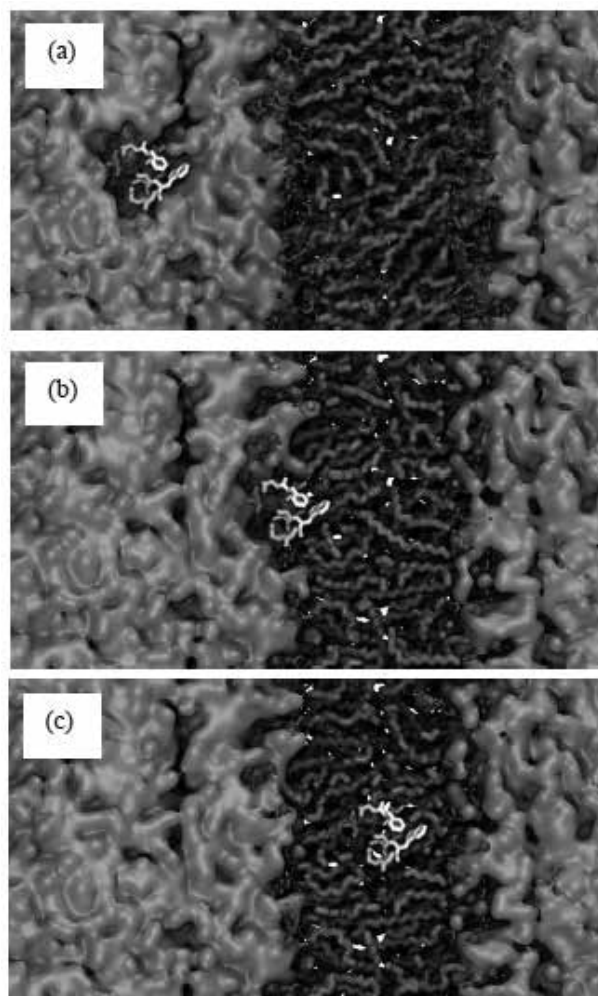


Figura 2. Sistemas gerados com a bicamada de POPC e POPG utilizando o método desenvolvido: (a) com o peptídeo localizado na solução. (b) com o peptídeo localizado na interface água/bicamada. (c) com o peptídeo localizado no interior da bicamada.

sistemas 2 (linha vermelha) e 3 (linha azul) apresentam valor mínimo de RMSD em torno de 0,1 Å alcançado com menos passos. Esses valores de RMSD menores que 1 Å apontam que em ambos os casos (bicamada pura e simples) a configuração estrutural da bicamada obtida após o processo de inserção do peptídeo é muito próxima da observada na bicamada original que estava equilibrada. Assim, os sistemas gerados pelo nosso método irão requerer muito menos tempo de equilíbrio que sistemas gerados por métodos onde se exclui grande quantidade de fosfolípidos para a inserção da proteína.

Por meio de uma varredura ao longo do eixo z (perpendicular a membrana) pode-se calcular a densidade de massa referente às moléculas de interesse em cada ponto do sistema, este mapeamento fornece o Perfil de Densidade de Massa. Com isso, é possível determinar a região média ocupada pelo solvente, pela bicamada e pela proteína, além de permitir estimar a espessura média da bicamada.

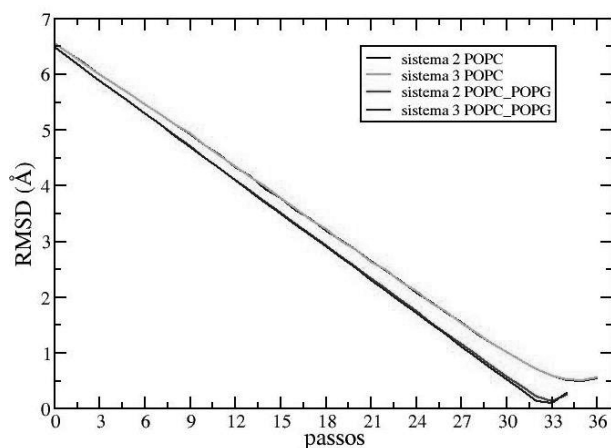


Figura 3. RMSD entre as posições dos átomos de fósforo da bicamada original e a bicamada no processo de fechamento após a inserção do peptídeo. São apresentados os resultados apenas para sistemas onde foi necessário abrir a bicamada para a inserção do peptídeo, no caso os sistemas 2 e 3 das bicamadas pura e mista. As linhas preta e verde representam os sistemas 2 e 3 da bicamada pura, respectivamente. As linhas vermelha e azul representam os sistemas 2 e 3 da bicamada mista.

Os gráficos do Perfil de Densidade de Massa (PDM) dos sistemas contendo bicamada de POPC (bicamada pura) e de POPC com POPG (bicamada mista) são mostrados nas figuras 4 e 5, respectivamente. Analisando as linhas vermelhas (PDM dos fosfolípidos) e azuis (PDM do grupo fosfato) de todos os gráficos observamos que ambas as bicamadas apresentam uma espessura média em torno de 40 Å mesmo após o processo de abertura e fechamento para a inserção do peptídeo. Isso mostra que o método aqui descrito perturba muito pouco as bicamadas com relação a sua espessura. Observando as linhas verdes vemos onde o peptídeo se localiza, em média, em cada sistema. O PDM da água indica coexistência com a região polar da bicamada na interface e é nulo na região no centro da membrana, como esperado.

Conclusão

A partir dos resultados e discussões realizadas acima, podemos concluir que o método proposto e o script implementado são eficientes para a inserção de proteínas em bicamadas lipídicas causando a mínima perturbação possível. O RMSD calculado mostra que a diferença entre as posições dos átomos de referência (fósforos) da bicamada original e da bicamada gerada ficou abaixo de 1 Å, com convergência mais rápida para a bicamada mista (POPC/POPG).

Através do gráfico do Perfil de Densidade de Massa observamos que a espessura da bicamada fica em torno de 40 Å em todos os sistemas, o que mostra que o método de inserção da proteína pouco altera a estrutura da bicamada. O PDM também nos mostra que nosso método também causa baixo ou nenhum impacto na solvatação da bicamada, já que a distribuição das moléculas de água permanece inalterada depois do processo de fechamento da bicamada.

Perspectivas Futuras

Os próximos passos serão a execução de simulações de Dinâmica Molecular dos sistemas gerados para o monitoramento de propriedades físico-químicas da bicamada como área por lípido, PDM e parâmetro de ordem. Observaremos quanto tempo de simulação será necessário para alcançarmos valores de referência e

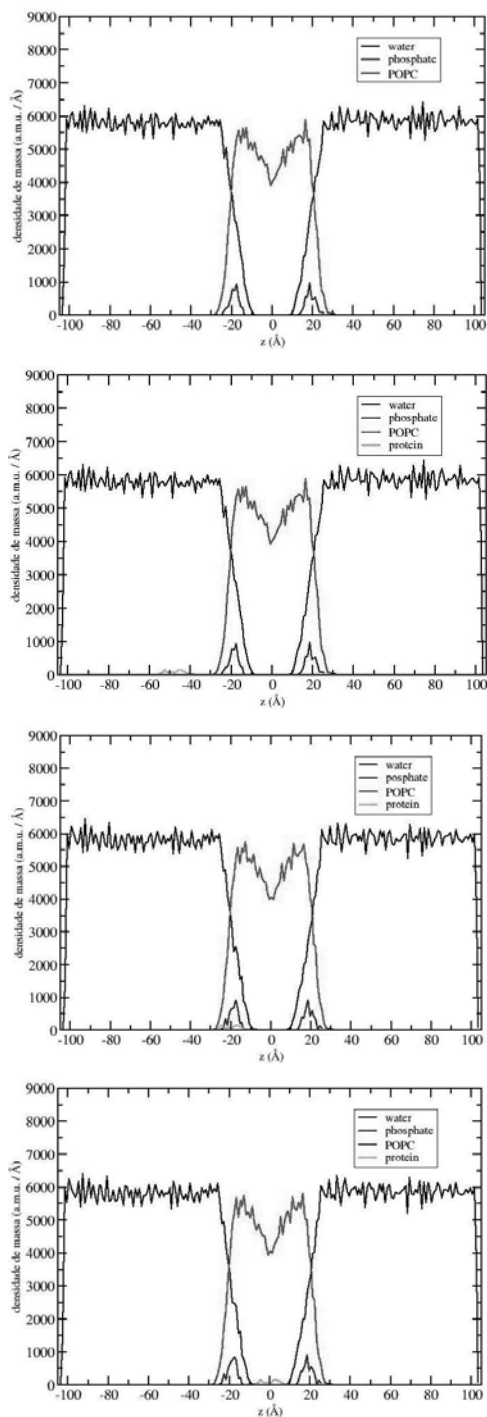


Figura 4. Perfil de Densidade de Massa (PDM) da bicamada pura de POPC em relação ao eixo z , onde em (a), (b), (c) e (d) a linha preta representa a água, a linha azul os grupos fosfato dos fosfolípidos, a linha vermelha o POPC e a verde o peptídeo.

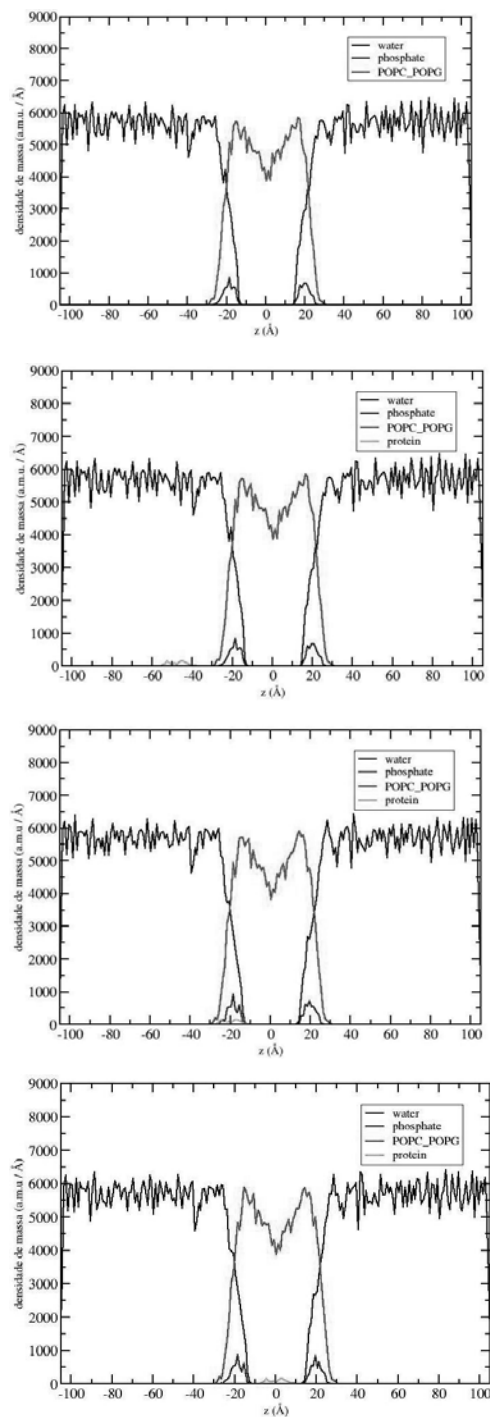


Figura 5. Perfil de Densidade de Massa (PDM) da bicamada mista de POPC e POPG em relação ao eixo z , onde em (a), (b), (c) e (d) a linha preta representa a água, a linha azul os grupos fosfato dos fosfolípidos, a linha vermelha o POPC ou POPG e a verde do peptídeo.

compararemos esses tempos com tempos obtidos a partir de simulações com sistemas gerados por outros métodos. Com isso teremos base para comparação de nosso método com outros já estabelecidos.

Agradecimentos

À Fapesp pelo apoio financeiro: processo nº 2010/18169-3, Fundação de Amparo à Pesquisa do Estado de São Paulo (FAPESP).

Esta pesquisa tornou-se possível graças aos recursos computacionais disponibilizados pelo Núcleo de Computação Científica (NCC/GridUNESP) da Universidade Estadual Paulista (UNESP)

Pesquisa desenvolvida com o auxílio do CENAPAD-SP (Centro Nacional de Processamento de Alto Desempenho em São Paulo), projeto UNICAMP / FINEP - MCT.

Luiz Fernando da Costa
Zonetti ^{a,b*} & Alexandre
Suman de Araújo^a

^a Universidade Estadual Paulista “Júlio de Mesquita Filho”, São José do Rio Preto /SP

^b Instituto Federal de Educação, Ciência e Tecnologia de São Paulo – Campus Birigui, Birigui/SP

*E-mail: luizfz@hotmail.com

Referências

1. Kandt, C., Ash, W. L. & Peter Tieleman, D. Setting up and running molecular dynamics simulations of membrane proteins. *Methods* 41, 475–488 (2007).
2. Humphrey, W., Dalke, A. & Schulten, K. VMD: Visual molecular dynamics. *J. Mol. Graph.* 14, 33–& (1996).
3. Phillips, J. C. et al. Scalable molecular dynamics with NAMD. *J. Comput. Chem.* 26, 1781–1802 (2005).
4. Giorgino, T. Computing 1-D atomic densities in macromolecular simulations: The density profile tool for VMD. *Comput. Phys. Commun.* 185, 317–322 (2014).
5. Wu, E. L. et al. CHARMM-GUI Membrane Builder toward realistic biological membrane simulations. *J. Comput. Chem.* 35, 1997–2004 (2014).
6. Brooks, B. R. et al. CHARMM: the biomolecular simulation program. *J. Comput. Chem.* 30, 1545–1614 (2009).
7. Jo, S., Kim, T. & Im, W. Automated Builder and Database of Protein/Membrane Complexes for Molecular Dynamics Simulations. *PLoS ONE* 2, e880 (2007).
8. Jo, S., Lim, J. B., Klauda, J. B. & Im, W. CHARMM-GUI Membrane Builder for Mixed Bilayers and Its Application to Yeast Membranes. *Biophys. J.* 97, 50–58 (2009).

Analysis of Aluminium-Magnesium Alloy Clusters Through Genetic Algorithm

Mateus A. M. Paiva & Breno R. L. Galvão

Introduction

Metal clusters have attracted a large scientific effort in the past few years due to their potential technological applications at the nanoscale. Mixed metal systems are known to have modified and often desirable properties relative to the pure phases of the individual metal, including improved corrosion resistance, low density and malleability.¹ Metal alloys composed of aluminum and magnesium have been widely recognized to be of importance in industry and aerospace manufacturing.²

In this work the structures and properties of Al-Mg alloys are investigated theoretically.

Methods

A modified genetic algorithm (GA) was employed in the search for the potential energy minimum associated with Al_xMg_y ($x+y \leq 35$) clusters using an empirical Gupta many-body potential.² The GA initially generates a number of random clusters. The energy of these random clusters are minimized locally and ranked by their energies. The best clusters are then selected as parents and crossed to generate a new population. Mutation is also performed in 15% probability by rotating parts of the cluster by random amounts. Convergence is achieved when no further improvement is reached after a given number of generations.

In order to avoid stagnation in a local minimum, the genetic algorithm here employed uses two different evolutionary operators: the operator history (OH) and the annihilator (A), which initiate new GA cycles in the search for different minima.^{3,4}

$$E_i = E_i^{\text{Band}} + E_i^{\text{rep}} \quad (1)$$

$$E_i^{\text{band}} = - \left[\sum_{j \neq i}^N \xi^2 \exp \left[-2q \left(\frac{r_{ij}}{r_0} - 1 \right) \right] \right]^{1/2} \quad (2)$$

$$E_i^{\text{rep}} = \sum_{j \neq i}^N A \exp \left[-p \left(\frac{r_{ij}}{r_0} - 1 \right) \right] \quad (3)$$

The term E_i band is an expression for many bodies and composes the attractive part of the energy, taking into account the character of the metal band connection. Equation 3 is interpreted as a repulsive contribution to ensure the stability of the structure. The parameters q , p , ξ and A were adjusted in the literature to pure clusters of Al and Mg, which we have employed in the present study. The parameters used are show in table 1. For the Al-Mg bonds, we used an average of such values.^{5,6}

Table 1 - Parameters for the Gupta potential for the Al-Mg system.

	Al-Al	Mg-Mg	Al-Mg
r_0 (Å)	2.8637	3.21	3.03685
A (eV)	0.1221	0.198722	0.160411
ξ (eV)	1.316	0.349712	0.832856
p	8.612	15.977780	12.29489
q	2.516	1.684590	2.100295

Results and Discussion

We have optimized the geometries of Al_xMg_y clusters for several compositions within fixed nuclearities of $x+y=5, 8, 10, 13, 15, 20, 25, 30$ and 35 atoms.

Specifically, the 13 atom clusters are considered a magic number² (increased stability) since it may form a symmetric icosahedron. Indeed, the literature shows the Al_{13} cluster to be a perfect icosahedron⁷, but Mg_{13} is not as symmetric².

The most stable structures obtained by our GA calculations for all possible compositions with 13 atom clusters are shown in Fig. 1. As seen, the icosahedral shape is lost for some of them Al_7Mg_6 , Al_6Mg_7 , Al_5Mg_8 , Al_4Mg_9 , $\text{Al}_3\text{Mg}_{10}$ and $\text{Al}_2\text{Mg}_{11}$. It is possible to notice the pattern of central aluminum atoms to take pyramidal and bipyramidal geometries, while magnesium does not demonstrate a clear pattern

The structures predicted in this work also show a tendency of aluminum atoms to occupy the center of the alloy clusters, while magnesium is segregated at the surface, as seen in Fig. 1.

The calculation of excess energies (Eq. 4), can provide insights on the preference of alloy formation over the corresponding pure cluster, showed that with about 40% aluminum, the alloy clusters are best stabilized, as seen in the graphic of Fig. 2.

$$E_{\text{excess}}(x) = \frac{E_{\text{clust}}(x)}{N} - \frac{E_{\text{pure}}^{\text{Mg}}(x)}{N} - \frac{E_{\text{pure}}^{\text{Al}}(x)}{N} \quad (4)$$

The calculation of second energy difference shows how much a cluster is stable compared to the neighbor. By calculating the second energy difference (Eq. 5), it is observed that $\text{Al}_3\text{Mg}_{10}$ and Al_5Mg_8 are particularly stable among the non icosahedral structures, while in the icosahedral ones (more than 8 Al atoms), there is no large peak, showing that they have similar stabilities in Fig. 3.

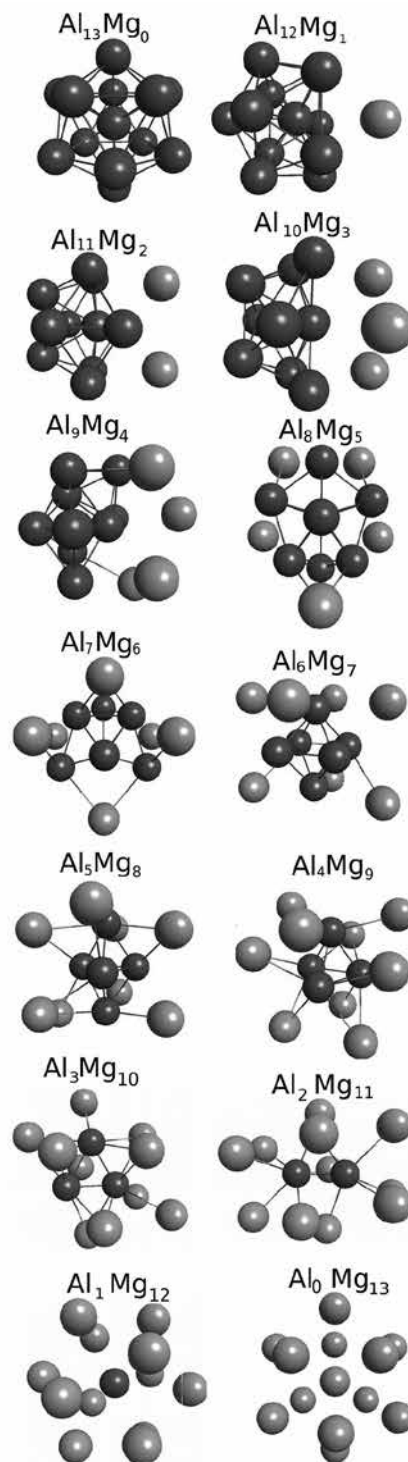


Figure 1. Alloy clusters of 13 atoms with different proportions of Al (green) and Mg (gray) .

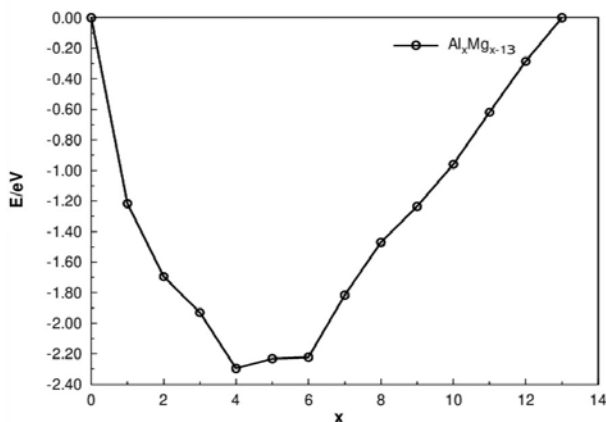


Figure 2. Graphic of excess of energy for cluster with 13 atoms

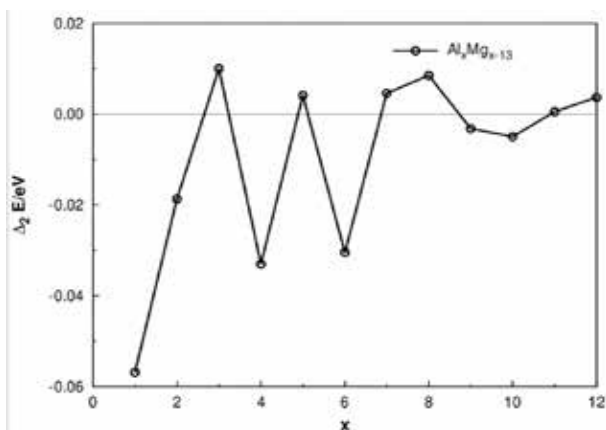


Figure 3 – Graphic of second energy difference for cluster with 13 atoms

$$\Delta_2 E(x) = \frac{2E_{\text{clust}}(x)}{N} - \frac{E_{\text{clust}}(x-1)}{N} - \frac{E_{\text{clust}}(x+1)}{N} \quad (5)$$

For clusters with 25 atoms, as with others nuclearities, the observations made for 13 atoms are applicable. As a seen in Fig. 4.

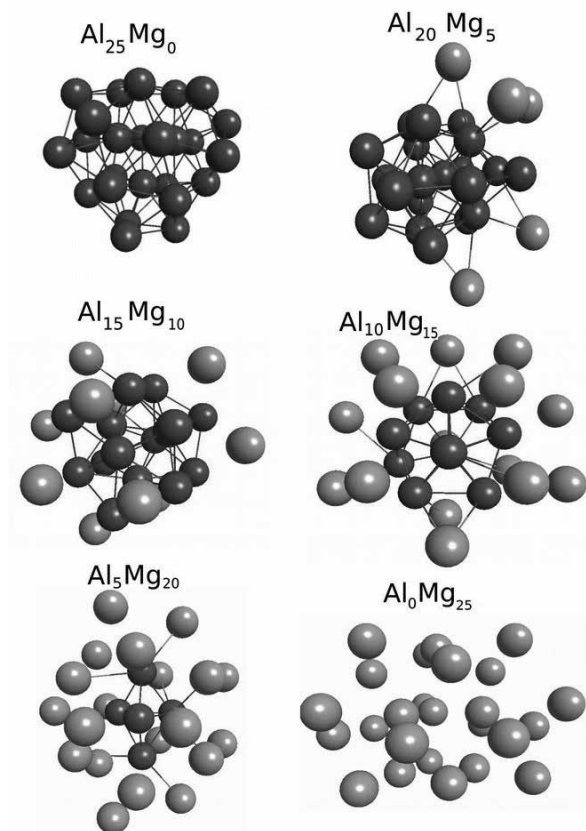


Figure 4. Alloy clusters of 25 atoms with different proportions of Al (green) and Mg (gray).

The central aluminum core tends to show the icosahedral shape whenever possible. Further calculations are being carried out, and confirmation of the structures employing ab initio methods is envisaged.

Conclusions

The modified genetic algorithm coupled with the empirical Gupta potential could predict the general trend of aluminum atoms occupying inner sites, with a ratio of 40%. Additional ab initio calculations will be carried out to confirm the results and to obtain new ones.

Acknowledgments

The authors are grateful for the support given from the FAPEMIG, and CEFET-MG.

1. E. Osorio et al., Phys. Chem. Chem. Phys. 15, 2222 (2013).
 2. Luo, Zhixun, et al. J. Am. Chem. Soc. 135, 4307 (2013)
 3. F. F. Guimarães, J. C. Belchior, R.L Johnston, C.J. Roberts, J.. Chem. Phys. 116, 8327 (2002)
 4. X. Li, Y. Qin, J. Fu, J. Zhao, Computational Materials Science 98, 328 (2015)
 5. Turner, Giles et al. The J. of Chem Physics 112.10, 4773-4778 (2000).
 6. Li, Xiaojie, et al. Computational Materials Science. 98 328-332 (2015).
 7. G. W. Turner, R. L. Johnston, N. T. Wilson, J. Chem. Phys. 112, 4773 (2000)
-

Mateus Augusto Martins de Paiva* & Breno R. L. Galvão

Departamento de Química, Centro Federal de Educação Tecnológica de Minas Gerais, Av. Amazonas 5253 - Nova Suíça - Belo Horizonte - MG – Brasil. 30.421-169

*E-mail: mts381@gmail.com

Parametrização de Campo de Força e Estudo Teórico do Comportamento Estrutural e Eletrônico de FAD e TPP – Cofatores da Enzima AHAS.

Renan F. Guerra & Eduardo F. Franca

Introdução

A enzima Acetohidroxiácido Sintase (AHAS) é encontrada em plantas e microrganismos já que está envolvida nos processos catalíticos e de biossíntese dos aminoácidos de cadeia ramificada (ACR). A AHAS é a primeira da rota biossintética dos mesmos e, portanto, alvo de herbicidas inibitórios que são usualmente empregados na agricultura, as sulfonilureias e imidazolinonas¹. Dessa forma, pode ser utilizada como alvo biológico, em métodos analíticos baseados em Microscopia de Força Atômica, na detecção desses agrotóxicos para controle ambiental mais rigoroso de culturas agrícolas para exportação.

A AHAS para exercer sua atividade catalítica necessita fundamentalmente de cofatores como os íons Mg^{2+} e K^{+} , e as biomoléculas FAD (Dinucleotídeo de Flavina e Adenina) e TPP (Tiamina Difosfato), como mostrado na Figura 1a e 1b, respectivamente. O papel dessas biomoléculas na enzima ainda permanece um enigma, mas sabe-se que são fundamentais para a integridade estrutural e atividade enzimática da mesma².

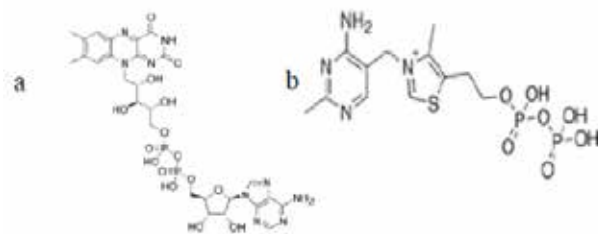


Figura 1. Estrutura molecular dos cofatores a) FAD e b) TPP.

O presente trabalho objetivou estudar o efeito da água na conformação estrutural e nas propriedades eletrônicas das moléculas de FAD e TPP em solução aquosa, haja vista que as propriedades moleculares desses co-fatores é afetada significativamente em fase condensada. Para tanto, foi utilizado um método híbrido de mecânica quântica e mecânica molecular (clássica), conhecido como QM/MM Sequencial, considerado adequado para estudos com esse foco já que a região de interesse (biomolécula) é tratada quanticamente e o meio no qual se encontra inserida (solvente) é tratada por cálculos

clássicos demandando menor custo computacional que os métodos puramente quânticos.

Métodos

Previamente, o campo de força das moléculas de FAD e TPP foram obtidos online utilizando o programa SwissParam³. Depois disso, as moléculas de FAD (carga -1) e TPP (carga -2) foram colocadas separadamente em uma caixa de simulação retangular a 1,5 nm do sistema e solvatada com moléculas de água do tipo Simple Point Charge (SPC) mantido em ensemble NPT (298 K and 1 bar). Íons sódio foram adicionados para neutralizar a carga do sistema. As dinâmicas moleculares foram realizadas utilizando o programa GROMACS 4.6 e o campo de força CHARMM 2.7 durante 4 e 10 ns para FAD e TPP, respectivamente.

Para cada ps de simulação a estrutura eletrônica das moléculas foi obtida utilizando cálculos semi-empíricos single point, com o hamiltoniano PM7 e o programa MOPAC 2012.

Os resultados foram analisados utilizando os programas Jmol, VMD e GRACE.

Resultados e Discussão

Para a estrutura do FAD o programa SwissParam gerou todos os parâmetros de campo de força (ligados e não-ligados) adequados para a descrição do composto utilizando simulação por dinâmica molecular. Para a molécula do TPP nem todos os diedros próprios foram identificados pela ferramenta online e, portanto, não tiveram seus parâmetros gerados. Na Tab. 1 estão listados os diedros não identificados para a estrutura do TPP (a cada linha da tabela os parâmetros para os diedros são os mesmos).

Tabela 1. Diedros próprios não identificados pelo programa SwissParam para a molécula TPP e parametrizados separadamente.

1	C3 C2 C1	H1	N1 C2 C1	H1
		H2		H2
		H3		H3
2	C2 C3 C11	C12	C2 C3 S1	C12
		H13		H13
		H14		H14
3	N1 C5 C2	C6	N1 C5 C4	C6
		H5		H5
		H6		H6

Dessa forma, a alternativa encontrada foi obter tais parâmetros a partir de uma molécula com estrutura análoga à do TPP. Gutowski (1979) propôs estruturas análogas ao Thiamine Pyrophosphate (TPP) de modo que a estrutura mais semelhante é o Thiamine Thiothiazolone Pyrophosphate (TTTPP) - a única diferença entre as estruturas é o átomo representado em rosa (H para o TPP e S para o TTTPP) conforme apresentado na Fig. 2 onde está apresentada a estrutura genérica para o TPP e seu análogo⁵.

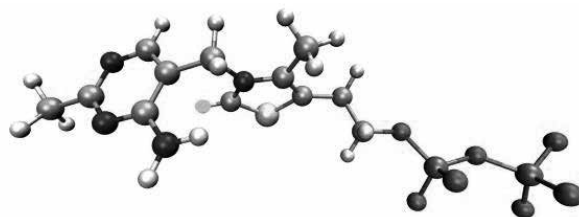


Figura 2. Estrutura geral do TPP e seus análogos.

Para a estrutura do TTTPP os diedros foram adequadamente descritos e os parâmetros utilizados na descrição do TPP no campo de força. Após a parametrização foi aplicada a metodologia QM/MM para ambos cofatores da enzima AHAS.

O cálculo da raiz quadrada do desvio quadrático médio (RMSD) com relação à estrutura inicial aponta para um desvio máximo de 0,46 e 0,34 nm para as moléculas de FAD e TPP, respectivamente, relacionado a flutuações conformacionais das estruturas em solução aquosa ao longo da trajetória. Isso está relacionado ao fato de a molécula de FAD apresentar uma estrutura consideravelmente maior e, portanto, maior número de graus de liberdade.

Em relação aos orbitais de fronteira, HOMO e LUMO, verificou-se que a variação estrutural para a molécula do FAD resultou na diminuição de energia em aproximadamente 0,295 eV. Os orbitais HOMO encontram-se localizados no agrupamento SO₄ tanto para estrutura inicial quanto para a estrutura final (Fig. 3a). Para a estrutura mais estável (Fig. 3b), no entanto, ocorre um deslocamento do HOMO diminuindo a extensão do mesmo de 5 para apenas 2 átomos, conforme apresentado nas representações das Fig. 3a e 3b.

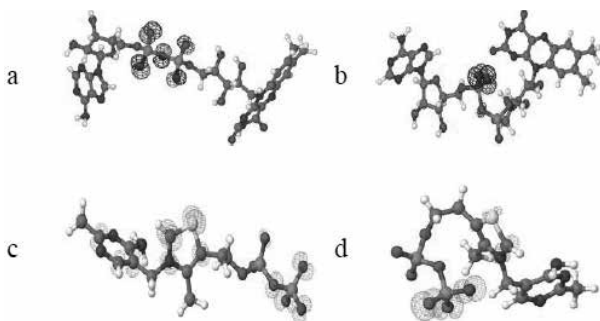


Figura 3. Orbitais moleculares HOMO nas estruturas inicial (a e c) e mais estável em solução aquosa (b e d) para as moléculas de FAD e TPP, respectivamente.

Para a molécula de TPP a estrutura mais estável ocorre após aproximadamente 7 ns de simulação, de modo que a diminuição energética ocasionada pela variação estrutural é de 0,574 eV. Esta estabilização energética se deve ao fato da relevante variação na conformação estrutural sofrida pela molécula, conforme se observa ao comparar as estruturas apresentadas nas Fig. 3c e 3d. Os orbitais HOMO na estrutura inicial se encontram distribuídos ao longo da molécula, no entanto, na estrutura mais estável os mesmos se encontram predominantemente localizados sob os átomos de oxigênio do agrupamento PO_4 da extremidade da estrutura.

A estrutura mais estável da molécula do FAD se apresenta numa conformação mais fechada ocasionada pela ocorrência de duas ligações de hidrogênio intramoleculares (Fig. 4) que apresentam tempo de vida médio de 3,49 ps e momento dipolar em solução aquosa maior em 1,97 Debyes. No entanto, para a molécula do TPP a considerável variação na estrutura é gerada apenas pelo calor de formação que é de cerca de - 166,97 kJ.mol⁻¹.

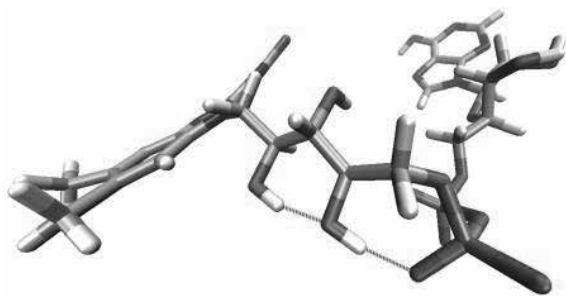


Figura 4. Ligações de Hidrogênio (vermelho) responsáveis pelo conformação mais estável da estrutura.

Dessa forma, torna-se possível afirmar que as moléculas de água tratadas como cargas pontuais foram responsáveis pela amostragem de estruturas mais estáveis para as duas moléculas em estudo.

Conclusões

O programa SwissParam foi eficiente e útil no processo de parametrização das moléculas do FAD e TPP, promovendo uma economia de tempo e memória computacional nessa etapa essencial das metodologias computacionais clássicas. A metodologia de QM/MM sequencial permitiu a descrição adequada do efeito do solvente explícito, temperatura e pressão na estrutura eletrônica do FAD e do TPP reafirmando a validade dos métodos híbridos no estudo de propriedades termodinâmicas de moléculas com elevado grau de liberdade como as estudadas.

Estruturas mais estáveis foram obtidas pela influência do solvente na estrutura eletrônica das moléculas de modo que as informações do presente trabalho serve de base para o estudo mais detalhado da função desempenhada pelos cofatores na enzima AHAS.

Agradecimentos

Os autores agradecem o apoio concedido pela CAPES, CNPQ, FAPEMIG e RQ-MG.

References

1. J. A. MCourt. R. G. Duggleby. Amino Acids. 31 (2), 173- 10,(2006)
2. J. A. MCourt. et. al. Proc. Natl. Acad. Sci. 103 (3), 569-573,(2006).
3. V. Zoete, M. A. Cuendet, A. Grosdidier, O. Micheelin. J. Comput. Chem. 32(11), 2359-2368, (2011).
4. B. R. BROOKS. et al. J. Comput. Chem., 30 (10), 1545-1614,(2009).
5. J. A. Gutowski, G. E. Lienhard. The Journal of Biological Chemistry. 251 (9), 2863-2866,(1976).

Renan F. Guerra* & Eduardo de Faria Franca

a Laboratório de Cristalografia e Química Computacional – Instituto de Química da Universidade Federal de Uberlândia (UFU)

*E-mail: renan_s13@hotmail.com

Stretching-Dependent Thermoelectric Properties of a BDT Single-Molecule Junction

Renato B. Pontes, Alberto Torres, Antônio J. R. da Silva & Adalberto Fazzio

Introduction

Understanding the physical and chemical properties of molecular junctions is fundamental for developing organic-based devices. In particular, a lot of effort has been made to investigate both the low bias conductance and the thermoelectric properties of molecules coupled to gold leads.

Recently, Venkataraman et al.¹ performed the first concomitant determination of conductance (G) and Seebeck coefficient (S) of a single molecule junction, via the direct measurement of electrical and thermoelectric currents, by using a scanning tunnelling microscope-based breakjunction technique (STM-MCBI). Thus, since the charge transport properties of molecular junctions depend on how the frontier orbitals are positioned in the vicinity of the Fermi level, a concurrent measurement of electrical and thermoelectric properties is now possible. Thus, it is interesting to consider what would happen with the thermoelectric properties of a single molecule junction as a function of the mechanical stretching. Here we show that the thermoelectric properties, thermopower (S), electronic heat conductance (kel) and efficiency, characterized by the figure of merit (ZT), can be tuned as a function of the electrode separation, in a single BDT molecule junction (Au/BDT/Au). We also propose a scheme to obtain the maximum ZT of molecular junctions in general².

Methods

Our results for the structural evolution of the junction Au/BDT/Au are based on first-principles spin-polarized total energy density functional theory (DFT) calculations^{3,4}. We use a PBE-GGA functional and norm-conserving pseudo-potentials as implemented in the SIESTA code^{5,6}. Numerical atomic orbitals are used as basis sets. We employed a split-valence double-zeta basis with a polarization function (DZP) for the whole system. The confining energy shift is 0.05 eV and an energy cut-off of 240 Ry is used to the grid integration. For the surface Brillouin zone (BZ) sampling we use a (4 x 4 x 1) Monkhorst-Pack set. Moreover, in our calculations the selfconsistency is achieved when the change in the total energy between cycles of the SCF procedure is below 10⁻⁴ eV and the density matrix change criterion of 10⁻⁴ is also satisfied. These criteria are enough to ensure convergence in the calculated total energy of 0.05 eV.

To obtain the geometries, the supercell is such that the molecule would be connected to the two sides of the Au slab. The Au slab is modelled by a (3 x 3) surface unit cell and five layers of gold. In all calculations the positions of the BDT atoms and the Au atoms on the first two layers at either side are allowed to relax until the forces are smaller than 0.02 eV/Å. All other atoms are held fixed at their bulk positions. The separation between the electrodes is increased in steps of 0.5 Å

and for each new supercell length the system is fully relaxed. The transport calculations are performed on TRANSAMPA code⁷⁻¹¹, which employs a non-equilibrium Green's function combined with density functional theory (NEGF-DFT).

Result and Discussion

Fig. 1(a–i) shows nine panels depicting the representative geometries of the different stages of the evolution of the Au/BDT/Au junction during a STM-MCBJ experiment. For small electrode separations (panels a and b), the molecule is nearly parallel to the surface and as the electrodes are moved apart, the BDT molecule is pulled to an upright conformation (panel h). By further stretching the single-molecule junction rupture of the Au–S bond occurs (panel i). A detailed discussion about the structural evolution of the Au/BDT/Au junction is presented by Pontes et al.¹¹

We show that the thermoelectric properties of a single molecule junction can be tuned by mechanic stretching. In Fig. 2, we show that the Seebeck coefficient is positive, indicating that it is dominated by the HOMO. Furthermore, it increases as the HOMO level, which is associated to the sulphur atom, tends towards energies close to the Fermi energy. To the end, by modelling the transmission coefficient of the system as a single Lorentzian peak (Fig. 3), we propose a scheme to obtain the maximum ZT of any molecular junction.

The scheme for maximizing the ZT involves two main points: (i) to obtain narrow resonances in the transmission coefficient spectrum and, (ii) the molecular orbital's energy shift, to tune the resonance. The narrow resonances can be obtained by mechanical stretching, as we previously showed. The molecular orbital's energy shift is possible by stretching, doping or even under an applied external electric field.

Conclusions

In conclusion, we investigate as a function of the stretching the behaviour of the thermoelectric properties – Seebeck coefficient (S), the electronic heat conductance (κ) and the figure of merit (ZT) – of a molecule-based

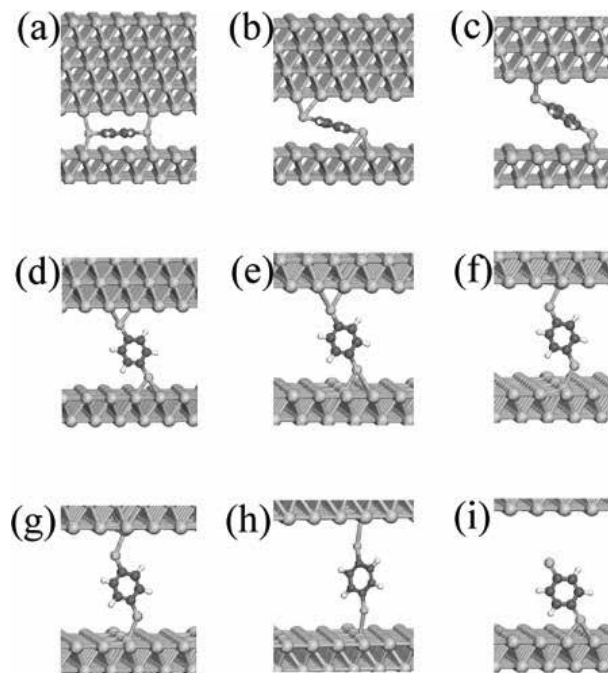


Figure 1. Ball-and-stick view of the optimized atomic structures, at different stages of the structural evolution of a single BDT molecule junction as a function of the stretching.

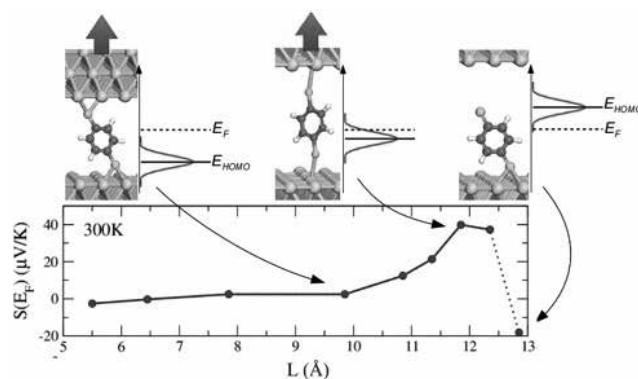


Figure 2. Seebeck coefficients, in the Fermi level [$S(E_F)$], as a function of the lead-lead separation, for the temperature of 300 K. The associated Au/BDT/Au geometry is also shown.

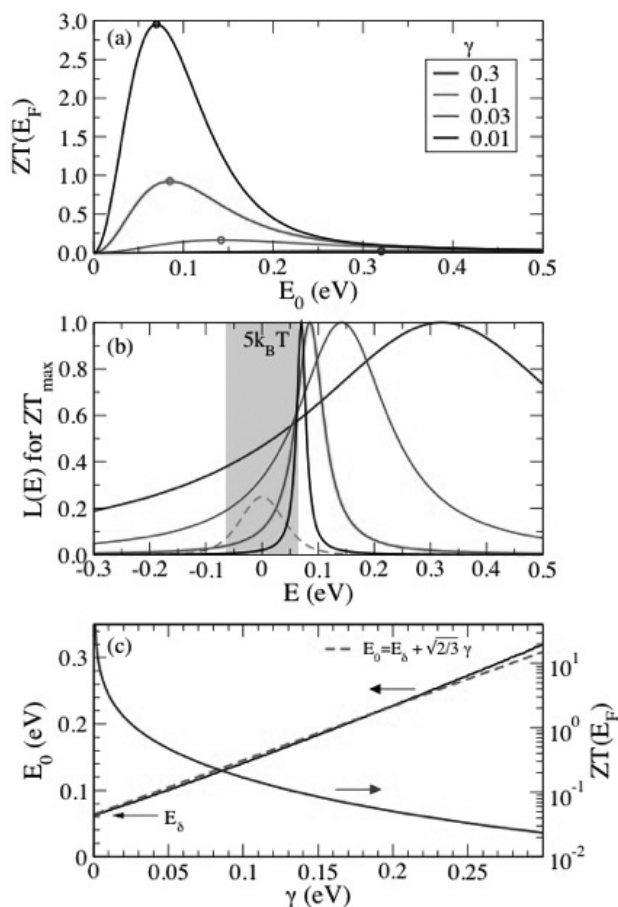


Figure 3. (a) Figure of merit, ZT , at the Fermi level, E_F , for Lorentzian transmittances as a function peak position, E_0 , for several widths, γ . (b) Lorentzian transmittances for the E_0 values which yield the maximum ZT in the upper panel, marked as dots in (a). (c) E_0 that $L(E)$ have to do in order to maximize ZT at the Fermi energy as function of the width, γ .

junction composed by a benzene-1,4-dithiol molecule (BDT) attached to Au(111) surfaces at room temperature. Based on our ab initio calculations, we show that the thermoelectric properties of a single molecule junction can be tuned by mechanic stretching. For the Au/BDT/Au junction, the Seebeck coefficient is positive, indicating that it is dominated by the HOMO. Furthermore, it increases as the HOMO level, which is associated to the sulphur atom, tends towards energies close to the Fermi energy. We also propose a simple and general scheme that can be used to obtain the maximum ZT of any molecular junction.

Acknowledgments

The authors are grateful for the support given by the Brazilian funding agencies: CAPES, CNPq, FAPEG and FAPESP.

References

1. J. R. Widawsky, P. Darancet, J. B. Neaton and L. Venkataraman, *Nano Lett.*, 12, 354–358, (2012).
2. A. Torres, R. B. Pontes, A. J. R. da Silva and A. Fazzio, *Phys. Chem. Chem. Phys.* 17, 5386–5392, (2015).
3. P. Hohenberg and W. Kohn, *Phys. Rev.*, 136, B864–B871, (1964).
4. W. Kohn and L. J. Sham, *Phys. Rev.* 140, A1133–A1138, (1965).
5. P. Ordejon, E. Artacho and J. M. Soler, *Phys. Rev. B: Condens. Matter Mater. Phys.* 53, R10441–R10444, (1996).
6. D. Sanchez-Portal, P. Ordejon, E. Artacho and J. M. Soler, *Int. J. Quantum Chem.* 65, 453–461, (1997).
7. F. D. Novaes, A. J. R. da Silva and A. Fazzio, *Braz. J. Phys.*, 36, 799–807, (2001).
8. J. Taylor, H. Guo and J. Wang, *Phys. Rev. B: Condens. Matter Mater. Phys.* 63, 245407, (2001).
9. M. Brandbyge, J. L. Mozos, P. Ordejon, J. Taylor and K. Stokbro, *Phys. Rev. B: Condens. Matter Mater. Phys.* 65, 165401, (2002).
10. Y. Xue, S. Datta and M. A. Ratner, *Chem. Phys.* 281, 151–170, (2002). 11 J. E. Padilha, M. P. Lima, A. J. R. da Silva and A. Fazzio, *Phys. Rev. B: Condens. Matter Mater. Phys.*, 84, 113412, (2011).
11. R. B. Pontes, A. R. Rocha, S. Sanvito, A. Fazzio and A. J. R. daSilva, *ACS Nano*, 5, 795–804, (2011)

Renato B. Pontes^a, Alberto Torres^b, Antônio J. R. da Silva^b & Adalberto Fazzio^b

^a Instituto de Física, Universidade Federal de Goiás, CP 131, 74001-970, Goiânia, GO, Brazil.

Email: pontes@ufg.br

^b Instituto de Física, Universidade de São Paulo, CP 66318, 05315-970, São Paulo, SP, Brazil.

Molecular Modeling and Computer Simulation involving the Encapsulation of β -carot ene in Boron Nitride Nanotubes

Charles de A. O. Rocha, David L. Azevedo, Fábio F. Monteiro & Antonio L. de A. Fonseca

Introduction

The possibility of applying functionalized nanotubes with β -carotene in the form of nanocrystalline dyes in photovoltaic-type cells (DSSC) is the motivating element of this work. It is now known that the addition of nanocrystalline organic dyes possibly increases the efficiency of these electronic devices in converting solar energy into electrical energy. Vale, in due course, quotes the recent work of Grätzel et al.^{7,8,9} on this subject.

On the one instance, we have the β -carotene (BC), an orange pigment that has molecular formula $C_{40}H_{56}$. It is a natural dye that shows the photoluminescence phenomenon, a property proven by spectroscopy. On the other instance we pointed out the boron nitride nanotubes (BNNTs). These nanostructures have been theoretically predicted shortly after the discovery of carbon nanotubes (CNTs) by Rubio et al in 1994, and were experimentally manufactured by Chopra et al, 1995⁵. All BNNTs are broadband semiconductors with gaps of approximately 5.5 eV^{2,3,4}. Their high ionicity and high energy gap give them electronic properties greater uniformity and explain the use of these materials in the electronics field. In addition, BNNTs stand out for their chemical inertness and high thermal stability, potentially interesting properties for applications in the biomedicine field and the engineering of biomaterials³. Unfortunately, it is noted that the applications of this and of other boron nitride materials in biological domains remain largely unexplored⁶.

The objective of the present work is to investigate the encapsulation dynamics of BC molecule in single wall boron nitride nanotubes (SWBNNT) by means of computer simulations. Results produced by classical methods of molecular mechanics (MM) and Molecular Dynamics (MD) confirmed the encapsulation of said molecule in the two cases studied. In addition, density functional approximations associated with the Tight-Binding method to investigate possible changes in the electronic structure of the materials involved were carried out.

Thus, an interesting line of research is that which proposes the replacement of mesoporous titanium oxide by a sensitizer higher efficiency. Nanotubes functionalized with BC are potentially promising in this regard.

Methods

In this undertaking, we performed molecular dynamics computer simulations associated with the Universal Force Field (UFF) to investigate the possibility of encapsulation of BC molecule in a SWBNNT, within the conditions imposed. Classical results were combined with results based on Functional Tight-Binding Density (DFTB+) to investigate also changes resulting from this process. To perform these simulations, the Materials Studio was used, a Cerius computer simulation package as desktop.

The Molecular Mechanics (MM) is a classical and

simple method that uses newtonian mechanics equations to describe the potential energy surface (PES) and the physical properties of molecular systems through energy conformation calculation. In other words, with the application of MM you want to get the optimized settings of the systems under study. The option of working with the so-called Universal Force Field (UFF) is conveniently categorical since the process one wishes to perform involves the interaction of an organic system with an inorganic system. The simulations describe the encapsulation of β -carotene into two specific nanotubes: a chiral SWBNNT (13,5) and an Armchair SWBNNT (9,9), with lengths and diameters compatible with conditions already described in the literature for CNTs.

The encapsulation process occurs with the application of molecular dynamics (MD). This is the method used to describe the time evolution of systems, through numerical integration of Newton's laws. The results obtained by these means provided information for their elastic energies calculations characterizing possible deformations besides allowing estimations on the spontaneity of the process.

Finally, one obtains quantum properties of systems through application of DFTB + module contained the Cerius package. The DFTB + uses the Tight-binding method (TB) associated with the Density Functional Theory (DFT) to gain accuracy and efficiency. The TB is in turn an approximation method suitable to the first neighboring situation. From this, analysis of energy and DOS of original systems and encapsulated systems allow us to make inferences about the gaps and other changes in the electronic structure of same.

Results and Discussion

In this study, we initially tried to obtain the optimized and isolated structures of β -carotene molecule and the nanotubes (13, 5) and (9, 9). This optimization procedure involves the application of Force Field (UFF). Nanotubes were chosen with both open ends and lengths larger than the ones of the molecule so as to avoid edge effects. The BNNTs also have diameters compatible with the diameters of CNTs described in the experimental work of Yanagi et al. 1.

Once the structures in their most stable conformations were obtained, it urges to place it in appropriate

conditions for the initial development of the dynamics. Other procedures such as the choice of NVT ensemble and the randomness of the initial velocities seek to reproduce the experimental conditions in which the process usually occurs.

The stabilizing energy of the complexes SWBNNT + BC is obtained by comparing the energies of the complex before and after encapsulation. Stabilizing Energy Calculations confirmed the occurrence of encapsulation in its spontaneous form in both cases studied. Figure 1 and Figure 2 show, in sequence, the frames that highlight the encapsulation of BCat SWBNNT (13,5) and SWBNNT (9,9). Similarly, the elastic energy of the encapsulated BC was obtained by comparing the energy from the free molecule with the one from the encapsulated molecule. Results from this energy values explain the emergence of geometric deformations of the molecule as a consequence of its weak interactions with the nanotubes walls.

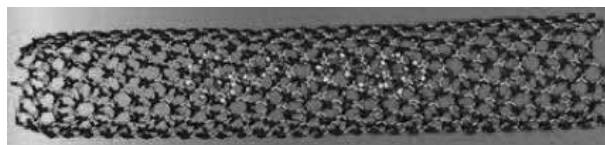


Figure 1. Frame in which the encapsulated BC in SWBNNT (13,5) is seen.

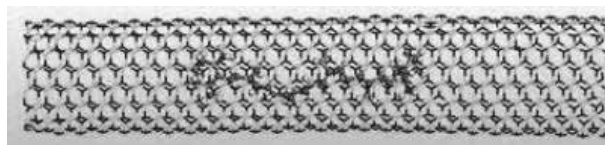


Figure 2. Frame in which the encapsulated BC in SWBNNT (9, 9) is seen.

Data on energy and the DOS of encapsulated SWBNNT complex (13, 5) + BC and SWBNNT (9,9) + BC have also been generated by application of DFTB + method. Figure 3 and Figure 4 relate the normalized DOS per unit of states with the energy of the corresponding nanotube.

So we can compare the gaps of the nanotube with the gap of the encapsulated complex. Each figure highlights the region near the Fermi zone. The difference between the gap of the nanotube before and after encapsulation is indicative of the BC electronic coupling involved in both cases.

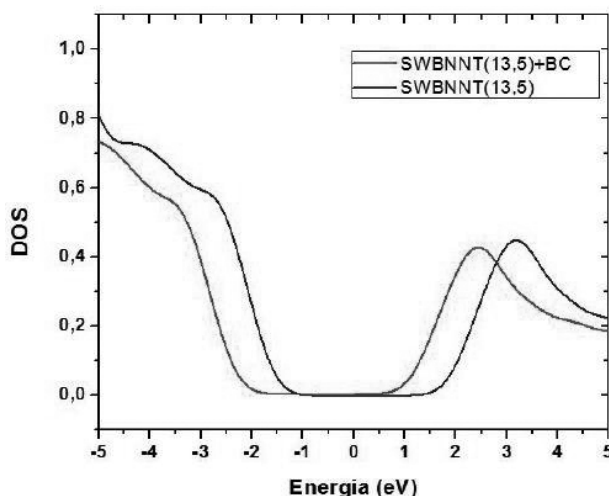


Figure 3. Curve depicting the DOS by unit of states as a function of the SWBNNT (13,5) energies. The blue line represents the pure nanotube and the red line represents the functionalized nanotube.

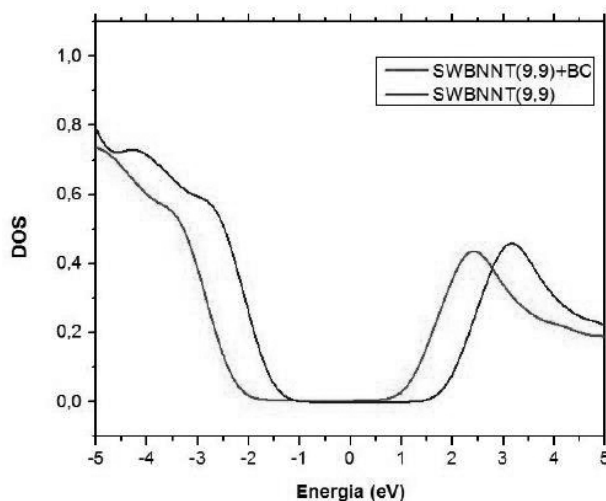


Figure 4. Curve depicting the DOS by unit of states as a function of the SWBNNT (9,9) energies. The blue line represents the pure nanotube and the red line represents the functionalized nanotube.

Conclusions

Our simulations showed that BC is encapsulated in SWBNNT nanotubes (13,5) and (9,9). Calculations relating to stabilization energies suggest that this process is spontaneous. Estimates of the elastic energy of BC point out deformations of the systems.

Analysis of the DOS of the investigated systems obtained by applying the DFTB + code, suggest the occurrence of electronic coupling due to the superposition of molecular orbitals.

Therefore, there have been changes in the electronic structure of the two nanotubes. Despite this evidence, the difference is remarkably small, so that both nanotubes keep their semiconductor properties.

Acknowledgments

The authors are grateful for the support given from the CNPq, INCT / Carbon Nanomaterials, CNPq / Network-Carbon Nanotube for Financial Support and CAPES.

References

1. Yanagi, K et al. Light-harvesting Function of β -carotene inside Carbon Nanotubes. *Phys. Rev.*, 2006.
2. Golberg, D., Bando, Y., Tang, C. C. and Zhi, C. Y., "Boron Nitride Nanotubes," *Adv. Mater.* 19(18), 2413-2432 (2007).
3. Golberg, D., Bando, Y., Huang, Y., Terao, T., Mitome, M., Tang, C. and Zhi, C., "Boron Nitride Nanotubes and Nanosheets," *ACS Nano* 4(6), 2979-2993 (2010).
4. Golberg, D., Bando, Y., Kurashima, K. and Sato, T., "Synthesis and characterization of ropes made of BN multiwalled nanotubes," *Scripta Mater.* 44(8-9), 1561-1565 (2001).
5. Chopra, N. G., Luyken, R. J., Cherrey, K., Crespi, V. H., Cohen, M. L., Louie, S. G. and Zettl, A., "Boron Nitride Nanotubes," *Science* 269(5226), 966-967 (1995).
6. Weng, Q. et al. Highly Water-soluble, Porous, and Biocompatible Boron Nitrides of Anticancer Drug Delivery. *ACS Nano*, 8 (6): 6123-6130, 2014.
7. M. Gratzel, Dye-sensitized solar cells, *J. Photochem. Photobio. C.* 4 (2003) 220 145-153. doi: 10.1016/S1389-5567(03)00026-1.
8. M. Gratzel. *Inorg. Chem.* 44, 6841, (2005).
9. A. Hagfeldt, M. Gratzel. *Acc. Chem. Res.* 33, 269, (2000).

Charles de A. O. Rocha^a,
David L. Azevedo^b, Fábio F.
Monteiro^b & Antonio L. de A.
Fonseca^b

^aUniversity of Brasília, UnB Faculty of Planaltina, 73.345-010, Brasília, Brazil

^bInstitute of Physics, University of Brasília, 70.919-970, Brasília, Brazil

*E-mail: charles.rocha@ifnmg.edu.br

Development of a Transition State Database from Chemical Reactions

Introduction

Studies of computational chemistry in recent decades have been growing exponentially, a simple Google search with the phrase 'Computational chemistry' in generates approximately 11,500,000 results and tends to increase more and more.

Currently, there are several theoretical methods based on computational chemistry, such as density functional theory and the semi-empirical method^{1,2}, which became a great choice for the prediction of some properties such as vibrational frequencies, potential energy surface, electronic parameters and energies, molecular properties and perhaps the most difficult of them, transition states structures.

Currently there are some recognized data banks and that are cataloged critical information in the molecular field, one can cite the crystallography data bank of Cambridge (CCDC), one facing in the area solid state, Virtual Atomic and Molecular Data Center (VAMDC). There are two national examples, the first database pharmacokinetics (PK / DB) and a second that is being developed with the approach of cataloging a database of natural products from Brazil^{3,4}.

Considering examples of molecular properties data bank and the great difficulty of calculating state transitions, this paper propose the built of a online system that suplemente this lack.

Methods

DFT and semiempirical methods combined with STQN method (Synchronous Transit-Guided Quasi-Newton)⁵ were used to find the transition states. All theoretical calculations were carried out using the G09⁶ program suite.

The reactions used to implementation in the data base were: hydrogens transfers, adding halide hydrogens in alkenes following Markovnikov mechanism, reaction aromatic nitration reaction of Morita-Baylis-Hilman, atmospheric reactions and obtaining inorganic cycles involving sulfur-phosphorus-nitrogen bond.

The database will be built in tables with descriptions of the reactions, their mechanism and downloads will be available at website.

Results and Discussion

The intention of the Transition Stats Data Bank (TSDB) is the user has the facility to find the transition state of the reaction of interest and describe analogues transition states with different functional groups. In the data bank, first, it is showed a generic description of the reaction and a second page shows the detailed mechanism, which it is available a Gaussian input file with transition state optimized in the PM6 or B3LYP/6-31G, see Figure 1. In addition, it will be possible to the user, also, deposit own transition states. The website will be hosted in the www.qtea.ueg.br/tsdb.

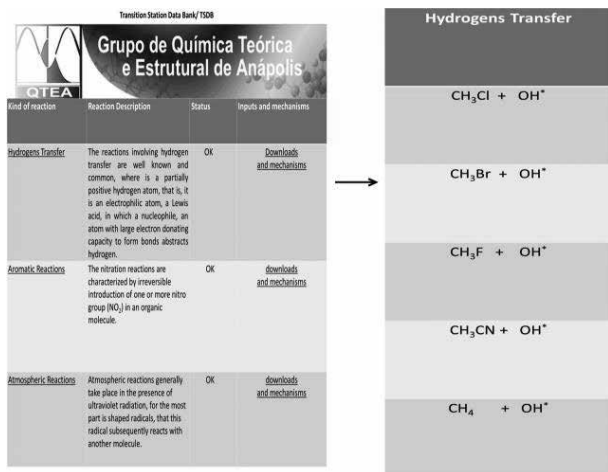


Figure 1: Website framework to find the optimized transition state.

To composition of the data bank, preliminary, we propose several transition states which are shown in a Table 1. The geometric parameters such as length bond formed and broken, angles and torsion angles are presented.

Conclusion

In summary, we propose the online framework of the data bank and we describe some transition states for specific chemical reactions. These transition states obtained assisted in the build on framework of the data bank.

The theory of the transition state is a great alternative to having theoretical results, such as electronic and thermodynamic properties with such perfect accuracy as those using experimental results. It can be observed that for the transition state calculation requires a long time because its difficulty requires the researcher a robust chemical sense. In this sense, the data bank can assist researchers to elucidate others reactions mechanism.

Acknowledgments

The authors are grateful for the support given from the FAPEG, CAPES, CNPQ and FINATEC.

References

- Kurt, A. P. A. METODOLOGIA SEMIEMPÍRICA UNIFICADA PARA A ESTIMATIVA DA CAPACIDADE DE CARGA DE ESTACAS, Universidade de São Paulo, **2010**.
- Júnior, J. de J. G. V. TEORIA DO FUNCIONAL DA DENSIDADE APLICADA AO ESTUDO DA INTERAÇÃO ENTRE OXIGÊNIO MOLECULAR E NANOCUSTERS DE PLATINA DOPADOS COM Al, Cr e V., Universidade de São Paulo, **2011**.
- Valli, M.; Dos Santos, R. N.; Figueira, L. D.; Nakajima, C. H.; Castro-Gamboa, I.; Andricopulo, A. D.; Bolzani, V. S. Development of a natural products database from the biodiversity of Brazil. J. Nat. Prod. 2013, 76, 439. <http://dx.doi.org/10.1021/np3006875> <http://www.ncbi.nlm.nih.gov/pubmed/23330984>.
- Moda, T. L.; Torres, L. G.; Carrara, A. E.; Andricopulo, A. D. PK/DB: Database for pharmacokinetic properties and predictive

Table 1: Geometric parameters obtained from chemical reactions studied

Reaction	d1	d2	A1	A2	T1	A2	T1
CH3Cl + OH-	1.25	1.24	108.4	103.3	0.00	103.34	0.00
CH3Br + OH*	1.31	1.18	107.8	99.4	0.00	99.44	-0.00
CH3F + OH*	1.19	1.30	107.8	95.6	-0.03	95.62	-0.03
CH3CN + OH*	1.22	1.24	106.7	99.7	0.10	99.71	0.10
CH4 + OH*	1.19	1.29	107.3	96.9	59.2	96.98	59.21
C2H7 + HX	1.87	1.30	150.6	100.7	33.3	100.70	33.30
C6H6 + NO2	-	2.01	-	107.0	60.4	107.03	60.46
C8H9N2O + C6H10O3	-	1.96	-	108.9	84.3	108.93	84.31
O3 + NO2	1.23	1.83	116.8	107.1	7.0	107.13	7.03
P2N2S2	1.50	2.19	129.3	90.2	179.9	90.24	179.9

d1 = distance broken bond; d2 = distance connection formed; A1 = lead angle being broken; A2 = lead angle being formed; T1 = Twist angle between the planes.

in silico ADME models. *Bioinformatics* **2008**, 24, 2270. <http://dx.doi.org/10.1093/bioinformatics/btn415> <http://www.ncbi.nlm.nih.gov/pubmed/18684738>.

5. Peng, C.; Schlegel, Bernhard, H. Combining Synchronous Transit and Quasi-Newton Methods to Find Transition States. *Isr. J. Chem.* **1993**, 33, 449. <http://dx.doi.org/10.1002/ijch.199300051>.
6. FRISCH, M. J. E. A. et al. Gaussian 09, Revision A. 02, Gaussian. Inc., Wallingford, CT, v. 200, **2002**.

F. O. S Neto & V. H
Carvalho*

Grupo de Química Teórica e Estrutural de Anápolis, Campus de
Ciências Exatas e Tecnológicas, Universidade Estadual de Goiás,
75001-970, Anápolis, Brasil

*E-mail: fatioleg@ueg.com

Instruções para Envio de Artigos para a Revista Processos Químicos

Prezado(a) autor(a),

Para que seu artigo possa entrar em nosso processo de avaliação, visando à possível publicação na revista Processos Químicos, ele deverá satisfazer às seguintes condições:

- ▶ Utilizar somente o editor Microsoft Word, numerando todas as páginas;
- ▶ Conter, no máximo, 40 laudas, incluindo Figuras, Tabelas, Esquemas etc.;
- ▶ Conter Resumo e *Abstract*, ambos com até 100 palavras;
- ▶ Conter Palavras-chave e *Keywords*, ambos com até 3 palavras;
- ▶ Título com, no máximo, 20 palavras;
- ▶ Titulação do autor (créditos). Dados pessoais do autor: endereço, telefone, e-mail;
- ▶ As figuras, tabelas, esquemas etc. devem ser colocados após as referências e devidamente identificados. Se escaneados, devem ser em alta resolução (800 dpi/ bitmap para traços) com extensão TIF ou JPEG. As fotos ou desenhos com cor (300 dpi/grayscale) devem ser enviados com extensão tif/jpg, para não termos problemas ao aplicá-las no padrão da Revista. Outras extensões possíveis: CDR, EPS ou CDX. No caso particular de esquemas contendo estruturas químicas, estas deverão ter sempre a mesma dimensão, para que possam ser reduzidas uniformemente. Considerar que as figuras deverão ter largura máxima de uma coluna (8,5 cm) ou, excepcionalmente, de 2 colunas (17,5 cm).

► As figuras (gráficos, esquemas, etc.) deverão ter qualidade gráfica adequada (usar somente fundo branco).

► A primeira página deverá conter o título do trabalho, nome e endereço dos autores (para a revista, a menor unidade é o departamento). Havendo autores com diferentes endereços, estes deverão se seguir imediatamente ao nome de cada autor. Os autores devem ser agrupados por endereço. Indicar com asterisco(*) o autor para correspondência, colocando seu e-mail no rodapé desta página (um só e-mail). A segunda página deverá conter o título, o resumo e o *abstract* do trabalho;

► As referências bibliográficas deverão ser numeradas e todas citadas ao final do artigo. Será utilizada a abreviatura da revista como definida no *Chemical Abstracts Service Source Index* (ver <http://www.cas.org/sent.html>). Caso a abreviatura autorizada de uma determinada revista não possa ser localizada e não for óbvio como o título deve ser abreviado, deve-se citar o título completo. Exemplos de citações:

1. Varma, R. S.; Singh, A. P.; J. Indian Chem. Soc. **1990**, 67, 518.
2. Provstyanoi, M. V.; Logachev, E. V.; Kochergin, P. M.; Beilis, Y. I.; Izv. Vyssh. Uchebn. Zadev.; Khim. Khim. Tekhnol. **1976**, 19, 708.
3. Lemos, T. L. G.; Andrade, C. H. S.; Guimarães, A. M.; Wolter-Filho, W.; Braz-Filho, R.; J. Braz. Chem. Soc. **1996**, 7, 123;
4. Ângelo, A. C. D.; de Souza, A.; Morgon, N. H.; Sambrano, J. R.; Quim. Nova **2001**, 24, 473.
5. Regitz, M. Em Multiple Bonds and Low Coordination in Phosphorus Chemistry; Regitz, M.; Scherer, O. J., eds.; Georg Thieme Verlag: Stuttgart, **1990**, cap. 2.
6. Cotton, F.A.; Wilkinson, G.; Advanced Inorganic Chemistry, 5th ed., Wiley: New York, **1988**.

► Espaço duplo entre linhas;

► Fonte: *Times New Roman* 12;

► A linguagem empregada deve ser atual. Isso implica a não utilização de termos, tais como: destarte, outrossim, descrever-se-á.

► O texto deve apresentar discurso impessoal, ou seja, expressões, tais como: constatamos, verificamos, utilizamos devem ser substituídas por constatou-se, foi verificado, utilizou-se.

► Enviar uma cópia do artigo, acompanhada de carta de encaminhamento à Editoria da Revista Processos Químicos, por meio do site **www.rpqsenai.org.br**. Maiores informações podem ser obtidas mediante endereço eletrônico: revistapq.senai@sistемаfieg.org.br.

VOCÊ É O PRIMEIRO INVESTIDOR DA SUA IDEIA

DEIXE O **EDITAL SENAI SESI DE INOVAÇÃO** SER O SEGUNDO.

O **EDITAL SENAI SESI DE INOVAÇÃO** É O INCENTIVO DE QUE MUITA IDEIA PRECISA PARA IR PARA FRENTE.

Se a sua empresa tem um projeto no âmbito industrial para inovação tecnológica ou melhoria da qualidade de vida do trabalhador, inscreva-o no **Edital SENAI SESI de Inovação**. Se você busca desenvolver novos produtos, processos e serviços inovadores, agora é sua chance. Com isso, os maiores vencedores são o aumento da competitividade e da produtividade das empresas.

SAIBA MAIS EM EDITALDEINOVACAO.COM.BR
E NÃO PERCA A OPORTUNIDADE DE FAZER
PARTE DO FUTURO DA INDÚSTRIA BRASILEIRA.

Innovate UK
Technology Strategy Board

Parceria:
 INOVATIVA
BRASIL

Ministério do
Desenvolvimento, Indústria
e Comércio Exterior

GOVERNO FEDERAL
BRASIL
PÁTRIA EDUCADORA

Realização:

 **Sistema
Indústria**

Iniciativa da CNI - Confederação
Nacional da Indústria